



**HAL**  
open science

# Compressible turbulent mixing subjected to strong radiation

Jean-Cédric Chkair

► **To cite this version:**

Jean-Cédric Chkair. Compressible turbulent mixing subjected to strong radiation. Mathematical Physics [math-ph]. Université de Paris, 2021. English. NNT : 2021UNIP7008 . tel-03445833

**HAL Id: tel-03445833**

**<https://theses.hal.science/tel-03445833>**

Submitted on 24 Nov 2021

**HAL** is a multi-disciplinary open access archive for the deposit and dissemination of scientific research documents, whether they are published or not. The documents may come from teaching and research institutions in France or abroad, or from public or private research centers.

L'archive ouverte pluridisciplinaire **HAL**, est destinée au dépôt et à la diffusion de documents scientifiques de niveau recherche, publiés ou non, émanant des établissements d'enseignement et de recherche français ou étrangers, des laboratoires publics ou privés.



Université de Paris

ED n°386 : École doctorale de Sciences Mathématiques de Paris Centre  
*Laboratoire Jacques-Louis Lions (UMR 7598)*

**THÈSE DE DOCTORAT**  
Spécialité : Mathématiques Appliquées

# Compressible turbulent mixing subjected to strong radiation

Par Jean-Cédric CHKAIR

Dirigée par :

M. Xavier BLANC	Professeur	Directeur
M. Olivier SOULARD	Ingénieur-chercheur, HDR	Co-directeur CEA
M. Jérôme GRIFFOND	Ingénieur-chercheur	Encadrant CEA

Présentée et soutenue publiquement le 29 mars 2021

Devant un jury composé de :

M. Olivier LAFITTE	Professeur	Université Sorbonne Paris Nord	France	Président
M. François LIGNIÈRES	DR CNRS	Université de Toulouse	France	Rapporteur
M. Daniel LIVESCU	Ingénieur-chercheur	Los Alamos National Laboratory	Etats-Unis	Rapporteur
Mme. Aurore NASO	CR CNRS	Centrale Lyon	France	Examineur
M. Robin J. R. WILLIAMS	Ingénieur-chercheur	Atomic Weapons Establishment	Royaume-Uni	Examineur
M. Xavier BLANC	Professeur	Université de Paris	France	Directeur
M. Olivier SOULARD	Ingénieur-chercheur, HDR	CEA	France	Co-directeur
M. Jérôme GRIFFOND	Ingénieur-chercheur	CEA	France	Encadrant



## Résumé

Les mélanges turbulents jouent un rôle prépondérant dans l'évolution des étoiles. Ils sont notamment nécessaires pour expliquer l'abondance de certains éléments ou pour rendre compte de la dissipation du moment angulaire observée dans certaines étoiles. Ces mélanges turbulents sont générés et entretenus par différents mécanismes : de la rotation aux instabilités magnétiques et au cisaillement. Parmi ces différents processus, les instabilités convectives de Rayleigh-Taylor ont déjà fait l'objet de nombreuses études théoriques, expérimentales et numériques.

Cependant, la majorité de ces études se limitent à des situations où les effets radiatifs sont absents. Au contraire, dans les étoiles, la prise en compte du rayonnement est essentielle : ce dernier est généralement plus efficace pour transporter les fluctuations de température que les mouvements turbulents eux-mêmes. La comparaison de ces deux modes de transport se fait à l'aide d'un nombre sans dimension appelé nombre de Péclet. Les mélanges turbulents des intérieurs stellaires impactés par l'instabilité de Rayleigh-Taylor sont alors caractérisés par un petit nombre de Péclet, inférieur à un.

L'objectif de ce travail est d'étudier les écoulements de mélanges turbulents générés par l'instabilité de Rayleigh-Taylor en présence de rayonnement, dans les limites des faibles nombres de Péclet. En particulier, le résultat majeur concerne la dérivation et la validation d'un modèle de turbulence de type RSM (Reynolds stress model) qui prend en compte les effets de mélange et qui soit adapté aux écoulements compressibles radiatifs dans la limite des faibles nombres de Péclet.

**Mots-clés:** astrophysique, étoile massive, turbulence stellaire, mélange thermohaline, nombre de Mach turbulent, nombre de Péclet turbulent, écoulement compressible, transfert radiatif, limite de diffusion, analyse asymptotique, simulations DNS et RANS, modèle RSM, instabilité de Rayleigh-Taylor, analyse linéaire de stabilité, instabilité "fingering", instabilité "oscillatory double-diffusive"

### Abstract

Turbulent mixing plays a preponderant role in the evolution of stars. In particular, they are necessary to explain the abundance of some elements or to account for the dissipation of angular momentum observed in some stars. These turbulent mixing are generated and maintained by various mechanisms: from rotation to magnetic instabilities and shearing. Among these different processes, Rayleigh-Taylor convective instabilities have already been the subject of numerous theoretical, experimental and numerical studies.

However, most of these studies are restricted to situations where radiation is absent. On the contrary, in stars, the consideration of radiation is essential: the latter is generally more effective in transporting temperature fluctuations than the turbulent motions themselves. The comparison of these two modes of transport is done using a dimensionless number called Péclet number. The turbulent stellar mixing impacted by the Rayleigh-Taylor instability is then characterized by a small number of Péclet below one.

The aim of this work is to study turbulent mixing flows generated by Rayleigh-Taylor instabilities in the presence of radiation, within the limits of low Péclet numbers. In particular, the major outcome deals with the derivation and the validation of a RSM (Reynolds stress model) type of turbulence model accounting for mixing effects and adapted to radiative compressible flows within the small Péclet limit.

**Keywords:** astrophysics, massive star, stellar turbulence, thermohaline mixing, turbulent Mach number, turbulent Péclet number, compressible flow, radiation transfer, diffusion limit, asymptotic analysis, DNS and RANS simulations, RSM model, Rayleigh-Taylor instability, linear stability analysis, “fingering” instability, “oscillatory double- diffusive” instability

# Acknowledgements

Landing on the end of my academic journey and berthing on the beginning of my professional career, this writing engraves the final stage of my sandy student life. Moreover, much more than a scientific endeavor, this human experience shaped my lonely wanderings into an entertaining daily routine.

Indeed, throughout my thesis, I have been extremely fortunate to meet and collaborate with people with whom I shared most of my time, many of my passions, a parcel of my madness and a bit of my sense of humour. Thus, this short missive embodies my deepest gratitude to all the persons who supported me during my hard times and it also conveys my sincere affection for my closest relatives and friends who remained at my side.

These last years, I have been working as a PhD. student under the direction of Pr. Xavier BLANC and with my advisors Dr. Olivier SOULARD and Dr. Jérôme GRIFFOND. Before that period, this is important to heed the fact that I had never done neither astrophysics nor radiation. Besides, I had obviously never handled turbulence or thermodynamics with such intensity and at this level of complexity.

I want, first of all, to acknowledge my PhD. supervisor Xavier B. for allowing me to catch this great opportunity. Your initial guidance was definitely essential in order to decipher the nebulous notions dealing with radiation. Although it is said that mathematics is a universal language, you were also my vital translator for the somewhat chastened register used by Chandrasekhar or Pomraning. Moreover, you developed my analytical mind by forcing me to associate my crazy derivations with physical concepts. I am deeply grateful to you for all the relentless proofreadings under the implausible deadlines imposed by my capricious schedule. You have often taken the burden of some administrative procedures from the doctoral school off my shoulders. I have been very lucky to meet you almost every week and to share with you my advancements, my declines and sometimes my relapses. Your meticulous guidelines have always been convoyed with a benevolent optimism, which was highly meaningful during hard times.

## Acknowledgements

---

I feel very grateful to my co-director and advisor Olivier S., who explained to me the main purposes of the thesis. You opened my eyes many times on its potential evolution and the numerous paths it can follow. By introducing me to stellar turbulence, I did not imagine to spend so much energy fighting against MESA with you during my first year. Your precious help allowed me to overcome the challenges related to stellar computation and the implementation of thermohaline models. At the risk of being mocked by my stinky colleagues, I am proud to write that Spyder is now my best friend. Although the thesis jury recognized the innovation and the relevance of the approximation, you have been the first instigator of it. Some steps of the asymptotic analysis would have been quite arduous to understand if you were not there! In particular, the mystery surrounding the generalized adiabatic coefficients and partial derivatives could be solved partly thanks to you! Usually, you were able to unravel humbly in one second the several issues that I confronted infernally in one week. Knowing my tendencies to easily digress, you have always been patient enough to correct me and to put me back on the right track, especially when writing the article or the manuscript. Incidentally, I will always remember the clarity and conciseness of your literary style. I also thank you for your support during the quarantine due to COVID-19, matching the period of my third year.

I also warmly thank my advisor Jérôme G., with whom I have spent the most of my time. You have helped me in so many ways and in so various fields, that I cannot count or remember them all. From the beginning to the end, you have been extremely patient and incredibly gifted at explaining difficult notions. Thank you for sharing with me your deep passion for turbulence and your fighting spirit in CFD. I will recall the nonstop evenings of numerical debugging for almost three long years, and almost everyday, and also our conversations until late, on the parking lot, even after opening hours. Your skills in numerical and physical analyses were particularly high standards and reminded me each day of the next objectives of the thesis. It helped me to remain focus on my teasing simulations and not to fall into despair in my gloomy, murky, shadowy, shady and somber but comfortable desk. I regret that the project with the interface reconstruction could not succeed but I assure you that these working hours have been very instructive anyway. Although the COVID ruined and shattered the awesome projects we wished to achieve during the last year, you provided a somptuous succour by presenting me to the stability world. We cannot deny that diving into the glee of the derivations and mathematical verifications of this chapter was deeply enjoyable. If I had to define you in one word, it would be “indefatigable”. To put it in a nutshell, you have been more than a advisor during all these years and I am sure that no one else would have done the same.

Moreover, I thank the persons involved in the prolongation of my thesis, who allowed me to finalize my work with some supplementary months: Emeric, Lydie, and whoever was concerned. Your endorsement and your support during this period were precious and crucial for my peace of mind.

Working in a research institute has been the greatest opportunity I had in order to achieve my professional goals, which effectively increased my passion in astrophysics and fluid mechanics and confirmed my fondness for aerodynamism.

I am extremely appreciative of all the jury for attending my defence, especially under the quite uncomfortable conditions due to the health crisis of the Corona virus. I know that finding the rightful schedule for the video conference has not been easy, especially with a time difference of several hours between France and the United States. I wish we all met personally and shared a buffet with french and libanese specialties. Nonetheless, I hope that you have enjoyed it!

I thank Mr. LAFITTE for embracing the role of jury president with such benevolence. Your blissful jokes quelled my anxious heart and soothed the atmosphere. Thank you for driving the session with efficiency while listening carefully to the questions of each member as well as my answers. I was quite interested by your remarks about new mathematical methods which regarded the final chapter of my work. It showed me that it can still be prone to improvement with a completely different point of view.

I am indebted to my referees: Mr. LIVESCU and Mr. LIGNIERES, for reviewing my manuscript. This is not necessarily something that everyone does with eagerness and a tremendous passion, or so I heard... The reports I have received from you were very favourable and they have been a first reward to my contributions. I acknowledge Mr. LIVESCU for his remarks which were extremely accurate and for complimenting me on the exhaustivity of my work. Your concern about the the re-contextualization of the instability in the stellar context, as well as some numerical aspects deepened my understanding of the relevance of studying turbulent mixing with radiation. I am beholden to Mr. LIGNIERES for his very laudatory report. Your own research was very close to mine and we have been able to exchange some heated ideas about the current issues regarding the modelization of turbulence in astrophysical situations. Your explanations and much experienced point of view about my turbulent model broadened my horizons.

I am grateful to my examiners: Mz. NASO and Mr. WILLIAMS who participated intensely to my defence and to the expansion of my comprehension of the thesis. I am first appreciative of Mz. NASO for enlarging the subject to some theories with very recent considerations, notably about rotation and shear effects. Your humility brought opening questions that lead to stimulating discussions. Secondly, I thank profusely Mr. WILLIAMS, who I have been lucky to meet twice at work during his seminars. By being the instigator of several founding papers related to the instability of Rayleigh-Taylor, your precise questions have been a pleasure to answer. Besides, they have always been supplemented by some praise regarding my results, which felt as a recognition of my efforts.

Although the defence has drawn to a close, a large amount of corrections stemmed from the miscellaneous controversies that befell during the presentation. Among them, some astrophysical precisions regarding the thermohaline instability have been added, as well as more details about the code **TRICLADE**, which is now present in appendix. However, others could not be appended exhaustively to this work due to a lack of time. Hence, I have been both delighted by the engrossment this thesis has aroused and sorrowful that some improvements could not be polished. In brief, the commentary I received from the jury testifies that the field of turbulence coupled to radiation is still predestined to enlarge, enrich and enlighten, just as stellar cores.

## Acknowledgements

---

The time has come to thank my dear colleagues for the memorable moments we have spent together, which will appear in a “cow love” fashion. For those who will have the bravery to grasp a piece of this section, please rest assured that a drinks party is foreseen by Providence in order to satisfy your thirst, appetite, lunacy, moral depravity and debauchery.

Charles, cheerful former postdoc, I will always remember our philosophical discussions about Truth or Beauty. Our breaks brought us precious moments: sangaku, riddles of all kinds and lots of laughter! Let us remain child at heart for eternity. I wish you happiness with your growing and pleasant family!

Adrien, lovely current postdoc, you know that the annual Fair of Beans is our pride, don't you? What a pleasure it was to share the same bakery and the same pizzeria. Having you as my office neighbour was very gratifying, especially to test my singing skills. Bring me some mustard from Dijon one day!

Lucile, spirited former PhD student, your hard-working behaviour, your unifying talents and your compassionate nature were probably your best assets to make everyone improve themselves. I owe a debt of gratitude to you for the numerous advices related to the thesis you gave me! Be filled with joy in the future!

Alexis, pervy former PhD student, I honestly wish to forget some conversations we had at lunch. Your hearty eater character was both your best and worst trait. Avoid being a frequent visitor to pole dancers so that you can take care of a progeny you may have!

Sophie, silent former PhD student, you are the woman the most trustworthy I have ever met for keeping a secret. I wish we had! We possessed at least a common passion for Mendelssohn, which forgives everything...

Florian, friendly former PhD student and co-desk, we shared the same advisors and much more! I remember your typical smiling face when we discussed about improbable subjects, such as how does an air-conditioner functions? Or why does pop music is hard to categorize? I still remember accompanying you during the last fateful weeks of the thesis! Your humanity and sense of humour were refreshing for the young PhD student I was.

Thibault, sporadic former PhD student, your intermittent presence has always spread its caustic good humour. Our passion for teaching, self-mockery and defying social conventions has made us piranhas with whimsical fins, shameless mischievous eyes and yet, with roughly big-hearted intentions, in the middle of an aquarium of questioning looks from our fellow salmon colleagues.

Mathieu, obscure former PhD student, you have been the first I met when arriving at the institute. Your reign of terror as the King of Darkness has been an inspiration for all the newcomers. We have been united by the passion of animes like Shokugeki no Soma! I tried my best to spread Despair and Pain along the corridors on behalf of your lessons, and succeeded in maturing into a charismatic dictator. As you always say: “it is with pressure that coal becomes diamond”!

Marie, skilful former PhD student, your delicacy was as soft as sandpaper and as subtle as an involuntary cremation. I remember our four main polemics about the value of conforming fries, the difference between Lebanese bread and pita, the spellings of zeugme and zeugma and the lack of consciousness of animals. What can I say? Except that I am right on all four anyway!

Giovanni, pasta-brand-like former PhD student, the summer school we went to brought us closer together as turbulent fighters! Your playfulness and spontaneity was extremely refreshing. You were one of the few people suffering from fluid mechanics like me. Hence, being able to interact with you was a profound relief.

Gregoire, nasal-voicy former PhD student, my visits to your office during my break time have marked the bond that brings us together through the strokes of your ruler. Although fatal errors and segmentation faults feature now your trademark, you have always been a reliable comrade struggling endlessly against “intabillities”. May you be happy in your new home, which will certainly host raclette parties.

Cécile, humane former PhD student and mate’o, we started and ended our demonic journey only a few months apart. How many evenings did we spend until closing time at the institute? Your good humour, intelligence and fighting spirit were an inspiration to me and to everyone else! Keep your overflowing curiosity and your love of chocolate to make yourself a little gourmet coffee when you have the blues. Thank you for sharing the throne during our “dinarchy”.

Christina, tender-hearted PhD student, we have shared almost all our years of thesis and the loss of our mental health together. Your gentleness and compassion were valuable during our writing periods. May your future profession give you a sense of complete fulfilment!

Augustin, pleasant PhD student, your spontaneous and always cheerful character allows you to relate to others very effortlessly. Although we were not office neighbours, it was always easy to start a conversation with you.

Ronan, depressive PhD student and co-desk, you were the one with whom I shared most of my funniest and nerve-wracking moments! How many days did we spend translating Fench expressions into English? How many hours did we spend calling each other on the phone at two meters from each other? Thank you for sharing your whiteboard against your will and for providing me with material as well as psychological support!

Eric, muppet PhD student, you were the strangest pledge on the team. Is there a bet you haven’t lost? Is there any respect you can ever get? However, as can be conveyed by any of our PhD colleagues: under some assumptions, your presence may be tractable.

Baptiste, blundering PhD student, your elegance was that of a cat that falls into the same gutter three times. Freedom and casualness seem to characterize you more than dignity or good manners. I will remember the conversations I had to follow in spite of myself, since you spoke so loudly that the walls reached their resonance frequency.

Albertine, fingering PhD student, a sustained register would be appropriate to describe your class, which echoed mine. But as we have so often demonstrated, our gestures were our best means of communication. Your respect for etiquette and your benevolent charisma lifted my spirits more than once! I will never forget the warm atmosphere that blossoms when you pass by and the social conventions that fall away when you open your mouth.

Victor, teasing PhD student, you have always been incredibly gifted at shattering dreams and hopes. That brings a tear or two to my eye. Who will argue with me about the definition of local thermodynamic equilibrium that everyone pretends to know?

Corentin, wacky PhD student, please tidy your knives correctly and learn to recognize silverware from food scraps. I hope you to reach balance and to hold you back in front of a madeleine. I leave irresponsibly the rest to my colleagues.

## Acknowledgements

---

Mathilde, jaded PhD student, who else but you can understand how to blithely disregard second-order terms, in the same way that we disdain our non-fluidic colleagues? Your duty will be to teach that turbulence must be so, with conviction as well as your toothless smile. The length of your hair is matched only by your wickedness!

Vincent, mysterious PhD student, your good taste in music regarding Two Steps From Hell will be your salvation for the rest of your thesis. Although our roads, like our offices, have diverged, I wish you all the hatred and madness that I have shown towards my comrades.

Olivier, lethargic PhD student, I wonder if we ever succeeded in getting you away from the enchained Duck? Anyway, our most passionate conversations concerned most of all LaTeX packages. As you can see in this work, I managed to put brackets to labelled subequations!!! Thank you for spending some evenings debugging with me!

Louise, stinky PhD student, I tried to recall the adjectives we both used to describe each other with such benevolence but cannot do so without a whiteboard full of madness. Remain the Knappounette you have always been and teach any newcomer not to play with your nerves.

Bastien, impassive PhD student, you have been the one I threatened most affectionately. Break your knees? Sink your teeth into your back? I'm sure your relief from my departure will keep you from locking yourself in your office!

I wish all the innocent former interns happiness and success: Clotilde, Audrey, Alexandre, Gobinath, Alexia, Paul, Leon, Yoann and Julien without forgetting the current baby ones Paul and Sébastien.

Finally, Sandra, the joking lady, your career journey has been admired by many of us: I hope you have the best in the world in the future, both in private and at work! Feel welcome at the institute in our crazy team!

At last, I feel grateful towards some employees, such as Mathieu for helping me so many times with the infernal code we worked on. I bid you the best! I address my thanks to Philippe, for your help in proofreading my article, in teaching me high standards thermodynamics and for your moral support. I remember also Monique and Audrey for providing me with everything I needed, and so many persons I cannot quote...

Finally, I thank deeply my close friends Elo and Cam as well as my cherished family, who have been of great support and kindness, and who shared my happiest and my darkest times.

Perennial Elo, we have known each other for almost 18 years and we are still as close as ever. Our friendship is still steadfast and the common trials we have gone through have only made us stronger. We have left our solitude to pursue an ever richer career of life and work. I hope to watch over you, even from afar, for the rest of our lives!

Conspiratorial Cam, your benevolence has been with me since engineering school and has never failed me. How many projects and crazy adventures have we shared? I thank you for all your messages always filled with tenderness. In spite of the excess of work that sometimes makes us catatonic, we always found the time to take news from each other!

Trustworthy father, you have always been my pillar and my confidant. These last years have been rich in emotions and in hazardous adventures, as unfortunate as they were unexpected. May your health remain vigorous and your peace of mind not be tormented any further. Thank you for teaching me to always keep my composure.

Attentive mother, you have been my cook... what would I have done without your Tupperware boxes? But much more than that! Your daily calls have been my greatest support and have brought me out of my loneliness, grief and melancholy. I probably inherited my fighting spirit from you!

Ugly sister, what kind of calls did we had during these years? That is impossible to determine. As you claimed, I will let you write a sentence that defines the embodiment of our bond and characterizes the deep respect you granted to me and my work: "I wish you a merry christmas youpi I'm the best sister he ever had in his entire life".

All of my colleagues, friends and family bestowed their trust upon me with sympathy and gave me wise recommendations for my professional future. I will finish with a poem I am particularly partial to, which captures my deepest thoughts and wishes far more effectively than any turbulence model could:

“  
When I consider every thing that grows  
Holds in perfection but a little moment,  
That this huge stage presenteth nought but shows  
Whereon the stars in secret influence comment;  
When I perceive that men as plants increase,  
Cheered and cheque'd even by the self-same sky,  
Vaunt in their youthful sap, at height decrease,  
And wear their brave state out of memory;  
Then the conceit of this inconstant stay  
Sets you most rich in youth before my sight,  
Where wasteful Time debateth with Decay,  
To change your day of youth to sullied night;  
And all in war with Time for love of you,  
As he takes from you, I engraft you new.  
”

---

WILLIAM SHAKESPEARE  
*Sonnets: Sonnet XV*

My aspiration is to contend with the erosion of time as well. Although the latter affects inescapably the human beings, it may collide with mortal but immortalized knowledge. Hence, as a passionate aeronautical engineer, an amateur teacher and a newborn doctor, I shall spread my own knowledge to any inquired generations. In this sense, may the world preserve a piece of its youth!

With warm regards,

Jean-Cédric CHKAIR

## Acknowledgements

---

# Introduction

Within stellar interiors, turbulent zones can appear under the action of a wide variety of mechanisms, ranging from shear and rotation to convection and double diffusion [Chandrasekhar, 1960, Prialnik, 2000]. The development of these turbulent zones usually entails the transport and mixing of elements that would have otherwise remained segregated and confined within bounded regions of the star. Through these effects, turbulence can have a lasting influence over the whole stellar evolution cycle. Among others, it can affect the life expectancy of stars, impact the observations susceptible to be made from Earth, and modify the abundance of some elements [Charbonnel & Zahn, 2007, Spiegel, 1969, Stevenson, 1982].

A distinct feature of stellar turbulent mixing zones stems from their interaction with radiation. In stellar interiors, the radiative field is in local equilibrium with the surrounding plasma and obeys the diffusion approximation. As a result, heat transfer is the sum of a thermal conduction term and of a radiative diffusion term. The latter is order of magnitudes higher than the former. It is so high that the Prandtl number,  $Pr$ , defined as the ratio of the viscosity to the sum of the thermal and radiative diffusivities, can reach values much smaller than one. Small-Prandtl-number fluids are certainly not uncommon on Earth. Liquid metals, such as those found in the Earth's core or in some nuclear reactors, exhibit Prandtl numbers ranging from  $10^{-1}$  to  $10^{-3}$ . However, these values remain much higher than those found in stellar interiors. For instance, in the radiative zone of the Sun, Prandtl numbers can become as small as  $10^{-9}$ . This difference in Prandtl numbers is not merely quantitative: It also changes the context into which turbulent convection takes place.

Along with conduction and radiation, turbulent convection is the third major process that is involved in the transport of heat. Its efficiency with respect to the other two processes can be weighed by the turbulent Péclet number,  $Pe_t$ . This nondimensional number compares the diffusivity of turbulent eddies, estimated from their typical size and velocity, to the sum of the thermal and radiative diffusivities – which, in our case, is essentially the radiative one.

Thus, in a stellar context, a small Péclet number indicates that radiation is much more efficient than turbulence at transporting heat, while a large Péclet number implies the contrary. Whether the Péclet number is small depends on the value of the Prandtl number,  $Pr$ , of the fluid. It also depends on the Reynolds number,  $Re_t$ , of the flow. Indeed, given its definition, the Péclet number is equal to the Prandtl number multiplied by the ratio of the turbulent diffusion to the plasma viscosity, which is nothing more than the Reynolds number  $Re_t$ :

$$Pe_t = Pr \cdot Re_t \quad .$$

Therefore, a small Péclet number can only be achieved provided the Prandtl number is much smaller than the inverse Reynolds number  $Pr \leq Re_t^{-1}$ . This is where the difference between the Prandtl numbers observed in stars and in liquid metals comes into play. Indeed, fully developed turbulence is usually attained for Reynolds numbers larger than  $10^3$ . As a result, in liquid metals, one can hardly combine a fully developed turbulent state with a small Péclet number. By contrast, with Prandtl numbers as low as  $10^{-9}$ , turbulence with high Reynolds and small Péclet numbers can exist in stellar interiors. And indeed, according to current state-of-the-art stellar simulations [Paxton *et al.*, 2013, 2019], turbulent mixing zones with small Péclet numbers are predicted to occur in most mid-sized and massive stars in their main sequence phase, their red-giant one, or both. As an example, at the frontier of the radiative core of a red giant of one solar mass, a turbulent mixing zone generated by a double-diffusive thermohaline instability is predicted to possess at its onset Péclet numbers on the order of  $10^{-2} - 10^{-1}$  and Reynolds numbers around  $10^6 - 10^7$ .

The existence of such mixing zones raises a challenge in terms of turbulence modelling. Indeed, while statistical closures for high-Péclet turbulence are well established and widespread, this is not the case for their small-Péclet-number counterparts. To date, most efforts addressing this issue have been circumscribed to the concept of “mixing length” introduced nearly a century ago by Prandtl [1925] and adapted for stellar convection [Biermann, 1932, Böhm-Vitense, 1953, 1958, Cox & Giuli, 1968]. This type of closure is in practice the one that is almost exclusively implemented in stellar evolution codes. A notable exception is the Reynolds stress model (RSM) proposed by Canuto [2011a,e], which usage remains unfortunately marginal. But independently from the particular modelling framework retained, a common point of these works lies in their attempt to capture the scaling of turbulent quantities in the limit of infinitely small Péclet numbers. This asymptotic limit is indeed one of the essential building blocks on which statistical models can be derived to deal with small Péclet turbulence. More precisely, the limit of infinitely small Péclet numbers is a singular limit of the Navier-Stokes equations. By applying an asymptotic analysis, a simplified approximation of the real flow can be formulated in which temperature fluctuations equilibrate instantaneously with their environment. This approach is similar to the one used for dealing with small turbulent Mach numbers,  $M_t$ . In that case, an asymptotic analysis allows us to derive an approximation of the real flow, called pseudocompressible, anelastic, or Boussinesq-Oberbeck, in which acoustical phenomena equilibrate instantaneously [Botta *et al.*, 1999, Durran, 1989, Gough, 1969, Shirdgaonkar & Lele, 2006, Soulard *et al.*, 2012, Spiegel & Veronis, 1960]. Small Péclet approximations are usually considered jointly with their small-Mach counterparts, which they complete and modify. This joint limit is appropriate for stellar turbulent flows which are in effect characterized by small turbulent Mach numbers,  $M_t$ .

Several works [Feireisl & Novotný, 2009, Lignieres, 1999, Novotny *et al.*, 2011, Spiegel, 1962] have thus been devoted to the study of the small Péclet–small Mach number limit, hereafter referred to uniquely as the small-Péclet-number limit in order to alleviate notations. However, some elements in these previous studies may not be fully adapted to the treatment of stellar turbulent mixing zones. For instance, in Spiegel [1962] and Lignieres [1999], an isovolume Boussinesq-like assumption is made prior to the asymptotic analysis, instead of being derived from it. The outcome of the analysis is consequently limited to small depth motions in addition to small Mach numbers [Spiegel & Veronis, 1960]. In Novotny *et al.* [2011] and Feireisl & Novotný [2009], a complete asymptotic analysis is conducted. However, the authors enforce a static reference state, while for turbulent applications, a mean varying state would be preferred. Besides, the analysis is restricted to perfect gases. But most importantly, none of the mentioned studies accounts for the presence of mixing, while it is one of the key aspects of stellar turbulence that needs to be dealt with. Therefore, an adaptation of existing small-Péclet-number asymptotic analyses is required for stellar applications, and elements of validation need to be provided. Another point that requires some clarification is the way a small-Péclet-number approximation can be used to derive statistical turbulent closures. The outcome of small-Péclet-number asymptotic analyses are expressions for the fluctuations of the velocity divergence and of the conduction term, as well as an order of magnitude for the pressure and temperature fluctuations. All of these elements impact the evolutions of the fluctuations of thermodynamical variables, such as density or temperature. They should consequently be accounted for in the formulation of any statistical model following the correlations between these variables and aiming at dealing with small-Péclet flows.

**Hence, this study consists in deriving and validating a RSM turbulence model accounting for mixing effects and adapted to radiative compressible flows within the ( $Pe_t \ll 1$ ) limit.**

First and foremost, the aim of the initial chapter is to characterize the properties of the turbulent mixing zones arising during stellar evolution. In particular, we focus on the estimation of orders of magnitude of the dimensionless numbers related to velocity fluctuations and molecular transport which notably arises from radiative transfer. To this purpose, we perform the simulations of a  $1 M_\odot$ , a  $5 M_\odot$  and a  $75 M_\odot$  stars, corresponding respectively to a low-mass, an intermediate-mass and a massive star, with the open-source astrophysical code *MESA*. The latter is chosen as it solves stellar structure equations including radiative diffusion as well as chemical transport. The three configurations will then allow to highlight the role played by the velocity fluctuations extracted from Prandtl [1925]’s models and the radiative diffusivity in the localization and the characterization of the turbulent zones evolving within ( $M_t \ll 1$  ;  $Pe_t \ll 1$ ) regimes.

The second part is dedicated to the study of the behaviour of hydro-radiative flows evolving in the limit of small Péclet numbers. The idea is to use an asymptotic analysis relying on infinitely small turbulent Mach and radiative Péclet numbers, treated both jointly, among the orders of the dimensionless numbers estimated in the first section. It is worth noting that the limit of infinitely small Péclet numbers is a singular limit of the Navier-Stokes equations. And by applying an asymptotic analysis, a simplified approximation of the real flow can be formulated in which temperature fluctuations equilibrate instantaneously with their environment.

This approach is, in fact, similar to the one used for dealing with small turbulent Mach numbers  $M_t$ . In that case, an asymptotic analysis allows to derive an approximation of the real flow, called pseudo-compressible, anelastic or Boussinesq-Oberbeck, in which acoustical phenomena equilibrate instantaneously (see [Soulard \*et al.\* \[2012\]](#)). It stems from the turbulent characteristic velocity being much smaller than the sound-crossing time. Hence, the simultaneous treatment of both limits allows the study to be fully adapted to the treatment of stellar turbulent mixing zones. Its impacts will regard several points. First, it will set the orders of magnitude of temperature and pressure fluctuations. Secondly, it will give rise to closures, suitable to RSM turbulent modelling, as asymptotic expressions for the fluctuating divergence and conduction terms. Thirdly, it will modify the stability criterion of a mean stratification. The latter will all be validated, along with the initial conditions of the asymptotic analysis, by performing stably stratified radiative Rayleigh-Taylor DNS simulations.

The third chapter deals with the adaptation of a ( $M_t \ll 1$ ) turbulent RSM model to the ( $Pe_t \ll 1$ ) limit, and its validation in “all Péclet” asymptotic regimes. The outcomes of the previous ( $M_t \ll 1$  ;  $Pe_t \ll 1$ ) asymptotic approach are one of the essential building blocks upon which statistical models can be derived to deal with small Péclet turbulence. The way a small Péclet number approximation can be used to derive statistical turbulent closures is explained as follow. The outcome of small Péclet number asymptotic analyses are expressions for the velocity divergence and the conduction term, as well as an order of magnitude for the pressure and temperature fluctuations. Since all of these elements impact the evolutions of the fluctuations of thermodynamical variables, such as density or temperature, they will consequently be accounted for in the formulation of the statistical model following the correlations between these variables and aiming at dealing with small Péclet flows. Hence, the validation of the model will use the closures derived in the asymptotic analysis and will rest upon the radiative Rayleigh-Taylor DNS simulations already studied and taken as reference.

In the last part, the aim is, firstly, to study the linear stability of stratified equilibria of binary mixtures under a gravitational field and, secondly, to improve the weighted “all Péclet” blending model proposed in the third part. In this way, a linear stability analysis based on an isothermal quasi-homogeneous approach is applied to the hydro-radiative governing equations. It will allow to derive stability criteria within all Mach, small Mach and small Mach-small Péclet regimes that involve viscosity, scalar diffusion and radiative conduction effects. In particular, the impacts of these latter on different flow configurations are emphasized through numerical resolutions, along with the characterization of “oscillating” and “non-oscillating” modes, highlighted using quasi-transverse approaches. In particular, the role played by the compressibility and the visco-dissipative coefficients on the stability of the flow field will be discussed. As for the model blending, its improvement will lie on the use of the stability condition found with the ( $M_t \ll 1$ ) dispersion relation. Indeed, by proceeding to an analogy regarding visco-diffusive contributions between the compressible radiative Navier-Stokes system and the turbulent RSM one, which both deal with binary radiative Rayleigh-Taylor mixtures, the behaviour of turbulent quantities will be assumed to be equivalent to their Navier-Stokes analogs. Ultimately, this method may provide a better suited transition parameter that bridges the range between asymptotic Péclet regimes.

# Contents

<b>Introduction</b>	<b>xiii</b>
<b>List of figures</b>	<b>1</b>
<b>List of tables</b>	<b>5</b>
<b>List of symbols</b>	<b>7</b>
<b>1 Properties of stellar turbulent mixing zones</b>	<b>15</b>
1.1 Introduction	16
1.2 Stellar structure equations	16
1.2.1 Conservation of mass, momentum, energy and mass fractions	16
1.2.2 Equation of state and radiative flux	18
1.2.3 Turbulent transport	19
1.3 Stellar turbulence models for convection and double diffusion	20
1.3.1 Convective and double-diffusive instabilities	20
1.3.1.1 Negligible heat flux (large Péclet number)	21
1.3.1.2 Very large heat flux (small Péclet number)	22
1.3.1.3 Summary and discussion	22
1.3.2 Modelling stellar turbulence in convective and thermohaline zones	23
1.3.2.1 Mixing length theory for turbulent convection	24
1.3.2.2 Modelling thermohaline turbulence	26
1.3.3 Discussion	28
1.4 Simulating stellar turbulence with MESA	29
1.4.1 Description of MESA and of the simulation parameters	29
1.4.2 Kippenhahn diagrams	30
1.4.3 Non-dimensional numbers	31
1.5 Conclusion	35

<b>2</b>	<b>Derivation and validation of a (<math>M_t \ll 1 ; Pe_t \ll 1</math>) asymptotic analysis</b>	<b>37</b>
2.1	Introduction . . . . .	38
2.2	Flow description . . . . .	39
2.2.1	Hydro-radiative instantaneous equations . . . . .	39
2.2.2	Velocity, pressure and temperature evolutions . . . . .	42
2.2.3	Average flow as a background state . . . . .	44
2.2.4	Dimensionless equations for the fluctuations . . . . .	45
2.2.4.1	Characteristic scales and dimensionless quantities . . . . .	45
2.2.4.2	Dimensionless numbers . . . . .	47
2.2.4.3	Dimensionless equations . . . . .	48
2.3	Small Mach-small Péclet number approximation ( $Pe_t \lesssim M_t \ll 1$ ) . . . . .	49
2.3.1	Main conditions . . . . .	49
2.3.1.1	Small Péclet number analysis in fluctuating temperature evolution	50
2.3.1.2	Small Mach number analysis in the fluctuating velocity and pressure evolutions . . . . .	51
2.3.1.3	Order of magnitude of the temperature fluctuations . . . . .	51
2.3.2	Main results of the asymptotic analysis . . . . .	52
2.3.2.1	Orders of magnitude of fluctuations . . . . .	52
2.3.2.2	General expressions for the divergence and the conduction terms	52
2.3.2.3	Expressions for the divergence and the conduction terms for a perfect gas . . . . .	53
2.3.2.4	Interpretation of the expressions for the divergence and the conduction terms for a matter perfect gas . . . . .	55
2.3.2.5	Comparison with the high Péclet limit . . . . .	56
2.3.3	Synthesis of the asymptotic analysis . . . . .	58
2.4	Small Péclet-small Mach number approximation ( $M_t \ll Pe_t \ll 1$ ) . . . . .	58
2.4.1	Main conditions . . . . .	58
2.4.1.1	Small Péclet number analysis in fluctuating temperature evolution	59
2.4.1.2	Small Mach number analysis in fluctuating velocity and pressure evolutions . . . . .	59
2.4.1.3	Order of magnitude of the temperature fluctuations . . . . .	60
2.4.2	Synthesis of the asymptotic analysis . . . . .	60
2.4.2.1	Orders of magnitude of fluctuations . . . . .	60
2.4.2.2	General expressions for the divergence and the conduction terms	61
2.5	Validation of the asymptotic analysis . . . . .	61
2.5.1	Numerical method . . . . .	61
2.5.2	Rayleigh-Taylor flow configuration . . . . .	62
2.5.3	Dimensionless numbers . . . . .	64
2.5.4	General evolution of the flow . . . . .	65
2.5.5	Validation of the asymptotic analysis . . . . .	68
2.6	Conclusion . . . . .	77

<b>3</b>	<b>Adaptation and validation of a (<math>M_t \ll 1</math>) RSM turbulence model to the (<math>Pe_t \ll 1</math>) regime</b>	<b>79</b>
3.1	Introduction	80
3.2	Adaptation of a RSM : the GSG turbulent model	81
3.2.1	Current version of the GSG model in the ( $Pe_t \gg 1$ ) limit	81
3.2.2	Adaptation of the Langevin PDF model to the ( $Pe_t \ll 1$ ) limit	85
3.2.3	Adaptation of the GSG model to the ( $Pe_t \ll 1$ ) limit	87
3.2.4	Blending between the two limits ( $Pe_t \gg 1$ ) and ( $Pe_t \ll 1$ )	88
3.3	Validation of the extended RSM	90
3.3.1	Calibration with respect to <b>TRICLADE</b> simulations	90
3.3.2	1D simulations with the GSG turbulence model	91
3.4	Conclusion	94
<b>4</b>	<b>Linear stability analysis</b>	<b>95</b>
4.1	Introduction	96
4.2	Governing equations and assumptions for the LSA	96
4.2.1	Hydro-radiative compressible governing equations	96
4.2.2	Quasi-homogeneous approach and isothermal equilibrium state	97
4.2.3	Assumptions regarding transport coefficients	99
4.2.3.1	Viscosity	99
4.2.3.2	Inter-species diffusion	100
4.2.3.3	Opacity	100
4.3	Dispersion relation within all Mach regime	101
4.3.1	Linear system	101
4.3.2	Dispersion relation at thermal equilibrium	102
4.3.2.1	Dispersion relation at thermal equilibrium for any wave angle	105
4.3.2.2	Non-radiative and non-diffusive limit	105
4.3.2.3	Dispersion relation at thermal equilibrium for transverse modes	106
4.3.2.4	Non-oscillating (or fingering) transverse mode	107
4.3.2.5	Pair of "oscillating" (or oscillatory double-diffusive convective) transverse modes	108
4.3.3	Dispersion relation in non-thermal equilibrium	109
4.4	Dispersion relation within the small Mach regime	112
4.4.1	Dispersion relation at thermal equilibrium for any wave angle	112
4.4.2	Dispersion relation at thermal equilibrium for transverse modes	114
4.4.2.1	Non-oscillating (or fingering) transverse mode	115
4.4.2.2	Pair of "oscillating" (or oscillatory double-diffusive convective) transverse modes	115
4.4.3	Large wave numbers limit: development in ( $1/k$ )	116
4.5	Small Mach-small Péclet regime	117
4.5.1	Dispersion relation at thermal equilibrium for any wave angle	117
4.5.2	Dispersion relation at thermal equilibrium for transverse modes	118
4.6	Numerical results	118
4.6.1	General dispersion relation at thermal equilibrium	118

## Contents

---

4.6.1.1	Non-dimensionalization for numerical resolution . . . . .	119
4.6.1.2	Expectations from local criteria . . . . .	120
4.6.1.3	Phenomenology . . . . .	121
4.6.1.4	Parametric variations . . . . .	124
4.6.2	Dispersion relation within the low Mach limit . . . . .	128
4.7	Extension to the non-isothermal case at thermal equilibrium . . . . .	130
4.7.1	Correction to the isothermal case . . . . .	130
4.7.1.1	Inter-species diffusion . . . . .	130
4.7.1.2	Opacity . . . . .	130
4.7.2	Dispersion relations at thermal equilibrium . . . . .	131
4.8	Link with Boussinesq approaches (pure hydrodynamic limit) . . . . .	132
4.9	Implications for the turbulent RSM model . . . . .	134
4.9.1	Analogy with the radiative turbulent RSM model . . . . .	135
4.9.2	Improvement of the model blending . . . . .	136
4.9.2.1	Marginal “fingering” stability and its implication on Rayleigh-Taylor production . . . . .	136
4.9.2.2	Blending models from LSA . . . . .	138
4.10	Conclusion . . . . .	143
<b>Conclusion</b>		<b>145</b>
<b>Extended summary in French</b>		<b>149</b>
<b>A Thermodynamics</b>		<b>177</b>
A.1	Generalized adiabatic exponents . . . . .	178
A.2	Thermodynamics of mixtures . . . . .	179
A.2.1	Mixture of perfect gases . . . . .	179
A.2.2	Black body radiation . . . . .	180
A.2.3	Mixture of perfect gases and black body radiation . . . . .	180
<b>B Asymptotic analysis extension</b>		<b>181</b>
B.1	Temperature and pressure equations . . . . .	182
B.2	Average and fluctuating velocity, temperature and pressure equations . . . . .	183
B.3	Development of fluctuating diffusion and conduction terms . . . . .	184
B.4	Small Mach-small Péclet asymptotic analysis in the presence of fast reactions . . . . .	186
B.4.1	Small Péclet . . . . .	186
B.4.2	Small Mach . . . . .	187
B.4.3	Synthesis . . . . .	187
<b>C Numerical methods</b>		<b>189</b>
C.1	TRICLADE . . . . .	190
C.1.1	Governing hydrodynamic mixing equations . . . . .	190
C.1.2	Governing hydro-radiative mixing equations . . . . .	191
C.1.3	Hyperbolic and parabolic systems . . . . .	192
C.1.4	Numerical flux . . . . .	192

C.1.5	Configuration of boundary conditions . . . . .	196
C.1.5.1	Material boundary conditions . . . . .	197
C.1.5.2	Radiative boundary conditions . . . . .	197
C.2	Numerical resolution . . . . .	199
	<b>Scientific production and communication</b>	<b>203</b>
	<b>Bibliography</b>	<b>247</b>



# List of Figures

1.1	Schematic representation of $\nabla_{\mu} - (\nabla_T - \nabla_{ad})$ stability for different stellar zones	24
1.2	Kippenhahn diagrams of a $1 M_{\odot}$ star from $t = 0.438\ 32$ Myr to $t = 13.349$ Gyr. The colored bar corresponds to the logarithm of nuclear reaction specific energy generation rate $[\log(\epsilon_{nuc})]$ . The helium core and the hydrogen burning shell are respectively identified by "He-core" and "H-burn.". Convection and thermohaline zones are shown and defined with respect to Sys. (1.19). The black triangle displayed over one of the dashed purple vertical lines showing specific times of evolution, represents the spatial profile plotted in Sec. 4.10. The "model number" corresponds to a non-linear representation of time. . . . .	31
1.3	Same as figure 1.2, but for a $5 M_{\odot}$ star from $t = 0.639\ 6$ Myr to $t = 0.106\ 2$ Gyr. . .	32
1.4	Same as figure 1.2, but for a $75 M_{\odot}$ star from $t = 0.0232\ 5$ Myr to $t = 3.657$ Myr. . .	32
1.5	Convective structure of stars during the main sequence phase. . . . .	33
1.6	Turbulent Mach, Reynolds and Péclet numbers, as well as pressure ratio $P^r/P^m$ , for a $1 M_{\odot}$ star (vertical hatching: thermohaline zone ; inclined hatching: convective zone). The profile is shown at $t = 11.333$ Gyr (see the black triangle at the top of the Kippenhahn diagram of Fig. 1.2). . . . .	34
1.7	Turbulent Mach, Reynolds and Péclet numbers, as well as pressure ratio $P^r/P^m$ , for a $5 M_{\odot}$ star (vertical hatching: thermohaline zone ; inclined hatching: convective zone). The profile is shown at $t = 0.105\ 4$ Gyr (see the black triangle at the top of the Kippenhahn diagram of Fig. 1.3). . . . .	35
1.8	Turbulent Mach, Reynolds and Péclet numbers, as well as pressure ratio $P^r/P^m$ , for a $75 M_{\odot}$ star (vertical hatching: thermohaline zone ; inclined hatching: convective zone). The profile is shown at $t = 3.591$ Myr (see the black triangle at the top of the Kippenhahn diagram of Fig. 1.4). . . . .	35
2.1	Time evolution of the turbulent Mach $M_t$ , Péclet $Pe_t$ and Reynolds $Re_{\lambda}$ numbers at the center of the mixing zone. . . . .	65
2.2	Spatial profiles of the pseudo-entropy $S$ , given by (2.74) for the high and small Péclet simulations at times $t = 0$ , $t = 17$ and $t = 34$ . . . . .	66

2.3	Shaded volume rendering of the light fluid concentration made visible from $c = 0.1$ (blue) to $c = 0.9$ (red). The heavy fluid is on the right and the light one on the left. The gravity vector is oriented to the left along the $x$ -axis, <i>i.e.</i> from the heavy to the light side. The rendering is shown at 3 different times $t = 4$ , $t = 17$ and $t = 34$ . Visually identical figures are obtained for all three simulations at $t = 4$ and $t = 17$ but large differences are observed here between the high Prandtl simulation HP and the small Prandtl simulation $SP_1$ at the final time $t = 34$ . . . . .	67
2.4	Time evolution of ratios $\eta_P$ and $\eta_T$ at the center of the mixing zone. . . . .	69
2.5	Cuts in the plane $y = 0$ at times $t = 17$ and $t = 34$ for simulation $SP_2$ displaying respectively: (a) and (c) the fluctuating conduction term $\mathcal{C}'$ computed by using its definition $\mathcal{C} = \partial_j (\lambda \partial_j T)$ ; (b) and (d) the asymptotic value of $\mathcal{C}'$ predicted by Eq. (2.57b). The color scale is the same in each figure. . . . .	71
2.6	Cuts in the plane $y = 0$ at times $t = 17$ and $t = 34$ for simulation $SP_2$ displaying respectively: (a) and (c) the fluctuating divergence $\text{div} \mathbf{u}'$ computed by using its definition $\text{div} \mathbf{u}' = \partial_j u'_j$ ; (b) and (d) the value of $\text{div} \mathbf{u}'$ predicted by Eq. (2.57a). The color scale is the same in each figure. . . . .	72
2.7	Spatial profiles of (a) $-\overline{\rho' \text{div} \mathbf{u}'}$ and (b) $\overline{u' \text{div} \mathbf{u}'}$ for simulation $SP_2$ at times $t = 17$ and $t = 34$ . Comparison between the ( $\mathbf{Pe}_t \ll 1$ ) <b>simulated</b> and ( $\mathbf{Pe}_t \ll 1$ ) <b>predicted</b> values, computed using the small-Péclet prediction Eq. (2.57a). The contributions from the stratification (“strat.”) and the molecular (“mix.”) terms to both predicted values are shown. . . . .	74
2.8	Spatial profiles of (a) $-\overline{\rho' \text{div} \mathbf{u}'}$ and (b) $\overline{u' \text{div} \mathbf{u}'}$ for simulation HP at times $t = 17$ and $t = 34$ . Comparison between the ( $\mathbf{Pe}_t \gg 1$ ) <b>simulated</b> and ( $\mathbf{Pe}_t \ll 1$ ) <b>predicted</b> values, computed using the small-Péclet prediction Eq. (2.57a). The contributions from the stratification (“strat.”) and the molecular (“mix.”) terms to both predicted values are shown. . . . .	75
2.9	Spatial profiles of (a) $-\overline{\rho' \text{div} \mathbf{u}'}$ and (b) $\overline{u' \text{div} \mathbf{u}'}$ for simulation $SP_2$ at times $t = 17$ and $t = 34$ . Comparison between the ( $\mathbf{Pe}_t \ll 1$ ) <b>simulated</b> and ( $\mathbf{M}_t \ll 1$ ) <b>predicted</b> values, computed using the small-Mach all-Péclet prediction Eq. (2.62) from Soulard <i>et al.</i> [2012]. The contributions from the stratification (“strat.”) and the molecular (“mix.”) terms to both predicted values are shown. . . . .	76
3.1	Time evolution of the turbulent kinetic energy $\tilde{k}$ at ( $x = 0$ ). Comparison between the DNS and the 1D-RANS simulations. . . . .	92
3.2	Time evolution of the normalized specific volume variance $\tilde{\tau}''^2 / \tilde{\tau}^2$ at ( $x = 0$ ). Comparison between the DNS and the 1D-RANS simulations. . . . .	93
3.3	Time evolution of the turbulent mixing zone width $\mathcal{L}_{\text{TMZ}} = 6 \int_{L_x} \tilde{c} (1 - \tilde{c}) dx$ . Comparison between the DNS and the 1D-RANS simulations. . . . .	93
4.1	Maps of $\max_{\{k_\perp/k\}} \omega_i$ in the planes $(\mathcal{A}_r, \log_{10} [1/\text{Le}])$ and $(\log_{10} [\mathcal{D}_c], \log_{10} [1/\text{Le}])$ by numerical resolution of the roots of the dispersion relation (4.36). Superposition of (semi)-analytical neutrality curves obtained for transverse modes $k_\perp = k$ exact or approximate with respect to relations (4.41) and (4.42) for the “non-oscillating” mode and Eqs. (4.47), (4.48) and (4.49) for “oscillating” modes. . . . .	121

4.2 Plot in the complex plane of the modes corresponding to the five roots of the dispersion relation (4.36) for the transverse modes ( $k_{\perp} = k$ ). The variation on  $\mathcal{D}_c/\chi_{\text{equi}}^r$  corresponds to a vertical path in Figs. 4.1. . . . . 122

4.3 Evolution with respect to the wave angle measured by  $k_{\perp}/k$  of the real part (dashed lines) and the imaginary part (solid lines) of the least stable or unstable mode; comparison of compressible results with the low Mach “all Péclet” and the low Mach-low Péclet limit. The three figures displays three values of the ratio  $Le^{-1} = \mathcal{D}_c/\chi_{\text{equi}}^r$  : 0.1, 1 and 10 . . . . . 123

4.4 Contours of neutrality in the planes  $(\mathcal{A}_r, \log_{10} [1/Le])$  and  $(\log_{10} [\mathcal{D}_c], \log_{10} [1/Le])$ : unstable zone on the left and stable one on the right. Numerical reference (solid lines): maximization on all modes and all quantities  $k_{\perp}/k$  of the roots of the relation dispersion (4.36). (Semi)-analytical neutrality curves obtained for the transverse modes  $k_{\perp} = k$ : dashed lines:  $\mathcal{N}_{\text{Non-osc.}}$  and  $\mathcal{N}_{\text{Osc.}}$ ; dotted lines:  $\mathcal{N}_{\text{Non-osc.}}^0$  and  $\mathcal{N}_{\text{Osc.}}^0$ . . . . . 124

4.5 Contours of neutrality in the planes  $(\mathcal{A}_r, \log_{10} [1/Le])$  and  $(\log_{10} [\mathcal{D}_c], \log_{10} [1/Le])$ : unstable zone on the left and stable one on the right. Numerical reference (solid lines): maximization on all modes and all quantities  $k_{\perp}/k$  of the roots of the relation dispersion (4.36). (Semi)-analytical neutrality curves obtained for the transverse modes  $k_{\perp} = k$ : dashed lines:  $\mathcal{N}_{\text{Non-osc.}}$  and  $\mathcal{N}_{\text{Osc.}}$  ; dotted lines:  $\mathcal{N}_{\text{Non-osc.}}^0$  and  $\mathcal{N}_{\text{Osc.}}^0$ . . . . . 125

4.6 Contours of neutrality in the planes  $(\mathcal{A}_r, \log_{10} [1/Le])$  and  $(\log_{10} [\mathcal{D}_c], \log_{10} [1/Le])$ : unstable zone on the left and stable one on the right. Numerical reference (solid lines): maximization on all modes and all quantities  $k_{\perp}/k$  of the roots of the relation dispersion (4.36). (Semi)-analytical neutrality curves obtained for the transverse modes  $k_{\perp} = k$ : dashed lines:  $\mathcal{N}_{\text{Non-osc.}}$  and  $\mathcal{N}_{\text{Osc.}}$  ; dotted lines:  $\mathcal{N}_{\text{Non-osc.}}^0$  and  $\mathcal{N}_{\text{Osc.}}^0$ . . . . . 126

4.7 Contours of neutrality in the planes  $(\mathcal{A}_r, \log_{10} [1/Le])$  and  $(\log_{10} [\mathcal{D}_c], \log_{10} [1/Le])$ : unstable zone on the left and stable one on the right. Numerical reference (solid lines): maximization on all modes and all quantities  $k_{\perp}/k$  of the roots of the relation dispersion (4.36). (Semi)-analytical neutrality curves obtained for the transverse modes  $k_{\perp} = k$ : dashed lines:  $\mathcal{N}_{\text{Non-osc.}}$  and  $\mathcal{N}_{\text{Osc.}}$  ; dotted lines:  $\mathcal{N}_{\text{Non-osc.}}^0$  and  $\mathcal{N}_{\text{Osc.}}^0$ . . . . . 127

4.8 Plot in the complex plane of the modes corresponding to the roots of the dispersion relations for the transverse modes  $k_{\perp} = k$ . Variation on  $Le^{-1} = \mathcal{D}_c/\chi_{\text{equi}}^r$  (rainbow-colored). Circles: roots of the general relation (4.36); crosses: roots of the relation (4.66) within the low Mach (“all Péclet”) limit; blacks squares: roots of the relation (4.76) within the low Mach-low Péclet limit. Corresponds to a vertical path in Fig. 4.9-(a). Left: for  $k = 5$ , the five modes of Eq. (4.36); right : for  $k = 10$ , zoom on the three central modes of Eq. (4.36) matching the three modes of Eq. (4.66). . . . . 128

4.9	Maps of $\max_{\{k_{\perp}/k\}} \omega_i$ in the planes $(\mathcal{A}_r, \log_{10} [1/Le])$ and $(\log_{10} [\mathcal{D}_c], \log_{10} [1/Le])$ by numerical resolution of the roots of the dispersion relation (4.36). Superposition of (semi)-analytical neutrality curves obtained for transverse modes $k_{\perp} = k$ (“non-oscillating” mode and “oscillating”) with respect to the general relation (red and blue curves), within the small Mach “all Péclet” limit (green curves) and within the low Mach-low Péclet limit (dashed purple lines). . . . .	129
4.10	Stability map with the same legends as Fig. 4.1. The neutrality hypersurfaces of the GSG model are added : vertical lines for the asymptotic formulations of the model valid for $(Pe_t \gg 1)$ or $(Pe_t \ll 1)$ together with curves $\mathcal{N}_{GSG}^a$ and $\mathcal{N}_{GSG}^b$ for the blended GSG model related respectively to the weighting functions (4.99) and (4.100). . . . .	139
4.11	Same legends as in Figs. 3.1, 3.2 and 3.3, <i>i.e.</i> time evolutions of the turbulent kinetic energy, the normalized specific volume variance and the turbulent mixing zone width. Comparison between the 1D-RANS simulations run with the calibrated blending model and the corrected one denoted “a”. . . . .	140
4.12	Same legends as in Figs. 3.1, 3.2 and 3.3, <i>i.e.</i> time evolutions of the turbulent kinetic energy, the normalized specific volume variance and the turbulent mixing zone width. Comparison between the 1D-RANS simulations run with the calibrated blending model and the corrected one denoted “b”. . . . .	142
C.1	HLLC approximate Riemann solver. . . . .	194
C.2	Spatial profiles of the rate of cell size to Kolmogorov length scale $\frac{\delta x}{\eta}$ at (a) $t = 17$ and (b) $t = 34$ . . . . .	200
C.3	Temporal evolution of the rate of cell size to Kolmogorov length scale $\frac{\delta x}{\eta}$ at the center of the mixing zone. . . . .	200
C.4	Spatial profiles of the rate of physical to total dissipation $\frac{\varepsilon_{\phi}}{\varepsilon_{tot}}$ at (a) $t = 17$ and (b) $t = 34$ . . . . .	201
C.5	Temporal evolution of the rate of physical to total dissipation $\frac{\varepsilon_{\phi}}{\varepsilon_{tot}}$ at the center of the mixing zone. . . . .	201
C.6	Screenshots of the video ( <a href="#">slide 17</a> ) displaying the $(Pe_t \ll 1)$ (top) and the $(Pe_t \gg 1)$ (bottom) simulations at dimensionless times. Slices containing the gravity vector directed from right to left, and displaying the ombroscopy, the pseudo-entropy and the temperature fields. Each quantity shares the same color scale, except for the temperature one in the $(Pe_t \ll 1)$ situation that has been reduced. . . . .	239

# List of Tables

A	Astronomical constants from C. Caso [1998]. . . . .	12
B	Fundamental constants with $a_R = 4\sigma_{SB}/c\ell$ , $m_H = 1/\mathcal{N}_A$ and $\mathcal{R} = k_B/m_H$ from Cohen & Taylor [1987a, 1995, 1987b]. . . . .	13
C	CGS and SI units of usual quantities. . . . .	13
D	Initial Solar abundances of stellar isotopes in mass fractions from Asplund <i>et al.</i> [2009]. . . . .	14
A	Rosseland opacities defining each of the three simulations performed for the validation. The acronyms SP and HP stand respectively for small Prandtl and high Prandtl. For information, each simulation of $0.94 \times 10^9$ cells has been performed in 25 000 iterations by 66 560 h.Pe $\sim$ 2 800 days.Pe. . . . .	64
A	Turbulent model coefficients used for 1D simulations of Sec. 3.3.2 . . . . .	91
A	Récapitulatif des hypersurfaces de neutralité. . . . .	169
A	Table of thermodynamic relations . . . . .	179



# List of symbols

## Acronyms:

- \* CEA Commissariat à l’Energie Atomique et aux énergies alternatives
- \* FT Fourier-transform
- \* HLLC Harten-Lax-Von Leer-Contact (numerical flux)
- \* KH Kelvin-Helmholtz
- \* LJLL Laboratoire Jacques-Louis Lions
- \* LSA Linear Stability Analysis
- \* LTE Local Thermodynamic Equilibrium
- \* MESA Modules for Experiments in Stellar Astrophysics
- \* MIST MESA Isochrones and Stellar Tracks (project)
- \* ML(T) Mixing Length (Theory)
- \* NS Navier-Stokes
- \* ODDC Oscillatory Double-Diffusive Convection
- \* (P)MS (Pre-)Main-Sequence
- \* RGB Red-Giant Branch
- \* RTI Rayleigh-Taylor Instability
- \* TMZ Turbulent Mixing Zone

## Abbreviations:

- \* conv. convective
- \* const. constant
- \* dyn. dynamical
- \* equi. thermal equilibrium (assuming LTE)
- \* ini. initial
- \* nuc. nuclear
- \* thrm. thermohaline

### Mathematical notations:

- \*  $q$  scalar quantity
- \*  $\mathbf{q}$  vector quantity
- \*  $q_j$  vector quantity coefficient
- \*  $q_{ij}$  matrix or order 2 tensor quantity coefficient
- \*  $\delta_{ij}$  Kronecker symbol
- \*  $\bar{q}$  mean quantity of the background field relative to linear perturbations
- \*  $q'$  perturbation of a quantity relative to linear perturbations
- \*  $\hat{q}$  Fourier-transformed quantity relative to linear perturbations
- \*  $\bar{q}$  Reynolds average of a quantity
- \*  $\tilde{q}$  Favre average of a quantity
- \*  $q'$  Reynolds fluctuation of a quantity
- \*  $q''$  Favre fluctuation of a quantity
- \*  $q^*$  dimensionless quantity
- \*  $q'^{(n)}$   $n^{\text{th}}$  term in the development of  $q'$  in powers of  $M_t$  in the small Mach-small Péclet asymptotic analysis
- \*  $D_t q$  Lagrangian time derivative of a quantity
- \*  $\text{div}(\mathbf{q})$  spatial divergence of a quantity
- \*  $\nabla q$  spatial gradient operator applied to a quantity
- \*  $\partial_t q$  partial derivative of a quantity with respect to the time  $t$
- \*  $\partial_j q$  partial derivative of a quantity with respect to the  $j^{\text{th}}$  spatial coordinate
- \*  $q_{,\rho}$  derivative of a quantity with respect to density at constant temperature and concentration (or mean molecular weight)
- \*  $q_{,T}$  derivative of a quantity with respect to temperature at constant density and concentration (or mean molecular weight)
- \*  $q_{,\alpha}$  derivative of a quantity with respect to concentration at constant density and temperature
- \*  $q_{,\mu}$  derivative of a quantity with respect to mean molecular weight at constant density and temperature

### Subscripts and superscripts:

- \*  $q_\alpha$  quantity related to species  $\alpha$ ,
- \*  $q^i$  quantity related to ions
- \*  $q^e$  quantity related to electrons
- \*  $q^m$  quantity related to matter (containing ions and electrons)
- \*  $q^r$  quantity related to radiation

## Roman letters:

* $A_t$	[ $\emptyset$ ]	Atwood number
* $A_r$	[ $\emptyset$ ]	twice the negative Atwood number regarding the contrast of molar masses
* Bo	[ $\emptyset$ ]	Boltzmann number
* $c_\alpha$	[ $\emptyset$ ]	concentration or mass fraction of species $\alpha$
* $c_p$	[erg.g <sup>-1</sup> .K <sup>-1</sup> ]	total specific heat capacity at constant pressure
* $c_p^m$	[erg.g <sup>-1</sup> .K <sup>-1</sup> ]	matter specific heat capacity at constant pressure
* $c_p^r$	[erg.g <sup>-1</sup> .K <sup>-1</sup> ]	radiative specific heat capacity at constant pressure
* $c_s$	[cm.s <sup>-1</sup> ]	speed of sound
* $c_v$	[erg.g <sup>-1</sup> .K <sup>-1</sup> ]	total specific heat capacity at constant volume
* $c_v^i$	[erg.g <sup>-1</sup> .K <sup>-1</sup> ]	ionic specific heat capacity at constant volume
* $c_v^e$	[erg.g <sup>-1</sup> .K <sup>-1</sup> ]	electronic specific heat capacity at constant volume
* $c_v^m$	[erg.g <sup>-1</sup> .K <sup>-1</sup> ]	matter specific heat capacity at constant volume
* $c_v^r$	[erg.g <sup>-1</sup> .K <sup>-1</sup> ]	radiative specific heat capacity at constant volume
* $\mathcal{C}$	[erg.cm <sup>-3</sup> .s <sup>-1</sup> ]	conduction term regarding total thermal diffusion
* d	[cm]	distance between the observer and the star
* $D, D_c$	[cm <sup>2</sup> .s <sup>-1</sup> ]	coefficient of diffusion of the binary mixture
* $D^{(\alpha)}$	[cm <sup>2</sup> .s <sup>-1</sup> ]	coefficient of diffusion of the species $\alpha$
* $D_{\text{conv.}}$	[cm <sup>2</sup> .s <sup>-1</sup> ]	turbulent convective diffusion coefficient
* $D_{\text{thrm.}}$	[cm <sup>2</sup> .s <sup>-1</sup> ]	turbulent thermohaline diffusion coefficient
* $D_P$	[erg.cm <sup>-3</sup> .s <sup>-1</sup> ]	diffusion term related to pressure evolution
* $D_T$	[erg.cm <sup>-3</sup> .s <sup>-1</sup> ]	diffusion term related to temperature evolution
* Da	[ $\emptyset$ ]	Damkhöler number
* e	[erg.g <sup>-1</sup> ]	total specific energy
* $e^i$	[erg.g <sup>-1</sup> ]	ionic specific energy
* $e^e$	[erg.g <sup>-1</sup> ]	electronic specific energy
* $e^m$	[erg.g <sup>-1</sup> ]	matter specific energy
* E	[erg]	total energy
* $E^r$	[erg.cm <sup>-3</sup> ]	radiative energy density
* $\mathcal{F}_\alpha$	[g.cm <sup>-2</sup> .s <sup>-1</sup> ]	scalar diffusion flux of species $\alpha$
* $\mathcal{F}^i$	[erg.cm <sup>-2</sup> .s <sup>-1</sup> ]	ionic flux
* $\mathcal{F}^e$	[erg.cm <sup>-2</sup> .s <sup>-1</sup> ]	electronic flux
* $\mathcal{F}^m$	[erg.cm <sup>-2</sup> .s <sup>-1</sup> ]	material flux
* $\mathcal{F}^r$	[erg.cm <sup>-2</sup> .s <sup>-1</sup> ]	radiative flux
* $\mathcal{F}_{\alpha,t}$	[g.cm <sup>-2</sup> .s <sup>-1</sup> ]	turbulent concentration flux of species $\alpha$
* $\mathcal{F}_{\alpha,t,\text{conv.}}$	[g.cm <sup>-2</sup> .s <sup>-1</sup> ]	turbulent convective scalar flux of species $\alpha$
* $\mathcal{F}_{\alpha,t,\text{thrm.}}$	[g.cm <sup>-2</sup> .s <sup>-1</sup> ]	turbulent thermohaline scalar flux of species $\alpha$
* $\mathcal{F}_{\text{conv.}}$	[erg.cm <sup>-2</sup> .s <sup>-1</sup> ]	convective heat flux

## List of symbols

---

* $\mathcal{F}_t$	[erg.cm <sup>-2</sup> .s <sup>-1</sup> ]	turbulent heat flux
* $Fr_a$	[∅]	Froude number related to acceleration
* $Fr_s$	[∅]	Froude number related to deformation
* $g$	[cm.s <sup>-2</sup> ]	local stellar gravity
* $h$	[erg.g <sup>-1</sup> ]	total specific enthalpy
* $h^m$	[erg.g <sup>-1</sup> ]	matter specific enthalpy
* $h^r$	[erg.g <sup>-1</sup> ]	radiative specific enthalpy
* $H_P$	[cm]	pressure scale height
* $k$	[cm <sup>2</sup> .s <sup>-2</sup> ]	turbulent kinetic energy
* $k_x$	[cm <sup>-1</sup> ]	x-component of the wave number
* $k_y$	[cm <sup>-1</sup> ]	y-component of the wave number
* $k_z$	[cm <sup>-1</sup> ]	z-component of the wave number
* $Ka_P$	[∅]	von Kármán number related to pressure
* $Ka_T$	[∅]	von Kármán number related to temperature
* $\ell_0$	[cm]	characteristic turbulent length
* $L$	[erg.s <sup>-1</sup> ]	interior luminosity of the star
* $L_{star}$	[erg.s <sup>-1</sup> ]	luminosity of the star
* $L_P$	[cm]	characteristic scale for the mean pressure gradient
* $L_T$	[cm]	characteristic scale for the mean temperature gradient
* $Le$	[∅]	Lewis number
* $m$	[g]	interior mass of the star
* $M$	[g]	total mass of the star
* $M_{ini.}$	[g]	initial mass of the star
* $\mathcal{M}$	[g.mol <sup>-1</sup> ]	molar mass
* $\mathcal{M}_\alpha$	[g.mol <sup>-1</sup> ]	molar mass of species $\alpha$
* $\mathcal{M}_l$	[g.mol <sup>-1</sup> ]	molar mass of the light fluid
* $\mathcal{M}_h$	[g.mol <sup>-1</sup> ]	molar mass of the heavy fluid
* $M_t$	[∅]	turbulent Mach number
* $N_s$	[∅]	total number of species of the mixture
* $N$	[s <sup>-1</sup> ]	Brunt-Väissälä frequency
* $N_\mu$	[s <sup>-1</sup> ]	Brunt-Väissälä frequency related to $\mu$
* $P$	[g.cm <sup>-1</sup> .s <sup>-2</sup> ]	total pressure of the field
* $P^i$	[g.cm <sup>-1</sup> .s <sup>-2</sup> ]	ionic pressure of the field
* $P^e$	[g.cm <sup>-1</sup> .s <sup>-2</sup> ]	electronic pressure of the field
* $P^m$	[g.cm <sup>-1</sup> .s <sup>-2</sup> ]	matter pressure of the field (ions and electrons)
* $P^r$	[g.cm <sup>-1</sup> .s <sup>-2</sup> ]	radiative pressure of the field
* $Pe_t$	[∅]	turbulent (radiative) Péclet number
* $Pr$	[∅]	Prandtl number
* $r_\alpha$	[erg.g <sup>-2</sup> .K <sup>-1</sup> ]	specific ideal gas constant of species $\alpha$
* $r$	[cm]	interior radius of the star

* $R$	[cm]	radius of the star
* $R$	[ $\emptyset$ ]	Mihalas number
* $Re_t$	[ $\emptyset$ ]	turbulent Reynolds number
* $Re_\lambda$	[ $\emptyset$ ]	Reynolds number based on the Taylor micro-scale
* $s$	[erg.g <sup>-1</sup> .K <sup>-1</sup> ]	specific total entropy
* $s^m$	[erg.g <sup>-1</sup> .K <sup>-1</sup> ]	specific material entropy
* $s^r$	[erg.g <sup>-1</sup> .K <sup>-1</sup> ]	specific radiative entropy
* $\mathcal{S}_\alpha$	[g.cm <sup>-3</sup> .s <sup>-1</sup> ]	source term of species $\alpha$
* $(\mathcal{S}_\alpha)_{\text{nuc.}}$	[s <sup>-1</sup> ]	source term arising from nuclear reactions
* $\mathcal{S}^i$	[erg.cm <sup>-3</sup> .s <sup>-1</sup> ]	source term related to ions
* $\mathcal{S}^e$	[erg.cm <sup>-3</sup> .s <sup>-1</sup> ]	source term related to electrons
* $\mathcal{S}^r$	[erg.cm <sup>-3</sup> .s <sup>-1</sup> ]	source term related to photons
* $S_{ij}$	[s <sup>-1</sup> ]	instantaneous strain-rate tensor
* $Sc$	[ $\emptyset$ ]	Schmidt number
* $t$	[s]	time
* $T$	[K]	temperature of the field
* $T^i$	[K]	ionic temperature of the field
* $T^e$	[K]	electronic temperature of the field
* $T^m$	[K]	matter temperature of the field (ions and electrons)
* $T^r$	[K]	radiative temperature of the field
* $u_0$	[cm.s <sup>-1</sup> ]	characteristic turbulent velocity
* $v_{\text{conv.}}$	[cm.s <sup>-1</sup> ]	convective velocity
* $v_{\text{thrm.}}$	[cm.s <sup>-1</sup> ]	thermohaline velocity
* $W^{i-e}$	[erg.cm <sup>-3</sup> .s <sup>-1</sup> ]	ion-electron exchange term
* $Z_\alpha$	[ $\emptyset$ ]	ionization degree of species $\alpha$

### Greek letters:

* $\alpha_{\text{MLT}}$	[ $\emptyset$ ]	mixing length parameter
* $\alpha_{\text{thrm.}}$	[ $\emptyset$ ]	thermohaline mixing length parameter
* $\beta$	[ $\emptyset$ ]	ratio of matter pressure to total pressure
* $\gamma_1, \gamma_2, \gamma_3$	[ $\emptyset$ ]	polytropic coefficients
* $\Gamma_1, \Gamma_2, \Gamma_3$	[ $\emptyset$ ]	generalized adiabatic exponents
* $\varepsilon$	[cm <sup>2</sup> .s <sup>-3</sup> ]	viscous dissipation rate of kinetic energy
* $\varepsilon_g$	[erg.g <sup>-1</sup> .s <sup>-1</sup> ]	expansion or contraction source term
* $\varepsilon_{\text{nuc.}}$	[erg.g <sup>-1</sup> .s <sup>-1</sup> ]	nuclear source term
* $\kappa^r$	[cm <sup>2</sup> .g <sup>-1</sup> ]	Rosseland mean opacity
* $\kappa_b$	[g.cm <sup>-1</sup> .s <sup>-1</sup> ]	bulk viscosity
* $\kappa_\mu$	[cm <sup>2</sup> .s <sup>-1</sup> ]	compositional diffusivity
* $\lambda^e$	[erg.cm <sup>-1</sup> .s <sup>-1</sup> .K <sup>-1</sup> ]	electronic thermal conductivity

## List of symbols

---

* $\lambda^i$	[erg.cm <sup>-1</sup> .s <sup>-1</sup> .K <sup>-1</sup> ]	ionic thermal conductivity
* $\lambda^m$	[erg.cm <sup>-1</sup> .s <sup>-1</sup> .K <sup>-1</sup> ]	matter thermal conductivity
* $\lambda^r$	[erg.cm <sup>-1</sup> .s <sup>-1</sup> .K <sup>-1</sup> ]	radiative thermal conductivity
* $\lambda_w$	[cm]	wavelength related to the linear perturbation
* $\Lambda^r$	[cm]	mean free path of photons
* $\Lambda_{\text{conv.}}$	[cm]	convective mixing length
* $\Lambda_{\text{MLT}}$	[cm]	mixing length
* $\Lambda_{\text{thrm.}}$	[cm]	thermohaline mixing length
* $\mu$	[g.mol <sup>-1</sup> ]	mean molecular weight (equivalent molar mass)
* $\mu_v$	[g.cm <sup>-1</sup> .s <sup>-1</sup> ]	dynamic or shear viscosity
* $\nu_t$	[cm <sup>2</sup> .s <sup>-1</sup> ]	turbulent diffusivity
* $\nu_v$	[cm <sup>2</sup> .s <sup>-1</sup> ]	kinematic viscosity
* $\Pi_{ij}$	[g.cm <sup>-1</sup> .s <sup>-2</sup> ]	viscosity tensor
* $\rho$	[g.cm <sup>-3</sup> ]	density of the gas
* $\tau$	[cm <sup>3</sup> .g <sup>-1</sup> ]	specific volume of the field
* $\tau_0$	[s]	characteristic turbulent time
* $\tau_{\text{diff}}$	[∅]	inverse Lewis number
* $\tau_{\text{dyn.}}$	[s]	stellar dynamical timescale
* $\tau_{\text{nuc.}}$	[s]	stellar nuclear timescale
* $\tau_{s_0}$	[s]	characteristic reaction time
* $\tau_{\text{star}}$	[s]	stellar evolution timescale
* $\tau_{\text{KH}}$	[s]	stellar thermal (or “Kelvin-Helmholtz”) timescale
* $\chi$	[cm <sup>2</sup> .s <sup>-1</sup> ]	thermal diffusivity
* $\chi^r$	[cm <sup>2</sup> .s <sup>-1</sup> ]	radiative diffusivity
* $\omega$	[s <sup>-1</sup> ]	characteristic turbulent frequency
* $\omega$	[s <sup>-1</sup> ]	complex frequency related to the linear perturbation
* $\omega_r$	[s <sup>-1</sup> ]	circular frequency related to the linear perturbation
* $\omega_i$	[s <sup>-1</sup> ]	growth rate related to the linear perturbation
* $\omega_{\text{Pet}}$	[∅]	weighting function of the blending model
* $\Omega^{e-r}$	[erg.cm <sup>-3</sup> .s <sup>-1</sup> ]	electron-radiation exchange term

## Astronomical constants:

Constant	Symbol	Value	SI unit	CGS unit
Solar mass	$M_{\odot}$	1.989 1	10 <sup>30</sup> kg	10 <sup>33</sup> g
Solar radius	$R_{\odot}$	6.959 8	10 <sup>8</sup> m	10 <sup>10</sup> cm
Solar luminosity	$L_{\odot}$	3.851 5	10 <sup>26</sup> J.s <sup>-1</sup>	10 <sup>10</sup> erg.s <sup>-1</sup>

Table A – Astronomical constants from C. Caso [1998].

## Fundamental constants:

Constant	Symbol	Value	SI unit	CGS unit
Speed of light	$c_\ell$	2.997 924 58	$10^8 \text{ m.s}^{-1}$	$10^{10} \text{ cm.s}^{-1}$
Gravitational constant	$G$	6.672 59	$10^{-11} \text{ m}^3.\text{kg}^{-1}.\text{s}^{-2}$	$10^{-8} \text{ cm}^3.\text{g}^{-1}.\text{s}^{-2}$
Boltzmann constant	$k_B$	1.380 658	$10^{-23} \text{ J.K}^{-1}$	$10^{-16} \text{ erg.K}^{-1}$
Stefan Boltzmann constant	$\sigma_{SB}$	5.670 51	$10^{-8} \text{ J.m}^{-2}.\text{s}^{-1}.\text{K}^{-4}$	$10^{-5} \text{ erg.cm}^{-2}.\text{s}^{-1}.\text{K}^{-4}$
Radiation constant	$a_R$	7.564 6	$10^{-16} \text{ J.m}^{-3}.\text{K}^{-4}$	$10^{-15} \text{ erg.cm}^{-3}.\text{K}^{-4}$
Avogadro number	$\mathcal{N}_A$	6.022 136 7	$10^{23} \text{ mol}^{-1}$	$10^{23} \text{ mol}^{-1}$
$^1\text{H}$ atom mass	$m_H$	1.673 534 4	$10^{-27} \text{ kg}$	$10^{-24} \text{ g}$
Ideal gas constant	$\mathcal{R}$	8.314 510	$10^3 \text{ J.kg}^{-1}.\text{K}^{-1}$	$10^7 \text{ erg.g}^{-1}.\text{K}^{-1}$

Table B – Fundamental constants with  $a_R = 4\sigma_{SB}/c_\ell$ ,  $m_H = 1/\mathcal{N}_A$  and  $\mathcal{R} = k_B/m_H$  from [Cohen & Taylor \[1987a, 1995, 1987b\]](#).

## Unit symbols:

CGS quantities	Usual symbols	CGS units	Equivalents in SI units
Position, length	$x, \ell$	cm	$10^{-2} \text{ m}$
Mass	$m$	g	$10^{-3} \text{ kg}$
Velocity	$v$	$\text{cm.s}^{-1}$	$10^{-2} \text{ m.s}^{-1}$
Acceleration	$a$	Gal (= $\text{cm.s}^{-2}$ )	$10^{-2} \text{ m.s}^{-2}$
Force	$f$	dyn (= $\text{g.cm.s}^{-2}$ )	$10^{-5} \text{ N}$
Energy	$E$	erg (= $\text{g.cm}^2.\text{s}^{-2}$ )	$10^{-7} \text{ J}$ (= $\text{kg.m}^2.\text{s}^{-2}$ )
Power	$\Phi$	$\text{erg.s}^{-1}$	$10^{-7} \text{ W}$
Pressure	$P$	Ba (= $\text{g.cm}^{-1}.\text{s}^{-2}$ )	$10^{-1} \text{ Pa}$
Dynamic viscosity	$\mu_v$	P (= $\text{g.cm}^{-1}.\text{s}^{-1}$ )	$10^{-1} \text{ Pa.s}$
Kinematic viscosity	$\nu_v$	St (= $\text{cm}^2.\text{s}^{-1}$ )	$10^{-4} \text{ m}^2.\text{s}^{-1}$
Time	$t$	s	1 s
Temperature	$T$	K	1 K
Molar mass	$\mathcal{M}$	$\text{g.mol}^{-1}$	$1 \text{ kg.mol}^{-1}$

Table C – CGS and SI units of usual quantities.

## Stellar isotopes:

Atomic number $Z$	Element	Atomic mass $A$	Initial Solar composition
1	H	1	$6.999\,999\,999\,999\,996\,2 \times 10^{-1}$
		2	0
2	He	3	$2.979\,763\,525\,113\,860\,4 \times 10^{-5}$
		4	$2.799\,702\,023\,647\,487\,3 \times 10^{-1}$
3	Li	6	0
		7	$1.382\,164\,456\,646\,894\,4 \times 10^{-8}$
4	Be	9	$2.365\,695\,637\,446\,254\,8 \times 10^{-10}$
6	C	12	$3.495\,153\,653\,574\,131\,9 \times 10^{-3}$
		13	$4.242\,674\,968\,419\,376\,9 \times 10^{-5}$
7	N	14	$1.032\,206\,117\,859\,104\,8 \times 10^{-3}$
		15	$4.065\,070\,828\,640\,580\,4 \times 10^{-6}$
8	O	16	$8.552\,447\,874\,100\,123\,4 \times 10^{-3}$
		17	$3.389\,296\,467\,143\,779\,9 \times 10^{-6}$
		18	$1.929\,785\,274\,002\,505\,5 \times 10^{-5}$
9	F	19	$7.548\,397\,077\,763\,601\,2 \times 10^{-7}$
10	Ne	20	$1.734\,857\,398\,108\,492\,6 \times 10^{-3}$
		21	$4.367\,048\,660\,566\,071\,0 \times 10^{-6}$
		22	$1.403\,184\,362\,329\,398\,6 \times 10^{-4}$
11	Na	23	$4.371\,918\,939\,278\,856\,1 \times 10^{-5}$
12	Mg	24	$8.253\,943\,857\,640\,752\,2 \times 10^{-4}$
		25	$1.088\,835\,049\,467\,064\,4 \times 10^{-4}$
		26	$1.245\,691\,377\,843\,899\,0 \times 10^{-4}$
13	Al	27	$8.321\,549\,675\,386\,420\,8 \times 10^{-5}$
14	Si	28	$9.137\,143\,164\,801\,017\,1 \times 10^{-4}$
		29	$4.805\,344\,954\,247\,566\,2 \times 10^{-5}$
		30	$3.276\,726\,835\,098\,454\,7 \times 10^{-5}$
15	P	31	$8.712\,272\,916\,529\,238\,9 \times 10^{-6}$
16	S	32	$4.383\,344\,319\,351\,613\,3 \times 10^{-4}$
		33	$3.568\,028\,864\,112\,964\,2 \times 10^{-6}$
		34	$2.339\,770\,121\,091\,554\,0 \times 10^{-3}$

Table D – Initial Solar abundances of stellar isotopes in mass fractions from [Asplund \*et al.\* \[2009\]](#).

# 1

## Properties of stellar turbulent mixing zones

“ Come with me home.  
The stars rise, the moon bends her arc,  
Each glowworm winks her spark,  
Let us get home before the night grows dark:  
For clouds may gather  
Though this is summer weather,  
Put out the lights and drench us through;  
Then if we lost our way what should we do?”

CHRISTINA ROSSETTI  
*Poems and Prose: Goblin Market*

### Contents

<b>1.1</b>	<b>Introduction</b> . . . . .	<b>16</b>
<b>1.2</b>	<b>Stellar structure equations</b> . . . . .	<b>16</b>
1.2.1	Conservation of mass, momentum, energy and mass fractions . .	16
1.2.2	Equation of state and radiative flux . . . . .	18
1.2.3	Turbulent transport . . . . .	19
<b>1.3</b>	<b>Stellar turbulence models for convection and double diffusion</b> . . . .	<b>20</b>
1.3.1	Convective and double-diffusive instabilities . . . . .	20
1.3.2	Modelling stellar turbulence in convective and thermohaline zones	23
1.3.3	Discussion . . . . .	28
<b>1.4</b>	<b>Simulating stellar turbulence with MESA</b> . . . . .	<b>29</b>
1.4.1	Description of MESA and of the simulation parameters . . . . .	29
1.4.2	Kippenhahn diagrams . . . . .	30
1.4.3	Non-dimensional numbers . . . . .	31
<b>1.5</b>	<b>Conclusion</b> . . . . .	<b>35</b>

### 1.1 Introduction

In the introduction of the manuscript, we argued that turbulent mixing zones with small Péclet, small Mach and high Reynolds numbers could be formed in stars. The purpose of this chapter is to defend and illustrate this assertion. To this end, we propose to perform simulations of the evolution of several stars with the open-source one-dimensional stellar-evolution code called MESA.

Before that, we first recall in Sec. 1.2 the general principles allowing to derive stellar evolution equations, such as those solved in MESA. Then, in Sec. 1.3, we describe how turbulence is generally accounted for in stellar evolution simulations. Finally, in Sec. 4.10, we perform simulations for three different stars, a low-mass star of mass  $1M_{\odot}$ , an intermediate-mass star of mass  $5M_{\odot}$  and a massive star of mass  $75M_{\odot}$ , with the notation  $M_{\odot}$  corresponding to one “solar mass” in astrophysical units. We then extract non-dimensional numbers from these simulations and discuss their significance.

### 1.2 Stellar structure equations

Our understanding of stellar structure is based on the pioneering works of Lane [1869], Schwarzschild [1906] and Eddington [1916], among others, who provided the foundations of stellar evolution theories. They were the firsts who considered stars as spherical systems of mass  $M$  and radius  $R$  obeying a mechanical and thermal equilibrium. A more recent and updated account of these works can be found in the books of Maeder [2009], Chandrasekhar [1957, 1960] and Prialnik [2000].

#### 1.2.1 Conservation of mass, momentum, energy and mass fractions

Assuming the spherical symmetry of the star, stellar structure equations are derived by considering the conservation of mass, momentum, energy and species mass fractions for an infinitely thin spherical shell located at a given radius  $r(t)$  that moves in a Lagrangian fashion. Instead of  $r$ , one may also choose to identify the shell position with the value of the mass it encloses:

$$m(t) = \int_0^{r(t)} dm = \int_0^{r(t)} 4\pi r^2 \rho(x, t) dx \quad , \quad (1.1)$$

with  $\rho(r, t)$  the value of the density at radius  $r$  and time  $t$ . The interest of this change of variable lies in the fact that  $m$  has a bounded range of variation:

$$0 \leq m(t) \leq M(t) \leq M_{\text{ini}} \quad ,$$

with  $M(t)$  and  $M_{\text{ini}}$  respectively the total and the initial mass of the star. The radius  $r(t)$  also appears to be bounded since:

$$0 \leq r(t) \leq R(t) \quad ,$$

but the stellar radius  $R(t)$  can increase or decrease by several orders of magnitude during the life of a star.

When deriving the mass, momentum, energy and mass fraction conservation equations, one has to account for the time variations of the radius  $r$  of the spherical shell, of its density  $\rho$ , of its total energy  $E$  and of the value of the mass fractions  $c_\alpha$  of its  $N_s$  species. However, these variations occur on widely different timescales and significant simplifications can be brought to the overall system. In particular, the dynamical timescale  $\tau_{\text{dyn.}}$  and the thermal timescale  $\tau_{\text{KH}}$  are much smaller than  $\tau_{\text{star}}$ , the typical lifespan of a star:

$$\tau_{\text{dyn.}} \sim \sqrt{R^3 / (G \cdot M)} \ll \tau_{\text{star}} \quad \text{and} \quad \tau_{\text{KH}} \sim G \cdot M^2 / (R \cdot L_{\text{star}}) \ll \tau_{\text{star}} \quad ,$$

where  $G$  is the gravitational constant and  $L_{\text{star}}$  is the luminosity of the star.<sup>1</sup> As an illustration, for a star of one solar mass,  $\tau_{\text{dyn.}}$  is  $10^{14}$  times smaller than  $\tau_{\text{star}}$  while  $\tau_{\text{KH}}$  is  $10^2$  times smaller [Maeder, 2009].

The smallness of the dynamical and thermal timescales allows one to neglect the time derivatives of  $r$ ,  $\rho$  and  $E$  appearing in the conservation equations of mass, momentum and energy. In other words, a hydrostatic and thermal equilibrium is assumed to be reached within the star. Any departure from this equilibrium is damped either on a timescale  $\tau_{\text{dyn.}}$  or a timescale  $\tau_{\text{KH}}$  which are both negligible compared to typical stellar ages.

By contrast, the stellar chemical composition is modified by nucleosynthesis, and a small fraction  $\epsilon$  of its rest-mass energy  $E \equiv M \cdot c_\ell^2$ , with  $c_\ell$  the speed of light, is converted into potential energy. The timescale of this process is called nuclear timescale  $\tau_{\text{nuc.}}$  and is usually much larger than the lifespan of a star:

$$\tau_{\text{nuc.}} \sim \epsilon \cdot M \cdot c_\ell^2 / L_{\text{star}} \gg \tau_{\text{star}} \quad , \quad (1.2)$$

where  $\epsilon \sim 10^{-3}$  can be estimated knowing the rate of the typical binding energy of a nucleon to its rest-mass energy [Prialdnik, 2000]. Thus, as opposed to the hydrodynamical and thermal balances, the chemical evolution of the star cannot be approached using a quasi-steady assumption. Instead, it is this process which sets the pace of the star life cycle.

Within these assumptions, one can describe the evolution of a star by expressing the conservation of mass, momentum and energy in a quasi-steady way, while letting the species mass fraction evolve in time because of nuclear reactions. The ensuing system takes the following form:

$$\left\{ \begin{array}{l} \frac{\partial r}{\partial m} = \frac{1}{4\pi r^2 \rho} \quad , \end{array} \right. \quad (1.3a)$$

$$\left\{ \begin{array}{l} \frac{\partial P}{\partial m} = -\frac{Gm}{4\pi r^4} \quad , \end{array} \right. \quad (1.3b)$$

$$\left\{ \begin{array}{l} \frac{\partial L}{\partial m} = \epsilon_{\text{nuc.}} + \epsilon_g \quad , \end{array} \right. \quad (1.3c)$$

$$\left\{ \begin{array}{l} \partial_t c_\alpha = (\mathcal{S}_\alpha)_{\text{nuc.}} \quad . \end{array} \right. \quad (1.3d)$$

---

<sup>1</sup>Let us recall that  $L_{\text{star}}$  corresponds to the energy radiated by the star per unit time and is analogous to a power. It is related to  $I$ , the radiation flux measuring the brightness of the star as observed from earth by:  $L_{\text{star}} \equiv 4\pi d^2 I$ , where  $d$  is the distance to the star.

## 1.2. Stellar structure equations

---

In these equations, we already introduced  $r$  and  $m$ , as the shell radius and enclosed mass,  $\rho$  as the density,  $c_\alpha$  as the species mass fraction and  $G$  as the gravitational constant. In addition,  $P$  is the total pressure, *i.e.* the sum of the material pressure  $P^m$  and the radiative pressure  $P^r$ :

$$P = P^m + P^r \quad ,$$

and  $L$  is the power flowing in and out of the spherical shell *i.e.*, the energy flux integrated over the spherical shell surface. Therefore, at the outer boundary  $m = M$ , its value is the luminosity of the star  $L(M) = L_{\text{star}}$ . The source term  $\epsilon_{\text{nuc}}$  gives the rate of energy produced by nuclear reactions minus the energy lost by the formation of neutrino particles. The source term  $\epsilon_g$  corresponds to the rate of energy provided to the system during a change of structure, *e.g.* during an expansion or a contraction. Finally,  $(\mathcal{S}_\alpha)_{\text{nuc}}$  is a source term arising from the nuclear reactions affecting the species  $\alpha$ . These different source terms are not detailed here, but the interested reader can find their expression in [Prialnik \[2000\]](#) for example.

The first equation of this system, Eq. (1.3a), corresponds to the conservation of mass. Equation (1.3b) expresses the hydrostatic equilibrium occurring in the star: the gravity force driving matter towards the core of the star is balanced by the thermal and radiative pressure gradient. Equation (1.3c) asserts the thermal equilibrium of the star: the power flowing in and out of the shell is balanced by the power produced within the shell through nuclear reactions and gravitational changes. Finally, Eq. (1.3d) tells how species mass fractions are modified by nuclear reactions. This last equation stands apart from the other three since it is the only one that involves a time derivative. As already explained, the slow nuclear fusion process taking place in the star sets the rhythm of its evolution while other processes are fast enough to be approximated in a quasi-steady way.

### 1.2.2 Equation of state and radiative flux

The conservation of mass, momentum, energy and mass fractions given by Sys. (1.3) must be supplemented by additional assumptions and relations. In particular, an equation of state is required to express the material pressure as a function of density, concentrations and temperature. For simplicity, we will hereafter assume that the plasma follows the law of perfect gases and that:

$$P^m = \rho \frac{\mathcal{R}}{\mu} T \quad , \quad (1.4)$$

where  $\mathcal{R}$  is the ideal gas constant and  $\mu$  is the “mean molecular weight”, which depends on the mass fractions of the species, on their molecular weights and ionization degrees. Details about the precise expression of  $\mu$  can be found in [Prialnik \[2000\]](#).

Concerning the temperature  $T$  appearing in the previous expression, let us mention that the conditions required to attain a local thermodynamic equilibrium are met in stellar flows. As a result, since thermal equilibrium between matter and radiation fields is also assumed, the temperature  $T^e$  and  $T^i$  of the electrons and ions of the plasma, as well as the temperature  $T^r$  of the radiative field are all equal:

$$T = T^e = T^i = T^r \quad .$$

Besides, the radiative field obeys the diffusion approximation [Mihalas & Mihalas, 2013]. The radiative pressure is given by:

$$P^r = \frac{1}{3} a_R T^4 \quad , \quad (1.5)$$

where  $a_R$  is the radiation constant. Moreover, if we assume that energy is primarily transported by radiation, then the energy flux  $L$  can be related to the temperature gradient and to the Rosseland mean opacity  $\kappa^r$ . The diffusion approximation of the radiative flux yields:

$$\frac{\partial T}{\partial m} = - \frac{3}{4 a_R c_\ell} \frac{\kappa^r}{T^3} \frac{L}{(4\pi r^2)^2} \quad . \quad (1.6)$$

The Rosseland mean opacity  $\kappa^r$  is a function of density, concentrations and temperature:

$$\kappa^r \equiv \kappa^r(\rho, c_\alpha, T) \quad . \quad (1.7)$$

Estimates for this opacity in stellar interiors can be found in Chandrasekhar [1960] or Prialnik [2000].

### 1.2.3 Turbulent transport

System (1.3) supplemented by the equation of state (1.4) and the diffusion approximation of the radiative flux (1.6) allows to compute the evolution of stars. However, in practice, its range of validity remains very limited since all phenomena linked to turbulence are neglected.

Two main effects can be expected from the presence of turbulent motions. First, turbulence contributes to the transport of energy. As a result, the energy flux  $L$  must not only account for a radiative component, as given by Eq. (1.6), but also for a turbulent one. Second, turbulence also induces a transport of the species mass fractions that must be included in Eq. (1.3d). In other words, the presence of a turbulent field leads to modify Sys. (1.3) and Eq. (1.6) as follows:

$$\left\{ \begin{array}{l} \frac{\partial r}{\partial m} = \frac{1}{4\pi r^2 \rho} \quad , \quad (1.8a) \\ \frac{\partial P}{\partial m} = - \frac{Gm}{4\pi r^4} \quad , \quad (1.8b) \\ \frac{\partial L}{\partial m} = \epsilon_{\text{nuc.}} + \epsilon_g \quad , \quad (1.8c) \\ \frac{\partial T}{\partial m} = - \frac{3}{4 a_R c_\ell} \frac{\kappa^r}{T^3} \frac{1}{4\pi r^2} \left( \frac{L}{4\pi r^2} + \mathcal{F}_t \right) \quad , \quad (1.8d) \\ \partial_t c_\alpha = - \frac{1}{\rho r^2} \frac{\partial}{\partial r} (r^2 \mathcal{F}_{\alpha,t}) + (\mathcal{S}_\alpha)_{\text{nuc.}} \quad . \quad (1.8e) \end{array} \right.$$

In this system, we have highlighted in purple the two main modifications brought by the presence of turbulence: a turbulent heat flux  $\mathcal{F}_t$  is added to the definition of  $L$ , in addition to the radiative flux. Besides, a turbulent concentration flux  $\mathcal{F}_{\alpha,t}$  is also added in the evolution equations of each species mass fraction.

### 1.3. Stellar turbulence models for convection and double diffusion

---

The question that remains is how can  $\mathcal{F}_t$  and  $\mathcal{F}_{\alpha,t}$  be closed. This question will be examined in the next section for the particular case of turbulent motions generated by convective and double diffusive instabilities.

## 1.3 Stellar turbulence models for convection and double diffusion

As mentioned in the introduction, a large number of hydrodynamical instabilities take place in stellar interiors, some linked to shear, others to rotation, convection or double-diffusion. Each of these instabilities, either independently or in conjunction with others, can trigger the development of turbulent regions within stellar interiors. In this section, we will arbitrarily assume that turbulence is generated exclusively by convective and double-diffusive instabilities. We will leave aside all other instabilities and their potential effects on turbulence modelling. Indeed, our purpose is not to be exhaustive but rather to highlight the physical properties of these two particular turbulent regimes.

### 1.3.1 Convective and double-diffusive instabilities

A linear analysis of the stability of a stratified equilibrium in a gravitational field will be led in chapter 4. In this section, we only aim to provide simple arguments allowing to understand the onset of convective and double-diffusive instabilities.

To this end, let us consider a small parcel of fluid of mass  $m$  and let us assume that this parcel is displaced radially from its equilibrium position  $r = r_1$  to a higher position  $r = r_2 = r_1 + dr$ , with  $dr > 0$  a small distance. At  $r = r_1$ , the mean density, pressure, temperature and molecular weights are respectively equal to  $\rho_1, P_1, T_1$  and  $\mu_1$ , while at  $r = r_2$  they are equal to  $\rho_2, P_2, T_2$  and  $\mu_2$ . Given the hydrostatic condition, one has  $P_2 < P_1$ , but there is no condition on the sign of the gradient of  $T$  and  $\mu$  and no condition on the order of  $T_1$  and  $T_2$  and  $\mu_1$  and  $\mu_2$ .

Before being displaced, the particle has the same characteristics as its environment, *i.e.* its state is given by  $\rho_1, P_1, T_1$  and  $\mu_1$ . But when it arrives at  $r = r_2$ , its state has evolved and is now given by  $\rho_\star, P_\star, T_\star$  and  $\mu_\star$ . Provided the displacement of the particle is slow compared to the speed of sound, the pressure of the particle can be considered to adjust instantaneously to its environment so that:

$$P_\star = P_2 \quad .$$

However, the particle density  $\rho_\star$  is not necessarily equal to the density  $\rho_2$  of its new environment. Then, if  $\rho_\star < \rho_2$ , the particle will be less dense than its surrounding and will keep on rising due to buoyancy. By contrast, if  $\rho_\star > \rho_2$ , it will be denser and instead of rising, it will fall back towards its initial position. In the first case, the displacement of the particle is amplified and the stratification is unstable. In the second case, the displacement of the particle is damped and the stratification is stable.

To determine the value of  $\rho_\star$ , we will consider two distinct cases. In the first one, we will assume that the heat flux is negligible while in the second one that it is very large. These two cases are relevant respectively to the high and small Péclet regime discussed in the introduction.

### 1.3.1.1 Negligible heat flux (large Péclet number)

In the first case, we will assume that the transport of heat and species mass fraction is negligible. With this assumption, the particle undergoes an adiabatic adjustment of its pressure. Therefore, given that infinitesimal changes are considered, one has:

$$\rho_\star = \rho_1 + \left. \frac{\partial \rho}{\partial P} \right|_{s, c_\alpha} (P_2 - P_1) \quad , \quad (1.9)$$

where  $\left. \frac{\partial \rho}{\partial P} \right|_{s, c_\alpha}$  is the partial derivative of the density with respect to pressure taken at constant entropy and constant composition. By comparison, the value of  $\rho_2$  is related to the gradient of  $P$  and  $\rho$  by:

$$\rho_2 = \rho_1 + \frac{\partial \rho / \partial r}{\partial P / \partial r} (P_2 - P_1) \quad . \quad (1.10)$$

Comparing the two values, we deduce that  $\rho_\star > \rho_2$  provided:

$$\left. \frac{\partial P}{\partial \rho} \right|_{s, c_\alpha} < \frac{\partial P / \partial r}{\partial \rho / \partial r} \quad .$$

When this condition is verified, the stratification is stable. This latter condition can be expressed in a different way by introducing the adiabatic exponent  $\Gamma_1$  defined as (see Eq. (A.1) of App. A.1):

$$\Gamma_1 = \left( \frac{d \ln P}{d \ln \rho} \right)_{s, c_\alpha} \quad ,$$

and also by defining the stratification frequency  $N$ , also called Brunt-Väissälä frequency:

$$N^2 = \frac{1}{\rho} \nabla P \left( \frac{\nabla \rho}{\rho} - \frac{1}{\Gamma_1 P} \nabla P \right) = \frac{1}{\rho} \frac{\partial P}{\partial r} \left( \frac{\nabla \rho}{\rho} \frac{\partial \rho}{\partial r} - \frac{1}{\Gamma_1 P} \frac{\partial P}{\partial r} \right) \quad . \quad (1.11)$$

With these quantities, the stability criterion becomes:

$$N^2 < 0 : \text{stable stratification} \quad \text{and} \quad N^2 > 0 : \text{unstable stratification} \quad . \quad (1.12)$$

This stability criterion has been derived in many different contexts under this form (see for instance the book by Landau & Lifshitz [1958] on Fluid Mechanics). In astrophysics, this criterion, called Ledoux [1958] criterion, has been derived by Kato [1966] and expressed using idiosyncratic notations that are found nowhere else and are rather confusing. For the sake of completeness, we nonetheless report this alternative formulation of Eq. (1.12):

$$\nabla_T < \nabla_L : \text{stable stratification} \quad \text{and} \quad \nabla_T > \nabla_L : \text{unstable stratification} \quad (1.13)$$

where:

$$\nabla_T = \frac{P}{T} \frac{\partial T / \partial r}{\partial P / \partial r} \quad , \quad \nabla_L = \nabla_{\text{ad}} - \frac{\chi_\mu}{\chi_T} \nabla_\mu \quad , \quad \nabla_{\text{ad}} = \frac{P}{T} \left( \frac{\partial T}{\partial P} \right)_{s, c_\alpha} \quad , \quad \nabla_\mu = \frac{P}{\mu} \frac{\partial \mu / \partial r}{\partial P / \partial r} \quad , \quad (1.14)$$

$$\chi_\mu = \left( \frac{\partial \ln P}{\partial \ln \mu} \right)_{\rho, T} \quad , \quad \chi_T = \left( \frac{\partial \ln P}{\partial \ln T} \right)_{\rho, c_\alpha} \quad \text{and} \quad \chi_\rho = \left( \frac{\partial \ln P}{\partial \ln \rho} \right)_{T, c_\alpha} \quad . \quad (1.15)$$

### 1.3. Stellar turbulence models for convection and double diffusion

---

The symbols  $\nabla_T$ ,  $\nabla_{ad}$ ,  $\nabla_L$  and  $\nabla_\mu$  are named “gradients” but are dimensionless quantities. The symbol  $\nabla_T$  can be interpreted as a measure of the variation of the temperature  $T$  with respect to the pressure depth of the star. The symbol  $\nabla_{ad}$  is the value that  $\nabla_T$  has when the stratification is isentropic. The symbol  $\nabla_L$  is called the “Ledoux” gradient and  $\nabla_\mu$  the composition gradient. Some of these “gradients” are thermodynamic coefficients, like  $\nabla_{ad}$ , others are computed from actual fields, like  $\nabla_T$  and  $\nabla_\mu$ . Others are a heterogeneous combination of both, like  $\nabla_L$ . Note that  $\chi_\rho$  is not used in relation (1.13), but has been added for the sake of completeness.

#### 1.3.1.2 Very large heat flux (small Péclet number)

In the second case, we assume that the diffusion of the species mass fraction remains negligible but that the heat flux is so intense that the particle reaches not only an acoustic equilibrium but also a thermal one. Then, one has not only  $P_\star = P_2$  but also  $T_\star = T_2$ , while the mean molecular weight has not changed:  $\mu_\star = \mu_1$ . Therefore, according to the equation of state (1.4), the value of  $\rho_\star$  is given by:

$$\rho_\star = \mu_1 \frac{P_2 - \frac{1}{3}a_R T_2^4}{\mathcal{R}T_2} .$$

Using the same equation of state, one also has:

$$\rho_2 = \mu_2 \frac{P_2 - \frac{1}{3}a_R T_2^4}{\mathcal{R}T_2} .$$

Comparing these two values, one obtains that  $\rho_\star > \rho_2$  if  $\mu_1 > \mu_2$ . Thus, the flow is stable when

$$\frac{\partial \mu}{\partial r} < 0 .$$

This condition is valid when the heat flux is very large and when  $\partial P / \partial r < 0$ . As in the previous case, it is possible to express this stability condition using a frequency. We introduce  $N_\mu$  defined as:

$$N_\mu^2 = -\frac{\nabla P}{\rho} \cdot \frac{\nabla \mu}{\mu} = -\frac{1}{\rho} \frac{\partial P}{\partial r} \frac{1}{\mu} \frac{\partial \mu}{\partial r} . \quad (1.16)$$

Then, the stability of the stratification can be expressed as:

$$N_\mu^2 < 0 : \text{stable stratification} \quad \text{and} \quad N_\mu^2 > 0 : \text{unstable stratification} . \quad (1.17)$$

With astrophysical notations, this criterion can also be written as:

$$\nabla_\mu > 0 : \text{stable stratification} \quad \text{and} \quad \nabla_\mu < 0 : \text{unstable stratification} . \quad (1.18)$$

#### 1.3.1.3 Summary and discussion

By studying the behavior of a small parcel of fluid, we were able to exhibit the stability criteria of the stratification in presence of a very small and a very large heat flux. The criterion (1.12) obtained in the negligible heat flux limit marks the onset of a convection. As for the criterion (1.17) obtained in the very large heat flux case, it stems from a particular asymptotic case of a double-diffusive instability.

The latter type of instability can be observed whenever two scalars (temperature, concentration) contribute to the density and have opposite stratifications. The corresponding stability criterion in the general case is of course more complex than equation (1.17), which, again, is only meaningful when the heat flux is very large (*i.e.* small Péclet number).

All in all, the simple example considered here allows to understand the physical mechanism at work in these instabilities. However, it cannot replace a full linear stability analysis (as was derived by Kato [1966] for astrophysical convection). In chapter 4, such an analysis will be performed. It will result in more general conditions allowing to bridge the two extreme limits of very large and very small heat fluxes. Note also that these two limits and their corresponding instability criteria will be discussed in chapter 2, as part of the asymptotic analysis of small Péclet number flows.

To complete this short introduction on buoyancy driven instabilities, it is customary in the stellar context to split double-diffusive instabilities in two categories. The first one is called “thermohaline” and the second one “semi-convective”. The criteria for differentiating these two instabilities as well as the convective instability are expressed with the gradient notations as follows:

$$\text{Stability : } \nabla_{\mu} > 0 \quad \text{and} \quad \nabla_T - \nabla_{\text{ad}} < 0 \quad , \quad (1.19a)$$

$$\text{Convective instability : } \nabla_T - \nabla_{\text{ad}} > -\frac{\chi_{\mu}}{\chi_T} \nabla_{\mu} \quad , \quad (1.19b)$$

$$\text{Thermohaline instability : } \nabla_T - \nabla_{\text{ad}} < -\frac{\chi_{\mu}}{\chi_T} \nabla_{\mu} \quad , \quad \nabla_{\mu} < 0 \quad \text{and} \quad \nabla_T - \nabla_{\text{ad}} < 0 \quad , \quad (1.19c)$$

$$\text{Semi-convective instability : } \nabla_T - \nabla_{\text{ad}} < -\frac{\chi_{\mu}}{\chi_T} \nabla_{\mu} \quad , \quad \nabla_{\mu} > 0 \quad \text{and} \quad \nabla_T - \nabla_{\text{ad}} > 0 \quad . \quad (1.19d)$$

These relationships are illustrated in figure 1.1, which is an adaptation of the one found in Salaris & Cassisi [2017].

### 1.3.2 Modelling stellar turbulence in convective and thermohaline zones

Equations (1.12) and (1.17), and their generalization (1.19), allow to identify stellar regions in which convective and double-diffusive instabilities occur. In these regions, small perturbations around the mean stratification will be amplified until a turbulent regime is reached. Then, in these regions, one needs to account for the turbulent heat and concentration fluxes,  $\mathcal{F}_t$  and  $\mathcal{F}_{\alpha,t}$ , appearing in Eqs. (1.8d) and (1.8e).

In this section, we will detail how these turbulent fluxes are modelled in two particular cases: first, when turbulent motions stem from convection and second, when they stem from the thermohaline instability. Neither the case of the semi-convective instability nor the cases when turbulence is generated by other types of instabilities as already stated at the beginning of this chapter, will be discussed in the following.

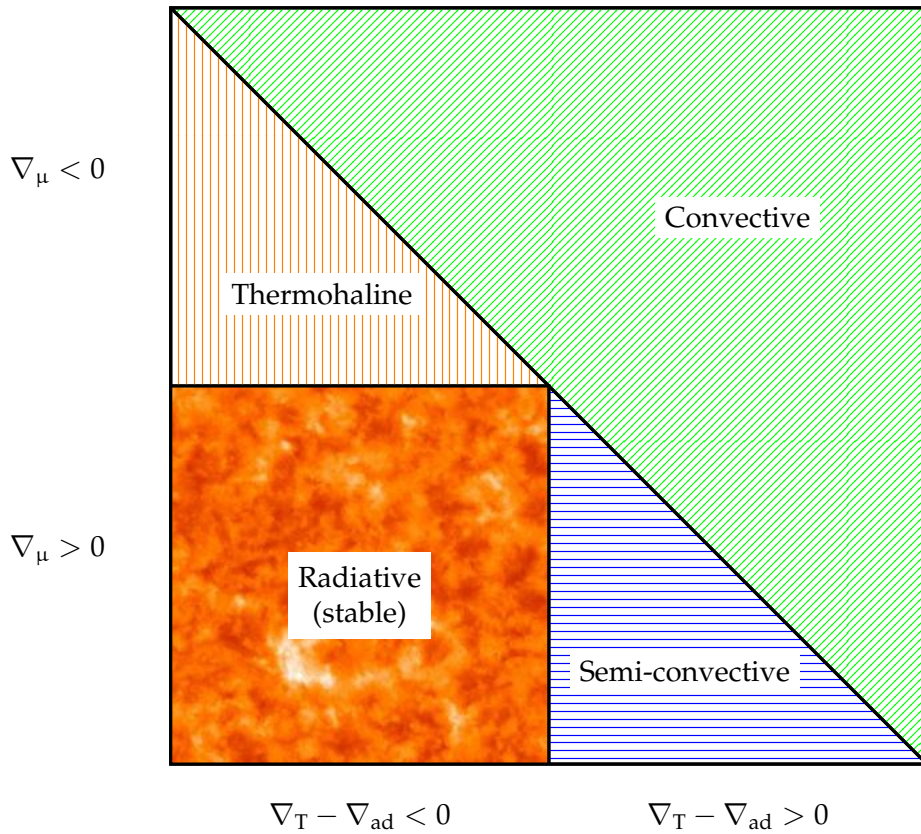


Figure 1.1 – Schematic representation of  $\nabla_{\mu} - (\nabla_T - \nabla_{ad})$  stability for different stellar zones. The diagonal line from the top left to the bottom right represents  $\nabla_L$ . This figure is adapted from Salaris & Cassisi [2017].

### 1.3.2.1 Mixing length theory for turbulent convection

In most stellar evolution calculations, the turbulent fluxes  $\mathcal{F}_t$  and  $\mathcal{F}_{\alpha,t}$  are modelled in convective zones by applying the mixing length theory (MLT) originally proposed by Prandtl [1925] a century ago. This concept of mixing length was then adapted for stellar convection by Biermann [1932] whose work aimed at estimating the depth of stellar convection zones. It relied on the consideration of a stellar flow bubble element moving adiabatically. Böhm-Vitense [1953, 1958] generalized this treatment, improving MLT models by focusing on the transition region between convective and radiative zones. Her model is currently the most used for stellar convective zones. The theory was then formalized based on the mixing length theory of convection from Cox & Giuli [1968].

The MLT states that turbulence in a convective zone can be considered as a group of convective elements (“eddies”) that have the same physical properties – they are assumed to be submitted to small variations with respect to their environment – and the same characteristic dimension in all directions with respect to the radius of the star. This characteristic dimension is called the mixing length and is denoted by  $\Lambda_{MLT}$ :

$$\Lambda_{MLT} \equiv \text{mixing length} \quad .$$

The mixing length can be interpreted as a mean free path, *i.e.* the distance that a turbulent eddy travels before its energetic and thermal content reaches an equilibrium with its surrounding. Usually,  $\Lambda_{\text{MLT}}$  is expressed as a fraction of the total pressure scale height  $H_P$  defined by:

$$H_P = -\frac{dr}{d \ln P} = \frac{P}{\rho g} \quad \text{with} \quad g = \frac{Gm}{r^2} \quad ,$$

where  $g$ ,  $G$  and  $m$  stand respectively for the local stellar gravity, the gravitational constant and the stellar interior mass. The MLT assumes that, after a certain distance of the order of  $H_P$ , a travelling fluid element will stop and invert its motion. Hence, at a radial distance  $r$ , one assumes:

$$\Lambda_{\text{MLT}} = \alpha_{\text{MLT}} \cdot H_P \quad .$$

The so-called mixing length parameter  $\alpha_{\text{MLT}}$  (of order unity) is calibrated *a priori* on heuristic considerations. Its typical values range from 0.5 to 2.5 and depends on the mass and on the metallicity of the star [Joyce & Chaboyer, 2018]. However, note that its impact regards mostly the thickness of the outer convective region of solar-type stars. The most common method to fix  $\alpha_{\text{MLT}}$  is to make a calibration on the Sun and attempting to match the estimated effective temperature of its photosphere.

In addition to  $\Lambda_{\text{MLT}}$ , one must also specify the typical velocity  $v_{\text{conv.}}$  of the turbulent eddies. To this end, one makes the assumption that the eddy has a density difference  $\delta\rho$  with its surrounding and has been accelerated by the gravitational field  $g$  over a distance proportional to  $\Lambda_{\text{MLT}}$ . The corresponding velocity is given by:

$$v_{\text{conv.}} \propto \sqrt{\max\left(-g \frac{\delta\rho}{\rho}, 0\right)} \Lambda_{\text{MLT}} \quad ,$$

where the max operator aims to filter out the stable case. To estimate  $\delta\rho$ , one can apply the same reasoning as the one used to determine the stability criterion (1.12). In particular, one can estimate  $\delta\rho$  as  $\delta\rho = \rho_\star - \rho_2$  with  $\rho_\star$  given by Eq. (1.9) and  $\rho_2$  given by Eq. (1.10). This leads to:

$$v_{\text{conv.}} \propto \Lambda_{\text{MLT}} \sqrt{\max(N^2, 0)} = \sqrt{\max\left(-g \left(\frac{1}{\rho} \frac{\partial\rho}{\partial r} - \frac{1}{\Gamma_1 P} \frac{\partial P}{\partial r}\right), 0\right)} \quad , \quad (1.20)$$

with  $N^2$  given by Eq. (1.11). An additional ingredient of the model consists in writing the turbulent heat flux in the form:

$$\mathcal{F}_{\text{conv.}} \propto \rho c_p \cdot v_{\text{conv.}} \cdot \delta T \quad ,$$

with  $c_p$  the specific heat at constant pressure. In this equation, the temperature difference can be estimated just as  $\delta\rho$  was, *i.e.* by considering the difference  $T_\star - T_2$  stemming from the adiabatic displacement of a small parcel of fluid over the distance  $\Lambda_{\text{MLT}}$ . This leads to define:

$$\delta T = \left[ \frac{\partial T}{\partial r} - \left( \frac{\partial T}{\partial P} \right)_{s, c_\alpha} \frac{\partial P}{\partial r} \right] \frac{\Lambda_{\text{MLT}}}{2} = (\nabla_T - \nabla_{\text{ad}}) \cdot \frac{T}{H_P} \cdot \frac{\Lambda_{\text{MLT}}}{2} \quad . \quad (1.21)$$

### 1.3. Stellar turbulence models for convection and double diffusion

Note that when the variations of the molecular weight  $\mu$  are neglected, the convective velocity can also be expressed as a function of  $\nabla_T - \nabla_{\text{ad}}$ . In that case, one has:

$$\text{for } \mu = \text{const.} \quad , \quad v_{\text{conv.}} \propto \Lambda_{\text{MLT}} \sqrt{\frac{g}{H_P} \cdot \frac{\chi_T}{\chi_\rho} (\nabla_T - \nabla_{\text{ad}})} \quad ,$$

This formula is the one usually found in the literature, even though Eq. (1.20) is slightly more general. These closures allow to model the turbulent heat flux  $\mathcal{F}_t$ . There only remains to close the turbulent scalar flux  $\mathcal{F}_{\alpha,t}$ . This is achieved by making a diffusion approximation:

$$\mathcal{F}_{\alpha,t,\text{conv.}} = -\rho \mathcal{D}_{\text{conv.}} \frac{\partial c_\alpha}{\partial r} \quad ,$$

where the turbulent diffusion coefficient is defined using  $v_{\text{conv.}}$  and  $\Lambda_{\text{MLT}}$ :

$$\mathcal{D}_{\text{conv.}} \propto v_{\text{conv.}} \cdot \Lambda_{\text{MLT}} \quad .$$

To sum up, in the convective regime and neglecting the variations of  $\mu$ , the turbulent heat and concentration fluxes can be modelled as follows:

**Main hypothesis: turbulence model in convective zones with constant  $\mu$**

$$\Lambda_{\text{MLT}} = \alpha_{\text{MLT}} \cdot H_P \quad (1.22a)$$

$$v_{\text{conv.}} = \Lambda_{\text{MLT}} \sqrt{a_{\text{MLT}} \cdot \frac{g}{H_P} \cdot \frac{\chi_T}{\chi_\rho} (\nabla_T - \nabla_{\text{ad}})} \quad (1.22b)$$

$$\mathcal{F}_t = \mathcal{F}_{\text{conv.}} = \rho c_p \cdot T \cdot b_{\text{MLT}} \cdot v_{\text{conv.}} \cdot \frac{\Lambda_{\text{MLT}}}{H_P} (\nabla_T - \nabla_{\text{ad}}) \quad (1.22c)$$

$$\mathcal{F}_{\alpha,t} = \mathcal{F}_{\alpha,t,\text{conv.}} = -\rho \mathcal{D}_{\text{conv.}} \frac{\partial c_\alpha}{\partial r} \quad \text{with} \quad \mathcal{D}_{\text{conv.}} = c_{\text{MLT}} \cdot v_{\text{conv.}} \cdot \Lambda_{\text{MLT}} \quad (1.22d)$$

Four constants  $\alpha_{\text{MLT}}$ ,  $a_{\text{MLT}}$ ,  $b_{\text{MLT}}$  and  $c_{\text{MLT}}$  must be prescribed in this model. This can be done by making calibrations on stars which properties are well known, such as the Sun. A variant of this model has been proposed by Tassoul *et al.* [1990] in order to account for non-adiabatic stratifications. In this variant, the adiabatic temperature “gradient”  $\nabla_{\text{ad}}$  is replaced by  $\nabla_{\text{conv.}}$ , the average temperature gradient of the whole material field contained within the convective zone. Notable studies [Canuto, 1996, Canuto & Mazzitelli, 1991, 1992, Heiter *et al.*, 2002, Kippenhahn, 1994, Weiss & Charbonnel, 2004] have been dedicated to the improvement of mixing length models. They essentially aimed at assessing the amount of radiative heat loss  $\delta T$  as defined by Eq. (1.21), interpreted as the loss of energy of a moving convective fluid particle during its travel in the stellar medium.

#### 1.3.2.2 Modelling thermohaline turbulence

In Sec. 1.3.1, we put forward a second mechanism (among many) leading to the generation of turbulent motions, namely the thermohaline instability [Charbonnel & Zahn, 2007, Lignieres, 1999, Prat, 2013, Traxler *et al.*, 2011, Ulrich, 1972, Wachlin *et al.*, 2014]. When the radiative heat flux is very large, the thermohaline instability occurs when the criterion (1.17) is met and, under more general conditions, it occurs when the inequalities of Eq. (1.19c) are verified.

In most stellar simulations, the influence of thermohaline turbulence on heat transport is neglected:

$$\mathcal{F}_t = 0 \quad .$$

It is implicitly assumed that thermohaline turbulence takes place in a regime where the radiative transport is overwhelming, *i.e.* in a small Péclet regime. The only turbulent effect that is left is the turbulent transport of the species mass fractions. As previously, this transport is modelled with a diffusion assumption:

$$\mathcal{F}_{\alpha,t,\text{thrm.}} = -\rho \mathcal{D}_{\text{thrm.}} \frac{\partial c_\alpha}{\partial r} \quad .$$

Ulrich [1972] was the first to derive a closure for  $\mathcal{D}_{\text{thrm.}}$ . By considering the results of a linear analysis of the thermohaline instability, he proposed the following expression:

$$\mathcal{D}_{\text{thrm.}} = \alpha_{\text{thrm.}} \cdot \frac{\chi^r}{R_0} \quad \text{with} \quad R_0 = -\frac{2\rho c_p}{3} \cdot \frac{\chi_T}{\chi_\mu} \cdot \frac{\nabla_T - \nabla_{\text{ad}}}{\nabla_\mu} \quad , \quad (1.23)$$

where  $\alpha_{\text{thrm.}}$  is a calibrated constant and  $\chi^r$  is the radiative diffusivity:

$$\chi^r = \frac{\lambda^r}{\rho c_p} \quad \text{with} \quad \lambda^r = \frac{4}{3} \cdot \frac{\text{aRC}\ell}{\rho \kappa^r} \cdot T^3 \quad . \quad (1.24)$$

Following this work, other closures, *e.g.* [Brown *et al.*, 2013, Denissenkov, 2010, Garaud, 2018, Kippenhahn *et al.*, 1980], have been derived from linear stability analyses. In particular, the model of Brown *et al.* [2013] relies on a small Prandtl asymptotic analysis. Let us recall that the Prandtl number characterizes the ratio of kinematic viscosity  $\nu_v$  to radiative diffusivity, *i.e.*:

$$\text{Pr} = \frac{\nu_v}{\chi^r} \quad ,$$

as seen in the introduction of the manuscript. The thermohaline characteristic mixing length  $\Lambda_{\text{thrm.}}$ , velocity  $v_{\text{thrm.}}$  and turbulent diffusion coefficient  $\mathcal{D}_{\text{thrm.}}$  are expressed as:

$$\Lambda_{\text{thrm.}} = 2\pi \left[ \frac{(1 + \text{Sc}^{-1}) \nu_v \chi^r}{\frac{g}{T} \cdot \frac{\chi_T}{\chi_\rho} \left( \frac{\partial T}{\partial r} - \left( \frac{\partial T}{\partial P} \right)_{s,c_\alpha} \frac{\partial P}{\partial r} \right)} \right]^{1/4} \quad \text{with} \quad \text{Sc} = \frac{\nu_v}{\kappa_\mu} \quad , \quad (1.25a)$$

$$v_{\text{thrm.}} = \text{const.} \cdot \frac{\lambda_w \sqrt{2}}{\Lambda_{\text{thrm.}}} \cdot \chi^r \left[ \frac{\frac{g}{T} \cdot \frac{\chi_T}{\chi_\rho} \left( \frac{\partial T}{\partial r} - \left( \frac{\partial T}{\partial P} \right)_{s,c_\alpha} \frac{\partial P}{\partial r} \right)}{\nu_v \chi^r} \right]^{1/4} \quad , \quad (1.25b)$$

$$\mathcal{D}_{\text{thrm.}} = \text{const.} \cdot \chi^r \cdot \frac{\lambda_w^2}{k_z^2 (\lambda_w + \tau_{\text{diff}} \cdot k_z^2)} \quad \text{with} \quad \tau_{\text{diff}} = \frac{\kappa_\mu}{\chi^r} = \text{Sc} \cdot \text{Pr} \quad , \quad (1.25c)$$

where  $\text{Sc}$  and  $\tau_{\text{diff}}$  are respectively the Schmidt and the inverse Lewis number. They are both related to molecular transport and characterize rates of diffusive coefficients. More precisely, the first is the rate of kinematic viscosity to compositional diffusivity  $\kappa_\mu$ , related to the mean molecular mass  $\mu$  (see Eq. (1.4)). And the second is the ratio of the latter to radiative conductivity.

### 1.3. Stellar turbulence models for convection and double diffusion

---

As for  $\lambda_w$  and  $k_z$ , they stand respectively for the wavelength of the fastest growing mode of the linear perturbation and the magnitude of its corresponding horizontal wave number (matching the radial direction in the stellar structure equations formalism). From the dispersion relation derived by [Baines & Gill \[1969\]](#), one may easily assess them as:

$$\lambda_w \approx \begin{cases} \sqrt{\text{Pr}} & \text{if } r_{\text{thrm.}} \ll \text{Pr} \ll 1, \\ \sqrt{\frac{\text{Pr} \cdot \tau_{\text{diff}}}{r_{\text{thrm.}}}} & \text{if } \text{Pr} \ll r_{\text{thrm.}} \ll 1, \end{cases} \quad \text{and} \quad k_z^2 \approx \frac{1}{\sqrt{1 + \tau_{\text{diff}}/\text{Pr}}} \quad \text{with} \quad r_{\text{thrm.}} = \frac{R_0 - 1}{\tau_{\text{diff}}^{-1} - 1}.$$

However, as noticed by [Garaud \[2018\]](#), the semi-analytical model of [Brown \*et al.\* \[2013\]](#) defined by Sys. (1.25) does not account for rotation, magnetism or shearing effects. The latter are very likely to modify the mixing efficiency of thermohaline convection.

#### 1.3.3 Discussion

Mixing length models, such as those detailed in this section, are the most frequently used in stellar evolution simulations. The main reason explaining this popularity is a practical one: these models are simple to implement and, once calibrated, they yield relevant predictions. Still, they usually do not manage to reproduce accurately all the phenomena they are meant to capture. For instance, [Salaris & Cassisi \[2017\]](#) point out that the MLT is often at odds with several helioseismic data.

To overcome these shortcomings, several authors have proposed other types of models. In particular, in a series of papers, [Canuto \[2011a,b,c,d,e\]](#) has advocated the use of Reynolds Stress Models (RSM) to deal with stellar turbulent mixing. In RSMs, the flow is decomposed into a mean and a fluctuating part. Then, evolution equations for the second-order correlations of the fluctuations of velocity, concentration and temperature (or any other relevant field) are derived and closed. RSMs allow for a richer description of the turbulent field than MLT does. However, this comes at the cost of solving extra transport equations, in addition to those introduced in Sys. (1.8).

This computational burden probably explains why RSMs have failed to materialize as an alternative to mixing length models. Another possible reason is that the number of RSMs available to describe stellar mixing flows remains limited. Yet, numerous variants of RSMs have been derived and used in other domains. Some of them [[Besnard \*et al.\*, 1989](#), [Grégoire \*et al.\*, 2005](#), [Schiestel, 2010](#)] are even designed to predict flows dominated by convective-like instabilities. But most of these non-stellar models usually do not capture all the physical phenomena involved in stellar flows. While their core features could be preserved, they would still require some adaptation before being applied to stellar simulations.

Among the elements lacking to RSMs, such as the ones of [Grégoire \*et al.\* \[2005\]](#) and [Besnard \*et al.\* \[1989\]](#), is the fact that they are not meant to predict double-diffusive instabilities. In particular, they are not meant to capture the small Péclet limit of these instabilities, such as described in Sec. 1.3.1.2. This question will be discussed further in chapter 3. More precisely, it will be shown how a small Péclet-small Mach number asymptotic analysis can help adapting RSMs to a stellar context. As for the asymptotic analysis, it will be presented in chapter 2.

## 1.4 Simulating stellar turbulence with MESA

In Sec. 1.2, we detailed how stellar evolution equations can be derived to simulate the evolution of a star. In Sec. 1.3, we indicated how turbulence can be taken into account in these equations, at least in the cases when it is generated by convective and thermohaline instabilities. In the present section, we now aim to describe results obtained by solving these equations and models for three types of stars: a low-mass, an intermediate-mass and a massive star, respectively with an initial mass of 1, 5 and  $75 M_{\odot}$ , with the notation  $M_{\odot}$  corresponding to one “solar mass” in astrophysical units.

### 1.4.1 Description of MESA and of the simulation parameters

To perform our simulations, we use an open-source code called Modules for Experiments in Stellar Astrophysics (MESA) [Paxton *et al.*, 2010]. This code solves structure equations which become equivalent to Sys. (1.8) described in Sec. 1.2, when a thermal and hydrostatic equilibrium is reached. MESA allows to account for convection using several variants of the mixing length theory (MLT), such as the one proposed by Cox & Giuli [1968] or Henyey *et al.* [1965]. These different variants always take a form close to the one described by Sys. (1.22). As for thermohaline turbulence, it is treated using the model by Ulrich [1972], as given by Eq. (1.23). The physics contained by MESA is not restricted to the few elements that have been described so far in this manuscript. A full description of the capabilities of MESA can be found in the series of papers [Paxton *et al.*, 2010, 2013, 2015, 2018, 2019].

Our simulations were set up using input data from the “MESA Isochrones and Stellar Tracks” (MIST) project [Choi *et al.*, 2016, Dotter, 2016]. The goal of the MIST project was to use MESA in order to compute stellar evolutions<sup>2</sup> for a wide variety of stars, with masses between  $0.1 \leq M/M_{\odot} \leq 200$  and metallicities between  $-2$  and  $0.5$ . For our simulations, we used the files corresponding to initial masses of  $1M_{\odot}$ ,  $5M_{\odot}$  and  $75M_{\odot}$  and to an initial composition identical to the Sun’s [Asplund *et al.*, 2009] (see Tab. D). For simplicity, the stars were also assumed to be non-rotating.

A pre-main sequence model with a core temperature of  $T = 5 \times 10^5$  K is chosen for the eponymous evolutionary phase in order to avoid nuclear burning (beginning at  $T \approx 10^6$  K). Note that although this stage is necessary to start the simulation, it is not studied or shown in the next sections. MESA then creates a starting stellar model with a uniform composition and contraction. The constants  $\alpha_{\text{MLT}}$  and  $\alpha_{\text{thrm.}}$  respectively stemming from the “standard” and thermohaline convective models of Henyey *et al.* [1965] and Ulrich [1972] are set as  $\alpha_{\text{MLT}} = 1.82$  and  $\alpha_{\text{thrm.}} = 666$ . The complete set of parameters can be retrieved in Choi *et al.* [2016].

<sup>2</sup>The input files used for these reference simulations have been made freely available on the MIST project website “<http://waps.cfa.harvard.edu/MIST>”.

### 1.4.2 Kippenhahn diagrams

The Kippenhahn diagram allows to identify the different turbulent mixing regions appearing during stellar evolution. The diagrams obtained from the MESA simulations of a  $1M_{\odot}$ , a  $5M_{\odot}$  and a  $75M_{\odot}$  star are respectively displayed in Figs. 1.2, 1.3 and 1.4. The turbulent zones are shown along the Lagrangian mass  $m(r)$  with respect to the stellar time scale. Equivalently, a “model number” can be used instead of time in order to emphasize periods where important events occur. It corresponds to quasi-stationary converged states of spatial stellar profiles with respect to  $m(r)$ . In terms of physical time, the frequency of these “model numbers” depends on the characteristic timescales of stellar evolution. Then, from the very slow main-sequence to the fast giant branch phase, the number of its iteration automatically increases.

This choice of representation is motivated by a global identification of stellar stages and a better visualization of the mixing zones appearing in the early life of the stars. Some reference times are arbitrarily displayed along Figs. 1.2, 1.3 and 1.4 in order to overcome the lacks of this perspective.

In the Kippenhahn diagrams, convection and thermohaline mixing zones are located using the criteria given by Sys. (1.19). Besides, they also displays the nuclear reaction specific energy generation rate  $[\log(\epsilon_{\text{nuc}})]$  from which neutrinos reactions have been subtracted, as defined in Sys. (1.3). These diagrams are shown for the duration of the main-sequence and the beginning of red-giant branch of these three stars. The transition towards the red-giant phase can be identified on the Kippenhahn diagrams by spotting the occurrence of a hydrogen burning shell, located by the legend “H-burn.”, surrounding the helium core, written “He-core”, and highlighted by the blue color of  $\log(\epsilon_{\text{nuc}})$ . More precisely, the main-sequence and the red-giant-branch stages are respectively denoted MS and RGB in red at the top of each diagram with an approximative reference time, representative of the transition between both continuous processes. They may be estimated at:

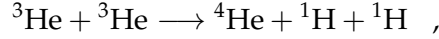
$$\begin{cases} t \approx 10.287 \text{ Gyr} & \text{for the } 1 M_{\odot} \text{ star} \quad , \\ t \approx 102.7 \text{ Myr} & \text{for the } 5 M_{\odot} \text{ star} \quad , \\ t \approx 3.588 \text{ Myr} & \text{for the } 75 M_{\odot} \text{ star} \quad . \end{cases}$$

When comparing these diagrams, one can observe that during the main sequence and most of the red-giant phase, convection occurs in the outer layers of the lightest star while it occurs in the core of the two highest mass stars.

Moreover, during the MS, the  $75 M_{\odot}$  star suffers from a substantial mass loss mainly due to stellar winds and hence, loses most of its envelope. The transition from a convective envelope to a convective core as the mass increases is well documented and some explanation about its existence can be found for instance in Prialnik [2000]. Figure 1.5 illustrates this transition for the main sequence phase.

Regarding thermohaline mixing, we can observe that the conditions required for its development are met for all three stars during the red-giant phase. Close to the burning hydrogen shell, and mostly below it, MESA predicts the existence of a thermohaline mixing zone.

As pointed out by Eggleton *et al.* [2006], a slight decrease of the mean molecular weight [Ulrich, 1972] occurs close to the hydrogen burning shell, because of the particular nuclear reaction taking place in this region, namely:



which converts two nuclei into three nuclei. The mean mass per nucleus drops from three to two. This decrease can give rise to an inversion of the gradient of the mean molecular weight  $\mu$ , and to conditions which favor the development of the thermohaline instability.

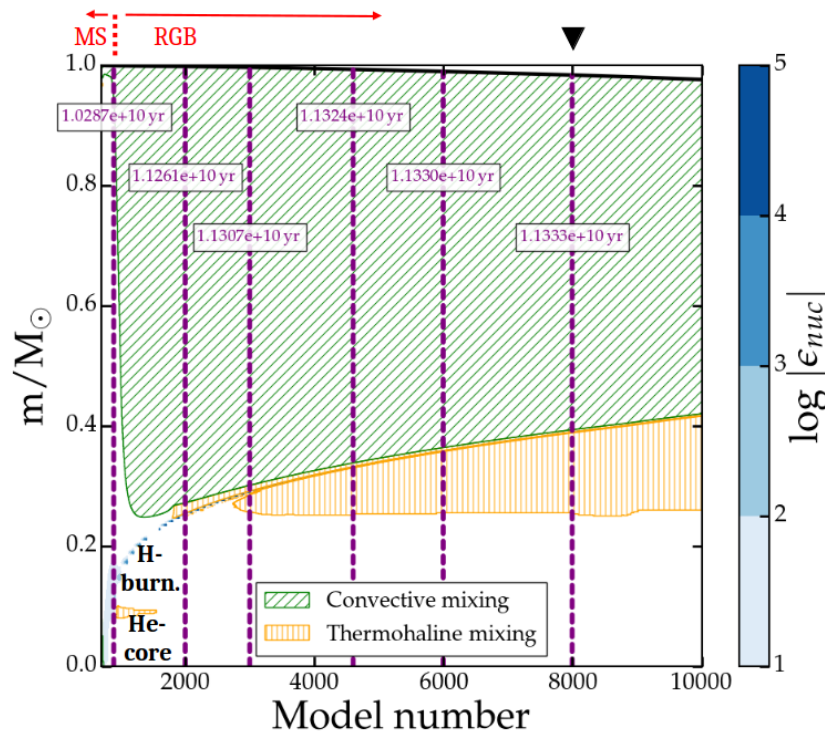


Figure 1.2 – Kippenhahn diagrams of a  $1 M_{\odot}$  star from  $t = 0.43832$  Myr to  $t = 13.349$  Gyr. The colored bar corresponds to the logarithm of nuclear reaction specific energy generation rate  $[\log(\epsilon_{\text{nuc}})]$ . The helium core and the hydrogen burning shell are respectively identified by “He-core” and “H-burn.”. Convection and thermohaline zones are shown and defined with respect to Sys. (1.19). The black triangle displayed over one of the dashed purple vertical lines showing specific times of evolution, represents the spatial profile plotted in Sec. 4.10. The “model number” corresponds to a non-linear representation of time.

### 1.4.3 Non-dimensional numbers

Thanks to the Kippenhahn diagram, we have identified regions where convective and thermohaline turbulent mixing takes place. We can now examine the value of the non-dimensional numbers characterizing these turbulent zones.

More precisely, our focus is on the turbulent Mach, Reynolds and Péclet numbers, respectively denoted by  $M_t$ ,  $Re_t$  and  $Pe_t$ . As explained in the introduction these numbers play a key role in defining the turbulent state of the flow and in specifying how heat transport by conduction and radiation interacts with the turbulent field. First of all, let us recall that  $M_t$ ,  $Re_t$  and  $Pe_t$

### 1.4. Simulating stellar turbulence with MESA

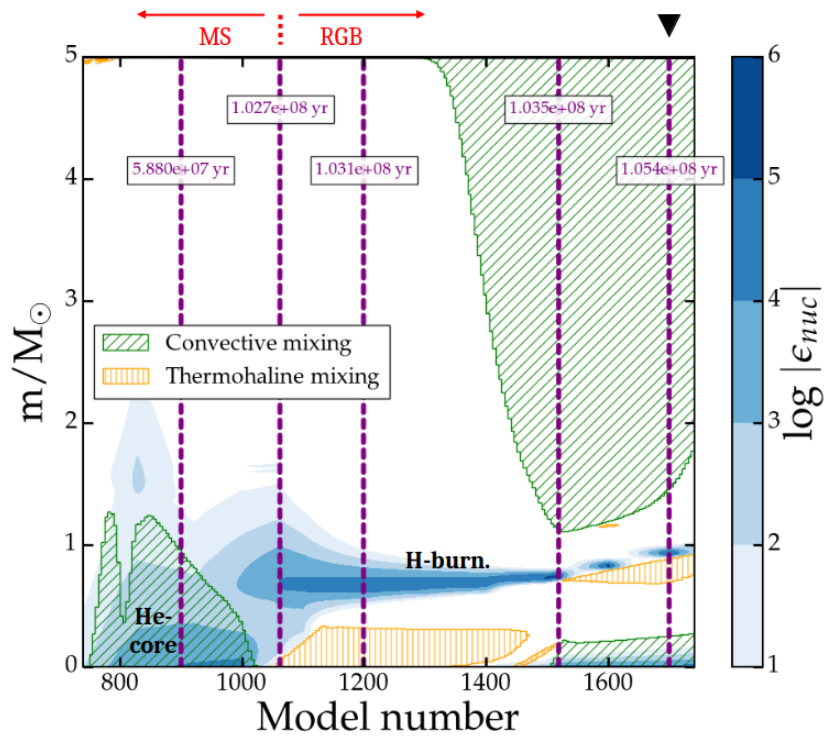


Figure 1.3 – Same as figure 1.2, but for a  $5 M_{\odot}$  star from  $t = 0.6396$  Myr to  $t = 0.1062$  Gyr.

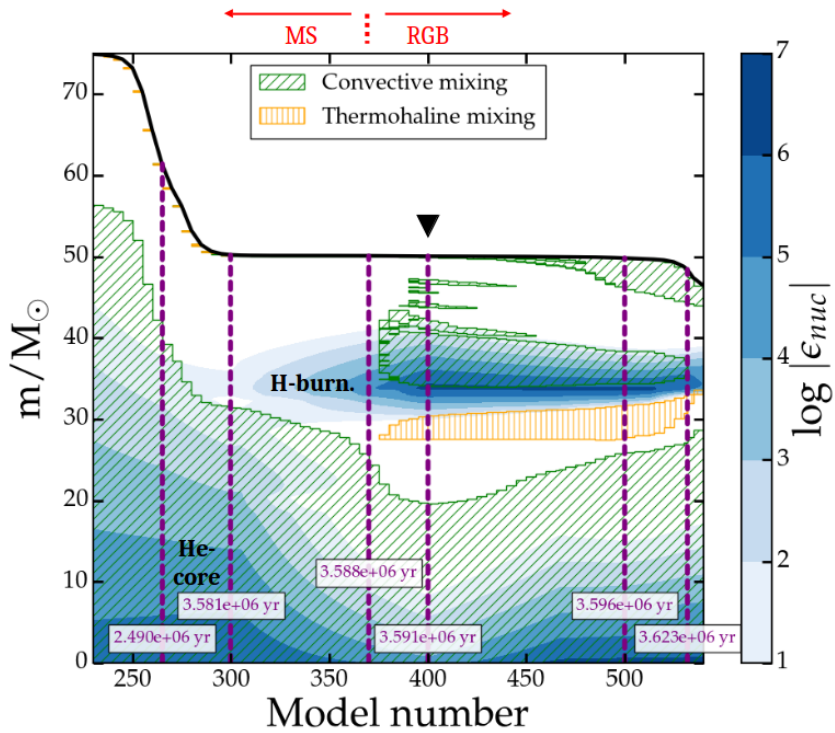


Figure 1.4 – Same as figure 1.2, but for a  $75 M_{\odot}$  star from  $t = 0.02325$  Myr to  $t = 3.657$  Myr.

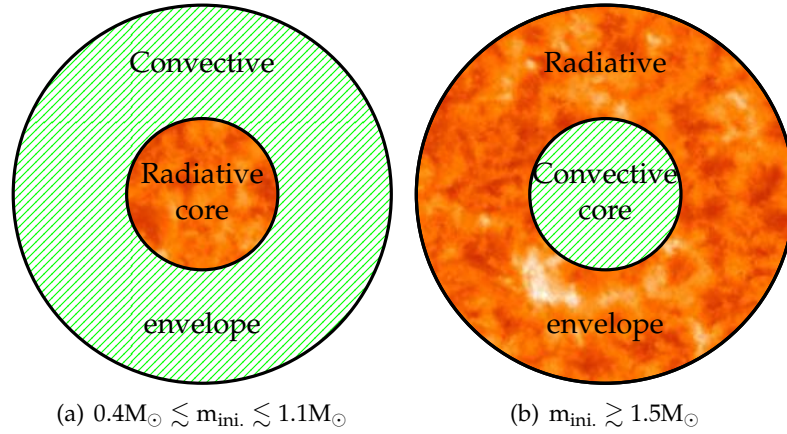


Figure 1.5 – Convective structure of stars during the main sequence phase.

are defined by:

$$M_t = \frac{u_0}{c_s} \quad , \quad \text{Re}_t = \frac{\nu_t}{\nu_v} \quad \text{and} \quad \text{Pe}_t = \frac{\nu_t}{\chi^r} \quad , \quad (1.26)$$

where  $u_0$  is the characteristic value of the turbulent velocity,  $\nu_t$  is the diffusivity of turbulent eddies,  $\nu_v$  is the kinematic viscosity and  $\chi^r$  is the radiative diffusivity defined by Eq. (1.24).

The values of  $\chi^r$  and  $c_s$  can be determined knowing respectively the Rosseland mean opacity  $\kappa^r$  and the generalized adiabatic exponent  $\Gamma_1$ . These quantities are provided directly as output of the code MESA. For the kinematic viscosity  $\nu_v$ , we use the “Pseudo-ion in Jellium” model of Arnault [2013]. The latter predicts viscosity and diffusion coefficients in plasmas where several constituent are being mixed. It is well suited to the strongly coupled regime which is encountered in stellar flows.

Concerning the quantities related to turbulence,  $u_0$  and  $\nu_t$ , we proceed as follows. In convective regions, we use the convective velocity  $v_{\text{conv.}}$  and the convective diffusion coefficient  $\mathcal{D}_{\text{conv.}}$ , as defined in Sys. (1.22). In other words, we set:

$$\text{Convective zone : } u_0 = v_{\text{conv.}} \quad \text{and} \quad \nu_t = \mathcal{D}_{\text{conv.}} \quad .$$

In thermohaline regions, we use the model of Brown *et al.* [2013] to estimate the turbulent velocity and diffusivity:

$$\text{Thermohaline zone : } u_0 = v_{\text{thrm.}} \quad \text{and} \quad \nu_t = \mathcal{D}_{\text{thrm.}} \quad ,$$

with  $\mathcal{D}_{\text{thrm.}}$  and  $v_{\text{thrm.}}$  given by Eqs. (1.25c) and (1.25b).

With these prescriptions, we can compute the turbulent Mach, Péclet and Reynolds numbers in our three MESA simulations. Profiles of these quantities are plotted in Figs. 1.6-1.8 at the onset of the red-giant phase of each star. In addition, the ratio of radiative to material pressure  $P^r/P^m$ , *i.e.* the ratio of Eq. (1.5) to Eq. (1.4), is displayed at the same time. They are supplied as outputs of MESA.

## 1.4. Simulating stellar turbulence with MESA

It can be seen that in convective zones, one always has:

$$\text{Convective zone : } M_t \ll 1 \text{ , } Pe_t \gg 1 \text{ and } Re_t \gg 1 \text{ .}$$

In thermohaline zones, however, one has:

**Main result: orders of magnitude of  $M_t$  and  $Pe_t$  in thermohaline zones**

$$\text{Thermohaline zone : } M_t \ll 1 \text{ and } Pe_t \ll 1 \text{ with } M_t \ll Pe_t \text{ .}$$

As for the Reynolds number, it remains moderate for the low and intermediate mass stars but becomes large for massive stars:

$$\text{Thermohaline zone : } Re_t \gtrsim 1 \text{ for } M = 1M_\odot \text{ or } 5M_\odot \text{ and } Re_t \gg 1 \text{ for } M = 75M_\odot \text{ .}$$

Finally, the radiative pressure  $P^r$  is negligible with respect to the material one  $P^m$  in the lightest stars, whatever the mixing zone considered:

$$P^r \ll P^m \text{ for } M = 1M_\odot \text{ or } 5M_\odot \text{ .}$$

However, in the same zones, the radiative contribution to total pressure becomes much significant for massive stars:

**Result: contribution of  $P^r$  with respect to  $P^m$  in massive stars**

$$P^r \gtrsim P^m \text{ for } M = 75M_\odot \text{ .}$$

While not plotted here, similar observations would be made at other times in the red-giant phase.

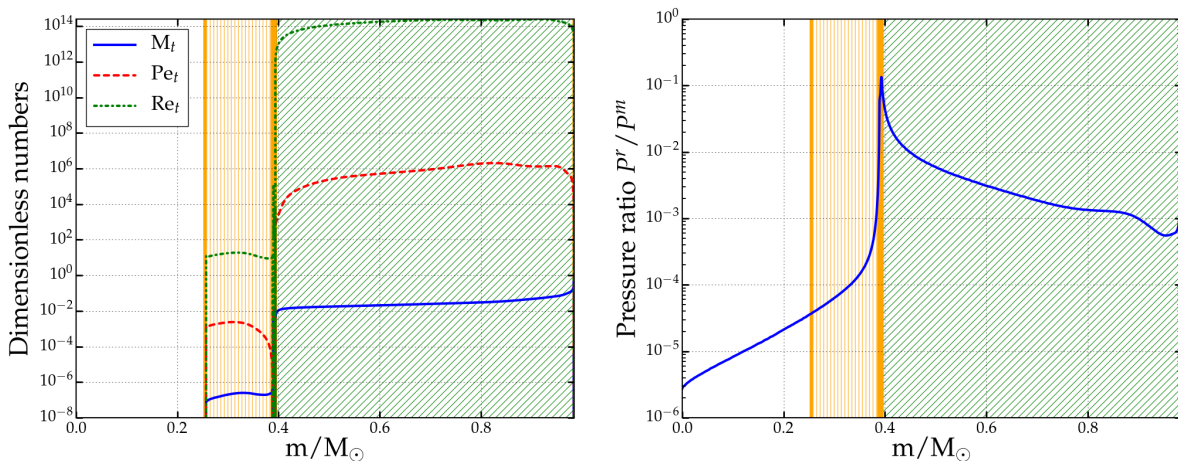


Figure 1.6 – Turbulent Mach, Reynolds and Péclet numbers, as well as pressure ratio  $P^r/P^m$ , for a  $1 M_\odot$  star (vertical hatching: thermohaline zone ; inclined hatching: convective zone). The profile is shown at  $t = 11.333$  Gyr (see the black triangle at the top of the Kippenhahn diagram of Fig. 1.2).

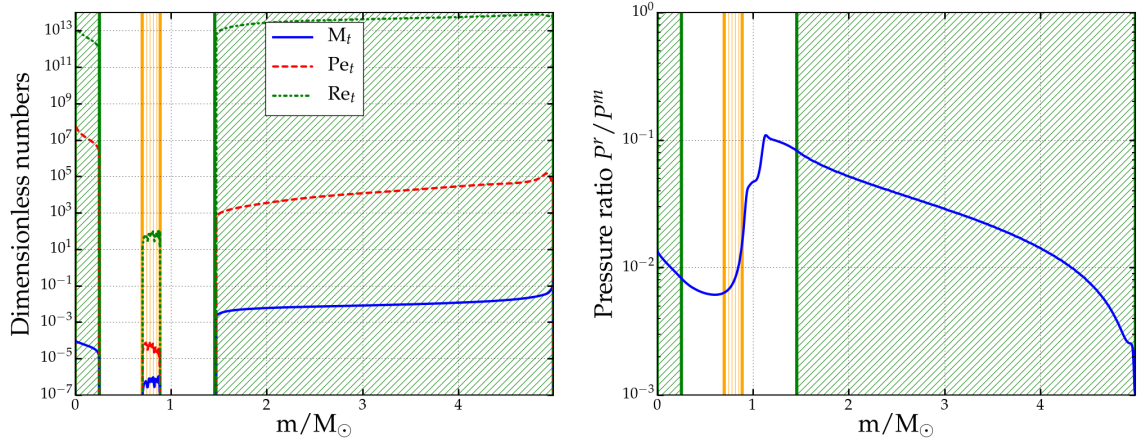


Figure 1.7 – Turbulent Mach, Reynolds and Péclet numbers, as well as pressure ratio  $P^r/P^m$ , for a  $5 M_\odot$  star (vertical hatching: thermohaline zone ; inclined hatching: convective zone). The profile is shown at  $t = 0.1054$  Gyr (see the black triangle at the top of the Kippenhahn diagram of Fig. 1.3).

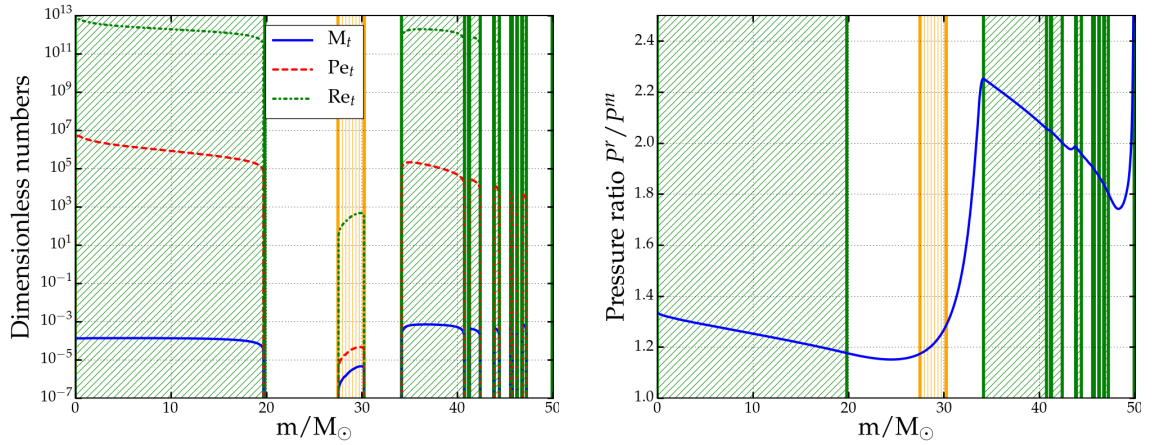


Figure 1.8 – Turbulent Mach, Reynolds and Péclet numbers, as well as pressure ratio  $P^r/P^m$ , for a  $75 M_\odot$  star (vertical hatching: thermohaline zone ; inclined hatching: convective zone). The profile is shown at  $t = 3.591$  Myr (see the black triangle at the top of the Kippenhahn diagram of Fig. 1.4).

## 1.5 Conclusion

We performed simulations with MESA of a low-mass star of mass  $1M_\odot$ , an intermediate-mass star of mass  $5M_\odot$  and a massive star of mass  $75M_\odot$ . We then identified the regions where convective and thermohaline mixing take place. Finally, we computed the turbulent Mach, Péclet and Reynolds number in these regions. The main conclusion is that small Mach and small Péclet numbers are observed in the thermohaline regions, and that, in addition, a high Reynolds number and a substantial amount of radiative pressure compared to the matter one, are reached when the star is massive. By contrast, convective regions are characterized by small Mach and high Péclet numbers, along with high Reynolds numbers.

As explained in the introduction, small Mach small Péclet turbulent flows raise several challenges in terms of modelling. Some of them are addressed in the next chapters.

## 1.5. Conclusion

---

# 2

## Derivation and validation of a ( $M_t \ll 1; Pe_t \ll 1$ ) asymptotic analysis

“ Careless of flowers that in perennial blow,  
Round the moist marge of Persian fountains cling;  
Heedless of Alpine torrents thundering  
Through icy portals radiant as heaven’s bow;  
I seek the birth-place of a native Stream.  
All hail ye mountains, hail thou morning light!  
Better to breathe upon this aëry height  
Than pass in needless sleep from dream to dream;

WILLIAM WORDSWORTH  
*The River Duddon: A Series of Sonnets*

### Contents

<b>2.1</b>	<b>Introduction</b> . . . . .	<b>38</b>
<b>2.2</b>	<b>Flow description</b> . . . . .	<b>39</b>
2.2.1	Hydro-radiative instantaneous equations . . . . .	39
2.2.2	Velocity, pressure and temperature evolutions . . . . .	42
2.2.3	Average flow as a background state . . . . .	44
2.2.4	Dimensionless equations for the fluctuations . . . . .	45
<b>2.3</b>	<b>Small Mach-small Péclet number approximation (<math>Pe_t \lesssim M_t \ll 1</math>)</b> . . .	<b>49</b>
2.3.1	Main conditions . . . . .	49
2.3.2	Main results of the asymptotic analysis . . . . .	52
2.3.3	Synthesis of the asymptotic analysis . . . . .	58
<b>2.4</b>	<b>Small Péclet-small Mach number approximation (<math>M_t \ll Pe_t \ll 1</math>)</b> . . .	<b>58</b>
2.4.1	Main conditions . . . . .	58
2.4.2	Synthesis of the asymptotic analysis . . . . .	60
<b>2.5</b>	<b>Validation of the asymptotic analysis</b> . . . . .	<b>61</b>
2.5.1	Numerical method . . . . .	61
2.5.2	Rayleigh-Taylor flow configuration . . . . .	62
2.5.3	Dimensionless numbers . . . . .	64
2.5.4	General evolution of the flow . . . . .	65
2.5.5	Validation of the asymptotic analysis . . . . .	68
<b>2.6</b>	<b>Conclusion</b> . . . . .	<b>77</b>

## 2.1 Introduction

In the previous chapter 1, we detailed how turbulent mixing zones encountered in the cores of mid-size to massive stars can undergo phases characterized by a small turbulent Mach number  $M_t$  and a small turbulent Péclet number  $Pe_t$ :

$$M_t \ll 1 \quad \text{and} \quad Pe_t \ll 1 \quad .$$

Let us recall that the Péclet number is here defined as the ratio between the radiation transport timescale and the turbulent one:

$$Pe_t \equiv \frac{\tau_{\text{radiation}}}{\tau_{\text{turbulence}}} \quad ,$$

and that the turbulent Mach number compares the turbulent characteristic velocity to the speed of sound:

$$M_t \equiv \frac{u_0}{c_s} \quad .$$

The asymptotic analysis of small-Mach number flows is a core element of fluid mechanics. It is involved in the study of flows as diverse as those encountered in geophysics (ocean, atmosphere [Botta *et al.*, 1999, Durran, 1989, Shirgaonkar & Lele, 2006]), engine combustion (aeronautics, automotive industry [de Charentenay *et al.*, 2001]), supernova explosions [Almgren *et al.*, 2008, 2006a,b] or inertial confinement fusion experiments [Sanz *et al.*, 2006].

The objective of these asymptotic analyses is to determine an approximation of the real flow allowing to filter out acoustical phenomena. The latter are indeed reaching an equilibrium with their environment on a timescale much shorter than the hydrodynamic one. Small-Mach asymptotic approximations allow to determine this equilibrium without the need to compute the fast acoustical interactions which have been required to reach it.

Similarly, when the Péclet number is small, an asymptotic analysis can be carried out in order to formulate an approximation of the real flow allowing to capture a thermal equilibrium resulting from the fast transport of temperature fluctuations by the radiative field. Small-Péclet approximations are usually considered jointly with small Mach number approximations, that they complete and modify. They have been the subject of numerous studies regarding stellar cores such as Spiegel [1962], Gough [1969], Lignieres [1999], Feireisl & Novotný [2009], Novotný *et al.* [2011], Prat [2013] and Maity & Kumar [2014]. However, none of these studies account for the presence of mixing which is one of the key aspects of stellar turbulence we would like to deal with. In particular, these previous analyses cannot be used to capture double-diffusive instabilities [Graud, 2018, Schmitt, 1994]. Besides, non-ideal equations of state are often involved in stellar interiors and the radiative pressure is not necessarily negligible in massive stars. Finally, nuclear reactions may take place in such stellar flows. These aspects have mostly been left aside in the previously mentioned studies and their impact on small Mach-small Péclet approximations should be considered.

The main objective of this chapter is thus to derive a small Mach-small Péclet number approximation that is valid for stellar mixing zones in the presence of a non-negligible radiative pressure and of reactions.

In the first section, an asymptotic analysis based on the evolution equations of the fluctuations of velocity, temperature and pressure is proposed. This operation allows to determine asymptotic expressions relating the fluctuating velocity divergence  $\text{div}\mathbf{u}'$  and the fluctuating heat conduction term  $\mathcal{C}'$  to other flow parameters. We then discuss how these expressions can be used to determine the stability criterion of a mean stratification. In particular, we show that this criterion is not the same in the small and high Péclet limits.

The second section deals with the validation of the approach, using the compressible Navier-Stokes code **TRICLADE** [Griffond & Souldard, 2014]. For this purpose, three DNS simulations of a radiative Rayleigh-Taylor instability are performed, each expected to evolve within different orders of turbulent Péclet numbers. The verification of the main conditions of the ( $M_t \ll 1$  ;  $Pe_t \ll 1$ ) approximation are obtained, along with the predicted orders of  $P'/\bar{P}$  and  $T'/\bar{T}$ . The validity of  $\text{div}\mathbf{u}'$  and  $\mathcal{C}'$  asymptotic expressions are shown to be qualitatively consistent with their simulated values at different times. Besides, the predictions of their density- and velocity-related correlations agree with their differentiated computations. Finally, the change of stability criterion related to the mean stratification is proven to be effective within each Péclet asymptotic regime.

## 2.2 Flow description

### 2.2.1 Hydro-radiative instantaneous equations

The flow field considered is a plasma defined by its density  $\rho$ , its velocity  $\mathbf{u}$ , the mass fractions (or concentrations) of the present ions  $c_\alpha$  for  $\{\alpha = 1, \dots, N_s\}$  with  $N_s$  the number of species and its specific internal energy  $e^m$  of ions and electrons. The plasma is also submitted to a gravitational force  $\mathbf{g}$  and is coupled to a radiative field of volumetric energy  $E^r$ . Within stellar interiors, the latter obeys the equilibrium diffusion approximation, as found in Mihalas & Mihalas [2013].

The evolution of the hydro-radiative flow is then given by the following equations, which correspond to Navier-Stokes equations, retrievable for instance in Giovangigli [2012], coupled with radiation treated in the diffusion limit:

$$\begin{cases} D_t \rho = -\rho \text{div} \mathbf{u} \quad , & (2.1a) \\ \rho D_t u_i = -\partial_i P - \partial_j \Pi_{ij} + \rho g_i \quad , & (2.1b) \\ \rho D_t c_\alpha = -\partial_j \mathcal{F}_{\alpha j} + \mathcal{S}_\alpha \quad , & (2.1c) \\ \rho D_t e^i = \rho \varepsilon - P^i \text{div} \mathbf{u} - \partial_j \mathcal{F}_j^i + W^{i-e} + \mathcal{S}^i \quad , & (2.1d) \\ \rho D_t e^e = -P^e \text{div} \mathbf{u} - \partial_j \mathcal{F}_j^e - \Omega^{e-r} - W^{i-e} + \mathcal{S}^e \quad , & (2.1e) \\ D_t E^r = -(E^r + P^r) \text{div} \mathbf{u} - \partial_j \mathcal{F}_j^r + \Omega^{e-r} + \mathcal{S}^r \quad , & (2.1f) \end{cases}$$

with the notations  $\partial_j \cdot$ ,  $D_t \cdot$  and  $\text{div} \cdot$  referring respectively to the partial derivative with respect

## 2.2. Flow description

---

to the spatial coordinate  $x_j$ , to the Lagrangian time derivative and to the divergence operator. In particular, one has the velocity divergence written as  $\text{div} \mathbf{u} = \partial_j u_j$ , and, for any quantity  $q$ ,  $D_t q = \partial_t q + u_j \partial_j q$  with  $\partial_t$  the partial derivative with respect to the time  $t$ . Note also that the Einstein convention on the summation of indices is used for latin letters. However, it will not be so for greek indices, in particular for the index  $\alpha$  attached to the species. For ease of expression, the superscripts “i”, “e”, “m” and “r” regarding flow variables are related respectively to the field of ions, electrons, matter (containing ions and electrons) and radiation.

The pressure and specific energy of the material medium, written respectively  $P^m$  and  $e^m$ , are considered to be the sum of their ionic and electronic parts, such that:

$$P^m = P^i + P^e \quad \text{and} \quad e^m = e^i + e^e \quad .$$

As for the pressure  $P$  appearing in the momentum equation (2.1b), it is the total pressure of the radiative flow, *i.e.* the sum of the material and radiative pressures, denoted  $P^m$  and  $P^r$ :

$$P = P^m + P^r \quad . \quad (2.2)$$

In low- and intermediate-mass stars, such as the Sun, radiative pressure is usually negligible compared to material pressure. However, this is not the case in massive ones, where both components can be of the same order, as shown in chapter 1.

Besides, the medium is supposed to be optically thick and hence, the assumption of local thermodynamic equilibrium as well as of thermal equilibrium between matter and radiation entail the ionic, electronic and radiative temperatures to be equal:

$$T^i = T^e = T^r \quad .$$

As a result, a single temperature  $T$  is needed to describe radiation and matter. Within the setting of Sys. (2.1) and following the previous properties, it may be noticed that, the total specific energy  $e$  can be expressed with respect to its material and volumetric radiative parts, such that:

$$e = e^m + E^r / \rho \quad . \quad (2.3)$$

In this way, relating to Eqs. (2.2) and (2.3), the same sum of matter and radiative contributions is applied to the specific total enthalpy  $h$ . The latter is defined by:

$$h = e + P / \rho = h^m + h^r \quad \text{with} \quad \begin{cases} h^m = e^m + P^m / \rho \quad , \\ h^r = (E^r + P^r) / \rho \quad . \end{cases}$$

Since the flow obeys the equilibrium diffusion approximation, the radiative pressure and energy are expressed as:

$$P^r = \frac{1}{3} E^r \quad \text{and} \quad E^r = a_R T^4 \quad , \quad (2.4)$$

where the radiation constant  $a_R = 4\sigma_{SB}/c_\ell$  is obtained from the Stefan-Boltzmann constant  $\sigma_{SB}$  and the light speed  $c_\ell$ .

The gravitational force  $\mathbf{g}$  has been introduced in Eq. (2.1b). In the same relation, the viscosity tensor  $\Pi_{ij}$  is defined by:

$$\Pi_{ij} = -2\mu_v \left( S_{ij} - \frac{1}{3} \text{div} \mathbf{u} \delta_{ij} \right) , \quad (2.5)$$

where  $S_{ij} = (\partial_j u_i + \partial_i u_j) / 2$  stands for the instantaneous strain-rate tensor and  $\mu_v = \rho \nu_v$  is the dynamic viscosity of the plasma with  $\nu_v$  its kinematic viscosity. The associated viscous dissipation rate  $\varepsilon$  is defined by:

$$\rho \varepsilon = -\Pi_{ij} S_{ji} . \quad (2.6)$$

In Eq. (2.1c), the diffusion flux of the species mass fraction  $c_\alpha$  is defined, as in [Giovangigli \[2012\]](#), by a Fickian approximation of the form:

$$\mathcal{F}_{\alpha j} = \begin{cases} -\rho \mathcal{D}^{(\alpha)} \partial_j c_\alpha & \text{for } \alpha = 1, \dots, N_s - 1 \quad , \\ -\sum_{\alpha=1}^{N_s-1} \mathcal{F}_{\alpha j} & \text{for } \alpha = N_s \quad , \end{cases} \quad (2.7)$$

where  $\mathcal{D}^{(\alpha)}$  is the diffusion coefficient of the species  $\alpha$ . Note that the validation proposed in this work in Sec. 2.5 regards a binary mixture ( $N_s = 2$ ) which means that, for both gases, there is a single inter-species diffusion coefficient that will be noted  $\mathcal{D}$ .

The terms denoted  $S_\alpha$ ,  $S^i$ ,  $S^e$  and  $S^r$  appearing in concentration and energy equations characterize respectively the source terms of the species  $\alpha$ , of ions, of electrons and of the radiation field. The ion-electron and the electron-radiation exchange terms, written respectively  $W^{i-e}$  and  $\Omega^{e-r}$ , are the coupling terms defined in energy equations (2.1d), (2.1e) and (2.1f).

Finally, referring to Sys. (2.1), the last unspecified terms are the ionic, electronic, radiative and total energy fluxes, denoted respectively  $\mathcal{F}_j^i$ ,  $\mathcal{F}_j^e$ ,  $\mathcal{F}_j^r$  and  $\mathcal{F}_j$ . Given that  $e$  is the total specific energy,  $\mathcal{F}_j$  has two contributions, a material one  $\mathcal{F}_j^m$ , which combines the ionic and electronic parts, and a radiative one  $\mathcal{F}_j^r$ :

$$\mathcal{F}_j = \mathcal{F}_j^m + \mathcal{F}_j^r \quad \text{with} \quad \mathcal{F}_j^m = \mathcal{F}_j^i + \mathcal{F}_j^e .$$

The material term  $\mathcal{F}_j^m$  is itself split into a thermal conduction contribution and an enthalpy mixing one:

$$\mathcal{F}_j^m = -\lambda^m \partial_j T + \sum_{\alpha} h_{,\alpha}^m \mathcal{F}_{\alpha j} ,$$

where  $\lambda^m$  is the thermal conductivity of the plasma and  $h_{,\alpha}^m$  represents, as will be explicitly expressed by Eq. (2.10), the differential of the material enthalpy  $h^m$  with respect to the mass fraction  $c_\alpha$  of the species  $\alpha$  at constant other thermodynamic variables.

As for the radiative flux, the equilibrium diffusion assumption allows to express it as:

$$\mathcal{F}_j^r = -\lambda^r \partial_j T \quad \text{with} \quad \lambda^r = \frac{4}{3} \frac{c_\ell a_R}{\rho \kappa^r} T^3 .$$

## 2.2. Flow description

---

In this expression,  $\kappa^r$  is the Rosseland opacity and is related to the Rosseland mean free path  $\Lambda^r$ , according to Chandrasekhar [1957], by:

$$\kappa^r = \frac{1}{\rho \Lambda^r} .$$

Let us remark that a total conductivity  $\lambda$  can be defined by summing the radiative and material contributions  $\lambda = \lambda^m + \lambda^r$ .

It is worth noting that, given the equilibrium diffusion assumption, a global specific heat of the photon-ion-electron continuum can be defined by differentiating the total specific energy  $e$  with respect to the temperature  $T$  and the density  $\rho$ . This yields the following specific total heat at constant volume  $c_v$  such that:

$$c_v = c_v^m + c_v^r \quad \text{with} \quad c_v^m = \sum_{\alpha} c_{v,\alpha}^m c_{\alpha} \quad \text{and} \quad c_v^r = \frac{4a_R T^3}{\rho} ,$$

where  $c_{v,\alpha}^m$  stands for the specific heat at constant volume of each species  $\alpha$ . As shown by the expression of the radiative specific heat  $c_v^r$ , it depends on temperature and density, in opposition to  $c_v^m$  in the case of ideal gases. From there, one can also define a total temperature diffusivity  $\chi$  using the total conductivity  $\lambda$  and the total specific heat  $c_v$ :

$$\chi = \frac{\lambda}{\rho c_v} ,$$

which accounts for the contributions of matter and radiation.

At last, the pressures and internal energies are considered to be differentiable functions of the temperature, density and concentrations only, so that:

$$P \equiv P(\rho, T, c_{\alpha}) \quad \text{and} \quad e \equiv e(\rho, T, c_{\alpha}) . \quad (2.8)$$

### 2.2.2 Velocity, pressure and temperature evolutions

The asymptotic analysis proposed below in Sec. 2.3 will deal with the properties of the velocity field  $\mathbf{u}$ , of the total pressure  $P$  and of the temperature  $T$ . The evolution equation of  $\mathbf{u}$  is given in Eq. (2.1b) but those of  $P$  and  $T$  still need to be made explicit.

The evolution of these two quantities can be deduced from relations (2.8) applied to Sys. (2.1) by using the differentiation chain rule with  $P$  and  $e$ , namely by writing that:

$$D_t P = P_{,T} D_t T + P_{,\rho} D_t \rho + \sum_{\alpha} P_{,\alpha} D_t c_{\alpha} \quad \text{and} \quad D_t e = e_{,T} D_t T + e_{,\rho} D_t \rho + \sum_{\alpha} e_{,\alpha} D_t c_{\alpha} , \quad (2.9)$$

where the notations  $f_{,T}$ ,  $f_{,\rho}$  and  $f_{,\alpha}$  for a function  $f(\rho, T, c_{\alpha})$  have the meanings:

$$f_{,T} = \partial_T f|_{\rho, c_{\alpha}} , \quad f_{,\rho} = \partial_{\rho} f|_{T, c_{\alpha}} \quad \text{and} \quad f_{,\alpha} = \partial_{c_{\alpha}} f|_{\rho, T, c_{\beta \neq \alpha}} . \quad (2.10)$$

Then, by combining these equations and after using some of Maxwell's thermodynamical relations, one obtains the following result for the total pressure P:

$$D_t P = -\gamma_1 P \text{div} \mathbf{u} + (\gamma_3 - 1) \mathcal{C} + \mathcal{S}_P + \mathcal{D}_P \quad , \quad (2.11)$$

and, for the temperature T:

$$D_t T = -(\gamma_2 - 1) T \text{div} \mathbf{u} + \frac{\mathcal{C}}{\rho c_v} + \frac{\mathcal{S}_T}{\rho c_v} + \frac{\mathcal{D}_T}{\rho c_v} \quad , \quad (2.12)$$

with the notations:

$$\begin{aligned} \mathcal{S}_P &= (\gamma_3 - 1) \mathcal{S} - \sum_{\alpha} [(\gamma_3 - 1) e_{r,\alpha} - P_{r,\alpha}/\rho] \mathcal{S}_{\alpha} \quad , \quad \mathcal{S}_T = \mathcal{S} - \sum_{\alpha} e_{r,\alpha} \mathcal{S}_{\alpha} \quad , \\ \mathcal{S} &= \rho \varepsilon + \mathcal{S}^i + \mathcal{S}^e + \mathcal{S}^r \quad , \quad c_v = e_{T} \quad . \end{aligned}$$

In Eqs. (2.11) and (2.12),  $\mathcal{C}$  stands for the total conduction term and  $\mathcal{D}_P$  and  $\mathcal{D}_T$  account for the effects of molecular diffusion and dissipation on P and T:

$$\mathcal{C} = \partial_j (\lambda \partial_j T) \quad , \quad (2.13)$$

$$\mathcal{D}_P = \gamma_3 \sum_{\alpha} \left[ \frac{P_{r,\alpha}}{\rho} \partial_j (\rho \mathcal{D}^{(\alpha)} \partial_j c_{\alpha}) \right] + \rho (\gamma_3 - 1) \sum_{\alpha} \left[ \mathcal{D}^{(\alpha)} \partial_j h_{r,\alpha} \partial_j c_{\alpha} \right] \quad , \quad (2.14)$$

$$\mathcal{D}_T = \sum_{\alpha} \left[ \frac{P_{r,\alpha}}{\rho} \partial_j (\rho \mathcal{D}^{(\alpha)} \partial_j c_{\alpha}) + \rho \mathcal{D}^{(\alpha)} \partial_j h_{r,\alpha} \partial_j c_{\alpha} \right] \quad . \quad (2.15)$$

The coefficients  $\gamma_1$ ,  $\gamma_2$  and  $\gamma_3$  are generalized adiabatic exponents defined for a continuum made of matter and radiation, as explicited in [Mihalas & Mihalas \[2013\]](#), by:

$$\gamma_1 = \frac{\rho}{P} \left( \frac{\partial P}{\partial \rho} \right)_{s,c_{\alpha}} \quad , \quad \gamma_2 = 1 + \frac{\rho}{T} \left( \frac{\partial T}{\partial \rho} \right)_{s,c_{\alpha}} \quad \text{and} \quad \gamma_3 = 1 + \frac{1}{\rho} \left( \frac{\partial P}{\partial e} \right)_{\rho,c_{\alpha}} \quad , \quad (2.16)$$

where  $s$  stands for the specific entropy. Note that with the notations found in [Mihalas & Mihalas \[2013\]](#), one has  $\gamma_1 = \Gamma_1$  but  $\gamma_2 = \Gamma_3$ . As for  $\gamma_3$ , it is not directly linked to an isentropic process and has been arbitrarily added to the list of adiabatic exponents for ease of expression. Note also that the generalized adiabatic exponents are usually different from one another and also from the ratio of specific heat  $\gamma$  defined by:

$$\gamma = \frac{c_p}{c_v} \quad ,$$

where  $c_v$  is the total specific heat at constant volume, which has already been introduced, and  $c_p$  is the total specific heat at constant pressure. All these coefficients are also usually different from the adiabatic exponent  $\gamma^m$  characterizing the plasma without radiation. They nevertheless coincide for a perfect gas without radiation, where in this case:

$$\gamma_1 = \gamma_2 = \gamma_3 = \gamma = \gamma^m \quad .$$

As a last note, Eqs. (2.11) and (2.12) remain the same whether the plasma behaves as an ideal gas or not. The differences between two different equations of state would only appear in the

## 2.2. Flow description

---

actual values of the generalized adiabatic exponents, which definitions extend beyond the ideal gas framework. They can be expressed in terms of differentials of temperature and density, by developing the definitions (2.16) with relations (2.9):

$$\gamma_1 = \frac{P,T}{\rho e,T} \left( 1 - \frac{\rho^2 e_{,\rho}}{P} \right) + \frac{\rho P_{,\rho}}{P} \quad , \quad \gamma_2 = 1 + \frac{P - \rho^2 e_{,\rho}}{\rho e,T} \quad , \quad \gamma_3 = 1 + \frac{P,T}{\rho e,T} \quad . \quad (2.17)$$

To summarize, the system of equations (2.1b), (2.11) and (2.12) pertaining to velocity, pressure and temperature used for the next analysis is:

$$\begin{cases} D_t u_i = -\frac{\partial_i P}{\rho} - \frac{\partial_j \Pi_{ij}}{\rho} + g_i \quad , & (2.18a) \\ D_t P = -\gamma_1 P \operatorname{div} \mathbf{u} + (\gamma_3 - 1) \mathcal{C} + \mathcal{S}_P + \mathcal{D}_P \quad , & (2.18b) \\ D_t T = -(\gamma_2 - 1) T \operatorname{div} \mathbf{u} + \frac{\mathcal{C}}{\rho c_v} + \frac{\mathcal{S}_T}{\rho c_v} + \frac{\mathcal{D}_T}{\rho c_v} \quad . & (2.18c) \end{cases}$$

### 2.2.3 Average flow as a background state

A crucial element when performing a small Mach number or a small Péclet number asymptotic study is to choose a reference state that will allow to split quantities into a background component and a deviation from this background. It is this deviation which properties will be determined by the analysis.

Most often, the background state is set according to some *a priori* knowledge of the flow, for instance by enforcing a particular stratification or by assuming some form of quasi-stationarity. However, this method may sometimes entail some unwarranted restrictions and prevent the result from being applicable to more general situations. Here, given the turbulence modelling context of this study, we choose a slightly different way of setting the background state of our asymptotic analysis. More precisely, we will perform our analysis by splitting quantities into a statistical ensemble mean and its corresponding fluctuation. Thus, the background state obeys its own set of evolution equations and is not determined by a priori assumptions. Note that, in a stellar context, the spherical symmetry of the configuration allows to assimilate ensemble means with spatial averages over the surface of spheres of a given radius. This ergodic definition of the ensemble mean can be useful in a practical context but will not be used hereafter.

For variable density flows, it is usual to work with “Favre” density-weighted statistics and “Reynolds” unweighted statistics. For any quantity  $q$ , the Reynolds and Favre averages are denoted respectively by  $\bar{q}$  and  $\tilde{q}$ . They are related by the identity:

$$\tilde{q} = \frac{\overline{\rho q}}{\bar{\rho}} \quad .$$

The corresponding fluctuations are:

$$q' = q - \bar{q} \quad \text{and} \quad q'' = q - \tilde{q} \quad ,$$

and are related by  $q'' = \overline{q''} + q'$ .

Then, by averaging Sys. (2.18), as shown in detail in App. B through classical techniques available for instance in Schiestel [2010], the set of averaged equations governing the reference state around which the asymptotic analysis will be performed is obtained. By subtracting each of these equations from their respective instantaneous counterparts, one obtains the following evolutions for the fluctuating velocity, pressure and temperature:

$$\left\{ \begin{array}{l} D_t \mathbf{u}_i'' = -u_j'' \partial_j \tilde{u}_i - \frac{\partial_i P'}{\rho} + \frac{\rho'}{\rho} \frac{\partial_i \bar{P}}{\bar{\rho}} - \left( \frac{\partial_j \Pi_{ij}}{\rho} \right)'' + \mathcal{R}_i^u \quad , \end{array} \right. \quad (2.19a)$$

$$\left\{ \begin{array}{l} D_t P' = -u_j' \partial_j \bar{P} - \bar{\gamma}_1 \bar{P} \text{div} \mathbf{u}' - \gamma_1' \bar{P} \text{div} \bar{\mathbf{u}} - \bar{\gamma}_1 P' \text{div} \bar{\mathbf{u}} + (\bar{\gamma}_3 - 1) C' + \gamma_3' \bar{C} \\ \quad + D_P' + \mathcal{S}_P' + \mathcal{R}^P \quad , \end{array} \right. \quad (2.19b)$$

$$\left\{ \begin{array}{l} D_t T' = -u_j' \partial_j \bar{T} - (\bar{\gamma}_2 - 1) \bar{T} \text{div} \mathbf{u}' - \gamma_2' \bar{T} \text{div} \bar{\mathbf{u}} - (\bar{\gamma}_2 - 1) T' \text{div} \bar{\mathbf{u}} + \left( \frac{C}{\rho c_v} \right)' \\ \quad + \left( \frac{D_T}{\rho c_v} \right)' + \left( \frac{\mathcal{S}_T}{\rho c_v} \right)' + \mathcal{R}^T \quad , \end{array} \right. \quad (2.19c)$$

with:

$$\left\{ \begin{array}{l} \mathcal{R}_i^u = \partial_j \left( \bar{\rho} \widetilde{u_i'' u_j''} \right) / \bar{\rho} \quad , \\ \mathcal{R}^P = \overline{u_j' \partial_j P'} - \left( \gamma_1' P' - \overline{\gamma_1' P'} \right) \text{div} \bar{\mathbf{u}} - \left( \gamma_1' \text{div} \mathbf{u}' - \overline{\gamma_1' \text{div} \mathbf{u}'} \right) \bar{P} - \bar{\gamma}_1 \left( P' \text{div} \mathbf{u}' - \overline{P' \text{div} \mathbf{u}'} \right) \\ \quad + \gamma_3' C' - \bar{\gamma}_3 \bar{C}' - \left( \gamma_1' P' \text{div} \mathbf{u}' - \overline{\gamma_1' P' \text{div} \mathbf{u}'} \right) \quad , \\ \mathcal{R}^T = \overline{u_j' \partial_j T'} - \left( \gamma_2' T' - \overline{\gamma_2' T'} \right) \text{div} \bar{\mathbf{u}} - \left( \gamma_2' \text{div} \mathbf{u}' - \overline{\gamma_2' \text{div} \mathbf{u}'} \right) \bar{T} - (\bar{\gamma}_2 - 1) \left( T' \text{div} \mathbf{u}' - \overline{T' \text{div} \mathbf{u}'} \right) \\ \quad + C' \left( \frac{1}{\rho c_v} \right)' - C' \left( \frac{1}{\rho c_v} \right)' - \left( \gamma_2' T' \text{div} \mathbf{u}' - \overline{\gamma_2' T' \text{div} \mathbf{u}'} \right) \quad . \end{array} \right.$$

Second order contributions, *i.e.* those involving the product of two or more fluctuating quantities have been gathered in the terms  $\mathcal{R}_i^u$ ,  $\mathcal{R}^P$  and  $\mathcal{R}^T$ . These contributions are not necessarily negligible but their role on the forthcoming analysis remains very limited. Equations (2.19a), (2.19b) and (2.19c) are the core equations that will serve for the small Péclet number analysis detailed in Sec. 2.3.

## 2.2.4 Dimensionless equations for the fluctuations

The last step before performing the small Péclet number asymptotic analysis consists in making Eqs. (2.19a), (2.19b) and (2.19c) dimensionless. In this regard, it is important to recognize that the mean and fluctuating fields have different characteristic scales. Hence, two sets of non-dimensionalizing parameters must be provided: one for the mean field, the other for the fluctuating field.

### 2.2.4.1 Characteristic scales and dimensionless quantities

First of all, the intensity of turbulent fluctuations, regarding the velocity  $\mathbf{u}''$ , the relative density  $\rho'/\bar{\rho}$ , the concentration  $c'_\alpha$  and the adiabatic exponents  $\gamma_1'$ ,  $\gamma_2'$ ,  $\gamma_3'$  are respectively characterized by  $u_0$ ,  $\epsilon_{\rho_0}$ ,  $\epsilon_{c_0}$  and  $\epsilon_{\gamma_0}$ .

## 2.2. Flow description

---

Besides, the characteristic length and time scales of turbulent eddies are denoted by  $\ell_0$  and  $\tau_0$ . They are related to the characteristic turbulent velocity by:

$$\tau_0 \sim \frac{\ell_0}{u_0} \sim \frac{1}{\omega_0} , \quad (2.21)$$

with  $\omega_0$  defined as characteristic turbulent frequency. As for the mean scales of density, pressure and temperature, they are respectively defined by the values of  $\rho_0$ ,  $P_0$  and  $T_0$ . For the sake of simplicity, the characteristic sound celerity  $c_{s_0}$  and heat coefficient at constant volume  $c_{v_0}$  are chosen as

$$c_{s_0} \sim \sqrt{\frac{P_0}{\rho_0}} \quad \text{and} \quad c_{v_0} \sim \frac{P_0}{\rho_0 T_0} . \quad (2.22)$$

Characteristic scales for the gradients of the mean field must also be provided. The characteristic scales of the mean strain and acceleration are respectively denoted by  $S_0$  and  $G_0$ . Besides, length scales for the mean gradients of temperature  $L_{T_0}$  and pressure  $L_{P_0}$  are also introduced:

$$L_{T_0} \sim \frac{T_0}{|\nabla T|_0} \quad \text{and} \quad L_{P_0} \sim \frac{P_0}{|\nabla P|_0} \sim \frac{c_{s_0}^2}{G_0} . \quad (2.23)$$

Concerning the pressure and temperature source terms, we assume that the order of magnitude of the fluctuating source terms relative to their mean is given by the parameter  $\epsilon_{s_0}$ :

$$\frac{S'_P}{\overline{S}_P} \sim \frac{S'_T}{\overline{S}_T} \sim \epsilon_{s_0} .$$

Besides, a characteristic reaction time  $\tau_{s_0}$  is introduced in order to specify the order of magnitude of the mean source terms:

$$\frac{\overline{S}_P}{\overline{P}} \sim \frac{\overline{S}_T}{\overline{\rho} c_v \overline{T}} \sim \frac{1}{\tau_{s_0}} .$$

Finally, characteristic values for the kinematic viscosity  $\nu_v$ , for the diffusion coefficients  $\mathcal{D}^{(\alpha)}$ , for the total thermal diffusivity  $\chi$  and for the are also introduced. They are respectively denoted by  $\nu_{v_0}$ ,  $\mathcal{D}_0^{(\alpha)}$  and  $\chi_0$ .

Dimensionless quantities from the mean and fluctuating fields, including the dimensionless time  $t^*$  and space  $\mathbf{x}^*$ , are then:

$$\begin{aligned} t^* &= \frac{t}{\tau_0} , \quad \mathbf{x}^* = \frac{\mathbf{x}}{\ell_0} , \quad \mathbf{u}''^* = \frac{\mathbf{u}''}{u_0} , \quad \gamma'_{1,2,3}{}^* = \frac{\gamma'_{1,2,3}}{\epsilon_{\gamma_0}} , \quad c'_{\alpha}{}^* = \frac{c'_{\alpha}}{\epsilon_{c_0}} , \\ \rho'^* &= \frac{\rho'}{\rho_0 \epsilon_{\rho_0}} , \quad P'^* = \frac{P'}{P_0} , \quad T'^* = \frac{T'}{T_0} , \quad \bar{\rho}^* = \frac{\bar{\rho}}{\rho_0} , \quad \bar{P}^* = \frac{\bar{P}}{P_0} , \quad \bar{T}^* = \frac{\bar{T}}{T_0} , \\ \left. \frac{\partial_i \bar{P}}{\bar{\rho}} \right|^* &= \frac{1}{G_0} \frac{\partial_i \bar{P}}{\bar{\rho}} , \quad \left. \frac{\partial_i \bar{P}}{\bar{P}} \right|^* = L_{P_0} \frac{\partial_i \bar{P}}{\bar{P}} , \quad \left. \frac{\partial_i \bar{T}}{\bar{T}} \right|^* = L_{T_0} \frac{\partial_i \bar{T}}{\bar{T}} , \quad \partial_j \tilde{u}_i|^* = \frac{1}{S_0} \partial_j \tilde{u}_i . \end{aligned}$$

As shown hereinabove, the fluctuations of pressure and temperature are not made dimensionless in the same way as other fluctuating variables. Indeed, the asymptotic analysis of Sec. 2.3 imposes the orders of  $\rho'$ ,  $c'_{\alpha}$  and  $\mathbf{u}''$  whereas the orders of  $P'$  and  $T'$  are deduced from it.

The conduction term is non-dimensionalized by:

$$\bar{C}^* = \frac{L_{T_0}^2}{\lambda_0 T_0} \bar{C} \quad \text{and} \quad C'^* = \frac{\ell_0^2}{\lambda_0 T_0} C' \quad , \quad (2.24)$$

with  $\lambda_0$  the order of the thermal conductivity. Apart from the thermal conductivity present in the conduction term, transport terms do not play a significant role in the asymptotic analysis and are then dimensionalized within a simplified approach. A characteristic kinematic viscosity and an inter-species diffusion coefficient are written respectively  $\nu_{v_0}$  and  $\mathcal{D}_0^{(\alpha)}$ , from which the transport terms can be made dimensionless as:

$$\left( \frac{\Pi_{ij}}{\rho} \right)'^* = \frac{\ell_0}{u_0 \nu_{v_0}} \left( \frac{\Pi_{ij}}{\rho} \right)' \quad , \quad \mathcal{D}_P'^* = \frac{\ell_0^2}{P_0 \mathcal{D}_0^{(\alpha)} \epsilon_{c_0}} \mathcal{D}_P' \quad \text{and} \quad \left( \frac{D_T}{\rho c_v} \right)'^* = \frac{\ell_0^2}{T_0 \mathcal{D}_0^{(\alpha)} \epsilon_{c_0}} \left( \frac{D_T}{\rho c_v} \right)' \quad . \quad (2.25)$$

Finally, the non-dimensionalized source terms can be written:

$$S_P'^* = \frac{\tau_{s_0}}{P_0 \epsilon_{s_0}} S_P' \quad \text{and} \quad \left( \frac{S_T}{\rho c_v} \right)'^* = \frac{\tau_{s_0}}{T_0 \epsilon_{s_0}} \left( \frac{S_T}{\rho c_v} \right)' \quad . \quad (2.26)$$

where  $\epsilon_{s_0}$  is the relative order of magnitude of the source term.

#### 2.2.4.2 Dimensionless numbers

The previous characteristic scales allow to carry out the derivation of the dimensionless equations. The latter involve a set of dimensionless numbers comparing the relative magnitude a few physical mechanisms.

Similarly as the quantities  $\epsilon_{\rho_0}$ ,  $\epsilon_{c_0}$ ,  $\epsilon_{\gamma_0}$  and  $\epsilon_{s_0}$ , the turbulent Mach number  $M_t$  characterizes the importance of compressibility effects in turbulent eddies. It is defined, as written in Sec. 2.1, as the ratio of the fluctuating velocity to the speed of sound, such that, from Eqs. (2.21) and (2.22):

$$M_t = \frac{u_0}{c_{s_0}} \quad .$$

The Froude numbers denoted  $Fr_s$  and  $Fr_a$ , are respectively related to strain and acceleration.  $Fr_s$  is the ratio of the characteristic turbulent frequency, defined in Eq. (2.21), to the mean scale of deformation and  $Fr_a$  measures the relative magnitude of the mean and the fluctuating acceleration of the flow. These numbers characterize then the turbulence production by mean gradients:

$$Fr_s = \frac{\omega_0}{S_0} \quad \text{and} \quad Fr_a = \frac{\omega_0 u_0}{G_0 \epsilon_{\rho_0}} \quad .$$

The von Kármán numbers, related to pressure  $Ka_P$  and temperature  $Ka_T$  are defined as the ratio of the turbulent length scale, from Eq. (2.21), to respectively the length scales of mean pressure and temperature gradients, defined in Eq. (2.23). Each compares two length scales, such that:

$$Ka_P = \frac{\ell_0}{L_{P_0}} \quad \text{and} \quad Ka_T = \frac{\ell_0}{L_{T_0}} \quad .$$

## 2.2. Flow description

Molecular transport regards basic dimensionless numbers such as the turbulent Reynolds number  $Re_t$ , the Prandtl number  $Pr$  and the Schmidt number  $Sc$ . The Reynolds number gives a measure of the rate of inertial forces to viscous forces in the flow and the Prandtl number is the ratio of the kinematic viscosity to the thermal diffusivity. As for the Schmidt number, it expresses the rate of kinematic viscosity to scalar diffusion. Thus:

$$Re_t = \frac{u_0 \ell_0}{\nu_{v_0}} \quad , \quad Pr = \frac{\nu_{v_0}}{\chi_0} \quad \text{and} \quad Sc = \frac{\nu_{v_0}}{D_0^{(\alpha)}} \quad .$$

The Péclet number  $Pe_t$  is related to the conduction through the Reynolds and the Prandtl number. As previously stated in Sec. 2.1, it compares the transport time scale by radiative conduction to the turbulent time scale and therefore the relative importance of the radiative transport to the turbulent one, such that:

$$Pe_t = \frac{u_0 \ell_0}{\chi_0} = Pr \cdot Re_t \quad \text{with} \quad \chi_0 = \frac{\lambda_0}{\rho_0 c_{v_0}} \quad .$$

Finally, the Damköhler number  $Da$  gives the ratio of the turbulent characteristic time (see Eq. (2.21)), to the mean reaction characteristic time :

$$Da = \frac{\tau_0}{\tau_{s_0}} \quad .$$

Its order of magnitude shows whether reactions are slow or fast with respect to the turbulent evolution.

### 2.2.4.3 Dimensionless equations

For the sake of simplicity, the asterisks superscripts are dropped. Hence, by using  $\ell_0$  and  $\tau_0$  for space and time as well as the other quantities where appropriate, one can now non-dimensionalize Eqs. (2.19a), (2.19b) and (2.19c). One obtains finally:

$$\left\{ \begin{array}{l} D_t u_i'' = - \left[ \frac{1}{M_t^2} \right] \frac{\partial_i P'}{\rho} - \left[ \frac{1}{Fr_s} \right] u_j'' \partial_j \tilde{u}_i + \left[ \frac{1}{Fr_a} \right] \frac{\rho'}{\rho} \frac{\partial_i \bar{P}}{\bar{\rho}} - \left[ \frac{1}{Re_t} \right] \left( \frac{1}{\rho} \partial_j \Pi_{ij} \right)'' + \mathcal{R}_i^u \quad , \quad (2.27a) \end{array} \right.$$

$$\left\{ \begin{array}{l} D_t P' = - \bar{\gamma}_1 \bar{P} \text{div} \mathbf{u}' + \left[ \frac{1}{Pe_t} \right] (\bar{\gamma}_3 - 1) \mathcal{C}' - \left[ \frac{1}{Fr_s} \right] \bar{\gamma}_1 P' \partial_j \bar{u}_j - [Ka_P] u_j' \partial_j \bar{P} \\ \quad - \left[ \frac{\epsilon_{\gamma_0}}{Fr_s} \right] \gamma_1' \bar{P} \partial_j \bar{u}_j + \left[ \frac{\epsilon_{\gamma_0} Ka_T^2}{Pe_t} \right] \gamma_3' \bar{C} + \left[ \frac{\epsilon_{c_0}}{Sc Re_t} \right] D_P' + [Da \epsilon_{s_0}] S_P' + \mathcal{R}^P \quad , \quad (2.27b) \end{array} \right.$$

$$\left\{ \begin{array}{l} D_t T' = - (\bar{\gamma}_2 - 1) \bar{T} \text{div} \mathbf{u}' + \left[ \frac{1}{Pe_t} \right] \frac{\mathcal{C}'}{\rho c_v} - \left[ \frac{1}{Fr_s} \right] (\bar{\gamma}_2 - 1) T' \partial_j \bar{u}_j - [Ka_T] u_j' \partial_j \bar{T} \\ \quad - \left[ \frac{\epsilon_{\gamma_0}}{Fr_s} \right] \gamma_2' \bar{T} \partial_j \bar{u}_j + \left[ \frac{\epsilon_{\gamma_0} Ka_T^2}{Pe_t} \right] \left( \frac{1}{\rho c_v} \right)' \bar{C} + \left[ \frac{\epsilon_{c_0}}{Sc Re_t} \right] \left( \frac{D_T}{\rho c_v} \right)' \\ \quad + [Da \epsilon_{s_0}] \left( \frac{S_T}{\rho c_v} \right)' + \mathcal{R}^T \quad . \quad (2.27c) \end{array} \right.$$

## 2.3 Small Mach-small Péclet number approximation ( $Pe_t \lesssim M_t \ll 1$ )

This section is the corner stone of the study and defines the main conditions used for the approximation. It emphasises the role played by the turbulent Mach number in the evolution of the fluctuating velocity and the influence of the Péclet number regarding the fluctuating temperature and pressure evolutions. Its outcomes concern the orders of magnitude of some thermodynamic fluctuating variables, as well as the expressions of the divergence of the velocity fluctuations  $\text{div} \mathbf{u}'$  and of the fluctuations of the conduction term  $C'$ .

### 2.3.1 Main conditions

As a first hypothesis, the asymptotic development of Eqs. (2.27a), (2.27b) and (2.27c) supposes, for an integer  $n$  greater or equal to 1, the flow to behave under the main conditions:

**Main conditions: orders of magnitude of  $M_t$  and  $Pe_t$**

$$M_t \ll 1 \quad \text{and} \quad Pe_t \sim M_t^n \ll 1 \quad . \quad (2.28)$$

In this configuration, the Péclet number is considered to be either smaller than or on the same order as the Mach number. However, a reverse development is investigated latter, in Sec. 2.4, where the flow admits  $M_t$  to be even smaller than  $Pe_t$ , such that ( $Pe_t \ll 1$ ) and ( $M_t \sim Pe_t^n \ll 1$ ).

The following secondary conditions are considered here. First, the order of fluctuations of the adiabatic exponents, of the concentration and of the density are assumed to be small, so that:

$$\epsilon_{\gamma_0} \sim M_t \ll 1 \quad , \quad \epsilon_{c_0} \sim M_t \ll 1 \quad \text{and} \quad \epsilon_{\rho_0} \sim M_t \ll 1 \quad . \quad (2.29)$$

Secondly, the flow is considered in a quasi-equilibrium state, which means that the mean production terms are of the same order as the dissipation ones. Hence,

$$Fr_a \sim 1 \quad \text{and} \quad Fr_s \sim 1 \quad . \quad (2.30)$$

And finally, the characteristic turbulent length scale is supposed small regarding the ones of temperature and pressure gradients:

$$Ka_T \sim Ka_P \sim M_t \ll 1 \quad . \quad (2.31)$$

The Reynolds and Schmidt numbers are assumed to verify:

$$Re_t \gtrsim 1 \quad \text{and} \quad Sc \cdot Re_t \gtrsim 1 \quad . \quad (2.32)$$

This assumption is compatible with both high and moderate Reynolds numbers. Regarding the reactive source terms, we assume that reactions have moderate velocities and that their fluctuations relative to their mean is small (the case of fast reaction rates is examined in App. B):

$$Da \sim 1 \quad \text{and} \quad \epsilon_{s_0} \sim M_t \ll 1 \quad . \quad (2.33)$$

### 2.3. Small Mach-small Péclet number approximation ( $\text{Pe}_t \lesssim \text{M}_t \ll 1$ )

---

The fluctuating quantities  $\mathbf{u}'$ ,  $\rho'$ ,  $P'$ ,  $\gamma'$  and  $T'$  are developed as functions of  $\text{M}_t$ . For any fluctuating quantity  $q'$ , we have:

$$q' = q^{(0)} + \text{M}_t q^{(1)} + \text{M}_t^2 q^{(2)} + \mathcal{O}\left(\text{M}_t^3\right) . \quad (2.34)$$

They are then inserted in the dimensionless Eqs. (2.27a), (2.27b) and (2.27c), corresponding respectively to the evolutions of the fluctuating velocity, pressure and temperature. In the next sections, the combined effects of small Mach and small Péclet limits are featured.

#### 2.3.1.1 Small Péclet number analysis in fluctuating temperature evolution

The asymptotic developments are first inserted in the fluctuating temperature evolution Eq. (2.27c). While focusing on the terms of order  $\text{Pe}_t^{-1} = \text{M}_t^n$ , the following result can be derived:

$$\frac{\mathcal{C}'^{(0)}}{\rho c_v} = 0 . \quad (2.35)$$

The conduction term can also take the dimensionless form:

$$\mathcal{C}' = \partial_j \left[ \bar{\lambda} \partial_j T' + [\text{Ka}_T] \lambda' \partial_j \bar{T} + \lambda' \partial_j T' - \overline{\lambda' \partial_j T'} \right] . \quad (2.36)$$

The fluctuations of the conductivity  $\lambda \equiv \lambda(\rho, T, c_\alpha)$  are supposed to be linearized under the form:

$$\lambda' = [\epsilon_{\rho_0}] \rho' \bar{\lambda}_{,\rho} + T' \bar{\lambda}_{,T} + [\epsilon_{c_0}] \sum_{\alpha} c'_{\alpha} \bar{\lambda}_{,\alpha} . \quad (2.37)$$

With the hypotheses  $\text{Ka}_T \sim \text{M}_t$  and  $\epsilon_{\rho_0} \sim \epsilon_{c_0} \sim \text{M}_t$ :

$$\mathcal{C}'^{(0)} = \partial_j \left[ \bar{\lambda} \partial_j T'^{(0)} + \bar{\lambda}_{,T} \left( T'^{(0)} \partial_j T'^{(0)} - \overline{T'^{(0)} \partial_j T'^{(0)}} \right) \right] . \quad (2.38)$$

Hence, excluding particular cases, Eqs. (2.35) and (2.38) lead to:

$$T'^{(0)} = 0 . \quad (2.39)$$

Moreover, when ( $n > 1$ ), from the orders varying from  $\text{M}_t^{-(n-1)}$  to  $\text{M}_t^{-1}$  in Eq. (2.27c) that:

$$\frac{\mathcal{C}'^{(1)}}{\rho c_v} = \dots = \frac{\mathcal{C}'^{(n-1)}}{\rho c_v} = 0 . \quad (2.40)$$

Taking into account that  $T'^{(0)} = 0$ , the first equality implies  $\mathcal{C}'^{(1)} = \partial_j \left[ \bar{\lambda} \partial_j T'^{(1)} \right]$ . Hence, excluding particular solutions, one has  $T'^{(1)} = 0$ . By recurrence, one finally deduces that:

$$T'^{(1)} = \dots = T'^{(n-1)} = 0 . \quad (2.41)$$

Thus, at order 0 and 1,

$$\begin{cases} 0 = -(\bar{\gamma}_2 - 1) \bar{T} \text{div} \mathbf{u}'^{(0)} + \left[ \frac{M_t^n}{Pe_t} \right] \frac{C'^{(n)}}{\bar{\rho}_{c_v}} , & (2.42a) \\ 0 = -(\bar{\gamma}_2 - 1) \bar{T} \text{div} \mathbf{u}'^{(1)} + \left[ \frac{M_t^n}{Pe_t} \right] \frac{C'^{(n+1)}}{\bar{\rho}_{c_v}} - \left[ \frac{Ka_T}{M_t} \right] u_j'^{(0)} \partial_j \bar{T} - \left[ \frac{\epsilon_{\gamma_0}}{M_t Fr_s} \right] \gamma_2'^{(0)} \bar{T} \partial_j \bar{u}_j \\ + \left[ \frac{\epsilon_{\gamma_0} Ka_T^2}{M_t Pe_t} \right] \left( \frac{1}{\bar{\rho}_{c_v}} \right)'^{(0)} \bar{C} + \left[ \frac{\epsilon_{c_0}}{M_t Sc Re_t} \right] \left( \frac{D_T}{\bar{\rho}_{c_v}} \right)'^{(0)} + [Da \epsilon_{s_0}] \left( \frac{S_T}{\bar{\rho}_{c_v}} \right)'^{(0)} . & (2.42b) \end{cases}$$

Thus, a first estimate of the order of  $T'$  and a first series of relations relating  $\text{div} \mathbf{u}'$  and  $C'$  to other fluctuations is obtained.

### 2.3.1.2 Small Mach number analysis in the fluctuating velocity and pressure evolutions

The asymptotic expansions are injected into the fluctuating velocity evolution Eq. (2.27a). By gathering the terms of order  $M_t^{-2}$  and  $M_t^{-1}$ , the following classical result is readily obtained:

$$P'^{(0)} = P'^{(1)} = 0 . \quad (2.43)$$

The previous result is then inserted in Eq. (2.27b), the fluctuating pressure evolution equation. Hence, at order 0 and 1,

$$\begin{cases} 0 = -\bar{\gamma}_1 \bar{P} \text{div} \mathbf{u}'^{(0)} + \left[ \frac{M_t^n}{Pe_t} \right] (\bar{\gamma}_3 - 1) C'^{(n)} , & (2.44a) \\ 0 = -\bar{\gamma}_1 \bar{P} \text{div} \mathbf{u}'^{(1)} + \left[ \frac{M_t^n}{Pe_t} \right] (\bar{\gamma}_3 - 1) C'^{(n+1)} - \left[ \frac{Ka_P}{M_t} \right] u_j'^{(0)} \partial_j \bar{P} - \left[ \frac{\epsilon_{\gamma_0}}{M_t Fr_s} \right] \gamma_1'^{(0)} \bar{P} \partial_j \bar{u}_j \\ + \left[ \frac{\epsilon_{\gamma_0} Ka_T^2}{M_t Pe_t} \right] \gamma_3'^{(0)} \bar{C} + \left[ \frac{\epsilon_{c_0}}{M_t Sc Re_t} \right] D_P'^{(0)} + [Da \epsilon_{s_0}] S_P'^{(0)} . & (2.44b) \end{cases}$$

Again, an estimate of orders of  $P'$  and a second series of relations relating  $\text{div} \mathbf{u}'$  and  $C'$  to other fluctuations is obtained. The system (2.44) is the same as the one obtained in a standard small Mach number analysis, without taking into account the Péclet number. This system has been derived for instance in [Souillard et al. \[2012\]](#). The only difference comes from the conduction term  $C$  that appears to be unknown and of the same order as the divergence term  $\text{div} \mathbf{u}'$ .

### 2.3.1.3 Order of magnitude of the temperature fluctuations

Relation (2.41) shows that the first non-zero order of  $T'$  is  $T'^{(n)}$ . However, the combination of order 0 Eqs. (2.42a) and (2.44a) gives:

$$\begin{cases} \text{div} \mathbf{u}'^{(0)} = 0 , & (2.45a) \\ C'^{(n)} = 0 . & (2.45b) \end{cases}$$

The latter relation implies that  $T'^{(n)} = 0$ . The first non-zero order of  $T'$  is then  $T'^{(n+1)}$ .

## 2.3. Small Mach-small Péclet number approximation ( $Pe_t \lesssim M_t \ll 1$ )

### 2.3.2 Main results of the asymptotic analysis

The asymptotic analysis being done, we would like to recast its main results in a dimensional form, more useful for practical applications. From now on, we come back to the original notations, prior to dropping the \* superscripts used to differentiate dimensional and dimensionless variables. Hence, the fluctuations return to their original definitions and denote dimensional variables from here.

#### 2.3.2.1 Orders of magnitude of fluctuations

The pressure fluctuations  $P'$  are of order  $M_t^2$  and the temperature ones  $T'$  are of order  $M_t^{n+1} \sim Pe_t \cdot M_t$ . In general, one can write, for  $Pe_t \lesssim M_t \ll 1$ :

**Main result: orders of magnitude of pressure and temperature fluctuations**

$$\frac{P'}{\bar{P}} \sim M_t^2 \ll M_t \quad \text{and} \quad \frac{T'}{\bar{T}} \sim Pe_t \cdot M_t \ll M_t \quad . \quad (2.46)$$

A point must be emphasized here. In the case of moderate reaction velocities ( $[Da\epsilon_{s_0}] \sim 1$ ) and when the Péclet number is of order  $M_t$ , temperature fluctuations  $T'$  are also of order  $M_t$ . Their level can be compared to other thermodynamic quantities and, as a result, temperature effects cannot be neglected. Furthermore, as shown in App. B, fast reaction rates ( $[Da\epsilon_{s_0}] \gg 1$ ) would maintain temperature fluctuations of similar level as the ones of other thermodynamic quantities, even when the Péclet number is small with respect to  $M_t$ .

#### 2.3.2.2 General expressions for the divergence and the conduction terms

From relations (2.42b) and (2.44b), one can write the following dimensionned system relating the fluctuation of the conduction term  $C'$  and the fluctuating divergence term  $\text{div}\mathbf{u}'$ :

$$\begin{cases} (\bar{\gamma}_2 - 1) \bar{T} \text{div}\mathbf{u}' - \frac{C'}{\rho c_v} = -u'_j \partial_j \bar{T} - \gamma'_2 \bar{T} \partial_j \bar{u}_j + \left(\frac{1}{\rho c_v}\right)' \bar{C} + \left(\frac{\mathcal{D}_T}{\rho c_v}\right)' + \left(\frac{\mathcal{S}_T}{\rho c_v}\right)' & , \quad (2.47a) \\ \bar{\gamma}_1 \bar{P} \text{div}\mathbf{u}' - (\bar{\gamma}_3 - 1) C' = -u'_j \partial_j \bar{P} - \gamma'_1 \bar{P} \partial_j \bar{u}_j + \gamma'_3 \bar{C} + \mathcal{D}'_P + \mathcal{S}'_P & . \quad (2.47b) \end{cases}$$

Equations. (2.47a) and (2.47b) express the respective equilibria of  $T'$  and  $P'$ . They link the velocity divergence and the conduction term and describe their variation according to gradients of pressure and temperature, as well as diffusion terms. Their combined existence emphasizes the dependency of the small Péclet approximation to its small Mach counterpart. This aspect is not necessarily accounted for in Spiegel [1962] or Lignieres [1999].

The relations of the system (2.47) allows to express  $C'$  and  $\text{div}\mathbf{u}'$  as functions of other fluctuating quantities. The development of diffusion terms  $\bar{\mathcal{D}}_T$ ,  $\mathcal{D}'_T$ ,  $\bar{\mathcal{D}}_P$  and  $\mathcal{D}'_P$ , as well as source terms  $\bar{\mathcal{S}}_T$ ,  $\mathcal{S}'_T$ ,  $\bar{\mathcal{S}}_P$  and  $\mathcal{S}'_P$  is carried on while considering a high Reynolds limit. It means that the latter is sufficiently high to neglect mean diffusive terms and to conserve only second derivatives of fluctuating quantities, as detailed in App. B.

Referring to Eqs. (B.5a) and (B.5b):

$$\overline{\mathcal{D}}_T = 0 \quad , \quad \mathcal{D}'_T \approx \sum_{\alpha} \overline{P}_{,\alpha} \mathcal{D}^{(\alpha)} \partial_{jj}^2 c'_{\alpha} \quad , \quad (2.48a)$$

$$\overline{\mathcal{D}}_P = 0 \quad , \quad \mathcal{D}'_P \approx \sum_{\alpha} \overline{\gamma}_3 \overline{P}_{,\alpha} \mathcal{D}^{(\alpha)} \partial_{jj}^2 c'_{\alpha} \quad , \quad (2.48b)$$

$$\overline{\mathcal{S}}_T = - \sum_{\alpha} \overline{e}_{,\alpha} \overline{\mathcal{S}}_{\alpha} + \overline{\mathcal{S}} \quad , \quad \mathcal{S}'_T = - \sum_{\alpha} (e_{,\alpha} \mathcal{S}_{\alpha})' + \mathcal{S}' \quad , \quad (2.48c)$$

$$\overline{\mathcal{S}}_P = \sum_{\alpha} \frac{\overline{P}_{,\alpha} \overline{\mathcal{S}}_{\alpha}}{\overline{\rho}} + (\overline{\gamma}_3 - 1) \overline{\mathcal{S}}_T \quad , \quad \mathcal{S}'_P = \sum_{\alpha} \left( \frac{P_{,\alpha} \mathcal{S}_{\alpha}}{\rho} \right)' + (\overline{\gamma}_3 - 1) \mathcal{S}'_T \quad . \quad (2.48d)$$

Finally, in the high Reynolds limit, the system (2.47) becomes:

**Main result: general expressions of  $\text{divu}'$  and  $C'$**

$$\left\{ \begin{aligned} \text{divu}' &= - u'_j \frac{\overline{\gamma}}{\overline{\gamma}_1} \left( \frac{\partial_j \overline{P}}{\overline{P}} - x^P \frac{\partial_j \overline{T}}{\overline{T}} \right) + \frac{\overline{\gamma}}{\overline{\gamma}_1 \overline{P}} (\overline{\mathcal{S}}_T + \overline{\mathcal{C}}) \left[ \gamma'_3 - (\overline{\gamma}_3 - 1) \left( \frac{\overline{\rho c_v}}{\rho c_v} \right)' \right] \\ &\quad - \frac{\overline{\gamma}}{\overline{\gamma}_1} (\gamma'_1 - x^P \gamma'_2) \partial_j \overline{u}_j + \frac{\overline{\gamma}}{\overline{\gamma}_1 \overline{P}} \sum_{\alpha} \left[ \overline{P}_{,\alpha} \mathcal{D}^{(\alpha)} \partial_{jj}^2 c'_{\alpha} + \left( \frac{P_{,\alpha} \mathcal{S}_{\alpha}}{\rho} \right)' \right] \quad , \end{aligned} \right. \quad (2.49a)$$

$$\left\{ \begin{aligned} \frac{C'}{\overline{\gamma} \overline{\rho c_v}} &= u'_j \left( \partial_j \overline{T} - \frac{\overline{\gamma}_2 - 1}{\overline{\gamma}_1} \overline{T} \frac{\partial_j \overline{P}}{\overline{P}} \right) + \left( \frac{\overline{\mathcal{C}} + \overline{\mathcal{S}}_T}{\overline{\rho c_v}} \right) \left[ \frac{\overline{\gamma}_2 - 1}{\overline{\gamma}_3 - 1} x^P \frac{\gamma'_3}{\overline{\gamma}_1} - \left( \frac{\overline{\rho c_v}}{\rho c_v} \right)' \right] \\ &\quad + (\overline{\gamma}_2 - 1) \overline{T} \left( \frac{\gamma'_2}{\overline{\gamma}_2 - 1} - \frac{\gamma'_1}{\overline{\gamma}_1} \right) \partial_j \overline{u}_j - \frac{\mathcal{S}'_T}{\overline{\gamma} \overline{\rho c_v}} + \frac{\overline{\gamma}_2 - 1}{\overline{\gamma}_3 - 1} \frac{x^P}{\overline{\gamma}_1 \overline{\rho c_v}} \sum_{\alpha} \left( \frac{P_{,\alpha} \mathcal{S}_{\alpha}}{\rho} \right)' \\ &\quad + \left( \frac{\overline{\gamma}}{\overline{\gamma}_1} \frac{\overline{\gamma}_2 - 1}{\overline{\gamma}_3 - 1} x^P - 1 \right) \sum_{\alpha} \frac{\overline{P}_{,\alpha} \mathcal{D}^{(\alpha)} \partial_{jj}^2 c'_{\alpha}}{\overline{\gamma} \overline{\rho c_v}} \quad , \end{aligned} \right. \quad (2.49b)$$

with:

$$\overline{\gamma} = \frac{\overline{\gamma}_1}{\overline{\gamma}_1 - (\overline{\gamma}_2 - 1) x^P} \quad \text{and} \quad x^P = \frac{(\overline{\gamma}_3 - 1) \overline{\rho c_v} \overline{T}}{\overline{P}} \quad . \quad (2.50)$$

### 2.3.2.3 Expressions for the divergence and the conduction terms for a perfect gas

If ions and electrons are supposed to behave as a perfect gas, the matter pressure  $P^m$  can be expressed as:

$$P^m = P^i + P^e = \rho r T = (\gamma^m - 1) \rho c_v^m T \quad \text{with} \quad r = \sum_{\alpha} r_{\alpha} c_{\alpha} \quad \text{and} \quad r_{\alpha} = \frac{\mathcal{R} (1 + \mathcal{Z}_{\alpha})}{\mathcal{M}_{\alpha}} \quad , \quad (2.51)$$

with  $\mathcal{R}$  is the ideal gas constant,  $\mathcal{Z}_{\alpha}$  is the ionization degree and  $\mathcal{M}_{\alpha}$  its molar mass<sup>1</sup>. The fluctuations of the adiabatic indices  $\gamma^m$ ,  $\gamma_1$ ,  $\gamma_2$  and  $\gamma_3$  are supposed negligible, so that:

$$\gamma'_1 = \gamma'_2 = \gamma'_3 = \gamma^{m'} = 0 \quad . \quad (2.52)$$

<sup>1</sup>In an astrophysical context, the molecular weight  $\mu$  is interpreted as an equivalent molar mass of the mixing gas.

### 2.3. Small Mach-small Péclet number approximation ( $\text{Pe}_t \lesssim \text{M}_t \ll 1$ )

Accordingly, the previous system (2.49) simplifies into:

$$\left\{ \begin{array}{l} \text{div}\mathbf{u}' = -u'_j \frac{\bar{\gamma}}{\bar{\gamma}_1} \left( \frac{\partial_j \bar{P}}{\bar{P}} - x^P \frac{\partial_j \bar{T}}{\bar{T}} \right) + \frac{\bar{\gamma}}{\bar{\gamma}_1 \bar{P}} \sum_{\alpha} \left[ \bar{P}_{,\alpha} \mathcal{D}^{(\alpha)} \partial_{jj}^2 c'_{\alpha} + \left( \frac{P_{,\alpha} \mathcal{S}_{\alpha}}{\rho} \right)' \right] , \\ \frac{C'}{\bar{\gamma} \rho c_v} = u'_j \left( \partial_j \bar{T} - \frac{\bar{\gamma}_2 - 1}{\bar{\gamma}_1} \bar{T} \frac{\partial_j \bar{P}}{\bar{P}} \right) - \frac{S'_T}{\bar{\gamma} \rho c_v} + \frac{\bar{\gamma}_2 - 1}{\bar{\gamma}_3 - 1} \frac{x^P}{\bar{\gamma}_1 \rho c_v} \sum_{\alpha} \left( \frac{P_{,\alpha} \mathcal{S}_{\alpha}}{\rho} \right)' \\ \quad + \left( \frac{\bar{\gamma}}{\bar{\gamma}_1} \frac{\bar{\gamma}_2 - 1}{\bar{\gamma}_3 - 1} x^P - 1 \right) \sum_{\alpha} \frac{\bar{P}_{,\alpha} \mathcal{D}^{(\alpha)} \partial_{jj}^2 c'_{\alpha}}{\bar{\gamma} \rho c_v} . \end{array} \right. \quad (2.53a)$$

$$\left\{ \begin{array}{l} \frac{C'}{\bar{\gamma} \rho c_v} = u'_j \left( \partial_j \bar{T} - \frac{\bar{\gamma}_2 - 1}{\bar{\gamma}_1} \bar{T} \frac{\partial_j \bar{P}}{\bar{P}} \right) - \frac{S'_T}{\bar{\gamma} \rho c_v} + \frac{\bar{\gamma}_2 - 1}{\bar{\gamma}_3 - 1} \frac{x^P}{\bar{\gamma}_1 \rho c_v} \sum_{\alpha} \left( \frac{P_{,\alpha} \mathcal{S}_{\alpha}}{\rho} \right)' \\ \quad + \left( \frac{\bar{\gamma}}{\bar{\gamma}_1} \frac{\bar{\gamma}_2 - 1}{\bar{\gamma}_3 - 1} x^P - 1 \right) \sum_{\alpha} \frac{\bar{P}_{,\alpha} \mathcal{D}^{(\alpha)} \partial_{jj}^2 c'_{\alpha}}{\bar{\gamma} \rho c_v} . \end{array} \right. \quad (2.53b)$$

In order to facilitate these derivations, it is worth noticing that the coefficients of Eq. (2.50) may be simplified into expressions depending on the ratio  $\beta = P^m/P$ , considering the thermodynamic expressions from App. A, such that:

$$\frac{\bar{\gamma}}{\bar{\gamma}_1} = \frac{1}{\beta} , \quad x^P = 4 - 3\bar{\beta} \quad \text{and} \quad \bar{\gamma}_2 = \bar{\gamma}_3 . \quad (2.54)$$

Moreover, the equation of state given by  $P = P^m + P^r$  implies:

$$\frac{\partial_j \bar{P}}{\bar{P}} = \bar{\beta} \left( \frac{\partial_j \bar{\rho}}{\bar{\rho}} + \frac{\partial_j \bar{r}}{\bar{r}} \right) + (4 - 3\bar{\beta}) \frac{\partial_j \bar{T}}{\bar{T}} , \quad (2.55)$$

which leads finally to simpler expressions for the closures<sup>2</sup> of  $\text{div}\mathbf{u}'$  and  $C'$ .

The general expressions of the fluctuating terms  $\text{div}\mathbf{u}'$  and  $C'$  regarding the hydro-radiative flow are finally:

**Result: expressions of  $\text{div}\mathbf{u}'$  and  $C'$  for a perfect gas plus radiation model**

$$\left\{ \begin{array}{l} \text{div}\mathbf{u}' = -u'_j \left( \frac{\partial_j \bar{\rho}}{\bar{\rho}} + \frac{\partial_j \bar{r}}{\bar{r}} \right) + \sum_{\alpha} \frac{r_{\alpha}}{\bar{r}} \left[ \mathcal{D}^{(\alpha)} \partial_{jj}^2 c'_{\alpha} + \left( \frac{\mathcal{S}_{\alpha}}{\rho} \right)' \right] , \\ C' = u'_j \left[ \bar{\rho} c_v \partial_j \bar{T} - x^P \bar{P} \left( \frac{\partial_j \bar{\rho}}{\bar{\rho}} + \frac{\partial_j \bar{r}}{\bar{r}} \right) \right] - S'_T + x^P \bar{P} \sum_{\alpha} \frac{r_{\alpha}}{\bar{r}} \left( \frac{\mathcal{S}_{\alpha}}{\rho} \right)' \\ \quad + 4\bar{P}^r \sum_{\alpha} \frac{r_{\alpha}}{\bar{r}} \mathcal{D}^{(\alpha)} \partial_{jj}^2 c'_{\alpha} . \end{array} \right. \quad (2.57a)$$

$$\left\{ \begin{array}{l} C' = u'_j \left[ \bar{\rho} c_v \partial_j \bar{T} - x^P \bar{P} \left( \frac{\partial_j \bar{\rho}}{\bar{\rho}} + \frac{\partial_j \bar{r}}{\bar{r}} \right) \right] - S'_T + x^P \bar{P} \sum_{\alpha} \frac{r_{\alpha}}{\bar{r}} \left( \frac{\mathcal{S}_{\alpha}}{\rho} \right)' \\ \quad + 4\bar{P}^r \sum_{\alpha} \frac{r_{\alpha}}{\bar{r}} \mathcal{D}^{(\alpha)} \partial_{jj}^2 c'_{\alpha} . \end{array} \right. \quad (2.57b)$$

<sup>2</sup>Hence, if no source terms are considered, Sys (2.57) takes the simplified form:

$$\left\{ \begin{array}{l} \text{div}\mathbf{u}' = -u'_j \left( \frac{\partial_j \bar{\rho}}{\bar{\rho}} + \frac{\partial_j \bar{r}}{\bar{r}} \right) + \sum_{\alpha} \frac{r_{\alpha}}{\bar{r}} \left( \mathcal{D}^{(\alpha)} \partial_{jj}^2 c'_{\alpha} \right) , \\ C' = u'_j \left[ \bar{\rho} c_v \partial_j \bar{T} - x^P \bar{P} \left( \frac{\partial_j \bar{\rho}}{\bar{\rho}} + \frac{\partial_j \bar{r}}{\bar{r}} \right) \right] + 4\bar{P}^r \sum_{\alpha} \frac{r_{\alpha}}{\bar{r}} \mathcal{D}^{(\alpha)} \partial_{jj}^2 c'_{\alpha} , \end{array} \right. \quad (2.56a)$$

$$\left\{ \begin{array}{l} C' = u'_j \left[ \bar{\rho} c_v \partial_j \bar{T} - x^P \bar{P} \left( \frac{\partial_j \bar{\rho}}{\bar{\rho}} + \frac{\partial_j \bar{r}}{\bar{r}} \right) \right] + 4\bar{P}^r \sum_{\alpha} \frac{r_{\alpha}}{\bar{r}} \mathcal{D}^{(\alpha)} \partial_{jj}^2 c'_{\alpha} , \end{array} \right. \quad (2.56b)$$

which is the form retained for the validations carried out in Secs. 2.5 and 3.

These expressions can be compared with the ones present in the literature. As mentioned in the introduction, previous works have been devoted to the study of the small Péclet-small Mach number limit. In Feireisl & Novotný [2009] and Novotný *et al.* [2011], the following expressions are proposed:

$$\text{div}\mathbf{u}' = -u'_j \frac{\partial_j \bar{\rho}}{\bar{\rho}} \quad \text{and} \quad \frac{C'}{\bar{\rho}c_v} = -(\gamma^m - 1)\bar{T}u'_j \frac{\partial_j \bar{\rho}}{\bar{\rho}} \quad , \quad (2.58)$$

while in the work of Lignieres [1999], based on the Boussinesq approximation, the following results are obtained:

$$\text{div}\mathbf{u}' = 0 \quad \text{and} \quad \frac{C'}{\bar{\rho}c_v} = u'_j \partial_j \bar{T} \quad . \quad (2.59)$$

The anelastic approximation of Gough [1969] provides:

$$\text{div}\mathbf{u}' = -u'_j \frac{\partial_j \bar{\rho}}{\bar{\rho}} \quad \text{and} \quad C' = u'_j \left( \bar{\rho}c_v \partial_j \bar{T} - \bar{P} \frac{\partial_j \bar{\rho}}{\bar{\rho}} \right) \quad . \quad (2.60)$$

#### 2.3.2.4 Interpretation of the expressions for the divergence and the conduction terms for a matter perfect gas

The first term on the right-hand side of Eq. (2.57a) expresses the volume adjustment of a mass element moving along a pressure and temperature gradient. That adjustment is not the same as the one observed in a high Péclet situation. In that case, the volume adjusts to the pressure gradient according to the relation (2.62) from Soulard *et al.* [2012].

The second term of Eq. (2.57a) shows that the volume of a mass element is also modified by the molecular diffusion and reactions of species provided they have different gas constants, which effects have not been proposed in the analysis of Novotný *et al.* [2011] or Gough [1969].

The expression derived in Feireisl & Novotný [2009] and Novotný *et al.* [2011] can be seen as a particular case of the one proposed here. Equation (2.58) reverts to Eqs. (2.57a) and (2.57b) when all species are identical, *i.e.* when there is no mixing involved in the flow and  $\bar{r} = \text{cst}$ , when there is no temperature gradient and when the radiative pressure is negligible compared to the material pressure ( $P^r \ll P^m$ ). These are indeed some of the conditions under which the asymptotic analysis of Feireisl & Novotný [2009] and Novotný *et al.* [2011] is performed.

As for the expression of Lignieres [1999], it can also be interpreted as a particular case of Eqs. (2.57a) and (2.57b). Equations (2.59) and (2.57a)-(2.57b) become equivalent provided mixing is discarded and provided the density gradient is zero.

The asymptotic expression of Gough [1969] is again a particular limit of Eqs. (2.57a) and (2.57b). Equation (2.60) reverts to Eq. (2.57a) and (2.57b) when mixing is not considered and in the limit of weak radiative pressure (with respect to its material counterpart). Thus, it involves a mean temperature gradient in addition to the expression of Novotný *et al.* [2011].

### 2.3. Small Mach-small Péclet number approximation ( $Pe_t \lesssim M_t \ll 1$ )

---

Finally, the expression of Eq. (2.57a) does not depend on the radiation field but is only affected by matter properties.

The second relation Eq. (2.57b) corresponds to the thermal equilibrium existing between the conduction term on the left-hand side and two different sources of temperature fluctuations on the right-hand side. The first source arises from the displacement of fluid particles along an adiabatic temperature gradient. The second one involves a combined effect of radiation and species diffusion. Indeed, Eq. (2.57b) indicates the thermal equilibrium of a fluid particle submitted to reactions, mixing and moving along an adiabatic temperature gradient. Without gradient of concentration, that gradient is directly given by the pseudo-entropy gradient, given by:

$$\bar{\rho} \bar{T} \partial_j \bar{s} |_{\alpha} = \bar{\rho} c_v \partial_j \bar{T} - x^P \bar{P} \frac{\partial_j \bar{\rho}}{\bar{\rho}} . \quad (2.61)$$

Temperature equilibrium then applies along the entropy gradient, which is different from the studies established in Lignieres [1999] and Novotny *et al.* [2011] where only the temperature gradient plays a role. This pseudo-entropy gradient may be also retrieved in the expression (2.60) of Gough [1969], but only in the limit of negligible radiative pressure. In the presence of gradient of concentration, the temperature equilibrium deviates from its isentropic character.

#### 2.3.2.5 Comparison with the high Péclet limit

In order to better understand the role played by the smallness of the Péclet number, it is worth comparing the results derived above against those obtained in the small Mach-high Péclet limit, as studied by Soulard *et al.* [2012].

First of all, for ( $Pe_t \gg 1$ ), there is no temperature equilibrium. Accordingly, there is no constraint for the order of magnitude of the fluctuating temperature  $T'$  and no relation equivalent to Eq. (2.57b). What remains is the pressure equilibrium and its consequences: the order of magnitude for  $P'$  in Eq. (2.46) and an expression for the divergence equivalent to Eq. (2.57a). Based on Soulard *et al.* [2012], this expression takes the form:

$$\text{div} \mathbf{u}' = -u'_j \frac{\partial_j \bar{P}}{\gamma_1 \bar{P}} + \text{Molecular terms} . \quad (2.62)$$

When all molecular diffusion coefficients are equal, the molecular terms in the above relation simplify into a diffusion term on density fluctuations and become equivalent to the diffusion term appearing in Eq. (2.57a). Therefore, notwithstanding the properties of  $T'$ , the main difference between the small and high Péclet limit comes from the way the volume of fluid particles adjust to the mean gradients of pressure and temperature, as expressed by the first term on the right-hand sides of Eqs. (2.57a) and (2.62). This difference has important repercussions, and in particular for defining the stability criterion of a mean stratification.

To illustrate this point, let us consider the linear inviscid stability of a flow having a mean density, temperature and concentration stratification satisfying the hydro-static equilibrium con-

dition:

$$\frac{\partial_i \bar{P}}{\bar{\rho}} = g_i \quad .$$

This problem can be studied by looking at the linearized equations for the density and velocity fluctuations, deduced from Sys. (2.18):

$$\partial_t u'_i = \frac{\rho'}{\rho} \frac{\partial_i \bar{P}}{\bar{\rho}} \quad \text{and} \quad \partial_t \frac{\rho'}{\rho} = -\text{div} \mathbf{u}' - u'_j \frac{\partial_j \bar{\rho}}{\bar{\rho}} \quad . \quad (2.63)$$

When inserting the value of the velocity divergence expression (2.62) obtained in the inviscid high Péclet limit, the second equation becomes:

$$\partial_t \frac{\rho'}{\rho} = -u'_j \left( \frac{\partial_j \bar{\rho}}{\bar{\rho}} - \frac{\partial_j \bar{P}}{\gamma_1 \bar{P}} \right) \quad .$$

When inserting the expression (2.57a) obtained in the inviscid small Péclet limit, this same equation becomes:

$$\partial_t \frac{\rho'}{\rho} = u'_j \frac{\partial_j \bar{r}}{\bar{r}} \quad .$$

From there, one obtains that a stratification is stable provided:

**Main result: stability criterion in both asymptotic regimes**

$$\left\{ \begin{array}{l} \text{for } (Pe_t \ll 1) \quad , \quad \frac{\partial_j \bar{r}}{\bar{r}} \frac{\partial_j \bar{P}}{\bar{\rho}} < 0 \quad , \quad (2.64a) \\ \text{for } (Pe_t \gg 1) \quad , \quad \left( \frac{\partial_j \bar{P}}{\gamma_1 \bar{P}} - \frac{\partial_j \bar{\rho}}{\bar{\rho}} \right) \frac{\partial_j \bar{P}}{\bar{\rho}} < 0 \quad . \quad (2.64b) \end{array} \right.$$

Note that these results are obtained here in the high-Reynolds limit for two asymptotic regimes. Notice also that these relations are equivalent to the stability criteria (1.12) and (1.17) derived in chapter 1. As a complement for intermediate regimes, a linear stability analysis (LSA) of Sys (2.1) is carried out in chapter 4, accounting for compressibility and visco-diffusive effects thanks to an isothermal quasi-homogeneous approach. This study concerns all Mach, small Mach and small Mach-small Péclet regimes with or without thermal equilibrium between matter and radiation.

In the large Péclet limit, stability is defined by the orientation of the acceleration with respect to the density gradient corrected by an adiabatic pressure gradient. The corrected density gradient can be rewritten as:

$$\frac{\partial_j \bar{\rho}}{\bar{\rho}} - \frac{\partial_j \bar{P}}{\gamma_1 \bar{P}} = \frac{\partial_j \bar{\rho}}{\bar{\rho}} - \frac{\partial_{\bar{P}} \bar{\rho} |_{\bar{s}, \bar{c}}}{\bar{\rho}} \partial_j \bar{P} = \frac{\partial_{\bar{s}} \bar{\rho} |_{\bar{P}, \bar{c}}}{\bar{\rho}} \partial_j \bar{s} + \sum_{\alpha} \frac{\partial_{c_{\alpha}} \bar{\rho} |_{\bar{P}, \bar{s}, \bar{c}_{\beta \neq \alpha}}}{\bar{\rho}} \partial_j \bar{c}_{\alpha} \quad ,$$

where  $\bar{s}$  is the entropy of the photon-matter continuum. Note that  $\partial_{\bar{s}} \bar{\rho} |_{\bar{P}, \bar{c}} < 0$  for ideal gases with radiation. Hence, in the absence of mean concentration gradients, the stability of a stratification in the high Péclet limit is determined by the relative orientation of the acceleration and the entropy gradient. When concentration gradients exist, the stability is not set uniquely by the the entropy gradient but the latter can still be expected to play a significant role.

## 2.4. Small Péclet-small Mach number approximation ( $M_t \ll Pe_t \ll 1$ )

---

By contrast, in the small Péclet limit, the stability is determined by the relative orientations of the acceleration and of the gradient of the gas constant  $\bar{r}$ , defined in Eq. (2.51), related to the molar mass of the fluid. Entropy does not play a role any longer and only the gradients of the concentrations of the different species influence the stability of the flow. The latter result can be understood as a special asymptotic case of the double-diffusion (thermohaline) instability encountered in geophysical and stellar flows, as in Schmitt [1994] and Garaud [2018].

### 2.3.3 Synthesis of the asymptotic analysis

An asymptotic analysis of a radiative flow within ( $M_t \ll 1$  ;  $Pe_t \ll 1$ ) limits, with  $Pe_t \lesssim M_t$ , has been achieved in this part. The main results regard the orders of magnitude of the pressure and temperature fluctuations, respectively ( $P'/\bar{P} \sim M_t^2$ ) and ( $T'/\bar{T} \sim Pe_t \cdot M_t$ ), as well as general asymptotic expressions for the fluctuating velocity divergence  $\text{div}\mathbf{u}'$  and the fluctuating conduction  $C'$  terms, as shown by Sys. (2.49). The same kind of study with ( $M_t \ll Pe_t$ ) is proposed hereinafter.

## 2.4 Small Péclet-small Mach number approximation ( $M_t \ll Pe_t \ll 1$ )

This section is dedicated to the investigation of the small Péclet-small Mach number limit. This limit is similar to the one studied before except that the Mach number is now considered to be much smaller than the Péclet number while the converse, or at least  $M_t \sim Pe_t$ , was assumed before. As will be seen below, exchanging the order of these two parameters does not modify the main results described in the previous sections.

### 2.4.1 Main conditions

As opposed to the latter study, we now assume that the main conditions of the asymptotic analysis are:

**Main conditions: orders of magnitude of  $M_t$  and  $Pe_t$**

$$Pe_t \ll 1 \quad \text{and} \quad M_t \sim Pe_t^n \ll 1 \quad \text{with} \quad n > 1 \quad .$$

The turbulent field is still assumed in quasi-equilibrium and an hypothesis of high Reynolds number holds to keep molecular effects, such that the following secondary conditions:

$$Fr_a \sim 1 \quad , \quad Fr_s \sim 1 \quad , \quad Re_t \gtrsim 1 \quad \text{and} \quad Sc \cdot Re_t \gtrsim 1 \quad ,$$

assumed in Sec. 2.3.1 remain. In this way, this analysis considers also small fluctuations of adiabatic exponents, of concentration and of density, such that:

$$\epsilon_{\gamma_0} \sim Pe_t \ll 1 \quad , \quad \epsilon_{c_0} \sim Pe_t \ll 1 \quad \text{and} \quad \epsilon_{\rho_0} \sim Pe_t \ll 1 \quad ,$$

and the characteristic turbulent length scale is supposed small with respect to the temperature and pressure gradients length scales:

$$Ka_P \sim Pe_t \ll 1 \quad \text{and} \quad Ka_T \sim Pe_t \ll 1 \quad .$$

Regarding the reactive source terms, the following order is imposed:

$$Da \sim 1 \quad \text{and} \quad \epsilon_{s_0} \ll 1 \quad ,$$

so that reactions have moderate velocities. The fluctuating quantities  $\mathbf{u}'$ ,  $\rho'$ ,  $P'$ ,  $\gamma'$  and  $T'$  are developed as functions of  $Pe_t$ . For any fluctuating quantity  $q'$ , we have:

$$q' = q^{(0)} + Pe_t q^{(1)} + Pe_t^2 q^{(2)} + \mathcal{O}\left(Pe_t^3\right) \quad .$$

As in Sec. 2.3, they are inserted into the dimensionless evolution equations of the fluctuating velocity, pressure and temperature, respectively Eqs. (2.27a), (2.27b) and (2.27c). Hence, the next paragraphs tend to reproduce the same steps detailed in Sec. 2.3 with only slight variations.

#### 2.4.1.1 Small Péclet number analysis in fluctuating temperature evolution

The asymptotic developments are first inserted in the fluctuating temperature evolution Eq. (2.27c). By focusing on the terms of order  $Pe_t^{-1}$ , the following result can be derived:

$$\frac{\mathcal{C}'^{(0)}}{\rho c_v} = 0 \quad , \quad (2.65)$$

which leads to:

$$T'^{(0)} = 0 \quad , \quad (2.66)$$

which in turn implies  $\mathcal{C}'^{(1)} = \partial_j [\bar{\lambda} \partial_j T'^{(1)}]$ . Then, at order 0 and 1, one has:

$$\left\{ \begin{array}{l} 0 = -(\bar{\gamma}_2 - 1) \bar{T} \text{div} \mathbf{u}'^{(0)} + \frac{\mathcal{C}'^{(1)}}{\rho c_v} \quad , \quad (2.67a) \\ D_t T'^{(1)} = -(\bar{\gamma}_2 - 1) \bar{T} \text{div} \mathbf{u}'^{(1)} + \frac{\mathcal{C}'^{(2)}}{\rho c_v} - \left[ \frac{1}{Fr_s} \right] (\bar{\gamma}_2 - 1) T'^{(1)} \partial_j \bar{u}_j - \left[ \frac{Ka_T}{Pe_t} \right] u_j'^{(0)} \partial_j \bar{T} \\ \quad - \left[ \frac{\epsilon_{\gamma_0}}{Pe_t Fr_s} \right] \gamma_2'^{(0)} \bar{T} \partial_j \bar{u}_j + \left[ \frac{\epsilon_{\gamma_0} Ka_T^2}{Pe_t^2} \right] \left( \frac{1}{\rho c_v} \right)'^{(0)} \bar{C} + \left[ \frac{\epsilon_{c_0}}{Pe_t Sc Re_t} \right] \left( \frac{D_T}{\rho c_v} \right)'^{(0)} \\ \quad + [Da \epsilon_{s_0}] \left( \frac{S_T}{\rho c_v} \right)'^{(0)} \quad . \quad (2.67b) \end{array} \right.$$

Thus, a first estimate of orders of  $T'$  and a first series of relations relating  $\text{div} \mathbf{u}'$  and  $\mathcal{C}'$  to other fluctuations is obtained. It is worth noting that, unlike in Sec. 2.3, nothing tends to suggest  $T'^{(1)} = 0$  in the second equation.

#### 2.4.1.2 Small Mach number analysis in fluctuating velocity and pressure evolutions

The asymptotic developments are secondly inserted in the fluctuating velocity evolution Eq. (2.27a). By gathering the terms of order  $M_t^{-2} = Pe_t^{-2n}$  and  $M_t^{-1} = Pe_t^{-2n+1}$ , one has again (with here  $n > 1$

## 2.4. Small Péclet-small Mach number approximation ( $M_t \ll Pe_t \ll 1$ )

by assumption):

$$P'^{(0)} = P'^{(1)} = \dots = P'^{(2n-1)} = 0 \quad . \quad (2.68)$$

The previous result is then inserted in Eq. (2.27b), the fluctuating pressure evolution equation. Hence, at order 0 and 1, one has:

$$\begin{cases} 0 = -\bar{\gamma}_1 \bar{P} \text{div} \mathbf{u}'^{(0)} + (\bar{\gamma}_3 - 1) C'^{(1)} \quad , & (2.69a) \\ 0 = -\bar{\gamma}_1 \bar{P} \text{div} \mathbf{u}'^{(1)} + (\bar{\gamma}_3 - 1) C'^{(2)} - \left[ \frac{Ka_P}{Pe_t} \right] u_j'^{(0)} \partial_j \bar{P} - \left[ \frac{\epsilon_{\gamma_0}}{Pe_t Fr_s} \right] \gamma_1'^{(0)} \bar{P} \partial_j \bar{u}_j \\ \quad + \left[ \frac{\epsilon_{\gamma_0} Ka_T^2}{Pe_t^2} \right] \gamma_3'^{(0)} \bar{C} + \left[ \frac{\epsilon_{c_0}}{Pe_t Sc Re_t} \right] D_P'^{(0)} + [Da \epsilon_{s_0}] S_P'^{(0)} \quad . & (2.69b) \end{cases}$$

Again, an estimate of orders of  $P'$  and a second series of relations relating  $\text{div} \mathbf{u}'$  and  $C'$  to other fluctuations is obtained. The system (2.69) is the same one as Sys. (2.42), with  $C'^{(1)}$  and  $C'^{(2)}$  respectively in place of  $C'^{(n)}$  and  $C'^{(n+1)}$ .

### 2.4.1.3 Order of magnitude of the temperature fluctuations

The result from relation (2.69) showed that the first order not equal to naught of  $T'$  is  $T'^{(1)}$ . However, like in Sec. 2.3, this result is amended when combining Eqs. (2.67a) and (2.69a) leading to:

$$\begin{cases} \text{div} \mathbf{u}'^{(0)} = 0 \quad , & (2.70a) \\ C'^{(1)} = 0 \quad . & (2.70b) \end{cases}$$

The latter relation implies that

$$T'^{(1)} = 0 \quad .$$

Hence, the first non-zero order of  $T'$  is then  $T'^{(2)}$ , which is one order less than the first estimate.

## 2.4.2 Synthesis of the asymptotic analysis

The second asymptotic analysis is now finished and, like in the first one, the main results are now presented in their dimensional form. It regards in particular, the relative orders of  $P'$  and  $T'$ , the asymptotic expression of  $\text{div} \mathbf{u}'$  as well as the evolution equation for  $C'$ .

### 2.4.2.1 Orders of magnitude of fluctuations

The pressure fluctuations  $P'$  are of order  $Pe_t^{2n} \sim M_t^2$  and the temperature ones  $T'$  are of order  $Pe_t^2$ . One can write, for ( $M_t \ll Pe_t \ll 1$ ):

**Main result: orders of magnitude of pressure and temperature fluctuations**

$$\frac{P'}{\bar{P}} \sim M_t^2 \sim Pe_t^{2n} \ll Pe_t \quad \text{and} \quad \frac{T'}{\bar{T}} \sim Pe_t^2 \ll Pe_t \quad . \quad (2.71)$$

Therefore, pressure and temperature fluctuations have a smaller order than density or concentration ones. Thus, they can be neglected regarding the latter as long as they do not appear in  $\mathcal{C}'$  or in the pressure gradient.

### 2.4.2.2 General expressions for the divergence and the conduction terms

Since  $T^{(1)} = 0$ , the Lagrangian time derivative of  $T^{(1)}$  appearing in equation (2.67) can be neglected. As a result, the outcome of the asymptotic analysis concerning the divergence and the conduction terms reverts exactly to the one derived in Sec. 2.3.

#### Main result: general expressions of $\text{div}\mathbf{u}'$ and $\mathcal{C}'$

The expressions of the conduction term  $\mathcal{C}'$  and the fluctuating divergence term  $\text{div}\mathbf{u}'$  are given by the two equations of system (2.47). Their simplification to the case of ideal gases is given by system (2.57).

## 2.5 Validation of the asymptotic analysis

The current section deals with the validation of these results through the use of a hydrodynamic code, presented in Sec. 2.5.1, in which the treatment of radiation has been implemented. To this purpose, in order to highlight the impacts of the small Péclet-small Mach number approximation, direct numerical simulations (DNS) of a radiative turbulent mixing zone are performed with the in-house **TRICLADE** code.

### 2.5.1 Numerical method

**TRICLADE** is a massively parallel code intended to solve turbulent mixing of perfect gases in a variable-density context (see [Shanmuganathan et al. \[2014\]](#) and [Thorner et al. \[2017\]](#)). The present computations are performed with an extension of the code to radiative equations implemented thanks to an operator splitting between the standard hydrodynamic visco-diffusive part and the radiative gray part including radiation-matter coupling and radiative diffusivity. In the radiative version of **TRICLADE**, the total energy is split into its material and radiative components. Hence, the following two equations are solved:

$$\begin{cases} \rho D_t e^m = -P^m \text{div}\mathbf{u} - \partial_j \mathcal{F}_j^m - \Omega^{m-r} + \rho \varepsilon & , \\ \rho D_t (E^r / \rho) = -P^r \text{div}\mathbf{u} - \partial_j \mathcal{F}_j^r + \Omega^{m-r} & , \end{cases}$$

where  $\Omega^{m-r}$  is the radiation-matter exchange term:

$$\Omega^{m-r} = \rho \kappa^r c_\ell \left( a_R T^m - E^r \right) \quad \text{with} \quad T^m = e^m / c_v^m .$$

It corresponds to a simplified version of the gray radiation hydrodynamics system derived in [Zhang et al. \[2011\]](#) within the flux-limited diffusion approximation. The asymptotic value  $1/3$  of the optically-thick limit is used here for the flux limiter and the Eddington factor; then, the corrections of order  $|\mathbf{u}|/c_\ell$  are neglected and the Planck mean interaction coefficient is taken equal to opacity  $\kappa^r$  for the sake of simplicity.

## 2.5. Validation of the asymptotic analysis

For the hydrodynamic part of the code, the monotonic upstream centered scheme for conservation laws (MUSCL) finite-volume Godunov method referred to as M5 in Kim & Kim [2005] is used. With respect to the standard version of TRICLADE, only a slight modification of the HLLC numerical flux is required to account for the additional  $E^r$  variable. This modification is described in App. C, along with some information regarding the boundary conditions implemented in TRICLADE. It includes as well some details about the numerical resolution of the simulations.

As for the gray coupling diffusion sub-system for  $(e^m, E^r)$ , a simple implementation relies on the fact that TRICLADE only works on cartesian grids. It is solved by dimensional splitting into three successive 1D implicit systems. The non-linear term  $T^{m4}$  at final time step is linearized as in Commercon *et al.* [2011]; in this way, when using three-point stencils to discretize the first order derivative of  $E^r$ , each 1D implicit problem is solved by inverting one three-diagonal system for  $E^r$  followed by an update of  $e^m$ . To avoid anisotropic artifacts, alternate directions orders are used from one iteration to the next. This procedure is valid in the limit of vanishing decoupling of matter and radiative temperatures like in the test cases of this section.

In the following sections, the cartesian frame  $(x_1, x_2, x_3)$  introduced in the derivation of the approximation will be also referred to with the notation  $(x, y, z)$ :  $(x_1, x_2, x_3) \equiv (x, y, z)$ .

### 2.5.2 Rayleigh-Taylor flow configuration

The test flow under consideration is a statistically axisymmetric turbulent mixing zone induced by a Rayleigh–Taylor instability (RTI) at a planar interface between two different fluids treated as perfect gases. This simplified configuration does not occur as such in stellar interiors. Its interest lies in the fact that it combines some of the elementary mechanisms which are at work in stellar flows. In particular, it involves mixing, convection, radiation and Péclet number effects. It consequently constitutes a relevant testing ground for our predictions.

The initial state of the simulations is defined as follows. The two fluids are separated by an interface, located at  $(x = x_0)$ , which is unstable with respect to a constant gravitational field  $\mathbf{g}$  oriented along the  $x$ -axis toward negative values of  $x$ , *i.e.* pointing from the heavy fluid side ( $x > 0$ ) to the light fluid side ( $x < 0$ ). The latter axis is referred to as the inhomogeneous or longitudinal direction, while the  $(y, z)$ -axes correspond to the transverse or homogeneous directions. The mean state is fixed by enforcing a hydrostatic equilibrium with an isothermal condition. More precisely, the initial profiles along the longitudinal direction are defined by:

$$\bar{T}(x) = T_0 \quad , \quad \bar{P}(x) = \bar{\rho}(x) \frac{\mathcal{R}}{\mathcal{M}(x)} T_0 + \frac{a_R T_0^4}{3} \quad \text{with} \quad \bar{\rho}(x) = \rho_0 \frac{\mathcal{M}(x)}{\mathcal{M}_0} \exp\left(\frac{\mathcal{M}(x) \mathbf{g}_x}{\mathcal{R} T_0}\right) \quad ,$$

$$\text{where } \mathcal{M}(x) = \begin{cases} \mathcal{M}_l & \text{if } x < x_0 \quad , \\ \mathcal{M}_h & \text{if } x > x_0 \quad , \end{cases} \quad \text{and} \quad \mathcal{M}_0 = \frac{\mathcal{M}_h + \mathcal{M}_l}{2} \quad .$$

Note that the two molar masses should be understood as effective masses, accounting for the actual molar mass divided by  $(1 + \mathcal{Z})$ , consistent with the equation of state (2.8). Their contrast is characterized by the Atwood number:

$$\mathcal{A}_t = \frac{\mathcal{M}_h - \mathcal{M}_l}{\mathcal{M}_h + \mathcal{M}_l} \quad .$$

At initial time, the interface is left flat but a small perturbation of the velocity field is introduced around it. The perturbation spectrum has a hat profile delimited by the wavelengths  $\lambda_{\min}$  and  $\lambda_{\max} = 2\lambda_{\min}$  and an intensity characterized by a turbulent Mach number  $M_{t_0}$ .

From now on, all quantities are non-dimensionalized by the following reference scales: the maximum wavelength of the perturbation spectrum  $\lambda_{\max}$ , the acceleration  $\mathcal{A}_t g$  and the arithmetic average of the densities of the two fluids at the interface. Besides, two dimensionless numbers are introduced in order to account for the local properties of the radiating fluid, see [Mihalas & Mihalas \[2013\]](#). The contribution of the radiation energy compared to the one of the stellar material may be expressed with the Mihalas number  $R$ . As for the Boltzmann number  $Bo$ , it yields the relative importance between radiative and matter energy transport.

They are respectively estimated at the initial interface location with:

$$R = \frac{\rho e^m}{E^r} \quad \text{and} \quad Bo = \frac{\rho h^m c_{s_0}}{\sigma_{SB} T^4} \quad ,$$

where all the quantities have the same meanings as in [Sec. 2.2.4](#). Note that the initial speed of sound is chosen as the characteristic velocity for the Boltzmann number. The temperature reference scale is finally defined from the other reference scales so as to maintain the Mihalas number.

For the sake of simplicity, both gases of the binary mixture have equal adiabatic indices  $\gamma_0$ , kinematic viscosity  $\nu_v$ , species diffusion coefficient  $\mathcal{D}$  and opacity  $\kappa^r$  and these properties are assumed to be constant.

Within this non-dimensional setting and choices, the main parameters defining the simulations are:

$$\begin{aligned} \mathcal{A}_t &= 0.26 \quad , \quad R = 1.24 \quad , \quad Bo = 3.75 \times 10^{-2} \quad , \quad \gamma_0 = \frac{5}{3} \quad , \quad \rho_0 = 1 \quad , \quad \lambda_{\max} = 1 \quad , \\ M_{t_0} &= 5 \times 10^{-3} \quad , \quad T_0 = 3.16 \quad , \quad \frac{\mathcal{M}_0 g}{\mathcal{R} T_0} = 3.89 \times 10^{-2} \quad , \quad \nu_v = \mathcal{D} = 9.2 \times 10^{-3} \quad . \end{aligned}$$

The fact that ( $R > 1$ ) indicates that material energy and pressure dominate radiative ones and the fact that ( $Bo \ll 1$ ) shows that the radiative flux overwhelms the material enthalpy flux. Such conditions can be found in the interior of massive stars, where the radiative pressure is not negligible as opposed to intermediate-mass stars.

As for the numerical parameters, the domain is of size  $(L_x \times L_y \times L_z) = (87.5 \times 100 \times 100)$  and is discretized using a Cartesian structured mesh with  $(N_x \times N_y \times N_z) = (896 \times 1024 \times 1024)$  cells. Periodic conditions are imposed in the transverse homogeneous directions, along the  $(y, z)$ -axes. Slip wall boundary conditions are considered for the fluids and Dirichlet ones for the radiative energy in the  $x$ -axis.

## 2.5. Validation of the asymptotic analysis

Three simulations are carried out: one with a very small Prandtl number, another with a large Prandtl number and a third with a moderately small Prandtl number. The Prandtl number is here defined as the value at initial time and at the interface of:

$$\text{Pr} = \frac{\nu_v}{\lambda/(\rho c_p)} = \frac{3\rho c_p}{4c_\ell a_R T^3} \rho_0 \kappa^r \nu_v \quad .$$

The first simulation is expected to yield a small Péclet number and aims at verifying the results of the asymptotic analysis. Then, by comparison with the second one, it allows to differentiate the behaviours of the induced turbulent mixing arising within both asymptotic regimes. The intermediate Prandtl simulation is meant to test the limits of the approximation. To vary the Prandtl number, the radiative conductivity is modified by changing the opacity  $\kappa^r$ . The opacity values chosen for each simulation are given in Table A along with the Prandtl number and with a name attributed to each simulation.

Simulation acronym	Opacity $\kappa^r$	Prandtl number Pr
SP <sub>1</sub>	8.64	$2.36 \times 10^{-4}$
SP <sub>2</sub>	$8.64 \times 10^1$	$2.36 \times 10^{-3}$
HP	$8.64 \times 10^4$	2.36

Table A – Rosseland opacities defining each of the three simulations performed for the validation. The acronyms SP and HP stand respectively for small Prandtl and high Prandtl. For information, each simulation of  $0.94 \times 10^9$  cells has been performed in 25 000 iterations by 66 560 h.Pe  $\sim$  2 800 days.Pe.

To conclude the flow description, let us remark that the problem is statistically one-dimensional only depending on the inhomogeneous direction  $x$ . Thus, by ergodicity, statistical averages can be computed by integration on the homogeneous directions. For any quantity  $q$ , we define:

$$\bar{q}(x) = \frac{1}{L_y L_z} \iint q(x, y, z) dy dz \quad .$$

### 2.5.3 Dimensionless numbers

In order to verify the main conditions of the asymptotic analysis, assumed in Sec. 2.3, we proceed to compute the following dimensionless numbers: the turbulent Mach number  $M_t$ , the turbulent Reynolds number  $\text{Re}_\lambda$  based on the Taylor micro-scale, as well as the turbulent Péclet number  $\text{Pe}_t$ . All those numbers are extracted from the simulations at the initial position of the interface ( $x = x_0$ ), using the following definitions:

$$M_t \equiv \frac{\sqrt{\bar{k}}}{c_s} \quad , \quad \text{Re}_\lambda \equiv \frac{2\sqrt{15}}{3} \sqrt{\frac{\rho \bar{k}^2}{\mu_v \bar{\varepsilon}}} \quad , \quad \text{Pe}_t \equiv \frac{\overline{\rho c_p} \nu_t}{\lambda} \quad ,$$

$$\text{with } \nu_t = \frac{C_\mu \bar{k}^2}{\bar{\varepsilon}} \quad , \quad \bar{k} = \frac{1}{2} \overline{u'_i u'_i} \quad , \quad \bar{\varepsilon} = 2\nu_v \overline{(\partial_j u'_i)^2} \quad . \quad (2.73)$$

These definitions involve the turbulent kinetic energy  $\bar{k}$ , its dissipation  $\bar{\varepsilon}$  and the turbulent viscosity  $\nu_t$ . The constant  $C_\mu$  is set to 0.1 as in standard  $\bar{k} - \bar{\varepsilon}$  models [Schiestel, 2010].

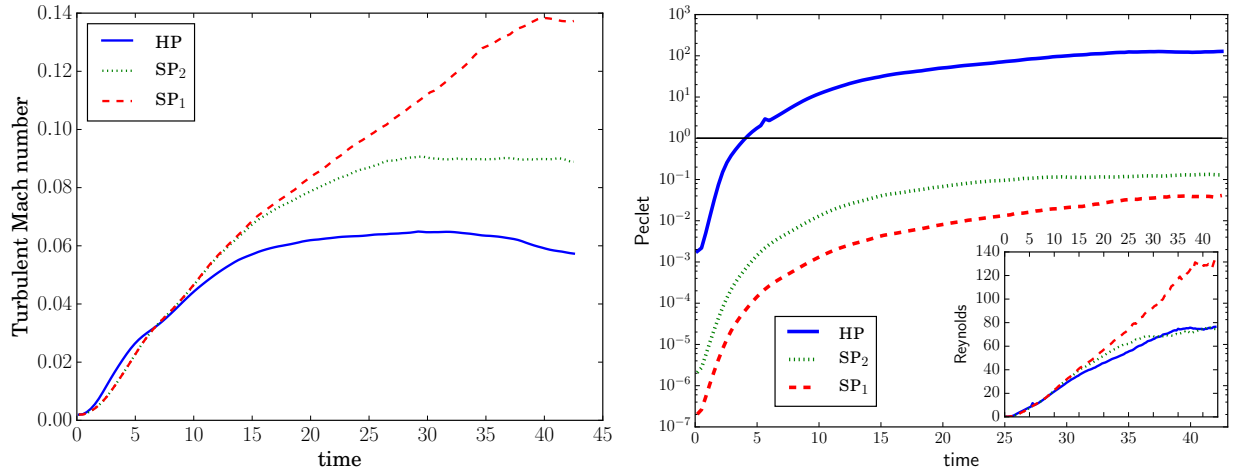


Figure 2.1 – Time evolution of the turbulent Mach  $M_t$ , Péclet  $Pe_t$  and Reynolds  $Re_\lambda$  numbers at the center of the mixing zone.

First, the desired condition ( $M_t \ll 1$ ), displayed in Fig. 2.1, is met for the three configurations since the turbulent Mach number is always observed to remain lower than 0.14. Regarding the turbulent Péclet number, its evolution is also shown in Fig. 2.1. At large enough times for the flow to be turbulent ( $t \gtrsim 15$ ), the Péclet reaches values on the order of  $10^{-2}$ ,  $10^{-1}$  and  $10^2$  respectively for the low, intermediate and high Prandtl simulations. As for the Reynolds number  $Re_\lambda$ , its value is shown in Fig. 2.1. It keeps increasing in time and finally reaches the value ( $Re_\lambda \sim 115$ ) for the small Prandtl simulation and ( $Re_\lambda \sim 70$ ) for the other two configurations.

To sum up, the following conditions are reached for each simulations, from approximately ( $t \gtrsim 15$ ):

$$\begin{cases} SP_1 & : (Re_\lambda \gg 1) \text{ and } (Pe_t \ll M_t \ll 1) , \\ SP_2 & : (Re_\lambda \gg 1) \text{ and } (Pe_t \sim M_t \ll 1) , \\ HP & : (Re_\lambda \gg 1) , (M_t \ll 1) \text{ and } (Pe_t \gg 1) . \end{cases}$$

Thus, the main conditions of relations (2.28) leading to the asymptotic expansion detailed in Sec. 2.3 are verified for the simulations  $SP_1$  and  $SP_2$ . By contrast, the simulation  $HP$  evolves in the opposite Péclet limit.

Note that the secondary conditions introduced in 2.3.1 are also verified in all three simulations. The Froude numbers are on the order or much larger than one, the relative concentration and density variances within the mixing zones are small and the mean pressure and temperature scales are much larger than the turbulent scale.

## 2.5.4 General evolution of the flow

The development of the instability between the two fluids is illustrated in Fig. 2.3. The latter displays a volume rendering of the concentration at three different times and for the simulations  $SP_1$  and  $HP$ .

## 2.5. Validation of the asymptotic analysis

More precisely, it shows the mixing zone shortly after the initial time ( $t = 4$ ) and at a transitional time ( $t = 17$ ). These times are only presented for the high Péclet simulation HP. Indeed, until ( $t \approx 17$ ), the binary mixtures of the small and high Péclet simulations are visually indistinguishable. However, at later times, in the fully turbulent regime, a clear discrepancy between the two simulations is seen. In the high Prandtl simulation HP, the mixing zone saturates whereas in the small Prandtl simulation  $SP_1$ , the dominant and most energetic scales of turbulence keep increasing.

This discrepancy can be explained by the difference in the stability criteria obtained in the high and small Péclet limit, as detailed in Sec. 2.3.2.5. For the high Péclet limit, the stability criterion is linked to the density gradient corrected by an adiabatic pressure gradient. This quantity can be integrated over the inhomogeneous direction to yield a dimensionless pseudo-entropy:

$$S = \int_{-30}^x \left( \frac{\partial_{\xi} \bar{P}}{\bar{\gamma}_1 \bar{P}} - \frac{\partial_{\xi} \bar{\rho}}{\bar{\rho}} \right) d\xi . \quad (2.74)$$

Given the orientation of the gravity in the simulations (leading to  $\partial_x \bar{P} < 0$ ) and the stability criterion (2.64b), the stratification in the high Péclet case is stable if  $S$  increases with  $x$  ( $\partial_x S > 0$ ), unstable if  $S$  decreases with  $x$  ( $\partial_x S < 0$ ) and neutral if  $S$  is uniform ( $\partial_x S = 0$ ).

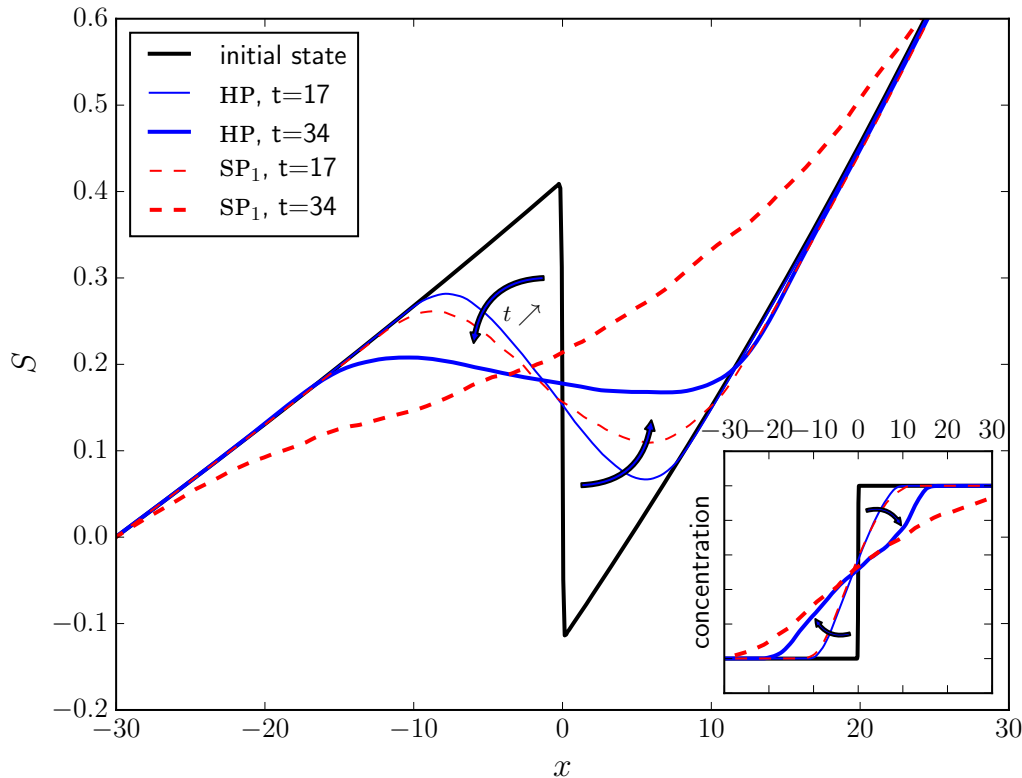


Figure 2.2 – Spatial profiles of the pseudo-entropy  $S$ , given by (2.74) for the high and small Péclet simulations at times  $t = 0$ ,  $t = 17$  and  $t = 34$ .

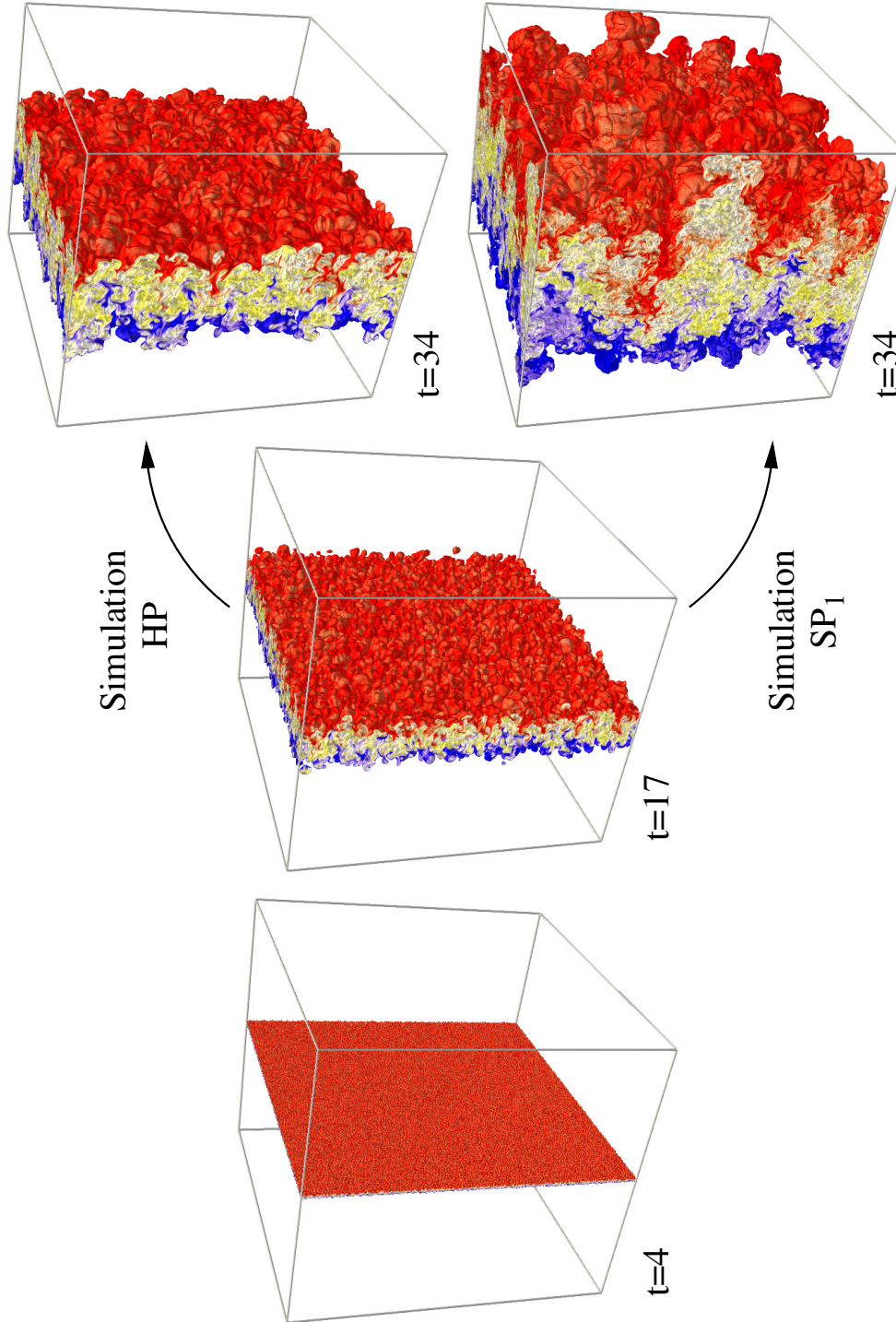


Figure 2.3 – Shaded volume rendering of the light fluid concentration made visible from  $c = 0.1$  (blue) to  $c = 0.9$  (red). The heavy fluid is on the right and the light one on the left. The gravity vector is oriented to the left along the x-axis, *i.e.* from the heavy to the light side. The rendering is shown at 3 different times  $t = 4$ ,  $t = 17$  and  $t = 34$ . Visually identical figures are obtained for all three simulations at  $t = 4$  and  $t = 17$  but large differences are observed here between the high Prandtl simulation HP and the small Prandtl simulation SP1 at the final time  $t = 34$ .

## 2.5. Validation of the asymptotic analysis

---

In the present simulations, the spatial profiles of the pseudo-entropy  $S$  are not monotonous. These profiles are shown for the high and small Prandtl simulations in Fig. 2.2 at times  $t = 0$ ,  $t = 17$  and  $t = 34$ . The initial profile of  $S$  is the same for all simulations and is imposed by the isothermal hydrostatic condition. More precisely, at  $t = 0$ , one observes a rapid decrease of  $S$  at the interface between both gases while  $S$  increases on each side of this interface. In other words, according to the high-Péclet number criterion (2.64b), the interface is initially unstable while the subdomains it separates are stable. As mixing unfolds, the initial rapid interfacial decrease of  $S$  extends and flattens out until an almost uniform profile is reached within the extent of the mixing zone. For the high Prandtl number simulation HP, this flat profile of  $S$  means that the stratification has reached an almost neutral state and that the instability is not fed any longer. Thus, turbulence starts decaying and eventually dissipates. The mixing zone stops growing.

This phenomenology is not observed for the small Prandtl simulation  $SP_1$ . As can be seen in Fig. 2.2, for  $SP_1$ , the profile of  $S$  never stops diffusing. Even after crossing the high Péclet neutral threshold, it keeps increasing over the whole spatial domain. To explain this major difference, one must recall that the stability criteria in the small and high Péclet limits are not the same. In the small Péclet case, the stability of a stratification is determined by Eq. (2.64a). It is completely independent of the entropy stratification and only depends on the gas constant gradient  $\partial_x \bar{r}$ . The latter exists if the two gases being mixed have different molar masses and if there is a mean concentration gradient. In the small Prandtl simulations performed here, evolving in a small Péclet regime, given the orientation of the gravity field and the initial repartition of the molar masses, the stability of the stratification is eventually given by the sign of  $\partial_x \bar{c}$ , the mean concentration gradient of the light fluid. More precisely, the stratification in the small Péclet limit is stable if  $\bar{c}$  decreases with  $x$  ( $\partial_x \bar{c} < 0$ ), unstable if  $\bar{c}$  increases ( $\partial_x \bar{c} > 0$ ) and neutral if  $\bar{c}$  is constant ( $\partial_x \bar{c} = 0$ ). The mean concentration has a monotonously decreasing spatial profile at all times ( $\partial_x \bar{c} \leq 0$ ) as shown in the insert of Fig. 2.2. Therefore, the stratification of the small Prandtl  $SP_1$  simulation is always unstable. As a result, in the small Péclet regime, the mixing zone grows until it reaches the boundaries of the flow domain.

As a conclusion, the different mixing width evolutions observed in simulations  $SP_1$  and HP are coherent with the stability criteria predicted in Sec. 2.3.2.5. These criteria reflect the influence of the Péclet number and are a direct consequence of the asymptotic approximation derived in Sec. 2.3. Thus, the qualitatively different behaviours between simulations  $SP_1$  and HP (identical except for the opacity value), are a first validation of the asymptotic results. A direct verification is proposed in the next subsection.

### 2.5.5 Validation of the asymptotic analysis

One of the main predictions of the asymptotic analysis is the order of magnitude of the pressure and temperature fluctuations, as given by Eq. (2.46). To assess this prediction, we plot in Fig. 2.4 the temporal evolutions of the ratios  $\eta_P$  and  $\eta_T$  at the center of the mixing zone, defined by:

$$\eta_P = \frac{\sqrt{P'P'}}{\bar{P} \cdot M_t^2} \quad \text{and} \quad \eta_T = \frac{\sqrt{T'T'}}{\bar{T} \cdot Pe_t \cdot M_t} \quad .$$

For Eq. (2.46) to be verified, these ratios must be on the order of 1. As can be seen in Fig. 2.4, the ratio  $\eta_P$  tends to 1 in the turbulent regime for each configuration, showing that the fluctuating pressure is on the order of  $M_t^2$ . This scaling is expected because it results from the small turbulent Mach number asymptotics whatever the Péclet number. Since the turbulent Mach number hardly reaches 0.14, as previously mentioned, all three simulations evolve in a small Mach regime and give rise to pressure fluctuations of the same order.

As for the ratio  $\eta_T$ , it is of order unity for the two small Prandtl simulations  $SP_1$  and  $SP_2$  whose turbulent mixing occur in a small Péclet regime. The prediction (2.46) is thus verified. On the opposite, the order of  $\eta_T$  in the high Prandtl simulation  $HP$  significantly departs from the others:  $\eta_T$  actually tends towards zero. There is indeed no condition for the fluctuating temperature in the high Péclet analysis [Soulard *et al.*, 2012].

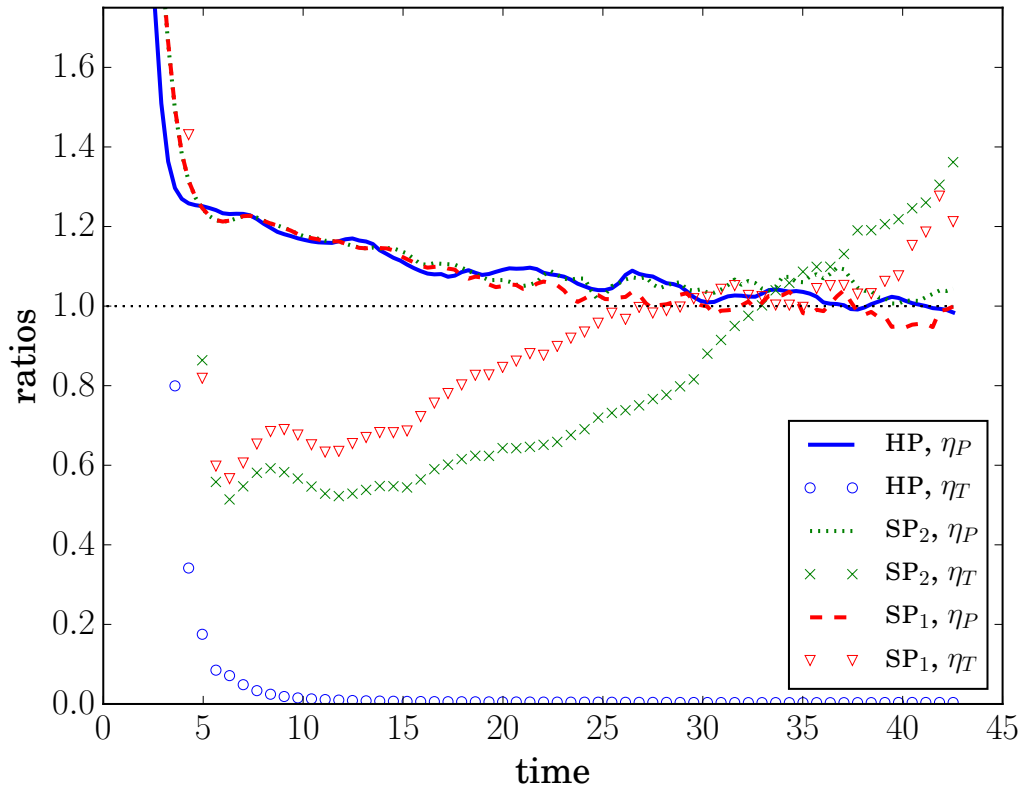


Figure 2.4 – Time evolution of ratios  $\eta_P$  and  $\eta_T$  at the center of the mixing zone.

The other major predictions derived from the asymptotic analysis of Sec. 2.3 are the values of the fluctuating velocity divergence  $\text{div} \mathbf{u}'$  and of the fluctuating conduction term  $\mathcal{C}'$ . These predictions are respectively expressed in Eqs. (2.57a) and (2.57b). To evaluate their quality, we compare “simulated” and “predicted” values of  $\text{div} \mathbf{u}'$  and  $\mathcal{C}'$ . On the one hand, the “simulated” values are obtained by taking the fluctuating part of  $\text{div} \mathbf{u}$  and  $\mathcal{C}$  computed from the actual fields using their definitions  $\text{div} \mathbf{u} = \partial_j u_j$  and  $\mathcal{C} = \partial_j (\lambda \partial_j T)$ . On the other hand, the “predicted” values are directly computed as the right-hand side of Eqs. (2.57a) and (2.57b) using the same actual simulations.

## 2.5. Validation of the asymptotic analysis

Two-dimensional fields (slices in the plane  $y = 0$ ) are shown in Figs. 2.5 and 2.6 to compare the simulated and predicted values of  $C'$  and  $\text{div}\mathbf{u}'$  respectively. They are extracted from the simulation  $\text{SP}_2$  at a transition time  $t = 17$  and at  $t = 34$ , a time at which the small Péclet asymptotic results should apply according to Fig. 2.1. The same structures can indeed be identified, from  $t = 17$ , in both parts of Fig. 2.5 and, since the color scale is the same, the overall agreement on the intensity of the fluctuating conduction  $C'$ -fields can be guessed. The main difference comes from the occurrence of some localized extrema in the simulated field which seem to be filtered out by the use of formula (2.57b). The same comments apply to the fluctuating velocity divergence shown in Fig. 2.6 including the filtering effect of the asymptotic expression Eq. (2.57a). The striking likeness between Fig. 2.5 and 2.6 comes from the fact the stratification term is dominant in Eqs. (2.57b) and (2.57a) in that case and the mean flow is isothermal. Both fields then roughly look like  $u'_j (\partial_j \bar{\rho} / \bar{\rho} + \partial_j \bar{r} / \bar{r})$  and the large difference in the prefactors is hidden in the difference in color scale between both figures.

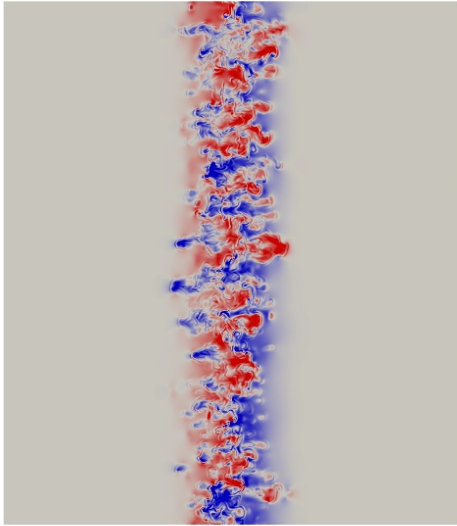
Figures 2.5 and 2.6 provide a qualitative assessment of the asymptotic results derived in Sec. 2.3.2.2. A quantitative validation can be performed by measuring the correlations of  $\text{div}\mathbf{u}'$  with other flow variables. For modelling purposes, that will be made clear in chapter 3, we focus on the correlations of  $\text{div}\mathbf{u}'$  with  $\rho'$  and  $u'_x$ , namely:  $\overline{\rho' \text{div}\mathbf{u}'}$  and  $\overline{u'_x \text{div}\mathbf{u}'}$ . Besides, the predicted value of  $\text{div}\mathbf{u}'$  is split into its two contributions: the one coming from the mean stratification and the one coming from molecular mixing effects. More precisely, from Eq. (2.57a), the correlations  $\overline{\rho' \text{div}\mathbf{u}'}$  and  $\overline{u'_x \text{div}\mathbf{u}'}$  are expressed as:

$$\overline{q' \text{div}\mathbf{u}'} = \overline{q' \text{div}\mathbf{u}'}^{\text{strat.}} + \overline{q' \text{div}\mathbf{u}'}^{\text{mix.}} \quad \text{with} \quad \begin{cases} \overline{q' \text{div}\mathbf{u}'}^{\text{strat.}} &= -\overline{q' u'_x} \left( \frac{\partial_x \bar{\rho}}{\bar{\rho}} + \frac{\partial_x \bar{r}}{\bar{r}} \right) , \\ \overline{q' \text{div}\mathbf{u}'}^{\text{mix.}} &= \frac{\Delta r}{\bar{r}} q' \left[ \frac{\partial_j (\rho D \partial_j c')}{\rho} \right]' , \end{cases}$$

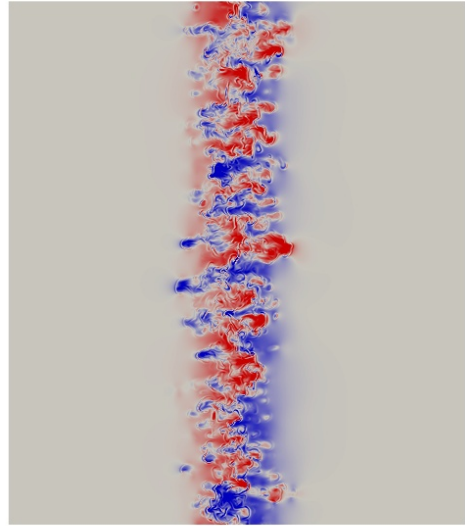
where the quantity  $q'$  stands for  $u'_x$  or  $\rho'$  and where  $\Delta r = \mathcal{R}/\mathcal{M}_l - \mathcal{R}/\mathcal{M}_h$ . The simulated and predicted correlations  $\overline{\rho' \text{div}\mathbf{u}'}$  and  $\overline{u'_x \text{div}\mathbf{u}'}$  of the simulations  $\text{SP}_2$  and HP are shown respectively in Figs. 2.7 and 2.8, along with the components of the predicted value, at times  $t = 17$  and  $t = 34$ .

Regarding the small-Prandtl simulation of Fig. 2.7, a good agreement between the simulation and the prediction is observed for both correlations at both times indicating that Eq. (2.57a) provides quantitatively accurate estimates. The contributions of the stratification and of the molecular mixing have opposite signs because of the instability: the baroclinic production related to the stratification tends to enhance the turbulence in this unstable configuration whereas the molecular diffusion tends to dissipate the turbulence.

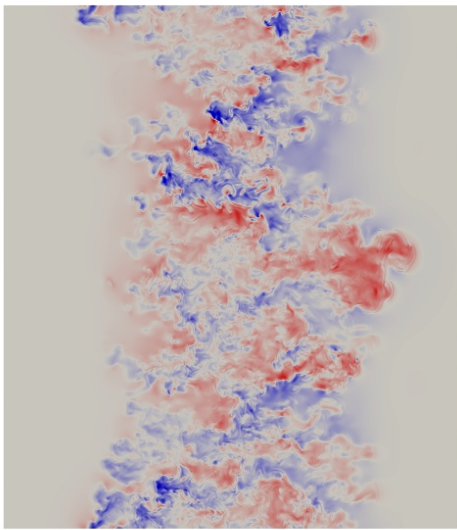
By contrast, if the same comparisons are performed using the high-Prandtl simulation HP instead of the small-Prandtl simulation  $\text{SP}_2$ , strong differences are observed, as expected. Indeed, as shown by Fig. 2.8, the small Péclet prediction Eq. (2.57a) can obviously not be applied to HP which evolves in a large Péclet regime according to Fig. 2.1. What remains however, is the opposition of signs between the stratification and the molecular diffusion contributions. The two parts of the correlations may then still be interpreted as respectively a production and a destruction process.



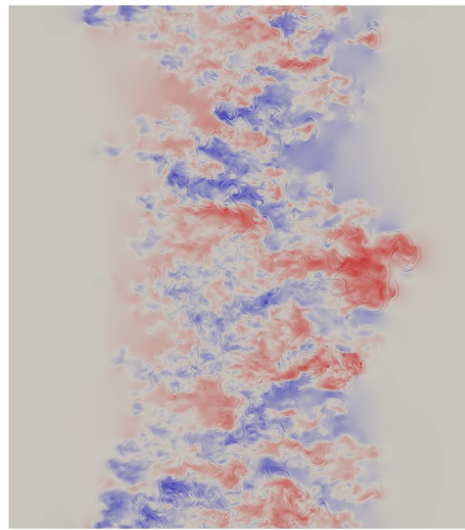
(a) Simulated value of  $C'$  at time  $t = 17$



(b) Predicted value of  $C'$  at time  $t = 17$



(c) Simulated value of  $C'$  at time  $t = 34$

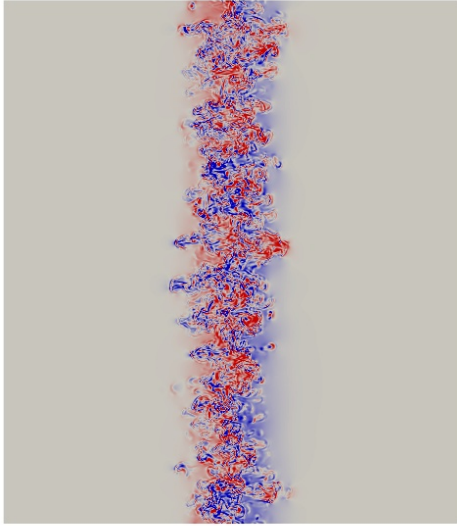


(d) Predicted value of  $C'$  at time  $t = 34$

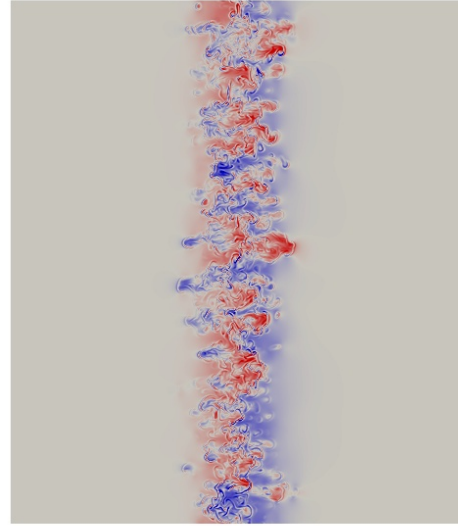
Figure 2.5 – Cuts in the plane  $y = 0$  at times  $t = 17$  and  $t = 34$  for simulation  $SP_2$  displaying respectively: (a) and (c) the fluctuating conduction term  $C'$  computed by using its definition  $C = \partial_j (\lambda \partial_j T)$ ; (b) and (d) the asymptotic value of  $C'$  predicted by Eq. (2.57b). The color scale is the same in each figure.

## 2.5. Validation of the asymptotic analysis

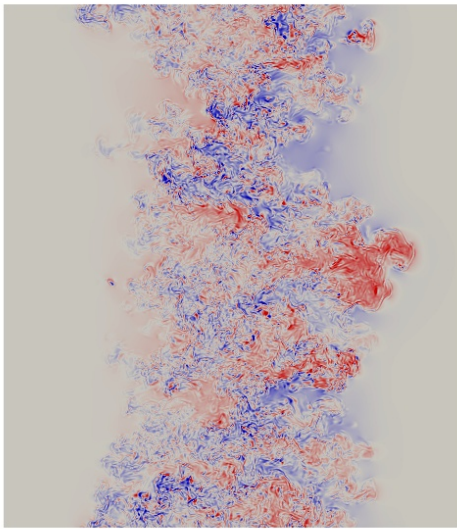
---



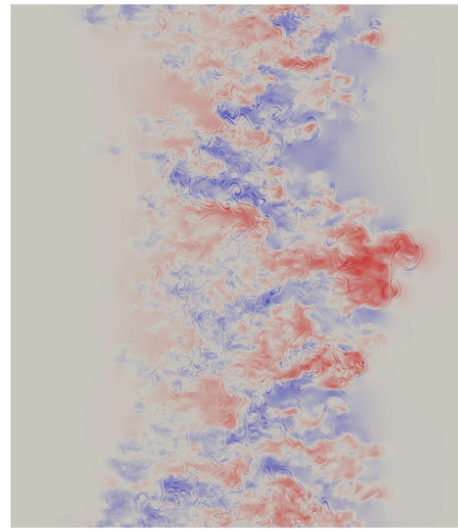
(a) Simulated value of  $\text{div}\mathbf{u}'$  at time  $t = 17$



(b) Predicted value of  $\text{div}\mathbf{u}'$  at time  $t = 17$



(c) Simulated value of  $\text{div}\mathbf{u}'$  at time  $t = 34$



(d) Predicted value of  $\text{div}\mathbf{u}'$  at time  $t = 34$

Figure 2.6 – Cuts in the plane  $y = 0$  at times  $t = 17$  and  $t = 34$  for simulation  $\text{SP}_2$  displaying respectively: (a) and (c) the fluctuating divergence  $\text{div}\mathbf{u}'$  computed by using its definition  $\text{div}\mathbf{u}' = \partial_j \mathbf{u}'_j$ ; (b) and (d) the value of  $\text{div}\mathbf{u}'$  predicted by Eq. (2.57a). The color scale is the same in each figure.

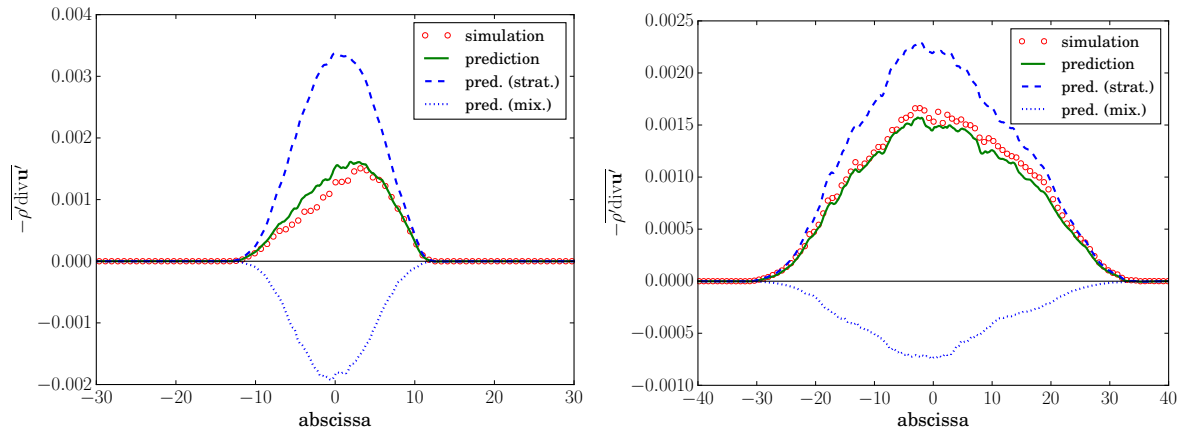
Finally, for both simulations SP<sub>2</sub> and HP represented in Figs. 2.7 and 2.8, the Reynolds number increases as time elapses so that the intensity of the molecular contribution is seen to decrease with respect to the stratification contribution.

A crucial information for turbulence modelling is highlighted in Fig. 2.9. The prediction of the divergence term of Eq. (2.62) has been derived by Soulard *et al.* [2012] within the ( $M_t \ll 1$ ) limit without any assumption on the order of  $Pe_t$  and should be valid for all value of  $Pe_t$ . Figure 2.9 indeed confirms its validity for the small-Prandtl simulation SP<sub>2</sub> while Fig. 2.7 has already shown it in the low-Péclet regime. What makes the small-Péclet prediction of Eq. (2.57a) essential for turbulence modelling is the partition between the stratification and the molecular terms. The latter can indeed not be directly taken into account and should be modelled as dissipative processes. The fact that the contribution  $\overline{q' \text{div} \mathbf{u}'}_{(2.62)}^{\text{mix.}}$  can change its sign and become positive in Fig. 2.9 when the partition of Eq. (2.62) is applied in the small-Péclet regime indicates that its interpretation as a pure destruction term becomes erroneous. The  $\overline{q' \text{div} \mathbf{u}'}_{(2.62)}^{\text{mix.}}$  must therefore be re-interpreted as the sum of a destruction term and an additional stratification one ensuing from the small-Péclet effects when ( $Pe_t \ll 1$ ). Such a re-interpretation finally leads to the partition of Eq. (2.57a) amenable to turbulence modelling when ( $Pe_t \ll 1$ ) as illustrated by the minus sign of  $\overline{q' \text{div} \mathbf{u}'}^{\text{mix.}}$  in Fig. 2.7.

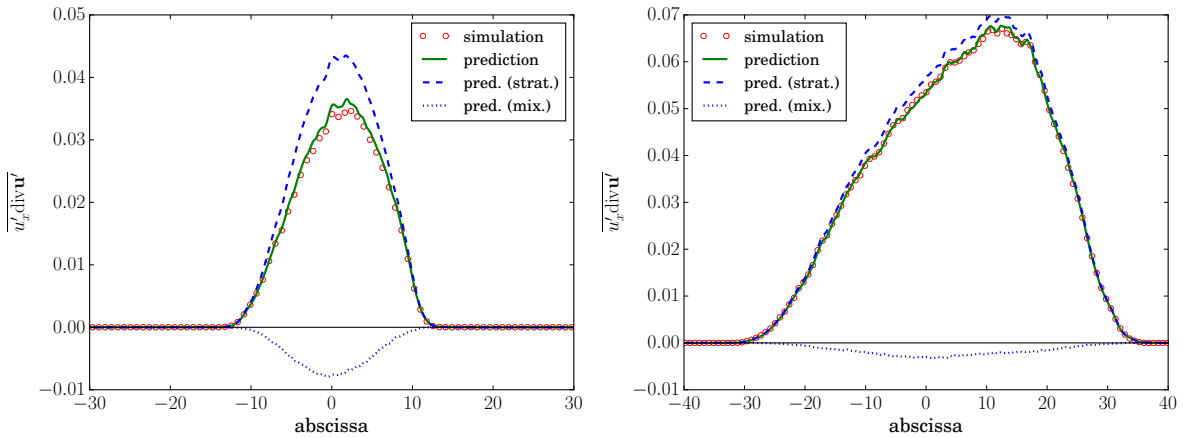
Hence, the comparison between Figs. 2.7 and 2.9 renders explicit the relevance of the small Mach-small Péclet approximation. Indeed, the characterization of the velocity divergence and of the conduction terms allows to target accurately the role played by each of their contributions in an infinitely small Prandtl regime. It will notably clarify the discrepancies of modellization in the next chapter, carried out for both asymptotic Péclet limits.

Finally, to sum up this section, the main results of the ( $M_t \ll 1$  ;  $Pe_t \ll 1$ ) approximation derived in Sec. 2.3 have been verified. The orders of magnitude of  $T'$  and  $P'$  and the values of  $\text{div} \mathbf{u}'$  and  $C'$  are all coherent with the asymptotic predictions.

## 2.5. Validation of the asymptotic analysis

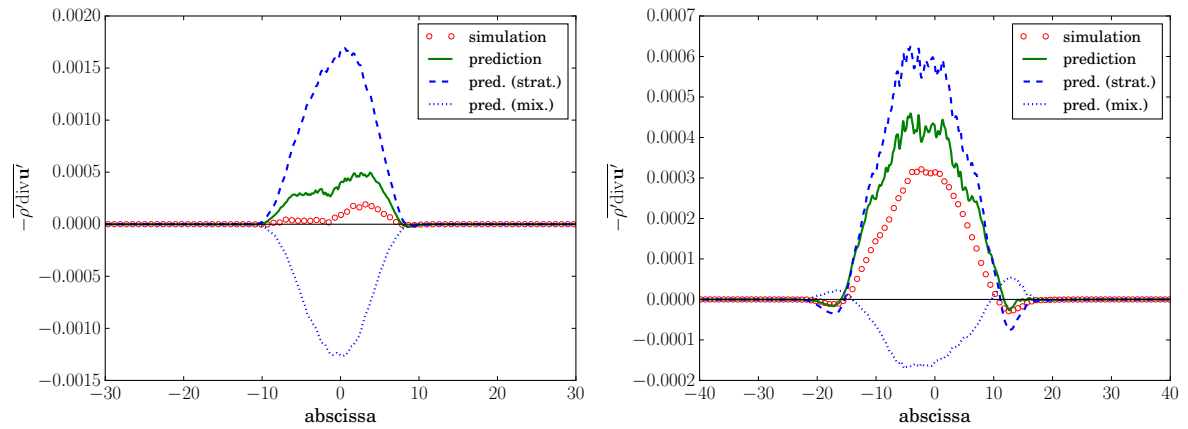


(a) Correlation  $-\overline{\rho' \text{div} \mathbf{u}'}$  at  $t = 17$  and  $t = 34$

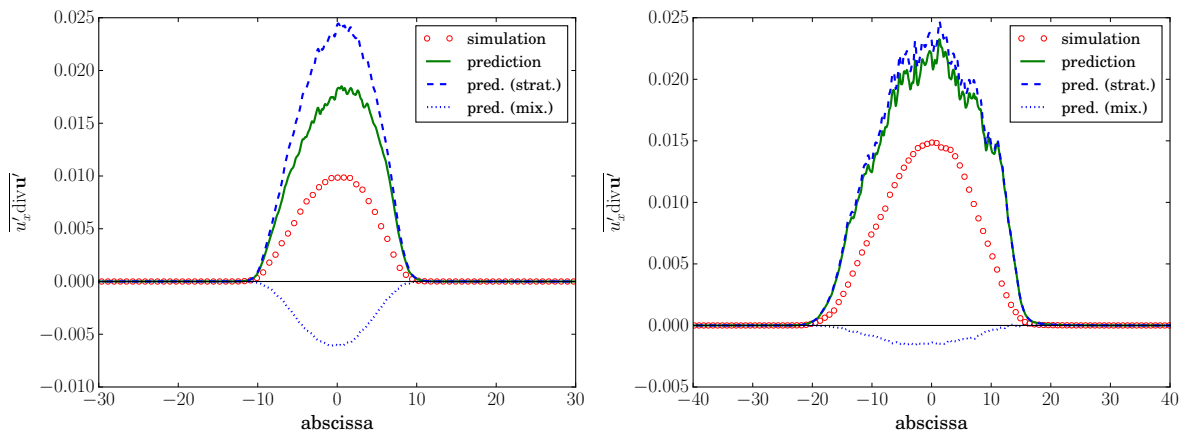


(b) Correlation  $\overline{u'_x \text{div} \mathbf{u}'}$  at  $t = 17$  and  $t = 34$

Figure 2.7 – Spatial profiles of (a)  $-\overline{\rho' \text{div} \mathbf{u}'}$  and (b)  $\overline{u'_x \text{div} \mathbf{u}'}$  for simulation  $\text{SP}_2$  at times  $t = 17$  and  $t = 34$ . Comparison between the ( $\text{Pe}_t \ll 1$ ) **simulated** and ( $\text{Pe}_t \ll 1$ ) **predicted** values, computed using the small-Péclet prediction Eq. (2.57a). The contributions from the stratification (“strat.”) and the molecular (“mix.”) terms to both predicted values are shown.



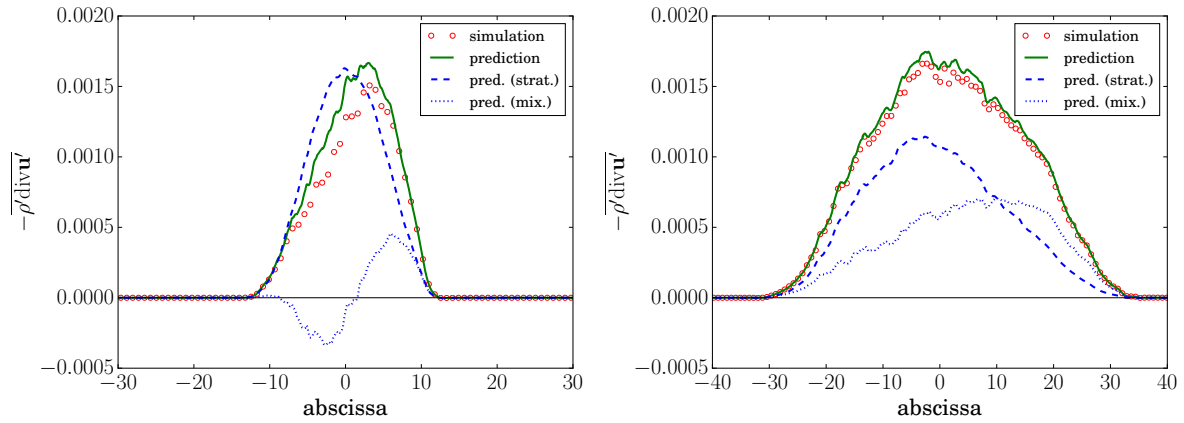
(a) Correlation  $-\overline{\rho' \text{div} u'}$  at  $t = 17$  and  $t = 34$



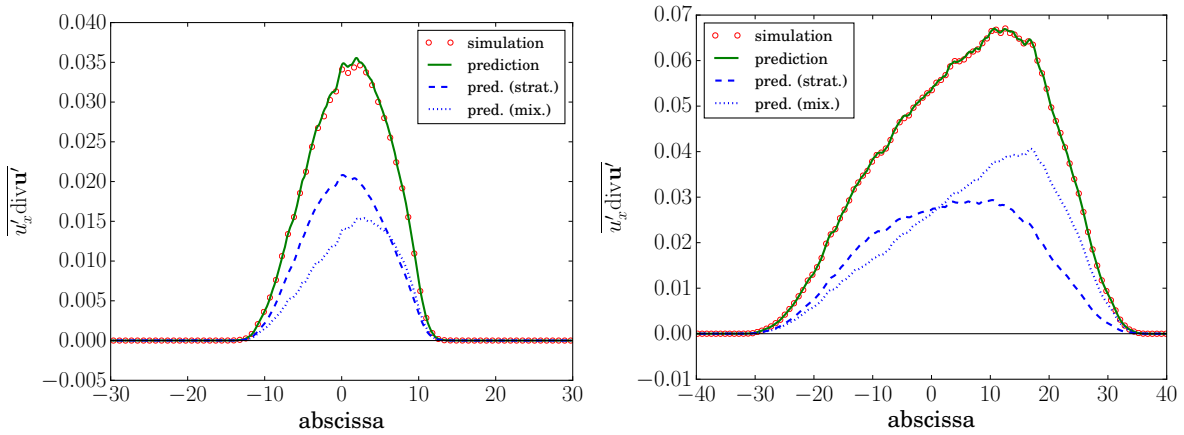
(b) Correlation  $\overline{u'_x \text{div} u'}$  at  $t = 17$  and  $t = 34$

Figure 2.8 – Spatial profiles of (a)  $-\overline{\rho' \text{div} u'}$  and (b)  $\overline{u'_x \text{div} u'}$  for simulation HP at times  $t = 17$  and  $t = 34$ . Comparison between the ( $Pe_t \gg 1$ ) **simulated** and ( $Pe_t \ll 1$ ) **predicted** values, computed using the small-Péclet prediction Eq. (2.57a). The contributions from the stratification (“strat.”) and the molecular (“mix.”) terms to both predicted values are shown.

## 2.5. Validation of the asymptotic analysis



(a) Correlation  $-\overline{\rho' \text{div} \mathbf{u}'}$  at  $t = 17$  and  $t = 34$



(b) Correlation  $\overline{u'_x \text{div} \mathbf{u}'}$  at  $t = 17$  and  $t = 34$

Figure 2.9 – Spatial profiles of (a)  $-\overline{\rho' \text{div} \mathbf{u}'}$  and (b)  $\overline{u'_x \text{div} \mathbf{u}'}$  for simulation  $SP_2$  at times  $t = 17$  and  $t = 34$ . Comparison between the ( $Pe_t \ll 1$ ) **simulated** and ( $M_t \ll 1$ ) **predicted** values, computed using the small-Mach all-Péclet prediction Eq. (2.62) from [Soulard \*et al.\* \[2012\]](#). The contributions from the stratification (“strat.”) and the molecular (“mix.”) terms to both predicted values are shown.

## 2.6 Conclusion

In this work, an asymptotic analysis of radiative mixing flows has been performed in the joint limit of small turbulent Mach number and small turbulent Péclet number. It predicts the scalings of pressure and temperature fluctuations in addition to providing approximations for the fluctuations of the thermal conduction and of the velocity divergence fields. The latter estimates turn out to be the cornerstone for the improvement of RANS turbulence modeling when the radiative conduction overwhelms the turbulent diffusivity. This aspect is discussed in the next chapter.

## 2.6. Conclusion

---

# 3

## Adaptation and validation of a ( $M_t \ll 1$ ) RSM turbulence model to the ( $Pe_t \ll 1$ ) regime

“For, though thy long dark lashes low depending,  
The soul of melancholy Gentleness  
Gleams like a Seraph from the sky descending,  
Above all pain, yet pitying all distress;  
At once such majesty with sweetness blending,  
I worship more, but cannot love thee less.”

LORD BYRON  
*Sonnet – to Geneva*

### Contents

<b>3.1 Introduction</b> . . . . .	<b>80</b>
<b>3.2 Adaptation of a RSM : the GSG turbulent model</b> . . . . .	<b>81</b>
3.2.1 Current version of the GSG model in the ( $Pe_t \gg 1$ ) limit . . . . .	81
3.2.2 Adaptation of the Langevin PDF model to the ( $Pe_t \ll 1$ ) limit . . . . .	85
3.2.3 Adaptation of the GSG model to the ( $Pe_t \ll 1$ ) limit . . . . .	87
3.2.4 Blending between the two limits ( $Pe_t \gg 1$ ) and ( $Pe_t \ll 1$ ) . . . . .	88
<b>3.3 Validation of the extended RSM</b> . . . . .	<b>90</b>
3.3.1 Calibration with respect to <b>TRICLADE</b> simulations . . . . .	90
3.3.2 1D simulations with the GSG turbulence model . . . . .	91
<b>3.4 Conclusion</b> . . . . .	<b>94</b>

## 3.1 Introduction

Small Mach number approximations, considered independently from small Péclet number ones, have a paramount influence on the formulation of statistical turbulent models. For instance, most closures for the fluctuating pressure gradient used in second order models [Launder *et al.*, 1975, Schiestel, 2010], probability density function (PDF) models [Kuznetsov & Sabelnikov, 1990, Pope, 1985] or spectral models [Sagaut & Cambon, 2018] are derived by assuming that the pressure field obeys a Poisson equation. Let us recall that the latter equation stems from the existence of a constraint on the velocity divergence, which is itself one of the main outcomes of small Mach number asymptotic analyses. Furthermore, the velocity divergence constraint allows for an explicit treatment of several compressibility effects. As reviewed by Livescu [2020] for instance, binary mixtures may lead to possibly strong density variations, stemming from large pressure, temperature or composition fluctuations. These effects can then be taken into account in a model with or without additional closures [Shimomura, 1999, So *et al.*, 2000, Soulard *et al.*, 2012]. In particular, in Soulard *et al.* [2012], it was shown how the velocity divergence constraint can be used to derive closed evolution equations for the variance and flux of the density field. These equations, in conjunction with additional equations for the Reynolds stresses (velocity co-variances) and for the kinetic energy dissipation, form the basis of a class of augmented Reynolds stress models (RSM) which have proved to be efficient for solving variable-density turbulence. Among those augmented RSM, one can cite the BHR model [Besnard *et al.*, 1989] and the GSG model [Grégoire *et al.*, 2005]. The latter is the model which adaptation was proposed in Soulard *et al.* [2012] and which will be the focus of this chapter.

As discussed in the previous chapter, the outcome of small Mach number approximations is different in the high and small Péclet limits. In particular, the constraint on the velocity divergence takes a different expression when both the Mach and Péclet numbers are small. This can be seen by comparing equation (2.62), valid for high Péclet numbers, to equation (2.57a), valid for small Péclet numbers. As a result, models which are based on the high Péclet version of the velocity divergence constraint are not adapted to deal with small Péclet flows and need to be modified to account for this particular limit.

Such adaptations have scarcely been considered in the literature. Indeed, flows combining small Péclet, small Mach and high Reynolds numbers are rarely – if ever at all – observed in traditional engineering applications, for which most turbulence models have been developed. By contrast, these conditions are frequently met in stellar applications (see chapter 1). In this context, several closures have consequently been proposed in order to capture small Péclet regimes. However, most efforts have been devoted to improve models based on Prandtl’s mixing length theory [Browning *et al.*, 2004, Canuto, 1996, Canuto & Mazzitelli, 1991, 1992, Heiter *et al.*, 2002, Kippenhahn, 1994, Meakin & Arnett, 2007, Prat, 2013, Viallet *et al.*, 2015, Weiss & Charbonnel, 2004, Zahn, 1991]. This type of models is indeed the one that is almost exclusively used in stellar evolution codes. A notable exception is the RSM proposed by Canuto [2011a]. In this model, an explicit dependency on the Péclet number is introduced. However, this model rests upon an iso-volume hypothesis which, as we saw in chapter 2, is not necessarily compatible with an asymptotic analysis coupling both the ( $M_t \ll 1$ ) and ( $Pe_t \ll 1$ ) limits.

Given this relative scarcity of turbulence models valid in the small Péclet limit, it would be especially interesting to derive a methodology for adapting high Péclet turbulence models to the small Péclet case. Such a methodology would allow to transpose the vast number and well-established properties of these existing models to the small Péclet case. The purpose of this chapter is to illustrate, with a concrete example, how such a methodology can be set up. To this end, we consider the particular case of the GSG model [Grégoire *et al.*, 2005]. This second-order RSM model is indeed particularly interesting for stellar applications since it is meant to treat variable density turbulent mixing zones submitted to a wide variety of convective instabilities. Besides, its derivation is explicitly based on the outcome of a small Mach, high Péclet asymptotic analysis. Therefore, the modifications linked to the value of the Péclet number will be easier to highlight and to implement.

The first part of this chapter details the adaptation of the ( $M_t \ll 1$ ) GSG model. It begins with the description of the current closure of the fluctuating divergence term, already accounting for the ( $Pe_t \gg 1$ ) limit. Then, in order to proceed to the ( $Pe_t \ll 1$ ) regime, one replaces the high Péclet relation of the fluctuating divergence by its small Péclet counterpart (Eq. (2.57a)). The stratification and the scalar diffusion terms of  $\text{div}\mathbf{u}'$  retrieved from the ( $M_t \ll 1 ; Pe_t \ll 1$ ) approximation are respectively modeled as a production and a dissipation term. The closures regarding the evolutions of the mass flux and the specific volume variance are modified accordingly. The adaptation ends with the proposition of a model blending the high and small Péclet limits.

The second part is dedicated to the validation of the extended model. To this purpose, a preliminary adjustment is needed. The RSM turbulent model coefficients are calibrated by reference to the three radiative Rayleigh-Taylor DNS already used in chapter 2 and named  $SP_1$ ,  $SP_2$  and HP (see Sec. 2.5.2). The turbulent quantities are then compared together in order to verify that the impacts of radiative effects on the physics of the instability are well predicted by the adapted GSG model. In particular, the kinetic energy, the normalized specific volume variance and the mixing length are proven to have different behaviours with respect to both Péclet asymptotic regimes.

## 3.2 Adaptation of a RSM : the GSG turbulent model

### 3.2.1 Current version of the GSG model in the ( $Pe_t \gg 1$ ) limit

The GSG model of Grégoire *et al.* [2005] is a second-order turbulence model, originally conceived for compressible gaseous mixtures induced by hydrodynamic instabilities such as the Richtmyer-Meshkov (RM) or Rayleigh-Taylor (RT) instabilities [Zhou, 2017]. In its latest version [Griffond *et al.*, 2010], this RSM follows the evolution of the Reynolds stress tensor  $\widetilde{R}_{ij} = \widetilde{u_i''u_j''}$ , of the turbulent energy dissipation rate  $\widetilde{\varepsilon}$ , of the specific volume turbulent flux  $\widetilde{\tau''u_i''}$  and of the specific volume variance  $\widetilde{\tau''\tau''}$ .

For any given quantity  $q$ , we recall that  $\bar{q}$  and  $\tilde{q} = \overline{\rho q}/\bar{\rho}$  denote its Reynolds and Favre averages, while  $q' = q - \bar{q}$  and  $q'' = q - \tilde{q}$  denote the corresponding fluctuations. We also recall that the specific volume is the inverse of the density and that its mean, flux and variance are

### 3.2. Adaptation of a RSM : the GSG turbulent model

exactly related to those of  $\rho$ , as follows:

$$\tau = \frac{1}{\rho} \quad , \quad \tilde{\tau} = \frac{1}{\bar{\rho}} \quad , \quad \frac{\widetilde{\tau''u_j''}}{\tilde{\tau}} = -\frac{\overline{\rho'u_j''}}{\bar{\rho}} = \overline{u_j''} \quad \text{and} \quad \frac{\widetilde{\tau''\tau''}}{\tilde{\tau}^2} = -\overline{\rho'[1/\rho]'} \quad .$$

These relations show that the velocity  $\overline{u_j''}$  is directly related to the mass flux; that is why it is sometimes abusively called "mass flux". We will also hereafter denote by  $\tilde{k}$  the turbulent kinetic energy and by  $\tilde{\omega}$  the turbulent frequency:

$$\tilde{k} = \frac{1}{2}\widetilde{R_{kk}} \quad \text{and} \quad \tilde{\omega} = \frac{\tilde{\varepsilon}}{\tilde{k}} \quad .$$

With these notations, the GSG model derived in Grégoire *et al.* [2005] and adapted in Griffond *et al.* [2010] takes the following form for the mean quantities

$$\left\{ \begin{array}{l} \partial_t \bar{\rho} + \partial_1 (\bar{\rho} \tilde{u}_1) = 0 \quad , \quad (3.1a) \\ \partial_t (\bar{\rho} \tilde{u}_i) + \partial_1 (\bar{\rho} \tilde{u}_i \tilde{u}_1) + \partial_1 (\bar{P}^m + \bar{P}^r) = \bar{\rho} g_i + \partial_1 (\bar{\rho} \widetilde{R_{il}}) \quad , \quad (3.1b) \\ \partial_t (\bar{\rho} \tilde{e}^m) + \partial_1 (\bar{\rho} \tilde{e}^m \tilde{u}_1) + \bar{P}^m \partial_1 \tilde{u}_1 = \partial_1 (\bar{\rho} C_e \mathcal{D}_{ij} \partial_j \tilde{e}^m) + \bar{\rho} \tilde{\varepsilon} - \bar{P}^m \partial_1 \overline{u_1''} \quad , \quad (3.1c) \\ \partial_t \bar{E}^r + \partial_1 (\bar{E}^r \tilde{u}_1) + \bar{P}^r \partial_1 \tilde{u}_1 = \partial_1 \left( \frac{c_\ell}{3\bar{\rho} \tilde{\kappa}^r} \partial_1 \bar{E}^r \right) - \bar{P}^r \partial_1 \overline{u_1''} - \partial_1 (\bar{E}^r \overline{u_1''}) \quad , \quad (3.1d) \\ \partial_t (\bar{\rho} \tilde{c}) + \partial_1 (\bar{\rho} \tilde{c} \tilde{u}_1) = \partial_1 (\bar{\rho} C_c \mathcal{D}_{ij} \partial_j \tilde{c}) \quad , \quad (3.1e) \end{array} \right.$$

where the diffusion tensor  $\mathcal{D}_{ij} = (\tilde{k}/\tilde{\varepsilon}) \widetilde{R_{ij}}$  stems from a first gradient closure as proposed by Daly & Harlow [1970] and applies to energy and scalar diffusion with the modelling constants  $C_e$  and  $C_c$  respectively. As for the second-order correlations appearing in Sys. (3.1), they evolve according to:

$$\begin{aligned} \widetilde{D_t R_{ij}} &= P_{ij} + P_{ij}^H - \gamma^S \left( P_{ij} - \frac{P_{kk}}{3} \delta_{ij} \right) - \gamma^H \left( P_{ij}^H - \frac{P_{kk}^H}{3} \delta_{ij} \right) - (C_1 \tilde{\omega} + \Omega_R) \left( \widetilde{R_{ij}} - \frac{2}{3} \tilde{k} \delta_{ij} \right) - \frac{2}{3} \tilde{\varepsilon} \delta_{ij} \\ &\quad + \frac{1}{\bar{\rho}} \partial_1 \left( \bar{\rho} C_d \frac{\tilde{k}}{\tilde{\varepsilon}} \widetilde{R_{kl}} \partial_k \widetilde{R_{ij}} \right) \quad , \quad (3.2a) \end{aligned}$$

$$\begin{aligned} \widetilde{D_t \frac{\tau''u_1''}{\tilde{\tau}}} &= - \left( \frac{\partial_1 \tilde{\tau}}{\tilde{\tau}} + \frac{\partial_1 \bar{P}}{\gamma_1 \bar{P}} \right) \widetilde{R_{il}} - (1-\gamma^S) \frac{\widetilde{\tau''u_1''}}{\tilde{\tau}} \partial_1 \tilde{u}_i - (1-\gamma^H) \frac{\partial_1 \bar{P}}{\bar{\rho}} \frac{\widetilde{\tau''\tau''}}{\tilde{\tau}^2} - (C_{u2}^* \tilde{\omega} + \frac{\Omega_R}{2}) \frac{\widetilde{\tau''u_1''}}{\tilde{\tau}} \\ &\quad + \partial_1 \left( \bar{\rho} C_d \frac{\tilde{k}}{\tilde{\varepsilon}} \widetilde{R_{kl}} \partial_k \widetilde{\tau''u_1''} \right) \quad , \quad (3.2b) \end{aligned}$$

$$\widetilde{D_t \frac{\tau''\tau''}{\tilde{\tau}^2}} = -2 \left( \frac{\partial_1 \tilde{\tau}}{\tilde{\tau}} + \frac{\partial_1 \bar{P}}{\gamma_1 \bar{P}} \right) \frac{\widetilde{\tau''u_1''}}{\tilde{\tau}} - C_{\rho 2}^* \tilde{\omega} \frac{\widetilde{\tau''\tau''}}{\tilde{\tau}^2} + \frac{1}{\tilde{\tau}} \partial_1 \left( \bar{\rho} C_d \frac{\tilde{k}}{\tilde{\varepsilon}} \widetilde{R_{kl}} \partial_k \widetilde{\tau''\tau''} \right) \quad , \quad (3.2c)$$

$$\widetilde{D_t \tilde{\varepsilon}} = -C_{\varepsilon 1}^c \tilde{\omega} \frac{P_{kk}}{2} - C_{\varepsilon 0} \tilde{\omega} \frac{P_{kk}^H}{2} - C_{\varepsilon 3}^{1D} \tilde{\varepsilon} \partial_1 \tilde{u}_1 - C_{\varepsilon 2} \tilde{\omega} \tilde{\varepsilon} + \frac{1}{\bar{\rho}} \partial_1 \left( \bar{\rho} C_e \frac{\tilde{k}}{\tilde{\varepsilon}} \widetilde{R_{kl}} \partial_k \tilde{\varepsilon} \right) \quad , \quad (3.2d)$$

where:

$$\left\{ \begin{array}{l} P_{ij} = -\widetilde{R_{ik}} \partial_k \tilde{u}_j - \widetilde{R_{jk}} \partial_k \tilde{u}_i \quad \text{is the shear production term} \quad , \\ P_{ij}^H = \widetilde{u_1'' \tau''} \partial_j \bar{P} + \widetilde{u_1'' \tau''} \partial_j \bar{P} \quad \text{is the enthalpic production term} \quad . \end{array} \right.$$

The value of  $C_{u2}^*$  and  $C_{\rho2}^*$  are related to  $C_{u2}$  and  $C_{\rho2}$  by adding a compressibility correction analogous to the one proposed by [Chassaing \[2001\]](#) for shear flows:

$$C_{u2}^* = C_{u2} \left( 1 + \sqrt{\frac{\widetilde{\tau''\tau''}}{\widetilde{\tau}^2}} \right) \quad \text{and} \quad C_{\rho2}^* = C_{\rho2} \left( 1 + \sqrt{\frac{\widetilde{\tau''\tau''}}{\widetilde{\tau}^2}} \right) .$$

The coefficient  $C_{\epsilon3}^{1D}$  is related to  $C_{\epsilon3}$  following the prescription of [Gauthier & Bonnet \[1990\]](#):

$$C_{\epsilon3}^{1D} = \frac{2}{3} \left( C_{\epsilon1}^d - C_{\epsilon1}^c \right) + C_{\epsilon3} .$$

The values of the modelling constants are given later in Tab. A after calibration for the validation case.

On the right-hand side of equation (3.2a), the terms proportional to  $\gamma^S$  and  $\gamma^H$  arise from the “isotropization of the production” closure, as found in the work of [Launder \*et al.\* \[1975\]](#) or [Bailly \*et al.\* \[1997\]](#). The term proportional to  $C_1$  is [Rotta \[1951\]](#)’s model of return to isotropy.

In the equations for  $\widetilde{\tau''u_i''}$  and  $\widetilde{\tau''\tau''}$ , one observes a production arising from the stratification in specific volume and pressure and proportional to  $\frac{\partial \widetilde{\tau}}{\widetilde{\tau}} + \frac{\partial \widetilde{P}}{\widetilde{P}}$ . This term arises from the expression of the velocity divergence derived for the high Péclet case (see Eq. (2.62)). The steps connecting the value of the fluctuating velocity divergence to the evolution of  $\widetilde{\tau''u_i''}$  and  $\widetilde{\tau''\tau''}$  can be found in [Soulard \*et al.\* \[2012\]](#) for the high Péclet case. They will be detailed in the next section for the small Péclet case.

Another element that plays an important role in the GSG model is the frequency  $\Omega_R$ . It is defined by:

$$\Omega_R = \max \left( 0, \Omega_R^0 - (C_1 - 1) \widetilde{\omega} \right) \quad \text{with} \quad \Omega_R^0 = \gamma^S \frac{P_{kk}}{2k} + \gamma^H \frac{P_{kk}}{2k} .$$

This frequency ensures that the model is realisable in the particular situations when shear and enthalpic production terms become too negative i.e, when “de-production” becomes too strong. By ‘realisability’, we mean here that the tensor  $\mathbb{X}$  of the second order correlations of  $u_i''$  and  $\tau''$  remains semi-definite positive at all times:

$$\mathbb{X} = \begin{bmatrix} \widetilde{\mathbf{u}'' \otimes \mathbf{u}''} & \widetilde{\mathbf{u}'' \tau''} \\ \widetilde{\mathbf{u}'' \tau''} & \widetilde{\tau'' \tau''} \end{bmatrix} \geq 0 .$$

To guarantee this property, the GSG model has been derived using the methodology proposed by [Pope \[1994\]](#). More precisely, the GSG system is written from Langevin models for the evolution of the velocity and specific volume fields. Then, starting from this closed set of stochastic equations, evolution equations for the second order correlations of  $\mathbf{u}''$  and  $\tau''$  can be derived. As a last step, third-order turbulent transport terms were closed using a turbulent diffusion hypothesis.

### 3.2. Adaptation of a RSM : the GSG turbulent model

As a result of this procedure, the GSG model defined by Sys. (3.2) is statistically equivalent to the following PDF Langevin model in *homogeneous turbulence*:

$$D_t \mathbf{q}'' = \mathbf{G}|_{\text{Pe}_t \gg 1} \cdot \mathbf{q}'' + \mathbf{H}|_{\text{Pe}_t \gg 1} \cdot \dot{\mathbf{W}} \quad , \quad (3.3)$$

where  $\mathbf{q}''$  stands for the composite vector of velocity and specific volume fluctuations:

$$\mathbf{q}'' = \left( \mathbf{u}'', \frac{\tau''}{\bar{\tau}} \right) \quad .$$

In Eq. (3.3),  $D_t$  is the Lagrangian derivative along the stochastic trajectory and  $\mathbf{W}$  a vector of independant Brownian processes. The tensors  $\mathbf{G}|_{\text{Pe}_t \gg 1}$  and  $\mathbf{H}|_{\text{Pe}_t \gg 1}$  are defined as:

$$\mathbf{G}|_{\text{Pe}_t \gg 1} = \begin{pmatrix} -(1 - \gamma^S) \nabla \otimes \tilde{\mathbf{u}} - \frac{1}{2} \mathbb{I} (\Omega_R + C_1 \tilde{\omega}) & -(1 - \gamma^H) \frac{\nabla \bar{P}}{\bar{\rho}} \\ - \left( \frac{\nabla \tilde{\tau}}{\bar{\tau}} + \frac{\nabla \bar{P}}{\bar{\gamma} \bar{P}} \right) & - (C_{u2}^* - \frac{1}{2} C_1) \tilde{\omega} \end{pmatrix} \quad ,$$

$$\mathbf{H}|_{\text{Pe}_t \gg 1} = \begin{pmatrix} \sqrt{\frac{2}{3} \tilde{\mathbf{k}}} \left[ (C_1 - 1) \tilde{\omega} + \Omega_R - \Omega_R^0 \right] \mathbb{I} & \mathbf{0} \\ \mathbf{0} & \sqrt{(2C_{u2}^* - C_{\rho 2}^* - C_1) \tilde{\omega} \frac{\tau'' \tau''}{\bar{\tau}^2}} \end{pmatrix} \quad ,$$

where  $\mathbb{I}$  is the identity tensor and  $\nabla$  refers to the spatial gradient operator. From the expression of  $\mathbf{H}|_{\text{Pe}_t \gg 1}$ , one can see that  $\Omega_R$  has been defined in order to guarantee the positivity of the term under the first square root and hence the realisability of the model.

As a last remark, Sys. (3.2) can be recast in a more compact form using the definitions of  $\mathbb{X}$ ,  $\mathbf{G}|_{\text{Pe}_t \gg 1}$  and  $\mathbf{H}|_{\text{Pe}_t \gg 1}$ :

$$\widetilde{D}_t \mathbb{X} = \mathbf{G}|_{\text{Pe}_t \gg 1} \cdot \mathbb{X} + \mathbb{X} \cdot \mathbf{G}|_{\text{Pe}_t \gg 1}^t + \mathbf{H}|_{\text{Pe}_t \gg 1} \cdot \mathbf{H}|_{\text{Pe}_t \gg 1}^t + \mathbb{D}_t \quad , \quad (3.4)$$

with

$$\mathbb{D}_t = \begin{bmatrix} \frac{1}{\bar{\rho}} \nabla \cdot \left( \bar{\rho} C_d \frac{\tilde{\mathbf{k}}}{\tilde{\varepsilon}} \widetilde{\mathbf{u}'' \otimes \mathbf{u}''} \cdot (\nabla \cdot \widetilde{\mathbf{u}'' \otimes \mathbf{u}''} \right) & \nabla \cdot \left( \bar{\rho} C_d \frac{\tilde{\mathbf{k}}}{\tilde{\varepsilon}} \widetilde{\mathbf{u}'' \otimes \mathbf{u}''} \cdot \nabla \widetilde{\mathbf{u}'' \tau''} \right) \\ \nabla \cdot \left( \bar{\rho} C_d \frac{\tilde{\mathbf{k}}}{\tilde{\varepsilon}} \widetilde{\mathbf{u}'' \otimes \mathbf{u}''} \cdot \nabla \widetilde{\mathbf{u}'' \tau''} \right) & \frac{1}{\bar{\tau}} \nabla \cdot \left( \bar{\rho} C_d \frac{\tilde{\mathbf{k}}}{\tilde{\varepsilon}} \widetilde{\mathbf{u}'' \otimes \mathbf{u}''} \cdot \nabla \widetilde{\tau''^2} \right) \end{bmatrix} \quad .$$

This alternative formulation allows to highlight the connection between the GSG model and its underlying PDF model. It also puts forward the intrinsic structure of the evolution of  $\mathbb{X}$  that guarantees that it remains positive semi-definite. Note also that the subscript  $|_{\text{Pe}_t \gg 1}$  has been used in order to recall that the GSG model and its corresponding PDF model are valid in the high Péclet limit.

### 3.2.2 Adaptation of the Langevin PDF model to the ( $Pe_t \ll 1$ ) limit

As explained in the previous section, the GSG model has been derived from a stochastic Langevin model closing the evolutions of  $\mathbf{u}''$  and  $\tau''$  (see Eq. (3.3)). Let us focus on the evolution of  $\tau''$  and see how it can be closed in the small Péclet limit. Starting from the conservation of mass equation, one obtains that:

$$D_t \frac{\tau''}{\bar{\tau}} = \left(1 + \frac{\tau''}{\bar{\tau}}\right) \left(\operatorname{div} \mathbf{u}' - u_j'' \frac{\partial_j \tilde{\tau}}{\bar{\tau}} + \partial_j (\bar{\rho} u_j'' \tau'')\right) .$$

In a PDF model solving the evolutions of  $\mathbf{u}''$  and  $\tau''$ , every term appearing on the right-hand side of this equation is known except for one :  $\operatorname{div} \mathbf{u}'$ . This is precisely where the asymptotic analysis detailed in chapter 2 takes all its interest. Indeed, this analysis provides an expression for  $\operatorname{div} \mathbf{u}'$ . For the sake of simplicity, we will only consider here the case when the fluids being mixed are non-reactive perfect gases having the same diffusion coefficient ( $D^{(\alpha)} = D$  for all  $\alpha$ ). In that case, following Eq. (2.57a) of chapter 2, we obtain that, in the limits ( $M_t \ll 1$ ) and ( $Pe_t \ll 1$ ):

$$\operatorname{div} \mathbf{u}' = -u_j' \left( \frac{\partial_j \bar{\rho}}{\bar{\rho}} + \frac{\partial_j \bar{r}}{\bar{r}} \right) + \sum_{\alpha} \frac{r_{\alpha}}{\bar{r}} \left( D \partial_{jj}^2 c'_{\alpha} \right) ,$$

where we recall that:

$$r = \sum_{\alpha} r_{\alpha} c_{\alpha} \quad \text{with} \quad r_{\alpha} = \frac{\mathcal{R} (1 + Z_{\alpha})}{\mathcal{M}_{\alpha}} ,$$

with  $Z_{\alpha}$  standing for the ionization degree and  $\mathcal{M}_{\alpha}$  for the molar mass of species  $\alpha$ .

In the asymptotic analysis of chapter 2, we also showed that the fluctuations of temperature and pressure can be neglected with respect to the fluctuations of other thermodynamic variables. Thus, the molecular term appearing in the velocity divergence can be directly related to the fluctuations of specific volume  $\tau''$  as follows:

$$\frac{\tau''}{\bar{\tau}} \approx \frac{r''}{\bar{r}} = \frac{r_{\alpha}}{\bar{r}} c''_{\alpha} .$$

Neglecting the difference between  $\tilde{r}$  and  $\bar{r}$ , we can then rewrite the expression for the velocity divergence as:

$$\operatorname{div} \mathbf{u}' = -u_j' \left( \frac{\partial_j \bar{\rho}}{\bar{\rho}} + \frac{\partial_j \tilde{r}}{\bar{r}} \right) + D \partial_{jj}^2 \left( \frac{\tau''}{\bar{\tau}} - \frac{\bar{\tau}''}{\bar{\tau}} \right) .$$

The latter term is negligible in the high Reynolds number limit but has been kept in order to guarantee that the mean of  $\operatorname{div} \mathbf{u}'$  is zero. From this expression, one deduces that in the small Péclet-small Mach limit, the evolution of  $\tau''$  is given by:

$$\begin{aligned} \text{For } (Pe_t \ll 1) \quad , \quad D_t \frac{\tau''}{\bar{\tau}} = & \left(1 + \frac{\tau''}{\bar{\tau}}\right) \left[ -u_j'' \frac{\partial_j \tilde{r}}{\bar{r}} + D \partial_{jj}^2 \frac{\tau''}{\bar{\tau}} \right. \\ & \left. + \partial_j (\bar{\rho} u_j'' \tau'') - \bar{\rho} u_j'' \tau'' \left( \frac{\partial_j \bar{\rho}}{\bar{\rho}} + \frac{\partial_j \tilde{r}}{\bar{r}} \right) - D \partial_{jj}^2 \frac{\bar{\tau}''}{\bar{\tau}} \right] . \end{aligned}$$

### 3.2. Adaptation of a RSM : the GSG turbulent model

This substitution is not yet sufficient to obtain a closed PDF model. Indeed, the molecular diffusion term appearing on the right-hand side is still unknown in a one-point PDF framework. However, a wide literature exists on how to close such molecular diffusion terms [Pope, 2000, 1985]: standard micromixing models can be applied. In this work, we decide to use a Langevin model. More precisely, we propose the following expression:

$$\left(1 + \frac{\tau''}{\tilde{\tau}}\right) \mathcal{D}\partial_{ij}^2 \left(\frac{\tau''}{\tilde{\tau}} - \overline{\frac{\tau''}{\tilde{\tau}}}\right) \equiv -C_{\rho 1} \tilde{\omega} \frac{\tau''}{\tilde{\tau}} + \sqrt{C_{\rho 0} \tilde{\omega} \frac{\tau''^2}{\tilde{\tau}^2}} \dot{W} \quad ,$$

where  $\dot{W}$  is the time derivative of a Brownian noise and  $C_{\rho 1}$  and  $C_{\rho 0}$  are two constants. Injecting this expression into the evolution of  $\tau''$ , we eventually obtain that:

$$\text{For } (Pe_t \ll 1) \quad , \quad D_t \frac{\tau''}{\tilde{\tau}} = \left(1 + \frac{\tau''}{\tilde{\tau}}\right) \left[ -u_j'' \frac{\partial \tilde{r}}{\tilde{\tau}} + \partial_j \left( \overline{\rho u_j'' \tau''} \right) - \overline{\rho u_j'' \tau''} \left( \frac{\partial_j \bar{\rho}}{\bar{\rho}} + \frac{\partial_j \tilde{r}}{\tilde{\tau}} \right) \right] - C_{\rho 1} \tilde{\omega} \frac{\tau''}{\tilde{\tau}} + \sqrt{C_{\rho 0} \tilde{\omega} \frac{\tau''^2}{\tilde{\tau}^2}} \dot{W} \quad .$$

This closed expression can be used as such in a PDF model. However, when used to derive a RSM, the presence of the prefactor  $\left(1 + \frac{\tau''}{\tilde{\tau}}\right)$  will lead to the creation of third order unknown correlations. To avoid this issue, we propose to simplify further this model and to neglect  $\frac{\tau''}{\tilde{\tau}}$ , assuming that density fluctuations are small. This assumption is actually consistent with the asymptotic analysis of chapter 2. With this additional simplification, our final model for the evolution of the specific volume fluctuations is:

**Result: model for the evolution of the specific volume within the  $(Pe_t \ll 1)$  limit**

$$\text{For } (Pe_t \ll 1) \quad , \quad D_t \frac{\tau''}{\tilde{\tau}} = -u_j'' \frac{\partial \tilde{r}}{\tilde{\tau}} - C_{\rho 1} \tilde{\omega} \frac{\tau''}{\tilde{\tau}} + \sqrt{C_{\rho 0} \tilde{\omega} \frac{\tau''^2}{\tilde{\tau}^2}} \dot{W} + \partial_j \left( \overline{\rho u_j'' \tau''} \right) - \overline{\rho u_j'' \tau''} \left( \frac{\partial_j \bar{\rho}}{\bar{\rho}} + \frac{\partial_j \tilde{r}}{\tilde{\tau}} \right) \quad . \quad (3.5)$$

This expression can be compared against the one obtained in the high-Péclet case. Using equation (3.3), the evolution of  $\tau''$  in the high-Péclet limit can be written as:

$$\text{For } (Pe_t \gg 1) \quad , \quad D_t \frac{\tau''}{\tilde{\tau}} = -u_j'' \left( \frac{\partial_j \tilde{\tau}}{\tilde{\tau}} + \frac{\partial_j \bar{P}}{\gamma_1 \bar{P}} \right) - \left( C_{u2}^* - \frac{1}{2} C_1 \right) \tilde{\omega} \frac{\tau''}{\tilde{\tau}} + \sqrt{\left( 2C_{u2}^* - C_{\rho 2}^* - C_1 \right) \tilde{\omega} \frac{\tau''^2}{\tilde{\tau}^2}} \dot{W} + \partial_j \left( \overline{\rho u_j'' \tau''} \right) - \overline{\rho u_j'' \tau''} \left( \frac{\partial_j \bar{\rho}}{\bar{\rho}} + \frac{\partial_j \tilde{r}}{\tilde{\tau}} \right) \quad . \quad (3.6)$$

Thus, the main difference between the high and small Péclet cases comes from the way  $\tau''/\tilde{\tau}$  reacts to a mean stratification. In the high Péclet case,  $\tau''/\tilde{\tau}$  varies when the pseudo-entropy gradient  $\left(\frac{\partial_j \tilde{\tau}}{\tilde{\tau}} + \frac{\partial_j \bar{P}}{\gamma_1 \bar{P}}\right)$  is different from zero, while in the small Péclet case, it varies when the molecular weight gradient is different from zero. This difference has already been highlighted in chapter 2. In Sec. 2.3.2.5, it was shown that this difference was responsible for the modification of the stability criterion of a mean stratification between the high and small Péclet cases.

Another difference may arise from the choice of the coefficients defining the micromixing model in the high and small Péclet cases. However, without further information, there is no particular reason to calibrate different constants in the two cases. Hence, from here on, we will assume that micromixing is treated identically when ( $Pe_t \ll 1$ ) and ( $Pe_t \gg 1$ ) so that:

$$C_{\rho 1} = C_{u2}^* - C_1/2 \quad \text{and} \quad C_{\rho 0} = 2C_{u2}^* - C_{\rho 2}^* - C_1 \quad . \quad (3.7)$$

Combining the Langevin model for  $\tau''/\tilde{\tau}$  with the Langevin model for the velocity field already defined in equation (3.3), we eventually obtain a PDF model valid in the small Péclet limit. In homogeneous turbulence, this model simplifies to the following expression:

**Result: adapted PDF model within the ( $Pe_t \ll 1$ ) limit**

$$D_t \mathbf{q}'' = \mathbf{G}|_{Pe_t \ll 1} \cdot \mathbf{q}'' + \mathbf{H}|_{Pe_t \ll 1} \cdot \mathbf{W} \quad , \quad (3.8)$$

where we recall that  $\mathbf{q}'' = \left( \mathbf{u}'', \frac{\tau''}{\tilde{\tau}} \right)$  and where the tensors  $\mathbf{G}|_{Pe_t \ll 1}$  and  $\mathbf{H}|_{Pe_t \ll 1}$  are defined by:

$$\mathbf{G}|_{Pe_t \ll 1} = \begin{pmatrix} -(1 - \gamma^S) \nabla \otimes \tilde{\mathbf{u}} - \frac{1}{2} \mathbb{I} (\Omega_R + C_1 \tilde{\omega}) & -(1 - \gamma^H) \frac{\nabla \bar{P}}{\bar{\rho}} \\ -\frac{\nabla \tilde{r}}{\tilde{\tau}} & -(C_{u2}^* - \frac{1}{2} C_1) \tilde{\omega} \end{pmatrix} \quad ,$$

$$\mathbf{H}|_{Pe_t \ll 1} = \mathbf{H}|_{Pe_t \gg 1} = \begin{pmatrix} \sqrt{\frac{2}{3}} \tilde{k} \left[ (C_1 - 1) \tilde{\omega} + \Omega_R - \Omega_R^0 \right] \mathbb{I} & \mathbf{0} \\ \mathbf{0} & \sqrt{(2C_{u2}^* - C_{\rho 2}^* - C_1) \tilde{\omega} \frac{\tau'' \tau''}{\tilde{\tau}^2}} \end{pmatrix} \quad .$$

Since  $\mathbf{H}|_{Pe_t \ll 1} = \mathbf{H}|_{Pe_t \gg 1}$ , we will from here on drop the two subscripts and use the notation:

$$\mathbf{H}|_{Pe_t \ll 1} = \mathbf{H}|_{Pe_t \gg 1} = \mathbf{H} \quad .$$

The difference between the high and small Péclet limits only lies with the definition of  $\mathbf{G}$ .

### 3.2.3 Adaptation of the GSG model to the ( $Pe_t \ll 1$ ) limit

By multiplying the stochastic equation (3.8) by  $\mathbf{q}'' = \left( \mathbf{u}'', \frac{\tau''}{\tilde{\tau}} \right)$  and taking the average of the result, equations for the second order correlations of  $u_i''$  and  $\tau''$  are obtained. In doing so, third order correlations appear and are closed using a turbulent diffusion assumption. When using the correlation tensor  $\mathbb{X}$ , the resulting model can be expressed as follows:

**Result: GSG model in the ( $Pe_t \ll 1$ ) limit**

$$\tilde{D}_t \mathbb{X} = \mathbf{G}|_{Pe_t \ll 1} \cdot \mathbb{X} + \mathbb{X} \cdot \mathbf{G}|_{Pe_t \ll 1}^t + \mathbf{H} \cdot \mathbf{H}^t + \mathbb{D}_t \quad . \quad (3.9)$$

Comparing this equation to its high Péclet equivalent one (3.4), we see that the main modification brought by the small Péclet analysis comes from the definition of  $\mathbf{G}|_{Pe_t \ll 1}$  with respect to  $\mathbf{G}|_{Pe_t \gg 1}$ . The small Péclet version of the model introduces a dependency to the gradient of  $\nabla \tilde{r}/\tilde{\tau}$  instead of the gradient of the pseudo-entropy  $\left( \frac{\nabla \tilde{\tau}}{\tilde{\tau}} + \frac{\nabla \bar{P}}{\bar{\rho}} \right)$  in the high Péclet case. These two gradients appear in the evolution equations of the variance and flux of the specific volume. This modification will be made clearer in the next section.

### 3.2. Adaptation of a RSM : the GSG turbulent model

#### 3.2.4 Blending between the two limits ( $Pe_t \gg 1$ ) and ( $Pe_t \ll 1$ )

Equations (3.4) and (3.9) define the GSG model respectively in the high and small Péclet regimes. To obtain a model valid for all Péclet values, we propose to perform a weighted average of these two versions of the model. To this end, we introduce the weighting function  $\omega_{Pe_t}$  defined as:

$$\omega_{Pe_t} = \frac{Pe_t^{\lim}}{Pe_t^{\lim} + Pe_t} . \quad (3.10)$$

The weight  $\omega_{Pe_t}$  is equal to 0 in the limit ( $Pe_t \gg 1$ ) and to 1 in the limit ( $Pe_t \ll 1$ ). The transition between the two limits is controlled by the arbitrary parameter  $Pe_t^{\lim}$ . Using this weight, we can now blend the two Péclet limits as follows.

**Main result: model blending for both ( $Pe_t \gg 1$ ) and ( $Pe_t \ll 1$ ) limits**

$$\widetilde{D}_t \mathbb{X} = \mathbf{G} \cdot \mathbb{X} + \mathbb{X} \cdot \mathbf{G}^t + \mathbf{H} \cdot \mathbf{H}^t + \mathbf{D}_t \quad \text{with} \quad \mathbf{G} = \omega_{Pe_t} \mathbf{G}|_{Pe_t \ll 1} + (1 - \omega_{Pe_t}) \mathbf{G}|_{Pe_t \gg 1} . \quad (3.11)$$

The explicit expression of the tensor  $\mathbf{G}$  is:

$$\mathbf{G} = \begin{pmatrix} -(1 - \gamma^S) \nabla \otimes \tilde{\mathbf{u}} - \frac{1}{2} \mathbb{I} (\Omega_R + C_1 \tilde{\omega}) & -(1 - \gamma^H) \frac{\nabla \bar{P}}{\bar{p}} \\ \theta_1^{Pe_t} - \frac{\partial_1 \tilde{\tau}}{\tilde{\tau}} & -(C_{u2}^* - \frac{1}{2} C_1) \tilde{\omega} \end{pmatrix} ,$$

where:

$$\theta_1^{Pe_t} - \frac{\partial_1 \tilde{\tau}}{\tilde{\tau}} = - \left[ \omega_{Pe_t} \frac{\partial_1 \tilde{r}}{\tilde{r}} + (1 - \omega_{Pe_t}) \left( \frac{\partial_1 \tilde{\tau}}{\tilde{\tau}} + \frac{\partial_1 \bar{P}}{\gamma_1 \bar{P}} \right) \right] . \quad (3.12)$$

Given the definition of  $\omega_{Pe_t}$ , one verifies that:

$$\left\{ \begin{array}{l} \text{for } Pe_t \rightarrow \infty , \quad \theta_1^{Pe_t} - \frac{\partial_1 \tilde{\tau}}{\tilde{\tau}} \rightarrow - \left( \frac{\partial_1 \tilde{\tau}}{\tilde{\tau}} + \frac{\partial_1 \bar{P}}{\gamma_1 \bar{P}} \right) , \\ \text{for } Pe_t \rightarrow 0 , \quad \theta_1^{Pe_t} - \frac{\partial_1 \tilde{\tau}}{\tilde{\tau}} \rightarrow - \frac{\partial_1 \tilde{r}}{\tilde{r}} . \end{array} \right. \quad (3.13a)$$

$$\left\{ \begin{array}{l} \text{for } Pe_t \rightarrow \infty , \quad \theta_1^{Pe_t} - \frac{\partial_1 \tilde{\tau}}{\tilde{\tau}} \rightarrow - \left( \frac{\partial_1 \tilde{\tau}}{\tilde{\tau}} + \frac{\partial_1 \bar{P}}{\gamma_1 \bar{P}} \right) , \\ \text{for } Pe_t \rightarrow 0 , \quad \theta_1^{Pe_t} - \frac{\partial_1 \tilde{\tau}}{\tilde{\tau}} \rightarrow - \frac{\partial_1 \tilde{r}}{\tilde{r}} . \end{array} \right. \quad (3.13b)$$

Several additional parameters have been introduced to perform the blending. First of all, the Péclet number has been defined, up to now, by comparing characteristic scales of the flow. Such a definition cannot be used in practice. Instead, we propose to define the Péclet number used in the GSG model by:

$$Pe_t \equiv \frac{\bar{c}_p \nu_t}{\tilde{\tau} \lambda^r} \quad \text{with} \quad \nu_t = \frac{C_\mu \tilde{k}^2}{\tilde{\varepsilon}} . \quad (3.14)$$

These definitions involve the specific heat capacity at constant pressure  $\bar{c}_p$ , the radiative conductivity  $\lambda^r$ , and the turbulent viscosity  $\nu_t$ . The latter is classically estimated on empirical grounds from the turbulent kinetic energy  $\tilde{k}$ , its dissipation  $\tilde{\varepsilon}$  and a constant  $C_\mu$  set to 0.1. The second parameter that needs to be defined is the transition Péclet number  $Pe_t^{\lim}$ . To fix its value, we use two methods. The first one is described in the next section: using the Rayleigh-Taylor simulations presented in chapter 2, we fit  $Pe_t^{\lim}$  in order to match their results with the GSG model. As

explained in Sec. 3.3.1, this process yields the following estimate for  $Pe_t^{\text{lim}}$ :

$$Pe_t^{\text{lim}} = 2C_\mu = 0.2 \quad . \quad (3.15)$$

To try and overcome the empirical nature of this procedure, we also developed another approach in chapter 4. This second method relies on a linear stability analysis of the visco-diffusive hydro-radiative equations and an analogy between the molecular diffusivity and its turbulent counterpart. The weighting function  $\omega_{Pe_t}$  is then chosen in order that the neutral stability of the turbulent model matches the one of its laminar diffusive counterpart

From a practical point of view, other remarks should be made. While we developed the asymptotic analysis of chapter 2 for fluids having a general equation of state, we restricted its use in this chapter to a mixture of ideal gases. The “all-Péclet” GSG model derived here is consequently only valid for such mixtures. To extend it to non-ideal gases, the most logical approach would consist in using the general formula for  $\text{div}\mathbf{u}'$  proposed in chapter 2. However, such an approach would require computing thermodynamical coefficients that are not necessarily available in simulation codes or that are expensive to compute. To avoid this drawback, we propose to make the following substitution:

$$\frac{\partial \tilde{r}}{\tilde{r}} \equiv \frac{\partial \overline{P^m}}{\overline{P^m}} - \frac{\partial \overline{T}}{\overline{T}} + \frac{\partial \tilde{\tau}}{\tilde{\tau}} \quad . \quad (3.16)$$

All the quantities involved in the right-hand side can be computed independently from the particular equation of state of the fluids and their sum reverts to the correct expression when the fluids are ideal.

To conclude this section, we can expand the tensorial equations (3.11) and obtain a more explicit form of the correction to Eq. (3.2) leading to the “all-Péclet” GSG model (together with the unchanged system (3.1) for mean quantities):

$$\begin{aligned} \widetilde{D}_t \widetilde{R}_{ij} &= P_{ij} + P_{ij}^H - \gamma^S \left( P_{ij} - \frac{P_{kk}}{3} \delta_{ij} \right) - \gamma^H \left( P_{ij}^H - \frac{P_{kk}^H}{3} \delta_{ij} \right) - (C_1 \tilde{\omega} + \Omega_R) \left( \widetilde{R}_{ij} - \frac{2}{3} \tilde{k} \delta_{ij} \right) - \frac{2}{3} \tilde{\varepsilon} \delta_{ij} \\ &\quad + \frac{1}{\rho} \partial_1 \left( \tilde{\rho} C_d \frac{\tilde{k}}{\tilde{\varepsilon}} \widetilde{R}_{kl} \partial_k \widetilde{R}_{ij} \right) \quad , \end{aligned} \quad (3.17a)$$

$$\begin{aligned} \widetilde{D}_t \frac{\widetilde{\tau'' u_i''}}{\tilde{\tau}} &= - (1 - \gamma^S) \frac{\tau'' u_1''}{\tilde{\tau}} \partial_1 \tilde{u}_i - (1 - \gamma^H) \frac{\partial_i \overline{P} \tau'' \tau''}{\tilde{\rho} \tilde{\tau}^2} - \left( \theta_1^{Pe_t} - \frac{\partial_1 \tilde{\tau}}{\tilde{\tau}} \right) \widetilde{R}_{il} - \left( C_{u2}^* \tilde{\omega} + \frac{\Omega_R}{2} \right) \frac{\tau'' u_i''}{\tilde{\tau}} \\ &\quad + \partial_1 \left( \tilde{\rho} C_d \frac{\tilde{k}}{\tilde{\varepsilon}} \widetilde{R}_{kl} \partial_k \widetilde{\tau'' u_i''} \right) \quad , \end{aligned} \quad (3.17b)$$

$$\widetilde{D}_t \frac{\widetilde{\tau'' \tau''}}{\tilde{\tau}^2} = -2 \left( \theta_1^{Pe_t} - \frac{\partial_1 \tilde{\tau}}{\tilde{\tau}} \right) \frac{\tau'' u_1''}{\tilde{\tau}} - C_{\rho 2}^* \tilde{\omega} \frac{\tau'' \tau''}{\tilde{\tau}^2} + \frac{1}{\tilde{\tau}} \partial_1 \left( \tilde{\rho} C_d \frac{\tilde{k}}{\tilde{\varepsilon}} \widetilde{R}_{kl} \partial_k \widetilde{\tau'' \tau''} \right) \quad , \quad (3.17c)$$

$$\widetilde{D}_t \tilde{\varepsilon} = -C_{\varepsilon 1}^c \tilde{\omega} \frac{P_{kk}}{2} - C_{\varepsilon 0} \tilde{\omega} \frac{P_{kk}^H}{2} - C_{\varepsilon 3}^{1D} \tilde{\varepsilon} \partial_1 \tilde{u}_1 - C_{\varepsilon 2} \tilde{\omega} \tilde{\varepsilon} + \frac{1}{\rho} \partial_1 \left( \tilde{\rho} C_e \frac{\tilde{k}}{\tilde{\varepsilon}} \widetilde{R}_{ll} \partial_l \tilde{\varepsilon} \right) \quad , \quad (3.17d)$$

### 3.3. Validation of the extended RSM

---

where according to Eqs. (3.12), (3.16), (3.10) and (3.14) with the fit of Eq. (3.15) for  $Pe_t^{\text{lim}}$ :

$$\theta_1^{Pe_t} - \frac{\partial_1 \tilde{\tau}}{\tilde{\tau}} = - \left[ \omega_{Pe_t} \left( \frac{\partial_1 \tilde{\tau}}{\tilde{\tau}} + \frac{\partial_1 \overline{P^m}}{\overline{P^m}} - \frac{\partial_1 \overline{T}}{\overline{T}} \right) + (1 - \omega_{Pe_t}) \left( \frac{\partial_1 \tilde{\tau}}{\tilde{\tau}} + \frac{\partial_1 \overline{P}}{\overline{P}} \right) \right]$$

with  $\omega_{Pe_t} = \frac{1}{1 + \frac{c_p \tilde{k}^2}{2\tilde{\tau} \lambda^* \tilde{\epsilon}}}$ .

Compared to the original GSG model given by Sys. (3.2), we observe that only a minor modification has been brought: the gradient of the pseudo-entropy  $\left( \frac{\nabla \tilde{\tau}}{\tilde{\tau}} + \frac{\nabla \overline{P}}{\overline{P}} \right)$  has been replaced by the weighted sum of gradients  $\left( \theta_1^{Pe_t} - \frac{\partial_1 \tilde{\tau}}{\tilde{\tau}} \right)$ . The latter tends to the pseudo-entropy gradient when  $(Pe_t \gg 1)$  and to  $\partial_1 \tilde{\tau} / \tilde{\tau}$  when  $(Pe_t \ll 1)$ . Despite affecting a very limited part of the model, the proposed modification may still lead to significant differences in the model behaviour. In order to illustrate this point, several test cases are detailed in the next section.

### 3.3 Validation of the extended RSM

In order to validate the closure (3.11), the three DNS of the radiative Rayleigh–Taylor mixing described in Sec. 2.5.2 are compared to three 1D RANS-simulations carried out with the modified GSG model. The latter are initialized at  $t = 9$  using 1D profiles for the averages and correlations computed from the DNS at the same time.

Indeed, the model is derived in the high-Reynolds limit and does not take the molecular viscosity and diffusion coefficients into account. It is therefore unable to closely match the transition to turbulence of the DNS and should be turned on only when the flow is close to turbulence. The same set of model coefficients is used in the three cases. They have been calibrated with respect to the method explained in the next section 3.3.1. The results of the simulations can then be compared to the DNS for the validation of the “all-Péclet” adaptation of the RANS model.

#### 3.3.1 Calibration with respect to TRICLADE simulations

Our purpose is the evaluation of the model adaptation to radiative effects, we therefore choose to calibrate some coefficients common to the original and the adapted model precisely for the three DNS in order to focus on the radiative correction. Once these are calibrated, the same integral procedure explained below allows to propose the fit for the parameter  $Pe_t^{\text{lim}}$  of the radiative correction.

The set of coefficients common to the original (3.2) and the adapted model (3.17) is

$$\mathfrak{E}_{\text{GSG}} = \left\{ \gamma^S, \gamma^H, C_1, C_d, C_{u2}, C_{\rho 2}, C_{\epsilon 0}, C_{\epsilon 1}^c, C_{\epsilon 1}^d, C_{\epsilon 2}, C_{\epsilon 3}, C_\epsilon, C_c, C_e \right\}. \quad (3.18)$$

Among these coefficients, some can be calibrated by integration of (3.17) over the domain, assuming the absence of fluxes at the boundaries, leading to :

$$\left\{ \begin{array}{l} \widetilde{D}_t \int \bar{\rho} (\widetilde{R}_{11} - \widetilde{R}_{tt}) dl = \int \left[ -2 (1-\gamma^S) \bar{\rho} \widetilde{R}_{11} \partial_1 \widetilde{u}_1 - 2 (1-\gamma^H) \partial_1 \bar{P} \widetilde{\rho} \widetilde{\tau}'' \widetilde{u}_1'' \right. \\ \left. - C_1 \widetilde{\omega} \bar{\rho} (\widetilde{R}_{11} - \widetilde{R}_{tt}) \right] dl \quad , \end{array} \right. \quad (3.19a)$$

$$\left\{ \begin{array}{l} \widetilde{D}_t \int \bar{\rho} \widetilde{\tau}'' \widetilde{u}_1'' dl = \int \left[ \bar{\rho} \widetilde{\tau}'' \widetilde{u}_1'' \partial_1 \widetilde{u}_1 - (1-\gamma^S) \bar{\rho} \widetilde{\tau}'' \widetilde{u}_1'' \partial_1 \widetilde{u}_1 - (1-\gamma^H) \bar{\rho} \partial_1 \bar{P} \widetilde{\tau}'' \widetilde{\tau}'' \right. \\ \left. + \left( \theta_1^{\text{Pe}_t} - \frac{\partial_1 \widetilde{\tau}}{\widetilde{\tau}} \right) \widetilde{R}_{11} - C_{u2}^* \widetilde{\omega} \bar{\rho} \widetilde{\tau}'' \widetilde{u}_1'' \right] dl \quad , \end{array} \right. \quad (3.19b)$$

$$\left\{ \begin{array}{l} \widetilde{D}_t \int \bar{\rho} \widetilde{\tau}'' \widetilde{\tau}'' dl = \int \left[ 2 \bar{\rho} \widetilde{\tau}'' \widetilde{\tau}'' \partial_1 \widetilde{u}_1 + 2 \left( \theta_1^{\text{Pe}_t} - \frac{\partial_1 \widetilde{\tau}}{\widetilde{\tau}} \right) \widetilde{\tau}'' \widetilde{u}_1'' - C_{\rho 2}^* \bar{\rho} \widetilde{\omega} \widetilde{\tau}'' \widetilde{\tau}'' \right] dl \quad . \end{array} \right. \quad (3.19c)$$

Since all the correlations of the model are at disposal for **TRICLADE** simulations, (3.19) yields three relations between the involved coefficients at each output time of each **TRICLADE** simulation. Among the model coefficients, some can be chosen on theoretical grounds,  $\gamma^S, \gamma^H$ , or have widely accepted values in the literature,  $C_1$ , we therefore choose to keep them as in Tab. A. Then, we are left for the two equations (3.19b) and (3.19c) with the three “unknown” coefficients  $C_{u2}, C_{\rho 2}$  and  $\text{Pe}_t^{\text{lim}}$  (hidden in  $\theta_1^{\text{Pe}_t}$  through (3.12) and (3.10)).

Both simulations  $\text{SP}_1$  and  $\text{HP}$  evolve close to an asymptotic regime and should therefore not depend much on  $\text{Pe}_t^{\text{lim}}$ . Substituting the suited limit (3.13) for  $\theta_1^{\text{Pe}_t}$  in (3.19) gives two sets of time-dependent fits  $C_{u2}(t)$  and  $C_{\rho 2}(t)$ . A third set can be evaluated from the  $\text{SP}_2$  simulation for each trial value for  $\text{Pe}_t^{\text{lim}}$ . The final fit (3.15) is chosen so as to collapse  $C_{u2}(t)$  and  $C_{\rho 2}(t)$  from  $\text{SP}_2$  with the previous sets obtained from  $\text{SP}_1$  and  $\text{HP}$ . The values in Tab. A for  $C_{u2}$  and  $C_{\rho 2}$  are chosen as averages of their time depending estimation after the onset of a fully turbulent regime.

The fact that the three sets obtained from the three simulations in different radiative regimes roughly collapse is itself a first validation of the model adaptation to radiative effects.

$\gamma^H$	$\gamma^S$	$C_1$	$C_{\epsilon 0}$	$C_{\epsilon 1}^c$	$C_{\epsilon 1}^d$	$C_{\epsilon 2}$	$C_{\epsilon 3}$	$C_{u2}$	$C_{\rho 2}$	$C_d$	$C_\epsilon$	$C_c$	$C_e$
0.3	0.6	1.8	1.42	1.44	2.0	1.92	-0.17	2.0	1.5	0.60	0.46	0.70	0.60

Table A – Turbulent model coefficients used for 1D simulations of Sec. 3.3.2

### 3.3.2 1D simulations with the GSG turbulence model

Figures 3.1, 3.2 and 3.3 compare turbulent quantities extracted from the three DNS  $\text{SP}_1, \text{SP}_2$  and  $\text{HP}$  to the ones predicted by the GSG model adapted to all Péclet regimes using the blending (3.11). Figures 3.1 and 3.2 plot the temporal evolution of the turbulent kinetic energy  $\widetilde{k}$  and the normalized specific volume variance  $\widetilde{\tau}''^2 / \widetilde{\tau}^2$  at the initial abscissa of the interface ( $x = x_0$ ) whereas Fig. 3.3 plots the width of the turbulent mixing zone defined as:

$$\mathcal{L}_{\text{TMZ}} = 6 \int_{L_x} \widetilde{c} (1 - \widetilde{c}) dx \quad .$$

### 3.3. Validation of the extended RSM

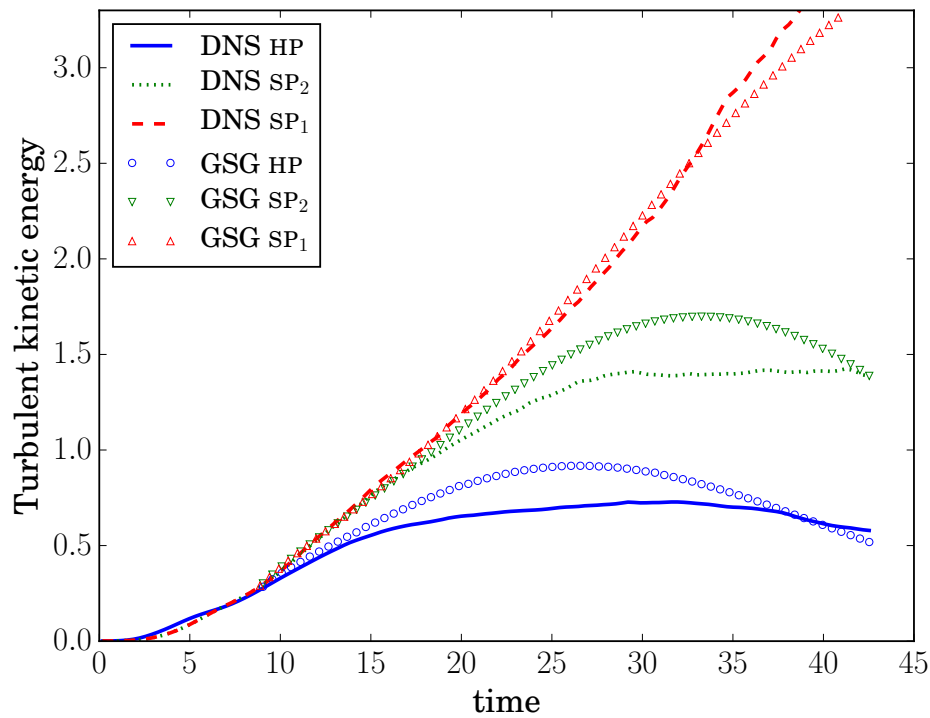


Figure 3.1 – Time evolution of the turbulent kinetic energy  $\tilde{k}$  at  $(x = 0)$ . Comparison between the DNS and the 1D-RANS simulations.

It can be seen that the extended GSG model reproduces the main trends observed in the simulations and allows to capture the differences between high and small Péclet regimes. For instance, in the large Péclet limit (HP), a decrease of the turbulent kinetic energy at  $(x = 0)$  is observed during the last third of the computation together with a slowdown of the TMZ expansion. This decline of the turbulent field has already been explained in Sec. 2.5.4. It is due to the fact that the mean pseudo-entropy  $S$  profile approaches its neutral value inside the TMZ so that the instability mechanism stops feeding the turbulent mixing zone whereas viscosity still dissipates the turbulent kinetic energy.

By contrast, in the small Péclet limit ( $SP_1$ ), the instability depends on the molar mass gradient which keeps always the same sign so that it endlessly transfers energy to the turbulent field. This explains the continuous growth in Fig. 3.1 and the accelerated expansion in Fig. 3.3.

The behaviour of the specific volume variance in Fig. 3.2 results from the competition between molecular diffusion tending to destroy the variance and turbulent transport of “fresh” pure fluid engulfed at the mixing zone edge and carried through the TMZ. Quicker expansion of the TMZ for  $SP_1$  allows to maintain a slow decay of the variance whereas molecular diffusion is almost not counter-balanced for HP.

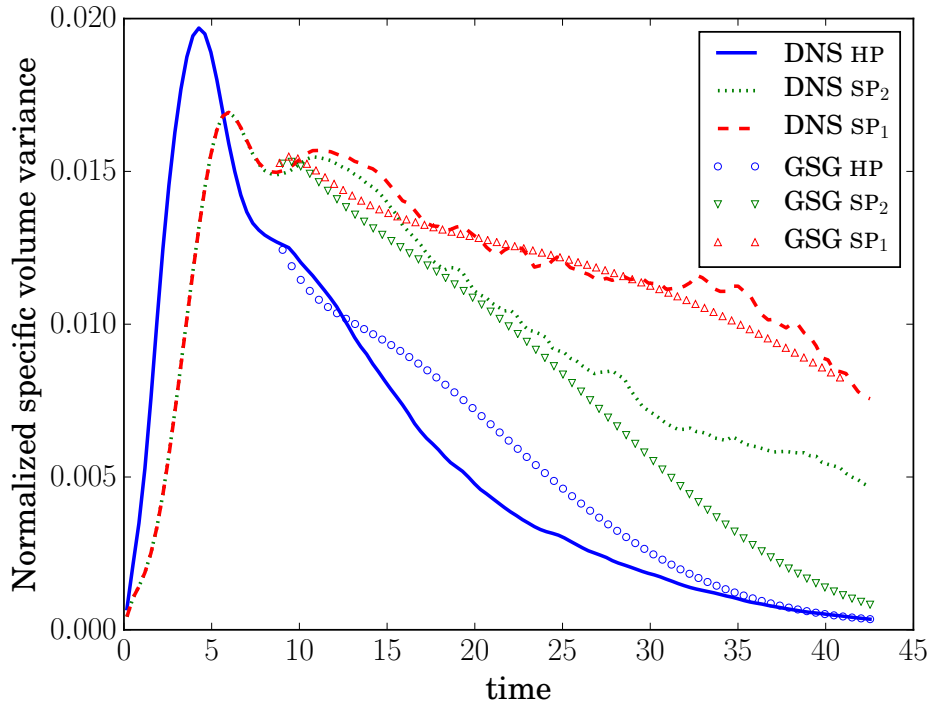


Figure 3.2 – Time evolution of the normalized specific volume variance  $\widetilde{\tau}''^2/\widetilde{\tau}^2$  at ( $x = 0$ ). Comparison between the DNS and the 1D-RANS simulations.

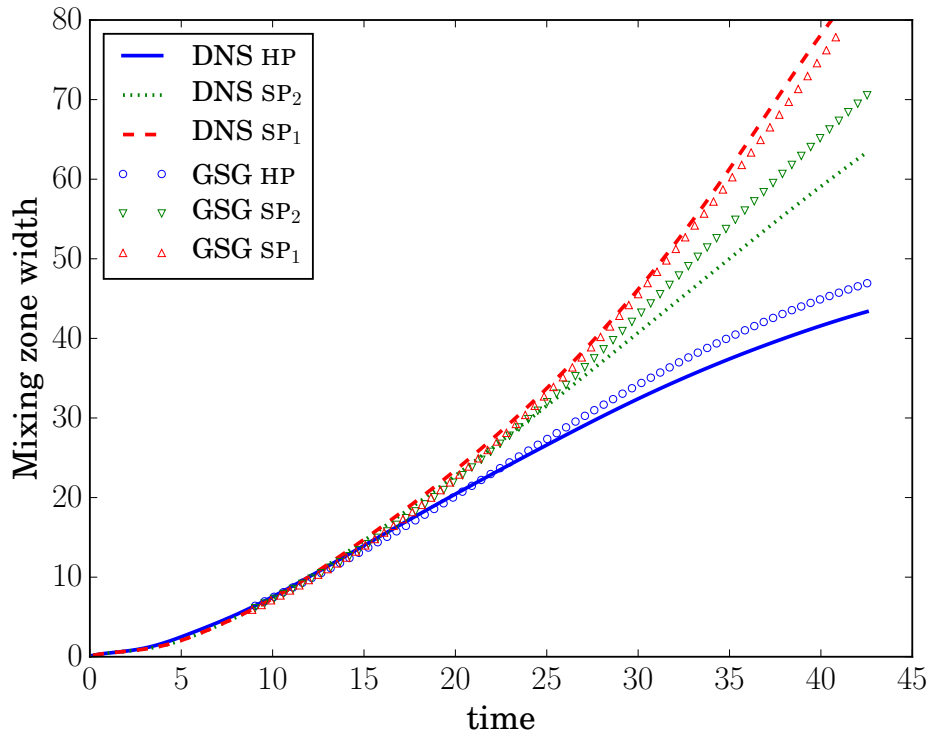


Figure 3.3 – Time evolution of the turbulent mixing zone width  $\mathcal{L}_{TMZ} = 6 \int_{L_x} \widetilde{c} (1 - \widetilde{c}) dx$ . Comparison between the DNS and the 1D-RANS simulations.

### 3.4. Conclusion

---

Between these two limiting cases, the intermediate Prandtl simulation  $SP_2$  exhibits a more subtle balance between the different mechanisms. Beginning in a small Péclet regime, it first follows the same evolution as  $SP_1$ , but doing so, its turbulent diffusivity quickly increases and so does its Péclet number as shown in Fig. 2.1. When the latter becomes non negligible the instability production reduces and becomes of a similar order as the molecular dissipation leading to a marginal evolution of the turbulent kinetic energy. Transfer of pure fluid from the TMZ edges then slows down letting the specific volume variance decrease much quicker in  $SP_2$  than in  $SP_1$ . Capturing this limiting behaviour is a challenge and the value  $Pe_t^{\text{lim}}$  in the blending of Eq. (3.11) is precisely chosen to get the transition in the right way.

Note that, plotted in Figs. 3.1 to 3.3, the original GSG model (3.2) would yield the same results as the large Péclet limit (HP), whatever the value of  $Pe_t$ .

To conclude, implementation of Eq. (2.57a) within the GSG RANS model proves successful in predicting the radiative RTI in the small Péclet limit. Extending the closure to all Péclet regimes thanks to the blending Eq. (3.11) allows the RSM to correctly capture the effects of the relative intensity of the radiative transfer and the turbulent transport in the turbulent mixing case under consideration.

### 3.4 Conclusion

A small Péclet-small Mach number analysis has been extended to radiative flows with mixing and radiation in the previous chapter 2. The results have then been used in this part in order to derive closures for the evolution of the density-linked correlations involved in a class of turbulent RSMs, such as the GSG and BHR models. Moreover, the validation has proven that mixing and radiative effects can be well captured by the adapted model. It regards more precisely the change of behaviour of the turbulent mixing zone due to the different stability criteria in each asymptotic regime. Finally, this work shows how to design turbulent models able to account for the effect of the relative magnitude of radiative conductivity and turbulent transport in the wide range of turbulent Péclet numbers encountered in stellar flows.

From now on, one will choose to focus on the stability of the turbulent model. In the last chapter of this work, one will provide a linear stability analysis (LSA) that includes viscosity, scalar diffusion and radiative conduction effects. One particular stability criterion will be used in order to improve the model blending defined in the adapted turbulent model by Eq. (3.11). The subsequent aim is to find a more suitable value for the prefactor  $Pe_t^{\text{lim}}$ , dealing with intermediate Péclet regimes.

# 4

## Linear stability analysis

“ When no loose gale disturbs the deep serene,  
And no dim cloud o’ercasts the solemn scene. ”

ALEXANDER POPE  
*The Iliad of Homer: A Nightpiece*

### Contents

<b>4.1 Introduction</b> . . . . .	<b>96</b>
<b>4.2 Governing equations and assumptions for the LSA</b> . . . . .	<b>96</b>
4.2.1 Hydro-radiative compressible governing equations . . . . .	96
4.2.2 Quasi-homogeneous approach and isothermal equilibrium state . . . . .	97
4.2.3 Assumptions regarding transport coefficients . . . . .	99
<b>4.3 Dispersion relation within all Mach regime</b> . . . . .	<b>101</b>
4.3.1 Linear system . . . . .	101
4.3.2 Dispersion relation at thermal equilibrium . . . . .	102
4.3.3 Dispersion relation in non-thermal equilibrium . . . . .	109
<b>4.4 Dispersion relation within the small Mach regime</b> . . . . .	<b>112</b>
4.4.1 Dispersion relation at thermal equilibrium for any wave angle . . . . .	112
4.4.2 Dispersion relation at thermal equilibrium for transverse modes . . . . .	114
4.4.3 Large wave numbers limit: development in $(1/k)$ . . . . .	116
<b>4.5 Small Mach-small Péclet regime</b> . . . . .	<b>117</b>
4.5.1 Dispersion relation at thermal equilibrium for any wave angle . . . . .	117
4.5.2 Dispersion relation at thermal equilibrium for transverse modes . . . . .	118
<b>4.6 Numerical results</b> . . . . .	<b>118</b>
4.6.1 General dispersion relation at thermal equilibrium . . . . .	118
4.6.2 Dispersion relation within the low Mach limit . . . . .	128
<b>4.7 Extension to the non-isothermal case at thermal equilibrium</b> . . . . .	<b>130</b>
4.7.1 Correction to the isothermal case . . . . .	130
4.7.2 Dispersion relations at thermal equilibrium . . . . .	131
<b>4.8 Link with Boussinesq approaches (pure hydrodynamic limit)</b> . . . . .	<b>132</b>
<b>4.9 Implications for the turbulent RSM model</b> . . . . .	<b>134</b>
4.9.1 Analogy with the radiative turbulent RSM model . . . . .	135
4.9.2 Improvement of the model blending . . . . .	136
<b>4.10 Conclusion</b> . . . . .	<b>143</b>

## 4.1 Introduction

This part is devoted to a linear stability analysis (LSA) of the stratified hydrostatic equilibrium considered in the previous chapters. Under an isothermal quasi-homogeneous assumption, stability criteria will be derived which involve viscosity, scalar diffusion and radiative conduction effects. Using the results of the asymptotic analysis of chapter 2 leads to stability criteria in the small Mach and small Mach-small Péclet regimes shedding light on how these approximations filter out some of the modes of the general dispersion relation.

Drawing an analogy between the physical visco-diffusive coefficients and their turbulent counterparts suggests a blending of the RANS model between the large and the small-Péclet regime based on a physical condition instead of the *ad hoc* fit introduced in chapter 3. Indeed, requiring that the neutral stability of the RSM in radiative Rayleigh-Taylor configurations matches the one of its laminar analogue allows to propose another weighting which bridges the range between low and high Péclet regimes.

## 4.2 Governing equations and assumptions for the LSA

### 4.2.1 Hydro-radiative compressible governing equations

As a starting point, the hydro-radiative compressible governing equations including viscosity and inter-species diffusion are written:

$$\begin{cases} \partial_t \rho + \partial_j (\rho u_j) & = 0 \quad , & (4.1a) \\ \partial_t (\rho u_i) + \partial_j (\rho u_i u_j) + \partial_i (P^m + P^r) & = \rho g_i - \partial_j \Pi_{ij} \quad , & (4.1b) \\ \partial_t (\rho e^m) + \partial_j (\rho e^m u_j) + P^m \partial_j u_j & = -c_\ell \rho \kappa^r (a_R T^{m4} - E^r) - \Pi_{ij} \partial_j u_i - \mathcal{Q}_c \quad , & (4.1c) \\ \partial_t E^r + \partial_j (E^r u_j + P^r u_j) - u_j \partial_j P^r & = +c_\ell \rho \kappa^r (a_R T^{m4} - E^r) + \mathcal{C} \quad , & (4.1d) \\ \partial_t (\rho c) + \partial_j (\rho c u_j) & = -\partial_j \mathcal{F}_{cj} \quad , & (4.1e) \end{cases}$$

with the same notations used as in chapter 2. A binary mixture of two ideal gases indexed “a” and “b” with the same adiabatic exponent  $\gamma_a = \gamma_b = \gamma^m$  is treated. According to Eqs. (2.5) and (2.7), the viscous stress tensor  $\Pi_{ij}$  and the scalar flux  $\mathcal{F}_{cj}$  are closed using respectively the relations:

$$\Pi_{ij} = -2\mu_v \left( S_{ij} - \frac{1}{3} \text{div} \mathbf{u} \delta_{ij} \right) \quad \text{and} \quad \mathcal{F}_{cj} = -\rho D_c \partial_j c \quad ,$$

with  $S_{ij} = (\partial_j u_i + \partial_i u_j) / 2$  the instantaneous strain-rate tensor,  $\mu_v = \rho \nu_v$  the dynamic viscosity of the mixture,  $\nu_v$  its kinematic viscosity,  $D_c$  the scalar diffusion coefficient and  $c$  the mass fraction of the gas indexed “a”. Then, one can write:

$$\mathcal{Q}_c = \partial_j [(h_a - h_b) \mathcal{F}_{cj}] = \partial_j \left[ -\rho D_c \frac{\gamma^m}{\gamma^m - 1} (r_a - r_b) T^m \partial_j c \right] \quad , \quad (4.2)$$

$$\mathcal{C} = \partial_j \left( \frac{c_\ell}{3\rho \kappa^r} \partial_j E^r \right) = \partial_j \left( \frac{4c_\ell T^{r3}}{\rho \kappa^r} \partial_j T^r \right) \quad , \quad (4.3)$$

As previously, the specific energies and pressures are related by  $e = e^m + E^r/\rho = c_v^m T^m + a_R T^r$  and  $P = P^m + P^r = \rho r T^m + a_R T^r/3$ . The ideal gas constant and the material specific heat capacity at constant volume of the mixture can be expressed in terms of the concentration as:

$$\begin{cases} r &= r_a c + r_b (1 - c) \\ c_v^m &= c_{va}^m c + c_{vb}^m (1 - c) \end{cases} \quad \text{with} \quad c_{va}^m = \frac{r_a}{\gamma_a - 1} \quad \text{and} \quad c_{vb}^m = \frac{r_b}{\gamma_b - 1} . \quad (4.4)$$

For ease of expression, pressure equations are substituted for energy equations (4.1c) and (4.1d). This leads to:

$$\begin{cases} \partial_t \left( \frac{P^m}{\gamma^m - 1} \right) + u_j \partial_j \left( \frac{P^m}{\gamma^m - 1} \right) + \frac{\gamma^m P^m}{\gamma^m - 1} \partial_j u_j &= -c_\ell \rho \kappa^r a_R \left( T^{m4} - T^{r4} \right) - \mathcal{Q}_c - \Pi_{ij} \partial_j u_i , \\ \partial_t (3P^r) + u_j \partial_j (3P^r) + 4P^r \partial_j u_j &= +c_\ell \rho \kappa^r a_R \left( T^{m4} - T^{r4} \right) + \partial_j \left( \frac{c_\ell}{\rho \kappa^r} \partial_j P^r \right) . \end{cases} \quad (4.5)$$

It is noteworthy that if thermal equilibrium between matter and radiation is considered,  $T^m = T^r$  and Sys. (4.5) may be replaced by Eq. (2.18b), derived in the asymptotic analysis regarding the total pressure evolution:

$$D_t P = -\gamma_1 P \partial_j u_j + (\gamma_3 - 1) \mathcal{C} + \mathcal{D}_P , \quad (4.6)$$

with, for a binary mixture of perfect gases, the conduction and the diffusion terms written as:

$$\mathcal{C} = \partial_j \left( \frac{4c_\ell T^3}{\rho \kappa^r} \partial_j T \right) , \quad (4.7)$$

$$\mathcal{D}_P = (\gamma_3 - 1) \left[ \rho \epsilon + \frac{\gamma^m}{\gamma^m - 1} \rho \mathcal{D}_c (r_a - r_b) \partial_j c \partial_j T \right] + \gamma_3 (r_a - r_b) T \partial_j (\rho \mathcal{D}_c \partial_j c) . \quad (4.8)$$

## 4.2.2 Quasi-homogeneous approach and isothermal equilibrium state

First of all, the linear stability analysis (LSA) requires the prescription of a base flow satisfying the governing equations. For any quantity  $q$ , the corresponding basic flow is denoted  $\bar{q}$ . We here consider hydrostatic equilibria (without any shear) in a gravity field oriented along the  $z$  direction. We then have:

$$\bar{q}(x, y, z, t) = \bar{q}(z) \quad \text{and} \quad \bar{\mathbf{u}} = 0 .$$

Small disturbances  $q'$  are superimposed to the base flow, so that any instantaneous quantity  $q$  is written:

$$q(x, y, z, t) = \bar{q}(z) + q'(x, y, z, t) .$$

Only the linear stability is studied here, meaning that all quadratic (or cubic) terms in the perturbation are neglected with respect to the linear ones. Under these assumptions, special solutions can be sought with the following normal mode form:

$$q'(x, y, z, t) = \check{q}(z) e^{i(k_x x + k_y y - \omega t)} ,$$

involving waves of wavelength  $\lambda_w = 2\pi/\sqrt{k_x^2 + k_y^2}$ . However, in order to make the calculations tractable, the stability of the system is investigated under a *quasi-homogeneous approach*. It

## 4.2. Governing equations and assumptions for the LSA

consists in using the additional assumption that the wavelength of the perturbations is small compared to the gradient length of the basic quantities, *i.e.* the length scales of their variations, hence  $\lambda_w \ll |\bar{q}/\partial_z \bar{q}|$ . The stability can then be considered over limited domains  $\mathcal{V}$  of spatial extension  $L$  such that:

$$\lambda_w \ll L \ll \left| \frac{\bar{q}}{\partial_z \bar{q}} \right| .$$

Choosing base flows with uniform gradients over the spatial domain  $\mathcal{V}$ , a development of  $\bar{q}$  around whatever point in  $\mathcal{V}$  leads to:

$$\bar{q}(z) = \bar{q}(z_0) \left[ 1 + (z - z_0) \frac{\partial_z \bar{q}}{\bar{q}} \right] + \mathcal{O}\left((z - z_0)^2\right) ,$$

implying that  $\bar{q}(z) \approx \bar{q}(z_0)$  since  $|z - z_0| \lesssim L$ . The quasi-homogeneous approach therefore yields the seemingly inconsistent assumptions whereby the basic quantities together with their gradient are both uniform:

**Main hypothesis: quasi-homogeneous approach**

$$\partial_z \bar{q} \approx \text{const.} \quad \text{and} \quad \bar{q}(z) \approx \text{const.} .$$

Such approximations are involved in the derivation of Boussinesq equations by Spiegel & Veronis [1960], which are used by Garaud [2018] for instance, as discussed later in Sec. 4.8.

Within the quasi-homogeneous assumption, the coefficients of the linear system resulting from the linearization of Sys. (4.1) are independent of  $(x, y, z, t)$ , *i.e.* constant. The normal modes, corresponding to the eigenmodes of the Fourier transform of the linear system can then be sought with the form:

$$\mathbf{q}'(x, y, z, t) = \hat{\mathbf{q}} e^{i(k_x x + k_y y + k_z z - \omega t)} \quad \forall \mathbf{q} \in \{\tau, \mathbf{u}, P, T, c\} . \quad (4.9)$$

To investigate the temporal stability, the wavevector  $\mathbf{k} = (k_x, k_y, k_z)$  is given as real ( $\mathbf{k} \in \mathbb{R}^3$ ) whereas  $\omega \in \mathbb{C}$  is complex with  $\omega_r$  the period and  $\omega_i$  the growth rate of the mode. The wavenumber is the norm of wavevector  $k = \sqrt{k_\perp^2 + k_z^2}$  with  $k_\perp = \sqrt{k_x^2 + k_y^2}$  the transverse wavenumber. The wavelength is related to the wavevector according to  $\lambda_w = 2\pi/k$ .

Although this limitation does not appear explicitly in the equations anymore, it is important to remember that resorting to the quasi-homogeneous approach implies that the results are only valid if the wavelength is small enough with respect to all mean gradient length scales, *i.e.*:

$$\lambda_w \ll \left| \frac{\bar{q}}{\partial_z \bar{q}} \right| \quad \text{or} \quad k \gg \left| \frac{\partial_z \bar{q}}{\bar{q}} \right| .$$

In addition to the hydrostatic equilibrium, *i.e.* ( $\bar{\mathbf{u}} = 0$ ), the basic state is assumed to be isothermal. When thermal equilibrium is achieved, the relation of equal temperatures gives:

$$\bar{T}^m = \bar{T}^r = \bar{T} .$$

Gravity is assumed oriented along the z-axis, such that  $\mathbf{g} = (0, 0, -g_0)$ . The isothermal condition implies a constant temperature ( $\partial_z \bar{T} = 0$ ) so that ( $\partial_z \bar{P} = \partial_z \bar{P}^m$ ). In this way, the equilibrium hypothesis yields ( $\bar{\tau} \partial_z \bar{P}^m = -g_0$ ) with  $\tau$  the specific volume and the equation of state entails:

$$\frac{\partial_z \bar{P}^m}{\bar{P}^m} + \frac{\partial_z \bar{\tau}}{\bar{\tau}} - \frac{\partial_z \bar{r}}{\bar{r}} = \frac{\partial_z \bar{T}^m}{\bar{T}^m} = 0 \quad .$$

where one recalls that the specific ideal gas constant  $r$  has been defined in Eq. (C.2). Because both gases of the mixture are chosen equal in Sec. 4.2.1, the ratio of material specific heats  $\gamma^m$  is constant and therefore equal to  $\bar{\gamma}^m$ . Then, the flow quantities are constrained by isothermal equilibrium with the relation:

$$\frac{\bar{\gamma}^m g_0}{\bar{c}_s^m} = \frac{\partial_z \bar{\tau}}{\bar{\tau}} - \mathcal{A}_r \partial_z \bar{c} \quad \text{with} \quad \bar{c}_s^m = \sqrt{\bar{\gamma}^m \bar{\tau} \bar{P}^m} \quad \text{and} \quad \mathcal{A}_r = \frac{r_a - r_b}{\bar{r}} \quad , \quad (4.10)$$

where  $\bar{c}_s^m$  is the material speed of sound and  $\mathcal{A}_r$  a parameter that may be interpreted as twice the negative Atwood number regarding the contrast of molar masses. At last, for the sake of simplicity, the concentration profile is supposed linear:

$$\partial_{zz}^2 \bar{c} = 0 \quad . \quad (4.11)$$

### 4.2.3 Assumptions regarding transport coefficients

In order to simplify some developments, some selected combinations will be treated as pure constants (*i.e.* nullity of their fluctuation and of their gradient). Then, in the next part, the notation  $[\rho q]$  is used temporarily for any quantity  $q$  to indicate that the combination  $[\rho q]$  is assumed to be purely constant.

#### 4.2.3.1 Viscosity

A constant dynamic viscosity  $\mu_v = [\rho \nu_v]$  is assumed with  $\nu_v$  the kinematic viscosity. Thus, the momentum equation (4.1b) becomes:

$$\partial_t (\rho u_i) + \partial_j (\rho u_i u_j) + \partial_i (P^m + P^r) = \rho g_i - [\rho \nu_v] \left( \partial_{jj}^2 u_i + \frac{1}{3} \partial_j \partial_j u_i \right) \quad ,$$

whose linearization around the equilibrium state<sup>1</sup> is:

$$\partial_t u_i' = -\bar{\tau} \partial_i P' - \tau' \partial_i \bar{P} + \bar{\tau} [\bar{\rho} \nu_v] \partial_{jj}^2 u_i' \quad .$$

Based on the homogeneous approach, one will consider  $\bar{\tau} [\bar{\rho} \nu_v] \approx \nu_v$ . This assumption implies the dissipation rate  $\varepsilon$ , as defined in Eq. (2.6), to follow:

$$\rho \varepsilon = -\Pi_{ij} \partial_j u_i = [\rho \nu_v] (\partial_j u_i)^2 \quad ,$$

<sup>1</sup>For the sake of simplicity, the term  $[\partial_i \partial_j u_j]$  is neglected meaning that the compressible contribution to the viscous dissipation is neglected with respect to the contribution of the incompressible velocity field.

## 4.2. Governing equations and assumptions for the LSA

---

whose linearization is strictly null, *i.e.*  $(\rho\varepsilon)' = 0$ .

### 4.2.3.2 Inter-species diffusion

The quantity  $[\rho\mathcal{D}_c]$  is also treated as a pure constant, so that the equation of concentration (4.1e) and the quantity  $\mathcal{Q}_c$  defined in Eq. (4.2) become:

$$D_t c = \tau [\rho\mathcal{D}_c] \partial_{jj}^2 c \quad \text{and} \quad \mathcal{Q}_c = -\frac{\gamma^m}{\gamma^m - 1} [\rho\mathcal{D}_c] (r_a - r_b) T^m \left( \partial_{jj}^2 c + \frac{\partial_j T^m}{T^m} \partial_j c \right) .$$

The linearization of these relations for an isothermal equilibrium leads to:

$$\partial_t c' = D_c \partial_{jj}^2 c' \quad \text{and} \quad \mathcal{Q}_c' = -\frac{\overline{\gamma^m}}{\overline{\gamma^m} - 1} D_c \mathcal{A}_r \overline{P^m} \left( \partial_{jj}^2 c' + \frac{\partial_z T^{m'}}{T^m} \partial_z \bar{c} \right) .$$

The hypothesis of constant  $[\rho\mathcal{D}_c]$  applied to Eq. (4.6), combined with the average isothermal condition allows to linearize the diffusion term  $\mathcal{D}_P$  recalled in Eq. (4.8). Then, by exploiting the hypothesis (4.11) and the previous relations, it can be written:

$$\mathcal{D}_P' = D_c \overline{P^m} \left( \overline{\gamma_3} \mathcal{A}_r \partial_{jj}^2 c' + \frac{\overline{\gamma^m} (\overline{\gamma_3} - 1)}{\overline{\gamma^m} - 1} \mathcal{A}_r \partial_z \bar{c} \frac{\partial_z T^{m'}}{T^m} \right) ,$$

and in the Fourier space (with definition (4.9)),

$$\widehat{\mathcal{D}}_P = -k^2 D_c \overline{P^m} \left( \overline{\gamma_3} \mathcal{A}_r \widehat{c} - \frac{\overline{\gamma^m} (\overline{\gamma_3} - 1)}{\overline{\gamma^m} - 1} \mathcal{A}_r \partial_z \bar{c} \frac{i k_z T^m}{k^2 T^m} \right) . \quad (4.12)$$

### 4.2.3.3 Opacity

Two hypotheses regarding the opacity can be ventured, without major complexification of the equations: it can be assumed that the quantities  $[\rho\kappa^r]$  or  $[\kappa^r]$  are purely constant. On the one hand, if  $[\rho\kappa^r]$  is constant, the linearization of the conduction term is simply:

$$C' = \frac{c_\ell}{[\rho\kappa^r]} \partial_{jj}^2 P^{r'} .$$

On the other hand, if  $[\kappa^r]$  is constant, since the isothermal condition implies the radiative pressure  $\overline{P^r}$  to be uniform, the linearization takes the form:

$$C' = \frac{c_\ell}{\overline{\rho} [\kappa^r]} \left( \partial_{jj}^2 P^{r'} + \frac{\partial_z \overline{\tau}}{\overline{\tau}} \partial_z P^{r'} \right) .$$

Hence, in the spectral space, the Fourier transform of  $C'$  can be expressed synthetically in terms of a factor  $h_{\rho\kappa^r}^{\text{const.}}$  by:

$$\widehat{C} = -k^2 h_{\rho\kappa^r}^{\text{const.}} \frac{4c_\ell \overline{P^r} \widehat{T^r}}{[\rho\kappa^r] \overline{T^r}} \quad \text{with} \quad h_{\rho\kappa^r}^{\text{const.}} = \begin{cases} 1 & \text{if } [\rho\kappa^r] = \text{const.} \\ 1 + \frac{i k_z \partial_z \overline{\tau}}{k^2 \overline{\tau}} & \text{if } [\kappa^r] = \text{const.} \end{cases} . \quad (4.13)$$

In the state of thermal equilibrium between matter and radiation, by using<sup>2</sup> Eq. (2.17), the radiative diffusivity coefficient  $\chi_{\text{equi.}}^r$  takes the form:

$$\chi_{\text{equi.}}^r = \left( \frac{\lambda^r}{\rho c_v} \right) = \frac{4(\bar{\gamma}_3 - 1) c_\ell \bar{P}^r}{[\rho \kappa^r] (\bar{P}^m + 4\bar{P}^r)} . \quad (4.14)$$

### 4.3 Dispersion relation within all Mach regime

#### 4.3.1 Linear system

The perturbed equations around the isothermal equilibrium state are hence:

$$\begin{cases} \partial_t \tau' + \mathbf{u}'_z \partial_z \bar{\tau} - \bar{\tau} \partial_j \mathbf{u}'_j & = 0 , & (4.15a) \\ \partial_t \mathbf{u}'_x + \bar{\tau} \partial_x (P^{m'} + P^{r'}) & = \nu_v \partial_{jj}^2 \mathbf{u}'_x , & (4.15b) \\ \partial_t \mathbf{u}'_y + \bar{\tau} \partial_y (P^{m'} + P^{r'}) & = \nu_v \partial_{jj}^2 \mathbf{u}'_y , & (4.15c) \\ \partial_t \mathbf{u}'_z + \bar{\tau} \partial_z (P^{m'} + P^{r'}) + \tau' \partial_z (\bar{P}^m + \bar{P}^r) & = \nu_v \partial_{jj}^2 \mathbf{u}'_z , & (4.15d) \\ \partial_t c' + \mathbf{u}'_z \partial_z \bar{c} & = \mathcal{D}_c \partial_{jj}^2 c' . & (4.15e) \end{cases}$$

In the next section, the isothermal case is considered so that  $(\partial_z \bar{P}^r = 0)$ . However, the term involving  $\partial_z \bar{P}^r$  in Eq. (4.15d) is kept for further generalization (see Sec. 4.7). The linearization of pressure equations (4.5) becomes:

$$\begin{cases} \frac{\partial_t P^{m'}}{\bar{\gamma}^m - 1} + \mathbf{u}'_z \frac{\partial_z \bar{P}^m}{\bar{\gamma}^m - 1} + \frac{\bar{\gamma}^m \bar{P}^m}{\bar{\gamma}^m - 1} \partial_j \mathbf{u}'_j & = -c_\ell a_R \left[ \rho \kappa^r (T^{m4} - T^{r4}) \right]' + \frac{\bar{\gamma}^m \bar{P}^m}{\bar{\gamma}^m - 1} \mathcal{D}_c \mathcal{A}_r \left( \partial_{jj}^2 c' + \frac{\partial_z T^{m'}}{\bar{T}^m} \partial_z \bar{c} \right) , \\ 3\partial_t P^{r'} + 4\bar{P}^r \partial_j \mathbf{u}'_j & = +c_\ell a_R \left[ \rho \kappa^r (T^{m4} - T^{r4}) \right]' + \frac{c_\ell}{[\rho \kappa^r]} h_{\rho \kappa^r}^{\text{const.}} \partial_{jj}^2 P^{r'} . \end{cases}$$

When thermal equilibrium is assumed, by using the previous relations and the fact that  $(\bar{c} = 0)$ , the linearization of Eq. (4.6) leads to:

$$\partial_t P' + \mathbf{u}'_z \partial_z \bar{P} = -\bar{\gamma}_1 \bar{P} \partial_j \mathbf{u}'_j + (\bar{\gamma}_3 - 1) C' + \mathcal{D}_P' . \quad (4.16)$$

Besides, temperatures can be substituted for variables of interest with the linearization of the equation of state:

$$P' = \bar{P}^m \left( \mathcal{A}_r c' - \frac{\tau'}{\bar{\tau}} + \frac{T^{m'}}{\bar{T}^m} \right) + 4\bar{P}^r \frac{T^{r'}}{\bar{T}^r} , \quad (4.17)$$

and within the limit of thermal equilibrium:

$$P' = \bar{P}^m \left( \mathcal{A}_r c' - \frac{\tau'}{\bar{\tau}} \right) + (\bar{P}^m + 4\bar{P}^r) \frac{T'}{\bar{T}} . \quad (4.18)$$

<sup>2</sup>where the thermodynamic relations of App. A are employed to derive the useful relation:

$$\frac{1}{\rho c_v} = \frac{(\bar{\gamma}_3 - 1) \bar{T}}{\bar{P}^m + 4\bar{P}^r} .$$

### 4.3. Dispersion relation within all Mach regime

#### 4.3.2 Dispersion relation at thermal equilibrium

The insertion of normal modes defined in Eq. (4.9) into Sys. (4.15) leads to:

$$\begin{cases} -i\omega\widehat{\tau} + \widehat{u}_z\partial_z\widehat{\tau} - \widehat{\tau}(ik_j\widehat{u}_j) & = 0 \quad , & (4.19a) \end{cases}$$

$$\begin{cases} -i\omega\widehat{u}_x + ik_x\widehat{\tau}(\widehat{p}^m + \widehat{p}^r) & = -v_v k^2 \widehat{u}_x \quad , & (4.19b) \end{cases}$$

$$\begin{cases} -i\omega\widehat{u}_y + ik_y\widehat{\tau}(\widehat{p}^m + \widehat{p}^r) & = -v_v k^2 \widehat{u}_y \quad , & (4.19c) \end{cases}$$

$$\begin{cases} -i\omega\widehat{u}_z + ik_z\widehat{\tau}(\widehat{p}^m + \widehat{p}^r) + \widehat{\tau}\partial_z\bar{P} & = -v_v k^2 \widehat{u}_z \quad , & (4.19d) \end{cases}$$

$$\begin{cases} -i\omega\widehat{c} + \widehat{u}_z\partial_z\widehat{c} & = -\mathcal{D}_c k^2 \widehat{c} \quad . & (4.19e) \end{cases}$$

Then, one deduces by combining velocity equations with respect to the x and y-axes (4.19b) and (4.19c) that:

$$ik_x\widehat{u}_x + ik_y\widehat{u}_y = i\frac{k_\perp^2}{\omega + iv_v k^2}\widehat{\tau}(\widehat{p}^m + \widehat{p}^r) \quad (4.20)$$

$$\text{with } k_\perp^2 = k_x^2 + k_y^2 \quad ,$$

Besides, from the scalar advection-diffusion relation (4.19e),

$$\widehat{c} = \frac{-i\partial_z\widehat{c}}{\omega + i\mathcal{D}_c k^2}\widehat{u}_z \quad , \quad (4.21)$$

which, inserted in Eq. (4.18), gives:

$$\frac{\widehat{T}}{\bar{T}} = \frac{\widehat{P}}{\bar{P}^m + 4\bar{P}^r} + \frac{\bar{P}^m}{\bar{P}^m + 4\bar{P}^r} \left( \frac{i\mathcal{A}_r\partial_z\widehat{c}}{\omega + i\mathcal{D}_c k^2}\widehat{u}_z + \frac{\widehat{\tau}}{\bar{\tau}} \right) \quad . \quad (4.22)$$

The Fourier transform of Eq. (4.16) becomes:

$$-i\omega\widehat{P} + \widehat{u}_z\partial_z\bar{P} = -\bar{\gamma}_1\bar{P}(ik_j\widehat{u}_j) + (\bar{\gamma}_3 - 1)\widehat{C} + \widehat{\mathcal{D}}_P \quad , \quad (4.23)$$

which results in the relation for  $\widehat{\mathcal{D}}_P$ :

$$\widehat{\mathcal{D}}_P = -(\bar{\gamma}_3 - 1)\widehat{C} + \mathcal{D}_c k^2 \bar{\gamma}_3 \bar{P}^m \frac{i\mathcal{A}_r\partial_z\widehat{c}}{\omega + i\mathcal{D}_c k^2}\widehat{u}_z - \chi_P^r k^2 \left[ \widehat{P} + \bar{P}^m \left( \frac{i\mathcal{A}_r\partial_z\widehat{c}}{\omega + i\mathcal{D}_c k^2}\widehat{u}_z + \frac{\widehat{\tau}}{\bar{\tau}} \right) \right] \quad , \quad (4.24)$$

where the following notation has been introduced:

$$\chi_P^r \equiv h_{\rho k^r}^{\text{const.}} \chi_{\text{equi.}}^r - \mathcal{D}_c \frac{\bar{P}^m}{\bar{P}^m + 4\bar{P}^r} \frac{\bar{\gamma}^m(\bar{\gamma}_3 - 1)}{\bar{\gamma}^m - 1} \mathcal{A}_r \partial_z \bar{c} \frac{i\mathbf{k}_z}{k^2} \quad . \quad (4.25)$$

Hence, using (4.20) and substituting temperatures for pressures with Eq. (4.22), the relation (4.16) becomes:

$$\begin{aligned} -i\omega\widehat{P} + \widehat{u}_z\partial_z\bar{P} &+ \bar{\gamma}_1\bar{P} \left[ i\frac{k_\perp^2}{\omega + iv_v k^2}\widehat{\tau}(\widehat{p}^m + \widehat{p}^r) + ik_z\widehat{u}_z \right] \\ &- \mathcal{D}_c k^2 \bar{\gamma}_3 \bar{P}^m \frac{i\mathcal{A}_r\partial_z\widehat{c}}{\omega + i\mathcal{D}_c k^2}\widehat{u}_z + \chi_P^r k^2 \left[ \widehat{P} + \bar{P}^m \left( \frac{i\mathcal{A}_r\partial_z\widehat{c}}{\omega + i\mathcal{D}_c k^2}\widehat{u}_z + \frac{\widehat{\tau}}{\bar{\tau}} \right) \right] = 0 \quad . \end{aligned}$$

The homogeneous linear system is then:

$$\begin{cases} -i\omega \frac{\hat{\tau}}{\bar{\tau}} - \left( \mathbf{i}k_z - \frac{\partial_z \bar{\tau}}{\bar{\tau}} \right) \hat{\mathbf{u}}_z - i \frac{k_z^2}{\omega + i\nu_v k^2} \bar{\tau} \left( \hat{\mathbf{p}}^m + \hat{\mathbf{p}}^r \right) & = 0, \\ \bar{\tau} \partial_z \bar{\mathbf{P}} \frac{\hat{\tau}}{\bar{\tau}} - i \left( \omega + i\nu_v k^2 \right) \hat{\mathbf{u}}_z + \mathbf{i}k_z \bar{\tau} \left( \hat{\mathbf{p}}^m + \hat{\mathbf{p}}^r \right) & = 0, \\ \left( \frac{\partial_z \bar{\mathbf{P}}}{\bar{\gamma}_1 \bar{\mathbf{P}}} + \mathbf{i}k_z \right) \hat{\mathbf{u}}_z + \left( \frac{-i\omega}{\bar{\gamma}_1 \bar{\tau} \bar{\mathbf{P}}} + i \frac{k_z^2}{\omega + i\nu_v k^2} \right) \bar{\tau} \left( \hat{\mathbf{p}}^m + \hat{\mathbf{p}}^r \right) - \mathcal{D}_c k^2 \frac{\bar{\gamma}_3 \bar{\mathbf{p}}^m}{\bar{\gamma}_1 \bar{\mathbf{P}}} \frac{i \mathcal{A}_r \partial_z \bar{c}}{\omega + i \mathcal{D}_c k^2} \hat{\mathbf{u}}_z \\ + \chi_P^r k^2 \frac{\bar{\mathbf{p}}^m}{\bar{\gamma}_1 \bar{\mathbf{P}}} \frac{\hat{\tau}}{\bar{\tau}} + \chi_P^r k^2 \frac{\bar{\mathbf{p}}^m}{\bar{\gamma}_1 \bar{\mathbf{P}}} \frac{i \mathcal{A}_r \partial_z \bar{c}}{\omega + i \mathcal{D}_c k^2} \hat{\mathbf{u}}_z + \chi_P^r k^2 \frac{1}{\bar{\gamma}_1 \bar{\tau} \bar{\mathbf{P}}} \bar{\tau} \left( \hat{\mathbf{p}}^m + \hat{\mathbf{p}}^r \right) & = 0, \end{cases} \quad (4.26)$$

which displays non-trivial solutions if and only if its determinant, denoted  $D_{\text{advr}}$ , is nought. The latter is developed with respect to the third line such that:

$$D_{\text{advr}} = D_{\text{adv}} + D_{\text{adr}}^{\mathcal{D}_c} + D_{\text{adr}}^r, \quad ,$$

with:

$$D_{\text{adv}} = \begin{vmatrix} -i\omega & - \left( \mathbf{i}k_z - \frac{\partial_z \bar{\tau}}{\bar{\tau}} \right) & -i \frac{k_z^2}{\omega + i\nu_v k^2} \\ \bar{\tau} \partial_z \bar{\mathbf{P}} & -i \left( \omega + i\nu_v k^2 \right) & + \mathbf{i}k_z \\ 0 & \left( \frac{\partial_z \bar{\mathbf{P}}}{\bar{\gamma}_1 \bar{\mathbf{P}}} + \mathbf{i}k_z \right) & + \left( \frac{-i\omega}{\bar{\gamma}_1 \bar{\tau} \bar{\mathbf{P}}} + i \frac{k_z^2}{\omega + i\nu_v k^2} \right) \end{vmatrix}, \quad (4.27a)$$

$$D_{\text{adr}}^{\mathcal{D}_c} = - \frac{\bar{\gamma}_3 \bar{\mathbf{p}}^m}{\bar{\gamma}_1 \bar{\mathbf{P}}} \frac{i \mathcal{D}_c k^2 \mathcal{A}_r \partial_z \bar{c}}{\omega + i \mathcal{D}_c k^2} \begin{vmatrix} -i\omega & - \left( \mathbf{i}k_z - \frac{\partial_z \bar{\tau}}{\bar{\tau}} \right) & -i \frac{k_z^2}{\omega + i\nu_v k^2} \\ \bar{\tau} \partial_z \bar{\mathbf{P}} & -i \left( \omega + i\nu_v k^2 \right) & + \mathbf{i}k_z \\ 0 & 1 & 0 \end{vmatrix}, \quad (4.27b)$$

$$D_{\text{adr}}^r = \chi_P^r k^2 \begin{vmatrix} -i\omega & - \left( \mathbf{i}k_z - \frac{\partial_z \bar{\tau}}{\bar{\tau}} \right) & -i \frac{k_z^2}{\omega + i\nu_v k^2} \\ \bar{\tau} \partial_z \bar{\mathbf{P}} & -i \left( \omega + i\nu_v k^2 \right) & + \mathbf{i}k_z \\ + \frac{\bar{\mathbf{p}}^m}{\bar{\gamma}_1 \bar{\mathbf{P}}} & + \frac{\bar{\mathbf{p}}^m}{\bar{\gamma}_1 \bar{\mathbf{P}}} \frac{i \mathcal{A}_r \partial_z \bar{c}}{\omega + i \mathcal{D}_c k^2} & + \frac{1}{\bar{\gamma}_1 \bar{\tau} \bar{\mathbf{P}}} \end{vmatrix}. \quad (4.27c)$$

The first determinant  $D_{\text{adv}}$  defined in Eq. (4.27a) is composed of an incompressible viscous and an acoustic contribution, denoted respectively  $D_{\text{icv}}$  and  $D_{\text{aav}}$ , such that:

$$D_{\text{adv}} = D_{\text{icv}} + \frac{D_{\text{aav}}}{\bar{\gamma}_1 \bar{\tau} \bar{\mathbf{P}}}, \quad ,$$

with:

$$D_{\text{icv}} = \begin{vmatrix} -i\omega & - \left( \mathbf{i}k_z - \frac{\partial_z \bar{\tau}}{\bar{\tau}} \right) & -i \frac{k_z^2}{\omega + i\nu_v k^2} \\ \bar{\tau} \partial_z \bar{\mathbf{P}} & -i \left( \omega + i\nu_v k^2 \right) & + \mathbf{i}k_z \\ 0 & + \mathbf{i}k_z & + i \frac{k_z^2}{\omega + i\nu_v k^2} \end{vmatrix}, \quad (4.28a)$$

$$D_{\text{aav}} = \begin{vmatrix} -i\omega & - \left( \mathbf{i}k_z - \frac{\partial_z \bar{\tau}}{\bar{\tau}} \right) & -i \frac{k_z^2}{\omega + i\nu_v k^2} \\ \bar{\tau} \partial_z \bar{\mathbf{P}} & -i \left( \omega + i\nu_v k^2 \right) & + \mathbf{i}k_z \\ 0 & \bar{\tau} \partial_z \bar{\mathbf{P}} & -i\omega \end{vmatrix}, \quad (4.28b)$$

### 4.3. Dispersion relation within all Mach regime

which gives:

$$i\omega D_{\text{adv}} = \frac{-\omega^3 (\omega + i\nu_v k^2)}{\gamma_1 \bar{\tau} \bar{P}} + \left( k^2 - \frac{\partial_z \bar{\tau}}{\bar{\tau}} \frac{\partial_z \bar{P}}{\gamma_1 \bar{P}} \right) \omega^2 + \frac{\omega k_{\perp}^2}{\omega + i\nu_v k^2} \bar{\tau} \partial_z \bar{P} \partial_z \bar{s} \quad , \quad (4.29)$$

where the basic pseudo-entropy gradient is defined as previously as:

$$\partial_z \bar{s} = \left( \frac{\partial_z \bar{\tau}}{\bar{\tau}} + \frac{\partial_z \bar{P}}{\gamma_1 \bar{P}} \right) \quad . \quad (4.30)$$

The second determinant  $D_{\text{adr}}^{\mathcal{D}_c}$  in Eq. (4.27b) comes from the contribution of inter-species diffusion and is developed such that:

$$i\omega D_{\text{adr}}^{\mathcal{D}_c} = -\frac{\gamma_3 \bar{P}^{\text{m}}}{\gamma_1 \bar{P}} \mathcal{D}_c k^2 \left( \frac{i\omega k_{\perp}^2}{\omega + i\nu_v k^2} \bar{\tau} \partial_z \bar{P} + \omega^2 k_z \right) \frac{\mathcal{A}_r \partial_z \bar{c}}{\omega + i\mathcal{D}_c k^2} \quad . \quad (4.31)$$

At last, the third determinant  $D_{\text{adr}}^{\mathcal{R}}$  in Eq. (4.27c), which provides the contribution of the radiative diffusivity, is computed as:

$$i\omega D_{\text{adr}}^{\mathcal{R}} = \chi_{\text{P}}^{\text{r}} k^2 \frac{\bar{P}^{\text{m}}}{\gamma_1 \bar{P}} \left[ -\frac{i\omega^2 (\omega + i\nu_v k^2)}{\bar{\tau} \bar{P}^{\text{m}}} + i\omega \left( k^2 + ik_z \frac{\partial_z \bar{\tau}}{\bar{\tau}} \right) + \left( \frac{i\omega k_{\perp}^2}{\omega + i\nu_v k^2} \bar{\tau} \partial_z \bar{P} + \omega^2 k_z \right) \frac{\mathcal{A}_r \partial_z \bar{c}}{\omega + i\mathcal{D}_c k^2} + i\omega \left( ik_z - \frac{\partial_z \bar{\tau}}{\bar{\tau}} \right) \frac{\partial_z \bar{P}}{\bar{P}^{\text{m}}} \right] \quad . \quad (4.32)$$

Finally, the dispersion relation:

$$i\omega \left( D_{\text{adv}} + D_{\text{adr}}^{\mathcal{D}_c} + D_{\text{adr}}^{\mathcal{R}} \right) = 0 \quad ,$$

is obtained by gathering Eqs. (4.29), (4.31) and (4.32) and by using the equilibrium relation:

$$\bar{\tau} \partial_z \bar{P} = -g_0 \quad .$$

Hence,

$$\begin{aligned} & \frac{\omega^3 (\omega + i\nu_v k^2)}{k^2 \bar{c}_s^2} - \left( 1 + \frac{\partial_z \bar{\tau}}{\bar{\tau}} \frac{g_0}{k^2 \bar{c}_s^2} \right) \omega^2 + \frac{k_{\perp}^2}{k^2} \frac{\omega}{\omega + i\nu_v k^2} g_0 \partial_z \bar{s} \\ & + \frac{i\mathcal{A}_r \partial_z \bar{c}}{\omega + i\mathcal{D}_c k^2} \left( \chi_{\text{P}}^{\text{r}} k^2 \frac{\bar{P}^{\text{m}}}{\gamma_1 \bar{P}} - \frac{\gamma_3 \bar{P}^{\text{m}}}{\gamma_1 \bar{P}} \mathcal{D}_c k^2 \right) \left( i\omega^2 \frac{k_z}{k^2} + \frac{k_{\perp}^2}{k^2} \frac{\omega g_0}{\omega + i\nu_v k^2} \right) \\ & - \frac{i\bar{P}^{\text{m}} \omega \chi_{\text{P}}^{\text{r}} k^2}{\gamma_1 \bar{P}} \left( 1 + i \frac{k_z}{k^2} \frac{\partial_z \bar{\tau}}{\bar{\tau}} \right) + \frac{i\chi_{\text{P}}^{\text{r}}}{\bar{c}_s^2} \left[ \omega^2 (\omega + i\nu_v k^2) + \omega g_0 \left( ik_z - \frac{\partial_z \bar{\tau}}{\bar{\tau}} \right) \right] = 0 \quad , (4.33) \end{aligned}$$

with  $\bar{c}_s = \sqrt{\gamma_1 \bar{\tau} \bar{P}}$  a modified speed of sound.

### 4.3.2.1 Dispersion relation at thermal equilibrium for any wave angle

Since a perfect gas plus radiation model is assumed, one may recall from thermodynamic relations of App. A.1 that:

$$\frac{1}{\bar{\gamma}} = \frac{1}{\bar{\gamma}_1} \frac{\bar{P}^m}{\bar{P}} \quad , \quad (4.34)$$

which allows to write Eq. (4.33) as:

$$\begin{aligned} & \frac{\omega^3 (\omega + i\nu_v k^2)}{k^2 \bar{c}_s^2} - \left(1 + \frac{\partial_z \bar{\tau}}{\bar{\tau}} \frac{g_0}{k^2 \bar{c}_s^2}\right) \omega^2 + \frac{k_\perp^2}{k^2} \frac{\omega}{\omega + i\nu_v k^2} g_0 \partial_z \bar{s} \\ & + \frac{i\mathcal{A}_r \partial_z \bar{c}}{\omega + i\mathcal{D}_c k^2} \frac{1}{\bar{\gamma}} \left(\chi_p^r k^2 - \bar{\gamma}_3 \mathcal{D}_c k^2\right) \left(i\omega^2 \frac{k_z}{k^2} + \frac{k_\perp^2}{k^2} \frac{\omega g_0}{\omega + i\nu_v k^2}\right) \\ & - i\omega \frac{1}{\bar{\gamma}} \chi_p^r k^2 \left(1 + i \frac{k_z}{k^2} \frac{\partial_z \bar{\tau}}{\bar{\tau}}\right) + \frac{i\chi_p^r}{\bar{c}_s^2} \left[\omega^2 (\omega + i\nu_v k^2) + \omega g_0 \left(ik_z - \frac{\partial_z \bar{\tau}}{\bar{\tau}}\right)\right] = 0 \end{aligned} \quad (4.35)$$

which can be expressed in the form of a fifth-order polynomial, better suited to numerical resolution:

$$\begin{aligned} & (\omega + i\nu_v k^2) (\omega + i\mathcal{D}_c k^2) \left[ \frac{\omega^2 (\omega + i\nu_v k^2)}{k^2 \bar{c}_s^2} - \left(1 + \frac{\partial_z \bar{\tau}}{\bar{\tau}} \frac{g_0}{k^2 \bar{c}_s^2}\right) \omega \right] \\ & - (\omega + i\nu_v k^2) (\omega + i\mathcal{D}_c k^2) \left[ \frac{i}{\bar{\gamma}} \chi_p^r k^2 \left(1 + \frac{\partial_z \bar{\tau}}{\bar{\tau}} \frac{ik_z}{k^2}\right) \right] \\ & + (\omega + i\nu_v k^2) (\omega + i\mathcal{D}_c k^2) \left[ \frac{i\chi_p^r k^2}{k^2 \bar{c}_s^2} \left[\omega (\omega + i\nu_v k^2) + g_0 \left(ik_z - \frac{\partial_z \bar{\tau}}{\bar{\tau}}\right)\right] \right] \\ & \quad + (\omega + i\mathcal{D}_c k^2) \left[ \frac{k_\perp^2}{k^2} g_0 \partial_z \bar{s} \right] \\ & \quad + i\mathcal{D}_c k^2 \mathcal{A}_r \partial_z \bar{c} \frac{1}{\bar{\gamma}} \left(\frac{\chi_p^r}{\mathcal{D}_c} - \bar{\gamma}_3\right) \left[i \frac{\omega k_z}{k^2} (\omega + i\nu_v k^2) + \frac{k_\perp^2}{k^2} g_0\right] = 0 \quad . \end{aligned} \quad (4.36)$$

### 4.3.2.2 Non-radiative and non-diffusive limit

In this paragraph, we intend to connect the previous dispersion relation (4.36) to the classical well-known Rayleigh-Taylor behaviour.

In the absence of radiation and inter-species diffusion, Eq. (4.36) reduces to a fourth-order polynomial straightforwardly soluble:

$$\frac{1}{k^2 \bar{c}_s^2} \left[\omega (\omega + i\nu_v k^2)\right]^2 - \left(1 + \frac{\partial_z \bar{\tau}}{\bar{\tau}} \frac{g_0}{k^2 \bar{c}_s^2}\right) \left[\omega (\omega + i\nu_v k^2)\right] + \frac{k_\perp^2}{k^2} g_0 \partial_z \bar{s} = 0 \quad . \quad (4.37)$$

Two pairs of solutions can be discriminated: one is related to acoustic effects whereas the other one persists in the incompressible limit. The latter describes the classical incompressible Rayleigh-Taylor instability with exponential growth when  $(g_0 \cdot \partial_z \bar{s} \leq 0)$  and neutral modes corresponding to gravity waves when  $(g_0 \cdot \partial_z \bar{s} \geq 0)$ .

The previous chapters have shown that the radiation can modify the stability condition in a way that will be described below. Especially, even if the radiation-free stable condition  $(g_0 \cdot \partial_z \bar{s} \geq 0)$  is met, strong radiative transport can destabilize the flow. One focuses particu-

### 4.3. Dispersion relation within all Mach regime

larly on the the two modes of (4.37) that can be approximated, in the incompressible ( $\overline{c_s} \rightarrow 0$ ) and inviscid ( $\nu_v \rightarrow 0$ ) limit, by:

$$\omega \approx \pm \frac{k_\perp}{k} \sqrt{g_0 \cdot \partial_z \overline{s}} \quad , \quad (4.38)$$

because, as will be seen further, these ‘‘oscillating’’ gravity waves can switch from stable to unstable behavior in the radiative case, depending on the Péclet number.

#### 4.3.2.3 Dispersion relation at thermal equilibrium for transverse modes

The previous dispersion relations (4.35) or (4.37) are difficult to solve analytically. Their numerical resolution indicates that the maximum growth rate is frequently obtained for the transverse modes, *i.e.* with  $k_\perp = k$  and  $k_z = 0$ . The latter observation suggests that the stable or unstable character of the flow can be evaluated from the sole analysis of the transverse modes. Although we did not manage to prove this assertion, useful results can be obtained thanks to this simplification and especially, analytical stability criteria can then be established. We tried to invalidate these criteria by numerical explorations but did not found any set of parameter leading to instability in contradiction with the transverse prediction.

Let  $\mathfrak{P}$  be the space of parameters which includes the visco-diffusive coefficients ( $\nu_v, \mathcal{D}_c, \chi_p^r$ ), the adiabatic exponents ( $\overline{\gamma}, \overline{\gamma}_3$ ), the gravity ( $g_0$ ), the wave vector components ( $k_\perp, k_z$ ), some mean quantities ( $\overline{c_s}, \overline{\tau}$ ) and the gradients ( $\partial_z \overline{c}, \partial_z \overline{\tau}, \partial_z \overline{s}$ ). For each set of parameters  $\mathfrak{p} \in \mathfrak{P}$ , the fifth-order polynomial (4.36) has five roots  $\omega^m$  for  $m \in \{1, 2, 3, 4, 5\}$ . From there, we discriminate five modes as the roots which can be continuously connected by letting  $\mathfrak{p}$  span the space  $\mathfrak{P}$ . The following study focuses on neutrality hypersurfaces, denoted  $\mathcal{N}$ , of the parameter space  $\mathfrak{P}$ . For each mode  $m$ , the neutrality hypersurface  $\mathcal{N}^m$  is defined such that, for  $\mathfrak{p} \in \mathcal{N}^m$ , one has:

$$\omega_i^m(\mathfrak{p}) = 0 \quad ,$$

with  $\omega_i^m = \Im(\omega^m)$  the imaginary part of the root  $\omega^m$  corresponding to mode  $m$ .

It is hoped that if all the transverse modes are stable, then all the modes are stable regardless of their wave vector. Under this assumption, the flow stability would be entirely driven by the transverse modes. Only numerical verifications can be proposed.

For the transverse modes  $k_\perp = k$  and  $k_z = 0$ , so according to Eq. (4.13), one has  $h_{\rho k^r}^{\text{const.}} = 1$  for both hypotheses about the opacity. According to Eq. (4.25), one has also  $\chi_p^r = \chi_{\text{equi.}}^r$ . By inserting  $k_\perp = k$  (equivalent to  $k_z = 0$ ) in Eq. (4.36), the polynomial becomes:

$$\begin{aligned} & \left( \omega + i\nu_v k^2 \right) \left( \omega + i\mathcal{D}_c k^2 \right) \left[ \frac{\omega + i\chi_{\text{equi.}}^r k^2}{k^2 \overline{c_s}^2} \left( \omega \left( \omega + i\nu_v k^2 \right) - g_0 \frac{\partial_z \overline{\tau}}{\overline{\tau}} \right) - \left( \omega + i\frac{1}{\overline{\gamma}} \chi_{\text{equi.}}^r k^2 \right) \right] \\ & + \left( \omega + i\mathcal{D}_c k^2 \right) \left( g_0 \partial_z \overline{s} \right) + i\mathcal{D}_c k^2 g_0 \mathcal{A}_r \partial_z \overline{c} \frac{1}{\overline{\gamma}} \left( \frac{\chi_{\text{equi.}}^r}{\mathcal{D}_c} - \overline{\gamma}_3 \right) = 0 \quad . \end{aligned} \quad (4.39)$$

Obtaining the neutrality relations under investigation amounts to find solutions to (4.39) with  $\omega_i = 0$ . Two different cases must be discriminated with respect to the real part  $\omega_r = \Re(\omega)$

which can be either zero or non-zero. When  $\omega_r = 0$ , the modes are “non-oscillating”. Crossing the neutrality surface leads to pure exponential growth without oscillation. This case can be related to the “fingering convection” of [Garaud \[2018\]](#) as discussed later in Sec. 4.8. On the other hand, when  $\omega_r \neq 0$ , the modes are “oscillating”. Crossing the neutrality surface leads to time-oscillations amplified in an exponential envelope. Except for acoustic waves, this second case can be related to the “oscillatory double-diffusive convective” instability of [Garaud \[2018\]](#).

From now onwards, basic dimensionless numbers related to molecular transport are introduced in order to characterize rates between visco-dissipative coefficients. The Schmidt number  $Sc$  and the radiative Lewis number  $Le$  are defined as the ratios of respectively the kinematic viscosity and the radiative diffusion to the scalar diffusivity:

$$Sc = \frac{\nu_v}{\mathcal{D}_c} \quad \text{and} \quad Le = \frac{\chi_{\text{equi}}^r}{\mathcal{D}_c} . \quad (4.40)$$

#### 4.3.2.4 Non-oscillating (or fingering) transverse mode

Let us write the polynomial from Eq. (4.39) as  $c_5\omega^5 + c_4\omega^4 + c_3\omega^3 + c_2\omega^2 + c_1\omega + c_0$ . Then, using (4.40), the zero-order coefficient is reduced to:

$$c_0 = +i\mathcal{D}_c k^2 \left( g_0 \mathcal{A}_r \partial_z \bar{c} \frac{1}{\bar{\gamma}} (Le - \bar{\gamma}_3) + g_0 \partial_z \bar{s} + \nu_v \chi_{\text{equi}}^r k^4 \left[ \frac{1}{\bar{\gamma}} + \frac{g_0}{k^2 c_s^2} \frac{\partial_z \bar{\tau}}{\bar{\tau}} \right] \right) .$$

When  $c_0$  vanishes,  $\omega = 0$  is an eigenvalue. Since the real part of the eigenvalue  $\omega$  is nought,  $\omega_r = 0$ , this mode is “non-oscillating” and since its imaginary part is also nought  $\omega_i = 0$ , it is neutral. This condition is verified if:

**Main result:**  $(\forall \mathbf{M}_t ; \forall \mathbf{Pe}_t)$  neutrality hyper-surface for the “non-oscillating” mode

$$\mathcal{N}_{\text{Non-osc.}} : \quad g_0 \mathcal{A}_r \partial_z \bar{c} \frac{1}{\bar{\gamma}} (Le - \bar{\gamma}_3) + g_0 \partial_z \bar{s} + (\mathcal{D}_c k^2)^2 Sc Le \left[ \frac{1}{\bar{\gamma}} + \frac{g_0}{k^2 c_s^2} \frac{\partial_z \bar{\tau}}{\bar{\tau}} \right] = 0 . \quad (4.41)$$

which defines the neutrality hyper-surface associated with this “non-oscillating” mode. Note that Eq. (4.41) is an exact relation for the transverse modes.

Besides, this relation (4.41) simplifies into a useful limit when  $\left[ (\mathcal{D}_c k^2)^2 \rightarrow 0 \right]$  because it is valid in relevant zones for turbulent modelling and because it will be used later for the specification of an all-Péclet blending of the RANS model. It gives:

**Result:**  $(\forall \mathbf{M}_t ; \forall \mathbf{Pe}_t ; \mathcal{D}_c^2 k^4 \rightarrow 0)$  neutrality hyper-surface for the “non-oscillating” mode

$$\mathcal{N}_{\text{Non-osc.}}^0 : \quad \mathcal{A}_r \partial_z \bar{c} \frac{1}{\bar{\gamma}} (Le - \bar{\gamma}_3) + \partial_z \bar{s} = 0 . \quad (4.42)$$

This mode is specific to the diffusive-radiative case and has no counterpart in the relation (4.37). As already mentioned can be related to the “fingering convection” of [Garaud \[2018\]](#) as discussed later in Sec. 4.8.

### 4.3. Dispersion relation within all Mach regime

#### 4.3.2.5 Pair of “oscillating” (or oscillatory double-diffusive convective) transverse modes

Let us now turn to the case of oscillating modes with  $\omega_r \neq 0$ . Within their hyper-surface of neutrality ( $\omega_i = 0$ ), these modes are real valued, *i.e.*  $\omega = \omega_r \in \mathbb{R}$ . Hence, they must simultaneously satisfy two equations corresponding to the real and imaginary parts of the dispersion equation:

$$\begin{aligned} & \left( \omega^2 - \nu_v \mathcal{D}_c k^4 \right) \left[ \frac{1}{k^2 \bar{c}_s^2} \left( \omega^2 - g_0 \frac{\partial_z \bar{\tau}}{\bar{\tau}} - \nu_v \chi_{\text{equi.}}^r k^4 \right) - 1 \right] \\ & - (\nu_v + \mathcal{D}_c) k^2 \left[ \frac{\nu_v k^2 \omega^2}{k^2 \bar{c}_s^2} + \chi_{\text{equi.}}^r k^2 \left( \frac{1}{k^2 \bar{c}_s^2} \left( \omega^2 - g_0 \frac{\partial_z \bar{\tau}}{\bar{\tau}} \right) - \frac{1}{\bar{\gamma}} \right) \right] + g_0 \partial_z \bar{S} = 0 \quad , \end{aligned} \quad (4.43)$$

for the real part (where a factor  $\omega$  has been suppressed, corresponding to the “non-oscillating” mode treated previously in Sec. 4.3.2.4) and:

$$\begin{aligned} & i \left[ (\nu_v + \mathcal{D}_c) k^2 \omega^2 \right] \left[ \frac{1}{k^2 \bar{c}_s^2} \left( \omega^2 - g_0 \frac{\partial_z \bar{\tau}}{\bar{\tau}} - \nu_v \chi_{\text{equi.}}^r k^4 \right) - 1 \right] \\ & + i \left( \omega^2 - \nu_v \mathcal{D}_c k^4 \right) \left[ \frac{\nu_v k^2 \omega^2}{k^2 \bar{c}_s^2} + \chi_{\text{equi.}}^r k^2 \left( \frac{1}{k^2 \bar{c}_s^2} \left( \omega^2 - g_0 \frac{\partial_z \bar{\tau}}{\bar{\tau}} \right) - \frac{1}{\bar{\gamma}} \right) \right] \\ & + i \mathcal{D}_c k^2 \left[ g_0 \partial_z \bar{S} + g_0 \mathcal{D}_c \mathcal{A}_r \partial_z \bar{c} \frac{1}{\bar{\gamma}} \left( \chi_{\text{equi.}}^r - \mathcal{D}_c \bar{\gamma}_3 \right) \right] = 0 \quad , \end{aligned} \quad (4.44)$$

for the imaginary part. As both of these equations are biquadratic, it amounts to solve jointly in  $\mathbb{R}$  the equations of the system:

$$\begin{cases} X^2 - 2b_1 X + c_1 = 0 \quad , \\ a_2 X^2 - 2b_2 X + c_2 = 0 \quad , \end{cases} \quad (4.45)$$

where  $X = \omega^2$  must be a real positive number and with:

$$\begin{cases} 2b_1 = k^2 \bar{c}_s^2 + g_0 \frac{\partial_z \bar{\tau}}{\bar{\tau}} + \left( \mathcal{D}_c k^2 \right)^2 [\text{Le} (1 + 2\text{Sc}) + \text{Sc} (2 + \text{Sc})] \quad , \\ c_1 = k^2 \bar{c}_s^2 g_0 \partial_z \bar{S} + \left( \mathcal{D}_c k^2 \right)^2 \left[ \text{Sc} \left( k^2 \bar{c}_s^2 + g_0 \frac{\partial_z \bar{\tau}}{\bar{\tau}} \right) + (1 + \text{Sc}) \text{Le} \left( \frac{1}{\bar{\gamma}} k^2 \bar{c}_s^2 + g_0 \frac{\partial_z \bar{\tau}}{\bar{\tau}} \right) \right] \\ \quad + \left( \mathcal{D}_c k^2 \right)^4 \text{Sc}^2 \text{Le} \quad , \\ a_2 = 1 + 2\text{Sc} + \text{Le} \quad , \\ 2b_2 = (1 + \text{Sc}) \left( k^2 \bar{c}_s^2 + g_0 \frac{\partial_z \bar{\tau}}{\bar{\tau}} \right) + \text{Le} \left( \frac{1}{\bar{\gamma}} k^2 \bar{c}_s^2 + g_0 \frac{\partial_z \bar{\tau}}{\bar{\tau}} \right) + \left( \mathcal{D}_c k^2 \right)^2 \text{Sc} [\text{Sc} + (2 + \text{Sc}) \text{Le}] \quad , \\ c_2 = k^2 \bar{c}_s^2 g_0 \partial_z \bar{S} + k^2 \bar{c}_s^2 g_0 \mathcal{A}_r \partial_z \bar{c} \frac{1}{\bar{\gamma}} (\text{Le} - \bar{\gamma}_3) + \left( \mathcal{D}_c k^2 \right)^2 \text{Sc} \text{Le} \left( \frac{1}{\bar{\gamma}} k^2 \bar{c}_s^2 + g_0 \frac{\partial_z \bar{\tau}}{\bar{\tau}} \right) \quad . \end{cases} \quad (4.46)$$

A first method consists in writing Sys. (4.45) as:

$$\begin{cases} X^2 - 2b_1 X + c_1 = 0 \quad , \\ X = \frac{(a_2 c_1 - c_2)}{(2b_1 a_2 - 2b_2)} \quad , \end{cases}$$

so that the relation defining the location of critical stability becomes:

$$\begin{cases} \frac{(a_2 c_1 - c_2)^2}{(2b_1 a_2 - 2b_2)^2} - 2b_1 \frac{(a_2 c_1 - c_2)}{(2b_1 a_2 - 2b_2)} + c_1 = 0 \quad , \\ \frac{(a_2 c_1 - c_2)}{(2b_1 a_2 - 2b_2)} \geq 0 \quad , \end{cases}$$

and then:

**Main result:**  $(\forall \mathbf{M}_t ; \forall \mathbf{Pe}_t)$  neutrality hyper-surface for the "oscillating" modes (1<sup>st</sup> method)

$$\mathcal{N}_{\text{Osc.}}^X : \begin{cases} (a_2 c_1 - c_2)^2 - 2b_1 (a_2 c_1 - c_2) (2b_1 a_2 - 2b_2) + c_1 (2b_1 a_2 - 2b_2)^2 = 0 & , \\ \frac{(a_2 c_1 - c_2)}{(2b_1 a_2 - 2b_2)} \geq 0 & , \end{cases} \quad (4.47)$$

where the inequality expresses the fact the hypothesis of  $(\omega^2 \geq 0)$  must be satisfied in this section. This formula does not discriminate between the two pairs of possible modes and may cause parasitic solutions to appear. The selection of modes should therefore be examined.

An approximate method circumventing the problem of solution selection is to make the hypothesis  $(c_1/b_1^2 \ll 1)$ , which gives:

$$\frac{g_0}{k^2 c_s^2} \partial_z \bar{s} \ll \left( 1 + \frac{g_0}{k^2 c_s^2} \frac{\partial_z \bar{\tau}}{\bar{\tau}} \right)^2 ,$$

and to treat the problem in the dominant order  $\mathcal{O}(c_1/b_1^2)$ . This leads first to  $X_- = c_1/(2b_1)$  and  $X_+ = 2b_1 - c_1/(2b_1)$  where  $X_-$  is the solution corresponding to gravity waves. The insertion of  $X_-$  in the other relation implies then:

**Main result:**  $(\forall \mathbf{M}_t ; \forall \mathbf{Pe}_t)$  neutrality hyper-surface for the "oscillating" modes (2<sup>nd</sup> method)

$$\mathcal{N}_{\text{Osc.}} : (2b_1) c_2 - (2b_2) c_1 = 0 \quad \text{with} \quad \frac{c_1}{2b_1} \geq 0 . \quad (4.48)$$

Formula (4.48) can be simplified into a compact formula but of limited validity by keeping in Eq. (4.46) only the dominant order  $\mathcal{O}(\mathcal{D}_c k^2)$ . It comes then when  $\left[ (\mathcal{D}_c k^2)^2 \rightarrow 0 \right]$ :

**Result:**  $(\forall \mathbf{M}_t ; \forall \mathbf{Pe}_t ; \mathcal{D}_c^2 k^4 \rightarrow 0)$  neutrality hyper-surface for the "oscillating" modes

$$\mathcal{N}_{\text{Osc.}}^0 : g_0 \mathcal{A}_r \partial_z \bar{c} \frac{1}{\bar{\gamma}} (\text{Le} - \bar{\gamma}_3) - g_0 \left( \text{Sc} + \text{Le} \frac{\frac{1}{\bar{\gamma}} + \frac{g_0}{k^2 c_s^2} \frac{\partial_z \bar{\tau}}{\bar{\tau}}}{1 + \frac{g_0}{k^2 c_s^2} \frac{\partial_z \bar{\tau}}{\bar{\tau}}} \right) \partial_z \bar{s} = 0 . \quad (4.49)$$

As previously mentioned, this pair of modes can be related to the "oscillatory double-diffusive convection" (ODDC) of [Garaud \[2018\]](#) as explained later in Sec. 4.8.

### 4.3.3 Dispersion relation in non-thermal equilibrium

A more general dispersion relation can be obtained by relaxing the assumption of thermal equilibrium. Only the total pressure equation is modified within the non-thermal equilibrium framework with respect to the thermal equilibrium case. Then, one focuses on the pressure equations (4.5) where, contrary to the perturbations, the basic state is assumed to be at thermal equilibrium in order to write the perturbed coupling term as:

$$c_{\ell} a_R \left[ \rho \kappa^r \left( T^{m4} - T^{r4} \right) \right]' = 4c_{\ell} \rho \kappa^r a_R \left( \frac{T^{m4}}{T^m} - \frac{T^{r4}}{T^r} \right) = 4c_{\ell} \rho \kappa^r a_R \bar{T}^4 \left( \frac{T^{m'}}{T^m} - \frac{T^{r'}}{T^r} \right) .$$

### 4.3. Dispersion relation within all Mach regime

In the spectral space, one has:

$$\begin{cases} -i\omega\widehat{P}^m + \widehat{u}_z\partial_z\overline{P}^m + \overline{\gamma^m}\overline{P}^m ik_j\widehat{u}_j & = -4(\overline{\gamma^m} - 1) c_\ell [\rho\kappa^r] a_R \overline{T}^4 \left( \frac{\widehat{T}^m}{\overline{T}^m} - \frac{\widehat{T}^r}{\overline{T}^r} \right) \\ & + \overline{\gamma^m} \mathcal{D}_c \mathcal{A}_r \overline{P}^m \left( ik_z \frac{\widehat{T}^m}{\overline{T}^m} \partial_z \overline{c} - k^2 \widehat{c} \right) , \\ -i\omega\widehat{P}^r + \widehat{u}_z\partial_z\overline{P}^r + \frac{4}{3}\overline{P}^r ik_j\widehat{u}_j & = +\frac{4}{3}c_\ell [\rho\kappa^r] a_R \overline{T}^4 \left( \frac{\widehat{T}^m}{\overline{T}^m} - \frac{\widehat{T}^r}{\overline{T}^r} \right) - \frac{c_\ell h_{\rho\kappa^r}^{\text{const.}}}{3[\rho\kappa^r]} k^2 \overline{P}^r , \end{cases} \quad (4.50)$$

from which the combination gives:

$$\begin{aligned} -i\omega\widehat{P} & + (4 - 3\overline{\gamma^m}) i\omega\widehat{P}^r + \widehat{u}_z\partial_z\overline{P} + \left[ \overline{\gamma^m}\overline{P}^m + 4(\overline{\gamma^m} - 1)\overline{P}^r \right] ik_j\widehat{u}_j \\ & = \overline{\gamma^m} \mathcal{D}_c \mathcal{A}_r \overline{P}^m \left( ik_z \frac{\widehat{T}^m}{\overline{T}^m} \partial_z \overline{c} - k^2 \widehat{c} \right) - \frac{(\overline{\gamma^m} - 1)c_\ell h_{\rho\kappa^r}^{\text{const.}}}{[\rho\kappa^r]} k^2 \overline{P}^r \frac{\widehat{P}^r}{\overline{P}^r} . \end{aligned} \quad (4.51)$$

In addition, radiative pressure and temperature are related by  $\left( \widehat{P}^r / \overline{P}^r = 4\widehat{T}^r / \overline{T}^r \right)$  so that the equation of state entails:

$$\widehat{P} = \overline{P}^m \left( \mathcal{A}_r \widehat{c} - \frac{\widehat{\tau}}{\overline{\tau}} + \frac{\widehat{T}^m}{\overline{T}^m} \right) + \widehat{P}^r . \quad (4.52)$$

Then, the combination of Eq. (4.52) and the equation for  $\widehat{P}^r$  of Sys. (4.50) results in:

$$(-i\omega + \zeta_r) \frac{\widehat{P}^r}{\overline{P}^r} = 4c_\ell [\rho\kappa^r] \left[ \frac{\widehat{P}}{\overline{P}^m} - \left( \mathcal{A}_r \widehat{c} - \frac{\widehat{\tau}}{\overline{\tau}} \right) \right] - \frac{4}{3} ik_j \widehat{u}_j , \quad (4.53)$$

with the notation:

$$\zeta_r = \frac{c_\ell h_{\rho\kappa^r}^{\text{const.}}}{3[\rho\kappa^r]} k^2 + c_\ell [\rho\kappa^r] \frac{\overline{P}^m + 4\overline{P}^r}{\overline{P}^m} . \quad (4.54)$$

The corrections to thermal equilibrium appear as supplementary terms, defined by:

$$\left( \frac{\widehat{P}^r}{\overline{P}^r} \right)_{\text{equi.}} = \frac{4\overline{P}^m}{\overline{P}^m + 4\overline{P}^r} \left[ \frac{\widehat{P}}{\overline{P}^m} - \left( \mathcal{A}_r \widehat{c} - \frac{\widehat{\tau}}{\overline{\tau}} \right) \right] \quad \text{and} \quad \left( \frac{\widehat{T}^r}{\overline{T}^r} \right)_{\text{equi.}} = \frac{\overline{P}^m}{\overline{P}^m + 4\overline{P}^r} \left[ \frac{\widehat{P}}{\overline{P}^m} - \left( \mathcal{A}_r \widehat{c} - \frac{\widehat{\tau}}{\overline{\tau}} \right) \right] , \quad (4.55)$$

and from Eq. (4.52):

$$\frac{\widehat{T}^m}{\overline{T}^m} - \left( \frac{\widehat{T}^r}{\overline{T}^r} \right)_{\text{equi.}} = -\frac{\overline{P}^r}{\overline{P}^m} \left[ \frac{\widehat{P}^r}{\overline{P}^r} - \left( \frac{\widehat{P}^r}{\overline{P}^r} \right)_{\text{equi.}} \right] . \quad (4.56)$$

The limit of thermal equilibrium is consequently introduced with the previous formulae from Eq. (4.51) by:

$$\begin{aligned} & -i\omega\widehat{P} + (4 - 3\overline{\gamma^m}) \overline{P}^r i\omega \left( \frac{\widehat{P}^r}{\overline{P}^r} \right)_{\text{equi.}} + \widehat{u}_z\partial_z\overline{P} + \left[ \overline{\gamma^m}\overline{P}^m + 4(\overline{\gamma^m} - 1)\overline{P}^r \right] ik_j\widehat{u}_j \\ & = +\overline{\gamma^m} \mathcal{D}_c \mathcal{A}_r \overline{P}^m \left[ ik_z \left( \frac{\widehat{T}^m}{\overline{T}^m} \right)_{\text{equi.}} \partial_z \overline{c} - k^2 \widehat{c} \right] - \frac{(\overline{\gamma^m} - 1)c_\ell h_{\rho\kappa^r}^{\text{const.}}}{[\rho\kappa^r]} k^2 \overline{P}^r \left( \frac{\widehat{P}^r}{\overline{P}^r} \right)_{\text{equi.}} \\ & + \overline{\gamma^m} \mathcal{D}_c \mathcal{A}_r \overline{P}^m ik_z \partial_z \overline{c} \left[ \frac{\widehat{T}^m}{\overline{T}^m} - \left( \frac{\widehat{T}^m}{\overline{T}^m} \right)_{\text{equi.}} \right] - \frac{(\overline{\gamma^m} - 1)c_\ell h_{\rho\kappa^r}^{\text{const.}}}{[\rho\kappa^r]} k^2 \overline{P}^r \left[ \frac{\widehat{P}^r}{\overline{P}^r} - \left( \frac{\widehat{P}^r}{\overline{P}^r} \right)_{\text{equi.}} \right] \\ & - (4 - 3\overline{\gamma^m}) \overline{P}^r i\omega \left[ \frac{\widehat{P}^r}{\overline{P}^r} - \left( \frac{\widehat{P}^r}{\overline{P}^r} \right)_{\text{equi.}} \right] . \end{aligned} \quad (4.57)$$

In order to express the factor  $\left[ \hat{P}^r / \bar{P}^r - \left( \hat{P}^r / \bar{P}^r \right)_{\text{equi.}} \right]$ , Eqs. (4.53) and (4.55) are combined so that:

$$\frac{1}{4} (\omega + i\zeta_r) \left[ \frac{\hat{P}^r}{\bar{P}^r} - \left( \frac{\hat{P}^r}{\bar{P}^r} \right)_{\text{equi.}} \right] = -\frac{\bar{P}^m}{\bar{P}^r} \left[ \left( \frac{\bar{P}^r}{\bar{P}^m + 4\bar{P}^r} \omega + i \frac{h_{\rho\kappa}^{\text{const.}} \chi_{\text{equi.}}^r k^2}{12(\gamma_3 - 1)} \right) \left( \frac{\hat{P}^r}{\bar{P}^m} + \frac{i\mathcal{A}_r \partial_z \bar{c}}{\omega + i\mathcal{D}_c k^2} \hat{u}_z + \frac{\hat{\tau}}{\bar{\tau}} \right) + \frac{\bar{P}^r}{3\bar{P}^m} \left[ k_z \hat{u}_z + \frac{k_{\perp}^2}{\omega + i\nu_v k^2} \bar{\tau} \left( \hat{P}^m + \hat{P}^r \right) \right] \right] .$$

Equations (4.20) and (4.21) applied to isothermal equilibrium, which condition is recalled as  $\left[ \partial_z \bar{\tau} / \bar{\tau} - \mathcal{A}_r \partial_z \bar{c} = -\partial_z \bar{P}^m / \bar{P}^m \right]$ , leads to:

$$-i\omega \left( \mathcal{A}_r \hat{c} - \frac{\hat{\tau}}{\bar{\tau}} \right) = \frac{-\partial_z \bar{P}^m}{\bar{P}^m} \hat{u}_z - \mathcal{A}_r \mathcal{D}_c k^2 \hat{c} - ik_j \hat{u}_j ,$$

so that, using Eq. (4.56) and the thermodynamic relations:

$$\begin{cases} \frac{\gamma^m - 1}{\gamma_3 - 1} &= 1 - (4 - 3\gamma^m) \frac{4\bar{P}^r}{\bar{P}^m + 4\bar{P}^r} , \\ \frac{\gamma^m - 1}{\gamma_3 - 1} \gamma_1 \left( \bar{P}^m + \bar{P}^r \right) &= \gamma^m \bar{P}^m + 4(\gamma^m - 1) \bar{P}^r - (4 - 3\gamma^m) \frac{4\bar{P}^r}{\bar{P}^m + 4\bar{P}^r} \bar{P}^m , \end{cases}$$

derived from App. A, Eq. (4.57) in the limit of thermal equilibrium takes the simple form:

$$-i\omega \hat{P} + \hat{u}_z \partial_z \bar{P} + \gamma_1 \bar{P} ik_j \hat{u}_j + \gamma_3 \bar{P}^m \mathcal{D}_c k^2 \mathcal{A}_r \hat{c} + \chi_P^r k^2 \left[ \hat{P} + \bar{P}^m \left( \frac{i\mathcal{A}_r \partial_z \bar{c}}{\omega + i\mathcal{D}_c k^2} + \frac{\hat{\tau}}{\bar{\tau}} \right) \right] + \mathfrak{C}_{\text{Non-equi.}} = 0 ,$$

which correction is:

$$\mathfrak{C}_{\text{Non-equi.}} = k^2 \left[ \chi_{\text{Non-equi.}}^P \hat{P} + \bar{P}^m \left( \chi_{\text{Non-equi.}}^{u_z} \frac{i\mathcal{A}_r \partial_z \bar{c}}{\omega + i\mathcal{D}_c k^2} \hat{u}_z + \chi_{\text{Non-equi.}}^{\tau} \frac{\hat{\tau}}{\bar{\tau}} \right) \right] . \quad (4.58)$$

Finally, the pressure equation can be written as:

$$\begin{aligned} & -i\omega \bar{P} + \hat{u}_z \partial_z \bar{P} + \gamma_1 \bar{P} \left( i \frac{k_{\perp}^2}{\omega + i\nu_v k^2} \bar{\tau} \left( \hat{P}^m + \hat{P}^r \right) + ik_z \hat{u}_z \right) - \mathcal{D}_c k^2 \gamma_3 \bar{P}^m \frac{i\mathcal{A}_r \partial_z \bar{c}}{\omega + i\mathcal{D}_c k^2} \hat{u}_z \\ & + k^2 \left[ \left( \chi_P^r + \chi_{\text{Non-equi.}}^P \right) \hat{P} + \bar{P}^m \frac{i\mathcal{A}_r \partial_z \bar{c}}{\omega + i\mathcal{D}_c k^2} \left( \chi_P^r + \chi_{\text{Non-equi.}}^{u_z} \right) \hat{u}_z + \bar{P}^m \left( \chi_P^r + \chi_{\text{Non-equi.}}^{\tau} \right) \frac{\hat{\tau}}{\bar{\tau}} \right] = 0 , \end{aligned}$$

from which the dispersion relation in non-thermal equilibrium is deduced from the one at thermal equilibrium by the sole substitution of the three occurrences of  $\chi_P^r$  by the appropriate terms  $\left( \chi_P^r + \chi_{\text{Non-equi.}}^P \right)$ ,  $\left( \chi_P^r + \chi_{\text{Non-equi.}}^{u_z} \right)$  and  $\left( \chi_P^r + \chi_{\text{Non-equi.}}^{\tau} \right)$ . They are defined according to:

$$\begin{cases} \chi_{\text{Non-equi.}}^{\tau} &= -\frac{\bar{P}^m + 4\bar{P}^r}{\bar{P}^r} \frac{\mathfrak{C}_{\text{Non-equi.}}^0}{\omega + i\zeta_r} \left[ \frac{\bar{P}^r}{\bar{P}^m + 4\bar{P}^r} \omega + i \frac{h_{\rho\kappa}^{\text{const.}} \chi_{\text{equi.}}^r k^2}{12(\gamma_3 - 1)} \right] , \\ \chi_{\text{Non-equi.}}^{u_z} &= -\frac{\bar{P}^m + 4\bar{P}^r}{\bar{P}^r} \frac{\mathfrak{C}_{\text{Non-equi.}}^0}{\omega + i\zeta_r} \left( \left[ \frac{\bar{P}^r}{\bar{P}^m + 4\bar{P}^r} \omega + i \frac{h_{\rho\kappa}^{\text{const.}} \chi_{\text{equi.}}^r k^2}{12(\gamma_3 - 1)} \right] - \frac{\bar{P}^r}{3\bar{P}^m} k_z \frac{\omega + i\mathcal{D}_c k^2}{i\mathcal{A}_r \partial_z \bar{c}} \right) , \\ \chi_{\text{Non-equi.}}^P &= -\frac{\bar{P}^m + 4\bar{P}^r}{\bar{P}^r} \frac{\mathfrak{C}_{\text{Non-equi.}}^0}{\omega + i\zeta_r} \left( \left[ \frac{\bar{P}^r}{\bar{P}^m + 4\bar{P}^r} \omega + i \frac{h_{\rho\kappa}^{\text{const.}} \chi_{\text{equi.}}^r k^2}{12(\gamma_3 - 1)} \right] - \frac{\bar{P}^r}{3\bar{P}^m} \frac{k_{\perp}^2}{\omega + i\nu_v k^2} \right) , \\ \mathfrak{C}_{\text{Non-equi.}}^0 &= \frac{1}{k^2} \left( \chi_P^r k^2 + \frac{\gamma^m (\gamma_3 - 1)}{\gamma^m - 1} \mathcal{D}_c k^2 \frac{ik_z}{k^2} \mathcal{A}_r \partial_z \bar{c} + \frac{(\gamma_3 - 1)(4 - 3\gamma^m)}{\gamma^m - 1} \frac{4\bar{P}^r}{\bar{P}^m + 4\bar{P}^r} i\omega \right) , \end{cases} \quad (4.59)$$

where the prefactor  $\frac{\bar{P}^m + 4\bar{P}^r}{\bar{P}^r}$  has been isolated since it diverges within the low radiation limit.

#### 4.4. Dispersion relation within the small Mach regime

The dispersion relation is deduced straightforwardly from the one (4.36) at thermal equilibrium and gives the following polynomial:

$$\begin{aligned}
& (\omega + i\nu_v k^2) (\omega + iD_c k^2) (\omega + i\zeta_r) \left[ \frac{\omega^2 (\omega + i\nu_v k^2)}{k^2 \bar{c}_s^2} - \left(1 + \frac{\partial_z \bar{\tau}}{\bar{\tau}} \frac{g_0}{k^2 \bar{c}_s^2}\right) \omega \right] \\
& - (\omega + i\nu_v k^2) (\omega + iD_c k^2) (\omega + i\zeta_r) \left[ i \frac{1}{\bar{\gamma}} \left( X_P^r + X_{\text{Non-equi.}}^r \right) k^2 \left(1 + \frac{\partial_z \bar{\tau}}{\bar{\tau}} \frac{ik_z}{k^2}\right) \right] \\
& + (\omega + i\nu_v k^2) (\omega + iD_c k^2) (\omega + i\zeta_r) \left[ \frac{i \left( X_P^r + X_{\text{Non-equi.}}^r \right) k^2}{k^2 \bar{c}_s^2} \left( \omega (\omega + i\nu_v k^2) + g_0 \left( ik_z - \frac{\partial_z \bar{\tau}}{\bar{\tau}} \right) \right) \right] \\
& + (\omega + iD_c k^2) (\omega + i\zeta_r) \left[ \frac{k_\perp^2}{k^2} g_0 \partial_z \bar{s} \right] \\
& + iD_c k^2 (\omega + i\zeta_r) \mathcal{A}_r \partial_z \bar{c} \frac{1}{\bar{\gamma}} \left( \frac{X_P^r + X_{\text{Non-equi.}}^{uz}}{D_c} - \bar{\gamma}_3 \right) \left( i \frac{\omega k_z}{k^2} (\omega + i\nu_v k^2) + \frac{k_\perp^2}{k^2} g_0 \right) = 0 \quad .
\end{aligned} \tag{4.60}$$

This sixth-order polynomial admits an additional root compared to the case at thermal equilibrium. The limit of thermal equilibrium can be found within the  $(\zeta_r \rightarrow \infty)$  limit of Eq. (4.60). This is indeed consistent with the fact that according to Eq. (4.54), the relaxation frequency towards thermal equilibrium, namely  $(c_\ell [\rho \kappa^r])$ , is one of the two contributions to  $\zeta_r$  (see Eq. (4.54)). The second one is rather associated to the radiative diffusivity and depends on the wave number  $k$ . Large values<sup>3</sup> of  $\zeta_r$  are more likely to entail minor modifications regarding the roots of dispersion relations. Hence, the additional coefficients from Sys. (4.59) related to this parameter will not be mentioned in the next sections.

The dispersion relations with or without the assumption of thermal equilibrium differ by the fact that, in Eq. (4.60), the coefficients at non-thermal equilibrium are functions of the growth rate  $\omega$ , unlike the coefficients at thermal equilibrium of Eq. (4.36), that are all independent of  $\omega$ .

#### 4.4 Dispersion relation within the small Mach regime

After the general compressible results, we now turn to the small Mach regime which is more akin to connections with the asymptotic analysis of chapter 2 and the modelling of chapter 3.

Besides, since the norm  $k$  of the wave vector  $\mathbf{k}$  does not play any role in the next part, only the influence of the wave angle defined by  $k_\perp/k$  is studied in the following dispersion relations.

##### 4.4.1 Dispersion relation at thermal equilibrium for any wave angle

The low Mach model has been derived at thermal equilibrium by Soulard *et al.* [2012] and recalled in the asymptotic analysis of chapter 2 by Eq. (2.62). It leads to the prediction:

$$\partial_j u_j' = -u_z' \frac{\partial_z \bar{P}}{\bar{\gamma}_1 \bar{P}} + \frac{\bar{\gamma}_3 - 1}{\bar{\gamma}_1 \bar{P}} c' + \frac{1}{\bar{\gamma}_1 \bar{P}} \mathcal{D}_P' \quad ,$$

hence, in the spectral space:

$$\hat{u}_z \partial_z \bar{P} = -\bar{\gamma}_1 \bar{P} (i\mathbf{k}_j \hat{u}_j) + (\bar{\gamma}_3 - 1) \hat{C} + \hat{\mathcal{D}}_P \quad , \tag{4.61}$$

<sup>3</sup>For a “large”  $\zeta_r$ , the non-thermal equilibrium correction becomes negligible and the additional root is simply  $\omega \approx -i\zeta_r$ : it is thus always very stable.

which differs from the complete equation (4.23) only by the absence of the term  $-i\omega\widehat{P}$  on the right-hand side. Then, if all terms from Eq. (4.22) are kept, Eq. (4.61) can be expanded into:

$$\begin{aligned} \widehat{u}_z \partial_z \bar{P} + \overline{\gamma_1} \bar{P} \left[ i \frac{k_\perp^2}{\omega + i\nu_v k^2} \bar{\tau} (\widehat{P}^m + \widehat{P}^r) + ik_z \widehat{u}_z \right] \\ - \mathcal{D}_c k^2 \overline{\gamma_3} \overline{P}^m \frac{i \mathcal{A}_r \partial_z \bar{c}}{\omega + i \mathcal{D}_c k^2} \widehat{u}_z + \chi_P^r k^2 \left[ \widehat{P} + \overline{P}^m \left( \frac{i \mathcal{A}_r \partial_z \bar{c}}{\omega + i \mathcal{D}_c k^2} \widehat{u}_z + \frac{\widehat{\tau}}{\bar{\tau}} \right) \right] = 0 \quad . \end{aligned}$$

Moreover, as shown in Eq. (2.46), the low Mach model predicts that  $(P'/\bar{P})$  is on the order of  $M_t^2$ . Since the expression for the divergence term  $\text{div} \mathbf{u}'$  is given to the dominant order in Mach, the consistency of the approximations suggests to eliminate the terms in  $(P'/\bar{P})$  in the linearization of the state equation, which yields:

$$\frac{\widehat{\tau}}{\bar{\tau}} = \frac{\overline{P}^m}{\overline{P}^m + 4\overline{P}^r} \left( \frac{i \mathcal{A}_r \partial_z \bar{c}}{\omega + i \mathcal{D}_c k^2} \widehat{u}_z + \frac{\widehat{\tau}}{\bar{\tau}} \right) \quad , \quad (4.62)$$

and, using the latter relation into Eq. (4.22) yields:

$$\begin{aligned} \widehat{u}_z \partial_z \bar{P} + \overline{\gamma_1} \bar{P} \left[ i \frac{k_\perp^2}{\omega + i\nu_v k^2} \bar{\tau} (\widehat{P}^m + \widehat{P}^r) + ik_z \widehat{u}_z \right] \\ - \mathcal{D}_c k^2 \overline{\gamma_3} \overline{P}^m \frac{i \mathcal{A}_r \partial_z \bar{c}}{\omega + i \mathcal{D}_c k^2} \widehat{u}_z + \chi_P^r \overline{P}^m k^2 \left( \frac{i \mathcal{A}_r \partial_z \bar{c}}{\omega + i \mathcal{D}_c k^2} \widehat{u}_z + \frac{\widehat{\tau}}{\bar{\tau}} \right) = 0 \quad , \end{aligned} \quad (4.63)$$

and the homogeneous linear system becomes:

$$\begin{cases} -i\omega \frac{\widehat{\tau}}{\bar{\tau}} - \left( ik_z - \frac{\partial_z \bar{\tau}}{\bar{\tau}} \right) \widehat{u}_z - i \frac{k_\perp^2}{\omega + i\nu_v k^2} \bar{\tau} (\widehat{P}^m + \widehat{P}^r) & = 0 \quad , \\ \bar{\tau} \partial_z \bar{P} \frac{\widehat{\tau}}{\bar{\tau}} - i \left( \omega + i\nu_v k^2 \right) \widehat{u}_z + ik_z \bar{\tau} (\widehat{P}^m + \widehat{P}^r) & = 0 \quad , \\ \left( \frac{\partial_z \bar{P}}{\overline{\gamma_1} \bar{P}} + ik_z \right) \widehat{u}_z + i \frac{k_\perp^2}{\omega + i\nu_v k^2} \bar{\tau} (\widehat{P}^m + \widehat{P}^r) - \mathcal{D}_c k^2 \frac{\overline{\gamma_3} \overline{P}^m}{\overline{\gamma_1} \bar{P}} \frac{i \mathcal{A}_r \partial_z \bar{c}}{\omega + i \mathcal{D}_c k^2} \widehat{u}_z \\ + \chi_P^r k^2 \frac{\overline{P}^m}{\overline{\gamma_1} \bar{P}} \frac{\widehat{\tau}}{\bar{\tau}} + \chi_P^r k^2 \frac{\overline{P}^m}{\overline{\gamma_1} \bar{P}} \frac{i \mathcal{A}_r \partial_z \bar{c}}{\omega + i \mathcal{D}_c k^2} \widehat{u}_z & = 0 \quad . \end{cases} \quad (4.64)$$

As has been carried out for Sys. (4.26), the corresponding determinant is put under the form:

$$D_{\text{advr}}^{\text{SM}} = D_{\text{adv}}^{\text{SM}} + D_{\text{adr}}^{\mathcal{D}_c} + D_{\text{adr}}^{\text{r,SM}} \quad \text{with} \quad D_{\text{adv}}^{\text{SM}} = D_{\text{icv}} + \frac{D_{\text{aav}}^{\text{SM}}}{\overline{\gamma_1} \bar{\tau} \bar{P}} \quad ,$$

where only the determinants  $D_{\text{aav}}^{\text{SM}}$  and  $D_{\text{adr}}^{\text{r,SM}}$  differ from their ‘‘all Mach’’ counterpart. Indeed, the determinants associated to the scalar diffusion  $D_{\text{adr}}^{\mathcal{D}_c}$  and the incompressible viscous contribution  $D_{\text{icv}}$  are the same as defined in respectively Eqs. (4.27b) and (4.28a). As for the so-called ‘‘acoustic’’ contribution, its determinant  $D_{\text{aav}}^{\text{SM}}$  takes the form:

$$D_{\text{aav}}^{\text{SM}} = \begin{vmatrix} -i\omega & - \left( ik_z - \frac{\partial_z \bar{\tau}}{\bar{\tau}} \right) & -i \frac{k_\perp^2}{\omega + i\nu_v k^2} \\ \bar{\tau} \partial_z \bar{P} & -i \left( \omega + i\nu_v k^2 \right) & + ik_z \\ 0 & \bar{\tau} \partial_z \bar{P} & 0 \end{vmatrix} = -\bar{\tau} \partial_z \bar{P} \left( \omega k_z + i \frac{k_\perp^2}{\omega + i\nu_v k^2} \bar{\tau} \partial_z \bar{P} \right) \quad ,$$

which gives:

$$i\omega D_{\text{adv}}^{\text{SM}} = k^2 \left( 1 - \frac{ik_z}{k^2} \frac{\bar{\tau} \partial_z \bar{P}}{\overline{\gamma_1} \bar{\tau} \bar{P}} \right) \omega^2 + \frac{\omega k_\perp^2}{\omega + i\nu_v k^2} \bar{\tau} \partial_z \bar{P} \partial_z \bar{s} \quad ,$$

with the pseudo-entropy gradient recalled in Eq. (4.30).

#### 4.4. Dispersion relation within the small Mach regime

The radiative diffusivity contribution is characterized by the determinant  $D_{\text{adr}}^{\text{r,SM}}$  such that:

$$D_{\text{adr}}^{\text{r,SM}} = \chi_{\text{P}}^{\text{r}} k^2 \begin{vmatrix} -i\omega & -\left(ik_z - \frac{\partial_z \bar{\tau}}{\tau}\right) & -i \frac{k_{\perp}^2}{\omega + i\nu_{\text{v}} k^2} \\ \bar{\tau} \partial_z \bar{\text{P}} & -i \left(\omega + i\nu_{\text{v}} k^2\right) & +ik_z \\ +\frac{\bar{\text{P}}^{\text{m}}}{\bar{\gamma}_1 \bar{\text{P}}} & +\frac{\bar{\text{P}}^{\text{m}}}{\bar{\gamma}_1 \bar{\text{P}}} \frac{i\mathcal{A}_r \partial_z \bar{c}}{\omega + i\mathcal{D}_c k^2} & 0 \end{vmatrix} .$$

The dispersion relation (4.35) is modified accordingly within the ( $M_{\text{t}} \ll 1$ ) limit:

$$\begin{aligned} & - \left(1 + \frac{ik_z}{k^2} \frac{g_0}{k^2 c_s^2}\right) \omega^2 + \frac{k_{\perp}^2}{k^2} \frac{\omega}{\omega + i\nu_{\text{v}} k^2} g_0 \partial_z \bar{s} \\ & + \frac{i\mathcal{A}_r \partial_z \bar{c}}{\omega + i\mathcal{D}_c k^2} \frac{1}{\bar{\gamma}} \left(\chi_{\text{P}}^{\text{r}} k^2 - \bar{\gamma}_3 \mathcal{D}_c k^2\right) \left(i\omega^2 \frac{k_z}{k^2} + \frac{k_{\perp}^2}{k^2} \frac{\omega g_0}{\omega + i\nu_{\text{v}} k^2}\right) \\ & - i\omega \frac{1}{\bar{\gamma}} \chi_{\text{P}}^{\text{r}} k^2 \left(1 + i \frac{k_z}{k^2} \frac{\partial_z \bar{\tau}}{\tau}\right) = 0 , \end{aligned} \quad (4.65)$$

which can be put under the form of a third-degree polynomial better suited for numerical resolution:

$$\begin{aligned} & - \left(\omega + i\nu_{\text{v}} k^2\right) \left(\omega + i\mathcal{D}_c k^2\right) \begin{bmatrix} - \left(1 + \frac{ik_z}{k^2} \frac{g_0}{k^2 c_s^2}\right) \omega \\ i \frac{1}{\bar{\gamma}} \chi_{\text{P}}^{\text{r}} k^2 \left(1 + \frac{\partial_z \bar{\tau}}{\tau} \frac{ik_z}{k^2}\right) \\ \frac{k_{\perp}^2}{k^2} g_0 \partial_z \bar{s} \end{bmatrix} \\ & + \left(\omega + i\mathcal{D}_c k^2\right) \left[\frac{k_{\perp}^2}{k^2} g_0 \partial_z \bar{s}\right] \\ & + i\mathcal{D}_c k^2 \mathcal{A}_r \partial_z \bar{c} \frac{1}{\bar{\gamma}} \left(\frac{\chi_{\text{P}}^{\text{r}}}{\mathcal{D}_c} - \bar{\gamma}_3\right) \left(i \frac{\omega k_z}{k^2} \left(\omega + i\nu_{\text{v}} k^2\right) + \frac{k_{\perp}^2}{k^2} g_0\right) = 0 . \end{aligned} \quad (4.66)$$

The relevance of keeping the term  $\left[\frac{ik_z}{k^2} \frac{g_0}{k^2 c_s^2}\right]$  is questionable, since the latter is of order  $M_{\text{t}}^2$ . Let us note that the ( $\bar{c}_s^2 \rightarrow \infty$ ) limit of the general relation defined in Eq. (4.36) would give Eq. (4.66), provided this term is eliminated.

#### 4.4.2 Dispersion relation at thermal equilibrium for transverse modes

For transverse modes  $k_{\perp} = k$  and  $k_z = 0$ , so according to Eq. (4.13), one has  $h_{\rho\text{kr}}^{\text{const}} = 1$  for both assumptions about opacity. From Eq. (4.25), the equality  $\chi_{\text{P}}^{\text{r}} = \chi_{\text{equi}}^{\text{r}}$  is also verified. By inserting  $k_{\perp} = k$  and  $k_z = 0$  in Eq. (4.66), the polynomial becomes:

$$\begin{aligned} & - \left(\omega + i\nu_{\text{v}} k^2\right) \left(\omega + i\mathcal{D}_c k^2\right) \left(\omega + i \frac{1}{\bar{\gamma}} \chi_{\text{equi}}^{\text{r}} k^2\right) + \left(\omega + i\mathcal{D}_c k^2\right) g_0 \partial_z \bar{s} \\ & + i\mathcal{D}_c k^2 g_0 \mathcal{A}_r \partial_z \bar{c} \frac{1}{\bar{\gamma}} (\text{Le} - \bar{\gamma}_3) = 0 , \end{aligned} \quad (4.67)$$

which can be written as  $c_3 \omega^3 + ic_2 \omega^2 + c_1 \omega + ic_0 = 0$  with:

$$\begin{cases} c_0 = +\mathcal{D}_c k^2 \left(g_0 \mathcal{A}_r \partial_z \bar{c} \frac{1}{\bar{\gamma}} (\text{Le} - \bar{\gamma}_3) + g_0 \partial_z \bar{s} + \frac{1}{\bar{\gamma}} \nu_{\text{v}} \chi_{\text{equi}}^{\text{r}} k^4\right) , \\ c_1 = +g_0 \partial_z \bar{s} + k^4 \left(\mathcal{D}_c \frac{1}{\bar{\gamma}} \chi_{\text{equi}}^{\text{r}} + \nu_{\text{v}} \frac{1}{\bar{\gamma}} \chi_{\text{equi}}^{\text{r}} + \nu_{\text{v}} \mathcal{D}_c\right) , \\ c_2 = -k^2 \left(\nu_{\text{v}} + \mathcal{D}_c + \frac{1}{\bar{\gamma}} \chi_{\text{equi}}^{\text{r}}\right) , \\ c_3 = -1 . \end{cases} \quad (4.68)$$

#### 4.4.2.1 Non-oscillating (or fingering) transverse mode

As in the “all Mach” section 4.3.2.4, when  $c_0$  vanishes,  $\omega = 0$  is an eigenvalue and there is therefore a neutral mode. This condition is verified if:

**Main result: ( $M_t \ll 1 ; \forall Pe_t$ ) neutrality hyper-surface for the “non-oscillating” mode**

$$\mathcal{N}_{\text{Non-osc.}}^{\text{SM}} : \quad g_0 \mathcal{A}_r \partial_z \bar{c} \frac{1}{\gamma} (\text{Le} - \bar{\gamma}_3) + g_0 \partial_z \bar{s} + \frac{1}{\gamma} (\mathcal{D}_c k^2)^2 \text{ScLe} = 0 \quad , \quad (4.69)$$

which defines the neutrality hyper-surface associated with this “non-oscillating” mode. It corresponds to an exact relation for the transverse modes.

Besides, this relation simplifies into a useful limit when  $\left[ (\mathcal{D}_c k^2)^2 \rightarrow 0 \right]$  because it is valid in relevant zones for turbulent modelling and because it will be used later for the specification of an all-Péclet blending of the RANS model. It comes:

**Result: ( $M_t \ll 1 ; \forall Pe_t ; \mathcal{D}_c^2 k^4 \rightarrow 0$ ) neutrality hyper-surface for the “non-oscillating” mode**

$$\mathcal{N}_{\text{Non-osc.}}^{\text{SM}^0} : \quad g_0 \mathcal{A}_r \partial_z \bar{c} \frac{1}{\gamma} (\text{Le} - \bar{\gamma}_3) + g_0 \partial_z \bar{s} = 0 \quad , \quad (4.70)$$

which is identical to the “all Mach” relation (4.42) such that  $\mathcal{N}_{\text{Non-osc.}}^{\text{SM}^0} = \mathcal{N}_{\text{Non-osc.}}^0$ .

#### 4.4.2.2 Pair of “oscillating” (or oscillatory double-diffusive convective) transverse modes

As in the “all Mach” section 4.3.2.5, one focuses on the pair of “oscillating” transverse modes. Then, one looks again for their neutrality hyper-surface where these modes are by definition real  $\omega = \omega_r \in \mathbb{R}$  by writing that this  $\omega \in \mathbb{R}$  must simultaneously satisfy two equations corresponding to the real and imaginary parts of the dispersion equation:

$$\begin{cases} \left( \omega^2 - \nu_v \mathcal{D}_c k^4 \right) - (\nu_v + \mathcal{D}_c) \frac{1}{\gamma} \chi_{\text{equi.}}^r k^4 - g_0 \partial_z \bar{s} & = 0 \quad , \\ (\nu_v + \mathcal{D}_c) k^2 \omega^2 + \left( \omega^2 - \nu_v \mathcal{D}_c k^4 \right) \frac{1}{\gamma} \chi_{\text{equi.}}^r k^2 - \mathcal{D}_c k^2 \left[ g_0 \partial_z \bar{s} + g_0 \mathcal{A}_r \partial_z \bar{c} \frac{1}{\gamma} (\text{Le} - \bar{\gamma}_3) \right] & = 0 \quad . \end{cases} \quad (4.71)$$

The existence of real solutions to this set of equations imposes that:

$$\begin{cases} \nu_v \mathcal{D}_c k^4 + (\nu_v + \mathcal{D}_c) k^4 \frac{1}{\gamma} \chi_{\text{equi.}}^r + g_0 \partial_z \bar{s} & \geq 0 \quad , \\ \left( \nu_v + \mathcal{D}_c + \frac{1}{\gamma} \chi_{\text{equi.}}^r \right) k^2 \left( \nu_v \mathcal{D}_c k^4 + (\nu_v + \mathcal{D}_c) k^4 \frac{1}{\gamma} \chi_{\text{equi.}}^r + g_0 \partial_z \bar{s} \right) \\ \quad - \mathcal{D}_c k^2 \left[ \nu_v k^4 \frac{1}{\gamma} \chi_{\text{equi.}}^r + g_0 \partial_z \bar{s} + g_0 \mathcal{A}_r \partial_z \bar{c} \frac{1}{\gamma} (\text{Le} - \bar{\gamma}_3) \right] & = 0 \quad . \end{cases}$$

By introducing the dimensionless numbers  $\text{Sc}$  and  $\text{Le}$  of Eq. (4.40) related to molecular transport, the neutrality hyper-surface  $\mathcal{N}_{\text{Osc.}}^{\text{SM}}$  of the “oscillating” modes exists under the condition:

$$g_0 \partial_z \bar{s} + (\mathcal{D}_c k^2)^2 \left( \text{Sc} + (1 + \text{Sc}) \frac{1}{\gamma} \text{Le} \right) \geq 0 \quad ,$$

and is then defined by:

#### 4.4. Dispersion relation within the small Mach regime

**Main result: ( $M_t \ll 1 ; \forall Pe_t$ ) neutrality hyper-surface for the “oscillating” modes**

$$\mathcal{N}_{\text{Osc.}}^{\text{SM}} : \quad \left( Sc + \frac{1}{\gamma} Le \right) g_0 \partial_z \bar{s} - g_0 \mathcal{A}_r \partial_z \bar{c} \frac{1}{\gamma} (Le - \bar{\gamma}_3) + \left( \mathcal{D}_c k^2 \right)^2 (1 + Sc) \left( Sc + (1 + Sc) \frac{1}{\gamma} Le + \left( \frac{1}{\gamma} Le \right)^2 \right) = 0 \quad . \quad (4.72)$$

Besides, when  $\left[ \left( \mathcal{D}_c k^2 \right)^2 \rightarrow 0 \right]$ , this relation simplifies into:

**Result: ( $M_t \ll 1 ; \forall Pe_t ; \mathcal{D}_c^2 k^4 \rightarrow 0$ ) neutrality hyper-surface for the “oscillating” modes**

$$\mathcal{N}_{\text{Osc.}}^{\text{SM}^0} : \quad \left( Sc + \frac{1}{\gamma} Le \right) g_0 \partial_z \bar{s} - g_0 \mathcal{A}_r \partial_z \bar{c} \frac{1}{\gamma} (Le - \bar{\gamma}_3) = 0 \quad , \quad (4.73)$$

under the condition  $[g_0 \partial_z \bar{s} \geq 0]$ .

#### 4.4.3 Large wave numbers limit: development in $(1/k)$

The consistency of the homogeneous approach imposes that the wavelength of the perturbations is small with respect to the gradient length of the basic quantities, thus:

$$\frac{k_z}{k^2} \frac{\partial_z \bar{\tau}}{\bar{\tau}} \ll 1 \quad ,$$

and by considering an appropriate non-dimensionalization, it may be assumed:

$$\left\{ g_0, \frac{\partial_z \bar{\tau}}{\bar{\tau}}, \partial_z \bar{s}, \partial_z \bar{c} \right\} \sim \mathcal{O}(1) \quad .$$

Then, our results only apply to wavelength small before one. Let us note ( $\epsilon = 1/k$ ), a parameter with respect to which one can develop the dispersion relation. As one wishes to preserve the effects of the visco-diffusive coefficients, one assumes:

$$\left\{ \mathcal{D}_c k^2, \nu_v k^2, \chi_{\text{equi.}}^r k^2 \right\} \sim \mathcal{O}(1) \quad .$$

Then, one looks for solutions in the form  $[\omega = \omega_0 + \epsilon \omega_1 + \mathcal{O}(\epsilon^2)]$  to Eq. (4.66). By inserting them in Eq. (4.66), the development of  $\omega$  at the dominant order leads to<sup>4</sup>:

$$- \left( \omega_0 + i \nu_v k^2 \right) \left( \omega_0 + i \mathcal{D}_c k^2 \right) \left( \omega_0 + i \frac{1}{\gamma} \chi_{\text{equi.}}^r k^2 \right) + \left( \omega_0 + i \mathcal{D}_c k^2 \right) \frac{k_z^2}{k^2} g_0 \partial_z \bar{s} + i \mathcal{D}_c k^2 \frac{1}{\gamma} (Le - \bar{\gamma}_3) \frac{k_z^2}{k^2} g_0 \mathcal{A}_r \partial_z \bar{c} = 0 \quad . \quad (4.74)$$

This relation at the dominant order of large wave numbers is identical to the relation (4.67) applying to transverse modes, provided that  $\left( \frac{k_z^2}{k^2} g_0 \right)$  is substituted to  $g_0$ . The previous results regarding neutrality curves can then be trivially extended. Indeed, the neutrality curves

<sup>4</sup>where it results in  $\chi_p^r = \chi_{\text{equi.}}^r + \mathcal{O}(\epsilon)$  and, by anticipating the non-isothermal extension in Sec. 4.7, one also has  $\frac{\bar{\gamma}_3}{\gamma}^{\text{Non-isoth.}} = \frac{\bar{\gamma}_3}{\gamma} + \mathcal{O}(\epsilon)$ .

of the transverse modes are always of the form  $\left[ g_0 [\dots] + (\mathcal{D}_c k^2)^2 [\dots] = 0 \right]$  and become thus  $\left[ \frac{k_\perp^2}{k^2} g_0 [\dots] + (\mathcal{D}_c k^2)^2 [\dots] = 0 \right]$  once the substitution  $\left( \frac{k_\perp^2}{k^2} g_0 \leftarrow g_0 \right)$  is applied. The latter can then be written as  $\left[ g_0 [\dots] + \left( \frac{k}{k_\perp} \mathcal{D}_c k^2 \right)^2 [\dots] = 0 \right]$ , showing that the curves for  $\left( \frac{k_\perp^2}{k^2} < 1 \right)$  correspond to the ones of the transverse mode for a larger diffusion  $\left( \frac{k}{k_\perp} \mathcal{D}_c \right)$ . If the fact that the diffusion has generally a stabilizing effect is admitted, the transverse mode has indeed the most constraining neutrality curve among the different wave angles within the large wave number limit.

## 4.5 Small Mach-small Péclet regime

### 4.5.1 Dispersion relation at thermal equilibrium for any wave angle

The small Mach-small Péclet model has been derived at thermal equilibrium in chapter 2 and recalled by Sys. (2.56) such that:

$$\partial_j \mathbf{u}_j' = \mathbf{u}_z' \left( \frac{\partial_z \bar{\tau}}{\bar{\tau}} - \mathcal{A}_r \partial_z \bar{c} \right) + \mathcal{D}_c \mathcal{A}_r \partial_{jj}^2 c' \quad ,$$

hence, in the spectral space:

$$i k_j \hat{\mathbf{u}}_j = \hat{\mathbf{u}}_z \left( \frac{\partial_z \bar{\tau}}{\bar{\tau}} - \mathcal{A}_r \partial_z \bar{c} \right) - \mathcal{D}_c k^2 \mathcal{A}_r \hat{c} \quad , \quad (4.75)$$

which, combined with Eq. (4.20), gives:

$$i \frac{k_\perp^2}{\omega + i \nu_v k^2} \bar{\tau} \left( \hat{\mathbf{P}}^m + \hat{\mathbf{P}}^r \right) = \hat{\mathbf{u}}_z \left( -i k_z + \frac{\partial_z \bar{\tau}}{\bar{\tau}} - \frac{\omega \mathcal{A}_r \partial_z \bar{c}}{\omega + i \mathcal{D}_c k^2} \right) \quad .$$

The linear system can be put into a form comparable to the ones obtained with the previous approaches:

$$\begin{cases} -i \omega \frac{\hat{\tau}}{\bar{\tau}} - \left( i k_z - \frac{\partial_z \bar{\tau}}{\bar{\tau}} \right) \hat{\mathbf{u}}_z - i \frac{k_\perp^2}{\omega + i \nu_v k^2} \bar{\tau} \left( \hat{\mathbf{P}}^m + \hat{\mathbf{P}}^r \right) & = 0 \quad , \\ \bar{\tau} \partial_z \bar{\mathbf{P}}^{\hat{\tau}} - i \left( \omega + i \nu_v k^2 \right) \hat{\mathbf{u}}_z + i k_z \bar{\tau} \left( \hat{\mathbf{P}}^m + \hat{\mathbf{P}}^r \right) & = 0 \quad , \\ \left( \mathcal{A}_r \partial_z \bar{c} - \frac{\partial_z \bar{\tau}}{\bar{\tau}} + i k_z \right) \hat{\mathbf{u}}_z + i \frac{k_\perp^2}{\omega + i \nu_v k^2} \bar{\tau} \left( \hat{\mathbf{P}}^m + \hat{\mathbf{P}}^r \right) - \mathcal{D}_c k^2 \frac{i \mathcal{A}_r \partial_z \bar{c}}{\omega + i \mathcal{D}_c k^2} \hat{\mathbf{u}}_z & = 0 \quad , \end{cases}$$

which gives the dispersion relation:

$$- \left( \omega + i \mathcal{D}_c k^2 \right) \left( \omega + i \nu_v k^2 \right) k^2 \left( 1 + \frac{\partial_z \bar{\tau} i k_z}{\bar{\tau} k^2} \right) + k^2 \mathcal{A}_r \partial_z \bar{c} \left( i \frac{\omega k_z}{k^2} \left( \omega + i \nu_v k^2 \right) + \frac{k_\perp^2}{k^2} g_0 \right) = 0 \quad . \quad (4.76)$$

This relation (4.76) derived within the small Mach-small Péclet approximation is exactly the limit when  $(\chi_p^r \rightarrow \infty)$  of the relation (4.66) obtained for the small Mach (all Péclet) approximation:

$$\left( 1 - \frac{\mathcal{A}_r \partial_z \bar{c}}{1 + \frac{\partial_z \bar{\tau} i k_z}{\bar{\tau} k^2}} \frac{i k_z}{k^2} \right) \omega^2 + \left( i \nu_v k^2 + i \mathcal{D}_c k^2 + \frac{\mathcal{A}_r \partial_z \bar{c}}{1 + \frac{\partial_z \bar{\tau} i k_z}{\bar{\tau} k^2}} \nu_v k_z \right) \omega - \frac{\mathcal{A}_r \partial_z \bar{c}}{1 + \frac{\partial_z \bar{\tau} i k_z}{\bar{\tau} k^2}} \frac{k_\perp^2}{k^2} g_0 - \nu_v \mathcal{D}_c k^4 = 0 \quad .$$

## 4.6. Numerical results

### 4.5.2 Dispersion relation at thermal equilibrium for transverse modes

By inserting  $k_{\perp} = k$  and  $k_z = 0$  in Eq. (4.76), the polynomial becomes:

$$\left(\omega + i\mathcal{D}_c k^2\right) \left(\omega + i\nu_v k^2\right) - g_0 \mathcal{A}_r \partial_z \bar{c} g_0 = 0 \quad . \quad (4.77)$$

The solutions of the equation  $\left[\omega^2 + i(\mathcal{D}_c + \nu_v) k^2 \omega - \left(g_0 \mathcal{A}_r \partial_z \bar{c} + \mathcal{D}_c \nu_v k^4\right) = 0\right]$  of discriminant:

$$\Delta = 4 \left(g_0 \mathcal{A}_r \partial_z \bar{c} + \mathcal{D}_c \nu_v k^4\right) - (\mathcal{D}_c + \nu_v)^2 k^4 = 4g_0 \mathcal{A}_r \partial_z \bar{c} - (\mathcal{D}_c - \nu_v)^2 k^4 \quad ,$$

are:

$$2\omega_{\pm} = -i(\mathcal{D}_c + \nu_v) k^2 \pm \sqrt{4g_0 \mathcal{A}_r \partial_z \bar{c} - (\mathcal{D}_c - \nu_v)^2 k^4} \quad .$$

One of the two transverse modes (“+” root) is then unstable if:

$$g_0 \mathcal{A}_r \partial_z \bar{c} < -\mathcal{D}_c \nu_v k^4 \leq 0 \quad . \quad (4.78)$$

If the condition is not verified, the flow is stable with respect to the transverse modes but this does not prove its general stability.

Let us notice that for Eq. (4.78), the growth rate  $\omega_+$  is purely imaginary ( $\omega_+ \in i\mathbb{R}$ ), the unstable mode is thus “non-oscillating”. This is the limit of the “non-oscillating” mode whose hyper-surfaces of neutrality have been established in Eqs. (4.41) and (4.69).

As previously, one defines the neutrality hyper-surface of the transverse modes within the low Mach-low Péclet limit as:

**Main result: ( $M_t \ll 1$  ;  $Pe_t \ll 1$ ) neutrality hyper-surface for the “non-oscillating” modes**

$$\mathcal{N}_{\text{Non-osc.}}^{\text{SMSP}} : g_0 \mathcal{A}_r \partial_z \bar{c} + \mathcal{D}_c \nu_v k^4 = 0 \quad . \quad (4.79)$$

## 4.6 Numerical results

### 4.6.1 General dispersion relation at thermal equilibrium

In this section, one considers the general dispersion relation at thermal equilibrium (4.35) as well as the subsequent hyper-surfaces of neutrality. One is particularly interested in the inverse of the Lewis number  $Le^{-1}$  (see Eq. (4.40)), defined as:

$$Le^{-1} = \frac{\mathcal{D}_c}{\chi_{\text{equi}}^r} \quad .$$

Note that the latter ratio is an analogue of the Péclet number according to the analogy between physical diffusion-viscosity and turbulent diffusion-viscosity proposed below in Sec. 4.9.1 in the context of turbulence modelling.

#### 4.6.1.1 Non-dimensionalization for numerical resolution

This section shows numerical solutions of the dispersion relations for parameters made dimensionless as follows. The length scale  $\bar{\tau}/\partial_z\bar{\tau}$  and the acceleration scale  $g_0$  are chosen such that:

$$\frac{\partial_z\bar{\tau}}{\bar{\tau}} = 1 \quad \text{and} \quad g_0 = \pm 1 = -\bar{\tau}\partial_z\bar{P} \quad ,$$

where the sign of  $g_0$  changes with respect to the gradient of  $\bar{\tau}$ . In the next part, only the case  $g_0 = 1$  is treated *i.e.*  $\partial_z\bar{\tau}$  and  $\partial_z\bar{P}$  of opposite signs (*i.e.* stable case for an Euler configuration with neither diffusion nor radiation). As an isothermal binary mixture is considered, the equation of state gives:

$$\frac{\partial_z\bar{P}^m}{\bar{P}^m} + \frac{\partial_z\bar{\tau}}{\bar{\tau}} = \frac{\partial_z\bar{r}}{\bar{r}} + \frac{\partial_z\bar{T}}{\bar{T}} \quad ,$$

which can take the form:

$$\frac{\partial_z\bar{P}^m}{\bar{P}^m} - \mathcal{A}_r\partial_z\bar{c} = -1 \quad ,$$

where, relatively to the gradient length of density, the concentration gradient is reasonably<sup>5</sup> chosen as

$$\partial_z\bar{c} = 1 \quad ,$$

since only the product  $[\mathcal{A}_r\partial_z\bar{c}]$  matters. Hence,  $[\partial_z\bar{P}^m/\bar{P}^m = -1 + \mathcal{A}_r]$  and the pseudo-entropy gradient is:

$$\partial_z\bar{s} = 1 + \frac{\bar{P}^m}{\bar{\gamma}_1\bar{P}} (\mathcal{A}_r - 1) \quad ,$$

where the expression of  $\bar{\gamma}_1$  is given in App. A. By using the nullity of  $\partial_z\bar{P}^i$  due to the isothermal condition, the parameters are constrained by the relation:  $[\bar{\gamma}^m g_0 / \bar{c}_s^m{}^2 = \partial_z\bar{\tau}/\bar{\tau} - \mathcal{A}_r\partial_z\bar{c}]$ . Hence,

$$\pm \frac{\bar{\gamma}^m}{\bar{c}_s^m{}^2} = 1 - \mathcal{A}_r \quad .$$

The homogeneous approach of this study only makes sense for short enough wavelengths with respect to the gradient length, so one will just consider the modes ( $k \geq \partial_z\bar{\tau}/\bar{\tau}$ ).

Finally, the only free parameters defining the equilibrium state are  $\{\bar{\gamma}^m, \mathcal{A}_r, \frac{1}{\bar{\gamma}}\}$ , from which the quantities appearing in the dispersion relations are:

#### Free parameters: defining the equilibrium state

$$\left\{ \begin{array}{l} \frac{\partial_z\bar{\tau}}{\bar{\tau}} = \partial_z\bar{c} = 1 \quad , \\ g_0 = +1 \quad , \\ \frac{\bar{c}_s^m{}^2}{\bar{\gamma}^m} = \frac{1}{1-\mathcal{A}_r} \quad , \\ \partial_z\bar{s} = 1 + \frac{1}{\bar{\gamma}} (\mathcal{A}_r - 1) \quad , \end{array} \right. \quad \text{with} \quad \mathcal{A}_r = \frac{r_a - r_b}{\bar{r}} \quad \text{and} \quad \frac{1}{\bar{\gamma}} = \frac{\bar{P}^m}{\bar{\gamma}_1\bar{P}} \quad .$$

<sup>5</sup>It amounts to assume that the molar mass difference is the main source of density variation in the mixture.

## 4.6. Numerical results

### 4.6.1.2 Expectations from local criteria

Local inviscid and non-diffusive stability criteria have been proposed in chapter 1 and summarized by Sys. (1.19). Applied to the present isothermal configuration for binary mixture of gases with the same adiabatic exponent  $\gamma^m$ , we have:

$$\begin{aligned} \nabla_T &= 0 , \\ \nabla_T - \nabla_{\text{ad}} &= -\frac{\bar{\gamma}-1}{\bar{\gamma}} \frac{\bar{P}}{p^m+4p^r} , \\ \nabla_\mu &= -\frac{\bar{P}}{p^m} \frac{\mathcal{A}_r}{\mathcal{A}_r-1} , \\ \nabla_T - \nabla_{\text{ad}} + \frac{\chi_\mu}{\chi_T} \nabla_\mu &= \frac{\bar{P}}{p^m+4p^r} \left( \frac{\mathcal{A}_r}{\mathcal{A}_r-1} - \frac{\bar{\gamma}-1}{\bar{\gamma}} \right) . \end{aligned}$$

Due to the fact that we necessarily have  $[\nabla_T - \nabla_{\text{ad}} < 0]$ , the semi-convective instability cannot be encountered according to Sys. (1.19) and we are left with only three cases defined with respect to  $\mathcal{A}_r$  :

$$\begin{aligned} \text{stability :} & \quad 0 < \mathcal{A}_r < 1 , \\ \text{thermohaline instability :} & \quad -(\bar{\gamma}-1) < \mathcal{A}_r < 0 , \\ \text{convective instability :} & \quad \mathcal{A}_r < -(\bar{\gamma}-1) . \end{aligned}$$

The ( $\mathcal{A}_r > 0$ ) region indeed remain stable in the following and will not be shown in the figures whereas the convective region [ $\mathcal{A}_r < -(\bar{\gamma}-1)$ ] can be damped and stabilized at given non-zero wavenumbers by the viscosity<sup>6</sup>.

The most interesting region is  $[-(\bar{\gamma}-1) < \mathcal{A}_r < 0]$  where thermohaline instability can be expected according to the local criteria (1.19). Depending on the relative importance of the radiative and inter-species diffusion coefficients, it will be shown to have a complex structure with one stable sub-region and two sub-regions which are unstable with respect to two different kind of instabilities.

As a last remark, one can notice that the boundary  $[-(\bar{\gamma}-1) = \mathcal{A}_r]$  corresponds exactly to the condition:

$$\frac{\partial_j \bar{P}}{\bar{\gamma}_1 \bar{P}} - \frac{\partial_j \bar{\rho}}{\bar{\rho}} = 0 ,$$

while ( $\mathcal{A}_r = 0$ ) corresponds exactly to the condition:

$$\frac{\partial_j \bar{r}}{\bar{r}} = 0 ,$$

showing that both asymptotic conditions of Eq. (2.64) derived from the asymptotic analysis match the boundaries of the stability regions of the stratified equilibrium, according to the local criteria (1.19).

<sup>6</sup>The effect of the viscosity vanishes at large wavelength so that unstable waves probably exist whatever the dissipation but that limit is out of the validity region of the present quasi-homogeneous approach.

## 4.6.1.3 Phenomenology

Figure 4.1 shows plots of  $\omega_i$  in the planes  $(\mathcal{A}_r, \log_{10} [1/Le])$  and  $(\log_{10} [\mathcal{D}_c], \log_{10} [1/Le])$ . The gray-level plotted field is obtained by numerical resolution of the roots of the dispersion relation (4.36). The selected value of  $\omega_i$  is the maximum value on all five modes and on  $k_{\perp}/k \in [0, 1]$ . The wave number  $k = 10$  is used for the top of Fig. 4.1 whereas the bottom is given for  $k = 40$ . In the right side of each subfigure,  $(\omega_i < 0)$  which means that the flow is stable for these parameters with respect to the corresponding wave number. On the other hand, unstable zones (*i.e.*  $\omega_i > 0$ ) are met on the left side.

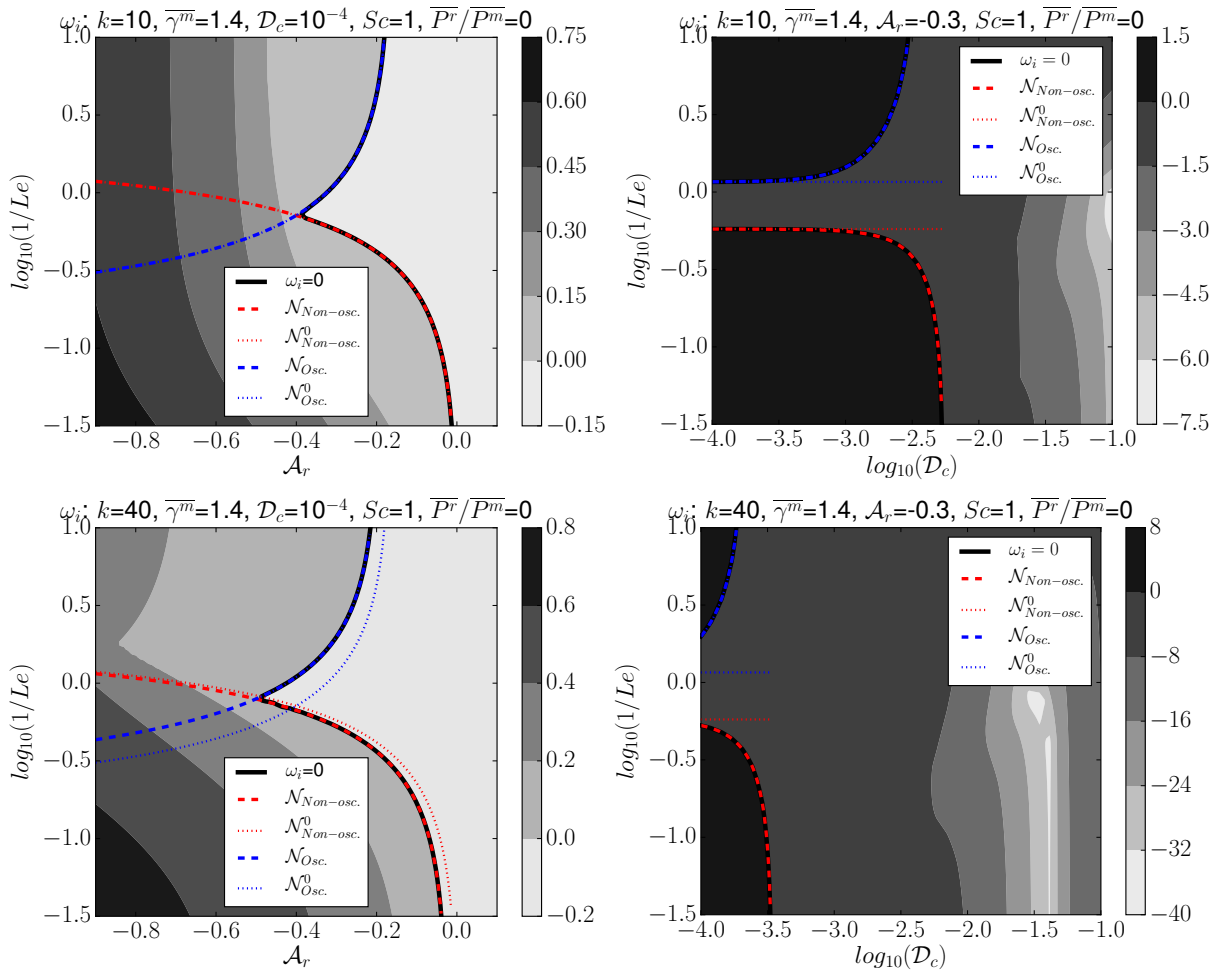


Figure 4.1 – Maps of  $\max_{\{k_{\perp}/k\}} \omega_i$  in the planes  $(\mathcal{A}_r, \log_{10} [1/Le])$  and  $(\log_{10} [\mathcal{D}_c], \log_{10} [1/Le])$  by numerical resolution of the roots of the dispersion relation (4.36). Superposition of (semi)-analytical neutrality curves obtained for transverse modes  $k_{\perp} = k$  exact or approximate with respect to relations (4.41) and (4.42) for the “non-oscillating” mode and Eqs. (4.47), (4.48) and (4.49) for “oscillating” modes.

The (semi)-analytical neutrality curves obtained for the transverse modes  $k_{\perp} = k$  are also reported. First, the dashed lines, denoted  $\mathcal{N}_{\text{Non-osc.}}$  and  $\mathcal{N}_{\text{Osc.}}$ , represent the “exact” curves respectively given by Eq. (4.41) and Eq. (4.48), computed for the “non-oscillating” mode (in red) and for the “oscillating” modes (in blue). Second, the dotted lines, denoted  $\mathcal{N}_{\text{Non-osc.}}^0$  and  $\mathcal{N}_{\text{Osc.}}^0$ , characterize the approximate curves with respect to respectively Eq. (4.41) and Eq. (4.48), calculated for the “non-oscillating” mode (in red) and for the “oscillating” modes (in blue).

## 4.6. Numerical results

One notes first in Fig. 4.1 that the union of  $\mathcal{N}_{\text{Non-osc.}}$  and  $\mathcal{N}_{\text{Osc.}}$  covers exactly the iso-value “0” of the numerical solution: this indicates that the first modes that become unstable are the transverse modes. The agreements between the “exact” and approximate curves  $\mathcal{N}_{\text{Non-osc.}}$  and  $\mathcal{N}_{\text{Non-osc.}}^0$ , as well as between  $\mathcal{N}_{\text{Osc.}}$  and  $\mathcal{N}_{\text{Osc.}}^0$ , are judged by comparing dashed and dotted lines. They are correct at moderate  $k$  and  $\mathcal{D}_c$  or, more accurately, within the  $\left[ \left( \mathcal{D}_c k^2 \right) \rightarrow 0 \right]$  limit.

One can also see in Fig. 4.1 that the “non-oscillating” mode defines an unstable zone in the lower left-hand corner of the subfigures while the “oscillating” modes define an unstable zone in the upper left-hand corner. This behavior is illustrated in Fig. 4.2 which also clarifies the designation of “oscillating” and “non-oscillating” modes.

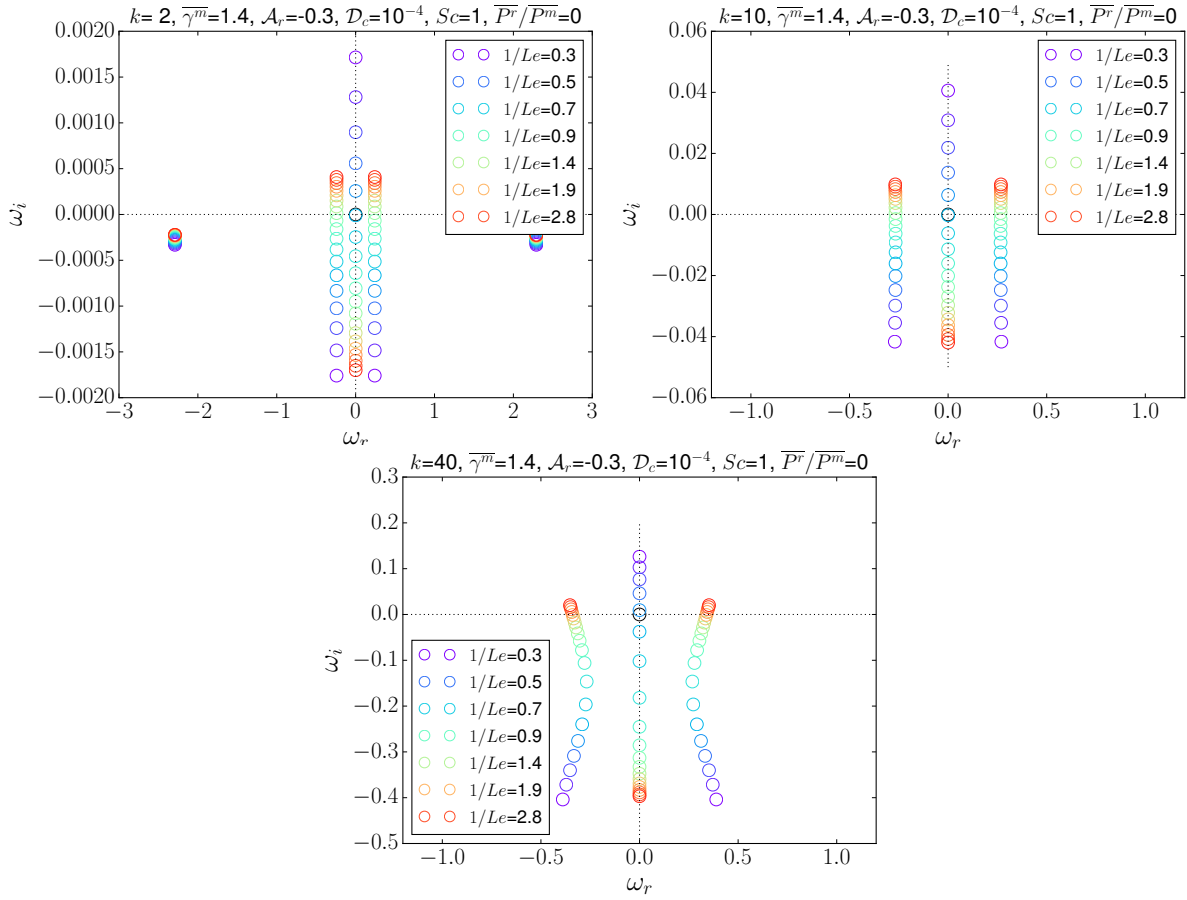


Figure 4.2 – Plot in the complex plane of the modes corresponding to the five roots of the dispersion relation (4.36) for the transverse modes ( $k_{\perp} = k$ ). The variation on  $\mathcal{D}_c/\chi_{\text{equi}}^{\text{f}}$  corresponds to a vertical path in Figs. 4.1.

Figure 4.2 shows a plot in the complex plane, when  $Le^{-1} = \mathcal{D}_c/\chi_{\text{equi}}^{\text{f}}$  varies, of transverse modes ( $k_{\perp} = k$ ) corresponding to the five roots of the dispersion relation (4.36). Except in Fig. 4.2-(a) where  $k = 2$  for a better legibility, the selected parameters correspond to vertical paths in Fig. 4.1 connecting two unstable zones through a stable one. The five modes are shown in Fig. 4.2-(a), whose pair of external modes is related to compressibility effects and is not relevant here. Figures 4.2-(b,c) propose a zoom on the modes labelled as “non-oscillating” ( $\omega_r = 0$ ) and “oscillating” ( $\omega_r \neq 0$ ). Figure 4.2 shows that the “non-oscillating” and the “oscillating” modes react in an opposite way to the evolution of the inverse of the Lewis number  $Le^{-1}$ .

Anticipating on the analogy between  $Pe_t$  and  $Le^{-1}$ , both comparing diffusive time scales (turbulent or molecular) to radiative transport time scales, the figure shows that the “non-oscillating” mode is stable at large Péclet number but is destabilized when it becomes small. The “oscillating” modes have the opposite behaviour. The destabilization of the “non-oscillating” mode, when the radiative diffusion becomes strong enough, is directly linked with the stability considerations introduced in Sec. 2.3.2.5 and exemplified by the difference between the three DNS presented in Sec. 2.5.

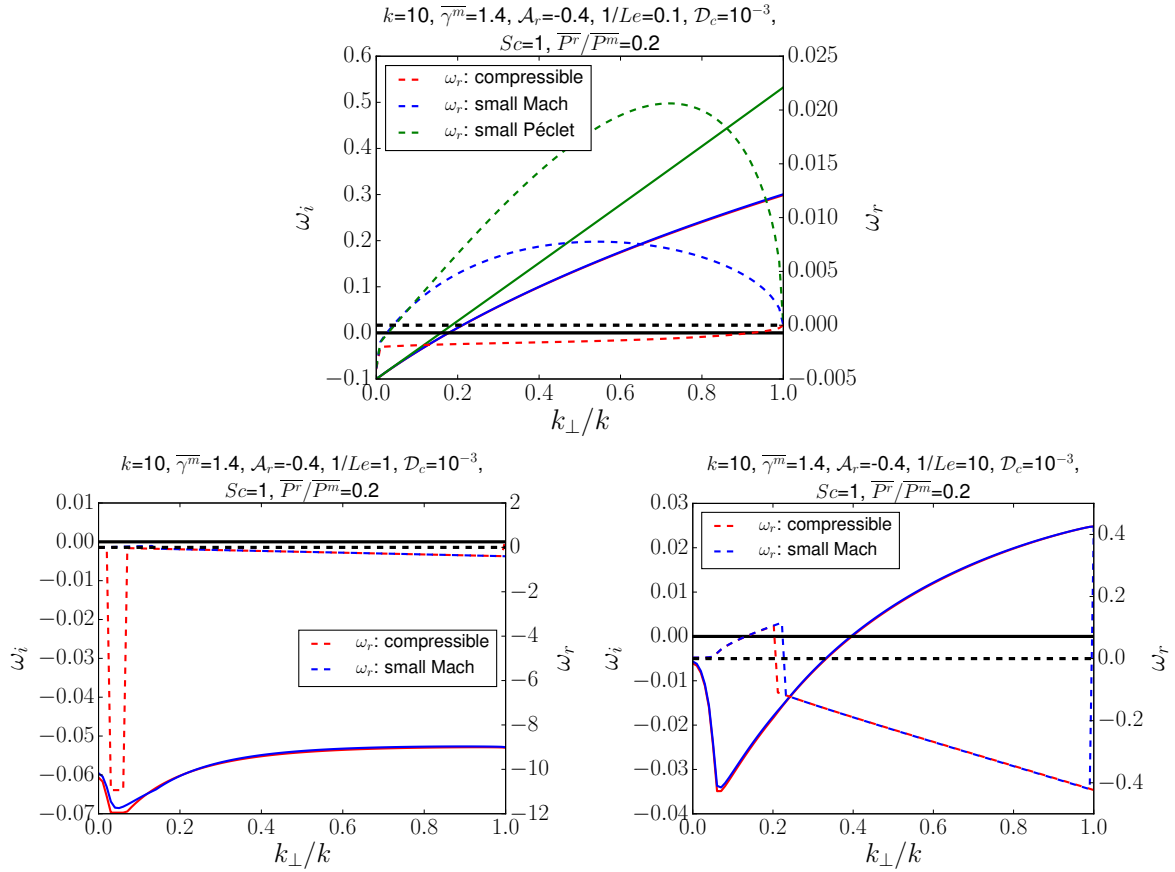


Figure 4.3 – Evolution with respect to the wave angle measured by  $k_{\perp}/k$  of the real part (dashed lines) and the imaginary part (solid lines) of the least stable or unstable mode; comparison of compressible results with the low Mach “all Péclet” and the low Mach-low Péclet limit. The three figures displays three values of the ratio  $Le^{-1} = \mathcal{D}_c / \chi_{\text{equi}}^r$  : 0.1, 1 and 10 .

Figure 4.3 shows the evolution of the real and imaginary parts of the least stable or unstable mode with respect to the wave angle measured by  $k_{\perp}/k$  for three values of  $Le^{-1} = \mathcal{D}_c / \chi_{\text{equi}}^r$  : 0.1, 1 and 10. It compares the solutions obtained from the compressible (4.36), the low Mach (4.66) and the low Mach-low Péclet (4.76) dispersion relations. A good agreement of the low Mach limit with the general solution can be noticed for the three Le numbers (the blue and red lines are almost superposed, at least for  $\omega_i$ ). For the tested parameters, the angle that maximizes  $\omega_i$  is  $k_{\perp}/k = 1$ . Figure 4.3-(a) is dominated by the mode referred to as “non-oscillating” (although  $\omega_r \neq 0$  for  $k_{\perp}/k \neq 1$ ) whereas Fig. 4.3-(c) is dominated by the pair of the so-called “oscillating” modes (the jump from a mode to another of the couple  $(\omega_1, \omega_2)$  characterized by  $\omega_2 \approx -\bar{\omega}_1$ , *i.e.* complex conjugate here, explains the discontinuity in the evolution of  $\omega_r$ ).

## 4.6. Numerical results

### 4.6.1.4 Parametric variations

Figures 4.4 to 4.7 show the effects of some parametric variations regarding the (numerical) general neutrality curves and for the exact transverse modes  $\mathcal{N}_{\text{Non-osc.}}$  and  $\mathcal{N}_{\text{Osc.}}$  or approximate in the  $\left[\left(\mathcal{D}_c k^2\right) \rightarrow 0\right]$  limit  $\mathcal{N}_{\text{Non-osc.}}^0$  and  $\mathcal{N}_{\text{Osc.}}^0$ . In all cases, the curve  $\mathcal{N}_{\text{Osc.}}^X$  according to Eq. (4.47) is also displayed but remains superimposed to  $\mathcal{N}_{\text{Osc.}}$  according to Eq. (4.48) for all the following curves.

Figure 4.4 shows the effect of the wave number. Recalling the stable region lies on the right side of each plot, one can see that it spreads out rapidly when the wave number grows. It may be due to the higher viscous attenuation at short wavelengths.

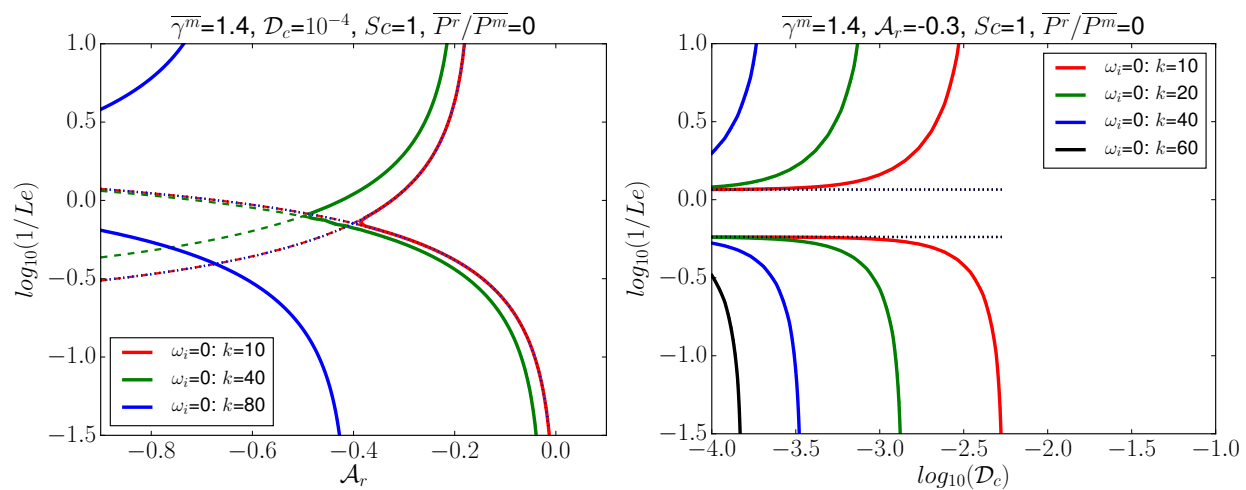


Figure 4.4 – Contours of neutrality in the planes  $(A_r, \log_{10}[1/Le])$  and  $(\log_{10}[\mathcal{D}_c], \log_{10}[1/Le])$ : unstable zone on the left and stable one on the right. Numerical reference (solid lines): maximization on all modes and all quantities  $k_{\perp}/k$  of the roots of the relation dispersion (4.36). (Semi)-analytical neutrality curves obtained for the transverse modes  $k_{\perp} = k$ : dashed lines:  $\mathcal{N}_{\text{Non-osc.}}$  and  $\mathcal{N}_{\text{Osc.}}$ ; dotted lines:  $\mathcal{N}_{\text{Non-osc.}}^0$  and  $\mathcal{N}_{\text{Osc.}}^0$ .

Figure 4.5 characterizes the effect of the material adiabatic exponent  $\gamma^m$ . The destabilization by the radiative conduction seems to be more likely to occur with the increase of compressibility of the gas. Indeed, the unstable region is much larger for a very compressible gas ( $\gamma^m = 1.1$ ) than for a weakly compressible one ( $\gamma^m = 1.66$ ).

Figure 4.6 points out the effect of the Schmidt number  $Sc$ . As previously, it can be interpreted by viscous attenuation which rises with the Schmidt number at fixed scalar diffusion coefficient  $\mathcal{D}_c$ . As expected, the increase of the kinematic viscosity seems to stabilize the flow field and enhances the stable zone located on the right side of each contours of Fig. 4.6.

Figure 4.7 displays the effect of radiation intensity, measured by  $\overline{Pr}/\overline{Pm}$  (taken at its zero limit in all previous figures). The growth of the radiative pressure tends to stabilize the flow.

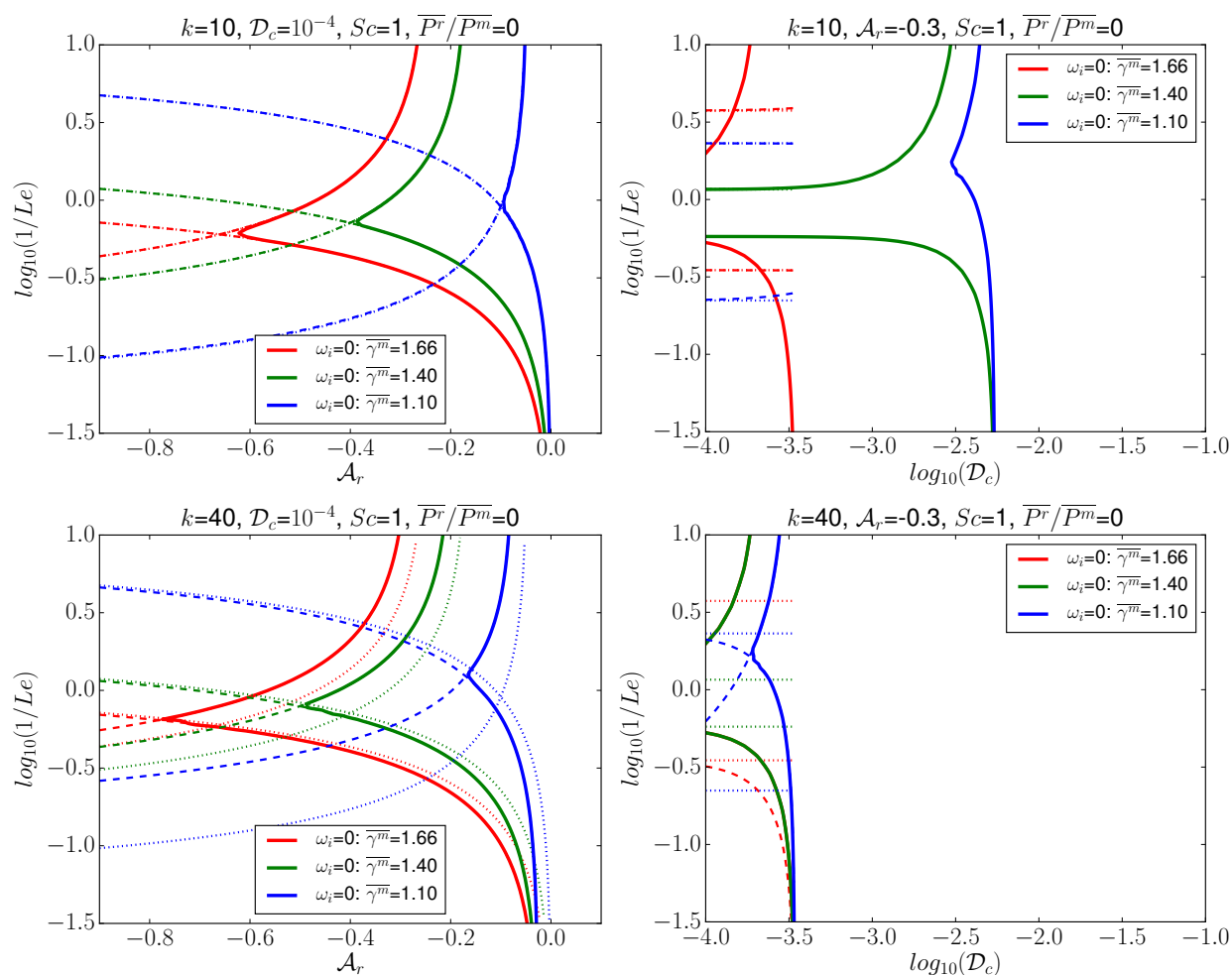


Figure 4.5 – Contours of neutrality in the planes  $(\mathcal{A}_r, \log_{10} [1/\text{Le}])$  and  $(\log_{10} [\mathcal{D}_c], \log_{10} [1/\text{Le}])$ : unstable zone on the left and stable one on the right. Numerical reference (solid lines): maximization on all modes and all quantities  $k_{\perp}/k$  of the roots of the relation dispersion (4.36). (Semi)-analytical neutrality curves obtained for the transverse modes  $k_{\perp} = k$ : dashed lines:  $\mathcal{N}_{\text{Non-osc.}}$  and  $\mathcal{N}_{\text{Osc.}}$ ; dotted lines:  $\mathcal{N}_{\text{Non-osc.}}^0$  and  $\mathcal{N}_{\text{Osc.}}^0$ .

## 4.6. Numerical results

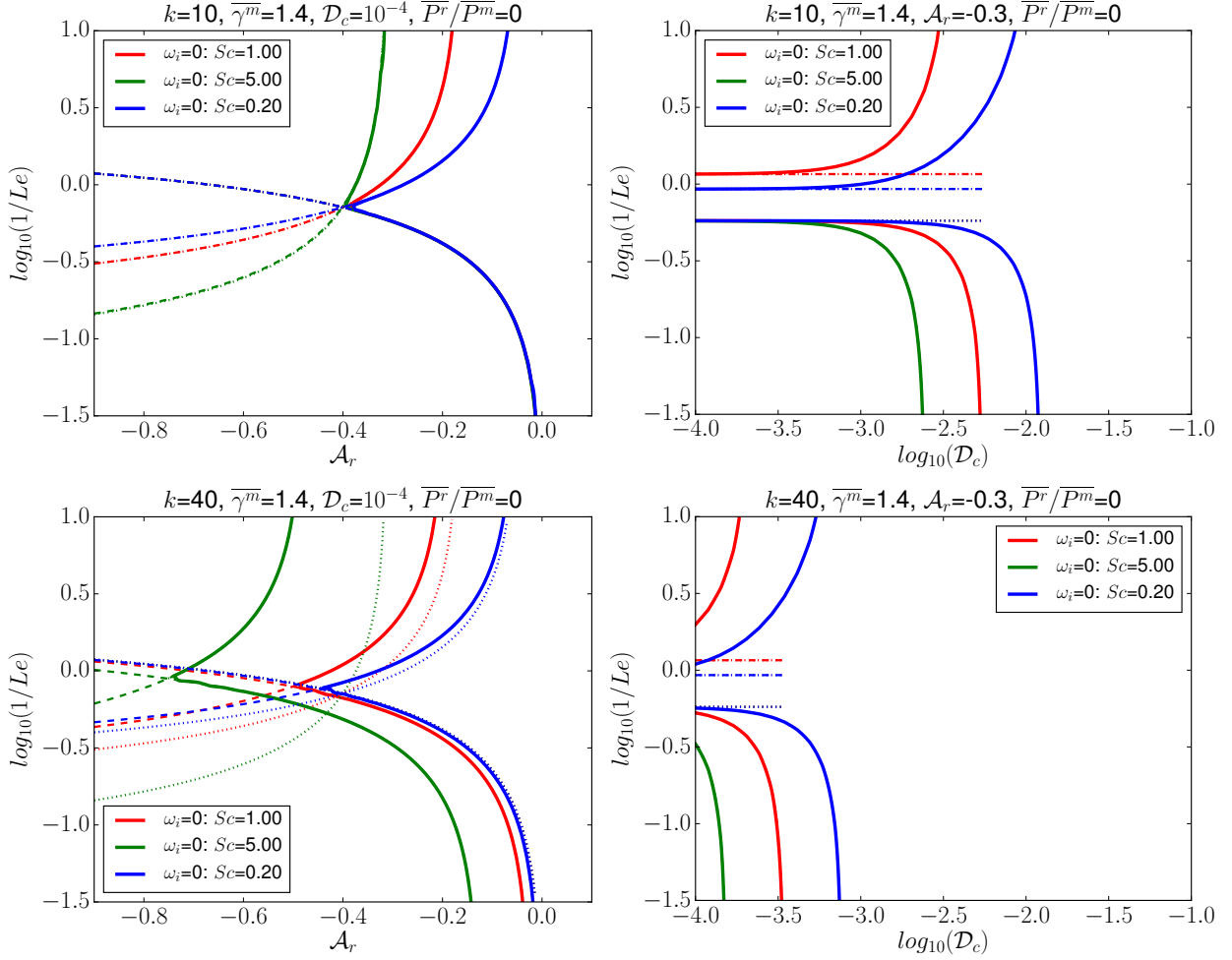


Figure 4.6 – Contours of neutrality in the planes  $(\mathcal{A}_r, \log_{10}[1/Le])$  and  $(\log_{10}[\mathcal{D}_c], \log_{10}[1/Le])$ : unstable zone on the left and stable one on the right. Numerical reference (solid lines): maximization on all modes and all quantities  $k_{\perp}/k$  of the roots of the relation dispersion (4.36). (Semi)-analytical neutrality curves obtained for the transverse modes  $k_{\perp} = k$ : dashed lines:  $\mathcal{N}_{\text{Non-osc.}}$  and  $\mathcal{N}_{\text{Osc.}}$ ; dotted lines:  $\mathcal{N}_{\text{Non-osc.}}^0$  and  $\mathcal{N}_{\text{Osc.}}^0$ .

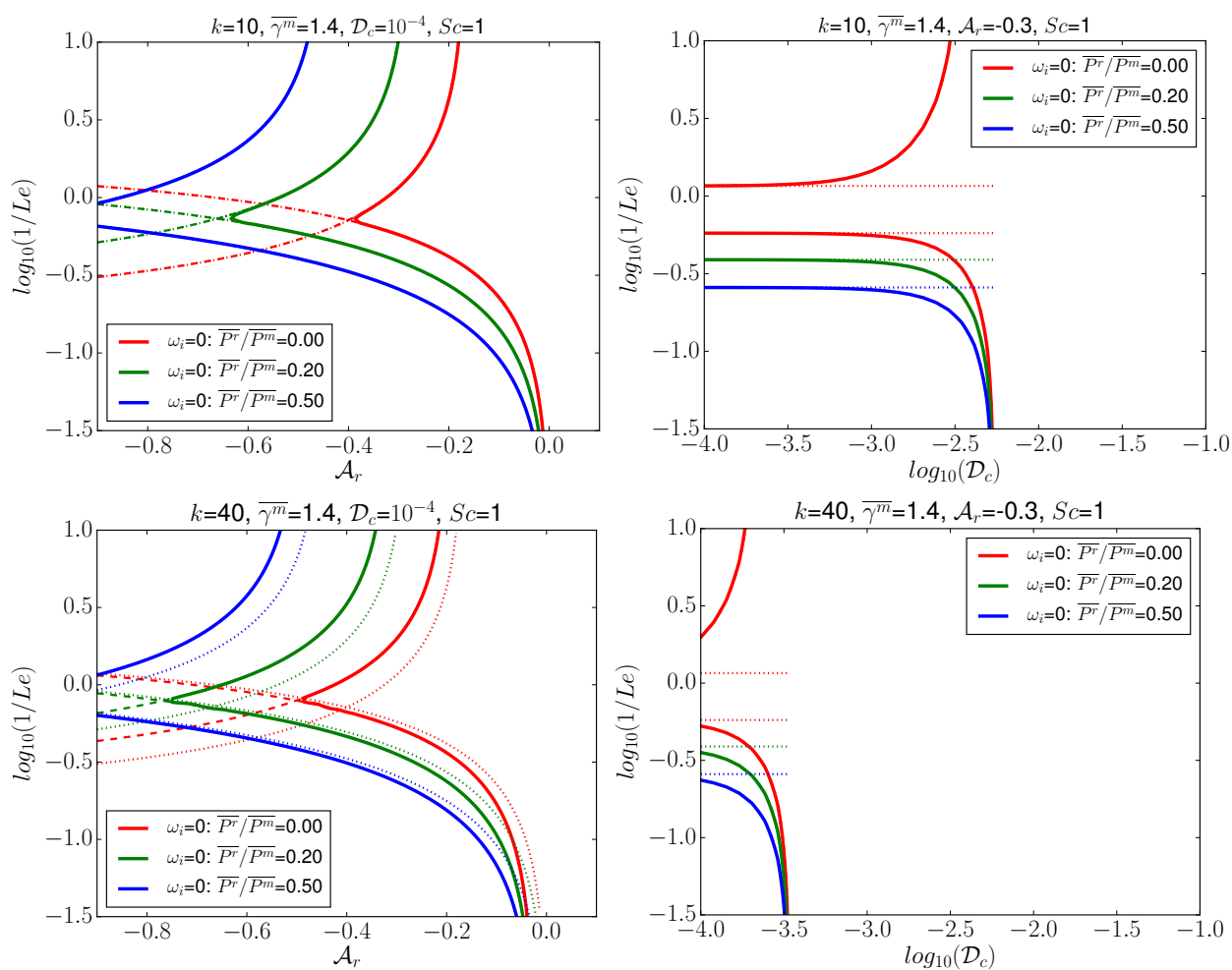


Figure 4.7 – Contours of neutrality in the planes  $(A_r, \log_{10}[1/Le])$  and  $(\log_{10}[D_c], \log_{10}[1/Le])$ : unstable zone on the left and stable one on the right. Numerical reference (solid lines): maximization on all modes and all quantities  $k_{\perp}/k$  of the roots of the relation dispersion (4.36). (Semi)-analytical neutrality curves obtained for the transverse modes  $k_{\perp} = k$ : dashed lines:  $\mathcal{N}_{\text{Non-osc.}}$  and  $\mathcal{N}_{\text{Osc.}}$ ; dotted lines:  $\mathcal{N}_{\text{Non-osc.}}^0$  and  $\mathcal{N}_{\text{Osc.}}^0$ .

## 4.6. Numerical results

### 4.6.2 Dispersion relation within the low Mach limit

In this section, the comparison between the general dispersion relation (4.36) at thermal equilibrium and the corresponding ones within the small Mach limit are considered, along with the subsequent neutrality hyper-surfaces.

Figure 4.8 deals with a plot in the complex plane of the roots of the dispersion relations (4.36), (4.66) and (4.76) when the ratio  $Le^{-1} = \mathcal{D}_c/\chi_{\text{equi}}^r$  varies. The roots of the general dispersion relation (4.36) and the one obtained within the low Mach “all Péclet” limit are respectively represented by circles and crosses with rainbow-colors encoding the value of  $Le^{-1}$ . The low Mach-low Péclet limit in Eq. (4.76) does not depend on the Lewis number, the two corresponding modes are depicted by black squares.

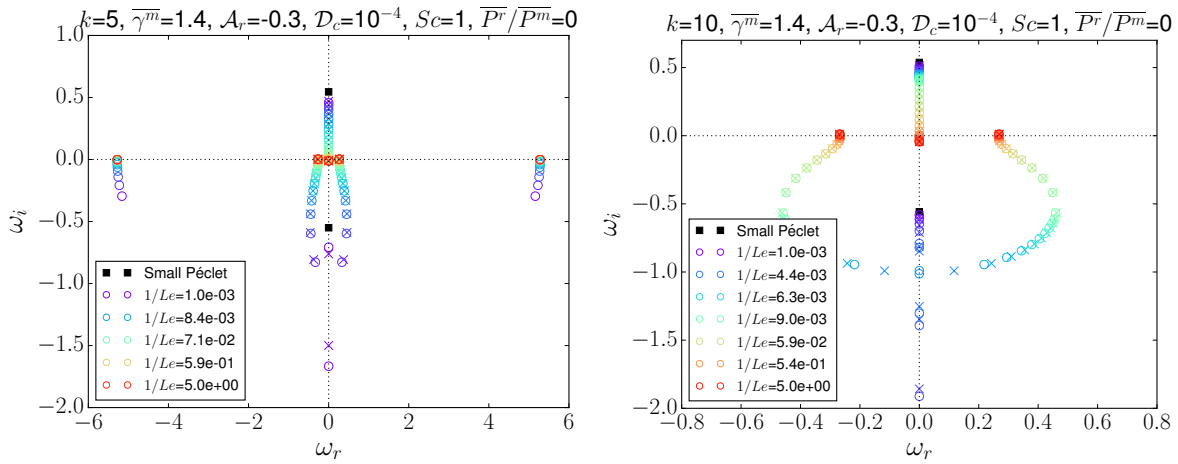


Figure 4.8 – Plot in the complex plane of the modes corresponding to the roots of the dispersion relations for the transverse modes  $k_{\perp} = k$ . Variation on  $Le^{-1} = \mathcal{D}_c/\chi_{\text{equi}}^r$ . (rainbow-colored). Circles: roots of the general relation (4.36); crosses: roots of the relation (4.66) within the low Mach (“all Péclet”) limit; blacks squares: roots of the relation (4.76) within the low Mach-low Péclet limit. Corresponds to a vertical path in Fig. 4.9-(a). Left: for  $k = 5$ , the five modes of Eq. (4.36); right : for  $k = 10$ , zoom on the three central modes of Eq. (4.36) matching the three modes of Eq. (4.66).

Figure 4.8-(a) confirms that the small Mach approximation filters out the acoustic modes of the general dispersion relation. The latter correspond to the left-most and right-most circles of the figure whereas the crosses of the small Mach approach are only present in the central zone with the three remaining modes. Figure 4.8-(b) proposes a zoom on the central zone for different parameters. It confirms that the two modes of the small Mach-small Péclet approximation match well the  $[\text{Le}^{-1} = \mathcal{D}_c/\chi_{\text{equi}}^r \rightarrow 0]$  limit of two of the three modes of the small Mach “all Péclet” approach, or of the central modes of the general relation. One remarks that the unstable solution ( $\omega_i > 0$ ) of the small Péclet regime can be continuously connected to the “non-oscillating” (“fingering”) mode described previously, whereas the stable one ( $\omega_i < 0$ ) is related to the two oscillating modes of “gravity waves” type.

Figure 4.9 plots the instability maps according to the same conventions as in Fig. 4.1 but adds neutrality curves (of transverse modes) from the low Mach “all Péclet” approach, given by Eqs. (4.72) and (4.73) and from the low Mach-low Péclet limit, given by Eq. (4.79). As already mentioned, the neutrality curves of the “non-oscillating” mode in the small Mach “all Péclet” approach are similar to the ones of the general case (exactly for  $\mathcal{N}_{\text{Non-osc.}}^{\text{SM}^0}$  and approximately for  $\mathcal{N}_{\text{Non-osc.}}^{\text{SM}}$ ) and have not been added here. As for the parameters of Fig. 4.9, the curves from the low Mach approach and the general ones are superimposed to the different levels of approximation (blue and green curves). The boundary characterized by the small Mach-small Péclet regime (dashed purple lines) defines a limit properly verified when  $(\text{Le}^{-1} = \mathcal{D}_c/\chi_{\text{equi}}^r \ll 1)$ .

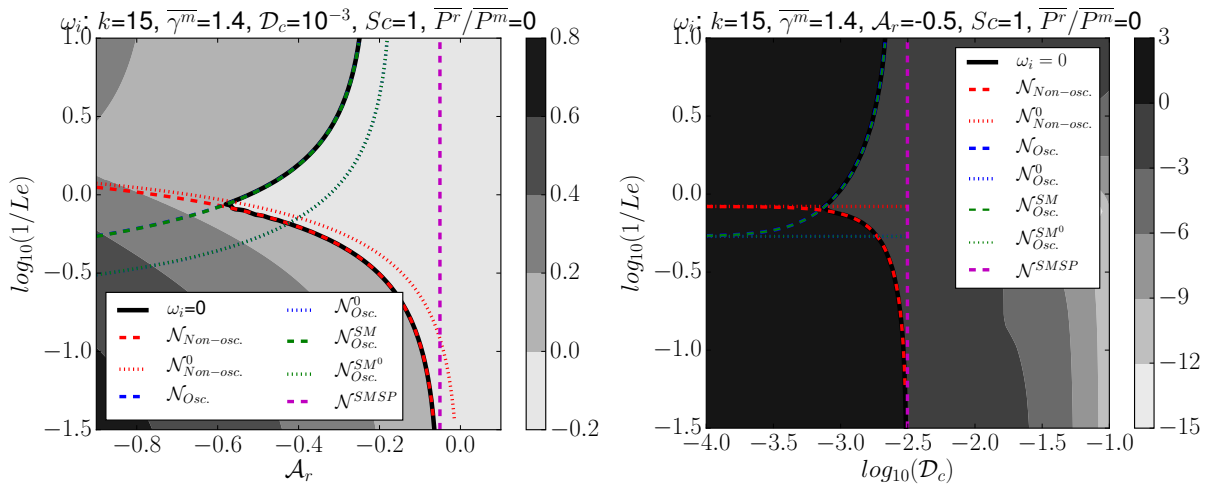


Figure 4.9 – Maps of  $\max_{\{k_{\perp}/k\}} \omega_i$  in the planes  $(A_r, \log_{10}[1/Le])$  and  $(\log_{10}[\mathcal{D}_c], \log_{10}[1/Le])$  by numerical resolution of the roots of the dispersion relation (4.36). Superposition of (semi)-analytical neutrality curves obtained for transverse modes  $k_{\perp} = k$  (“non-oscillating” mode and “oscillating”) with respect to the general relation (red and blue curves), within the small Mach “all Péclet” limit (green curves) and within the low Mach-low Péclet limit (dashed purple lines).

## 4.7 Extension to the non-isothermal case at thermal equilibrium

In this section, the isothermal hypothesis is removed in order to allow linear temperature profiles but by maintaining the simplification:

$$\partial_{zz}^2 \bar{T} = 0 \quad , \quad (4.80)$$

necessary to the existence of a stationary equilibrium solution when  $[\rho\kappa^r]$  is a pure constant. It follows that, since thermal equilibrium is assumed,  $\partial_z \bar{T}^m = \partial_z \bar{T}^r = \partial_z \bar{T}$ .

### 4.7.1 Correction to the isothermal case

The linearization of the conduction  $\mathcal{C}$  and the diffusion  $\mathcal{D}_P$  terms recalled by Eqs. (4.7) and (4.8) must be reconsidered in order to treat the non-isothermal case.

#### 4.7.1.1 Inter-species diffusion

As in Sec. 4.2.3.2, the quantity  $[\rho\mathcal{D}_c]$  is assumed to be purely constant. When this is applied to Eq. (4.6), this hypothesis allows to write:

$$\mathcal{D}_P' = (r_a - r_b) \left[ \frac{\gamma^m(\gamma_3 - 1)}{\gamma^m - 1} [\rho\mathcal{D}_c] \partial_j c \partial_j T^m + \gamma_3 T^m \partial_j ([\rho\mathcal{D}_c] \partial_j c) \right]' .$$

Note that the generalized adiabatic exponent  $\gamma_3$  may be linearized, using Tab. (A) in App. A, as:

$$\gamma_3' = \frac{4(\bar{\gamma}^m - 1)(2 - 3\bar{\gamma}^m)}{[1 + 12(\bar{\gamma}^m - 1)\bar{p}^r/\bar{p}^m]^2} \left( \frac{p^{r'}}{\bar{p}^m} - \frac{\bar{p}^r}{\bar{p}^m} \frac{p^{m'}}{\bar{p}^m} \right) \quad ,$$

but is not taken into account for the sake of simplicity and will be assumed to be negligible. Thus, using the assumption (4.11) of a linear concentration profile,

$$\mathcal{D}_P' = \mathcal{D}_c \bar{p}^m \left[ \bar{\gamma}_3 \mathcal{A}_r \partial_{jj}^2 c' + \frac{\bar{\gamma}^m(\bar{\gamma}_3 - 1)}{\bar{\gamma}^m - 1} \mathcal{A}_r \left( \partial_z \bar{c} \frac{\partial_z T^{m'}}{T^m} + \partial_z c' \frac{\partial_z \bar{T}^m}{T^m} \right) \right] \quad ,$$

hence, in the spectral space:

$$\widehat{\mathcal{D}}_P = -k^2 \mathcal{D}_c \bar{p}^m \left[ \bar{\gamma}_3 \mathcal{A}_r \widehat{c} - \frac{\bar{\gamma}^m(\bar{\gamma}_3 - 1)}{\bar{\gamma}^m - 1} \frac{i k_z}{k^2} \left( \mathcal{A}_r \partial_z \bar{c} \frac{\widehat{T}^m}{T^m} + \left[ \frac{\partial_z \bar{T}^m}{T^m} \mathcal{A}_r \widehat{c} \right] \right) \right] \quad . \quad (4.81)$$

#### 4.7.1.2 Opacity

Referring to Sec. 4.2.3.3, since only the treatment of the quantity  $[\rho\kappa^r]$  as a pure constant can give a stationary equilibrium state (except for a very particular choice of density and temperature profiles), the latter assumption is the only one retained. It implies the linearization of the conduction term  $\mathcal{C}$  to remain unchanged, such that:

$$c' = \frac{4c_l \bar{p}^r}{[\rho\kappa^r]} \frac{\partial_{jj}^2 T^{r'}}{T^r} \quad \text{and} \quad h_{\rho\kappa^r}^{\text{const.}} = 1 \quad .$$

It is worth noting that, under that assumption, the non-isothermal case at thermal equilibrium does differ from the isothermal one at thermal equilibrium only by the additional term  $\left[\frac{\partial_z \bar{T}^m}{\bar{T}^m} \mathcal{A}_r \bar{c}\right]$  appearing in Eq. (4.81).

#### 4.7.2 Dispersion relations at thermal equilibrium

A general expression for  $\widehat{\mathcal{D}}_P$  can be obtained by inserting Eq. (4.21) in Eq. (4.81), such that:

$$\widehat{\mathcal{D}}_P^{\text{Non-isoth.}} = \widehat{\mathcal{D}}_P^{\text{Isoth.}} - k^2 \mathcal{D}_c \bar{P}^m \frac{\bar{\gamma}^m (\bar{\gamma}_3 - 1)}{\bar{\gamma}^m - 1} \frac{i k_z \partial_z \bar{T}^m}{k^2 \bar{T}^m} \frac{i \mathcal{A}_r \partial_z \bar{c}}{\omega + i \mathcal{D}_c k^2} \widehat{u}_z, \quad (4.82)$$

with  $\widehat{\mathcal{D}}_P^{\text{Isoth.}}$  given by the formula (4.24). Then, by using this relation and Eq. (4.20), the formula (4.16) becomes:

$$\begin{aligned} -i\omega \widehat{P} + \widehat{u}_z \partial_z \bar{P} + \bar{\gamma}_1 \bar{P} \left[ i \frac{k_z^2}{\omega + i \nu_v k^2} \bar{\tau} \left( \widehat{P}^m + \widehat{P}^r \right) + i k_z \widehat{u}_z \right] \\ - \mathcal{D}_c k^2 \left( \bar{\gamma}_3 + \left[ \frac{\bar{\gamma}^m (\bar{\gamma}_3 - 1)}{\bar{\gamma}^m - 1} \frac{i k_z \partial_z \bar{T}^m}{k^2 \bar{T}^m} \right] \right) \bar{P}^m \frac{i \mathcal{A}_r \partial_z \bar{c}}{\omega + i \mathcal{D}_c k^2} \widehat{u}_z + \chi_P^r k^2 \left[ \widehat{P} + \bar{P}^m \left( \frac{i \mathcal{A}_r \partial_z \bar{c}}{\omega + i \mathcal{D}_c k^2} \widehat{u}_z + \frac{\widehat{\tau}}{\bar{\tau}} \right) \right] = 0. \end{aligned}$$

In order to derive the dispersion relation, one simply has to replace the term  $\bar{\gamma}_3$  by the quantity  $\left[ \bar{\gamma}_3 + \frac{\bar{\gamma}^m (\bar{\gamma}_3 - 1)}{\bar{\gamma}^m - 1} \frac{i k_z \partial_z \bar{T}^m}{k^2 \bar{T}^m} \right]$  in the determinant  $D_{\text{adr}}^{\mathcal{D}_c}$  related to inter-species diffusion. The propagation of the latter provides the following conclusions.

In the case of a compressible flow field within the ( $M_t \ll 1$ ) limit, the compressible formulae (4.35) and (4.36), as well as the low Mach ones (4.65) and (4.66) remain valid in the case of a mean uniform temperature gradient, provided that the coefficient  $(\bar{\gamma}_3/\bar{\gamma})$ , defined in Eq. (4.34) is substituted for  $(\bar{\gamma}_3/\bar{\gamma})^{\text{Non-isoth.}}$ , such that:

$$\frac{\bar{\gamma}_3}{\bar{\gamma}}^{\text{Non-isoth.}} = \frac{1}{\bar{\gamma}} \left( \bar{\gamma}_3 + \left[ \frac{\bar{\gamma}^m (\bar{\gamma}_3 - 1)}{\bar{\gamma}^m - 1} \frac{i k_z \partial_z \bar{T}^m}{k^2 \bar{T}^m} \right] \right) \quad \text{with} \quad \frac{1}{\bar{\gamma}} = \frac{\bar{P}^m}{\bar{\gamma}_1 \bar{P}}. \quad (4.83)$$

Thus, in the ( $M_t \ll 1$ ;  $Pe_t \ll 1$ ) limits, the dispersion relation (4.76) is not modified by the insertion of a temperature gradient.

Regarding the transverse modes, since the previous results have shown that  $\frac{\bar{\gamma}_3}{\bar{\gamma}}^{\text{Non-isoth.}} = \frac{\bar{\gamma}_3}{\bar{\gamma}}$  when  $k_z = 0$ , the dispersion relations for transverse modes are always identical in the isothermal case and with a uniform temperature gradient. It implies that the relations on the neutrality curves remain the same. However, let us notice that the value of  $\partial_z \bar{s}$  is modified by the addition of a non-zero temperature gradient. Moreover, the consistency of the homogeneous approach requires the wavelength of the perturbations to be small compared to the gradient length of mean quantities, that is:

$$\frac{k_z \partial_z \bar{T}}{k^2 \bar{T}} = \epsilon \ll 1.$$

Thus, if all terms of order higher than  $\mathcal{O}(\epsilon)$  are neglected, it entails that  $\frac{\bar{\gamma}_3}{\bar{\gamma}}^{\text{Non-isoth.}} = \frac{\bar{\gamma}_3}{\bar{\gamma}}$  and the temperature gradient vanishes from the dispersion relations. The isothermal relations are then also valid in non-isothermal cases.

## 4.8 Link with Boussinesq approaches (pure hydrodynamic limit)

The goal of this section is to connect our previous results with the ones obtained within the Boussinesq approximation by [Garaud \[2018\]](#) in the purely hydrodynamic regime. This regime is valid but considering only formula at thermal equilibrium and taking the ( $P^r/P^m \rightarrow 0$ ) limit (so that the different adiabatic exponents have the same value, as recalled in App. A).

The Boussinesq approximation assumes the nullity of the velocity divergence field, that is  $[\partial_j \mathbf{u}_j' = 0]$ . Thus, when it is combined with momentum equations:

$$\begin{cases} -i\omega \widehat{u}_x + ik_x \bar{\tau} (\widehat{P}^m + \widehat{P}^r) & = -\nu_v k^2 \widehat{u}_x \quad , \\ -i\omega \widehat{u}_y + ik_y \bar{\tau} (\widehat{P}^m + \widehat{P}^r) & = -\nu_v k^2 \widehat{u}_y \quad , \\ -i\omega \widehat{u}_z + ik_z \bar{\tau} (\widehat{P}^m + \widehat{P}^r) + \widehat{\tau} \partial_z \bar{P} & = -\nu_v k^2 \widehat{u}_z \quad , \\ + ik_j \widehat{u}_j & = 0 \quad , \end{cases}$$

which gives:

$$\begin{cases} \bar{\tau} (\widehat{P}^m + \widehat{P}^r) = \frac{ik_z}{k^2} \widehat{\tau} \partial_z \bar{P} \quad , \\ \frac{ik_z^2}{k^2} \bar{g}_0 \frac{\widehat{\tau}}{\bar{\tau}} = (\omega + i\nu_v k^2) \widehat{u}_z \quad . \end{cases} \quad (4.84)$$

The equation of state within the ( $M_t \ll 1$ ) limit, using the scalar equation (4.21), gives:

$$\frac{\widehat{T}}{\bar{T}} = \frac{\bar{P}^m}{\bar{P}^m + 4\bar{P}^r} \left( \frac{i\mathcal{A}_r \partial_z \bar{c}}{\omega + i\mathcal{D}_c k^2} \widehat{u}_z + \frac{\widehat{\tau}}{\bar{\tau}} \right) \quad .$$

Rather than relation (4.6) which deals with pressure evolution, the temperature equation is preferred. Then, from Eq. (2.18c) of the asymptotic analysis, one has:

$$D_t T = -(\gamma_2 - 1) T \partial_j u_j + \frac{\mathcal{C}}{\rho c_v} + \frac{\mathcal{D}_T}{\rho c_v} \quad , \quad (4.85)$$

with, for a binary mixture of perfect gases at at thermal equilibrium, the conduction and the diffusion terms, recalled from Eqs. (4.7) and (2.15), defined as:

$$\begin{cases} \mathcal{C} & = \partial_j \left( \frac{4c_\ell T^3}{\rho k^r} \partial_j T \right) \quad , \\ \mathcal{D}_T & = \rho \varepsilon + \frac{\gamma^m}{\gamma^m - 1} \rho \mathcal{D}_c (r_a - r_b) \partial_j c \partial_j T + (r_a - r_b) T \partial_j (\rho \mathcal{D}_c \partial_j c) \quad , \end{cases} \quad (4.86)$$

where the definition of  $\mathcal{C}$  is related to Eq. (4.7) and the one of  $\mathcal{D}_T$  brings very similar terms to  $\mathcal{D}_P$  in Eq. (4.8). Then, the linearization of Eq. (4.85) around the equilibrium state, which existence implies that  $[\bar{\mathcal{C}} + \bar{\mathcal{D}}_T = 0]$ , leads to:

$$\partial_t T' + \mathbf{u}'_z \partial_z \bar{T} = -(\bar{\gamma}_2 - 1) \bar{T} \partial_j \mathbf{u}'_j + \frac{\mathcal{C}'}{\rho c_v} + \frac{\mathcal{D}_T'}{\rho c_v} \quad .$$

Although the incompressibility assumption of Boussinesq has been exploited in Eq. (4.84), the ( $M_t \ll 1$ ) model is required in order to insert it into the system. We recall that:

$$\partial_j \mathbf{u}_j' = -\mathbf{u}'_z \frac{\partial_z \bar{P}}{\gamma_1 \bar{P}} + \frac{\bar{\gamma}_3 - 1}{\gamma_1 \bar{P}} c' + \frac{\mathcal{D}_P'}{\gamma_1 \bar{P}} ,$$

in which the condition  $[\partial_j \mathbf{u}_j' = 0]$  is not substituted here. Then,

$$\partial_t \mathbf{T}' + \mathbf{u}'_z \bar{T} \left( \frac{\partial_z \bar{T}}{\bar{T}} - \frac{(\bar{\gamma}_2 - 1)}{\gamma_1 \bar{P}} \partial_z \bar{P} \right) = \left( \frac{1}{\bar{P}^m + 4\bar{P}^r} - \frac{(\bar{\gamma}_2 - 1)}{\gamma_1 \bar{P}} \right) (\bar{\gamma}_3 - 1) \bar{T} c' + \frac{(\bar{\gamma}_3 - 1) \bar{T}}{\bar{P}^m + 4\bar{P}^r} \mathcal{D}_T' - \frac{(\bar{\gamma}_2 - 1) \bar{T}}{\gamma_1 \bar{P}} \mathcal{D}_P' .$$

with, by neglecting the perturbations of  $\bar{\gamma}_3$ , the perturbed diffusion terms expressed as:

$$\begin{cases} \mathcal{D}_P' = (\bar{\gamma}_3 - 1) \left[ \frac{\gamma^m}{\gamma^m - 1} \rho \mathcal{D}_c (r_a - r_b) \partial_j c \partial_j T^m \right]' + \bar{\gamma}_3 (r_a - r_b) [T^m \partial_j (\rho \mathcal{D}_c \partial_j c)]' , \\ \mathcal{D}_T' = \left[ \frac{\gamma^m}{\gamma^m - 1} \rho \mathcal{D}_c (r_a - r_b) \partial_j c \partial_j T^m \right]' + (r_a - r_b) [T^m \partial_j (\rho \mathcal{D}_c \partial_j c)]' . \end{cases}$$

Finally, in the ( $P^r/P^m \rightarrow 0$ ) limit, and by assuming that  $\{\gamma^m, \gamma, \gamma_1, \gamma_2, \gamma_3\}$  are equal, the equation of temperature evolution<sup>7</sup> becomes:

$$\partial_t \mathbf{T}' + \mathbf{u}'_z (\partial_z \bar{T} - \partial_z \bar{T}_{ad}) = \frac{1}{\bar{\gamma}} \chi_{equi}^r \partial_{jj}^2 \mathbf{T}' \quad \text{with} \quad \bar{T}_{ad} = -\frac{g_0}{c_p} ,$$

which is the linearized version of the fluctuating temperature evolution of [Garaud \[2018\]](#) where  $\frac{1}{\bar{\gamma}} \chi_{equi}^r$  matches the radiative diffusivity noted  $\kappa_T$  by the author. Then, in the pure hydrodynamic regime, we have:

$$\frac{\partial_t \mathbf{T}'}{\bar{T}} + \mathbf{u}'_z (\partial_z \bar{s} - \mathcal{A}_r \partial_z \bar{c}) = \frac{1}{\bar{\gamma}} \chi_{equi}^r \frac{\partial_{jj}^2 \mathbf{T}'}{\bar{T}} ,$$

hence,

$$-i \left( \omega + i \frac{1}{\bar{\gamma}} \chi_{equi}^r k^2 \right) \frac{\hat{\mathbf{T}}}{\bar{T}} + (\partial_z \bar{s} - \mathcal{A}_r \partial_z \bar{c}) \hat{\mathbf{u}}_z = 0 .$$

By taking the simplification within the ( $P^r/P^m \rightarrow 0$ ) limit of the relation derived from the equation of state in the ( $M_t \ll 1$ ) limit, and then the relation (4.84), one has the dispersion relation:

$$-i \left( \omega + i \frac{1}{\bar{\gamma}} \chi_{equi}^r k^2 \right) \left( \frac{i \mathcal{A}_r \partial_z \bar{c}}{\omega + i \mathcal{D}_c k^2} \hat{\mathbf{u}}_z + \frac{k^2}{ik_{\perp}^2 g_0} \left( \omega + i \nu_v k^2 \right) \hat{\mathbf{u}}_z \right) + (\partial_z \bar{s} - \mathcal{A}_r \partial_z \bar{c}) \hat{\mathbf{u}}_z = 0 ,$$

which can take the form:

$$\begin{aligned} & - \left( \omega + i \nu_v k^2 \right) \left( \omega + i \mathcal{D}_c k^2 \right) \left( \omega + i \frac{1}{\bar{\gamma}} \chi_{equi}^r k^2 \right) + \left( \omega + i \mathcal{D}_c k^2 \right) \frac{k_{\perp}^2}{k^2} g_0 \partial_z \bar{s} \\ & + i \mathcal{D}_c k^2 \left( \frac{1}{\bar{\gamma}} \text{Le} - 1 \right) \frac{k_{\perp}^2}{k^2} g_0 \mathcal{A}_r \partial_z \bar{c} = 0 . \end{aligned} \quad (4.87)$$

This relation is identical to the one of [Garaud \[2018\]](#). Besides, the dispersion relation (4.87) according to Boussinesq approximation matches the limit (4.74) of high wave numbers of the relation (4.66), obtained within the low Mach approach.

<sup>7</sup>Notice that, in the hydrodynamic regime, the quantity:

$$\frac{(\bar{\gamma}_3 - 1) \bar{T}}{\bar{P}^m + 4\bar{P}^r} \mathcal{D}_T' - \frac{(\bar{\gamma}_2 - 1) \bar{T}}{\gamma_1 \bar{P}} \mathcal{D}_P' = \frac{\bar{\gamma}^m}{\gamma^m - 1} \bar{\tau} [\rho \mathcal{D}_c] \mathcal{A}_r \bar{P}^m \left( \partial_z \bar{c} \frac{\partial_z T^m}{\bar{T}^m} + \partial_z c' \frac{\partial_z \bar{T}^m}{\bar{T}^m} \right) ,$$

is ignored in the Boussinesq approximation for unclear reasons.

## 4.9. Implications for the turbulent RSM model

---

It is worth noting that the effects of finite wave numbers does vanish from Eq. (4.87) only because the contributions  $\mathcal{D}_T'$  of the equations of  $T'$  and  $\mathcal{D}_P'$  of the small Mach fluctuating velocity divergence model have been discarded without any prior justification.

The Boussinesq approximation introduces two coefficients  $\alpha_T$  and  $\beta_c$ , related to:

$$\frac{\tau'}{\bar{\tau}} - \alpha_T T' + \beta_c c' = 0 \quad ,$$

that the equation of state allows to identify in the low Mach regime as:

$$\begin{cases} \alpha_T &= \frac{1}{T} \quad , \\ \beta_c &= -\mathcal{A}_r \quad . \end{cases}$$

Hence, the development of the main parameter is  $R_0$ , defined as:

$$R_0 = \frac{\alpha_T |\partial_z \bar{T} - \partial_z \bar{T}_{ad}|}{\beta_c |\partial_z \bar{c}|} = \frac{|\partial_z \bar{s} - \mathcal{A}_r \partial_z \bar{c}|}{-\mathcal{A}_r |\partial_z \bar{c}|} \quad .$$

According to the notations of [Garaud \[2018\]](#), the Prandtl number  $Pr$  and an equivalent of the inverse of the Lewis number  $Le$ , denoted  $\tau_{diff}$  are characterized by:

$$Pr = \bar{\gamma} \frac{\nu_v}{\chi_{equi}^r} \quad \text{and} \quad \tau_{diff} = \bar{\gamma} \frac{\mathcal{D}_c}{\chi_{equi}^r} \quad .$$

Thus, by using the fact that  $\left(\frac{\bar{\gamma}_3}{\bar{\gamma}} \rightarrow 1\right)$ , the stability limits defined in Eqs. (4.70) and (4.73) can be written as:

$$\begin{cases} \mathcal{N}_{Non-osc.}^{SM^0} &: \frac{\partial_z \bar{s} - \mathcal{A}_r \partial_z \bar{c}}{-\mathcal{A}_r \partial_z \bar{c}} = \tau_{diff}^{-1} \quad , \\ \mathcal{N}_{Osc.}^{SM^0} &: \frac{\partial_z \bar{s} - \mathcal{A}_r \partial_z \bar{c}}{-\mathcal{A}_r \partial_z \bar{c}} = \frac{Pr + \tau_{diff}}{Pr + 1} \quad , \end{cases}$$

which agree with the stability limits given in [Garaud \[2018\]](#) and confirm the identification of the previously described modes, such as the “non-oscillating” mode, related to the “fingering convection” (or thermohaline convection), as well as the “oscillating” modes, characterizing the “oscillatory double-diffusive convection” (or semi-convection).

## 4.9 Implications for the turbulent RSM model

Having obtained analytical criteria defining the marginal stability of radiative Rayleigh-Taylor configurations with respect to the efficiency of the radiative transport, we now try to use it in order to improve the blending of the RSM between the small and large Péclet regimes.

Since the previous results pertain to laminar flows with molecular visco-diffusive processes, they do not apply to the turbulent situations modelled by the RSM. However, an analogy can be drawn between the turbulent viscosity and diffusivity and their molecular counterparts.

### 4.9.1 Analogy with the radiative turbulent RSM model

The analogy is established by connecting the radiative visco-diffusive Sys. (4.1) with Sys. (3.1) governing the mean quantities of the RSM turbulent model, as introduced in chapter 3. To do so, flows under consideration are restricted to binary mixtures under isothermal conditions. Thermal equilibrium is assumed so that the coupling terms  $[\pm c_\ell \rho \kappa^r (a_R T^{m_4} - E^r)]$  of Eqs. (4.1c) and (4.1d) vanish. Then, by assuming that both gases share the same adiabatic exponent  $\gamma_a = \gamma_b = \gamma^m$  and using the relations of Sys. (C.2), one can simplify the diffusion of material energy  $[\partial_l (\bar{\rho} C_e \mathcal{D}_{lj} \partial_j \widetilde{e^m})]$  of Eq. (3.1c) within the quasi-isothermal limit by considering:

$$\partial_l \widetilde{e^m} = \partial_l \left( \widetilde{c_v^m T} \right) \approx \bar{T} \frac{c_{pa}^m - c_{pb}^m}{\gamma^m} \partial_l \widetilde{c} \quad .$$

Hence, the expression of the flux  $\mathcal{Q}_c$  from Eq. (4.2) takes the form:

$$\mathcal{Q}_c = \partial_j [(h_a - h_b) \mathcal{F}_{cj}] \approx \partial_j \left( \bar{\rho} \gamma^m \mathcal{D}_c \partial_j \widetilde{e^m} \right) \quad , \quad (4.88)$$

which clarifies the link between the enthalpic material flux from the Navier-Stokes system and the turbulent one.

Due to the assumption of quasi-homogeneity, the turbulent quantities are uniform in space. Thus, their gradient may not be considered in the analogy. Hence, the terms  $[\overline{P^m} \partial_l \overline{u_l''}]$  and  $[\overline{P^r} \partial_l \overline{u_l''}]$  from respectively Eqs. (3.1c) and (3.1d) disappear. Moreover, the quasi-isothermal limit implies the homogeneity of the radiative energy  $\overline{E^r}$ , which also removes the term  $[\partial_l (\overline{E^r} \overline{u_l''})]$  from the study. The analogies between the visco-diffusive coefficients of the hydro-radiative compressible governing equations (4.1) and of the radiative turbulent RSM system (3.1) are then:

$$\left\{ \begin{array}{ll} -\Pi_{il} \leftrightarrow \bar{\rho} \widetilde{R}_{il} & \text{from Eqs. (4.1b) and (3.1b)} \quad , \quad (4.89a) \\ \mathcal{D}_c \delta_{lj} \leftrightarrow C_c \mathcal{D}_{lj} = C_c \frac{\widetilde{k}}{\widetilde{\varepsilon}} \widetilde{R}_{lj} & \text{from Eqs. (4.1e) and (3.1e)} \quad , \quad (4.89b) \\ \gamma^m \mathcal{D}_c \delta_{lj} \leftrightarrow C_e \mathcal{D}_{lj} = C_e \frac{\widetilde{k}}{\widetilde{\varepsilon}} \widetilde{R}_{lj} & \text{from Eqs. (4.1c) and (3.1c)} \quad , \quad (4.89c) \\ -\Pi_{ij} \partial_j u_i \leftrightarrow \bar{\rho} \widetilde{\varepsilon} & \text{from Eqs. (4.1c) and (3.1c)} \quad , \quad (4.89d) \end{array} \right.$$

from which relations (4.89b) and (4.89c) are maintained consistent by imposing the condition:

$$C_e = \gamma^m C_c \quad .$$

The tensorial nature of the turbulent diffusivity has to be eliminated so that it can be compared to the isotropic molecular diffusion. In this way, the analogy:

$$\mathcal{D}_c \leftrightarrow \frac{2C_c}{3} \frac{\widetilde{k}^2}{\widetilde{\varepsilon}} \quad , \quad (4.90)$$

is proposed where the isotropic part of the Reynolds tensor is retained.

## 4.9. Implications for the turbulent RSM model

---

The Péclet number is the ratio of the turbulent diffusivity to the radiative diffusivity estimated in Eq. (4.14), *i.e.*:

$$\text{Pe}_t \equiv \bar{\gamma} \frac{\nu_t}{\chi^r} \quad \text{with} \quad \chi^r = \frac{\lambda^r}{\rho c_v} \quad , \quad (4.91)$$

Following the phenomenological definition of the Péclet number of Eq. (2.73), the turbulent diffusivity of RANS models is roughly estimated as  $\nu_t = \frac{C_\mu \tilde{k}^2}{\varepsilon}$  with  $C_\mu = 0.1$ . However, when dealing with the actual implementation of the turbulent diffusion of the RSM, the effective turbulent diffusivity of given computation is  $\nu_t = \frac{2C_c \tilde{k}^2}{3\varepsilon}$  where the modelling coefficient  $C_c$  may vary because of a calibration.

The analogous of the molecular diffusivity  $D_c$  is its turbulent counterpart  $\nu_t$  implying the following analogy between the Lewis and the Péclet number:

$$\text{Le}^{-1} \equiv \frac{D_c}{\chi^r} \leftrightarrow \frac{1}{\bar{\gamma}} \text{Pe}_t \equiv \frac{\nu_t}{\chi^r} \quad , \quad (4.92)$$

At last, the relation (4.89a), tends to impose a unit Schmidt number:

$$\text{Sc} = \frac{\nu_v}{D_c} \sim 1 \quad ,$$

for the following LSA to be relevant, with  $\nu_v$  the kinetic viscosity as expressed latter in Sec. 4.2.3.1.

### 4.9.2 Improvement of the model blending

In this last section, we decide to focus on the blending (see Eq. (3.11)) of the adapted RSM turbulent model derived in the previous chapter 3. Its form is recalled as:

$$\mathbf{G} = \omega_{\text{Pe}_t} \mathbf{G}|_{\text{Pe}_t \ll 1} + (1 - \omega_{\text{Pe}_t}) \mathbf{G}|_{\text{Pe}_t \gg 1} \quad \text{with} \quad \omega_{\text{Pe}_t} = \frac{\text{Pe}_t^{\text{lim}}}{\text{Pe}_t^{\text{lim}} + \text{Pe}_t} \quad ,$$

where the weighting function  $\omega_{\text{Pe}_t}$  has been introduced in order to bridge the range between Péclet asymptotic limits. Up to here, the parameter  $\text{Pe}_t^{\text{lim}}$  has been chosen by a fit on three numerical simulations. A more general choice based on physical considerations is now proposed from the LSA. In particular, the dispersion relation (4.42) corresponding to the “non-oscillating” mode related to “fingering convection” [Garaud, 2018] is taken as reference for this purpose because it expresses a key process in the effect of the radiative diffusivity on the stability of the turbulent configuration of chapter 2.

#### 4.9.2.1 Marginal “fingering” stability and its implication on Rayleigh-Taylor production

The stability criterion regarding a radiative RT configuration is first derived from the adapted turbulent model system (3.17). Considering an hydrostatic equilibrium in statistically homogeneous flow, the turbulent evolution equations that only include relevant production terms are:

$$\begin{cases} \widetilde{D}_t \widetilde{R}_{II} = -2 \left(1 - \frac{2}{3} \gamma^H\right) \frac{\partial_1 \bar{P}}{\bar{\rho}} \frac{\widetilde{\tau'' u_1''}}{\widetilde{\tau}} , & (4.93a) \\ \widetilde{D}_t \frac{\widetilde{\tau'' u_1''}}{\widetilde{\tau}} = - \left(1 - \gamma^H\right) \frac{\partial_1 \bar{P}}{\bar{\rho}} \frac{\widetilde{\tau'' \tau''}}{\widetilde{\tau}^2} + \left(\theta_1^{Pe_t} - \frac{\partial_1 \widetilde{\tau}}{\widetilde{\tau}}\right) \widetilde{R}_{II} , & (4.93b) \\ \widetilde{D}_t \frac{\widetilde{\tau'' \tau''}}{\widetilde{\tau}^2} = 2 \left(\theta_1^{Pe_t} - \frac{\partial_1 \widetilde{\tau}}{\widetilde{\tau}}\right) \frac{\widetilde{\tau'' u_1''}}{\widetilde{\tau}} , & (4.93c) \end{cases}$$

where ( $\gamma^H = 0.3$ ) from Tab. A and the transition parameter  $\theta_1^{Pe_t}$  given by (3.12) is:

$$\theta_1^{Pe_t} - \frac{\partial_1 \widetilde{\tau}}{\widetilde{\tau}} = - \left( \omega_{Pe_t} \frac{\partial_1 \widetilde{r}}{\widetilde{r}} + (1 - \omega_{Pe_t}) \left( \frac{\partial_1 \widetilde{\tau}}{\widetilde{\tau}} + \frac{\partial_1 \bar{P}}{\gamma_1 \bar{P}} \right) \right) .$$

The base flow is assumed to be in quasi-equilibrium, hence independent of time, so that:

$$\partial_{tt}^2 \frac{\widetilde{\tau'' u_1''}}{\widetilde{\tau}} = - \left(1 - \gamma^H\right) \frac{\partial_1 \bar{P}}{\bar{\rho}} \partial_t \frac{\widetilde{\tau'' \tau''}}{\widetilde{\tau}^2} + \left(\theta_1^{Pe_t} - \frac{\partial_1 \widetilde{\tau}}{\widetilde{\tau}}\right) \partial_t \widetilde{R}_{II} \quad (4.94)$$

since  $\widetilde{u}_j = 0$  due to hydrostatic equilibrium. Using Eqs. (4.93a) and (4.93c), the relation (4.94) becomes:

$$\partial_{tt}^2 \frac{\widetilde{\tau'' u_1''}}{\widetilde{\tau}} + 2 \left(2 - \frac{5\gamma^H}{3}\right) \left(\theta_1^{Pe_t} - \frac{\partial_1 \widetilde{\tau}}{\widetilde{\tau}}\right) \frac{\partial_1 \bar{P}}{\bar{\rho}} \frac{\widetilde{\tau'' u_1''}}{\widetilde{\tau}} = 0 . \quad (4.95)$$

Since  $(2 - 5\gamma^H/3) > 0$ , the stability is determined by the sign of:

$$\mathfrak{C}_{RT} = \left(\theta_1^{Pe_t} - \frac{\partial_1 \widetilde{\tau}}{\widetilde{\tau}}\right) \frac{\partial_1 \bar{P}}{\bar{\rho}} , \quad (4.96)$$

where the radiative RT is stable if  $\mathfrak{C}_{RT} \geq 0$  ("oscillating" solution) and unstable if  $\mathfrak{C}_{RT} < 0$  (solution with an exponentially increasing component).

Three limiting cases can be made explicit, including the incompressible one (within which the fluctuating velocity divergence tends to nought so that  $\partial_1 u_1' = 0$ , implying  $\theta_1^{Pe_t} = 0$ ). Hence, referring to Sys. (3.13), the system is stable provided that:

$$\mathfrak{C}_{RT} = \begin{cases} \partial_{1s} \frac{\partial_1 \bar{P}}{\bar{\rho}} < 0 \text{ for } (Pe_t \gg 1) , & (4.97a) \\ \frac{\partial_1 \widetilde{r}}{\widetilde{r}} \frac{\partial_1 \bar{P}}{\bar{\rho}} < 0 \text{ for } (Pe_t \ll 1) , & (4.97b) \\ \frac{\partial_1 \widetilde{\tau}}{\widetilde{\tau}} \frac{\partial_1 \bar{P}}{\bar{\rho}} < 0 \text{ for an incompressible flow} . & (4.97c) \end{cases}$$

One last remark concerns Eq. (4.97b). In the presence of a monofluid, its molar mass is uniform, and hence its specific gas constant verifies  $\partial_1 \widetilde{r} = 0$ . Thus, the RTI vanishes in the ( $Pe_t \ll 1$ ) limit.

## 4.9. Implications for the turbulent RSM model

The marginal stability of the GSG model is reached when (4.96) is equal to zero. By analogy with LSA results, we recast it as an equivalent neutrality hypersurface of the form:

### Main result: neutrality hyper-surface of the GSG model

$$\mathcal{N}_{\text{GSG}} : \quad g_0 \omega_{\text{Pe}_t} \frac{\partial_1 \bar{r}}{\bar{r}} + g_0 (1 - \omega_{\text{Pe}_t}) \partial_1 \bar{s} = 0 \quad (4.98)$$

### 4.9.2.2 Blending models from LSA

The LSA has shown that, for from small to moderate Péclet regimes, the stability of the flow field is dominated by non-oscillating modes related to the “fingering” instability [Garaud, 2018]. In the large wave numbers limit, such stability is given by relation (4.42), recalled as:

$$\mathcal{N}_{\text{Non-osc.}}^0 : \quad g_0 \mathcal{A}_r \partial_z \bar{c} \frac{1}{\bar{\gamma}} (\text{Le} - \bar{\gamma}_3) + g_0 \partial_z \bar{s} = 0 \quad \text{with} \quad \text{Le} \equiv \frac{\chi^r}{\mathcal{D}_c} \quad \text{and} \quad \mathcal{A}_r = \frac{r_a - r_b}{\bar{r}} \quad .$$

which can be rewritten

$$\mathcal{N}_{\text{Non-osc.}}^0 : \quad g_0 \left( 1 - \bar{\gamma}_3 \text{Le}^{-1} \right) \frac{\partial_z \bar{r}}{\bar{r}} + g_0 \bar{\gamma} \text{Le}^{-1} \partial_z \bar{s} = 0 \quad ,$$

which can be interpreted as a convex combination between molar mass and pseudo-entropy gradients driving the stability in asymptotic limits, provided that:

### Condition: GSG blending model “a” (first proposition)

$$0 \leq \frac{\bar{\gamma}_3}{\text{Le}} \leq 1 \quad .$$

Notice that this condition seems natural in view of the maps of Fig. 4.1, also displayed in Fig. 4.10. Indeed, since the flow is stable with respect to the “fingering” modes within the high Péclet regime, there is no marginal curve to match for the model in that region.

Then, referring to the analogy (4.92) that assumes  $\text{Le}^{-1} \equiv \mathcal{D}_c / \chi^r \leftrightarrow \text{Pe}_t / \bar{\gamma} \equiv \nu_t / \chi^r$ , the comparison between  $\mathcal{N}_{\text{Non-osc.}}^0$  and  $\mathcal{N}_{\text{GSG}}$  suggests to pose:

### Main result: weighting function of the blending model “a” (first proposition)

$$\omega_{\text{Pe}_t}^a \equiv \max \left( \frac{1 - (\bar{\gamma}_3 / \bar{\gamma}) \text{Pe}_t}{1 + (1 - (\bar{\gamma}_3 / \bar{\gamma})) \text{Pe}_t}, 0 \right) \quad , \quad (4.99)$$

In other words, it consists in introducing a weighting over the range  $\text{Pe}_t \in [0, \bar{\gamma} / \bar{\gamma}_3 [$  but reverts to the  $(\text{Pe}_t \gg 1)$  model as soon as  $(\text{Pe}_t > \bar{\gamma} / \bar{\gamma}_3)$ .

Figure 4.10 plots different neutral curves related to the model in the linear stability map of Fig. 4.1. The marginal stability of the high Péclet model and small Péclet limits of the model, respectively given by  $\partial_z \bar{s} = 0$  and  $\frac{\partial \bar{r}}{\bar{r}} = 0$ , stand as vertical lines in the map. As for the neutrality hyper-surface of the blending denoted  $\mathcal{N}_{GSG}^a$ , it lies on  $\mathcal{N}_{Non-osc.}^0$  for  $(Pe_t < \bar{\gamma}/\bar{\gamma}_3)$  and jumps on the high Péclet curve for  $(Pe_t > \bar{\gamma}/\bar{\gamma}_3)$ .

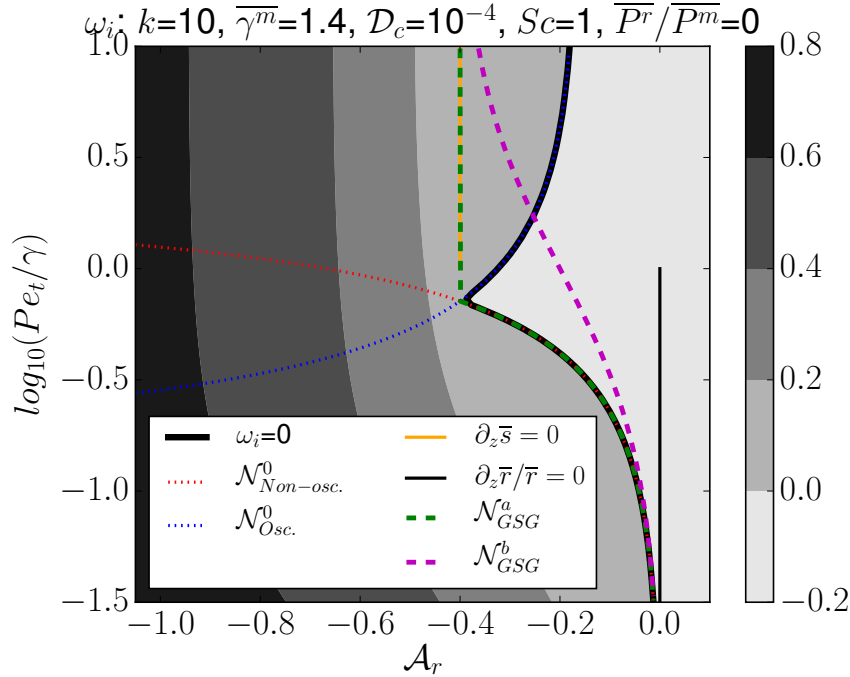


Figure 4.10 – Stability map with the same legends as Fig. 4.1. The neutrality hypersurfaces of the GSG model are added : vertical lines for the asymptotic formulations of the model valid for  $(Pe_t \gg 1)$  or  $(Pe_t \ll 1)$  together with curves  $\mathcal{N}_{GSG}^a$  and  $\mathcal{N}_{GSG}^b$  for the blended GSG model related respectively to the weighting functions (4.99) and (4.100).

The three simulations HP, SP<sub>1</sub> and SP<sub>2</sub> of Sec. 3.3.2 are run using this blending. The turbulent quantities showed in Figs. 3.1, 3.2 and 3.3, respectively the turbulent kinetic energy, normalized specific volume variance and turbulent mixing width, resulting from the 1D-RSM simulations, are represented in Fig. 4.11 as well. For the sake of clarity, the additional latin letter “(a)” to the legends HP, SP<sub>1</sub> and SP<sub>2</sub> refers to the cases including the blending model “a”.

The results of the blending based on the stability criterion shown with black curves are not so good as the ones precisely fitted to these DNS. The case with intermediate Péclet values especially seems to revert too quickly to a large Péclet behaviour. Since the abrupt change of the blending at  $(Pe_t = \bar{\gamma}/\bar{\gamma}_3)$  might explain this behaviour, we turn to a more continuous and less restrictive use of the stability criterion.

#### 4.9. Implications for the turbulent RSM model

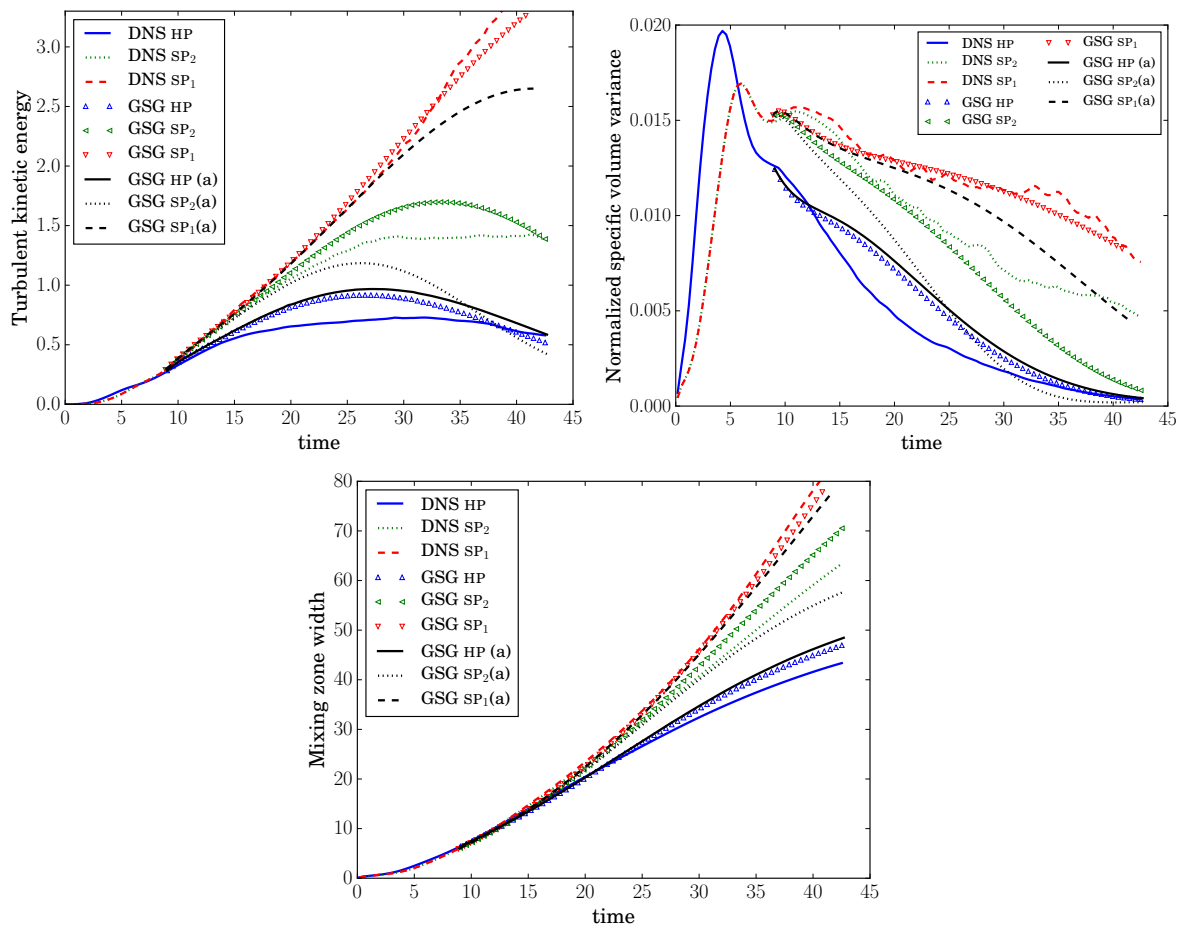


Figure 4.11 – Same legends as in Figs. 3.1, 3.2 and 3.3, *i.e.* time evolutions of the turbulent kinetic energy, the normalized specific volume variance and the turbulent mixing zone width. Comparison between the 1D-RANS simulations run with the calibrated blending model and the corrected one denoted “a”.

Instead of trying to impose the weight from the stability criterion everywhere, it can be written as a convex combination of both limits. We now keep the arbitrary functional form:

$$\omega_{\text{Pe}_t} = \frac{\text{Pe}_t^{\text{lim}}}{\text{Pe}_t^{\text{lim}} + \text{Pe}_t} ,$$

and only impose  $\text{Pe}_t^{\text{lim}}$  so that it matches the stability curve in the small Péclet limit. Since:

$$\omega_{\text{Pe}_t} \xrightarrow{\text{Pe}_t \rightarrow 0} 1 - \frac{\text{Pe}_t}{\text{Pe}_t^{\text{lim}}} ,$$

whereas,

$$\omega_{\text{Pe}_t}^a \xrightarrow{\text{Pe}_t \rightarrow 0} 1 - \text{Pe}_t ,$$

the choice  $\text{Pe}_t^{\text{lim}} = 1$  ensues, leading to:

**Main result: weighting function of the blending model “b” (second proposition)**

$$\omega_{\text{Pe}_t}^b \equiv \frac{1}{1 + \text{Pe}_t} , \tag{4.100}$$

which is displayed in Fig. 4.10 together with  $\omega_{\text{Pe}_t}^a$ . The corresponding neutrality hyper-surface  $\mathcal{N}_{\text{GSG}}^b$  smoothly joins the ( $\text{Pe}_t \ll 1$ ) and ( $\text{Pe}_t \gg 1$ ) limits.

The same figures 4.12 as previously are shown hereafter with the latin letter “(b)” following the legends HP, SP<sub>1</sub> and SP<sub>2</sub> referring to the Péclet simulations run with the blending model “b”. A quite satisfactory agreement is obtained since the results are close to the ones precisely fit to these numerical simulations. The physically motivated choice of the blending is therefore an interesting improvement provided by the linear stability analysis.

#### 4.9. Implications for the turbulent RSM model

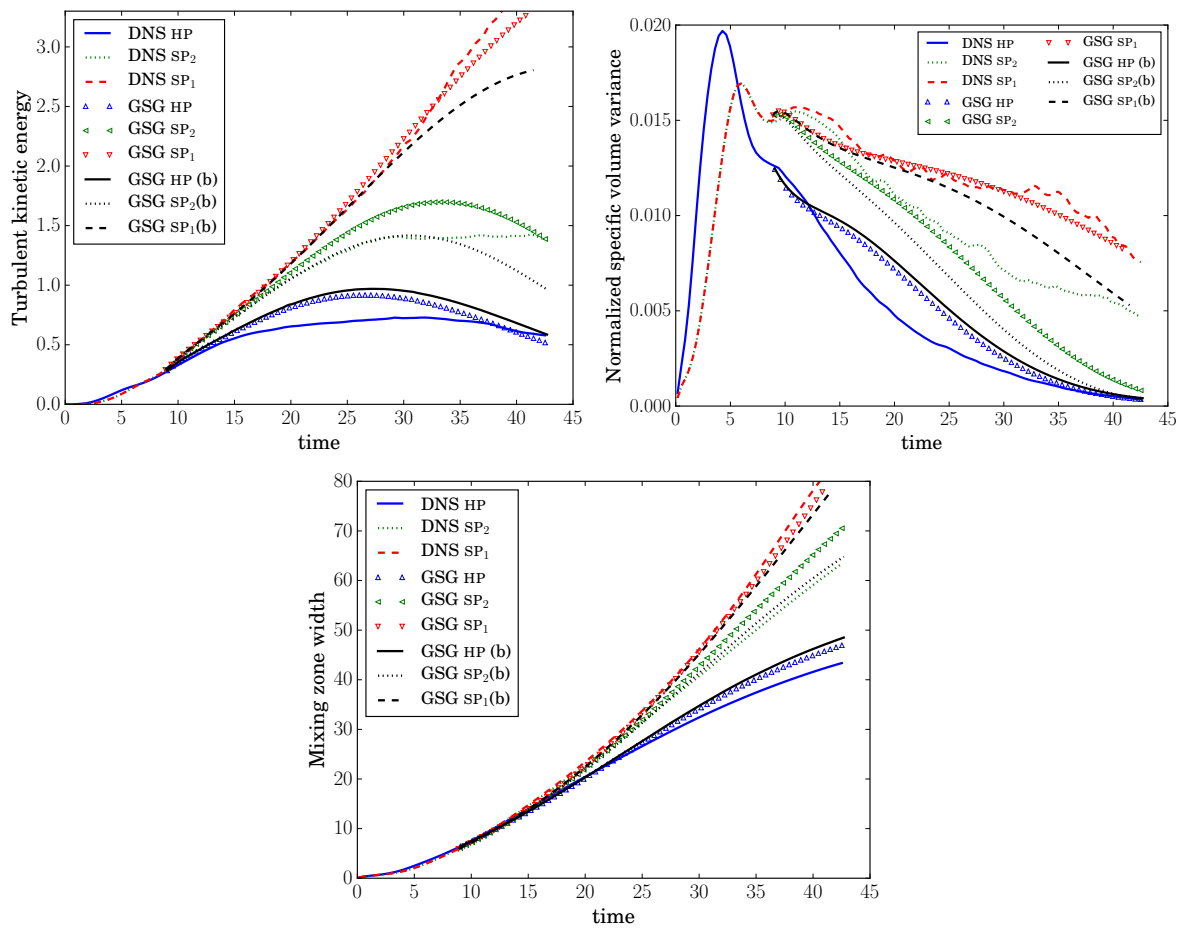


Figure 4.12 – Same legends as in Figs. 3.1, 3.2 and 3.3, *i.e.* time evolutions of the turbulent kinetic energy, the normalized specific volume variance and the turbulent mixing zone width. Comparison between the 1D-RANS simulations run with the calibrated blending model and the corrected one denoted “b”.

## 4.10 Conclusion

A linear analysis of the stability of a radiative Rayleigh-Taylor configuration has been performed in this part. Its application regards the set of compressible Navier-Stokes equations which includes notably visco-diffusive coefficients such as the kinematic viscosity  $\nu_v$ , the scalar diffusion  $\mathcal{D}_c$  and the radiative diffusivity  $\lambda^r$ . In order to make the calculation tractable, a quasi-homogeneous approach has been used assuming perturbations of small wavelength with respect to the gradient lengths of the equilibrium basic flow. The main results are the derivation of dispersion relations at the different levels of description: compressible (thermal equilibrium or not) small Mach ( $M_t \ll 1$ ), and small Mach-small Péclet ( $M_t \ll 1 ; Pe_t \ll 1$ ).

The compressible dispersion relation at thermal equilibrium involves five modes: a pair of acoustic modes, an “oscillating” pair and a “non-oscillating” mode. While the two first ones are confirmed to be filtered out in the ( $M_t \ll 1$ ) limit, the others react in an opposite way to the changes of the Lewis number  $Le$  or equivalently, of the turbulent Péclet number  $Pe_t$  in the RSM system. Referring to the terminology of [Garaud \[2018\]](#), the pair of “oscillating” modes can be directly related to the “oscillatory double-diffusive convection”, or semi-convection in the astrophysical context. Conversely, the “non-oscillating” mode refers to the “fingering convection” (or thermohaline convection). Parametric variations have been shown to illustrate the dependance of the radiative RTI to radiation intensity, viscosity, compressibility and wave number. Minor changes occur between situations with or without the assumption of thermal equilibrium between matter and radiation fields.

Finally, the stability criteria of the fingering instability in the limit of large wave numbers has been used in order to improve the blending model, bridging the gap between both Péclet asymptotic limits of the GSG RSM. While the observations of the turbulent quantities stemming from the simulations HP, SP<sub>1</sub> and SP<sub>2</sub> (run with corrected blendings) may not show outstanding improvements, correct trends obtained from the physically sounded derivation of the new blending are satisfactory.

## 4.10. Conclusion

---

# Conclusion

The main innovation of this work is the small Mach-small Péclet approximation, around which the developments of each following chapter articulates. This asymptotic analysis deals with general flow fields involving mixing and strong radiative effects.

The first chapter of this work confirmed the presence of two particular types of turbulent mixing zones, *i.e.* standard and double-diffusive thermohaline convection, arising during the main-sequence and the giant-branch evolutions of low, intermediate-mass and massive stars. For this purpose, a  $1 M_{\odot}$ , a  $5 M_{\odot}$  and a  $75 M_{\odot}$  stars have been simulated until the end of the giant phase with a 1D astrophysical code: **MESA**. The mixing regions of interest stem from the onset of large scaled convective motions applied to strongly stratified and optically thick media. They share the properties of being submitted to chemical mixing as well as to intense radiation. The latter dominates any other heat transport processes or viscous effects due to its enhanced interaction with the material field and is then treated in the diffusion limit. Thus, the computation of Prandtl [1925]’s mixing length models applied to convection zones has shown that turbulence in stars evolves generally under the limits of  $(\text{Re}_t \geq 1)$ ,  $(\text{Pr} \ll 1)$  and  $(\text{M}_t \leq 1)$ , where the smallness of the Mach number affords to filter out sound waves in the context of turbulence modelling. Some other relevant properties have been added, which are, on the one hand, that the turbulent length scale could be decoupled from the mean pressure and temperature gradient ones, *i.e.*  $(\text{Ka}_P \ll 1)$  and  $(\text{Ka}_T \ll 1)$ , and, on the other hand, that turbulence production by these same gradients may be of the same order as its dissipation:  $(\text{Fr}_a \sim 1)$  and  $(\text{Fr}_s \sim 1)$ . In particular, stellar flows in the deep interiors of stars are characterized by a state of local thermodynamic equilibrium where radiative and matter temperatures are assumed equal and where ionization is considered to be usually complete. The turbulent velocity results in being much smaller than the speed of sound:  $(\text{M}_t \ll 1)$ . This is precisely in these regions next to the core that thermohaline (or fingering) convection occurs, in response to a destabilizing composition gradient. The key parameter which differentiates it from standard convection is nothing else than the Péclet number  $\text{Pe}_t$ , which follows:

$$\begin{cases} \text{Pe}_t \gg 1 & \text{in convective zones} \quad , \\ \text{Pe}_t \ll 1 & \text{in thermohaline zones} \quad . \end{cases}$$

Hence, contrary to convection, fingering double-diffusion is characterized by a radiative diffusivity that overwhelms turbulence in terms of energy transport. Prandtl [1925]’s phenomenological models do not allow the capture of turbulent scales in the thermohaline limit. Indeed, they usually neglect the properties of convective structures such as the turbulent velocity for instance and do not account for variable density flows. Thus, following the study of Canuto [2011a,e]’s RSM dedicated to stellar convection modelling, the derivation of a stochastic model which can address these issues has resorted to be the sparehead of the thesis in order to define the turbulent statistical properties of such medium.

The second part deals with an asymptotic analysis performed in the joint limits of infinitely small turbulent Mach and Péclet numbers. These imposed orders of magnitude entail the equilibrium of respectively acoustical phenomena and temperature fluctuations with their environment. The hydro-radiative set of governing equations involves the compressible Navier-Stokes system coupled with radiation in the diffusion limit. The results concern first, the prediction of pressure and temperature fluctuations in terms of  $M_t$  and  $Pe_t$ . And second, the behaviour of the radiative flow is examined through the asymptotic expressions of the divergence of velocity fluctuations  $\text{div}\mathbf{u}'$  and the fluctuating heat conduction term  $\mathcal{C}' = \partial_j (\lambda \partial_j T)'$ . Based on a radiatively stably stratified Rayleigh-Taylor configuration, the validation of their predicted values has been verified both qualitatively and quantitatively with respect to their DNS simulated ones. They have been compared to other expressions existing in literature. Hence, the closures derived from these outcomes were proven to be suitable in a RSM turbulent model and could be used for the simulation of small Péclet regimes involving mixing. In addition, the stability criterion of a mean stratification is modified accordingly. It changes from depending on the pseudo-entropy gradient to the molar mass gradient in respectively the ( $Pe_t \gg 1$ ) and the ( $Pe_t \ll 1$ ) limits.

In the third chapter, an adaptation of a ( $M_t \ll 1$ ) RSM model, already compatible with the ( $Pe_t \gg 1$ ) limit, has been proposed in order to account for the effect of the relative magnitude of radiative conductivity and turbulent transport in the range of infinitely small turbulent Péclet numbers. For this purpose, the evolution of density-linked correlations followed by the GSG 1D-RANS model has been closed using the outcomes of the previous analysis. The validation of the model lied on the references of Rayleigh-Taylor DNS simulations already studied in the second part. The capture of radiative effects and mixing, such as the stability criterion, has been correctly carried out by the adapted model.

The last part focused on a linear stability analysis applied to equilibrium states of radiatively stratified binary mixtures in a gravitational field. Based on a quasi-homogeneous approach, the LSA is intended first to highlight the role played by radiative diffusion. Indeed, in the stability space, the key parameter that defines the switch to “fingering” instability, *i.e.* “thermohaline” convection in the astrophysical context, is the Lewis number  $Le$  derived from the radiative NS governing equations, or equivalently, the Péclet number  $Pe_t$  when turbulent equilibria are considered. It allows to evaluate the influence on the stability of different parameters (gas compressibility, Schmidt number, relative importance of the radiative contribution to the pressure). The second purpose of the LSA has been dedicated to the improvement of the blending model, dealing with intermediate Péclet regimes. The stated stability criterion characterizing the onset of “fingering” convection has been used in place of a convex combination which originally required compulsory calibration. Thus, the bridge between both asymptotic limits rests now on a physically sound basis.

To summarize, the small Mach-small Péclet approximation has been derived and validated in order to deal with general radiative flow fields involving mixing. The latter have been captured efficiently by an adapted RSM model, which is now able to capture ( $Pe_t \ll 1$ ) and ( $Pe_t \gg 1$ ) regimes, and even the main trends of intermediate Péclet regimes. Such phenomena occur in stellar media, where turbulence coupled with radiation plays a role of overriding importance in the transport of chemical isotopes. This plasma may involve in addition a large amount of multiphysical processes such as ionization, electron degeneracy, nuclear reactions, shear, magnetism... However, in this work, the application of the approximation has been restrained to radiative binary mixtures of perfect gases without the inclusion of source terms. It provides, for instance, an accurate turbulent model for the deep interiors of stars in their early phases of evolution. In particular, it deals with the ( $Pe_t \ll 1$ ) regimes of “thermohaline” convective zones containing H-He mixing. While already accounting for some relevant changes in the behaviour of intensely radiative fields, the properties of such plasma are far from being completely understood. The treatment of additional processes may entail to relax a certain amount of simplifications. Among them, one can suppose a non-thermal equilibrium between matter and radiation fields or a non-“grey” material hypothesis. An interesting feature concerns the implications of source terms, such as nuclear reactions. Indeed, the asymptotic analysis already predicts a change in the orders of magnitude of fluctuating temperatures, as derived in App. B.4. Besides, addressing some issues related to 1D astrophysical modelling can be an interesting path to follow. Following [Canuto \[2011a\]](#), the actual adapted GSG model could be directly solved within an astrophysical code or even be cast under the form of a local [Prandtl \[1925\]](#)’s model, which might then provide a better suited alternative than other existing phenomenological models.



## Extended summary in French

### Introduction

Dans les intérieurs stellaires, des zones turbulentes peuvent se développer sous l'action d'une grande variété de mécanismes, allant du cisaillement et de la rotation à la convection et à la double-diffusion [Chandrasekhar, 1960, Prialnik, 2000]. L'élargissement de ces zones entraîne généralement le transport et le mélange d'éléments qui, autrement, seraient restés ségrégués et confinés dans des régions limitées de l'étoile. Par ces effets, la turbulence peut avoir une influence durable sur l'ensemble du cycle d'évolution stellaire. Elle peut, entre autres, affecter la durée de vie des étoiles, avoir un impact sur les observations susceptibles d'être faites depuis la Terre, et modifier l'abondance de certains éléments [Charbonnel & Zahn, 2007, Spiegel, 1969, Stevenson, 1982].

Une caractéristique particulière des zones de mélange turbulent stellaire provient de leur interaction avec le rayonnement. Dans les intérieurs d'étoiles, le champ radiatif est en équilibre local avec le plasma environnant et obéit à l'approximation de diffusion. Par conséquent, le transfert de chaleur est la somme d'un terme de conduction thermique et d'un terme de diffusion radiative. Ce dernier est d'un ordre de grandeur supérieur au premier. Il est si élevé que le nombre de Prandtl  $Pr$ , défini comme le rapport de la viscosité sur la somme des diffusivités thermique et radiative, peut atteindre des valeurs bien inférieures à un. Les fluides à faible nombre de Prandtl ne sont certainement pas rares sur Terre. Les métaux liquides, comme ceux que l'on trouve dans le coeur terrestre ou dans certains réacteurs nucléaires, présentent des nombres de Prandtl allant de  $10^{-1}$  à  $10^{-3}$ . Cependant, ces valeurs restent bien supérieures à celles trouvées dans les intérieurs stellaires. Par exemple, dans la zone radiative du Soleil, les nombres de Prandtl peuvent devenir aussi petits que  $10^{-9}$ . Cette différence entre les nombres de Prandtl n'est pas seulement quantitative : elle modifie également le contexte dans lequel se produit la convection turbulente.

Avec la conduction et le rayonnement, la convection turbulente est le troisième processus majeur qui intervient dans le transport de la chaleur. Son efficacité par rapport aux deux autres processus peut être évaluée par le nombre de Péclet turbulent  $Pe_t$ . Ce nombre sans dimension compare la diffusivité des tourbillons turbulents, estimée à partir de leur taille et de leur vitesse typique, à la somme des diffusivités thermique et radiative – qui, dans notre cas, est essentiellement la diffusivité radiative. Ainsi, dans un contexte stellaire, un petit nombre de Péclet indique que le rayonnement est beaucoup plus efficace que la turbulence pour transporter la chaleur,

tandis qu'un grand nombre de Péclet implique le contraire. Le fait que le nombre de Péclet soit petit ou non dépend de la valeur du nombre de Prandtl  $Pr$  du fluide. Il dépend également du nombre de Reynolds  $Re_t$  de l'écoulement. En effet, compte tenu de sa définition, le nombre de Péclet est égal au nombre de Prandtl multiplié par le rapport de la diffusion turbulente sur la viscosité du plasma, qui n'est rien d'autre que le nombre de Reynolds  $Re_t$  :

$$Pe_t = Pr \cdot Re_t \quad .$$

Par conséquent, un petit nombre de  $Pe_t$  ne peut être obtenu que si le nombre de Prandtl est beaucoup plus petit que l'inverse du nombre de Reynolds :  $Pr \ll Re_t^{-1}$ . C'est ici qu'intervient la différence entre les nombres de Prandtl observés dans les étoiles et dans les métaux liquides. En effet, la turbulence pleinement développée est généralement atteinte pour des nombres de Reynolds supérieurs à  $10^3$ . Ainsi, dans les métaux liquides, on peut difficilement combiner un état turbulent pleinement développé avec un petit nombre de Prandtl. En revanche, avec des nombres de Prandtl aussi bas que  $10^{-9}$ , la turbulence avec des nombres de Reynolds élevés et de petits nombres de Péclet peut exister dans les intérieurs stellaires. En effet, selon les simulations stellaires les plus récentes [Paxton *et al.*, 2013, 2019], des zones de mélange turbulentes avec de petits nombres Péclet sont prédites dans la plupart des étoiles de taille intermédiaire et massive, soit dans leur phase de séquence principale, soit dans leur phase de géante rouge, soit encore dans les deux.

L'existence de telles zones de mélange soulève un défi en termes de modélisation de la turbulence. En effet, si les fermetures statistiques pour les turbulences à haut nombre de Péclet sont bien établies et répandues, il n'en va pas de même pour leurs homologues à petit nombre de Péclet. Jusqu'à présent, la plupart des efforts déployés pour résoudre ce problème ont été circonscrits au contexte de la théorie de la longueur de mélange, introduite il y a près d'un siècle par Prandtl [1925]. Ce type de fermeture est en pratique celui qui est presque exclusivement mis en œuvre dans les codes d'évolution stellaire. Une exception notable est le modèle de contrainte de Reynolds (RSM) proposé par Canuto [2011a,e], dont l'usage reste malheureusement marginal. Mais indépendamment du cadre de modélisation particulier retenu, un point commun de ces travaux réside dans leur tentative de capturer la mise à l'échelle des quantités turbulentes dans la limite des nombres de Péclet infiniment petits. Cette limite asymptotique est en effet l'un des fondements essentiels sur lesquels des modèles statistiques peuvent être dérivés pour traiter la turbulence à petits Péclets.

Plus précisément, la limite des nombres de Péclet infiniment petits est une limite singulière des équations de Navier-Stokes. En appliquant une analyse asymptotique, une approximation simplifiée de l'écoulement réel peut être formulée dans laquelle les fluctuations de température s'équilibrent instantanément avec leur environnement. Cette approche est similaire à celle utilisée pour traiter les petits nombres de Mach turbulents  $Ma_t$ . Dans ce cas, une analyse asymptotique permet de dériver une approximation de l'écoulement réel, dite pseudo-compressible, anélastique ou Boussinesq-Oberbeck, dans laquelle les phénomènes acoustiques s'équilibrent instantanément [Soulard *et al.*, 2012]. Les approximations petit Péclet sont généralement considérées conjointement avec leurs homologues à petit Mach, qu'elles complètent et modifient. Cette limite conjointe est appropriée pour les écoulements turbulents stellaires qui sont en effet caractérisés par de petits nombres de Mach turbulents  $Ma_t$ .

Plusieurs travaux [Lignieres, 1999, Novotny *et al.*, 2011, Spiegel, 1962] ont ainsi été consacrés à l'étude de la limite faible nombre de Péclet-faible nombre de Mach. Cependant, certains éléments de ces études antérieures peuvent ne pas être entièrement adaptés au traitement des zones de mélange turbulentes stellaires. Un autre point qui nécessite quelques éclaircissements est la façon dont une approximation faible Péclet peut être utilisée pour dériver des fermetures turbulentes statistiques. Les résultats des analyses asymptotiques faible Péclet sont des expressions pour la divergence des vitesses et le terme de conduction, ainsi qu'un ordre de grandeur pour les fluctuations de pression et de température. Tous ces éléments ont un impact sur l'évolution des fluctuations des variables thermodynamiques, telles que la densité ou la température. Ils doivent donc être pris en compte dans la formulation de tout modèle statistique suivant les corrélations entre ces variables et visant à traiter les écoulements bas Péclet.

**Ainsi, cette étude consiste à dériver et à valider un modèle de turbulence RSM, tenant compte des effets de mélange et adapté aux écoulements radiatifs compressibles, dans la limite ( $Pe_t \ll 1$ ).**

Afin d'atteindre ce but, nous caractérisons tout d'abord les propriétés des zones de mélange turbulentes qui apparaissent au cours de l'évolution stellaire. En particulier, nous nous concentrons sur les ordres de grandeur de l'estimation des nombres adimensionnels liés aux fluctuations de vitesse et au transport moléculaire qui découle notamment du transfert radiatif. Pour ce faire, nous réalisons des simulations d'étoiles de  $1M_{\odot}$ ,  $5M_{\odot}$  et  $75M_{\odot}$  avec le code astrophysique open-source MESA.

Nous procédons dans un second chapitre à une analyse asymptotique basée sur les évolutions des fluctuations de vitesse, de pression, de température et de concentration d'espèces adaptées aux écoulements hydro-radiatifs rencontrés dans les intérieurs stellaires. Ceci conduit à nos principaux résultats concernant les ordres de grandeur de la température et de la pression fluctuantes, ainsi qu'à des expressions pour la divergence de la vitesse fluctuante et le terme de conduction. Ensuite, ces prédictions sont validées en effectuant des simulations numériques d'une instabilité radiative de Rayleigh-Taylor dans le régime faible Péclet.

En troisième partie, l'impact de l'approximation pour les petits nombres de Péclet sur la modélisation de la turbulence est illustré en considérant un modèle à un point d'ordre 2 existant et en adaptant sa formulation. Le modèle retenu pour cette tâche est le modèle GSG [Grégoire *et al.*, 2005], qui est un modèle RSM conçu pour traiter les zones de mélange turbulent à densité variable à haut Péclet, soumises à différents types d'instabilités convectives, telles que celles rencontrées dans un contexte stellaire.

Enfin, le dernier chapitre du manuscrit est consacré, premièrement, à l'étude de la stabilité linéaire de mélanges binaires stratifiés en équilibre soumis à un champ de gravité et, d'autre part, à l'amélioration du modèle de raccord pondéré "tout Péclet" proposé dans la troisième partie. Une analyse de stabilité linéaire permettra de dériver des critères de stabilité dans les régimes tout Mach, bas Mach et bas Mach-bas Péclet impliquant des effets visco-diffusifs. En particulier, leurs impacts sur différentes configurations d'écoulement sera mis en évidence par des résolutions numériques, ainsi que par la caractérisation des modes "oscillants" et "non-oscillants". Quant au modèle de raccord, son amélioration reposera sur l'utilisation de la condition de stabilité trouvée avec la relation de dispersion ( $M_t \ll 1$ ).

## Chapitre 1 - Simulation de la turbulence stellaire avec MESA

Les modèles de longueur de mélange de Prandtl [1925], tels que ceux détaillés dans le chapitre 1 du manuscrit, sont les plus fréquemment utilisés dans les simulations d'évolution stellaire. La principale raison expliquant cette popularité est d'ordre pratique : ces modèles sont simples à mettre en œuvre et, une fois calibrés, ils donnent des prédictions pertinentes. Pourtant, ils ne parviennent généralement pas à reproduire avec précision tous les phénomènes qu'ils sont censés capturer. Par exemple, Salaris & Cassisi [2017] soulignent que la MLT est souvent en contradiction avec plusieurs données héliosismiques.

Pour pallier ces insuffisances, plusieurs auteurs ont proposé d'autres types de modèles. En particulier, dans une série d'articles, Canuto [2011a,b,c,d,e] a préconisé l'utilisation de modèles de type RSM (Reynolds Stress Model) pour traiter le mélange turbulent stellaire. Dans les RSM, l'écoulement est décomposé en une partie moyenne et une partie fluctuante. Ensuite, les équations d'évolution pour les corrélations de second ordre des fluctuations de la vitesse, de la concentration et de la température (ou de tout autre champ pertinent) sont dérivées et fermées. Les RSM permettent une description plus riche du champ turbulent que le MLT. Cependant, cela se fait au prix de la résolution d'équations de transport supplémentaires, en plus de celles introduites dans le système d'équations de structure stellaire.

Cette charge de calcul explique probablement pourquoi les RSM n'ont pas réussi à se matérialiser comme une alternative aux modèles de longueur de mélange. Une autre raison possible est que le nombre de RSM disponibles pour décrire les flux de mélange stellaire reste limité. Pourtant, de nombreuses variantes de RSM ont été dérivées et utilisées dans d'autres domaines. Certains d'entre eux [Besnard *et al.*, 1989, Grégoire *et al.*, 2005, Schiestel, 2010] sont même conçus pour prédire des écoulements dominés par des instabilités de type convectif. Mais la plupart de ces modèles non stellaires ne capturent généralement pas tous les phénomènes physiques impliqués dans les écoulements stellaires. Bien que leurs principales caractéristiques pourraient être préservées, elles nécessiteraient néanmoins une adaptation avant d'être appliquées aux simulations stellaires.

Parmi les éléments manquants aux RSM, tels que ceux de Grégoire *et al.* [2005] et Besnard *et al.* [1989], figure le fait qu'ils ne sont pas destinés à prédire les instabilités à double diffusion. En particulier, ils ne sont pas censés capturer la limite petit Péclet de ces instabilités.

### Description de MESA et des paramètres de simulation

Nous visons ici à décrire les résultats obtenus en résolvant les équations d'évolution de structure stellaire et les modèles pour trois types d'étoiles : une étoile de faible masse, une étoile de masse intermédiaire et une étoile massive, respectivement avec une masse initiale de 1, 5 et 75  $M_{\odot}$ , avec la notation  $M_{\odot}$  correspondant à une "masse solaire" en unités astrophysiques.

Pour réaliser nos simulations, nous utilisons un code open-source appelé Modules for Experiments in Stellar Astrophysics (MESA) [Paxton *et al.*, 2010]. MESA permet de prendre en compte la convection en utilisant plusieurs variantes de la théorie de la longueur de mélange (MLT), telle que celle proposée par Cox & Giuli [1968] ou Henyey *et al.* [1965]. Quant à la turbulence thermohaline, elle est traitée à l'aide du modèle de Ulrich [1972], tel que décrit dans le chapitre 1.

Pour nos simulations, nous avons utilisé les fichiers [Choi *et al.*, 2016, Dotter, 2016] correspondant à des masses initiales de  $1M_{\odot}$ ,  $5M_{\odot}$  et  $75M_{\odot}$  et à une composition initiale identique à celle du Soleil [Asplund *et al.*, 2009] (voir Tab. D). Pour des raisons de simplicité, les étoiles sont également supposées non rotatives.

## Diagrammes de Kippenhahn

Le diagramme de Kippenhahn permet d'identifier les différentes régions de mélange turbulent apparaissant au cours de l'évolution stellaire. Les diagrammes obtenus à partir des simulations MESA d'une étoile de  $1M_{\odot}$ ,  $5M_{\odot}$  et  $75M_{\odot}$  sont respectivement présentés dans les Figs. 1.2, 1.3 et 1.4. Les zones turbulentes sont représentées le long de la masse lagrangienne  $m(r)$  par rapport à l'échelle de temps stellaire. De manière équivalente, des "model number" peuvent être utilisés à la place du temps afin de souligner les périodes où des événements importants se produisent. Ils correspondent aux états convergents quasi-stationnaires de profils stellaires spatiaux par rapport à  $m(r)$ . En termes de temps physique, la fréquence des "model number" dépend des échelles de temps caractéristiques de l'évolution stellaire. Ainsi, de la lente séquence principale à la rapide branche des géantes, le nombre de ses itérations augmente automatiquement.

Dans les diagrammes de Kippenhahn, les zones de convection et de mélange thermohaline sont localisées en utilisant les critères dérivés par Kato [1966]. En outre, ils affichent également le taux de génération d'énergie spécifique des réactions nucléaires [ $\log(\epsilon_{\text{nuc}})$ ] duquel ont été soustraites les réactions neutrinos. Ces diagrammes sont présentés pour la durée de la séquence principale et le début de la branche des géantes rouges de ces trois étoiles. La transition vers la phase de géante rouge peut être identifiée sur les diagrammes de Kippenhahn en repérant l'apparition d'une coquille de combustion de l'hydrogène, localisée par la légende "H-burn.", entourant le cœur d'hélium, écrit "He-core", et mis en évidence par la couleur bleue de  $\log(\epsilon_{\text{nuc}})$ . Plus précisément, les étapes de la séquence principale et de la branche géante rouge sont respectivement notées MS et RGB en rouge en haut de chaque diagramme avec un temps de référence approximatif, représentatif de la transition entre les deux processus continus. En comparant ces diagrammes, on peut observer que pendant la séquence principale et la majeure partie de la phase des géantes rouges, la convection se produit dans les couches extérieures de l'étoile la plus légère alors qu'elle se produit dans le cœur des deux étoiles de masse la plus élevée.

En ce qui concerne la zone de mélange thermohaline, nous pouvons observer que les conditions requises pour son développement sont réunies pour les trois étoiles pendant la phase de géante rouge. Près de la coquille d'hydrogène en combustion, et surtout en dessous, MESA prédit l'existence d'une telle zone. Comme l'a souligné Eggleton *et al.* [2006], une légère diminution du poids moléculaire moyen [Ulrich, 1972] se produit à proximité de la coquille de combustion de l'hydrogène, en raison de la réaction nucléaire particulière qui a lieu dans cette région. Cette diminution peut donner lieu à une inversion du gradient de la masse moléculaire moyenne  $\mu$ , et à des conditions qui favorisent le développement de l'instabilité thermohaline.

## Nombres sans dimension

Grâce au diagramme de Kippenhahn, nous avons identifié les régions où se produit le mélange turbulent convectif et thermohaline. Nous pouvons maintenant examiner la valeur des nombres sans dimension qui caractérisent ces zones turbulentes.

Plus précisément, nous nous concentrons sur les nombres turbulents de Mach, Reynolds et Péclet, respectivement désignés par  $M_t$ ,  $Re_t$  et  $Pe_t$ . Comme expliqué dans l'introduction, ces nombres jouent un rôle clé pour définir l'état turbulent de l'écoulement et pour spécifier comment le transport de chaleur par conduction et rayonnement interagit avec le champ turbulent. Tout d'abord, rappelons que  $M_t$ ,  $Re_t$  et  $Pe_t$  sont définis par :

$$M_t = \frac{u_0}{c_s} \quad , \quad Re_t = \frac{\nu_t}{\nu_v} \quad \text{et} \quad Pe_t = \frac{\nu_t}{\chi^r} \quad ,$$

où  $u_0$  est la valeur caractéristique de la vitesse turbulente,  $\nu_t$  est la diffusivité des tourbillons turbulents,  $\nu_v$  est la viscosité cinématique et  $\chi^r$  est la diffusivité radiative.

Les valeurs de  $\chi^r$  et de  $c_s$  peuvent être déterminées en connaissant respectivement l'opacité moyenne de Rosseland  $\kappa^r$  et l'exposant adiabatique généralisé  $\Gamma_1$ . Ces quantités sont fournies directement en sortie du code MESA. Pour la viscosité cinématique  $\nu_v$ , nous utilisons le modèle "Pseudo-ion in Jellium" de Arnault [2013]. Ce dernier prédit les coefficients de viscosité et de diffusion dans les plasmas où plusieurs constituants sont mélangés. Il est bien adapté au régime fortement couplé qui est rencontré dans les écoulements stellaires.

Concernant les quantités liées à la turbulence,  $u_0$  et  $\nu_t$ , nous procédons comme suit. Dans les régions convectives, nous utilisons la vitesse de convection  $v_{\text{conv}}$  et le coefficient de diffusion convective  $\mathcal{D}_{\text{conv}}$ , tels que définis dans le modèle MLT défini dans le chapitre 1. En d'autres termes,  $u_0 = v_{\text{conv}}$  et  $\nu_t = \mathcal{D}_{\text{conv}}$ . Dans les régions thermohalines, nous utilisons le modèle de Brown *et al.* [2013] pour estimer la vitesse et la diffusivité turbulentes, soit,  $u_0 = v_{\text{thrm}}$  et  $\nu_t = \mathcal{D}_{\text{thrm}}$ . Grâce à ces prescriptions, nous pouvons calculer les nombres turbulents de Mach, de Péclet et de Reynolds dans nos trois simulations MESA. Les profils de ces quantités sont tracés dans la Fig. 1.8 au début de la phase de géante rouge de l'étoile. En outre, le rapport entre la pression radiative et la pression de matière  $P^r/P^m$ , est affiché en même temps. Ils sont fournis comme sorties de MESA.

On peut voir que dans les zones convectives, on a toujours :

$$\text{Zone convective : } M_t \ll 1 \quad , \quad Pe_t \gg 1 \quad \text{et} \quad Re_t \gg 1 \quad .$$

Dans les zones thermohalines, cependant, on a :

$$\text{Zone thermohaline : } M_t \ll 1 \quad \text{et} \quad Pe_t \ll 1 \quad \text{with} \quad M_t \ll Pe_t \quad .$$

Quant au nombre de Reynolds, il reste modéré pour les étoiles de faible et moyenne masse mais devient important pour les étoiles massives :

$$\text{Zone thermohaline : } Re_t \gtrsim 1 \quad \text{pour} \quad M = 1M_\odot \quad \text{ou} \quad 5M_\odot \quad \text{et} \quad Re_t \gg 1 \quad \text{pour} \quad M = 75M_\odot \quad .$$

Enfin, la pression radiative  $P^r$  est négligeable par rapport à celle de la matière  $P^m$  dans les étoiles les plus légères, quelle que soit la zone de mélange considérée : ( $P^r \ll P^m$ ) pour  $M = 1M_\odot$  ou  $5M_\odot$ . Cependant, dans les mêmes zones, la contribution radiative à la pression totale devient beaucoup plus importante pour les étoiles massives : ( $P^r \gtrsim P^m$ ) pour  $M = 75M_\odot$ .

## Chapitre 2 - Approximation faible Mach-faible Péclet

Nous rappelons que l'objectif de ce travail est d'étudier les écoulements turbulents ayant un petit nombre de Mach et un petit nombre de Péclet.

### Équations instantannées

Nous considérons un plasma défini par sa densité  $\rho$ , sa vitesse  $\mathbf{u}$ , les fractions massiques de ses  $N_s$  ions  $c_\alpha$  pour  $\{\alpha = 1, \dots, N_s\}$  et l'énergie massique interne  $e^m$  de ses ions et électrons. Ce plasma est soumis à une gravité  $\mathbf{g}$  et est couplé à un champ radiatif d'énergie volumique  $E^r$ . Le champ radiatif des intérieurs stellaires obéit à l'approximation de diffusion [Mihalas & Mihalas, 2013]. Par conséquent, une seule température  $T$  est nécessaire pour décrire le rayonnement et la matière. De plus, au lieu de  $e^m$  et  $E^r$ , il suffit de suivre l'énergie massique totale  $e$ , définie comme  $e = e^m + E^r/\rho$ . Ainsi, l'évolution de l'écoulement hydro-radiatif est donnée par :

$$\begin{aligned} D_t \rho &= -\rho \operatorname{div} \mathbf{u} \quad , \\ \rho D_t \mathbf{u}_i &= -\partial_i P - \partial_j \Pi_{ij} + \rho g_i \quad , \\ \rho D_t c_\alpha &= -\partial_j \mathcal{F}_{\alpha j} \quad , \\ \rho D_t e &= \rho \varepsilon - P \operatorname{div} \mathbf{u} - \partial_j \mathcal{F}_j \quad . \end{aligned}$$

Dans ces équations, les notations  $\partial_j \cdot$ ,  $D_t \cdot$  et  $\operatorname{div} \cdot$  font respectivement référence à la dérivée partielle par rapport à la coordonnée spatiale  $x_j$ , à la dérivée temporelle lagrangienne et à l'opérateur de divergence. En particulier, nous avons  $\operatorname{div} \mathbf{u} = \partial_j u_j$ , et, pour toute quantité  $q$ ,  $D_t q = \partial_t q + u_j \partial_j q$  avec  $\partial_t$  la dérivée partielle par rapport au temps  $t$ . Notons également que la convention d'Einstein sur la sommation des indices répétés est utilisée pour les lettres latines mais pas pour les indices grecs, en particulier pour l'indice  $\alpha$  attaché à l'espèce.

La pression  $P$  est la pression totale du flux radiatif, c'est-à-dire la somme des pressions matérielle et radiative, respectivement notées  $P^m$  et  $P^r$ , soit  $P = P^m + P^r$ . Dans les étoiles de masse intermédiaire, comme le Soleil, la pression radiative est généralement négligeable par rapport à la pression matière. Cependant, ce n'est pas le cas dans les étoiles massives, où les deux composantes peuvent être du même ordre, comme vu précédemment. Comme le champ radiatif obéit à l'approximation de la diffusion, la pression radiative peut être exprimée par  $P^r = E^r/3$  avec  $E^r = a_R T^4$ , où  $a_R$  est la constante de rayonnement. En ce qui concerne la pression matière  $P^m$ , nous supposons, par souci de simplicité, que le plasma est entièrement ionisé et se comporte comme un gaz parfait. Par conséquent, elle obéit à l'équation d'état  $P^m = \rho r T$  avec  $r = \sum_\alpha r_\alpha c_\alpha$  et  $r_\alpha = \mathcal{R} (1 + Z_\alpha) / \mathcal{M}_\alpha$ , où  $\mathcal{R}$  est la constante de gaz parfait,  $\mathcal{M}_\alpha$  est la masse molaire de l'ion  $\alpha$  et  $Z_\alpha$  est son degré d'ionisation. Pour les mêmes raisons, nous supposons ici que la chaleur spécifique à volume constant  $c_{v,\alpha}^m$  de chaque espèce  $\alpha$  est constante et que toutes les espèces  $\alpha$  partagent le même coefficient polytropique  $\gamma^m$ . Ainsi,  $e^m = c_v^m T$  avec  $c_v^m = \sum_\alpha c_{v,\alpha}^m c_\alpha$  et  $\gamma_\alpha = 1 + r_\alpha / c_{v,\alpha}^m = \gamma^m$  pour tout  $\alpha$ . Notons également que  $c_v^m$  inclut les contributions des ions et des électrons, mais pas celles des photons. Étant donné l'hypothèse de diffusion, on peut toutefois définir une chaleur spécifique globale du continuum photons-ions-électrons en différenciant l'énergie totale  $e$  par rapport à la température  $T$  à densité constante  $\rho$ . On obtient ainsi la chaleur spécifique totale à volume constant  $c_v = c_v^m + 4a_R T^3 / \rho$ .

Nous avons également introduit le tenseur de viscosité  $\Pi_{ij}$ , défini par  $\Pi_{ij} = -2\mu_v (S_{ij} - \frac{1}{3}\text{div}\mathbf{u}\delta_{ij})$ , où  $S_{ij} = (\partial_j u_i + \partial_i u_j) / 2$  et où  $\mu_v = \rho\nu_v$  est la viscosité dynamique du plasma avec  $\nu_v$  sa viscosité cinématique. La dissipation associée est définie par  $\rho\varepsilon = -\Pi_{ij}S_{ji}$ . Le flux de diffusion de la fraction massique de l'espèce  $c_\alpha$  est défini par une approximation Fickienne [Giovangigli, 2012] de la forme :  $\mathcal{F}_{\alpha j} = -\rho\mathcal{D}^{(\alpha)}\partial_j c_\alpha$  pour  $\alpha = \{1, \dots, N_s - 1\}$  et  $\mathcal{F}_{\alpha j} = -\sum_{\alpha=1}^{N_s-1} \mathcal{F}_{\alpha j}$  pour  $\alpha = N_s$ , où  $\mathcal{D}^{(\alpha)}$  est le coefficient de diffusion de l'espèce  $\alpha$ . Notons que la validation proposée dans cette étude concerne un mélange binaire ( $N_s = 2$ ) ce qui signifie que, pour les deux gaz, il existe un seul coefficient de diffusion interspécifique qui sera noté  $\mathcal{D}$ . Enfin, le dernier terme encore non spécifié est le flux d'énergie  $\mathcal{F}_j$ . Étant donné que  $e$  est l'énergie totale,  $\mathcal{F}_j$  a deux contributions, une matérielle  $\mathcal{F}_j^m$  et une radiative  $\mathcal{F}_j^r$  tel que  $\mathcal{F}_j = \mathcal{F}_j^m + \mathcal{F}_j^r$ . Le terme matériel  $\mathcal{F}_j^m$  est lui-même divisé en une contribution de conduction thermique et une contribution de mélange enthalpique  $\mathcal{F}_j^m = -\lambda^m\partial_j T + h_{,\alpha}^m\mathcal{F}_{\alpha j}$ , où  $\lambda^m$  est la conductivité thermique du plasma et  $h_{,\alpha}^m$  représente la différentielle de l'enthalpie  $h^m$  par rapport à la fraction massique  $c_\alpha$  de l'espèce  $\alpha$  à autres variables thermodynamiques constantes. Quant au flux radiatif, l'hypothèse de diffusion permet de l'exprimer comme  $\mathcal{F}_j^r = -\lambda^r\partial_j T$  avec  $\lambda^r = 4c_\ell a_R T^3 / (3\rho\kappa^r)$ , avec  $c_\ell$  la célérité de la lumière. Dans cette expression,  $\kappa^r$  est l'opacité de Rosseland et est liée au libre parcours moyen de Rosseland  $\Lambda^r$  par  $\kappa^r = 1/(\rho\Lambda^r)$ . Pour conclure, une conductivité totale  $\lambda$  peut être définie en additionnant les contributions radiative et matérielle, soit  $\lambda = \lambda^m + \lambda^r$ . À partir de là, on peut également définir une diffusivité thermique totale  $\chi$  en utilisant la conductivité totale  $\lambda$  et la chaleur spécifique totale  $c_v$  telle que  $\chi = \lambda/(\rho c_v)$ . Cette définition tient compte des contributions de la matière et du rayonnement.

## Pression et température

L'analyse asymptotique proposée ci-après traitera des propriétés du champ de vitesse  $\mathbf{u}$ , de la pression totale  $P$  et de la température  $T$ . L'équation d'évolution de  $\mathbf{u}$  est donnée dans le système hydro-radiatif défini précédemment. Quant à celles de  $P$  et de  $T$ , elles sont déduites en utilisant certaines relations thermodynamiques de Maxwell :

$$D_t P = -\Gamma_1 P \text{div}\mathbf{u} + (\Gamma_3 - 1)\mathcal{C} + \mathcal{D}_P \quad , \quad D_t T = -(\Gamma_2 - 1)T \text{div}\mathbf{u} + \frac{\mathcal{C}}{\rho c_v} + \frac{\mathcal{D}_T}{\rho c_v} \quad \text{et} \quad \mathcal{C} = \partial_j (\lambda \partial_j T) \quad .$$

Dans ces équations,  $\mathcal{C}$  représente le terme de conduction totale et  $\mathcal{D}_P$  et  $\mathcal{D}_T$  rendent compte des effets de la diffusion et de la dissipation moléculaires sur  $P$  et  $T$  :

$$\mathcal{D}_P = \Gamma_3 \sum_{\alpha} \frac{P_{,\alpha}}{\rho} \partial_j (\rho \mathcal{D}^{(\alpha)} \partial_j c_\alpha) (\Gamma_3 - 1) \rho \left( \varepsilon + \sum_{\alpha} \mathcal{D}^{(\alpha)} \partial_j h_{,\alpha}^m \partial_j c_\alpha \right) \quad \text{et} \quad \mathcal{D}_T = \sum_{\alpha} \frac{P_{,\alpha}}{\rho} \partial_j (\rho \mathcal{D}^{(\alpha)} \partial_j c_\alpha) \rho \left( \varepsilon + \sum_{\alpha} \mathcal{D}^{(\alpha)} \partial_j h_{,\alpha}^m \partial_j c_\alpha \right) \quad .$$

Les coefficients  $\gamma_1, \gamma_2$  et  $\gamma_3$  sont des exposants adiabatiques généralisés définis pour un continuum composé de matière et de rayonnement Mihalas & Mihalas [2013] par  $\Gamma_1 = \rho/P \cdot \partial P / \partial \rho|_{s,c}$ ,  $\Gamma_2 = 1 + \rho/T \cdot \partial T / \partial \rho|_{s,c}$  et  $\Gamma_3 = 1 + 1/\rho \cdot \partial P / \partial e|_{\rho,c}$ , où  $s$  est l'entropie. Notons qu'avec les notations trouvées dans Mihalas & Mihalas [2013], on a  $\gamma_1 = \Gamma_1$  mais  $\gamma_2 = \Gamma_3$ . Notons que les exposants adiabatiques généralisés sont généralement différents les uns des autres et également du rapport de chaleur spécifique  $\gamma$  défini par  $\gamma = c_p/c_v$ , où  $c_v$  est la chaleur spécifique totale à volume constant et  $c_p$  est la chaleur spécifique totale à pression constante. Tous ces coefficients sont aussi généralement différents de l'exposant adiabatique  $\gamma^m$  caractérisant le plasma sans rayonnement. Ils coïncident néanmoins pour un gaz parfait sans rayonnement.

## Écoulement moyen comme état de base

Un élément crucial lors de l'étude asymptotique à petit nombre de Mach ou à petit nombre de Péclet est de choisir un état de référence qui permettra de diviser les quantités en une composante de base et une déviation de cette base. C'est cet écart dont les propriétés seront déterminées par l'analyse. Plus précisément, nous effectuerons notre analyse en divisant les quantités en une moyenne d'ensemble statistique et sa fluctuation correspondante.

Pour les écoulement à densité variable, il est habituel de travailler avec les statistiques pondérées par la densité de "Favre" et les statistiques non pondérées de "Reynolds". Pour toute quantité  $q$ , les moyennes de Reynolds et de Favre sont désignées respectivement par  $\bar{q}$  et  $\tilde{q}$ . Elles sont liées par l'identité  $\tilde{q} = \bar{\rho q} / \bar{\rho}$ . Les fluctuations correspondantes sont  $q' = q - \bar{q}$  et  $q'' = q - \tilde{q}$ . Elles sont liées par  $q'' = \overline{q''} + q'$ .

## Équations sans dimension pour les fluctuations

La dernière étape avant d'effectuer l'analyse asymptotique à petit nombre de Péclet consiste à rendre sans dimension les équations d'évolution de la vitesse, de la pression et de la température fluctuantes. À cet égard, il est important de reconnaître que les champs moyens et fluctuants ont des échelles caractéristiques différentes. Par conséquent, deux ensembles de paramètres adimensionnants doivent être fournis : un pour le champ moyen, l'autre pour le champ fluctuant.

Tout d'abord, l'intensité des fluctuations turbulentes, concernant la vitesse  $u''$ , la densité relative  $\rho' / \bar{\rho}$ , la concentration  $c'_\alpha$  et les exposants adiabatiques  $\gamma'_1, \gamma'_2, \gamma'_3$  sont respectivement caractérisés par  $u_0, \epsilon_{\rho_0}, \epsilon_{c_0}$  et  $\epsilon_{\gamma_0}$ . Par ailleurs, les échelles de longueur et de temps caractéristiques des tourbillons turbulents sont désignées par  $\ell_0$  et  $\tau_0$ . Elles sont liées à la vitesse turbulente caractéristique par :  $\tau_0 = \ell_0 / u_0$ . Quant aux échelles moyennes de densité, pression et température, elles sont respectivement définies par les valeurs de  $\rho_0, P_0$  et  $T_0$ . Par souci de simplicité, la célérité du son caractéristique  $c_{s_0}$  et la capacité calorifique à volume constant  $c_{v_0}$  sont choisis égaux à  $c_{s_0} = \sqrt{P_0 / \rho_0}$  et  $c_{v_0} = P_0 / (\rho_0 T_0)$ . Les échelles caractéristiques des gradients du champ moyen doivent également être fournies. Les échelles caractéristiques de la déformation et de l'accélération moyennes sont respectivement désignées par  $S_0$  et  $G_0$ . En outre, des échelles de longueur pour les gradients moyens de température  $L_{T_0}$  et de pression  $L_{P_0}$  sont également introduites :  $L_{T_0} \sim T_0 / |\nabla T|_0$  et  $L_{P_0} \sim P_0 / |\nabla P|_0 \sim c_{s_0}^2 / G_0$ . Enfin, des valeurs caractéristiques pour la viscosité cinématique  $\nu_v$ , pour les coefficients de diffusion  $\mathcal{D}^{(\alpha)}$  et pour la diffusivité thermique totale  $\chi$  sont également introduites. Elles sont respectivement désignées par  $\nu_{v_0}, \mathcal{D}_0^{(\alpha)}$  et  $\chi_0$ .

En utilisant  $\ell_0$  et  $\tau_0$  pour l'espace et le temps et les autres quantités le cas échéant, nous pouvons adimensionner les équations fluctuantes (voir Eqs. (2.27a), (2.27b) et (2.27c)). Les nombres sans dimension apparaissant dans ces équations sont définis comme suit :  $M_t = u_0 / c_{s_0}$ ,  $Fr_s = 1 / (\tau_0 \cdot S_0)$ ,  $Fr_a = u_0 / (\tau_0 \cdot G_0 \cdot \epsilon_{\rho_0})$ ,  $Ka_P = \ell_0 / L_{P_0}$ ,  $Ka_T = \ell_0 / L_{T_0}$ ,  $Re_t = u_0 \cdot \ell_0 / \nu_{v_0}$ ,  $Pr = \nu_{v_0} / \chi_0$ ,  $Sc = \nu_{v_0} / \mathcal{D}_0$ ,  $Pe_t = u_0 \cdot \ell_0 / \chi_0 = Pr \cdot Re_t$ . Le nombre de Mach turbulent  $M_t$  caractérise l'intensité des fluctuations de la vitesse turbulente. Les nombres de Froude liés à la déformation  $Fr_s$  et à l'accélération  $Fr_a$  caractérisent la production de turbulence par les gradients moyens. Les nombres de von Karman, liés à la pression  $Ka_P$  et à la température  $Ka_T$  caractérisent les échelles de longueur des champs de pression et de température moyens. Les effets moléculaires et radiatifs sont pris en compte dans le nombre de Reynolds turbulent  $Re_t$ , le nombre de Schmidt  $Sc$ , le nombre de Prandtl  $Pr$  et le nombre de Péclet  $Pe_t$ .

## Conditions du développement asymptotique

Nous supposons par la suite que le nombre de Mach est petit et que le nombre de Péclet est éventuellement encore plus petit. Cette condition s'exprime comme suit :

$$M_t \ll 1 \quad \text{et} \quad Pe_t \sim M_t^n \ll 1 \quad \text{avec} \quad n \geq 1 \quad .$$

Des conditions secondaires doivent aussi être fournies (avec les autres nombres sans dimension,) considérées pertinentes pour les intérieurs stellaires. Premièrement, nous supposons l'ordre de grandeur des fluctuations de concentration et de densité faible :  $\epsilon_{c_0} \sim M_t \ll 1$  et  $\epsilon_{\rho_0} \sim M_t \ll 1$ . Ensuite, nous supposons que la turbulence diminue ou se trouve dans un état de quasi-équilibre. Cela implique que les termes de production moyenne sont au plus du même ordre que ceux de dissipation. Par conséquent, nous considérons que  $Fr_a \gtrsim 1$  et  $Fr_s \gtrsim 1$ . Nous supposons également que l'échelle de longueur des champs de température et de pression moyens est très grande par rapport à l'échelle de longueur turbulente :  $Ka_P \sim M_t \ll 1$  et  $Ka_T \sim Pe_t^{1/2} \ll 1$ . Enfin, on suppose que les termes visqueux et de dissipation vérifient  $Re_t \gtrsim 1$  et  $Sc \cdot Re_t \gtrsim 1$ .

## Résultats principaux du développement asymptotique

Nous procédons ici à l'analyse asymptotique. Les quantités fluctuantes sont développées comme fonctions du  $M_t$ . Pour toute fluctuation  $q'$ , on a  $q' = q^{(0)} + M_t \cdot q^{(1)} + M_t^2 \cdot q^{(2)} + \mathcal{O}(M_t^3)$ . Ces développements sont ensuite insérés dans les équations d'évolution dérivées précédemment (Eqs. (2.27a), (2.27b) et (2.27c)) et les termes d'ordres similaires sont rassemblés.

Tout d'abord, le terme de conduction dans l'équation d'évolution de la température fluctuante (2.27c) a un échelonnement singulier d'ordre  $Pe_t^{-1} = M_t^{-n}$ . Ensuite, y en rassemblant les termes d'ordre  $Pe_t^{-1} = M_t^{-n}$  à  $M_t^{-1}$  et en tenant compte des conditions secondaires, on déduit que :  $\mathcal{C}'^{(0)} = \mathcal{C}'^{(1)} = \dots = \mathcal{C}'^{(n-1)} = 0$  et  $T'^{(0)} = T'^{(1)} = \dots = T'^{(n-1)} = 0$ . Ce premier résultat montre que les fluctuations de température sont au moins d'ordre  $Pe_t = M_t^n$ . Quant à l'ordre de grandeur du champ de pression, il peut être déduit en notant que le terme de gradient de pression dans l'Eq. (2.27a) a un échelonnement singulier d'ordre  $M_t^{-2}$ . Ensuite, en rassemblant les termes d'ordre  $M_t^{-2}$  à  $M_t^{-1}$ , on déduit que :  $P'^{(0)} = P'^{(1)} = 0$ . Ce deuxième résultat montre que les fluctuations de pression sont d'ordre  $M_t^2$ . Il s'agit de l'échelle classique obtenue dans la plupart, sinon la totalité, des approximations à petit nombre de Mach. Lorsqu'elles sont injectés dans les définitions des indices adiabatiques, ces échelles de température et de pression impliquent, avec le fait que  $\gamma^m$  est constant, que :  $\gamma_1'^{(0)} = \gamma_2'^{(0)} = \gamma_3'^{(0)} = 0$ . Revenons aux équations (2.27b) et (2.27c) pour la température et la pression fluctuantes. A l'ordre  $M_t^0$ , on obtient une combinaison linéaire de  $\text{div} \mathbf{u}'^{(0)}$  et  $\mathcal{C}'^{(n)}$  du côté droit comprenant des termes nuls du côté gauche. Ainsi,  $\text{div} \mathbf{u}'^{(0)} = 0$  and  $\mathcal{C}'^{(n)} = 0$ . La dernière égalité implique que  $T'^{(n)} = 0$ . Ceci montre que la température est d'ordre  $M_t \cdot Pe_t$  et est bien plus petite que les deux  $M_t$  et  $Pe_t$ . Enfin, à l'ordre  $M_t$ , les Eqs. (2.27b) et (2.27c) fournissent deux relations reliant l'ordre principal de la divergence des vitesses à l'ordre principal du terme de conduction. Ces équations expriment les équilibres respectifs de  $T'$  et  $P'$ . Ils relient la divergence des vitesses et le terme de conduction et décrivent leur variation en fonction des gradients de pression et de température, ainsi que des termes de diffusion. Leur existence combinée souligne la dépendance de l'approximation faible Péclet à son homologue faible Mach.

## Prédictions en termes de variables dimensionnelles

Nous exprimons les principaux résultats de l'analyse sous forme dimensionnelle. Nous revenons donc aux variables originales, avant l'adimensionnement du système. Le premier résultat est que les fluctuations de  $P'$  et de  $T'$  sont respectivement d'ordre  $M_t^2$  et  $Pe_t \cdot M_t$  :

$$P'/\bar{P} \sim M_t^2 \ll M_t \quad \text{et} \quad T'/\bar{T} \sim Pe_t \cdot M_t \ll M_t .$$

Cela indique que les fluctuations de pression et de température sont faibles par rapport aux fluctuations des autres variables thermodynamiques. Ainsi, elles peuvent être négligées par rapport à ces dernières sauf lorsqu'elles interviennent dans des gradients ou des termes de diffusion.

Le deuxième résultat de l'analyse asymptotique est tiré des deux relations traduisant l'équilibre de  $P'$  et  $T'$ . Ces équations forment un système linéaire pour les deux quantités inconnues  $\text{div}\mathbf{u}'$  et  $C'$ . En inversant ce système, on obtient que :

$$\text{div}\mathbf{u}' = -u'_j \left( \frac{\partial_j \bar{\rho}}{\bar{\rho}} + \frac{\partial_j \bar{r}}{\bar{r}} \right) - \sum_{\alpha} \frac{r_{\alpha}}{\bar{r}} \frac{\partial_j \mathcal{F}_{\alpha j}'}{\bar{\rho}} \quad \text{et} \quad C' = u'_j \left[ \frac{\partial_j \bar{P}}{\bar{\rho} c_v} - x^P \bar{P} \left( \frac{\partial_j \bar{\rho}}{\bar{\rho}} + \frac{\partial_j \bar{r}}{\bar{r}} \right) \right] - 4\bar{P}^r \sum_{\alpha} \frac{r_{\alpha}}{\bar{r}} \frac{\partial_j \mathcal{F}_{\alpha j}'}{\bar{\rho}} ,$$

avec  $x^P = 4 - 3\bar{P}^m/\bar{P}$ . Le premier terme du côté droit de la première équation exprime l'ajustement volumique d'un élément de masse se déplaçant dans un environnement stratifié. Comme on peut le constater, cet ajustement ne dépend que de la valeur de la densité moyenne et de la constante des gaz parfaits et non de propriétés radiatives. Le second terme de la première équation montre que le volume d'un élément de masse est également modifié par la diffusion moléculaire des espèces à condition qu'elles aient des constantes de gaz différentes.

La deuxième relation correspond à l'équilibre thermique existant entre le terme de conduction du côté gauche et deux sources différentes de fluctuations de température du côté droit. Le premier terme source provient du déplacement des particules de fluide le long d'un gradient de température de type adiabatique. Le second implique un effet combiné du rayonnement et de la diffusion des espèces.

## Comparaison avec les résultats précédents et avec la limite grand Péclet

Un autre point de comparaison peut être fait pour mieux comprendre le rôle joué par la petitesse du nombre de Péclet. Tout d'abord, pour ( $Pe_t \gg 1$ ), il n'y a pas d'équilibre de température. Par conséquent, il n'y a pas de contrainte pour l'ordre de grandeur de  $T'$ . Il reste l'équilibre de pression et ses conséquences : l'ordre de grandeur de  $P'$  et une expression pour la terme de divergence. D'après [Soulard et al. \[2012\]](#), cette expression prend la forme :

$$\text{div}\mathbf{u}' = -u'_j \partial_j \bar{P} / (\bar{\gamma}_1 \bar{P}) + \text{Termes moléculaires.}$$

Lorsque tous les coefficients de diffusion moléculaire sont égaux, les termes moléculaires de la relation précédente se simplifient en un terme de diffusion sur les fluctuations de densité et deviennent équivalents au terme de diffusion apparaissant dans l'expression ( $Pe_t \ll 1$ ) de divergence. Par conséquent, nonobstant les propriétés de  $T'$ , la principale différence entre la limite petit et grand Péclet provient de la façon dont le volume des particules fluides s'ajuste aux gradients moyens de pression et de température, comme l'exprime le premier terme du côté droit des équations de  $\text{div}\mathbf{u}'$ .

Cette différence a des répercussions importantes, notamment pour définir le critère de stabilité d'une stratification moyenne. Pour illustrer ce point, considérons la stabilité linéaire inviscide d'un écoulement ayant une stratification moyenne de densité, température et concentration satisfaisant la condition d'équilibre hydrostatique  $\partial_i \bar{P} = \bar{\rho} g_i$ . De là, on obtient qu'une stratification est stable à condition que :

$$\text{pour } (Pe_t \ll 1) \quad , \quad \partial_j \bar{r} \cdot \partial_j \bar{P} / \bar{\rho} < 0 \quad \text{et} \quad \text{pour } (Pe_t \gg 1) \quad , \quad (\partial_j \bar{P} / \bar{\gamma}_1 \bar{P} - \partial_j \bar{\rho} / \bar{\rho}) \partial_j \bar{P} / \bar{\rho} < 0 \quad .$$

Dans la limite grand Péclet, la stabilité est définie par l'orientation de l'accélération par rapport au gradient de densité corrigé par un gradient de pression adiabatique. Ainsi, en l'absence de gradients de concentration moyens, la stabilité d'une stratification dans la limite haut Péclet est déterminée par l'orientation de l'accélération et du gradient d'entropie. Lorsque des gradients de concentration existent, la stabilité n'est pas déterminée uniquement par le gradient d'entropie, mais on peut s'attendre à ce que ce dernier joue un rôle important. En revanche, dans la limite petit Péclet, la stabilité est déterminée par les orientations de l'accélération et du gradient de la constante des gaz. L'entropie ne joue plus de rôle et seuls les gradients des concentrations des différentes espèces influencent la stabilité de l'écoulement. Ce dernier résultat peut être compris comme un cas asymptotique particulier de l'instabilité à double-diffusion (thermohaline) rencontrée dans les écoulements stellaires [Garaud, 2018].

## Validation de l'analyse asymptotique

Afin d'étudier l'impact de l'approximation bas Mach-bas Péclet, des simulations numériques (DNS) d'une zone de mélange turbulent radiatif sont réalisées avec le code TRICLADE.

### Configuration de l'écoulement de type Rayleigh-Taylor

L'écoulement test considéré est un mélange turbulent statistiquement axisymétrique induit par une instabilité de Rayleigh–Taylor (RTI) au niveau d'une interface planaire entre deux fluides différents. Cette configuration simplifiée ne se rencontre pas telle quelle dans les intérieurs d'étoiles. Son intérêt réside dans le fait qu'elle combine certains mécanismes élémentaires à l'œuvre dans les écoulements stellaires : du mélange, de la convection, du rayonnement et des effets de Péclet. Cela constitue donc un banc d'essai pertinent pour nos prédictions.

L'état initial des simulations est défini comme suit. Les deux fluides sont séparés par une interface, située à  $x = x_0$ , qui est instable par rapport à un champ gravitationnel constant  $\mathbf{g}$  orienté selon l'axe  $x$  vers des valeurs négatives de  $x$ , c'est-à-dire pointant du côté du fluide lourd ( $x > 0$ ) vers le côté du fluide léger ( $x < 0$ ). Ce dernier axe est appelé direction inhomogène ou longitudinale, tandis que les axes  $(y, z)$  correspondent aux directions transversales ou homogènes. L'état moyen est fixé en imposant un équilibre hydrostatique avec une condition isotherme. Les deux masses molaires  $\mathcal{M}_h$  et  $\mathcal{M}_l$  de chaque fluide doivent être interprétées comme des masses effectives, tenant compte de la masse molaire réelle divisée par  $1 + \mathcal{Z}$ , en accord avec l'équation d'état (2.8). Leur contraste est caractérisé par le nombre d'Atwood :  $\mathcal{A}_t = \frac{\mathcal{M}_h - \mathcal{M}_l}{\mathcal{M}_h + \mathcal{M}_l}$ . Au temps initial, l'interface est laissée plate mais une petite perturbation du champ de vitesse est introduite autour d'elle. Le spectre de la perturbation a un profil en "chapeau" délimité par les longueurs d'onde  $\lambda_{\min}$  et  $\lambda_{\max} = 2\lambda_{\min}$  et une intensité caractérisée par un nombre de Mach turbulent  $M_{t_0}$ .

En outre, deux nombres sans dimension [Mihalas & Mihalas, 2013] sont introduits afin de tenir compte des propriétés locales du fluide radiatif. La contribution de l'énergie de rayonnement par rapport à celle de la matière stellaire peut être exprimée par le nombre de Mihalas  $R$ . Quant au nombre de Boltzmann  $Bo$ , il donne l'importance relative entre le transport d'énergie radiatif et celui de la matière. Ils sont respectivement estimés au centre de la zone de mélange  $x = x_0$ , à l'emplacement initial de l'interface avec :  $R = \rho e^m / E^r$  et  $Bo = \rho h^m c_{s0} / (\sigma_{SB} T^4)$ , avec  $\sigma_{SB}$  la constante de Stefan-Boltzmann. Notons que la vitesse du son initiale est choisie comme vitesse caractéristique pour le nombre de Boltzmann. L'échelle de référence de la température est définie à partir des autres échelles de référence de manière à maintenir le nombre de Mihalas.

Par souci de simplicité, les deux gaz du mélange binaire ont les mêmes indices adiabatiques  $\gamma_0$ , viscosité cinématique  $\nu_v$ , coefficient de diffusion des espèces  $\mathcal{D}$  et opacité  $\kappa^r$  et ces propriétés sont supposées être constantes. Dans ce cadre, les principaux paramètres définissant les simulations sont  $\mathcal{A}_t = 0.26$ ,  $R = 1.24$ ,  $Bo = 3.75 \times 10^{-2}$ ,  $\gamma_0 = 5/3$ ,  $\rho_0 = 1$ ,  $\lambda_{\max} = 1$ ,  $M_{t0} = 5 \times 10^{-3}$ ,  $T_0 = 3.16$ ,  $\frac{M_{t0} g}{\mathcal{R} T_0} = 3.89 \times 10^{-2}$ ,  $\nu_v = \mathcal{D} = 9.2 \times 10^{-3}$ . Le fait que ( $R > 1$ ) indique que l'énergie et la pression matérielles dominent celles radiatives et le fait que ( $Bo \ll 1$ ) montre que le flux radiatif domine le flux enthalpique matériel. De telles conditions peuvent être trouvées à l'intérieur des étoiles massives, où la pression radiative n'est pas négligeable, contrairement aux étoiles de masse intermédiaire (comme vu dans le chapitre 1).

Trois simulations sont effectuées : une avec un très petit nombre de Prandtl, une autre avec un grand nombre de Prandtl et une troisième avec un nombre de Prandtl modérément petit. Le nombre de Prandtl est ici défini comme la valeur au temps initial et à l'interface de  $Pr = \rho c_p \cdot \nu_v / \chi = \rho_0 \kappa^r \nu_v \cdot 3 \rho c_p / (4 c_{\ell} a_{\mathcal{R}} T^3)$ . La première simulation est censée donner un petit nombre de Péclet et vise à vérifier les résultats de l'analyse asymptotique. Ensuite, par comparaison avec la deuxième simulation, elle permet de différencier les comportements du mélange turbulent induit dans les deux régimes asymptotiques. La simulation de Prandtl intermédiaire est destinée à tester les limites de l'approximation. Pour faire varier le nombre de Prandtl, la conductivité radiative est modifiée en changeant l'opacité  $\kappa^r$ . Les valeurs d'opacité choisies pour chaque simulation sont indiquées dans le tableau A ainsi que le nombre de Prandtl et avec un nom attribué à chaque simulation.

Pour conclure la description de l'écoulement, remarquons que le problème est statistiquement unidimensionnel, avec  $x$  la direction inhomogène. Ainsi, par ergodicité, les moyennes statistiques peuvent être calculées par intégration sur les directions homogènes. Pour toute quantité  $q$ , on a  $\bar{q}(x) = \frac{1}{L_y L_z} \iint q(x, y, z) \cdot dy dz$ .

## Nombres sans dimension

Afin de vérifier les conditions principales de l'analyse asymptotique, nous procédons au calcul des nombres adimensionnels suivants : le nombre de Mach turbulent  $M_t$ , le nombre de Reynolds turbulent  $Re_{\lambda}$  basé sur la micro-échelle de Taylor, ainsi que le nombre de Péclet turbulent  $Pe_t$ . Ces nombres sont extraits des simulations à la position initiale de l'interface  $x = x_0$  tels que :

$$M_t \equiv \frac{\sqrt{\bar{k}}}{c_s}, Re_{\lambda} \equiv \frac{2\sqrt{15}}{3} \sqrt{\frac{\bar{\rho} \bar{k}^2}{\mu_v \bar{\varepsilon}}}, Pe_t \equiv \frac{\bar{\rho} c_p \nu_t}{\lambda} \text{ avec } \nu_t = \frac{C_{\mu} \bar{k}^2}{\bar{\varepsilon}}, \bar{k} = \frac{1}{2} \overline{u'_i u'_i}, \bar{\varepsilon} = 2 \nu_v \overline{(\partial_j u'_i)^2} \quad ,$$

qui font intervenir l'énergie cinétique turbulente  $\bar{k}$ , sa dissipation  $\bar{\epsilon}$  et la viscosité turbulente  $\nu_t$ . La constante  $C_\mu$  est fixée à 0,1 comme dans les modèles standards  $\bar{k} - \bar{\epsilon}$  [Schiestel, 2010].

Tout d'abord, la condition souhaitée ( $M_t \ll 1$ ) est satisfaite pour les trois configurations puisque l'on observe que le nombre de Mach turbulent reste toujours inférieur à 0,14. En ce qui concerne le nombre de Péclet turbulent, son évolution est représentée sur la Fig. 2.1. Les conditions suivantes sont atteintes pour chaque simulation, à partir d'environ ( $t \gtrsim 15$ ) :

$$\left\{ \begin{array}{l} \text{SP}_1 \quad : \quad \text{Re}_\lambda \gg 1 \quad \text{et} \quad \text{Pe}_t \ll M_t \ll 1 \quad , \\ \text{SP}_2 \quad : \quad \text{Re}_\lambda \gg 1 \quad \text{et} \quad \text{Pe}_t \sim M_t \ll 1 \quad , \\ \text{HP} \quad : \quad \text{Re}_\lambda \gg 1 \quad , \quad M_t \ll 1 \quad \text{et} \quad \text{Pe}_t \gg 1 \quad . \end{array} \right.$$

Ainsi, les principales conditions des relations (2.28) sont vérifiées pour les simulations  $\text{SP}_1$  et  $\text{SP}_2$ . En revanche, la simulation HP évolue dans la limite de Péclet opposée.

### Évolution générale de l'écoulement

Le développement de l'instabilité entre les deux fluides est illustré dans la Fig. 2.3. Cette dernière montre un rendu volumique direct de la concentration du fluide léger à trois moments différents et pour les simulations  $\text{SP}_1$  et HP. Plus précisément, cette figure montre la zone de mélange peu après le temps initial ( $t = 4$ ) et à un temps de transition ( $t = 17$ ). Ces temps ne sont présentés que pour la simulation à haut Péclet HP. En effet, jusqu'à ( $t \approx 17$ ), les mélanges binaires des simulations à faible et fort Péclet sont visuellement indiscernables. Cependant, à des moments plus tardifs, dans le régime pleinement turbulent, une nette divergence entre les deux simulations est observée, comme le montre la Fig. 2.3. Dans la simulation à Prandtl élevé HP, la zone de mélange sature alors que dans la simulation à faible Prandtl  $\text{SP}_1$ , les échelles de turbulence dominantes et les plus énergétiques continuent d'augmenter.

Cette divergence peut être expliquée par la différence des critères de stabilité obtenus dans les limites haut et bas Péclet. Pour la limite grand Péclet, le critère de stabilité est lié au gradient de densité corrigé par un gradient de pression adiabatique. Cette quantité peut être intégrée sur la direction inhomogène pour donner une pseudo-entropie sans dimension :  $S = \int_{-30}^x [\partial_\xi \bar{P} / (\bar{\gamma}_1 \bar{P}) - \partial_\xi \bar{\rho} / \bar{\rho}] d\xi$ . Étant donné l'orientation de la gravité dans les simulations (conduisant à  $\partial_x \bar{P} < 0$ ), la stratification dans le cas Péclet élevé est stable si S augmente avec x ( $\partial_x S > 0$ ), instable si S diminue ( $\partial_x S < 0$ ) et neutre si S est constant ( $\partial_x S = 0$ ).

Dans les présentes simulations, les profils spatiaux de la pseudo-entropie S ne sont pas monotones. Ces profils sont illustrés pour les simulations de Prandtl élevé et faible sur la figure 2.2 aux temps  $t = 0$ ,  $t = 17$  et  $t = 34$ . Le profil initial de S est le même pour toutes les simulations et est imposé par la condition hydrostatique isotherme. Plus précisément, à  $t = 0$ , on observe une diminution rapide de S à l'interface entre les deux gaz tandis que S augmente de part et d'autre de cette interface. En d'autres termes, selon le critère du nombre de Péclet élevé, l'interface est initialement instable alors que les sous-domaines qu'elle sépare sont stables. Au fur et à mesure que le mélange se déroule, la diminution interfaciale initiale rapide de S s'étend et s'aplatit jusqu'à ce qu'un profil presque constant soit atteint dans l'étendue de la zone de mélange. Pour la simulation à haut nombre de Prandtl HP, ce profil plat de S signifie que la stratification a atteint un état presque neutre et que l'instabilité n'est plus alimentée. Ainsi, la turbulence commence à décroître et finit par se dissiper. La zone de mélange cesse de croître.

Cette phénoménologie n'est pas observée pour la simulation petit Prandtl  $SP_1$ . Comme on peut le voir sur la Fig. 2.2, pour  $SP_1$ , le profil de  $S$  ne cesse de se diffuser. Même après avoir franchi le seuil élevé de neutralité de Péclet, il continue d'augmenter sur l'ensemble du domaine spatial. Pour expliquer cette différence majeure, il faut rappeler que les critères de stabilité dans la limite petit et grand Péclet ne sont pas les mêmes. Dans le cas du petit Péclet, la stabilité d'une stratification est totalement indépendante de la stratification entropique et ne dépend que du gradient de la constante des gaz  $\partial_x \bar{c}$ . Ce dernier existe si les deux gaz mélangés ont des masses molaires différentes et s'il y a un gradient de concentration moyen. Dans les simulations à faible Prandtl qui évoluent dans un régime faible Péclet (étant donné l'orientation du champ de gravité et la répartition initiale des masses molaires), la stabilité de la stratification est donnée par le signe de  $\partial_x \bar{c}$ , soit par le gradient moyen de concentration du fluide léger. Plus précisément, la stratification dans la limite petit Péclet est stable si  $\bar{c}$  décroît avec  $x$  ( $\partial_x \bar{c} < 0$ ), instable si  $\bar{c}$  augmente ( $\partial_x \bar{c} > 0$ ) et neutre si  $\bar{c}$  est constant ( $\partial_x \bar{c} = 0$ ). La concentration moyenne a un profil spatial monotone décroissant à tout moment ( $\partial_x \bar{c} \leq 0$ ) comme le montre la Fig. 2.2. Par conséquent, la stratification de la simulation faible Prandtl  $SP_1$  est toujours instable. Par conséquent, le mélange pourrait théoriquement croître indéfiniment dans le régime petit Péclet.

En conclusion, les différentes évolutions de la largeur de mélange observées dans les simulations  $SP_1$  et  $HP$  sont cohérentes avec les critères de stabilité prédits et dérivés précédemment. Ces critères reflètent l'influence du nombre de Péclet et sont une conséquence directe de l'approximation asymptotique. Ainsi, les comportements qualitativement différents entre les simulations  $SP_1$  et  $HP$  (identiques sauf pour la valeur d'opacité), est une première validation des résultats asymptotiques. Une vérification directe est proposée au paragraphe suivant.

### Validation de l'analyse asymptotique

L'une des principales prédictions de l'analyse asymptotique est l'ordre de grandeur des fluctuations de pression et de température. Pour évaluer cette prédiction, nous traçons sur la Fig. 2.4 les évolutions temporelles des rapports  $\eta_P$  et  $\eta_T$  au centre de la zone de mélange, définis par :

$$\eta_P = \frac{\sqrt{P' \cdot P'}}{\bar{P} \cdot M_t^2} \quad \text{et} \quad \eta_T = \frac{\sqrt{T' \cdot T'}}{\bar{T} \cdot Pe_t \cdot M_t} .$$

Pour que ces prédictions soient vérifiées, ces rapports doivent être de l'ordre de 1.

Comme on peut le voir sur la Fig. 2.4, le rapport  $\eta_P$  tend vers 1 dans le régime turbulent pour chaque configuration, montrant que la pression fluctuante est de l'ordre de  $M_t^2$ . Cet échelonnement est attendu car il résulte de l'analyse asymptotique à faible nombre de Mach quel que soit le nombre de Péclet. Comme le Mach atteint à peine 0,14, les trois simulations évoluent dans un régime à faible Mach.

Quant au rapport  $\eta_T$ , il est de l'ordre de l'unité pour les deux simulations petit Prandtl  $SP_1$  et  $SP_2$  dont le mélange turbulent se produit dans un régime petit Péclet. La prédiction concernant l'ordre de  $T'$  est donc vérifiée. En revanche, l'ordre de  $\eta_T$  dans la simulation à haut Prandtl  $HP$  s'écarte significativement des autres :  $\eta_T$  tend en fait vers zéro. Il n'y a en effet aucune prédiction pour l'ordre de  $T'$  dans l'analyse haut Péclet de [Soulard et al. \[2012\]](#).

Les autres prédictions majeures dérivées de l'analyse asymptotique sont les valeurs de la divergence de vitesse fluctuante  $\text{div} \mathbf{u}'$  et du terme de conduction fluctuant  $\mathcal{C}'$  (Ces prédictions sont

respectivement exprimées dans les Eqs. (2.56a) et (2.56b)). Pour évaluer leur qualité, nous comparons les valeurs "simulées" et "prédites" de  $\text{div}\mathbf{u}'$  et  $C'$ . Les valeurs "simulées" sont obtenues en prenant la partie fluctuante de  $\text{div}\mathbf{u}$  et  $C$  calculée à partir des champs réels en utilisant leurs définitions. Les valeurs "prédites" sont directement calculées (comme le côté droit des équations (2.56a) et (2.56b)) en utilisant les mêmes simulations réelles.

Les champs bidimensionnels (coupes dans le plan  $y = 0$ ) sont représentés sur les Figs. 2.5 et 2.6 pour comparer les valeurs simulées et prédites de respectivement  $C'$  et  $\text{div}\mathbf{u}'$ . Elles sont extraites de la simulation  $SP_2$  à  $t = 34$ , un temps auquel les résultats de l'analyse asymptotique petit Péclet devraient s'appliquer selon la Fig. 2.1. Les mêmes structures peuvent en effet être identifiées dans les deux parties de la Fig. 2.5 et, puisque l'échelle de couleurs est la même, on peut supposer un accord global sur l'intensité des champs de conduction fluctuants  $C'$ . La principale différence vient de l'apparition de quelques extrema localisés dans le champ simulé qui semblent être filtrés par l'utilisation de la formule asymptotique (Eq. (2.56b)). Les mêmes commentaires s'appliquent à la divergence de vitesse fluctuante montrée dans la Fig. 2.6, y compris l'effet de filtrage de l'expression asymptotique de  $\text{div}\mathbf{u}'$ .

Les Figs. 2.5 et 2.6 fournissent une évaluation qualitative des résultats asymptotiques. Une validation quantitative peut être réalisée en mesurant les corrélations de  $\text{div}\mathbf{u}'$  avec d'autres quantités turbulentes. Pour des raisons de modélisation qui seront précisées plus loin, nous nous focalisons sur les corrélations  $\overline{\rho'\text{div}\mathbf{u}'}$  et  $\overline{u'_x\text{div}\mathbf{u}'}$ . La comparaison de ces corrélations calculées avec les valeurs simulées et prédites de  $\text{div}\mathbf{u}'$  constitue *a priori* des tests des fermetures turbulentes. En outre, la valeur prédite de  $\text{div}\mathbf{u}'$  est divisée en deux contributions : celle provenant de la stratification moyenne et celle provenant des effets du mélange moléculaire. Plus précisément, à partir de l'équation (2.56a), les corrélations  $\overline{\rho'\text{div}\mathbf{u}'}$  et  $\overline{u'_x\text{div}\mathbf{u}'}$  sont exprimées comme :

$$\overline{q'\text{div}\mathbf{u}'} = \overline{q'\text{div}\mathbf{u}'}^{\text{strat.}} + \overline{q'\text{div}\mathbf{u}'}^{\text{mix.}} \quad \text{avec} \quad \begin{cases} \overline{q'\text{div}\mathbf{u}'}^{\text{strat.}} &= -\overline{q'u'_x} (\partial_j \bar{\rho} / \bar{\rho} + \partial_j \bar{r} / \bar{r}) , \\ \overline{q'\text{div}\mathbf{u}'}^{\text{mix.}} &= \Delta r / \bar{r} \cdot \overline{q' [\partial_j (\rho D \partial_j c') / \rho]} , \end{cases}$$

où la quantité  $q'$  représente  $u_x$  ou  $\rho'$  et où  $\Delta r = \mathcal{R} / \mathcal{M}_l - \mathcal{R} / \mathcal{M}_h$ .

Les corrélations simulées et prédites  $\overline{\rho'\text{div}\mathbf{u}'}$  et  $\overline{u'_x\text{div}\mathbf{u}'}$  sont représentées sur les Figs. 2.7, ainsi que les composantes de la valeur prédite, aux temps  $t = 17$  et  $t = 34$ . Un bon accord entre la simulation et la prédiction est observé pour les deux corrélations aux deux temps, indiquant que l'expression asymptotique de  $\text{div}\mathbf{u}'$  fournit des estimations quantitativement précises. Les contributions de la stratification et du mélange moléculaire ont des signes opposés à cause de l'instabilité : la production barocline liée à la stratification tend à intensifier le flux de masse turbulent et la variance de la densité alors que la diffusion moléculaire tend à diminuer la valeur des corrélations de densité. Au fur et à mesure que le temps s'écoule, le nombre de Reynolds augmente et on constate que l'intensité relative de la contribution moléculaire diminue par rapport à la contribution de la stratification.

Pour résumer, les principaux résultats de l'approximation faible Mach-faible Péclet ont été vérifiés. Les ordres de grandeur de  $T'$  et  $P'$  et les valeurs de  $\text{div}\mathbf{u}'$  et  $C'$  sont tous cohérents avec les prédictions asymptotiques.

## Chapitre 3 - Application à la modélisation de la turbulence

L'une de nos principales motivations pour étudier la limite asymptotique faible Mach-faible Péclet est de comprendre comment les modèles de turbulence à un point du second ordre peuvent être conçus ou modifiés pour tenir compte de ce régime. Nous considérons la modélisation de type Reynolds Average Navier-Stokes (RANS) et nous nous concentrons sur la classe des modèles "Reynolds Stress model" (RSM). Un RSM particulier : le modèle GSG [Grégoire *et al.*, 2005], est utilisé ici pour tester des modifications. Il est en effet particulièrement intéressant pour les applications stellaires puisqu'il permet de traiter des zones de mélange turbulent à densité variable, soumises à une grande variété d'instabilités convectives. Cependant, dans sa formulation actuelle, il est restreint aux grands nombres de Péclet et doit être adapté à la limite faible Péclet.

### Adaptation d'un modèle de type Reynolds Stress Model

Le modèle GSG [Griffond & Souldard, 2014, Grégoire *et al.*, 2005] suit les évolutions des corrélations des champs de vitesse et de densité, notamment le flux de masse  $\overline{\rho' u'_i} / \bar{\rho}$  et la variance de la densité  $\overline{\rho'^2} / \bar{\rho}^2$ . L'évolution de la densité fluctuante est donnée au premier ordre par l'Eq. (2.63). Parmi les principales inconnues apparaissant dans les évolutions de  $\overline{\rho' u'_i} / \bar{\rho}$  et  $\overline{\rho'^2} / \bar{\rho}^2$  se trouvent respectivement les corrélations  $\overline{u'_i \text{div} \mathbf{u}'}$  et  $\overline{\rho' \text{div} \mathbf{u}'}$ . Dans la limite petit Péclet, ces termes peuvent être fermés en substituant la valeur de  $\text{div} \mathbf{u}'$  par son expression asymptotique. On obtient pour ( $\text{Pe}_t \ll 1$ ) avec  $q'$  représentant  $u'_i$  ou  $\rho'$   $\overline{q' \text{div} \mathbf{u}'}|_{\text{Pe}_t \ll 1} = -\overline{q' u'_j} [\partial_j \bar{\rho} / \bar{\rho} + \partial_j \bar{r} / \bar{r}] + \overline{q' \text{div} \mathbf{u}'}^{\text{mix}}$ , où  $\overline{q' \text{div} \mathbf{u}'}^{\text{mix}}$  est la contribution à  $\text{div} \mathbf{u}'$  liée au mélange moléculaire. Nous proposons de modéliser ces effets moléculaires comme une dissipation agissant sur les fluctuations de densité :  $\overline{q' \text{div} \mathbf{u}'}^{\text{mix}} \propto \omega \cdot \rho' q' / \bar{\rho}$ . Ainsi, le modèle suivant est obtenu dans la limite petit Péclet :

$$\overline{u'_i \text{div} \mathbf{u}'}|_{\text{Pe}_t \ll 1} = -\overline{u'_i u'_j} [\partial_j \bar{\rho} / \bar{\rho} + \partial_j \bar{r} / \bar{r}] + C_1 \omega \overline{\rho' u'_i} / \bar{\rho} \quad \text{et} \quad \overline{\rho' \text{div} \mathbf{u}'}|_{\text{Pe}_t \ll 1} = -\overline{\rho' u'_i} [\partial_j \bar{\rho} / \bar{\rho} + \partial_j \bar{r} / \bar{r}] + C_2 \omega \overline{\rho'^2} / \bar{\rho} .$$

où  $C_1$  et  $C_2$  sont des constantes et  $\omega = \bar{\varepsilon} / \bar{k}$  est la fréquence turbulente caractéristique.

Ces fermetures sont différentes de celles retenues dans la formulation initiale à grand Péclet du modèle GSG. En effet, sur la base de l'équation (2.62), la formulation actuelle du modèle GSG, proposée pour ( $\text{Pe}_t \gg 1$ ) dans Souldard *et al.* [2012] est :

$$\overline{u'_i \text{div} \mathbf{u}'}|_{\text{Pe}_t \gg 1} = -\overline{u'_i u'_j} \partial_j \bar{P} / (\bar{\gamma}_1 \bar{P}) + C_1 \omega \overline{\rho' u'_i} / \bar{\rho} \quad \text{et} \quad \overline{\rho' \text{div} \mathbf{u}'}|_{\text{Pe}_t \gg 1} = -\overline{\rho' u'_i} \partial_j \bar{P} / (\bar{\gamma}_1 \bar{P}) + C_2 \omega \overline{\rho'^2} / \bar{\rho} .$$

Par conséquent, la principale adaptation du modèle GSG à la limite petit Péclet nécessite la modification des termes de production apparaissant dans les équations de variance de densité et de flux de masse turbulente. Cette différence n'affecte pas seulement les niveaux des corrélations liées à la densité, elle modifie également le critère d'instabilité de flottabilité auquel le modèle est susceptible de réagir. Enfin, pour combler l'écart entre les petits et les grands nombres de Péclet, nous proposons d'effectuer un raccord pondéré des deux limites sous la forme :

$$\overline{q' \text{div} \mathbf{u}'} = (1 - \omega_{\text{Pe}_t}) \overline{q' \text{div} \mathbf{u}'}|_{\text{Pe}_t \ll 1} + \omega_{\text{Pe}_t} \overline{q' \text{div} \mathbf{u}'}|_{\text{Pe}_t \gg 1} \quad \text{avec} \quad \omega_{\text{Pe}_t} = \frac{\text{Pe}_t^{\text{lim}}}{\text{Pe}_t^{\text{lim}} + \text{Pe}_t} \quad \text{et} \quad \text{Pe}_t^{\text{lim}} = 2C_\mu = 0.2 ,$$

où la quantité  $q'$  représente  $u'_i$  ou  $\rho'$ . La valeur de  $\text{Pe}_t^{\text{lim}}$  est interprétée comme un paramètre de transition entre les régimes de Péclet élevé et faible.

## Validation du RSM étendu

Afin de valider le modèle de fermeture, les trois DNS du mélange Rayleigh-Taylor radiatif sont comparés aux trois RANS 1D effectuées avec le modèle GSG modifié. Ces dernières sont initialisées à  $t = 9$  avec des profils 1D pour les moyennes et les corrélations calculées à partir des DNS au même instant. Le même ensemble de coefficients de modèle est utilisé dans les trois cas.

Les Figs. 3.1, 3.2 et 3.3 comparent les quantités turbulentes extraites des trois DNS  $SP_1$ ,  $SP_2$  et HP à celles prédites par le modèle GSG adapté à tous les régimes de Péclet en utilisant le raccord précédent (voir Eq. (3.11)). Les Figs. 3.1 et 3.2 représentent l'évolution temporelle de l'énergie cinétique turbulente  $\tilde{k}$  et de la variance de la densité normalisée  $\overline{\rho'^2}/\bar{\rho}^2$  à l'abscisse initiale de l'interface  $x = x_0$  tandis que la figure 3.3 représente la largeur de la zone de mélange turbulent définie comme suit  $\mathcal{L}_{TMZ} = 6 \int_{L_x} \tilde{c} (1 - \tilde{c}) dx$ .

On peut constater que le modèle GSG étendu reproduit les principales tendances observées dans les simulations et permet de capturer les différences entre les régimes grand et petit Péclet. Par exemple, dans la limite grand Péclet (HP), une diminution de l'énergie cinétique turbulente à  $x = 0$  est observée pendant le dernier tiers du calcul ainsi qu'un ralentissement de l'expansion de la ZMT (Zone de Mélange Turbulent). Ce déclin du champ turbulent a déjà été expliqué précédemment. Elle est due au fait que le profil de pseudo-entropie moyenne  $S$  se rapproche de sa valeur neutre à l'intérieur de la ZMT de sorte que le mécanisme d'instabilité cesse d'alimenter la zone de mélange turbulent alors que la viscosité dissipe encore l'énergie cinétique turbulente.

En revanche, dans la limite petit Péclet ( $SP_1$ ), l'instabilité dépend du gradient de masse molaire qui garde le même signe de sorte qu'il transfère sans cesse de l'énergie au champ turbulent. Ceci explique la croissance continue dans la Fig. 3.1 et l'expansion accélérée dans la Fig. 3.3.

Le comportement de la variance de densité dans la Fig. 3.2 résulte de la compétition entre la diffusion moléculaire qui tend à détruire cette variance et du transport turbulent du fluide pur "frais", englouti au bord de la zone de mélange, et transporté à travers la ZMT. L'expansion plus rapide de la ZMT dans  $SP_1$  permet de maintenir une décroissance lente de la variance alors que la diffusion moléculaire n'est presque pas contrebalancée pour HP.

Entre ces deux cas limites, la simulation Prandtl intermédiaire  $SP_2$  présente un équilibre plus subtil entre les différents mécanismes. Commencant dans un régime à faible Péclet, elle suit d'abord la même évolution que  $SP_1$ , mais ce faisant, sa diffusivité turbulente augmente rapidement ainsi que son nombre de Péclet, comme le montre la Fig. 2.1. Lorsque ce dernier devient non négligeable, la production de l'instabilité se réduit et devient d'un ordre similaire à la dissipation moléculaire, conduisant à une évolution marginale de l'énergie cinétique turbulente. Le transfert de fluide pur depuis les bords de la ZMT ralentit alors, laissant la variance de densité diminuer beaucoup plus rapidement dans  $SP_2$  que dans  $SP_1$ . Capturer ce comportement limite est un défi et la valeur  $Pe_t^{\text{lim}}$  au sein du raccord est précisément choisie pour obtenir une transition correct.

En conclusion, l'application du modèle petit Mach-petit Péclet dans le modèle GSG RANS s'avère efficace pour prédire l'instabilité radiative dans la limite ( $Pe_t \ll 1$ ). L'extension de la fermeture pour tous les régimes de Péclet, grâce au modèle de raccord, permet au RSM de capturer correctement les effets de l'intensité relative du transfert radiatif et du transport turbulent dans le cas du mélange turbulent considéré.

## Chapitre 4 - Analyse linéaire de stabilité

Cette partie est consacrée à une analyse linéaire de stabilité (ALS) de l'équilibre hydrostatique stratifié du mélange binaire considéré dans les chapitres précédents. L'objectif subséquent de cette analyse est d'améliorer le modèle de raccord précédent qui, au lieu d'utiliser un ajustement *ad hoc*, pourra être basé sur des considérations physiques.

### Équations régissant l'écoulement et hypothèses pour l'ALS

#### Équations régissant l'écoulement hydro-radiatif compressible

On s'appuie sur les équations de Navier-Stokes couplées au champ radiatif, traité dans la limite de diffusion (Sys. (4.1)), qui incluent la viscosité et la diffusion interspécifique.

#### Approche quasi-homogène et état d'équilibre isotherme

L'analyse de stabilité linéaire (ALS) nécessite la prescription d'un écoulement de base satisfaisant le système précédent. Pour toute quantité  $q$ , l'écoulement de base correspondant est noté  $\bar{q}$ . Nous considérons ici l'équilibre hydrostatique (sans cisaillement) dans un champ de gravité orienté selon la direction  $z$ . On a alors  $\bar{q}(x, y, z, t) = \bar{q}(z)$  et  $\bar{\mathbf{u}} = 0$ . De petites perturbations  $q'$  sont superposées à l'écoulement de base, de sorte que toute quantité instantanée  $q$  s'écrit  $q(x, y, z, t) = \bar{q}(z) + q'(x, y, z, t)$ . On recherche des solutions spécifiques ayant la forme  $q'(x, y, z, t) = \check{q}(z) e^{i(k_x x + k_y y - \omega t)}$ , impliquant des perturbations de longueur d'onde  $\lambda_w = 2\pi / \sqrt{k_x^2 + k_y^2}$ . Afin de rendre les calculs réalisables, la stabilité du système est étudiée dans le cadre d'une approche quasi-homogène. On suppose donc que la longueur d'onde des perturbations est petite par rapport à la longueur de gradient des quantités de base :  $\lambda_w \ll |\bar{q} / \partial_z \bar{q}|$ . Cette approche donne donc lieu à des hypothèses apparemment incohérentes selon lesquelles les quantités de base et leur gradient sont tous deux uniformes :

$$\partial_z \bar{q} \approx \text{const.} \quad \text{and} \quad \bar{q}(z) \approx \text{const.} \quad .$$

Les modes normaux, correspondant aux modes propres de la transformée de Fourier du système linéaire, ont donc la forme  $q'(x, y, z, t) = \hat{q} e^{i(k_x x + k_y y + k_z z - \omega t)}$ . Pour étudier la stabilité temporelle, le vecteur d'onde  $\mathbf{k} = (k_x, k_y, k_z)$  est donné comme réel ( $\mathbf{k} \in \mathbb{R}^3$ ) tandis que  $\omega \in \mathbb{C}$  est complexe avec  $\omega_i = \Im(\omega)$  le taux de croissance du mode. Le nombre d'onde est la norme du vecteur d'onde  $k = \sqrt{k_x^2 + k_y^2 + k_z^2}$  avec  $k_\perp = \sqrt{k_x^2 + k_y^2}$  le nombre d'onde transverse. La longueur d'onde vérifie  $\lambda_w = 2\pi/k$ .

L'état de base est supposé isotherme. La gravité est supposée orientée le long de l'axe  $z$ , de sorte que  $\mathbf{g} = (0, 0, -g_0)$ . Comme les deux gaz du mélange sont choisis égaux, le rapport des chaleurs spécifiques des matériaux  $\gamma^m$  est constant et donc égal à  $\bar{\gamma}^m$ . Ensuite, les quantités de l'écoulement sont contraintes par l'équilibre isotherme avec la relation  $\bar{\gamma}^m g_0 / \bar{c}_s^m = \partial_z \bar{\tau} / \bar{\tau} - \mathcal{A}_r \partial_z \bar{c}$  avec  $\bar{c}_s^m = \sqrt{\bar{\gamma}^m \bar{\tau} \bar{P}^m}$  la vitesse du son matière et  $\mathcal{A}_r = (r_a - r_b) / \bar{r}$  un paramètre interprété comme le double du nombre négatif d'Atwood concernant le contraste des masses molaires. Enfin, pour des raisons de simplicité, le profil de concentration est supposé linéaire :  $\partial_{zz}^2 \bar{c} = 0$ .

## Relations de dispersion

### Relation de dispersion "tout Mach" à l'équilibre thermique pour tout angle d'onde

L'insertion des modes normaux dans les équations perturbées autour de l'état d'équilibre isotherme permet la dérivation de la relation de dispersion (Eq. (4.36)) à l'équilibre thermique pour tout angle d'onde et tout régime de Mach. Cette dernière prend la forme d'un polynôme d'ordre 5.

#### Limite non-radiative et non-diffusive

En particulier, en l'absence de rayonnement et de diffusion interspécifique, cette équation se réduit à un polynôme d'ordre 4 directement soluble :

$$\frac{1}{k^2 \bar{c}_s^2} \left[ \omega \left( \omega + i\nu_v k^2 \right) \right]^2 - \left( 1 + \frac{\partial_z \bar{\tau}}{\bar{\tau}} \frac{g_0}{k^2 \bar{c}_s^2} \right) \left[ \omega \left( \omega + i\nu_v k^2 \right) \right] + \frac{k_\perp^2}{k^2} g_0 \partial_z \bar{s} = 0 \quad .$$

Deux paires de solutions peuvent être distinguées : l'une est liée aux effets acoustiques tandis que l'autre persiste dans la limite incompressible. Cette dernière décrit l'instabilité classique incompressible de Rayleigh-Taylor avec une croissance exponentielle lorsque  $(g_0 \cdot \partial_z \bar{s} \leq 0)$  et des modes neutres correspondant aux ondes de gravité lorsque  $(g_0 \cdot \partial_z \bar{s} \geq 0)$ .

Les chapitres précédents ont montré que le rayonnement peut modifier la condition de stabilité d'une manière qui sera décrite ci-dessous. En particulier, même si la condition de stabilité sans rayonnement  $(g_0 \cdot \partial_z \bar{s} \geq 0)$  est respectée, un fort transport radiatif peut déstabiliser l'écoulement. On se concentre particulièrement sur les deux modes (de l'Eq. (4.37)) qui peuvent être approximés, dans la limite incompressible  $(\bar{c}_s \rightarrow 0)$  et inviscide  $(\nu_v \rightarrow 0)$ , par  $\omega \approx \pm \frac{k_\perp}{k} \sqrt{g_0 \cdot \partial_z \bar{s}}$ , car ces ondes de gravité "oscillantes" peuvent passer d'un comportement stable à un comportement instable dans le cas radiatif, en fonction du nombre de Péclet.

### Relation de dispersion à l'équilibre thermique pour les modes transverses

Les relations de dispersion évoquées précédemment sont difficiles à résoudre analytiquement. Leur résolution numérique indique que le taux de croissance maximal est fréquemment obtenu pour les modes transverses, soit pour  $k_\perp = k$  et  $k_z = 0$ . Cela suggère que le caractère stable ou instable de l'écoulement peut être évalué à partir de la seule analyse des modes transverses.

Soit  $\mathfrak{P}$  l'espace des paramètres qui comprend les coefficients visco-diffusifs  $(\nu_v, \mathcal{D}_c, \chi_p^r)$ , les exposants adiabatiques  $(\bar{\gamma}, \bar{\gamma}_3)$ , la gravité  $(g_0)$ , les composantes du vecteur onde  $(k_\perp, k_z)$ , certaines quantités moyennes  $(\bar{c}_s, \bar{\tau})$  et les gradients  $(\partial_z \bar{c}, \partial_z \bar{\tau}, \partial_z \bar{s})$ . Pour chaque ensemble de paramètres  $\mathfrak{p} \in \mathfrak{P}$ , le polynôme d'ordre 5 a cinq racines  $\omega^m$  pour  $m \in \{1, 2, 3, 4, 5\}$ . De là, nous distinguons cinq modes comme étant les racines qui peuvent être connectées de manière continue en laissant  $\mathfrak{p}$  couvrir l'espace  $\mathfrak{P}$ . L'étude suivante se concentre sur les hypersurfaces de neutralité, notées  $\mathcal{N}$ , de l'espace paramétrique  $\mathfrak{P}$ . Pour chaque mode  $m$ , on définit l'hypersurface de neutralité  $\mathcal{N}^m$  telle que, pour  $\mathfrak{p} \in \mathcal{N}^m$ , on a  $\omega_1^m(\mathfrak{p}) = 0$ , avec  $\omega_1^m = \Im m(\omega^m)$  la partie imaginaire de la racine  $\omega^m$  correspondant au mode  $m$ .

On espère que si tous les modes transverses sont stables, alors tous les modes sont stables quel que soit leur vecteur d'onde. La stabilité de l'écoulement serait alors entièrement pilotée par les modes transverses. Seules des vérifications numériques peuvent être proposées.

## Relations de dispersion "bas Mach" et "bas Mach-bas Péclet" à l'équilibre thermique pour tout angle d'onde

Pour rappel, le modèle bas Mach a été dérivé à l'équilibre thermique par [Souard \*et al.\* \[2012\]](#), et conduit à la prédiction :  $\partial_j \mathbf{u}_j' = -\mathbf{u}_z' \partial_z \bar{P} / (\bar{\gamma}_1 \bar{P}) + (\bar{\gamma}_3 - 1) \mathcal{C}' / (\bar{\gamma}_1 \bar{P}) + \mathcal{D}_p' / (\bar{\gamma}_1 \bar{P})$ . Lorsqu'insérée dans le système linéaire perturbé, cette relation donne lieu à une relation de dispersion (4.66) à l'équilibre thermique, pour tout angle d'onde et pour ( $M_t \ll 1$ ). De même, à partir de l'expression asymptotique de l'analyse bas Mach-bas Péclet, on dérive la prédiction :  $\partial_j \mathbf{u}_j' = \mathbf{u}_z' (\partial_z \bar{\tau} / \bar{\tau} - \mathcal{A}_r \partial_z \bar{c}) + \mathcal{D}_c \mathcal{A}_r \partial_{jj}^2 c'$ , ce qui, de la même manière que précédemment, conduit à une relation de dispersion (4.76) dans la limite ( $M_t \ll 1 ; Pe_t \ll 1$ ).

## Hypersurfaces de neutralité "tout Mach", "bas Mach" et "bas Mach-bas Péclet" à l'équilibre thermique pour les modes transverses

L'obtention des relations de neutralité étudiées revient à trouver des solutions pour toutes les relations de dispersion avec  $\omega_i = 0$ . Deux cas différents doivent être distingués en ce qui concerne la partie réelle  $\omega_r = \Re \epsilon(\omega)$  qui peut être soit nulle soit non nulle. Lorsque  $\omega_r = 0$ , les modes sont "non-oscillants". Le franchissement de la surface de neutralité conduit à une croissance exponentielle pure sans oscillation. Ce cas peut être rapproché de la convection "fingering" de [Garaud \[2018\]](#). D'autre part, lorsque  $\omega_r \neq 0$ , les modes sont "oscillants". Le franchissement de la surface de neutralité conduit à des oscillations temporelles amplifiées dans une enveloppe exponentielle. A l'exception des ondes acoustiques, ce second cas peut être rapproché de l'instabilité convective "oscillante double-diffusive" de [Garaud \[2018\]](#).

Les hypersurfaces de neutralités dérivés dans ce chapitre sont référencées dans le tableau A. Elles correspondent aux critères de stabilité marginale obtenus dans les régimes "tout Mach", "bas Mach" et "bas Mach-bas Péclet" à l'équilibre thermique pour les modes transverses, ainsi que leurs limites lorsque ( $\mathcal{D}_c^2 k^4 \rightarrow 0$ ), avec  $\mathcal{D}_c$  la diffusion scalaire. Cette dernière trouvera son utilité dans la spécification du raccord du modèle GSG modifié.

Régime (limite)	Dénomination de l'hypersurface de neutralité	Relation(s) de dispersion	Type de mode(s)
$\forall M_t ; \forall Pe_t$	$\mathcal{N}_{\text{Non-osc.}}$	Eq. (4.41)	non-oscillant
$\forall M_t ; \forall Pe_t ; \mathcal{D}_c^2 k^4 \rightarrow 0$	$\mathcal{N}_{\text{Non-osc.}}^0$	Eq. (4.42)	non-oscillant
$\forall M_t ; \forall Pe_t$	$\mathcal{N}_{\text{Osc.}}^X$ et $\mathcal{N}_{\text{Osc.}}$	Eqs. (4.47) et (4.48)	oscillants
$\forall M_t ; \forall Pe_t ; \mathcal{D}_c^2 k^4 \rightarrow 0$	$\mathcal{N}_{\text{Osc.}}^0$	Eq. (4.49)	oscillants
$M_t \ll 1 ; \forall Pe_t$	$\mathcal{N}_{\text{Non-osc.}}^{\text{SM}}$	Eq. (4.69)	non-oscillant
$M_t \ll 1 ; \forall Pe_t ; \mathcal{D}_c^2 k^4 \rightarrow 0$	$\mathcal{N}_{\text{Non-osc.}}^{\text{SM}0}$	Eq. (4.70)	non-oscillant
$M_t \ll 1 ; \forall Pe_t$	$\mathcal{N}_{\text{Osc.}}^{\text{SM}}$	Eq. (4.72)	oscillants
$M_t \ll 1 ; \forall Pe_t ; \mathcal{D}_c^2 k^4 \rightarrow 0$	$\mathcal{N}_{\text{Osc.}}^{\text{SM}0}$	Eq. (4.73)	oscillants
$M_t \ll 1 ; Pe_t \ll 1$	$\mathcal{N}_{\text{Non-osc.}}^{\text{SMSP}}$	Eq. (4.79)	non-oscillant

Table A – Récapitulatif des hypersurfaces de neutralité.

## Résultats numériques

### Relation de dispersion générale à l'équilibre thermique

On considère dans cette section la relation de dispersion générale à l'équilibre thermique (4.36) ainsi que les hyper-surfaces de neutralité subséquentes. On s'intéresse en particulier au ratio  $Le^{-1} = \mathcal{D}_c / \chi_{\text{equi}}^r$  (inverse du nombre de Lewis), avec  $\chi_{\text{equi}}^r$  la diffusivité radiative, qui constitue un analogue du nombre de Péclet si on établit l'analogie entre diffusion-viscosité physique et diffusion-viscosité turbulente dans le cadre d'une modélisation de la turbulence.

### Adimensionnement pour la résolution numérique

Les résolutions numériques sont obtenues pour un ensemble de paramètres d'adimensionnement choisi arbitrairement tel que les seuls paramètres libres définissant l'état d'équilibre sont  $\{\bar{\gamma}^m, \mathcal{A}_r, 1/\bar{\gamma}\}$ , desquels les quantités apparaissant dans les relations de dispersion sont issues, soit :  $\partial_z \bar{\tau} / \bar{\tau} = \partial_z \bar{c} = 1$ ,  $g_0 = +1$ ,  $\bar{c}_s^2 = \bar{\gamma} / (1 - \mathcal{A}_r)$ ,  $\partial_z \bar{s} = 1 + (\mathcal{A}_r - 1) / \bar{\gamma}$ , avec  $\mathcal{A}_r = (r_a - r_b) / \bar{r}$  et  $1/\bar{\gamma} = \bar{P}^m / (\bar{\gamma}_1 \bar{P})$ .

### Phénoménologie

La figure 4.1 montre les suivis de  $\omega_i$  dans les plans  $(\mathcal{A}_r, \log_{10} [1/Le])$  et  $(\log_{10} [\mathcal{D}_c], \log_{10} [1/Le])$ . Le champ tracé en niveaux de gris est obtenu par résolution numérique des racines de la relation (4.36). Dans le côté droit de chaque sous-figure, on a ( $\omega_i < 0$ ) : l'écoulement est donc stable pour le jeu de paramètres choisi. Des zones instables ( $\omega_i > 0$ ) sont situées sur le côté gauche.

On remarque d'abord sur la Fig. 4.1 que l'union de  $\mathcal{N}_{\text{Non-osc.}}$  et  $\mathcal{N}_{\text{Osc.}}$  couvre exactement l'isovaleur "0" de la solution numérique : ceci indique que les premiers modes qui deviennent instables sont les modes transverses. Les accords entre les courbes "exactes" et approximatives  $\mathcal{N}_{\text{Non-osc.}}$  et  $\mathcal{N}_{\text{Non-osc.}}^0$ , ainsi qu'entre  $\mathcal{N}_{\text{Osc.}}$  et  $\mathcal{N}_{\text{Osc.}}^0$ , sont jugés en comparant les lignes en pointillés et en tirets. Elles sont correctes pour des  $k$  et  $\mathcal{D}_c$  modérés ou, plus précisément, dans la limite  $[(\mathcal{D}_c k^2) \rightarrow 0]$ . On peut également voir sur la Fig. 4.1 que le mode "non-oscillant" définit une zone instable dans le coin inférieur gauche des sous-figures alors que les modes "oscillants" définissent une zone instable dans le coin supérieur gauche.

Ce comportement est illustré sur la Fig. 4.2 qui clarifie également la désignation des modes "oscillant" et "non-oscillant". La Fig. 4.2 montre un suivi dans le plan complexe, lorsque  $Le^{-1} = \mathcal{D}_c / \chi_{\text{equi}}^r$  varie, des modes transverses ( $k_{\perp} = k$ ) correspondant aux cinq racines de la relation de dispersion (4.36). A l'exception de la Fig. 4.2-(a) où  $k = 2$  pour une meilleure lisibilité, les paramètres sélectionnés correspondent aux chemins verticaux de la Fig. 4.1 reliant deux zones instables par une zone stable. Les cinq modes sont représentés sur la Fig. 4.2-(a), dont la paire de modes externes est liée aux effets de compressibilité et n'est pas pertinente ici. Les Figs. 4.2-(b,c) proposent un zoom sur les modes étiquetés "non-oscillant" ( $\omega_r = 0$ ) et "oscillant" ( $\omega_r \neq 0$ ). La Fig. 4.2 montre que les modes "non-oscillant" et "oscillant" réagissent de manière opposée à l'évolution de l'inverse du nombre de Lewis  $Le^{-1}$ .

En anticipant sur l'analogie entre  $Pe_t$  et  $Le^{-1}$  (tous deux comparant les échelles de temps diffusives, turbulentes ou moléculaires, aux échelles de temps du transport radiatif), la figure montre que le mode "non-oscillant" est stable à grand nombre de Péclet mais est déstabilisé quand ce dernier devient petit. Les modes "oscillants" ont un comportement opposé.

La figure 4.3 montre l'évolution des parties réelle et imaginaire du mode le moins stable ou instable par rapport à l'angle d'onde mesuré par  $k_{\perp}/k$  pour trois valeurs du rapport  $Le^{-1} = \mathcal{D}_c/\chi_{\text{equi}}^r$  : 0.1, 1 et 10. Elle compare les solutions obtenues à partir de la relation de dispersion (4.36) compressible, de la relation (4.66) bas Mach et de l'Eq. (4.76) bas Péclet. Un bon accord de la limite bas Mach avec la solution générale peut être remarqué pour les trois nombres de  $Le$  (les lignes bleues et rouges sont presque superposées, au moins pour  $\omega_i$ ). Pour les paramètres testés, l'angle qui maximise le  $\omega_i$  est  $k_{\perp}/k = 1$ . La Fig. 4.3-(a) est dominée par le mode dit "non-oscillant" (bien que  $\omega_r \neq 0$  pour  $k_{\perp}/k \neq 1$ ) alors que la figure 4.3-(c) est dominée par la paire de modes dits "oscillants" (le saut d'un mode à l'autre du couple  $(\omega_1, \omega_2)$  caractérisé par  $\omega_2 \approx -\overline{\omega_1}$ , soit le complexe conjugué ici, explique la discontinuité dans l'évolution de  $\omega_r$ ).

### Relation de dispersion dans la limite bas Mach et bas Mach-bas Péclet

Après les résultats généraux obtenus dans la limite compressible, nous nous intéressons au régime bas Mach qui s'apparente davantage à établir des connexions avec l'analyse asymptotique et la modélisation turbulente de ce travail. Pour ce faire, on considère la comparaison de la relation de dispersion générale à l'équilibre thermique (4.36) et des relations correspondantes en limite bas Mach et bas Mach-bas Péclet, ainsi que les hyper-surfaces de neutralité subséquentes.

La figure 4.8 traite d'un suivi dans le plan complexe des racines des relations de dispersion (4.36), (4.66) et (4.76) lorsque le rapport  $Le^{-1} = \mathcal{D}_c/\chi_{\text{equi}}^r$  varie. Les racines de la relation de dispersion générale (4.36) et celle obtenue dans la limite "tout Péclet" à bas Mach (Eq. (4.66)) sont respectivement représentées par des cercles et des croix dont les couleurs arc-en-ciel codent la valeur de  $Le^{-1}$ . La limite bas Mach-bas Péclet dans l'Eq. (4.76) ne dépend pas du nombre de Lewis et les deux modes correspondants sont représentés par des carrés noirs.

La figure 4.8-(a) confirme que l'approximation petit Mach filtre les modes acoustiques de la relation de dispersion générale. Ces derniers correspondent aux cercles les plus à gauche et les plus à droite de la figure alors que les croix de l'approche petit Mach ne sont présentes que dans la zone centrale avec les trois modes restants. La figure 4.8-(b) propose un zoom sur la zone centrale pour différents paramètres. Elle confirme que les deux modes de l'approximation petit Mach-petit Péclet correspondent bien à la limite  $[Le^{-1} = \mathcal{D}_c/\chi_{\text{equi}}^r \rightarrow 0]$  de deux des trois modes de l'approche petit Mach "tout Péclet", ou des modes centraux de la relation générale. On remarque que la solution instable ( $\omega_i > 0$ ) du régime petit Péclet peut être reliée de façon continue au mode "non-oscillant" ("fingering") décrit précédemment, alors que la solution stable ( $\omega_i < 0$ ) est reliée aux deux modes oscillants de type "ondes de gravité".

La Fig. 4.9 représente les cartes d'instabilité selon les mêmes conventions que dans la Fig. 4.1 mais ajoute les courbes de neutralité (des modes transverses) provenant de l'approche "tout Péclet" à faible Mach, donnée par les équations (4.72) et (4.73) et de la limite bas Mach-bas Péclet, donnée par l'équation (4.79). Comme déjà mentionné, les courbes de neutralité du mode "non oscillant" dans l'approche "tout Péclet" à petit Mach sont similaires à celles du cas général (exactement pour  $\mathcal{N}_{\text{Non-osc.}}^{\text{SM}^0}$  et approximativement pour  $\mathcal{N}_{\text{Non-osc.}}^{\text{SM}}$ ) et n'ont pas été ajoutées ici. Comme pour les paramètres de la Fig. 4.9, les courbes de l'approche à faible Mach et celles du cas général sont superposées aux différents niveaux d'approximation (courbes bleues et vertes). La frontière caractérisée par le régime petit Mach-petit Péclet (lignes pointillées violettes) définit une limite correctement vérifiée lorsque  $(\mathcal{D}_c/\chi_{\text{equi}}^r \ll 1)$ .

## Implications pour le modèle RSM turbulent

Ayant obtenu des critères analytiques définissant la stabilité marginale des configurations Rayleigh-Taylor radiatifs par rapport à l'efficacité du transport radiatif, nous essayons maintenant de les utiliser afin d'améliorer le raccord du RSM entre les petits et grands régimes de Péclet.

Les résultats précédents concernent des écoulements laminaires impliquant des processus moléculaires ne s'appliquant pas à la turbulence modélisée par le RSM. Cependant, une analogie peut être faite entre la viscosité, la diffusivité turbulente et leurs équivalents moléculaires.

### Analogie avec le modèle RSM radiatif turbulent

L'analogie est établie en connectant le Sys. (4.1) visco-diffusif radiatif avec le Sys. (3.1) régissant les quantités moyennes du modèle turbulent RSM, comme introduit dans le chapitre 3. Cela mène à une analogie entre le nombre de Péclet turbulent et le nombre de Lewis :  $Le^{-1} \leftrightarrow Pe_t/\bar{\gamma}$ .

### Amélioration du modèle de raccord

Nous nous concentrons sur le raccord (3.11) du modèle RSM adapté, où la fonction de pondération  $\omega_{Pe_t}$  a été introduite afin de combler l'écart entre les limites asymptotiques de Péclet. Jusqu'à présent, le paramètre  $Pe_t^{lim}$  a été choisi par un ajustement sur trois simulations numériques. Un choix basé sur des considérations physiques est maintenant proposé à partir de l'ALS.

### Stabilité marginale "fingering" et son implication dans la production de Rayleigh-Taylor

Le critère de stabilité concernant une configuration RT radiatif est d'abord dérivé du système (3.17) du modèle turbulent adapté. Par conséquent, le système est stable à condition que :

$$\partial_1 \bar{s} \cdot \frac{\partial_1 \bar{P}}{\bar{\rho}} < 0 \text{ pour } (Pe_t \gg 1) \quad \text{et} \quad \frac{\partial_1 \tilde{r}}{\tilde{r}} \cdot \frac{\partial_1 \bar{P}}{\bar{\rho}} < 0 \text{ pour } (Pe_t \ll 1) \quad .$$

La stabilité marginale du modèle GSG est atteinte lorsque l'Eq. (4.96) est égal à zéro. Par analogie avec les résultats de l'ALS, elle se réécrit comme une hypersurface de neutralité équivalente :

$$\mathcal{N}_{GSG} : \quad g_0 \omega_{Pe_t} \frac{\partial_1 \tilde{r}}{\tilde{r}} + g_0 (1 - \omega_{Pe_t}) \partial_1 \bar{s} = 0 \quad .$$

### Modèles de raccord de l'ALS

L'ALS a montré que, pour des régimes de Péclet petits à modérés, la stabilité de l'écoulement est dominée par des modes non-oscillants liés à l'instabilité "fingering" [Garaud, 2018]. Dans la limite des grands nombres d'onde, une telle stabilité est donnée par la relation (4.42), qui peut être réécrite :

$$\mathcal{N}_{Non-osc.}^0 : \quad g_0 \left( 1 - \bar{\gamma}_3 Le^{-1} \right) \frac{\partial_z \tilde{r}}{\tilde{r}} + g_0 \bar{\gamma} Le^{-1} \partial_z \bar{s} = 0 \quad ,$$

et qui peut être interprété comme une combinaison convexe entre les gradients de masse molaire et de pseudo-entropie pilotant la stabilité dans les limites asymptotiques, à condition que :  $(0 \leq \bar{\gamma}_3/Le \leq 1)$ .

Ensuite, la comparaison entre  $\mathcal{N}_{\text{Non-osc.}}^0$  et  $\mathcal{N}_{\text{GSG}}$  suggère de poser :

$$\omega_{\text{Pe}_t}^a \equiv \max \left( \frac{1 - (\bar{\gamma}_3/\bar{\gamma})\text{Pe}_t}{1 + (1 - (\bar{\gamma}_3/\bar{\gamma}))\text{Pe}_t}, 0 \right) .$$

En d'autres termes, cela consiste à introduire une pondération sur l'intervalle  $\text{Pe}_t \in [0, \bar{\gamma}/\bar{\gamma}_3 [$ , puis on revient au modèle ( $\text{Pe}_t \gg 1$ ) dès que ( $\text{Pe}_t > \bar{\gamma}/\bar{\gamma}_3$ ).

La figure 4.10 trace différentes courbes de neutralité liées au modèle dans la carte de stabilité linéaire de la Fig. 4.1. La stabilité marginale du modèle grand Péclet et petit Péclet, respectivement données par  $\partial_z \bar{s} = 0$  et  $\partial_1 \tilde{r}/\tilde{r} = 0$ , se présente sous forme de lignes verticales dans la carte. Quant à l'hyper-surface de neutralité du raccord notée  $\mathcal{N}_{\text{GSG}}^a$ , elle se situe sur  $\mathcal{N}_{\text{Non-osc.}}^0$  pour ( $\text{Pe}_t < \bar{\gamma}/\bar{\gamma}_3$ ) et "saute" sur la courbe grand Péclet lorsque ( $\text{Pe}_t > \bar{\gamma}/\bar{\gamma}_3$ ).

Les simulations HP, SP<sub>1</sub> et SP<sub>2</sub> sont lancées en utilisant ce raccord. Les quantités turbulentes montrées sur les Figs. 3.1, 3.2 et 3.3, respectivement l'énergie cinétique turbulente, la variance de volume spécifique normalisé et la largeur de mélange, résultant des simulations 1D-RSM, sont également représentées sur la Fig. 4.11. Par souci de clarté, la lettre latine supplémentaire "(a)" aux légendes HP, SP<sub>1</sub> et SP<sub>2</sub> fait référence aux cas incluant le modèle de raccord "a".

Les résultats du raccord basé sur le critère de stabilité illustré par les courbes noires ne sont pas aussi bons que ceux précisément ajustés pour les DNS. Le cas avec des valeurs intermédiaires de Péclet, en particulier, semble revenir trop rapidement à un comportement grand Péclet. Comme le changement abrupt du raccord à ( $\text{Pe}_t = \bar{\gamma}/\bar{\gamma}_3$ ) pourrait expliquer ce comportement, nous nous tournons vers une utilisation plus continue et moins restrictive du critère de stabilité.

Ainsi, plutôt que d'imposer partout le poids du critère de stabilité, on peut l'écrire comme une combinaison convexe de deux limites. On conserve donc la forme fonctionnelle arbitraire  $\omega_{\text{Pe}_t} = \text{Pe}_t^{\text{lim}} / (\text{Pe}_t^{\text{lim}} + \text{Pe}_t)$  et on n'impose  $\text{Pe}_t^{\text{lim}}$  que pour qu'il corresponde à la courbe de stabilité dans la limite petit Péclet. Il s'ensuit le choix  $\text{Pe}_t^{\text{lim}} = 1$ , ce qui conduit à :

$$\omega_{\text{Pe}_t}^b \equiv \frac{1}{1 + \text{Pe}_t} ,$$

qui est représenté sur la Fig. 4.10 avec  $\omega_{\text{Pe}_t}^a$ . L'hyper-surface de neutralité correspondante  $\mathcal{N}_{\text{GSG}}^b$  relie de manière lisse les limites ( $\text{Pe}_t \ll 1$ ) et ( $\text{Pe}_t \gg 1$ ).

Les mêmes Figs. 4.12 que précédemment sont présentées avec la lettre latine "(b)" suivant les légendes HP, SP<sub>1</sub> et SP<sub>2</sub> faisant référence aux simulations de Péclet effectuées avec le modèle de raccord "b". Un accord tout à fait satisfaisant est obtenu puisque les résultats sont proches de ceux précisément ajustés à ces simulations numériques. Le choix du raccord qui est motivé par des considérations physiques est donc une amélioration intéressante fournie par l'ALS.

## Conclusion

La principale innovation de ce travail est l'approximation faible Mach-faible Péclet, autour de laquelle s'articulent chaque chapitre. Cette analyse asymptotique traite des écoulements généraux impliquant du mélange et de forts effets radiatifs.

Le premier chapitre de ce travail a confirmé la présence de deux types particuliers de zones de mélange turbulent, la convection thermohaline standard et double-diffusive, apparaissant au cours de l'évolution de la séquence principale et de la branche géante d'étoiles de faible, moyenne et grande masse. Dans ce but, des étoiles de  $1 M_{\odot}$ ,  $5 M_{\odot}$  et  $75 M_{\odot}$  ont été simulées jusqu'à la fin de la phase géante avec un code astrophysique 1D : **MESA**. Les régions de mélange d'intérêt proviennent de l'apparition de mouvements convectifs à grande échelle appliqués à des milieux fortement stratifiés et optiquement épais. Elles partagent les propriétés d'être soumises à un mélange chimique ainsi qu'à un rayonnement intense. Ce dernier domine tout autre processus de transport de chaleur ou effet visqueux en raison de son interaction accrue avec le champ de matière et est alors traité dans la limite de la diffusion. Ainsi, le calcul des modèles de longueur de mélange de Prandtl [1925] appliqués aux zones de convection a montré que la turbulence dans les étoiles évolue généralement dans les limites de  $(Re_t \geq 1)$ ,  $(Pr \ll 1)$  et  $(M_t \leq 1)$ , où la petitesse du nombre de Mach permet de filtrer les ondes sonores dans le contexte de la modélisation de la turbulence. En particulier, les écoulements stellaires dans les intérieurs profonds des étoiles sont caractérisés par un état d'équilibre thermodynamique local où les températures radiative et de la matière sont supposées égales et où l'ionisation est considérée comme généralement complète. La vitesse turbulente est donc beaucoup plus faible que la vitesse du son :  $(M_t \ll 1)$ . C'est précisément dans ces régions proches du noyau que se produit la convection thermohaline (ou "fingering"), en réponse à un gradient de composition déstabilisant. Le paramètre clé qui la différencie de la convection standard n'est autre que le nombre de Péclet  $Pe_t$ , qui suit :

$$\begin{cases} Pe_t \gg 1 & \text{dans les zones convectives} \quad , \\ Pe_t \ll 1 & \text{dans les zones thermohalines} \quad . \end{cases}$$

Ainsi, contrairement à la convection, la double-diffusion "fingering" est caractérisée par une diffusivité radiative qui surpasse la turbulence en termes de transport d'énergie. Les modèles phénoménologiques de Prandtl [1925] ne permettent pas la capture des échelles turbulentes dans la limite thermohaline. En effet, ils négligent généralement les propriétés des structures convectives telles que la vitesse turbulente par exemple et ne tiennent pas compte des écoulements à densité variable. Ainsi, suite à l'étude du RSM de Canuto [2011a,e] dédié à la modélisation de la convection stellaire, la dérivation d'un modèle stochastique permettant de traiter ces questions a été retenue comme le fer de lance de la thèse afin de définir les propriétés statistiques turbulentes d'un tel milieu.

La deuxième partie traite d'une analyse asymptotique réalisée dans les limites conjointes des nombres de Mach et de Péclet turbulents infiniment petits. Ces ordres de grandeur imposés impliquent l'équilibre des phénomènes acoustiques et des fluctuations de température avec leur environnement. Le jeu d'équations régissant l'hydro-radiation implique le système compressible de Navier-Stokes couplé au rayonnement dans la limite de diffusion. Les résultats concernent d'abord la prédiction des fluctuations de pression et de température en termes de  $M_t$  et  $Pe_t$ . Et deuxièmement, le comportement de l'écoulement radiatif est examiné à travers les expressions asymptotiques de la divergence des fluctuations de vitesse  $\text{div} \mathbf{u}'$  et du terme de conduction thermique fluctuant  $\mathcal{C}' = \partial_j (\lambda \partial_j T)'$ . Sur la base d'une configuration de Rayleigh-Taylor radiatif stablement stratifié, la validation de leurs valeurs prédites a été vérifiée à la fois qualitativement et quantitativement par rapport à celles simulées par le DNS. Par conséquent, les fer-

metures dérivées de ces résultats se sont avérées appropriées dans un modèle turbulent RSM et pourraient être utilisées pour la simulation de petits régimes de Péclet impliquant du mélange. En outre, le critère de stabilité d'une stratification moyenne est modifié en conséquence. Il ne dépend plus du gradient de pseudo-entropie mais du gradient de masse molaire, respectivement dans les limites de ( $Pe_t \gg 1$ ) et de ( $Pe_t \ll 1$ ).

Dans le troisième chapitre, une adaptation d'un modèle RSM ( $M_t \ll 1$ ), déjà compatible avec la limite ( $Pe_t \gg 1$ ), a été proposée afin de rendre compte de l'effet de l'ampleur relative de la conductivité radiative et du transport turbulent dans la gamme des nombres de Péclet turbulents infiniment petits. À cette fin, l'évolution des corrélations liées à la densité suivie par le modèle GSG 1D-RANS a été fermée en utilisant les résultats de l'analyse précédente. La validation du modèle s'est appuyée sur les références des simulations DNS de Rayleigh-Taylor déjà étudiées dans la deuxième partie. La capture des effets radiatifs et du mélange, comme le critère de stabilité, a été correctement réalisée par le modèle adapté.

La dernière partie a porté sur une analyse de stabilité linéaire appliquée aux états d'équilibre de mélanges binaires stratifiés radiatifs dans un champ gravitationnel. Basée sur une approche quasi-homogène, l'ALS vise d'abord à mettre en évidence le rôle joué par la diffusion radiative. En effet, dans l'espace de stabilité, le paramètre clé qui définit le passage à l'instabilité "fingering", c'est-à-dire à la convection "thermohaline" dans le contexte astrophysique, est le nombre de Lewis  $Le$ , ou de manière équivalente, le nombre de Péclet  $Pe_t$  lorsque des équilibres turbulents sont considérés. Un objectif de l'ALS a été consacré à l'amélioration du modèle de raccord, en traitant les régimes de Péclet intermédiaires. Le critère de stabilité caractérisant le début de la convection "fingering" a été utilisé à la place d'une combinaison convexe qui nécessitait à l'origine une calibration obligatoire. Ainsi, le pont entre les deux limites asymptotiques repose maintenant sur une base physiquement solide.

En résumé, l'approximation faible Mach-faible Péclet a été dérivée et validée afin de traiter des écoulements radiatifs généraux impliquant du mélange. Le modèle RSM adapté est maintenant capable de capturer les régimes ( $Pe_t \ll 1$ ) et ( $Pe_t \gg 1$ ), et même les tendances principales des régimes intermédiaires petit Péclet. De tels phénomènes se produisent dans les milieux stellaires, où la turbulence couplée au rayonnement joue un rôle prépondérant dans le transport des isotopes chimiques. Ce plasma peut aussi impliquer un grand nombre de processus multiphysiques tels que l'ionisation, la dégénérescence électronique, les réactions nucléaires, le cisaillement, le magnétisme... Cependant, dans ce travail, l'application de l'approximation a été restreinte aux mélanges binaires radiatifs de gaz parfaits, sans l'inclusion de termes sources. Bien que l'on puisse déjà expliquer certains changements pertinents dans le comportement des champs intensément radiatifs, les propriétés de ces plasmas sont loin d'être complètement comprises. Le traitement de processus supplémentaires peut nécessiter de relaxer un certain nombre de simplifications. Une caractéristique intéressante concerne les implications des termes sources, tels que les réactions nucléaires. En effet, l'analyse asymptotique prédit déjà un changement dans l'ordre de grandeur de  $T'$ , comme dérivé dans l'annexe B.4. En outre, la résolution de certains problèmes liés à la modélisation astrophysique 1D peut être une voie intéressante à suivre. Suivant [Canuto \[2011a\]](#), le modèle GSG adapté actuel pourrait être directement résolu dans un code astrophysique ou même être dérivé sous la forme d'un modèle de [Prandtl \[1925\]](#) local, qui pourrait alors fournir une alternative mieux adaptée que les autres modèles phénoménologiques existants.



# A

## Thermodynamics

### Contents

---

<b>A.1 Generalized adiabatic exponents</b> . . . . .	<b>178</b>
<b>A.2 Thermodynamics of mixtures</b> . . . . .	<b>179</b>
A.2.1 Mixture of perfect gases . . . . .	179
A.2.2 Black body radiation . . . . .	180
A.2.3 Mixture of perfect gases and black body radiation . . . . .	180

---

## A.1 Generalized adiabatic exponents

The assumption of local thermodynamic equilibrium implies some relations between the derivatives of pressure, temperature and density (see Chandrasekhar [1957] and Mihalas & Mihalas [2013]). These relations are defined by the coefficients  $\Gamma_1, \Gamma_2$  and  $\Gamma_3$ , named ‘‘generalized adiabatic exponents’’ by Chandrasekhar [1957], as well as the coefficients  $\gamma_1, \gamma_2, \gamma_3$  and  $\gamma$  defined in the asymptotic analysis of chapter 2. They satisfy:

$$\gamma_1 = \Gamma_1 = \left( \frac{d \ln P}{d \ln \rho} \right)_{s,\alpha} = \frac{P_{,T}}{\rho e_{,T}} \left( 1 - \frac{\rho^2 e_{,\rho}}{P} \right) + \frac{\rho P_{,\rho}}{P} , \quad (\text{A.1})$$

$$\frac{\Gamma_2}{\Gamma_2 - 1} = \left( \frac{d \ln P}{d \ln T} \right)_{s,\alpha} = \frac{T}{P} \left( P_{,T} + \rho^2 \frac{P_{,\rho} e_{,T}}{P - \rho^2 e_{,\rho}} \right) , \quad (\text{A.2})$$

$$\gamma_2 - 1 = \Gamma_3 - 1 = \left( \frac{d \ln T}{d \ln \rho} \right)_{s,\alpha} = \frac{P - \rho^2 e_{,\rho}}{\rho e_{,T} T} , \quad (\text{A.3})$$

$$\gamma_3 - 1 = \frac{1}{\rho} \left( \frac{\partial P}{\partial e} \right)_{\rho} = \frac{1}{\rho} \frac{P_{,T}}{e_{,T}} , \quad (\text{A.4})$$

$$\text{with } \gamma = \frac{C_p}{C_v} = 1 + \frac{P_{,T}}{e_{,T} P_{,\rho}} \left( \frac{P}{\rho^2} - e_{,\rho} \right) , \quad (\text{A.5})$$

where we recall that the shortcuts  $f_{,T}$  and  $f_{,\rho}$  stand for the differentiation with constant other variables in  $\{T, \rho, c_\alpha\}$ . The previous partial derivatives take the form:

$$P_{,T} = (\gamma_3 - 1) \rho c_v , \quad P_{,\rho} = \frac{\gamma_1 P}{\gamma \rho} , \quad e_{,T} = c_v \quad \text{and} \quad e_{,\rho} = \frac{P}{\rho^2} \left( 1 - \frac{\gamma_1}{\gamma} \frac{\gamma - 1}{\gamma_3 - 1} \right) . \quad (\text{A.6})$$

The following useful relations aims at facilitating some derivations in the asymptotic analysis of chapter 2:

$$\gamma = \frac{\gamma_1}{\chi_\rho} , \quad \gamma_2 - 1 = \frac{\gamma - 1}{\gamma} \frac{\gamma_1 P}{(\gamma_3 - 1) \rho c_v T} , \quad \frac{\Gamma_2}{\Gamma_2 - 1} = \frac{\Gamma_1}{\Gamma_3 - 1} = \frac{\chi_\rho}{\Gamma_3 - 1} + \chi_T , \quad (\text{A.7})$$

$$\frac{\gamma_1 P}{\gamma \rho} = \frac{\gamma_1^m P^m}{\gamma^m \rho} , \quad \gamma_1 P - (\gamma_3 - 1) (\gamma_2 - 1) \rho c_v T = \gamma_1^m P^m - (\gamma_3^m - 1) (\gamma_2^m - 1) \rho c_v^m T , \quad (\text{A.8})$$

$$\text{with } \chi_\rho = \left( \frac{\partial \ln P}{\partial \ln \rho} \right)_{T,\mu} , \quad \chi_T = \left( \frac{\partial \ln P}{\partial \ln T} \right)_{\rho,\mu} \quad \text{and} \quad \chi_\mu = \left( \frac{\partial \ln P}{\partial \ln \mu} \right)_{\rho,T} . \quad (\text{A.9})$$

If a perfect gas plus radiation model is considered, the equality ( $\gamma_2 = \gamma_3$ ) is satisfied. Besides, the usual astrophysical pressure exponents inspired from Cox & Giuli [1968] in Eq. (A.9) can be expressed in terms of the pressure ratio ( $\beta = P^m/P$ ) such that:

$$\chi_\rho = \frac{\rho P_{,\rho}}{P} = \beta , \quad \chi_T = \frac{TP_{,T}}{P} = 4 - 3\beta \quad \text{and} \quad \chi_\mu = \frac{\mu P_{,\mu}}{P} = -\beta . \quad (\text{A.10})$$

The generalized adiabatic exponents of Sys. (A.1) are gathered in Tab. A. They are expressed in terms of the pressure ratio  $\beta$ , depending on the type of system considered, as described hereafter.

Thermodynamic quantity	Perfect gas	Black body radiation	Mixture of a perfect gas and black body radiation
$\beta$	1	0	$\frac{P^m}{P}$
$\gamma_1 = \Gamma_1$	$\gamma^m$	$\gamma^r$	$\beta + \frac{(4-3\beta)^2(\gamma^m-1)}{12(1-\beta)(\gamma^m-1)+\beta}$
$\Gamma_2$	$\gamma^m$	$\gamma^r$	$\frac{\beta^2+(16-12\beta-3\beta^2)(\gamma^m-1)}{\beta^2+3(4-3\beta-\beta^2)(\gamma^m-1)}$
$\gamma_2 = \gamma_3 = \Gamma_3$	$\gamma^m$	$\gamma^r$	$1 + \frac{(4-3\beta)(\gamma^m-1)}{12(1-\beta)(\gamma^m-1)+\beta}$
$\gamma$	$\gamma^m$	$\infty$	$1 + \frac{(4-3\beta)^2(\gamma^m-1)}{12\beta(1-\beta)(\gamma^m-1)+\beta^2}$

Table A – Table of thermodynamic relations

## A.2 Thermodynamics of mixtures

The systems studied in this thesis are considered as mixtures of a perfect gas and radiation, which means that total pressures and specific internal energies depend on three thermodynamic variables, such as:

$$P \equiv P(\rho, T, \mu) \quad \text{and} \quad e \equiv e(\rho, T, \mu) \quad .$$

### A.2.1 Mixture of perfect gases

The equation of state of a perfect gas is given by relation (1.4). A mixture of  $k$  perfect gases of mean molecular weight  $\mu_k$  is considered as one perfect gas of mean molecular weight  $\mu$ . Then, the material pressure of this mixture of perfect gases is given by Dalton's law of partial pressures  $P_k^m$ , such that:

$$P^m = \sum_k P_k^m = \rho r T^m = \rho \mathcal{R} T^m \sum_k \frac{1}{\mu_k} = \rho \frac{\mathcal{R}}{\mu} T^m = (\gamma^m - 1) \rho e^m \quad , \quad (\text{A.11})$$

$$\gamma^m \equiv \frac{C_p^m}{C_v^m} \equiv \frac{c_p^m}{c_v^m} \quad \text{and} \quad e^m \equiv c_v^m T^m \quad , \quad (\text{A.12})$$

where  $\mu$  stands for the mean molecular weight of the mixture of perfect gases, each having a mean molecular weight  $\mu_k$ . As for  $e^m$  and  $T^m$ , they refer respectively to the material specific energy of the mixture and its temperature.

The mean molecular weight  $\mu$  can be interpreted as an equivalent molar mass  $\mathcal{M}$  of the perfect gas. In this way, the specific enthalpy, heat capacities and entropy are:

$$h^m \equiv c_p^m T^m = e^m + \frac{P^m}{\rho} \quad , \quad (\text{A.13})$$

$$c_p^m \equiv \frac{\gamma^m}{\gamma^m - 1} \frac{\mathcal{R}}{\mu} \quad , \quad c_v^m \equiv \frac{1}{\gamma^m - 1} \frac{\mathcal{R}}{\mu} \quad , \quad (\text{A.14})$$

$$s^m \equiv c_v^m \ln T^m - \frac{\mathcal{R}}{\mu} \ln \rho + s_0^m \quad , \quad (\text{A.15})$$

## A.2. Thermodynamics of mixtures

---

where  $c_v^m$  and  $c_p^m$  are matter specific heat capacities respectively at constant volume and pressure. The quantity  $s_0^m$  is a material specific entropy constant. Here, we assume that each component of the mixture is a monoatomic perfect gas, hence  $\gamma^m = 5/3$ .

### A.2.2 Black body radiation

As thermal radiation is considered isotropic in our applications, the thermal radiation pressure  $P^r$  and radiative energy  $E^r$  are related by the formula (2.4) and then:

$$P^r = \frac{1}{3}E^r = \frac{1}{3}a_R T^r{}^4 \quad , \quad (\text{A.16})$$

with  $T^r$  standing for the radiative temperature. Besides, the polytropic laws related to relations (A.1), (A.2) and (A.3) suppose that, for an isentropic process, the radiation field behaves like a perfect gas of polytropic coefficient equal to  $4/3$ . A radiative gamma  $\gamma^r$  (but having no physical meaning) is introduced such that ( $\gamma^r = 4/3$ ). The radiative specific enthalpy, heat capacities and entropy are respectively given by:

$$h^r \equiv \frac{E^r}{\rho} + \frac{P^r}{\rho} = \frac{4}{3} \frac{E^r}{\rho} \quad , \quad (\text{A.17})$$

$$c_p^r \equiv T^r \left( \frac{\partial s^r}{\partial T^r} \right)_{p^r} \longrightarrow \infty \quad , \quad c_v^r \equiv T^r \left( \frac{\partial s^r}{\partial T^r} \right)_v = 12 \frac{P^r}{\rho T^r} = \frac{4a_R T^r{}^3}{\rho} \quad , \quad (\text{A.18})$$

$$s^r \equiv \frac{4}{3} \frac{a_R T^r{}^3}{\rho} + s_0^r \quad , \quad (\text{A.19})$$

where  $c_v^r$  and  $c_p^r$  are radiative specific heat capacities respectively at constant volume and pressure. The quantity  $s_0^r$  is a radiative specific entropy constant. It is worth noting that the specific heat capacity of radiation at constant pressure  $c_p^r$  is infinite. Indeed, from Eq. (A.16), as the radiative pressure remains constant, the temperature follows the same behaviour. Hence, the amount of energy necessary to make the temperature of the system increase of 1 K would theoretically be infinite.

### A.2.3 Mixture of perfect gases and black body radiation

In this thesis, we consider a mixture of perfect gases and radiation. Since the material and radiative temperature are assumed equal ( $T = T^m = T^r$ ), the equation of state is:

$$P = P^m + P^r = \rho r T + a_R T^4 = (\gamma^m - 1) \rho e^m + a_R T^4 \quad , \quad (\text{A.20})$$

$$\text{with } \gamma^m \equiv \frac{c_p^m}{c_v^m} \quad \text{and} \quad e = e^m + \frac{E^r}{\rho} \quad . \quad (\text{A.21})$$

Again, the total specific enthalpy, heat capacity at constant volume and entropy are respectively given by:

$$h = h^m + h^r \quad , \quad c_v = c_v^m + c_v^r \quad \text{and} \quad s = s^m + s^r \quad , \quad (\text{A.22})$$

with all the quantities being defined in the previous sections A.2.1 and A.2.2.

# B

## Asymptotic analysis extension

### Contents

---

<b>B.1</b>	<b>Temperature and pressure equations . . . . .</b>	<b>182</b>
<b>B.2</b>	<b>Average and fluctuating velocity, temperature and pressure equations</b>	<b>183</b>
<b>B.3</b>	<b>Development of fluctuating diffusion and conduction terms . . . . .</b>	<b>184</b>
<b>B.4</b>	<b>Small Mach-small Péclet asymptotic analysis in the presence of fast reactions . . . . .</b>	<b>186</b>
B.4.1	Small Péclet . . . . .	186
B.4.2	Small Mach . . . . .	187
B.4.3	Synthesis . . . . .	187

---

## B.1 Temperature and pressure equations

The derivation of temperature and pressure equations is described as follow. As a reminder, the LTE as well as the thermal equilibrium allow to consider the following hypothesis:

$$T^i = T^e = T^r \equiv T \quad ,$$

where the superscripts “i”, “e” and “r” refer respectively to the ionic, electronic and radiative fields. Then, three equations for the temperature can be deduced from the ionic, electronic and radiative equations of energy, respectively Eqs. (2.1d), (2.1e) and (2.1f). They can be written:

$$D_t T = - \left( \gamma_2^i - 1 \right) T \text{div} \mathbf{u} + \frac{1}{\rho c_v^i} \left( \rho \varepsilon - \text{div} \mathcal{F}^i + \mathcal{S}^i + \sum_{\alpha} e_{,\alpha}^i \text{div} \mathcal{F}_{\alpha} + W^{i-e} \right) \quad (\text{B.1a})$$

$$= - \left( \gamma_2^e - 1 \right) T \text{div} \mathbf{u} + \frac{1}{\rho c_v^e} \left( -\text{div} \mathcal{F}^e + \mathcal{S}^e + \sum_{\alpha} e_{,\alpha}^e \text{div} \mathcal{F}_{\alpha} - W^{i-e} - \Omega^{e-r} \right) \quad (\text{B.1b})$$

$$= - \left( \gamma^r - 1 \right) T \text{div} \mathbf{u} + \frac{1}{\rho c_v^r} \left( -\text{div} \mathcal{F}^r + \mathcal{S}^r + \Omega^{e-r} \right) \quad , \quad (\text{B.1c})$$

with:

$$\begin{aligned} \gamma_1^i &= \frac{P_{,T}^i}{\rho e_{,T}^i} \left( 1 - \frac{\rho^2 e_{,\rho}^i}{P} \right) + \frac{\rho P_{,\rho}^i}{P} \quad , \quad \gamma_2^i = 1 + \frac{P - \rho^2 e_{,\rho}^i}{\rho e_{,T}^i T} \quad , \quad \gamma_3^i = 1 + \frac{P_{,T}^i}{\rho e_{,T}^i} \quad , \\ \gamma_1^e &= \frac{P_{,T}^e}{\rho e_{,T}^e} \left( 1 - \frac{\rho^2 e_{,\rho}^e}{P} \right) + \frac{\rho P_{,\rho}^e}{P} \quad , \quad \gamma_2^e = 1 + \frac{P - \rho^2 e_{,\rho}^e}{\rho e_{,T}^e T} \quad , \quad \gamma_3^e = 1 + \frac{P_{,T}^e}{\rho e_{,T}^e} \quad , \quad \gamma^r = \frac{4}{3} \quad , \\ c_v^i &= e_{,T}^i \quad , \quad c_v^e = e_{,T}^e \quad , \quad c_v^r = E_{,T}^r / \rho = 12P^r / (\rho T) \quad . \end{aligned}$$

As already defined in Sec. 2.2.1, the global specific heat capacity at constant volume  $c_v$  is developed as the sum of the ionic, electronic and radiative ones, specifically  $c_v^i$ ,  $c_v^e$  and  $c_v^r$ , such that:

$$c_v = c_v^i + c_v^e + c_v^r \quad .$$

In the same way, the total specific energy  $e$  is expressed in terms of internal energies of ions  $e^i$ , electrons  $e^e$  and radiation  $E^r / \rho$  such as:

$$e = e^i + e^e + E^r / \rho \quad .$$

The ionic, electronic and radiative fluxes are recalled to be  $\mathcal{F}^i$ ,  $\mathcal{F}^e$  and  $\mathcal{F}_{\alpha}$ , and  $\mathcal{S}^i$ ,  $\mathcal{S}^e$  and  $\mathcal{S}^r$  stand for the ionic, electronic and radiative source terms. Moreover, as in Sec. 2.2.2, the definitions of the polytropic coefficients are expressed in terms of generalized adiabatic coefficients, defined by [Mihalas & Mihalas \[2013\]](#) such that:

$$\begin{aligned} \gamma_1^i &= \Gamma_1^i \quad , \quad \gamma_1^e = \Gamma_1^e \quad , \quad \gamma_2^i = \Gamma_3^i \quad , \quad \gamma_2^e = \Gamma_3^e \quad , \\ \gamma_3^i &= 1 + \frac{1}{\rho} \left( \frac{\partial P^i}{\partial e^i} \right)_{\rho, c_{\alpha}} \quad \text{and} \quad \gamma_3^e = 1 + \frac{1}{\rho} \left( \frac{\partial P^e}{\partial e^e} \right)_{\rho, c_{\alpha}} \quad . \end{aligned}$$

The expressions of the exchange terms  $W^{i-e}$  and  $\Omega^{e-r}$  of Eqs. (2.1d)-(2.1f) are then deduced:

$$W^{i-e} = -\rho c_v^i T \text{div} \mathbf{u} \frac{(\gamma_2^e - \gamma^r) x^e - (\gamma_2^i - \gamma^r) (x^e + x^r)}{1 + x^e + x^r} - \frac{\text{div} \mathcal{F}^e + \text{div} \mathcal{F}^r - (x^e + x^r) \text{div} \mathcal{F}^i}{1 + x^e + x^r} + \frac{e_{,\alpha}^e - (x^e + x^r) e_{,\alpha}^i}{1 + x^e + x^r} \text{div} \mathcal{F}_\alpha + \frac{\mathcal{S}^e + \mathcal{S}^r - (x^e + x^r) (\rho \varepsilon + \mathcal{S}^i)}{1 + x^e + x^r} , \quad (\text{B.2a})$$

$$\Omega^{e-r} = -\rho c_v^i T \text{div} \mathbf{u} \frac{(\gamma_2^i - \gamma^r) + x^e (\gamma_2^e - \gamma^r)}{1 + x^e + x^r} x^r - \frac{x^r (\text{div} \mathcal{F}^i + \text{div} \mathcal{F}^e) - (1 + x^e) \text{div} \mathcal{F}^r}{1 + x^e + x^r} + \frac{e_{,\alpha}^e + e_{,\alpha}^i}{1 + x^e + x^r} x^r \text{div} \mathcal{F}_\alpha + \frac{x^r (\rho \varepsilon + \mathcal{S}^i + \mathcal{S}^e) - (1 + x^e) \mathcal{S}^r}{1 + x^e + x^r} , \quad (\text{B.2b})$$

$$\text{with } x^e = \frac{c_v^e}{c_v^i} \quad \text{and} \quad x^r = \frac{c_v^r}{c_v^i} .$$

By inserting these expressions in one of the three temperature equations of the system (B.1), the temperature evolution of Eq. (2.12) is obtained. Besides, the evolution of the total pressure regards these exchange terms as well. Hence, the pressure evolution of Eq. (2.11) is derived by replacing the equilibrium values of  $W^{i-e}$  and  $\Omega^{e-r}$  by respectively Eqs. (B.2a) and (B.2b).

The polytropic coefficients used in Eqs. (2.11) and (2.12) are defined from total pressures and energies. They are indeed related to ionic, electronic and radiative polytropic coefficients according to:

$$\gamma_1 = -\frac{\rho c_v^i T x^r (\gamma_2^i - \gamma^r) (\gamma_3^i - \gamma^r) + x^e [x^r (\gamma_2^e - \gamma^r) (\gamma_3^e - \gamma^r) + (\gamma_2^i - \gamma^e) (\gamma_3^i - \gamma^e)]}{P} + \frac{\gamma_1^i P^i + \gamma_1^e P^e + \gamma^r P^r}{P} , \quad \gamma_2 = \frac{\gamma_2^i + x^e \gamma_2^e + x^r \gamma^r}{1 + x^e + x^r} \quad \text{and} \quad \gamma_3 = \frac{\gamma_3^i + x^e \gamma_3^e + x^r \gamma^r}{1 + x^e + x^r} .$$

## B.2 Average and fluctuating velocity, temperature and pressure equations

This part is devoted to the derivations of the dimensionless equations for  $\mathbf{u}''$ ,  $P'$  and  $T'$ , as carried on with classical techniques by Schiestel [2010]. They are straightforwardly derived from the evolution equations of velocity, pressure and temperature. In this way, the Favre average is applied to Eq. (2.18a) and Reynolds averages are applied to Eqs. (2.18b) and (2.18c) so that the evolution equations of averages of velocity, temperature and pressure can be derived as:

$$\left\{ \begin{array}{l} \widetilde{D}_t \widetilde{u}_i = -\frac{\partial_i \bar{P}}{\bar{\rho}} - \frac{\partial_j \bar{\Pi}_{ij}}{\bar{\rho}} - \frac{\partial_j (\overline{\rho u_i'' u_j''})}{\bar{\rho}} + g_i , \\ \widetilde{D}_t \bar{P} = -\overline{\gamma_1 P \text{div} \mathbf{u}} - \overline{\gamma_1' P' \text{div} \mathbf{u}} - \overline{\gamma_1' \text{div} \mathbf{u}' P} - \overline{\gamma_1 P' \text{div} \mathbf{u}'} + (\overline{\gamma_3} - 1) \bar{C} + \overline{\gamma_3' C'} + \overline{\mathcal{S}_P} \\ \quad + \overline{D_P} - \overline{\mathbf{u}'' \partial_j \bar{P}} - \overline{u_j' \partial_j P'} - \overline{\gamma_1' P' \text{div} \mathbf{u}'} , \\ \widetilde{D}_t \bar{T} = -(\overline{\gamma_2} - 1) \overline{T \text{div} \mathbf{u}} - \overline{\gamma_2' T' \text{div} \mathbf{u}} - \overline{\gamma_2' \text{div} \mathbf{u}' T} - (\overline{\gamma_2} - 1) \overline{T' \text{div} \mathbf{u}'} \\ \quad + \left( \frac{\bar{C}}{\rho c_v} + \frac{\overline{\mathcal{S}_T}}{\rho c_v} + \frac{\overline{D_T}}{\rho c_v} \right) - \overline{\mathbf{u}'' \partial_j \bar{T}} - \overline{u_j' \partial_j T'} - \overline{\gamma_2' T' \text{div} \mathbf{u}'} . \end{array} \right. \quad (\text{B.3a})$$

$$\left. \begin{array}{l} \widetilde{D}_t \bar{P} = -\overline{\gamma_1 P \text{div} \mathbf{u}} - \overline{\gamma_1' P' \text{div} \mathbf{u}} - \overline{\gamma_1' \text{div} \mathbf{u}' P} - \overline{\gamma_1 P' \text{div} \mathbf{u}'} + (\overline{\gamma_3} - 1) \bar{C} + \overline{\gamma_3' C'} + \overline{\mathcal{S}_P} \\ \quad + \overline{D_P} - \overline{\mathbf{u}'' \partial_j \bar{P}} - \overline{u_j' \partial_j P'} - \overline{\gamma_1' P' \text{div} \mathbf{u}'} , \end{array} \right. \quad (\text{B.3b})$$

$$\left. \begin{array}{l} \widetilde{D}_t \bar{T} = -(\overline{\gamma_2} - 1) \overline{T \text{div} \mathbf{u}} - \overline{\gamma_2' T' \text{div} \mathbf{u}} - \overline{\gamma_2' \text{div} \mathbf{u}' T} - (\overline{\gamma_2} - 1) \overline{T' \text{div} \mathbf{u}'} \\ \quad + \left( \frac{\bar{C}}{\rho c_v} + \frac{\overline{\mathcal{S}_T}}{\rho c_v} + \frac{\overline{D_T}}{\rho c_v} \right) - \overline{\mathbf{u}'' \partial_j \bar{T}} - \overline{u_j' \partial_j T'} - \overline{\gamma_2' T' \text{div} \mathbf{u}'} . \end{array} \right. \quad (\text{B.3c})$$

### B.3. Development of fluctuating diffusion and conduction terms

with the notation  $\widetilde{D}_t q$  of any quantity  $q$  written:

$$\widetilde{D}_t q = \partial_t q + \widetilde{u}_j \partial_j q \quad .$$

The difference between those equations and the corresponding governing ones gives the evolutions of the fluctuations:

$$\left\{ \begin{array}{l} D_t u_i'' = -\frac{\partial_i P'}{\rho} - u_j'' \partial_j \widetilde{u}_i + \frac{\rho'}{\rho} \frac{\partial_i \bar{P}}{\bar{\rho}} - \left( \frac{1}{\rho} \partial_j \Pi_{ij} \right)'' + \frac{\partial_j (\widetilde{\rho u_i'' u_j''})}{\bar{\rho}} \quad , \quad (B.4a) \\ D_t P' = -\overline{\gamma_1 P' \text{div} \mathbf{u}'} - \gamma_1' \bar{P} \text{div} \bar{\mathbf{u}} - \overline{\gamma_1 P' \text{div} \bar{\mathbf{u}}} + (\overline{\gamma_3} - 1) \bar{C}' + \gamma_3' \bar{C} + \mathcal{D}'_P + \mathcal{S}'_P - u_j' \partial_j \bar{P} \\ \quad - (\gamma_1' P' - \overline{\gamma_1' P'}) \text{div} \bar{\mathbf{u}} - (\gamma_1' \text{div} \mathbf{u}' - \overline{\gamma_1' \text{div} \mathbf{u}'} ) \bar{P} - \overline{\gamma_1 (P' \text{div} \mathbf{u}' - \overline{P' \text{div} \mathbf{u}'})} \\ \quad + \gamma_3' \bar{C}' - \overline{\gamma_3' \bar{C}'} + \overline{u_j' \partial_j P'} - (\gamma_1' P' \text{div} \mathbf{u}' - \overline{\gamma_1' P' \text{div} \mathbf{u}'}) \quad , \quad (B.4b) \\ D_t T' = -(\overline{\gamma_2} - 1) \bar{T} \text{div} \mathbf{u}' - \gamma_2' \bar{T} \text{div} \bar{\mathbf{u}} - (\overline{\gamma_2} - 1) T' \text{div} \bar{\mathbf{u}} - u_j' \partial_j \bar{T} + C' \left( \frac{1}{\rho c_v} \right) \\ \quad + \bar{C} \left( \frac{1}{\rho c_v} \right)' + \left( \frac{\mathcal{D}_T}{\rho c_v} \right)' + \left( \frac{\mathcal{S}_T}{\rho c_v} \right)' - (\gamma_2' T' - \overline{\gamma_2' T'}) \text{div} \bar{\mathbf{u}} \\ \quad - (\gamma_2' \text{div} \mathbf{u}' - \overline{\gamma_2' \text{div} \mathbf{u}'}) \bar{T} - (\overline{\gamma_2} - 1) (T' \text{div} \mathbf{u}' - \overline{T' \text{div} \mathbf{u}'}) + C' \left( \frac{1}{\rho c_v} \right)' \\ \quad - C' \left( \frac{1}{\rho c_v} \right)' + \overline{u_j' \partial_j T'} - (\gamma_2' T' \text{div} \mathbf{u}' - \overline{\gamma_2' T' \text{div} \mathbf{u}'}) \quad . \quad (B.4c) \end{array} \right.$$

Finally, by neglecting terms of order 2 and 3, as well as making the system (B.4) dimensionless, the fluctuating equations of Sys. (2.27) can be derived.

### B.3 Development of fluctuating diffusion and conduction terms

The diffusion terms  $\mathcal{D}_P$  and  $\mathcal{D}_T$  related respectively to the pressure and temperature evolution are defined by Eqs. (2.14) and (2.15). As for the conduction term  $\mathcal{C}$ , its expression is given in Eq. (2.13). They are recalled as:

$$\begin{aligned} \mathcal{D}_P &= \gamma_3 \sum_{\alpha} \frac{P_{r,\alpha}}{\rho} \partial_j (\rho \mathcal{D}^{(\alpha)} \partial_j c_{\alpha}) + \rho (\gamma_3 - 1) \sum_{\alpha} \mathcal{D}^{(\alpha)} \partial_j h_{r,\alpha} \partial_j c_{\alpha} \quad , \\ \mathcal{D}_T &= \sum_{\alpha} \frac{P_{r,\alpha}}{\rho} \partial_j (\rho \mathcal{D}^{(\alpha)} \partial_j c_{\alpha}) + \rho \sum_{\alpha} \mathcal{D}^{(\alpha)} \partial_j h_{r,\alpha} \partial_j c_{\alpha} \quad , \\ \mathcal{C} &= \partial_j (\lambda \partial_j T) \quad \text{with} \quad \lambda = \lambda^m + \lambda^r \quad \text{and} \quad \lambda^r = \frac{4}{3} a_{RC\ell} \frac{T^3}{\rho \kappa^r} \quad . \end{aligned}$$

The transport coefficients such as the matter conductivity  $\lambda^m$ , the scalar diffusion  $\mathcal{D}^{(\alpha)}$  and the Rosseland opacity  $\kappa^r$  are assumed to be spatially constant such that, for a binary mixture of perfect gases coupled with radiation, the previous expressions may be simplified into:

**Hypothesis: constant transport coefficients**

$$\begin{aligned}
 \mathcal{D}_P &= \sum_{\alpha} \mathcal{D}^{(\alpha)} \left[ \frac{\gamma_3 P_{,\alpha}}{\rho} \left( \partial_j \rho \partial_j c_{\alpha} + \rho \partial_{jj}^2 c_{\alpha} \right) + \rho (\gamma_3 - 1) \partial_j h_{,\alpha} \partial_j c_{\alpha} \right] , \\
 \mathcal{D}_T &= \sum_{\alpha} \mathcal{D}^{(\alpha)} \left[ \frac{P_{,\alpha}}{\rho} \left( \partial_j \rho \partial_j c_{\alpha} + \rho \partial_{jj}^2 c_{\alpha} \right) + \rho \partial_j h_{,\alpha} \partial_j c_{\alpha} \right] , \\
 \mathcal{C} &= \lambda^m \partial_{jj}^2 T + \frac{4}{3} \frac{a_{RC\ell}}{\kappa^r} \partial_j \left[ \frac{T^3}{\rho} \partial_j T \right] .
 \end{aligned}$$

Notice that the quantities  $(P_{,\alpha}/\rho)$  and  $(h_{,\alpha})$  are functions of only one state variable, namely the temperature. Besides, for a hydro-radiative flow field, the radiative diffusion prevails over the material thermal diffusion, which corresponds to the first term on the right-hand side of  $\mathcal{C}$  being neglected with respect to the second one.

The fluctuations of these quantities are developed in terms of fluctuating density, concentration and temperature, as well as their gradients and second derivatives, such as:

$$\begin{aligned}
 \mathcal{D}'_P &= \sum_{\alpha} \mathcal{D}^{(\alpha)} \left[ \overline{\gamma_3 \left( \frac{P_{,\alpha}}{\rho} \right)} \left( \partial_j \bar{\rho} \partial_j c'_{\alpha} + \partial_j \rho' \partial_j \bar{c}_{\alpha} + \bar{\rho} \partial_{jj}^2 c'_{\alpha} + \rho' \partial_{jj}^2 \bar{c}_{\alpha} \right) + \overline{\gamma_3 \left( \frac{P_{,\alpha}}{\rho} \right)'} \left( \partial_j \bar{\rho} \partial_j \bar{c}_{\alpha} + \bar{\rho} \partial_{jj}^2 \bar{c}_{\alpha} \right) \right. \\
 &\quad \left. + (\overline{\gamma_3} - 1) \left( \rho' \partial_j \bar{h}_{,\alpha} \partial_j \bar{c}_{\alpha} + \bar{\rho} \partial_j h'_{,\alpha} \partial_j \bar{c}_{\alpha} + \bar{\rho} \partial_j \bar{h}_{,\alpha} \partial_j c'_{\alpha} \right) \right] , \tag{B.5a}
 \end{aligned}$$

$$\begin{aligned}
 \mathcal{D}'_T &= \sum_{\alpha} \mathcal{D}^{(\alpha)} \left[ \overline{\left( \frac{P_{,\alpha}}{\rho} \right)} \left( \partial_j \bar{\rho} \partial_j c'_{\alpha} + \partial_j \rho' \partial_j \bar{c}_{\alpha} + \bar{\rho} \partial_{jj}^2 c'_{\alpha} + \rho' \partial_{jj}^2 \bar{c}_{\alpha} \right) + \overline{\left( \frac{P_{,\alpha}}{\rho} \right)'} \left( \partial_j \bar{\rho} \partial_j \bar{c}_{\alpha} + \bar{\rho} \partial_{jj}^2 \bar{c}_{\alpha} \right) \right. \\
 &\quad \left. + \rho' \partial_j \bar{h}_{,\alpha} \partial_j \bar{c}_{\alpha} + \bar{\rho} \partial_j h'_{,\alpha} \partial_j \bar{c}_{\alpha} + \bar{\rho} \partial_j \bar{h}_{,\alpha} \partial_j c'_{\alpha} \right] , \tag{B.5b}
 \end{aligned}$$

$$\begin{aligned}
 \mathcal{C}' &= \frac{4}{3} \frac{a_{RC\ell}}{\kappa^r} \left[ \frac{\rho'}{\bar{\rho}} (-\mathfrak{X} - 2\mathfrak{Y} - 3) + \frac{\partial_j \rho'}{\partial_j \bar{\rho}} \mathfrak{Y} + \frac{T'}{\bar{T}} (2\mathfrak{X} + 3\mathfrak{Y} + 3\mathfrak{Z}) + \frac{\partial_j T'}{\partial_j \bar{T}} (2\mathfrak{X} + \mathfrak{Y}) + \frac{\partial_{jj}^2 T'}{\partial_{jj}^2 \bar{T}} \mathfrak{Z} \right] \\
 &\quad + \overline{\lambda^m} \partial_{jj}^2 T' , \tag{B.5c}
 \end{aligned}$$

$$\text{with } \mathfrak{X} = \frac{3\bar{T}^2 (\partial_j \bar{T}^2)}{\bar{\rho}} , \quad \mathfrak{Y} = -\frac{\bar{T}^3 (\partial_j \bar{\rho}) (\partial_j \bar{T})}{\bar{\rho}^2} , \quad \mathfrak{Z} = \frac{\bar{T}^3 \partial_{jj}^2 \bar{T}}{\bar{\rho}} .$$

In the high Reynolds limit, the dominant terms of the diffusion terms  $\mathcal{D}'_P$  and  $\mathcal{D}'_T$  are assumed to be the second derivatives of fluctuating quantities of the state variables, whence the approximations of the system (2.48).

## B.4 Small Mach-small Péclet asymptotic analysis in the presence of fast reactions

In the asymptotic analysis of Sec. 2.3, reactions are supposed to have no, a slow (*i.e.*  $[\text{Da}\epsilon_{s_0}] \ll 1$ ) or a moderate velocity such that ( $[\text{Da}\epsilon_{s_0}] \sim 1$ ). If the reactions are considered fast and the Péclet number  $\text{Pe}_t$  of the order  $M_t^2$ , one has:

$$\text{Da}\epsilon_{s_0} \sim \frac{1}{M_t} \gg 1 \quad \text{and} \quad \text{Pe}_t \sim M_t^2 .$$

In that case, the reasoning of Sec. 2.3 can be followed once again, provided that some modifications occur.

### B.4.1 Small Péclet

Likewise, the asymptotic developments regarding any fluctuating quantity  $q'$  are inserted into Eqs. (2.27b) and (2.27c), expressing respectively the evolutions of the fluctuating pressure and temperature. Let us recall that, for any  $q'$ :

$$q' = q^{(0)} + M_t q^{(1)} + M_t^2 q^{(2)} + \mathcal{O}(M_t^3) .$$

Then, by collecting terms of order  $\text{Pe}_t^{-1} = M_t^{-2}$  and  $M_t^{-1}$ , the following system is obtained:

$$\begin{cases} c^{(0)} = 0 , & \text{(B.6a)} \\ c^{(1)} = [\text{Da}\epsilon_{s_0}\text{Pe}_t] \mathcal{S}_T^{\prime(0)} = [\text{Da}\epsilon_{s_0}\text{Pe}_t] \frac{\mathcal{S}_P^{\prime(0)}}{\bar{\gamma}_3 - 1} . & \text{(B.6b)} \end{cases}$$

The same result as Eq. (2.39) is found by using Eq. (B.6a), such that:

$$T^{\prime(0)} = 0 .$$

Moreover, the expression of  $\mathcal{S}_P^{\prime(0)}$ , extracted from the source term  $\mathcal{S}_P'$  related to pressure, defined in Eq. (2.48d), is developed as:

$$\mathcal{S}_P^{\prime(0)} = \sum_{\alpha} \left( \frac{P_{r,\alpha} \mathcal{S}_{\alpha}}{\rho} \right)^{\prime(0)} + (\bar{\gamma}_3 - 1) \mathcal{S}_T^{\prime(0)} .$$

Then, the two other equalities from Eq. (B.6b) lead to:

$$\partial_j \left[ \lambda \partial_j T^{\prime(1)} \right] = [\text{Da}\epsilon_{s_0}\text{Pe}_t] \mathcal{S}_T^{\prime(0)} = [\text{Da}\epsilon_{s_0}\text{Pe}_t] \left[ \sum_{\alpha} \left( \frac{P_{r,\alpha} \mathcal{S}_{\alpha}}{\rho (\bar{\gamma}_3 - 1)} \right)^{\prime(0)} + \mathcal{S}_T^{\prime(0)} \right] . \quad \text{(B.7)}$$

It shows that an asymptotic development with ( $[\text{Da}\epsilon_{s_0}] \gg 1$ ) is only possible if the order of the quantity  $\sum_{\alpha} \left( \frac{P_{r,\alpha} \mathcal{S}_{\alpha}}{\rho (\bar{\gamma}_3 - 1)} \right)^{\prime(0)}$  is higher than the one of  $\mathcal{S}_T^{\prime(0)}$ .

For a ionized perfect gas, which equation of state is defined in Eq. (2.51), this compatibility condition implies for each species  $\alpha$ :

$$\frac{r_\alpha - \bar{r}}{\bar{r}} \ll 1 \quad .$$

This condition is assumed to be verified in the present asymptotic analysis. Hence, contrary to the case where reactions are slow, Eq. (B.7) entails that temperature fluctuations are of the order of  $M_t$  and not  $M_t^2$ .

Finally, the order 0 of Eq. (2.27c) gives another relation that link the fluctuating divergence  $\text{div}\mathbf{u}'^{(0)}$  and conduction  $C'^{(2)}$  terms, such as:

$$(\bar{\gamma}_2 - 1) \bar{T} \text{div}\mathbf{u}'^{(0)} - \left[ \frac{M_t^2}{\text{Pe}_t} \right] \frac{C'^{(2)}}{\bar{\rho}c_v} = [\text{Da}\epsilon_{s_0}] \mathcal{S}'_p^{(1)} \quad . \quad (\text{B.8})$$

#### B.4.2 Small Mach

Regarding the small Mach analysis, its contribution implies the same results as in Sec. 2.3, namely:

$$P'^{(0)} = P'^{(1)} = 0 \quad .$$

With this order of magnitude, Eq. (2.27b) at order 0 implies:

$$\bar{\gamma}_1 \bar{P} \text{div}\mathbf{u}'^{(0)} - \left[ \frac{M_t^2}{\text{Pe}_t} \right] (\bar{\gamma}_3 - 1) C'^{(2)} = [\text{Da}\epsilon_{s_0}] \mathcal{S}'_p^{(1)} \quad . \quad (\text{B.9})$$

This relation links, once again, the quantities  $\text{div}\mathbf{u}'^{(0)}$  and  $C'^{(2)}$  together. Thus, the combination of Eqs. (B.8) and (B.9) allows to derive their expressions with respect to other fluctuating variables, as obtained in the system (2.49).

#### B.4.3 Synthesis

This asymptotic analysis has proven that the following orders of magnitude are satisfied when the reaction rates are high:

$$\frac{P'}{\bar{P}} \sim M_t^2 \quad \text{and} \quad \frac{T'}{\bar{T}} \sim \text{Pe}_t [\text{Da}\epsilon_{s_0}] \sim M_t \quad .$$

Hence, fast reactions maintain a level of temperature fluctuations similar to the ones of other thermodynamic quantities. Then, the effects of temperature cannot be neglected anymore.

As for the expressions of the fluctuating divergence  $\text{div}\mathbf{u}'$  and conduction  $C'$  terms, they are compatible with the ones of the system (2.49), which are derived in the hypothesis of moderate reactions. According to the assumptions of rapid reactions or not, dominant terms are different, but both relations remain valid.

#### **B.4. Small Mach-small Péclet asymptotic analysis in the presence of fast reactions**

---

# C

## Numerical methods

### Contents

---

<b>C.1 TRICLADE</b> . . . . .	<b>190</b>
C.1.1 Governing hydrodynamic mixing equations . . . . .	190
C.1.2 Governing hydro-radiative mixing equations . . . . .	191
C.1.3 Hyperbolic and parabolic systems . . . . .	192
C.1.4 Numerical flux . . . . .	192
C.1.5 Configuration of boundary conditions . . . . .	196
<b>C.2 Numerical resolution</b> . . . . .	<b>199</b>

---

## C.1 TRICLADE

TRICLADE is an in-house CEA code originally conceived in order to solve purely hydrodynamic systems. In order to validate the asymptotic analysis carried out in chapter 2, the latter has been adapted for the simulations of a hydro-radiative instability. The implementation of radiation, carried out by J. GRIFFOND, led to specific treatments regarding the numerical flux as well as the material and radiative boundary conditions. They are presented in the next sections, along with some relevant information for the numerical resolution of simulations HP, SP<sub>1</sub> and SP<sub>2</sub>. Note that these three contributions have been part of this thesis.

### C.1.1 Governing hydrodynamic mixing equations

TRICLADE is originally dedicated to hydrodynamic applications for which the flow mixing treats the following Navier-Stokes equations (found for instance in Giovangigli [2012]) and an advection-diffusion equation related to the concentration:

$$\begin{cases} \partial_t \rho + \partial_j (\rho u_j) & = 0 \quad , \\ \partial_t (\rho u_i) + \partial_j (\rho u_i u_j) + \partial_i P^m & = \rho f_i - \partial_j \Pi_{ij} \quad , \\ \partial_t (\rho e^m) + \partial_j (\rho e^m u_j + P^m u_j) & = \mathcal{C} - \Pi_{ij} \partial_j u_i - \mathcal{Q}_c + \rho f_i u_i \quad , \\ \partial_t (\rho c) + \partial_j (\rho c u_j) & = -\partial_j \mathcal{F}_{cj} \quad , \end{cases}$$

with the notations  $\partial_t \cdot$  and  $\partial_j \cdot$  referring respectively to the partial derivative with respect to the time  $t$  and to the spatial coordinate  $x_j$ . The density and velocity components are denoted respectively  $\rho$  and  $u_i$ . Note also that the Einstein convention on the summation of indices is used for latin letters. For the sake of commodity, the superscript “m” regarding flow variables is related to the material field. In addition, a binary mixture of two ideal gases indexed “a” and “b” with the same adiabatic exponent  $\gamma_a = \gamma_b = \gamma^m$  is treated. They are submitted to volumetric forces  $f$ , usually considered as a homogeneous gravity  $g$  in this work. The viscous stress tensor  $\Pi_{ij}$  and the scalar flux  $\mathcal{F}_{cj}$  are closed using respectively the hypothesis of Stokes regarding Lamé coefficients and the Fick law:

$$\Pi_{ij} = -2\mu_v \left( S_{ij} - \frac{1}{3} \text{div} \mathbf{u} \delta_{ij} \right) \quad \text{and} \quad \mathcal{F}_{cj} = -\rho \mathcal{D}_c \partial_j c \quad ,$$

with  $S_{ij} = (\partial_j u_i + \partial_i u_j) / 2$  the instantaneous tensor of deformation,  $\mu_v = \rho \nu_v$  the dynamic viscosity of the mixture,  $\nu_v$  its kinematic viscosity,  $\mathcal{D}_c$  the scalar diffusion coefficient and  $c$  the mass fraction of the gas indexed “a”. The velocity divergence is written  $\text{div} \mathbf{u} = \partial_j u_j$ .

Besides, the notations  $\mathcal{C}$  and  $\mathcal{Q}_c$  are related respectively to the thermal conduction and to the sum of thermal and enthalpic fluxes. These quantities are then defined with respect to the Fourier law and based on an isothermal mixing model. Hence,

$$\begin{aligned} \mathcal{C} &= \partial_j (\lambda^m \partial_j T^m) \quad , \\ \mathcal{Q}_c &= \partial_j \left[ -\lambda^m \partial_j T^m + (h_a^m - h_b^m) \mathcal{F}_{cj} \right] = -\partial_j \left[ \lambda^m \partial_j T^m + \rho \mathcal{D}_c \frac{\gamma^m}{\gamma^m - 1} (r_a - r_b) T^m \partial_j c \right] \quad , \end{aligned}$$

with  $\lambda^m$  and  $T^m$  the material thermal diffusivity and temperature. The ideal gas constant and the material specific heat capacity at constant volume of the mixture can be expressed in terms of the concentration as:

$$\begin{cases} r &= r_a c + r_b (1 - c) \\ c_v^m &= c_{va}^m c + c_{vb}^m (1 - c) \end{cases} \quad \text{with} \quad c_{va}^m = \frac{r_a}{\gamma_a - 1} \quad \text{and} \quad c_{vb}^m = \frac{r_b}{\gamma_b - 1} .$$

At last, the material pressure  $P^m$ , specific energy  $e^m$  and specific enthalpy  $h^m$  rest upon a ideal gas model such that:

$$P^m = \rho r T^m \quad , \quad e^m = c_v^m T^m \quad \text{and} \quad h^m = e^m + P^m / \rho .$$

### C.1.2 Governing hydro-radiative mixing equations

After the implementation of radiation, the flow mixing is now solved by the following Navier-Stokes equations, coupled with radiation treated in the diffusion limit, and adding an advection-diffusion equation related to the concentration:

$$\begin{cases} \partial_t \rho + \partial_j (\rho u_j) &= 0 \quad , \\ \partial_t (\rho u_i) + \partial_j (\rho u_i u_j) + \partial_i P^m + \lambda_{\text{Edd}} \partial_i E^r &= \rho f_i - \partial_j \Pi_{ij} \quad , \\ \partial_t (\rho e^m) + \partial_j (\rho e^m u_j + P^m u_j) + \lambda_{\text{Edd}} u_j \partial_j E^r &= -c_\ell \rho \kappa^r (a_R T^{m4} - E^r) - \Pi_{ij} \partial_j u_i - \mathcal{Q}_c + \rho f_i u_i \quad , \\ \partial_t E^r + \partial_j \left( \frac{3 - f_{\text{Edd}}}{2} E^r u_j \right) - \lambda_{\text{Edd}} u_j \partial_j E^r &= +c_\ell \rho \kappa^r (a_R T^{m4} - E^r) + \mathcal{C} \quad , \\ \partial_t (\rho c) + \partial_j (\rho c u_j) &= -\partial_j \mathcal{F}_{cj} \quad , \end{cases}$$

with  $c_\ell$  the speed of light and  $a_R$  the radiation constant. As matter and radiative pressures are treated as scalars in the code, the total pressure as well as the radiative energy are expressed by:

$$P = P^m + P^r \quad \text{and} \quad E^r = a_R T^r{}^4 \quad \text{with} \quad P^r = \lambda_{\text{Edd}} E^r \quad ,$$

where  $T^r$  stands for the radiative temperature. The total conductivity  $\mathcal{C}$  takes the form:

$$\mathcal{C} = \partial_j \left( \lambda^m \partial_j T^m + \lambda_{\text{Edd}} \frac{c_\ell}{\rho \kappa^r} \partial_j E^r \right) = \partial_j \left( \lambda^m \partial_j T^m + \lambda^r \partial_j T^r \right) \quad \text{with} \quad \lambda^r = \lambda_{\text{Edd}} \frac{4a_R c_\ell T^r{}^3}{\rho \kappa^r} \quad ,$$

which may be simplified into  $\mathcal{C} = \partial_j (\lambda^r \partial_j T^r)$  since the radiative conductivity  $\lambda^r$  overwhelms the material one  $\lambda^m$  in one's present applications. The opacity is implemented with respect to the definition of Chandrasekhar [1957] and takes the form, for  $p$  and  $q$  fixed positive integers:

$$\kappa^r = \kappa_0^r \rho^p T^r{}^q \quad \text{with} \quad \kappa^r = \frac{1}{\rho \Lambda^r} \quad \text{and} \quad \kappa^r = \kappa_a^r c + \kappa_b^r (1 - c) \quad ,$$

where  $\kappa_0^r$  is a constant and  $\Lambda^r$  is the Rosseland mean free path. The Eddington factor  $f_{\text{Edd}}$  and the Eddington flux limiter  $\lambda_{\text{Edd}}$  are taken currently as  $f_{\text{Edd}} = \lambda_{\text{Edd}} = 1/3$ . They are related by:

$$f_{\text{Edd}} = \lambda_{\text{Edd}} + \lambda_{\text{Edd}}^2 R_{\text{Edd}}^2 \quad \text{and} \quad \lambda_{\text{Edd}} = \frac{2 + R_{\text{Edd}}}{6 + 3R_{\text{Edd}} + R_{\text{Edd}}^2} \quad \text{with} \quad R_{\text{Edd}} = \frac{\|\partial_t E^r\|}{\rho \kappa^r E^r} .$$

### C.1.3 Hyperbolic and parabolic systems

The governing hydro-radiative equations are split into two parts: one that couples radiation and the fluid in a hyperbolic subsystem and a parabolic formulation in which radiative diffusion and source-sink terms evolve. Removing the equation for the concentration, the first one yields:

$$\begin{cases} \partial_t \rho + \partial_j (\rho u_j) & = 0 , \\ \partial_t (\rho u_i) + \partial_j (\rho u_i u_j) + \partial_i P^m + \lambda_{\text{Edd}} \partial_i E^r & = 0 , \\ \partial_t (\rho e^m) + \partial_j (\rho e^m u_j + P^m u_j) + \lambda_{\text{Edd}} u_j \partial_j E^r & = 0 , \\ \partial_t E^r + \partial_j \left( \frac{3 - f_{\text{Edd}}}{2} E^r u_j \right) - \lambda_{\text{Edd}} u_j \partial_j E^r & = 0 , \end{cases}$$

and the second one holds:

$$\begin{cases} \partial_t \left( \rho e^m - \frac{1}{2} \rho u_i u_i \right) = -c_\ell \rho \kappa^r (a_R T^{m4} - E^r) + 2 \lambda_{\text{Edd}} \frac{u_j}{\rho} \partial_j E^r , \\ \partial_t E^r = +c_\ell \rho \kappa^r (a_R T^{m4} - E^r) - 2 \lambda_{\text{Edd}} \frac{u_j}{\rho} \partial_j E^r + C . \end{cases}$$

The diffusive relations are coupled due to the quasi-equilibrium of temperatures  $T^m \approx T^r$ . The conservative system of the seven variables  $(\rho, \mathbf{u}, e^m, c, E^r)$  can hence take the form:

$$\partial_t \mathbf{U} + \nabla \mathbf{F} + \mathbf{S}^{\text{ex.}} = 0 ,$$

$$\text{with } \mathbf{U} = \begin{pmatrix} \rho \\ \rho \mathbf{u} \\ \rho e^m \\ \rho c \\ E^r \end{pmatrix} , \quad \mathbf{F} = \begin{pmatrix} \rho \mathbf{u} \\ \rho \mathbf{u} \mathbf{u} + (P^m + P^r) \\ \rho e^m \mathbf{u} + (P^m + P^r) \mathbf{u} \\ \rho c \mathbf{u} \\ \frac{3 - f_{\text{Edd}} - 2 \lambda_{\text{Edd}}}{2} E^r \mathbf{u} \end{pmatrix} \quad \text{and} \quad \mathbf{S}^{\text{ex.}} = \begin{pmatrix} 0 \\ -E^r \nabla \lambda_{\text{Edd}} \\ -E^r \nabla (\lambda_{\text{Edd}} \mathbf{u}) \\ 0 \\ E^r \nabla (\lambda_{\text{Edd}} \mathbf{u}) \end{pmatrix} .$$

TRICLADE then solves these equations in two steps. First, the conservative form allows to define the fluxes at the faces of the cells with respect to an approximate Riemann solver and second, the exchange terms present in  $\mathbf{S}^{\text{ex.}}$  are accounted for with a centered treatment.

### C.1.4 Numerical flux

The original numerical flux used in the purely hydrodynamic version is the HLLC found in Toro [2013]. In the  $(R_{\text{Edd}} \rightarrow 0)$  limit, *i.e.* the  $(f_{\text{Edd}} = \lambda_{\text{Edd}} \rightarrow 1/3)$  limit, the conservative mono-dimensional system with respect to the x-axis provides:

$$\mathbf{U} = \begin{pmatrix} \rho \\ \rho u \\ \rho e^m \\ \rho c \\ E^r \end{pmatrix} , \quad \mathbf{F} = \begin{pmatrix} \rho u \\ \rho u u + (P^m + P^r) \\ \rho e^m u + (P^m + P^r) u \\ \rho c u \\ E^r u \end{pmatrix} \quad \text{and} \quad \mathbf{S}^{\text{ex.}} = \begin{pmatrix} 0 \\ 0 \\ -\frac{1}{3} E^r \partial_x u \\ 0 \\ \frac{1}{3} E^r \partial_x u \end{pmatrix} .$$

where  $P^r = E^r/3$  and  $P^m = (\gamma^m - 1)\rho e^m$  and from which the HLLC flux is adapted in order to account for the presence of the radiative terms. For the sake of compacity, only the projected velocity  $u$  along the  $x$ -axis of  $\mathbf{u}(u, v, w)$  is shown. The derivation of the numerical flux for all the velocity components can then be easily carried out by replacing  $u$  by  $v$  or  $w$ . In the next demonstrations, the equation for the concentration is dropped since its treatment is self-consistent and remains the same as in the pure hydrodynamic version.

The aim of this section is to derive an approximate Riemann solver dedicated to the hyperbolic subsystem of **TRICLADE**. In particular, it includes a three-dimensional and multi-component flow, *i.e.* the scalar advection-diffusion equation and the diffusion approximation related to the radiative field, all solved with respect to the cartesian frame  $(x, y, z)$ . This time again, only the  $x$ -component is shown for the sake of compacity, and since a “split”-Riemann solver is implemented in **TRICLADE**. Hence, one considers a domain having appropriate boundary conditions and confined in a control volume of dimensions  $(x \times t) \in ([x_L, x_R] \times [0, T])$ . The Riemann problem takes the form:

$$\partial_t \mathbf{U} + \partial_x (\mathbf{F}(\mathbf{U})) = 0 \quad ,$$

and where, assuming an explicit conservative relation:

$$\mathbf{U}_i^{n+1} = \mathbf{U}_i^n - \frac{\Delta t}{\Delta x} (\mathbf{F}_{i+1/2} - \mathbf{F}_{i-1/2}) \quad ,$$

such that  $\Delta t$  and  $\Delta x$  are respectively the time and space steps of the discretization and the numerical flux  $\mathbf{F}_{i+1/2}$  is the unknown to be determined.

The current HLLC numerical flux is inspired from the HLL one from [Harten \*et al.\* \[1983\]](#), in which the fastest signal velocities stemming from the initial discontinuity located at the interface is estimated by the means of a two-wave model for the structure of the exact solution. The accuracy of the HLLC comes from the assumption of a three wave model, as shown in [Fig. C.1](#), which tends to improve the resolution of the intermediate waves. According to [Toro \[2013\]](#), the approximate HLLC flux is given by:

$$\mathbf{F}_{i+1/2} = \begin{cases} F_L & \text{if } x/t \leq S_L \quad , \\ F_L^* & \text{if } S_L \leq x/t \leq S^* \quad , \\ F_R^* & \text{if } S^* \leq x/t \leq S_R \quad , \\ F_R & \text{if } S_R \leq x/t \quad , \end{cases} \quad \text{with } \mathbf{U}(x, t) = \begin{cases} U_L & \text{if } x/t \leq S_L \quad , \\ U_L^* & \text{if } S_L \leq x/t \leq S^* \quad , \\ U_R^* & \text{if } S^* \leq x/t \leq S_R \quad , \\ U_R & \text{if } S_R \leq x/t \quad , \end{cases}$$

where, by applying Rankine-Hugoniot conditions across each of the wave speeds  $S_L$ ,  $S^*$  and  $S_R$ , one has the relations:

$$\begin{cases} F_L^* = F_L + S_L (U_L^* - U_L) \quad , \\ F_R^* = F_R + S_R (U_R^* - U_R) \quad , \end{cases} \quad \text{and} \quad F_R^* = F_L^* + S^* (U_R^* - U_L^*) \quad ,$$

with the intermediate wave  $S^*$  originally taking the form:

$$S^* = \frac{P_R^m - P_L^m + \rho_L u_L (S_L - u_L) - \rho_R u_R (S_R - u_R)}{\rho_L (S_L - u_L) - \rho_R (S_R - u_R)} \quad . \quad (\text{C.5})$$

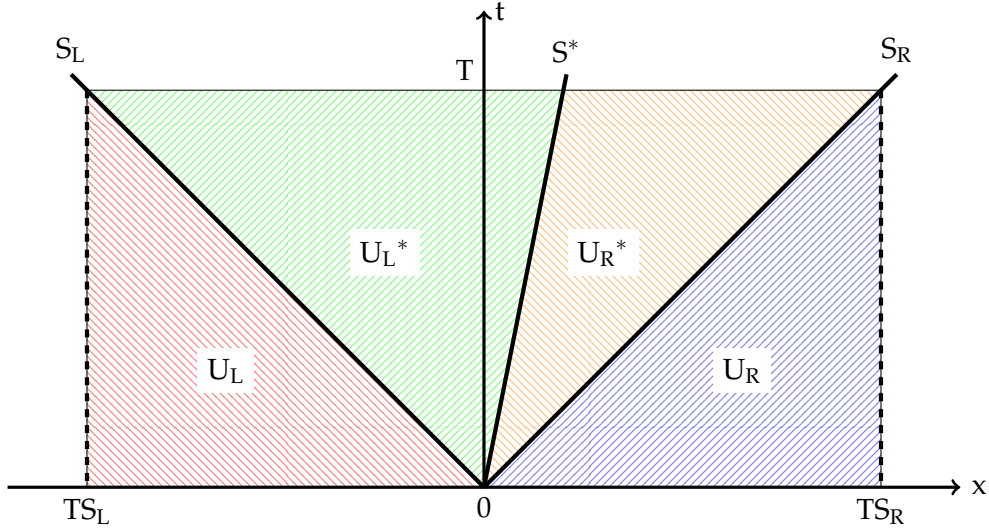


Figure C.1 – HLLC approximate Riemann solver. Representation of the wave structure derived from the Riemann problem in the control volume  $(x \times t) \in ([x_L, x_R] \times [0, T])$  such that  $x_L \leq T \cdot S_L$  and  $x_R \geq T \cdot S_R$  with  $T$  an arbitrary time and where  $S_L$  and  $S_R$  are the fastest signal velocities perturbing the initial data states respectively  $U_L$  and  $U_R$ .

In order to solve this problem, one needs to add supplementary conditions. The first ones regarding the pressure and the velocity are held by the exact solution and the second one allows to estimate the velocity in the star region to be characterized from the estimation of the wave  $S^*$ . They are both respectively written:

$$\begin{cases} P_L^* = P_R^* = P^* , & \text{and } S^* = u^* . \\ u_L^* = u_R^* = u^* , \end{cases}$$

Then, regarding the radiative diffusion equation, the simplest version of the approximation consists in treating the jump of radiative energy  $E^r$  such that it is hold by the discontinuity of contact:

$$E_L^{r*} = E_L^r \quad \text{and} \quad E_R^{r*} = E_R^r ,$$

but it is physically wrong. Then, the equivalents of relations:

$$S_L U_L^* - F_L^* = S_L U_L - F_L \quad \text{and} \quad S_R U_R^* - F_R^* = S_R U_R - F_R ,$$

become:

$$S_L \begin{pmatrix} \rho \\ \rho u \\ \rho e^m \\ E^r \end{pmatrix}_{L^*} - \begin{pmatrix} \rho_L^* S^* \\ (\rho u)_L^* S^* + (P_L^m + P_L^{r*}) \\ (\rho e^m)_L^* S^* + (P_L^m + P_L^{r*}) u^* \\ E_L^{r*} S^* \end{pmatrix} = S_L \begin{pmatrix} \rho_L \\ \rho_L u_L \\ \rho_L e_L^m \\ E_L^r \end{pmatrix} - \begin{pmatrix} \rho_L u_L \\ \rho_L u_L u_L + (P_L^m + P_L^r) \\ \rho_L e_L^m u_L + (P_L^m + P_L^r) u_L \\ E_L^r u_L \end{pmatrix} ,$$

and analogously by substituting L by R. Then the first line gives:

$$\rho_L^* = \frac{S_L \rho_L - \rho_L u_L}{S_L - S^*} = \rho_L \frac{S_L - u_L}{S_L - S^*} ,$$

which allows the second line to simplify into:

$$(P^{m*} + P^{r*}) - (P_L^m + P_L^r) = \rho_L(S^* - u_L)(S_L - u_L) \quad .$$

On the one hand, this relation permits to determine an estimation for the pressure when all the velocities are characterized. And on the other hand, the substitution of  $P^* = P^{m*} + P^{r*}$  yields the system:

$$(S_L - S^*) \begin{pmatrix} \rho \\ \rho u \\ \rho e^m \\ E^r \end{pmatrix}_{L^*} = (S_L - u_L) \begin{pmatrix} \rho_L \\ \rho_L u_L \\ \rho_L e_L^m \\ E_L^r \end{pmatrix} + \begin{pmatrix} 0 \\ (P^{m*} + P^{r*}) - (P_L^m + P_L^r) \\ (P^{m*} + P^{r*})u^* - (P_L^m + P_L^r)u_L \\ 0 \end{pmatrix} \quad ,$$

hence,

$$(S_L - S^*) \begin{pmatrix} \rho \\ \rho u \\ \rho e^m \\ E^r \end{pmatrix}_{L^*} = (S_L - u_L) \begin{pmatrix} \rho_L \\ \rho_L u_L \\ \rho_L e_L^m \\ E_L^r \end{pmatrix} + \begin{pmatrix} 0 \\ \rho_L(S^* - u_L)(S_L - u_L) \\ (P_L^m + P_L^r)(u^* - u_L) + \rho_L(S^* - u_L)(S_L - u_L)u^* \\ 0 \end{pmatrix} \quad ,$$

and finally,

$$(S_L - S^*) \begin{pmatrix} \rho \\ \rho u \\ \rho e^m \\ E^r \end{pmatrix}_{L^*} = (S_L - u_L) \begin{pmatrix} \rho_L \\ \rho_L S^* \\ \rho_L e_L^m \\ E_L^r \end{pmatrix} + \begin{pmatrix} 0 \\ 0 \\ (S^* - u_L) [(P_L^m + P_L^r) + \rho_L(S_L - u_L)u^*] \\ 0 \end{pmatrix} \quad .$$

From there, the material specific energy holds:

$$(\rho e^m)_{L^*} = \rho_L \frac{S_L - u_L}{S_L - S^*} \left( e_L^m + (S^* - u_L) \left[ S^* + \frac{(P_L^m + P_L^r)}{\rho_L(S_L - u_L)} \right] \right) \quad ,$$

and as for the volumetric radiative energy, one has:

$$E_{L^*}^r = \frac{S_L - u_L}{S_L - S^*} E_L^r \quad .$$

The same relation is obtained from the relation:

$$S_R u_R^* - F_R^* = S_R U_R - F_R \quad ,$$

by replacing L by R. Besides, the hypothesis of  $u_L^* = u_R^* = S^*$  is exploited so that one may derive the relations:

$$\begin{cases} (P^m + P^r)_{L^*} - (P_L^m + P_L^r) = \rho_L(S^* - u_L)(S_L - u_L) \quad , \\ (P^m + P^r)_{R^*} - (P_R^m + P_R^r) = \rho_R(S^* - u_R)(S_R - u_R) \quad , \end{cases}$$

which must be verified simultaneously for the equality:

$$P^{m*} + P^{r*} = (P^m + P^r)_{L^*} = (P^m + P^r)_{R^*} \quad ,$$

to be implicitly satisfied. It entails,

$$(P_L^m + P_L^r) + \rho_L(S^* - u_L)(S_L - u_L) = (P_R^m + P_R^r) + \rho_R(S^* - u_R)(S_R - u_R) \quad ,$$

and hence provides the contact wave speed:

$$S^* = \frac{(P_R^m + P_R^r) - (P_L^m + P_L^r) + \rho_L u_L (S_L - u_L) - \rho_R u_R (S_R - u_R)}{\rho_L (S_L - u_L) - \rho_R (S_R - u_R)} \quad ,$$

which allows to respect the consistency of the numerical flux for each conservative component. This expression is in accordance with the one found in MESA by Paxton *et al.* [2018] and can be compared to its pure hydrodynamic version (C.5).

Finally, TRICLADE can adopt two possible versions of the HLLC flux. The first one, denoted HLLC1, relates on the previous relations. The drawback of this method lies on the choice of the velocities  $S_L$  and  $S_R$ , based on Einfeldt [1988] according to Nishikawa & Kitamura [2008] that relies on a Roe solver. In this way, it seems appropriate to modify the different sound speeds in order to account for corrections due to radiative field and hence make the substitution:

$$\sqrt{\frac{\gamma^m P^m}{\rho}} \leftarrow \sqrt{\frac{\gamma^m P^m + 4P^r/3}{\rho}} \quad .$$

The second version HLLC2 uses approximate solvers of Toro [2013] which are only valid in pure hydrodynamic cases. It is then *a priori* less reliable than HLLC1.

### C.1.5 Configuration of boundary conditions

The numerical validation of Sec. 2 carried out with TRICLADE relates on the simulation of a radiative Rayleigh-Taylor instability. The turbulent flow induced by the latter evolves with respect to a statistically mono-dimensional field in the cartesian frame  $(x, y, z)$ . The configuration of boundary conditions is straightforward for both TRICLADE's subsystems in the homogeneous plan  $(y, z)$  where periodicity is chosen between each opposite faces along the  $y$ - and  $z$ -directions such that:

$$\begin{cases} \rho_{\text{dom.}} = \rho_{\text{opp.}} \quad , \\ \mathbf{u}_{\text{dom.}} = \mathbf{u}_{\text{opp.}} \quad , \\ e_{\text{dom.}}^m = e_{\text{opp.}}^m \quad , \end{cases}$$

where  $\rho$ ,  $\mathbf{u}$  and  $e^m$  stand respectively for the density, velocity vector and material specific energy. For the sake of commodity, the subscripts "dom." and "opp." regard respectively the inner computational boundary and its opposite edge.

However, the boundary conditions along the inhomogeneous  $x$ -axis needs specific treatments, as depicted in the two next paragraphs.

### C.1.5.1 Material boundary conditions

At first, classical slip wall boundary conditions are considered for the material subsystem, which reverses to the constraints on state variables:

$$\begin{cases} \rho_{\text{dom.}} = \rho_{\text{gho.}} , \\ \mathbf{u}_{\text{ndom.}} = \mathbf{u}_{\text{ngho.}} , \\ \mathbf{u}_{\text{tdom.}} = 0 , \\ e_{\text{dom.}}^m = e_{\text{gho.}}^m + \frac{1}{\gamma^m - 1} (g_j dx_j) , \end{cases}$$

where the notation  $dx_j$  refers to the total differential with respect to the spatial coordinate  $x_j$ . The Einstein convention on the summation of indices is used for  $j$  and the subscript "gho." regards the cells in the extended ghost zone.

The normal and tangential components of the velocity field are denoted respectively  $\mathbf{u}_n$  and  $\mathbf{u}_t$ , the material adiabatic exponent is written  $\gamma^m$  and the gravity components are represented by  $g_j$  with respect to the cartesian frame.

Hence, the slip boundary condition erases the normal component of each variable at the edge of the domain and keeps the tangential components untouched. However, these classical conditions appears to be incompatible with the implemented initial profiles, which is due very strong gradients appearing at the boundaries.

A slight correction consists hence in extending these profiles from the inner computational domain to the boundary domain. This extension to the ghost zones allows consequently to achieve a better hydrostatic equilibrium. They are continuously re-computed in these zones during the run of the simulations.

### C.1.5.2 Radiative boundary conditions

The diffusive subsystem requires effective radiative boundary conditions. The latter, known as the "Marshak" conditions, are derived in this part.

The equation of radiative transfer is a first order differential equation in space and time and hence includes boundary conditions in both of these variables. The system is supposed non-re-entrant, *i.e.* photons leaving the body cannot enter back in any part of it, and such that no photons may enter from any bounding surface at all. Hence, the specific intensity  $I$  in a grey atmosphere, *i.e.* independant of the frequency  $\nu$ , follows at the boundary:

$$I(\mathbf{x}, \mathbf{k}, t) = 0 ,$$

or so-called the "vacuum" or "free surface" boundary condition, with respect to Eq. (2.30) from Pomraning [2005]. The intensity  $I$  can be interpreted as a distribution function for photons that depends on the spatial position vector  $\mathbf{x}$ , the direction of travel of photon  $\mathbf{k}$  and the time  $t$ .

One of the main assumptions regarding the diffusion approximation of the radiative transfer equation is that the angular dependence of  $I$  can be characterized by two terms developed in a spherical harmonic expansion, such that:

$$I = \frac{1}{4\pi}I_0 + \frac{3}{4\pi}\mathbf{k} \cdot \mathbf{I}_1 \quad \text{with} \quad \begin{cases} I_0 = \int_{4\pi} I d\mathbf{k} , \\ I_1 = \int_{4\pi} I \mathbf{k} d\mathbf{k} , \end{cases} \quad (\text{C.8})$$

where  $I_0$  is a presumed dominant term and  $\mathbf{I}_1$  its first order anisotropy correction. Besides, inserting this equality (C.8) in the equation of transfer allows to characterize these unknowns as:

$$\begin{cases} I_0 = c_\ell E^r , \\ I_1 = \mathcal{F}^r , \end{cases} \quad \text{with} \quad E^r = a_R T^{r4} , \quad \mathcal{F}^r = -\frac{c_\ell \Lambda^r}{3} \nabla E^r \quad \text{and} \quad \Lambda^r = \frac{1}{\rho \kappa^r} , \quad (\text{C.9})$$

where  $c_\ell$ ,  $a_R$  and  $\Lambda^r$  stand respectively for the speed of light, the radiation constant and the mean free path of photon. The radiative energy  $E^r$  depends solely on the radiative temperature  $T^r$  and the radiative flux  $\mathcal{F}^r$  has one more dependance on the opacity  $\kappa^r$  and, in a much lesser extent, on the density  $\rho$  of the gaseous flow field. Then, the Marshak condition, taken from Eqs. (2.29) and (3.12) of Pomraning [2005], corresponds to the choice:

$$\int_{\mathbf{n} \cdot \mathbf{k} < 0} I(\mathbf{n} \cdot \mathbf{k}) d\mathbf{k} = \int_{\mathbf{n} \cdot \mathbf{k} < 0} \left( \frac{1}{4\pi}I_0 + \frac{3}{4\pi}\mathbf{k} \cdot \mathbf{I}_1 \right) (\mathbf{n} \cdot \mathbf{k}) d\mathbf{k} = 0 ,$$

where  $\mathbf{n}$  is a unit outward normal vector at the surface point  $\mathbf{x}$ . It reverses then to:

$$\frac{1}{4}I_0 - \frac{1}{2}\mathbf{n} \cdot \mathbf{I}_1 = 0 , \quad (\text{C.10})$$

and by inserting the expressions (C.9) of  $I_0$  and  $\mathbf{I}_1$  in Eq. (C.10), one obtains finally:

$$\frac{1}{2}E^r + \frac{1}{3\rho\kappa^r}\mathbf{n} \cdot \nabla E^r = 0 ,$$

which are implemented numerically as Robin conditions applied to the radiative energy. In TRICLADE, they regard the boundaries along the (inhomogeneous)  $x$ -axis and  $E^r$  is treated as a scalar. Hence one retains the simple form:

$$E^r + \frac{2}{3\rho\kappa^r}\mathbf{n} \cdot \nabla E^r = 0 .$$

Notice that the prefactor involving the opacity  $\kappa^r$  entails the second term on the left-hand side of the equation to be of greater order than the first one. This feature indicates that this equality may reverse to simple "Dirichlet" conditions applied to  $E^r$ :

$$E^r = 0 .$$

## C.2 Numerical resolution

In Sec. 2.5, we argued that the simulations HP, SP<sub>1</sub> and SP<sub>2</sub> were sufficiently resolved that they could be called DNS. This section aims to defend this assertion.

TRICLADE is a shock-capturing code which introduces a numerical dissipation  $\varepsilon_{\text{num}}$  that can be estimated from the budget of turbulent kinetic energy  $\widetilde{k} = \frac{1}{2}\widetilde{R}_{kk}$ :

$$\partial_t (\overline{\rho\widetilde{k}}) + \partial_x (\overline{\rho\widetilde{k}u_x}) + \partial_x \frac{\overline{\rho u_1'' u_1'' u_x''}}{2} + \overline{\rho R_{xx}} \partial_x \widetilde{u}_x + \overline{u_x''} \partial_x \overline{P} + \partial_x \overline{P' u_x''} - \overline{P' \partial_1 u_1''} + \partial_x \overline{u_1'' \Pi_{1x}} - \overline{\Pi_{11} \partial_1 u_1''} = 0 \quad , \quad (\text{C.11})$$

where  $\widetilde{R}_{ij} = \widetilde{u_i'' u_j''}$  is the Reynolds stress tensor and  $\Pi_{ij}$  the instantaneous tensor of deformation. This numerical dissipation can be assessed from the residue containing the following deviation from the average:

$$\overline{\rho\varepsilon_{\text{num}}} \equiv - \left[ \partial_t (\overline{\rho\widetilde{k}}) + \partial_x (\overline{\rho\widetilde{k}u_x}) + \partial_x \frac{\overline{\rho u_1'' u_1'' u_x''}}{2} + \overline{\rho R_{xx}} \partial_x \widetilde{u}_x + \overline{u_x''} \partial_x \overline{P} + \partial_x \overline{P' u_x''} - \overline{P' \partial_1 u_1''} + \partial_x \overline{u_1'' \Pi_{1x}} - \overline{\Pi_{11} \partial_1 u_1''} \right] .$$

Note that this term involves also the numerical diffusion but the latter vanishes when a spatial integration along the whole domain is performed. As for the physical dissipation  $\varepsilon_\phi$ , it is related to the last term on the right-hand side of Eq. (C.11) through:

$$\overline{\rho\varepsilon_\phi} = -\overline{\Pi_{11} \partial_1 u_1''} \quad ,$$

which allows to characterize the total dissipation  $\varepsilon_{\text{tot}}$  simply as the sum of its numerical and physical parts:

$$\varepsilon_{\text{tot}} = \varepsilon_{\text{num}} + \varepsilon_\phi \quad .$$

Figure C.2 shows the spatial profile along the x-axis of the ratio of the cell size  $\delta x$  to the Kolmogorov length scale  $\eta$ , such that:

$$\delta x = \frac{L_x}{N_x} \quad \text{and} \quad \eta = \left( \frac{\nu_v^3}{\varepsilon_{\text{tot}}} \right)^{1/4} \quad ,$$

at the transition time  $t = 17$  and at  $t = 34$ . Following the prescription of Pope [2000], small scales are well resolved if this ratio  $\frac{\delta x}{\eta}$  remains under the typical value of 2.1. This seems respected by the simulation HP at both times. As for the small-Prandtl simulations SP<sub>1</sub> and SP<sub>2</sub>, they are at the limit of resolution in both cases.

## C.2. Numerical resolution

Moreover, as confirmed by Fig. C.3 that displays the temporal evolution of this ratio at the initial position of the interface, the three simulations HP, SP<sub>1</sub> and SP<sub>2</sub> can be considered as highly resolved. The difference of evolution between the high and small Prandtl simulations stem from the behaviour of the RTI. It involves a higher turbulence intensity in the small Péclet regime where the kinetic energy keeps increasing, as seen in chapter 3 and a collapse of the turbulent field in the high Péclet limit. This explains why the high Prandtl simulation HP looks even better resolved than the others.

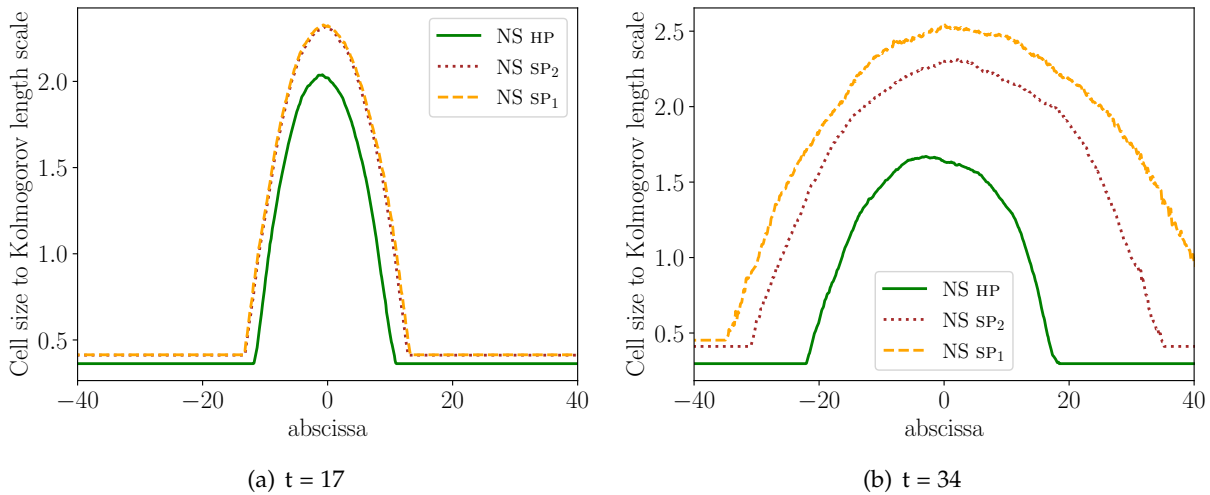


Figure C.2 – Spatial profiles of the rate of cell size to Kolmogorov length scale  $\frac{\delta x}{\eta}$  at (a)  $t = 17$  and (b)  $t = 34$ .

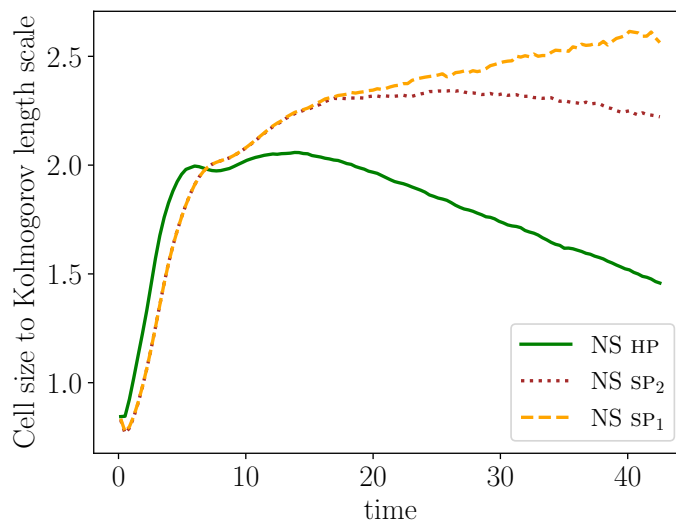


Figure C.3 – Temporal evolution of the rate of cell size to Kolmogorov length scale  $\frac{\delta x}{\eta}$  at the center of the mixing zone.

Figure C.4 displays the spatial profiles along the inhomogeneous direction of the ratio of physical to total dissipation  $\frac{\varepsilon_\phi}{\varepsilon_{\text{tot}}}$  at the times  $t = 17$  and  $t = 34$ . It remains superior to 80% for all simulations and seems to reach higher values, around 90%, in the high Prandtl one HP. Hence, they can all be considered as highly resolved. Furthermore, at  $t = 34$ , the thresholds of SP<sub>1</sub> and SP<sub>2</sub> spread over a larger zone than the one of HP. This is explained by the growth of the TMZ in the small Péclet regime, as explained in chapter 3.

Figure C.5 shows the computation of this ratio at the center of the mixing zone with respect to time. It confirms the last statements since the ratio  $\frac{\varepsilon_\phi}{\varepsilon_{\text{tot}}}$  does not seem to reach values under around 80%. Thus, as found previously with the use of the Kolmogorov length scale, all three simulations HP, SP<sub>1</sub> and SP<sub>2</sub> can be regarded as highly resolved.

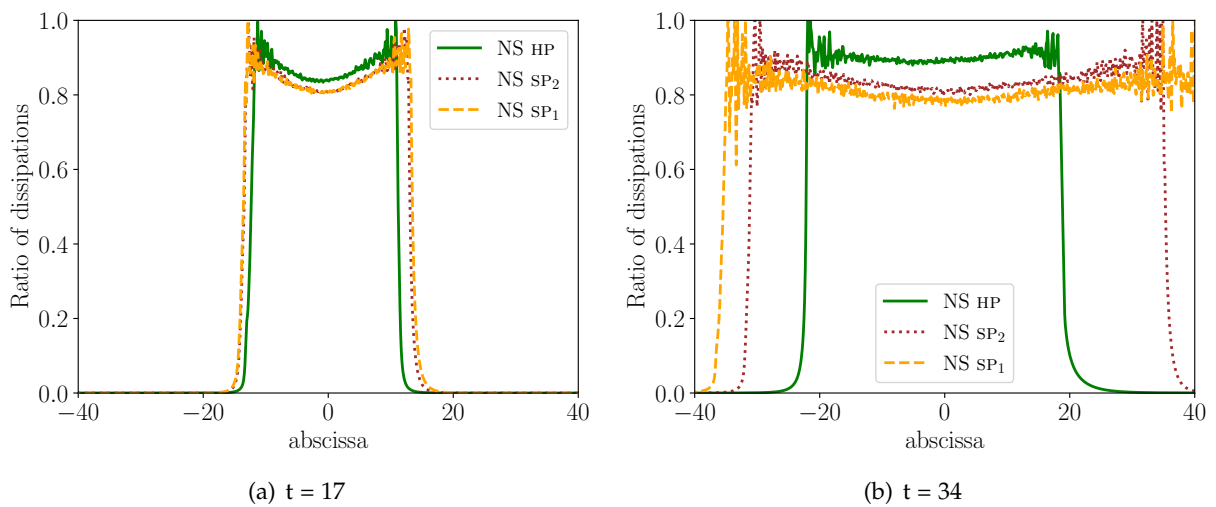


Figure C.4 – Spatial profiles of the rate of physical to total dissipation  $\frac{\varepsilon_\phi}{\varepsilon_{\text{tot}}}$  at (a)  $t = 17$  and (b)  $t = 34$ .

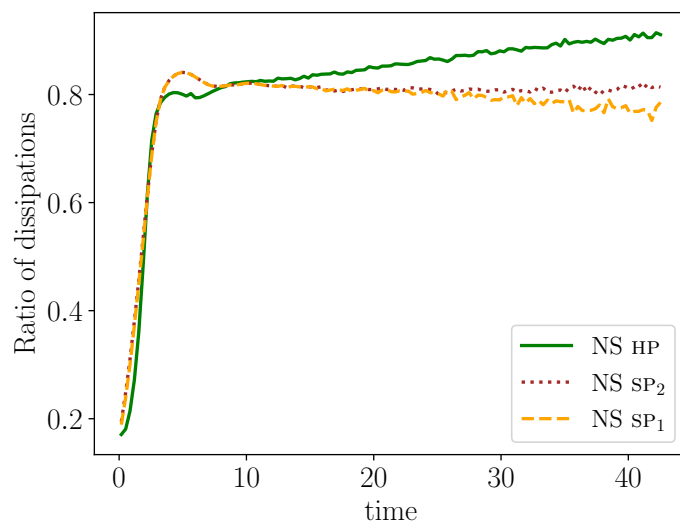


Figure C.5 – Temporal evolution of the rate of physical to total dissipation  $\frac{\varepsilon_\phi}{\varepsilon_{\text{tot}}}$  at the center of the mixing zone.



# Scientific production and communication

## Publication in a peer-reviewed journal (see hereinafter)

- \* **Chkair, J.-C., Soulard, O., Griffond, J. & Blanc, X.** | Physical Review E  
*Small-Peclet-number approximation for stellar turbulent mixing zones*  
August 2020

## Presentation of work at conferences

- \* **17th European Turbulence Conference (ETC17)**  
Turin - Italy | Oral talk  
*Modelling turbulence subjected to strong radiation*  
03 - 06 September 2019
- \* **12th Engineering Turbulence Modelling and Measurements (ETMM12)**  
Montpellier (La Grande-Motte) - France | Oral talk & proceeding  
*Small Péclet-small Mach number approximation and its implications on statistical turbulence models*  
26 - 28 September 2018

## General public conference and meeting (see hereinafter)

- \* **Science Festival ("Fête de la Science")**  
Bruyères-le-Châtel - France | Animation of the "turbulence" stand  
*Promotion of vocations in fluid mechanics*  
05 - 13 October 2019
- \* **Meeting with Plasma Master students**  
Bruyères-le-Châtel - France | Poster  
*Exchange on scientific experiments and projects*  
October 12, 2018

## Teaching activity

- \* **EPF engineering school**  
Sceaux - France | Mathematics exams (36h)  
*For 1<sup>st</sup> and 2<sup>nd</sup> year students in the integrated preparatory program*  
September 2018 - June 2019

**Small-Péclet-number approximation for stellar turbulent mixing zones**Jean-Cédric Chkair, Olivier Soulard, and Jérôme Griffond *CEA, DAM, DIF, F-91297 Arpajon, France*

Xavier Blanc

*Université de Paris, Sorbonne Université, CNRS, Laboratoire Jacques-Louis Lions, F-75013 Paris, France*

(Received 24 June 2020; accepted 7 August 2020; published 18 September 2020)

The purpose of this work is to derive a small turbulent Péclet–small turbulent Mach number approximation for hydroradiative turbulent mixing zones encountered in stellar interiors where the radiative conductivity can overwhelm the turbulent transport. To this end, we proceed to an asymptotic analysis and determine orders of magnitude for the fluctuating temperature and pressure, as well as closed expressions for the fluctuating conduction and velocity divergence. The latter is used to extend a Reynolds stress model to the small-Péclet regime. Three-dimensional direct numerical simulations of radiative Rayleigh-Taylor turbulent mixing zones are performed, first, to validate the asymptotic predictions and, second, to validate their use in the Reynolds stress model.

DOI: [10.1103/PhysRevE.102.033111](https://doi.org/10.1103/PhysRevE.102.033111)**I. INTRODUCTION**

Within stellar interiors, turbulent zones can appear under the action of a wide variety of mechanisms, ranging from shear and rotation to convection and double diffusion [1,2]. The development of these turbulent zones usually entails the transport and mixing of elements that would have otherwise remained segregated and confined within bounded regions of the star. Through these effects, turbulence can have a lasting influence over the whole stellar evolution cycle. Among others, it can affect the life expectancy of stars, impact the observations susceptible to be made from Earth, and modify the abundance of some elements [3–5].

A distinct feature of stellar turbulent mixing zones stems from their interaction with radiation. In stellar interiors, the radiative field is in local equilibrium with the surrounding plasma and obeys the diffusion approximation. As a result, heat transfer is the sum of a thermal conduction term and of a radiative diffusion term. The latter is order of magnitudes higher than the former. It is so high that the Prandtl number,  $Pr$ , defined as the ratio of the viscosity to the sum of the thermal and radiative diffusivities, can reach values much smaller than one. Small-Prandtl-number fluids are certainly not uncommon on Earth. Liquid metals, such as those found in the Earth's core or in some nuclear reactors, exhibit Prandtl numbers ranging from  $10^{-1}$  to  $10^{-3}$ . However, these values remain much higher than those found in stellar interiors. For instance, in the radiative zone of the Sun, Prandtl numbers can become as small as  $10^{-9}$ . This difference in Prandtl numbers is not merely quantitative: It also changes the context into which turbulent convection takes place.

Along with conduction and radiation, turbulent convection is the third major process that is involved in the transport of heat. Its efficiency with respect to the other two processes can be weighed by the turbulent Péclet number,  $Pe_t$ . This nondimensional number compares the diffusivity of turbulent

eddies, estimated from their typical size and velocity, to the sum of the thermal and radiative diffusivities—which, in our case, is essentially the radiative one. Thus, in a stellar context, a small Péclet number indicates that radiation is much more efficient than turbulence at transporting heat, while a large Péclet number implies the contrary. Whether the Péclet number is small depends on the value of the Prandtl number,  $Pr$ , of the fluid. It also depends on the Reynolds number,  $Re_t$ , of the flow. Indeed, given its definition, the Péclet number is equal to the Prandtl number multiplied by the ratio of the turbulent diffusion to the plasma viscosity, which is nothing more than the Reynolds number  $Re_t$ :  $Pe_t = Pr \times Re_t$ . Therefore, a small Péclet number can only be achieved provided the Prandtl number is much smaller than the inverse Reynolds number  $Pr \ll Re_t^{-1}$ . This is where the difference between the Prandtl numbers observed in stars and in liquid metals comes into play. Indeed, fully developed turbulence is usually attained for Reynolds numbers larger than  $10^3$ . As a result, in liquid metals, one can hardly combine a fully developed turbulent state with a small Péclet number. By contrast, with Prandtl numbers as low as  $10^{-9}$ , turbulence with high Reynolds and small Péclet numbers can exist in stellar interiors. And indeed, according to current state-of-the-art stellar simulations [6,7], turbulent mixing zones with small Péclet numbers are predicted to occur in most mid-sized and massive stars in their main sequence phase, their red-giant one, or both. As an example, at the frontier of the radiative core of a red giant of one solar mass, a turbulent mixing zone generated by a double-diffusive thermohaline instability is predicted to possess at its onset Péclet numbers on the order of  $10^{-2}$ – $10^{-1}$  and Reynolds numbers around  $10^6$ – $10^7$ .

The existence of such mixing zones raises a challenge in terms of turbulence modeling. Indeed, while statistical closures for high-Péclet turbulence are well established and widespread, the same cannot be said about their small-Péclet-number counterparts. To date, most efforts addressing this

issue have been circumscribed to the concept of “mixing length” introduced nearly a century ago by Prandtl [8] and adapted for stellar convection [9–12]. This type of closure is in practice the one that is almost exclusively implemented in stellar evolution codes. A notable exception is the Reynolds stress model (RSM) proposed by Canuto [13,14], which usage remains unfortunately marginal. But independently from the particular modeling framework retained, a common point of these works lies in their attempt to capture the scaling of turbulent quantities in the limit of infinitely small Péclet numbers. This asymptotic limit is indeed one of the essential building blocks on which statistical models can be derived to deal with small Péclet turbulence.

More precisely, the limit of infinitely small Péclet numbers is a singular limit of the Navier-Stokes equations. By applying an asymptotic analysis, a simplified approximation of the real flow can be formulated in which temperature fluctuations equilibrate instantaneously with their environment. This approach is similar to the one used for dealing with small turbulent Mach numbers,  $M_t$ . In that case, an asymptotic analysis allows us to derive an approximation of the real flow, called pseudocompressible, anelastic, or Boussinesq-Oberbeck, in which acoustical phenomena equilibrate instantaneously [15–20]. Small Péclet approximations are usually considered jointly with their small-Mach counterparts, which they complete and modify. This joint limit is appropriate for stellar turbulent flows which are in effect characterized by small turbulent Mach numbers,  $M_t$ .

Several works [21–25] have thus been devoted to the study of the small Péclet–small Mach number limit, hereafter referred to uniquely as the small-Péclet-number limit in order to alleviate notations. However, some elements in these previous studies may not be fully adapted to the treatment of stellar turbulent mixing zones. For instance, in Refs. [22,23], an isovolume Boussinesq-like assumption is made prior to the asymptotic analysis, instead of being derived from it. The outcome of the analysis is consequently limited to small depth motions in addition to small Mach numbers [15]. In Refs. [24,25], a complete asymptotic analysis is led. However, the authors enforce a static reference state, while for turbulent applications, a mean varying state would be preferred. Besides, the analysis is restricted to perfect gases. But most importantly, none of the mentioned studies [21–25] accounts for the presence of mixing, while it is one of the key aspects of stellar turbulence that needs to be dealt with. Finally, no verification of the derived asymptotic approximation is proposed. Therefore, an adaptation of existing small-Péclet-number asymptotic analyses is required for stellar applications, and elements of validation need to be provided.

Another point that requires some clarification is the way a small-Péclet-number approximation can be used to derive statistical turbulent closures. The outcome of small-Péclet-number asymptotic analyses are expressions for the fluctuations of the velocity divergence and of the conduction term, as well as an order of magnitude for the pressure and temperature fluctuations. All of these elements impact the evolutions of the fluctuations of thermodynamical variables, such as density or temperature. They should consequently be accounted for in the formulation of any statistical model following the correlations between

these variables and aiming at dealing with small-Péclet flows.

Thus, the main objective of this work is to derive and validate a small-Péclet-number approximation relevant to stellar turbulent mixing zones. As a secondary objective, we also aim to illustrate how this approximation can be used for the purpose of turbulence modeling. To attain these objectives, we first proceed with an asymptotic analysis based on the evolutions of the fluctuating velocity, pressure, temperature, and species concentration adapted to the hydroradiative flows encountered in stellar interiors. This leads to our main results regarding the orders of magnitude of the fluctuating temperature and pressure, as well as expressions for the fluctuating velocity divergence and for the conduction term. The obtained expressions are contrasted against the ones obtained in the high-Péclet case, as well as those derived in other works [21–24]. Then these predictions are validated by performing numerical simulations of a radiative Rayleigh-Taylor instability in the small-Péclet regime. This particular flow is not expected to occur as such in stellar interiors. Still, it retains many of the elementary ingredients that are relevant to stellar flows (including mixing, convective instability, stratification, and small Péclet numbers). It consequently constitutes a relevant test bed for validating our predictions. Finally, the impact of the small-Péclet-number approximation on turbulence modeling is illustrated by considering an existing second-order one point model and adapting its formulation. The model retained for this task is the Grégoire-Souffland-Gauthier (GSG) model [26], which is a RSM model designed for treating high-Péclet variable density turbulent mixing zones submitted to different types of convective instabilities, such as those encountered in a stellar context. While illustrated on this particular model, the procedure detailed here can in principle be used to adapt other existing RSM models. Besides, it is worth stressing that RSM models can be simplified into mixing-length models, as shown by Canuto [14].

The remaining of this work unfolds as follows. In Sec. II, the governing equations of the flow are detailed, made nondimensional and split into a mean and a fluctuating part. Then, in Sec. III, an asymptotic analysis of these equations is led. The result of this analysis is validated in Sec. IV. Finally, the adaptation of the GSG turbulence model to match the small-Péclet-number limit is unveiled in Sec. V.

## II. RADIATIVE MIXING FLOW DESCRIPTION

### A. Governing equations

We consider a plasma defined by its density  $\rho$ , its velocity  $\mathbf{u}$ , the mass fractions of its  $N_s$  species of ions  $c_\alpha$  for  $\{\alpha = 1, \dots, N_s\}$ , and the internal specific energy  $e^m$  of its ions and electrons. This plasma is submitted to a gravitational force  $\mathbf{g}$  and is coupled to a radiative field of volumetric energy  $E^r$ . With a good approximation, the radiative field of stellar interiors obeys the equilibrium diffusion approximation [27]. As a result, a single temperature  $T$  is needed to describe radiation and matter. Besides, instead of  $e^m$  and  $E^r$ , one only needs to follow the total specific energy  $e$ , defined as:

$$e = e^m + E^r / \rho.$$

Within this setting, the evolution of the hydroradiative flow considered in this work is given by the following equations:

$$D_t \rho = -\rho \operatorname{div} \mathbf{u}, \quad (1a)$$

$$\rho D_t u_i = -\partial_i P - \partial_j \Pi_{ij} + \rho g_i, \quad (1b)$$

$$\rho D_t c_\alpha = -\partial_j \mathcal{F}_{\alpha j}, \quad (1c)$$

$$\rho D_t e = \rho \varepsilon - P \operatorname{div} \mathbf{u} - \partial_j \mathcal{F}_j. \quad (1d)$$

In these equations, the notations  $\partial_j \cdot$ ,  $D_t \cdot$ , and  $\operatorname{div} \cdot$  refer, respectively, to the partial derivative with respect to the spatial coordinate  $x_j$ , to the Lagrangian time derivative and to the divergence operator. In particular, one has  $\operatorname{div} \mathbf{u} = \partial_j u_j$ , and, for any quantity  $q$ ,  $D_t q = \partial_t q + u_j \partial_j q$  with  $\partial_t$  the partial derivative with respect to the time  $t$ . Note also that the Einstein convention on the summation of indices is used for Latin letters. However, it will not be so for Greek indices, in particular for the index  $\alpha$  attached to the species.

An important point that needs to be stressed is that the pressure  $P$  appearing in Eqs. (1b) and (1d) is the total pressure of the radiative flow, i.e., the sum of the material and radiative pressures, respectively denoted by  $P^m$  and  $P^r$ :

$$P = P^m + P^r.$$

In intermediate mass stars, such as the Sun, radiative pressure is usually negligible compared to the material pressure. However, this is not the case in massive stars, where both components can be of the same order.

Appendix A describes the equations of state and the closures for the viscosity tensor  $\Pi_{ij}$ , dissipation  $\varepsilon$ , and the molecular fluxes  $\mathcal{F}_{\alpha j}$  and  $\mathcal{F}_j$  introduced to solve Eqs. (1). Among the main quantities used hereafter, let us mention the constant volume specific heat  $C_v$ , the total thermal conductivity  $\lambda$ , which are the sums of material and radiative contributions, respectively, and the thermal diffusivity  $\chi$  defined by  $\chi = \lambda/(\rho C_v)$ .

The asymptotic analysis proposed below in Sec. III deals with the properties of the velocity field  $\mathbf{u}$ , of the total pressure  $P$ , and of the temperature  $T$ . The evolution equation of  $\mathbf{u}$  is given in Eqs. (1a)–(1d) but those of  $P$  and  $T$  still need to be made explicit. The evolution of these two quantities can be deduced from Eqs. (1a)–(1d) by using the differentiation chain rule with  $P$  and  $e$ , namely by writing that  $D_t P = P_{,T} D_t T + P_{,\rho} D_t \rho + \sum_\alpha P_{,\alpha} D_t c_\alpha$  and that  $D_t e = e_{,T} D_t T + e_{,\rho} D_t \rho + \sum_\alpha e_{,\alpha} D_t c_\alpha$ , where the notations  $f_{,T}$ ,  $f_{,\rho}$ , and  $f_{,\alpha}$  for a function  $f(\rho, T, c_\alpha)$  have the meanings  $f_{,T} = \partial_T f|_{\rho, c_\alpha}$ ,  $f_{,\rho} = \partial_\rho f|_{T, c_\alpha}$ , and  $f_{,\alpha} = \partial_{c_\alpha} f|_{\rho, T, c_{\beta \neq \alpha}}$ . Then, by combining these equations and after using some of Maxwell's thermodynamical relations, one obtains the following result for the total pressure  $P$ :

$$D_t P = -\gamma_1 P \operatorname{div} \mathbf{u} + (\gamma_3 - 1) \mathcal{C} + \mathcal{D}_P, \quad (2)$$

and, for the temperature  $T$ :

$$D_t T = -(\gamma_2 - 1) T \operatorname{div} \mathbf{u} + \frac{\mathcal{C}}{\rho C_v} + \frac{\mathcal{D}_T}{\rho C_v}. \quad (3)$$

In these two equations,  $\mathcal{C}$  stands for the total conduction term

$$\mathcal{C} = \partial_j (\lambda \partial_j T), \quad (4)$$

and  $\mathcal{D}_P$  and  $\mathcal{D}_T$  account for the effects of molecular diffusion and dissipation on  $P$  and  $T$ . Complete formula for  $\mathcal{D}_P$ ,  $\mathcal{D}_T$ , and  $\gamma_i$  are given in Appendix A.

### B. Average flow as a background state

A crucial element when performing a small-Mach-number or a small-Péclet-number asymptotic study is to choose a reference state that will allow to split quantities into a background component and a deviation from this background. It is this deviation which properties will be determined by the analysis. Most often, the background state is set according to some *a priori* knowledge of the flow, for instance by enforcing a particular stratification or by assuming some form of quasistationarity. However, this method may sometimes entail some unwarranted restrictions and prevent the result from being applicable to more general situations. Here, given the turbulence modeling context of this study, we choose a slightly different way of setting the background state of our asymptotic analysis. More precisely, we will perform our analysis by splitting quantities into a statistical ensemble mean and its corresponding fluctuation. Thus, the background state obeys its own set of evolution equations and is not determined by *a priori* assumptions. Note that, in a stellar context, the spherical symmetry of the configuration allows to assimilate ensemble means with spatial averages over the surface of sphere of a given radius. This ergodic definition of the ensemble mean can be useful in a practical context but will not be used hereafter.

For variable density flows, it is usual to work with ‘‘Favre’’ density-weighted statistics and ‘‘Reynolds’’ unweighted statistics. For any quantity  $q$ , the Reynolds and Favre averages are denoted, respectively, by  $\bar{q}$  and  $\tilde{q}$ . They are related by the identity  $\tilde{q} = \bar{\rho q} / \bar{\rho}$ . The corresponding fluctuations are, respectively,  $q' = q - \bar{q}$  and  $q'' = q - \tilde{q}$ . They are related by  $q'' = \tilde{q}'' + q'$ . Since the unweighted average follows Reynolds rules [28], one has  $\tilde{\tilde{q}} = \tilde{q}$ .

By averaging Eqs. (1b), (2), and (3), one obtains the following result:

$$\tilde{D}_t \tilde{u}_i = -\frac{\partial_i \tilde{P}}{\bar{\rho}} - \frac{\partial_j \tilde{\Pi}_{ij}}{\bar{\rho}} - \frac{\partial_j (\tilde{\rho} u_i'' u_j'')}{\bar{\rho}} + g_i, \quad (5)$$

$$\tilde{D}_t \tilde{P} = -\gamma_1 \overline{P \operatorname{div} \mathbf{u}} - \partial_j \overline{u_j' P'} + \overline{P' \operatorname{div} \mathbf{u}'} - \overline{u_j'' \partial_j \tilde{P}} + (\gamma_3 - 1) \overline{\mathcal{C}} + \overline{\mathcal{D}_P}, \quad (6)$$

$$\tilde{D}_t \tilde{T} = -(\gamma_2 - 1) \overline{T \operatorname{div} \mathbf{u}} - \partial_j \overline{u_j' T'} + \overline{T' \operatorname{div} \mathbf{u}'} - \overline{u_j'' \partial_j \tilde{T}} + \left( \frac{\mathcal{C}}{\rho C_v} \right) + \left( \frac{\mathcal{D}_T}{\rho C_v} \right), \quad (7)$$

where the notation  $\tilde{D}_t q$  for a given quantity  $q$  stands for:

$$\tilde{D}_t q = \partial_t q + \tilde{u}_j \partial_j q.$$

This set of averaged equations governs the reference state around which the asymptotic analysis will be performed. By

subtracting each of these equations from their respective instantaneous counterparts, one obtains the following evolutions for the fluctuating velocity, pressure and temperature:

$$D_t u_i' = -u_j' \partial_j \tilde{u}_i - \frac{\partial_i P'}{\rho} + \frac{\rho'}{\rho} \frac{\partial_i \bar{P}}{\bar{\rho}} - \left( \frac{\partial_j \Pi_{ij}}{\rho} \right)' + \mathcal{R}_i^u, \quad (8)$$

$$D_t P' = -u_j' \partial_j \bar{P} - \bar{\gamma}_1 \bar{P} \text{div} \mathbf{u}' - \gamma_1' \bar{P} \text{div} \bar{\mathbf{u}} - \bar{\gamma}_1 P' \text{div} \bar{\mathbf{u}} + (\bar{\gamma}_3 - 1) C' + \gamma_3' \bar{C} + \mathcal{D}'_P + \mathcal{R}^P, \quad (9)$$

$$D_t T' = -u_j' \partial_j \bar{T} - (\bar{\gamma}_2 - 1) \bar{T} \text{div} \mathbf{u}' - \gamma_2' \bar{T} \text{div} \bar{\mathbf{u}} - (\bar{\gamma}_2 - 1) T' \text{div} \bar{\mathbf{u}} + \left( \frac{C}{\rho C_v} \right)' + \left( \frac{\mathcal{D}_T}{\rho C_v} \right)' + \mathcal{R}^T. \quad (10)$$

Second-order contributions, i.e., those involving the product of two or more fluctuating quantities have been regrouped in the terms  $\mathcal{R}_i^u$ ,  $\mathcal{R}^P$ , and  $\mathcal{R}^T$ . These contributions are not necessarily negligible but their role on the forthcoming analysis remains very limited. Hence, their expressions are not detailed here. They can, however, be found in Appendix B. Equations (8)–(10) are the core equations that will serve for the small-Péclet-number analysis detailed in Sec. III.

### C. Dimensionless equations for the fluctuations

The last step before performing the small-Péclet-number asymptotic analysis consists in making Eqs. (8)–(10) dimensionless. In this regard, it is important to recognize that the mean and fluctuating fields have different characteristic scales. Hence, two sets of nondimensionalizing parameters must be provided: one for the mean field and the other for the fluctuating field.

First, the intensity of turbulent fluctuations, regarding the velocity  $\mathbf{u}'$ , the relative density  $\rho'/\bar{\rho}$ , the concentration  $c'_\alpha$ , and the adiabatic exponents  $\gamma_1'$ ,  $\gamma_2'$ , and  $\gamma_3'$  are respectively characterized by  $u_0$ ,  $\epsilon_{\rho 0}$ ,  $\epsilon_{c 0}$ , and  $\epsilon_{\gamma 0}$ . Besides, the characteristic length and timescales of turbulent eddies are denoted by  $\ell_0$  and  $\tau_0$ . They are related to the characteristic turbulent velocity by  $\tau_0 = \ell_0/u_0$ .

As for the mean scales of density, pressure, and temperature, they are respectively defined by the values of  $\rho_0$ ,  $P_0$ , and  $T_0$ . For the sake of simplicity, the characteristic sound celerity  $c_{s0}$  and heat coefficient at constant volume  $C_{v0}$  are chosen equal to  $c_{s0} = \sqrt{P_0/\rho_0}$  and  $C_{v0} = P_0/(\rho_0 T_0)$ .

Characteristic scales for the gradients of the mean field must also be provided. The characteristic scales of the mean strain and acceleration are respectively denoted by  $S_0$  and  $G_0$ . Besides, length scales for the mean gradients of temperature  $L_{T_0}$  and pressure  $L_{P_0}$  are also introduced:  $L_{T_0} \sim T_0/|\nabla T|_0$  and  $L_{P_0} \sim P_0/|\nabla P|_0 \sim c_{s0}^2/G_0$ .

Finally, characteristic values for the kinematic viscosity  $\nu$ , for the diffusion coefficients  $\mathcal{D}^{(\alpha)}$  and for the total thermal diffusivity  $\chi$  are also introduced. They are respectively denoted by  $\nu_0$ ,  $\mathcal{D}_0$ , and  $\chi_0$ .

Using  $\ell_0$  and  $\tau_0$  for space and time and the other quantities where appropriate, we can now nondimensionalize

Eqs. (8)–(10). We obtain that:

$$D_t u_i' = - \left[ \frac{1}{\text{Fr}_s} \right] u_j' \partial_j \tilde{u}_i - \left[ \frac{1}{M_t^2} \right] \frac{\partial_i P'}{\rho} + \left[ \frac{1}{\text{Fr}_a} \right] \frac{\rho'}{\rho} \frac{\partial_i \bar{P}}{\bar{\rho}} - \left[ \frac{1}{\text{Re}_t} \right] \left( \frac{1}{\rho} \partial_j \Pi_{ij} \right)' + \mathcal{R}_i^u, \quad (11)$$

$$D_t P' = -[\text{Ka}_P] u_j' \partial_j \bar{P} - \bar{\gamma}_1 \bar{P} \text{div} \mathbf{u}' + \left[ \frac{1}{\text{Pe}_t} \right] (\bar{\gamma}_3 - 1) C' - \left[ \frac{1}{\text{Fr}_s} \right] \bar{\gamma}_1 P' \partial_j \bar{u}_j - \left[ \frac{\epsilon_{\gamma 0}}{\text{Fr}_s} \right] \gamma_1' \bar{P} \partial_j \bar{u}_j + \left[ \frac{\epsilon_{\gamma 0} \text{Ka}_T^2}{\text{Pe}_t} \right] \gamma_3' \bar{C} + \left[ \frac{\epsilon_{c 0}}{\text{ScRe}_t} \right] \mathcal{D}'_P + \mathcal{R}^P, \quad (12)$$

$$D_t T' = -[\text{Ka}_T] u_j' \partial_j \bar{T} - (\bar{\gamma}_2 - 1) \bar{T} \text{div} \mathbf{u}' + \left[ \frac{1}{\text{Pe}_t} \right] \frac{C'}{\bar{\rho} \langle C_v \rangle} - \left[ \frac{1}{\text{Fr}_s} \right] (\bar{\gamma}_2 - 1) T' \partial_j \bar{u}_j - \left[ \frac{\epsilon_{\gamma 0}}{\text{Fr}_s} \right] \gamma_2' \bar{T} \partial_j \bar{u}_j + \left[ \frac{\epsilon_{\gamma 0} \text{Ka}_T^2}{\text{Pe}_t} \right] \left( \frac{1}{\rho C_v} \right)' \bar{C} + \left[ \frac{\epsilon_{c 0}}{\text{ScRe}_t} \right] \left( \frac{\mathcal{D}_T}{\rho C_v} \right)' + \mathcal{R}^T. \quad (13)$$

The dimensionless numbers appearing in these equations are defined as follows:

$$M_t = \frac{u_0}{c_{s0}}, \text{Fr}_s = \frac{1}{\tau_0 S_0}, \text{Fr}_a = \frac{u_0}{\tau_0 G_0 \epsilon_{\rho 0}}, \quad (14)$$

$$\text{Ka}_P = \frac{\ell_0}{L_{P_0}}, \text{Ka}_T = \frac{\ell_0}{L_{T_0}}, \text{Re}_t = \frac{u_0 \ell_0}{\nu_0}, \quad (15)$$

$$\text{Pr} = \frac{\nu_0}{\chi_0}, \text{Sc} = \frac{\nu_0}{\mathcal{D}_0}, \text{Pe}_t = \frac{u_0 \ell_0}{\chi_0} = \text{PrRe}_t. \quad (16)$$

The turbulent Mach number,  $M_t$ , characterizes the intensity of the turbulent velocity fluctuations. The Froude numbers related to strain,  $\text{Fr}_s$ , and acceleration,  $\text{Fr}_a$ , characterize the turbulence production by mean gradients. The von Kármán numbers, related to pressure,  $\text{Ka}_P$ , and temperature,  $\text{Ka}_T$ , characterize the length scales of mean pressure and temperature fields. Molecular and radiative effects are accounted for in the turbulent Reynolds number,  $\text{Re}_t$ ; Schmidt number,  $\text{Sc}$ ; Prandtl number,  $\text{Pr}$ ; and Péclet number,  $\text{Pe}_t$ . Finally, the averaged specific heat  $\langle C_v \rangle$  is defined by:

$$\langle C_v \rangle^{-1} = \bar{\rho}^{-1} / (\rho C_v).$$

## III. SMALL MACH NUMBER–SMALL PÉCLET NUMBER APPROXIMATION

### A. Conditions of the asymptotic expansion

The objective of this work is to study turbulent flows having small Mach and small Péclet numbers. More precisely, we will hereafter assume that the Mach number is small and that the Péclet number is possibly even smaller. This condition is expressed as:

$$M_t \ll 1 \text{ and } \text{Pe}_t \sim M_t^n \ll 1 \text{ with } n \geq 1. \quad (17)$$

Secondary conditions must also be provided for the remaining dimensionless numbers. The following ones are expected to

be relevant to stellar interiors. First, we consider that the order of magnitude of the fluctuations of the adiabatic exponents, concentration and density, are small:

$$\epsilon_{\gamma_0} \sim M_t \ll 1, \quad \epsilon_{c_0} \sim M_t \ll 1, \quad \epsilon_{\rho_0} \sim M_t \ll 1.$$

Then, we assume that turbulence is either decaying or is in a quasiequilibrium state. This implies that the mean production terms are at most of the same order as the dissipation ones. Hence, we consider that:

$$\text{Fr}_a \gtrsim 1, \quad \text{Fr}_s \gtrsim 1.$$

We also assume that the length scale of the mean temperature and pressure fields are very large compared to the turbulent length scale:

$$\text{Ka}_P \sim M_t \ll 1, \quad \text{Ka}_T \sim \text{Pe}_t^{1/2} \ll 1.$$

Finally, the viscous and dissipation terms are assumed to verify:

$$\text{Re}_t \gtrsim 1, \quad \text{ScRe}_t \gtrsim 1.$$

### B. Main results of the asymptotic expansion

We now proceed with the asymptotic analysis. The fluctuating quantities, such as  $\mathbf{u}'$  or  $P'$ , are developed as functions of the small parameter  $M_t$ . For any fluctuating quantity  $q'$ , we write the following expansion:

$$q' = q'^{(0)} + M_t q'^{(1)} + M_t^2 q'^{(2)} + O(M_t^3).$$

These expansions are then inserted in the dimensionless equations (11)–(13) and terms of similar orders are collected.

First, the conduction term in the fluctuating temperature evolution equation (13) has a singular scaling of order  $\text{Pe}_t^{-1} = M_t^{-n}$ . Then, collecting terms of order  $\text{Pe}_t^{-1} = M_t^{-n}$  to  $M_t^{-1}$  in this equation and accounting for the secondary conditions on the orders of magnitude of density, concentration, and length scales, one deduces that:

$$\mathcal{C}'^{(0)} = \mathcal{C}'^{(1)} = \dots = \mathcal{C}'^{(n-1)} = 0, \quad (18)$$

$$\text{and } T'^{(0)} = T'^{(1)} = \dots = T'^{(n-1)} = 0. \quad (19)$$

This first result shows that the temperature fluctuation is at least of order  $\text{Pe}_t = M_t^n$ . This prediction will be refined below. As for the order of magnitude of the pressure field, it can be deduced by noting that the pressure gradient term in Eq. (11) has a singular scaling of order  $M_t^{-2}$ . Then, collecting terms of order  $M_t^{-2}$  to  $M_t^{-1}$ , one deduces that:

$$P'^{(0)} = P'^{(1)} = 0. \quad (20)$$

This second result shows that the pressure fluctuation is of order  $M_t^2$ . This is the classical scaling obtained in most, if not all, small-Mach-number approximations [15–20].

When inserted in the definitions of the adiabatic indices, these temperature and pressure scalings imply, along with the fact that  $\gamma_m$  is constant, that:

$$\gamma_1'^{(0)} = \gamma_2'^{(0)} = \gamma_3'^{(0)} = 0.$$

Returning to Eqs. (12) and (13) for the fluctuating temperature and pressure, this time at order  $M_t^0$ , one obtains a linear

combination of  $\text{div}\mathbf{u}'^{(0)}$  and  $\mathcal{C}'^{(n)}$  on the right-hand side and null terms on the left-hand side. As a result, one deduces that:

$$\text{div}\mathbf{u}'^{(0)} = 0 \text{ and } \mathcal{C}'^{(n)} = 0.$$

The last equality implies that  $T'^{(n)} = 0$ . This shows that within the assumptions retained in this study, the temperature fluctuation is of order  $M_t \text{Pe}_t$  and is much smaller than both  $M_t$  and  $\text{Pe}_t$ .

Finally, at order  $M_t$ , Eqs. (12) and (13) provide two relations linking the main order of the velocity divergence to the main order of the conduction term:

$$0 = -\bar{\gamma}_1 \bar{P} \text{div}\mathbf{u}'^{(1)} + \left[ \frac{M_t^n}{\text{Pe}_t} \right] (\bar{\gamma}_3 - 1) \mathcal{C}'^{(n+1)} - \left[ \frac{\text{Ka}_P}{M_t} \right] u_j'^{(0)} \partial_j \bar{P} + \left[ \frac{\epsilon_{c_0}}{M_t \text{ScRe}_t} \right] \mathcal{D}'_P^{(0)}, \quad (21)$$

$$0 = -(\bar{\gamma}_2 - 1) \bar{T} \text{div}\mathbf{u}'^{(1)} + \left[ \frac{M_t^n}{\text{Pe}_t} \right] \frac{\mathcal{C}'^{(n+1)}}{\bar{\rho}(C_v)} - \left[ \frac{\text{Ka}_T}{M_t} \right] u_j'^{(0)} \partial_j \bar{T} + \left[ \frac{\epsilon_{c_0}}{M_t \text{ScRe}_t} \right] \left( \frac{\mathcal{D}_T}{\rho C_v} \right)'^{(0)}. \quad (22)$$

Equations (21) and (22) express the respective equilibria of  $T'$  and  $P'$ . They link the velocity divergence and the conduction term and describe their variation according to gradients of pressure and temperature, as well as diffusion terms. Their combined existence emphasizes the dependency of the small-Péclet approximation to its small-Mach counterpart. In particular, it appears hard to justify how one may enforce beforehand the constraint  $\text{div}\mathbf{u}' = 0$  and then perform a small-Péclet analysis of the resulting incompressible system as was done in Refs. [22], [23], or [29].

### C. Predictions in terms of dimensional variables

The asymptotic analysis being done, we recast its main results in a dimensional form, more useful for practical applications. From now on, we come back to the original variables prior to performing the nondimensionalization of the system. Hence, the fluctuations return to their original definitions and denote dimensional variables from here.

The first result is as follows. The pressure fluctuation  $P'$  is of order  $M_t^2$  and the temperature fluctuation  $T'$  is of order  $\text{Pe}_t M_t$ :

$$\frac{P'}{P} \sim M_t^2 \ll M_t \text{ and } \frac{T'}{T} \sim \text{Pe}_t M_t \ll M_t. \quad (23)$$

These relations indicate that the fluctuations of pressure and temperature are small compared to the fluctuations of other thermodynamical variables. Thus, they can be neglected with respect to these other variables, except when involved in gradients or diffusion terms [15,16].

The second result of the asymptotic analysis is taken from relations (21) and (22). These equations form a linear system for the two unknown quantities  $\text{div}\mathbf{u}'$  and  $\mathcal{C}'$ . By inverting this system and expanding the definitions of the adiabatic indices,

one obtains that:

$$\text{div}\mathbf{u}' = -u'_j \left( \frac{\partial_j \bar{\rho}}{\bar{\rho}} + \frac{\partial_j \bar{r}}{\bar{r}} \right) - \sum_{\alpha} \frac{r_{\alpha}}{\bar{r}} \frac{\partial_j \mathcal{F}'_{\alpha j}}{\bar{\rho}}, \quad (24)$$

$$c' = u'_j \left[ \bar{\rho} \bar{C}_v \partial_j \bar{T} - x^p \bar{P} \left( \frac{\partial_j \bar{\rho}}{\bar{\rho}} + \frac{\partial_j \bar{r}}{\bar{r}} \right) \right], \\ - 4\bar{P} \sum_{\alpha} \frac{r_{\alpha}}{\bar{r}} \frac{\partial_j \mathcal{F}'_{\alpha j}}{\bar{\rho}},$$

$$\text{with } x^p = 4 - 3 \frac{\bar{P}^m}{\bar{P}}. \quad (25)$$

The first term on the right-hand side of Eq. (24) expresses the volume adjustment of a mass element moving in a stratified environment. As can be seen, this adjustment only depends on the value of the mean density and of the plasma gas constant and not on radiative properties. The second term of Eq. (24) shows that the volume of a mass element is also modified by the molecular diffusion of species provided they have different gas constants.

The second relation Eq. (25) corresponds to the thermal equilibrium existing between the conduction term on the left-hand side and two different sources of temperature fluctuations on the right-hand side. The first source term arises from the displacement of fluid particles along an adiabatic-like temperature gradient. The second one involves a combined effect of radiation and species diffusion.

Note that a generalized version of these relations can be found in Appendix C to account for nonideal equations of states and additional source terms.

#### D. Comparison with previous results and with the high-Péclet limit

As mentioned in the Introduction, previous works have been devoted to the study of the small Péclet–small Mach number limit. In Refs. [24,25], the following expressions are proposed:

$$\text{div}\mathbf{u}' = -u'_j \frac{\partial_j \bar{\rho}}{\bar{\rho}} \text{ and } \frac{c'}{\bar{\rho} \bar{C}_v} = -(\gamma_m - 1) \bar{T} u'_j \frac{\partial_j \bar{\rho}}{\bar{\rho}}, \quad (26)$$

while in Ref. [23], the following results are obtained:

$$\text{div}\mathbf{u}' = 0 \text{ and } \frac{c'}{\bar{\rho} \bar{C}_v} = u'_j \partial_j \bar{T}. \quad (27)$$

The expressions derived in Refs. [24,25] can be seen as particular cases of the ones proposed here. Equation (26) reverts to Eqs. (24) and (25) when all species are identical, i.e., when there is no mixing involved in the flow and  $\bar{r} = \text{Cst}$ , when there is no temperature gradient and when the radiative pressure is negligible compared to the material pressure  $P' \ll P^m$ . These are indeed some of the conditions under which the asymptotic analysis of Refs. [24,25] is performed.

As for the expression of Ref. [23], it can also be interpreted as a particular case of Eqs. (24) and (25). Equations (27), (24), and (25) become indeed equivalent provided mixing is discarded and provided the density gradient is zero.

Another point of comparison can be made to better understand Eqs. (24) and (25) and the role played by the smallness of the Péclet number. Equations (24) and (25) can

also be compared against their high-Péclet-number counterparts. First, for  $\text{Pe}_t \gg 1$ , there is no temperature equilibrium. Accordingly, there is no constraint for the order of magnitude of the fluctuating temperature  $T'$  and no relation equivalent to Eq. (25). What remains is the pressure equilibrium and its consequences: the order of magnitude for  $P'$  in Eq. (23) and an expression for the divergence equivalent to Eq. (24). Based on Ref. [20], this expression takes the form:

$$\text{div}\mathbf{u}' = -u'_j \frac{\partial_j \bar{P}}{\bar{\gamma}_1 \bar{P}} + \text{molecular terms}. \quad (28)$$

When all molecular diffusion coefficients are equal, the molecular terms in the above relation simplify into a diffusion term on density fluctuations and become equivalent to the diffusion term appearing in Eq. (24). Therefore, notwithstanding the properties of  $T'$ , the main difference between the small- and high-Péclet limits comes from the way the volume of fluid particles adjust to the mean gradients of pressure and temperature, as expressed by the first term on the right-hand sides of Eqs. (24) and (28). This difference has important repercussions, in particular for defining the stability criterion of a mean stratification. To illustrate this point, let us consider the linear inviscid stability of a static configuration (i.e., without shear nor any mean velocity) having a mean density, temperature, and concentration stratification satisfying the hydrostatic equilibrium condition  $\partial_j \bar{P} = \bar{\rho} g_j$ . This problem can be studied by looking at the linearized equations for the density and velocity fluctuations, deduced from Eqs. (1):

$$\partial_t u'_i = \frac{\rho'}{\rho} \frac{\partial_i \bar{P}}{\bar{\rho}} \quad \text{and} \quad \partial_t \frac{\rho'}{\rho} = -\text{div}\mathbf{u}' - u'_j \frac{\partial_j \bar{\rho}}{\bar{\rho}}. \quad (29)$$

When inserting the value of the velocity divergence expression (28) obtained the inviscid high-Péclet limit, the second equation becomes  $\partial_t \frac{\rho'}{\rho} = -u'_j \left( \frac{\partial_j \bar{\rho}}{\bar{\rho}} - \frac{\partial_j \bar{P}}{\bar{\gamma}_1 \bar{P}} \right)$ . When inserting expression (24) obtained in the inviscid small-Péclet limit, this same equation becomes  $\partial_t \frac{\rho'}{\rho} = u'_j \frac{\partial_j \bar{r}}{\bar{r}}$ . From there, one obtains that a stratification is stable provided:

$$\text{for } \text{Pe}_t \ll 1, \quad \frac{\partial_j \bar{r}}{\bar{r}} \frac{\partial_j \bar{P}}{\bar{\rho}} < 0, \quad (30)$$

$$\text{for } \text{Pe}_t \gg 1, \quad \left( \frac{\partial_j \bar{P}}{\bar{\gamma}_1 \bar{P}} - \frac{\partial_j \bar{\rho}}{\bar{\rho}} \right) \frac{\partial_j \bar{P}}{\bar{\rho}} < 0. \quad (31)$$

In the large-Péclet limit, stability is defined by the orientation of the mean pressure gradient with respect to the density gradient corrected by an adiabatic pressure gradient. The corrected density gradient can be rewritten as:

$$\frac{\partial_j \bar{P}}{\bar{\gamma}_1 \bar{P}} - \frac{\partial_j \bar{\rho}}{\bar{\rho}} = \frac{\partial_{\bar{P}} \bar{\rho} |_{\bar{s}, \bar{c}}}{\bar{\rho}} \partial_j \bar{P} - \frac{\partial_j \bar{\rho}}{\bar{\rho}} \\ = - \frac{\partial_{\bar{s}} \bar{\rho} |_{\bar{P}, \bar{c}}}{\bar{\rho}} \partial_j \bar{s} - \sum_{\alpha} \frac{\partial_{\bar{c}_{\alpha}} \bar{\rho} |_{\bar{P}, \bar{s}, \bar{c}_{\beta \neq \alpha}}}{\bar{\rho}} \partial_j \bar{c}_{\alpha},$$

where  $s$  is the entropy of the photon-matter continuum. Note that  $\partial_{\bar{s}} \bar{\rho} |_{\bar{P}, \bar{c}} < 0$  for ideal gases with radiation. Hence, in the absence of mean concentration gradients, the stability of a stratification in the high-Péclet limit is determined by the relative orientation of the mean pressure gradient and the

entropy gradient. When concentration gradients exist, the stability is not set uniquely by the entropy gradient but the latter can still be expected to play a significant role. In the limit of vanishing radiation  $\frac{\partial_j \bar{p}}{\bar{\rho}} - \frac{\partial_j \bar{p}}{\bar{\gamma}_1 \bar{p}}$  reverts to the inverse scale height of the potential density for a perfect gas and since  $\partial_j \bar{p}/\bar{\rho} = g_j$ , one recognizes that (31) becomes nothing else than the usual stability condition  $N^2 > 0$  expressed in terms of the Brunt-Väisälä frequency  $N$ .

By contrast, in the small-Péclet limit, the stability is determined by the relative orientations of the mean pressure gradient and the gradient of the gas constant. Entropy does not play a role any longer and only the gradients of the concentrations of the different species influence the stability of the flow. The latter result can be understood as a special asymptotic case of the double-diffusion (thermohaline) instability encountered in geophysical and stellar flows [30–32].

#### IV. VALIDATION OF THE ASYMPTOTIC ANALYSIS

In order to highlight the impacts of the small Péclet–small Mach number approximation, direct numerical simulations (DNS) of a radiative turbulent mixing zone are performed with the in-house TRICLADE code, see Appendix D.

In the following sections, the cartesian frame  $(x_1, x_2, x_3)$  introduced in the derivation of the asymptotic approximation will be also be referred to with the notation  $(x, y, z)$ :  $(x_1, x_2, x_3) \equiv (x, y, z)$ .

##### A. Rayleigh-Taylor flow configuration

The test flow under consideration is a statistically axisymmetric turbulent mixing induced by a Rayleigh-Taylor instability (RTI) at a planar interface between two different fluids. As explained in the Introduction, this simplified configuration does not occur as such in stellar interiors. Its interest lies in the fact that it combines some of the elementary mechanisms which are at work in stellar flows. In particular, it involves mixing, convection, radiation, and Péclet number effects. It consequently constitutes a relevant testing ground for our predictions.

The initial state of the simulations is defined as follows. The two fluids are separated by an interface, located at  $x = x_I$  (chosen at  $x_I = 0$  below), which is unstable with respect to a constant gravitational field  $\mathbf{g}$  oriented along the  $x$  axis toward negative values of  $x$  i.e., pointing from the heavy fluid side ( $x > x_I$ ) to the light fluid side ( $x < x_I$ ). The latter axis is referred to as the inhomogeneous or longitudinal direction, while the  $(y, z)$  axes correspond to the transverse or homogeneous directions. The mean state is fixed by enforcing a hydrostatic equilibrium with an isothermal condition. More precisely, the initial profiles along the longitudinal direction are defined by:

$$\bar{T}(x) = T_0, \quad \bar{P}(x) = \bar{\rho}(x) \frac{\mathcal{R}}{\mathcal{M}(x)} T_0 + \frac{a_R T_0^4}{3}$$

$$\text{with } \bar{\rho}(x) = \rho_0 \frac{\mathcal{M}(x)}{\mathcal{M}_0} \exp \left[ \frac{\mathcal{M}(x) g x}{\mathcal{R} T_0} \right]$$

$$\text{where } \mathcal{M}(x) = \begin{cases} \mathcal{M}_l & \text{if } x < x_I \\ \mathcal{M}_h & \text{if } x > x_I \end{cases} \text{ and } \mathcal{M}_0 = \frac{\mathcal{M}_h + \mathcal{M}_l}{2}.$$

Note that the two molar masses should be understood as effective masses, accounting for the actual molar mass divided by  $1 + \mathcal{Z}$ , consistent with the equation of state (A1). Their contrast is characterized by the Atwood number:

$$\mathcal{A} = \frac{\mathcal{M}_h - \mathcal{M}_l}{\mathcal{M}_h + \mathcal{M}_l}.$$

At initial time, the interface is left flat but a small perturbation of the velocity field is introduced around it. The perturbation spectrum has a hat profile delimited by the wavelengths  $\Lambda_{\min}$  and  $\Lambda_{\max} = 2\Lambda_{\min}$  and an intensity characterized by a turbulent Mach number,  $M_{t0}$ .

From now on, all quantities are nondimensionalized by the following reference scales: the maximum wavelength of the perturbation spectrum  $\Lambda_{\max}$ , the acceleration  $\mathcal{A}g$ , and the arithmetic average of the densities of the two fluids at the interface. Besides, two dimensionless numbers are introduced in order to account for the local properties of the radiating fluid, see Ref. [27]. The contribution of the radiation energy compared to the one of the stellar material may be expressed with the Mihalas number,  $R$ . As for the Boltzmann number,  $\text{Bo}$ , it yields the relative importance between radiative and matter energy transport. They are respectively estimated at the initial interface location with:

$$R = \frac{\rho e^m}{E^r} \text{ and } \text{Bo} = \frac{\rho h^m c_{s0}}{\sigma_{\text{SB}} T^4},$$

where all the quantities have the same meanings as in Sec. II C. Note that the initial speed of sound is chosen as the characteristic velocity for the Boltzmann number. The temperature reference scale is finally defined from the other reference scales so as to maintain the Mihalas number.

For the sake of simplicity, both gases of the binary mixture have equal adiabatic indices  $\gamma_0$ , kinematic viscosity  $\nu$ , species diffusion coefficient  $\mathcal{D}$ , and opacity  $\kappa^r$ , and these properties are assumed to be constant.

Within this nondimensional setting and choices, the main parameters defining the simulations are as follows:

$$\mathcal{A} = 0.26, \quad R = 1.24, \quad \text{Bo} = 3.75 \times 10^{-2},$$

$$\gamma_0 = \frac{5}{3}, \quad \rho_0 = 1, \quad \Lambda_{\max} = 1,$$

$$M_{t0} = 5 \times 10^{-3}, \quad T_0 = 3.16,$$

$$\frac{\mathcal{M}_0 g}{\mathcal{R} T_0} = 3.89 \times 10^{-2}, \quad \nu = \mathcal{D} = 9.2 \times 10^{-3}$$

The fact that  $R > 1$  indicates that material energy and pressure dominate radiative ones and the fact that  $\text{Bo} \ll 1$  shows that the radiative flux overwhelms the material enthalpy flux. Such conditions can be found in the interior of massive stars, where the radiative pressure is not negligible as opposed to intermediate-mass stars.

As for the numerical parameters, the domain is of size  $L_x \times L_y \times L_z = (87.5 \times 100 \times 100)$  and is discretized using a Cartesian structured mesh with  $N_x \times N_y \times N_z = (896 \times 1024 \times 1024)$  cells. Periodic conditions are imposed in the transverse homogeneous directions, along the  $(y, z)$  axes. Slip wall boundary conditions are considered for the fluids and Dirichlet ones for the radiative energy in the  $x$  axis.

TABLE I. Rosseland opacities and Prandtl numbers for each of the three simulations performed for the validation. The acronyms SP and HP stand, respectively, for small Prandtl and high Prandtl.

Simulation acronym	Opacity $\kappa^r$	Prandtl number Pr
SP <sub>1</sub>	8.64	$1.42 \times 10^{-4}$
SP <sub>2</sub>	$8.64 \times 10^1$	$1.42 \times 10^{-3}$
HP	$8.64 \times 10^4$	1.42

Three simulations are carried out: one with a very small Prandtl number, another with a large Prandtl number, and a third one with a moderately small Prandtl number. The Prandtl number is defined as the value at initial time and at the interface of:

$$\text{Pr} = \frac{\nu}{\lambda/(\rho C_v)} = \frac{3\rho C_v}{4c_\ell a_R T^3} \rho_0 \kappa^r \nu.$$

The first simulation is expected to yield a small Péclet number and aims at verifying the results of the asymptotic analysis. Then, by comparison with the second one, it allows to differentiate the behaviors of the induced turbulent mixing arising within both asymptotic regimes. The intermediate Prandtl simulation is meant to test the limits of the approximation. To vary the Prandtl number, the radiative conductivity is modified by changing the opacity  $\kappa^r$ . The opacity values chosen for each simulation are given in Table I along with the Prandtl number and with a name attributed to each simulation.

To conclude the flow description, let us remark that the problem is statistically one dimensional (1D), with  $x$  the inhomogeneous direction. Thus, by ergodicity, statistical averages can be computed by integration on the homogeneous directions. For any quantity  $q$ , we have:

$$\bar{q}(x) = \frac{1}{L_y L_z} \iint q(x, y, z) dy dz.$$

### B. Dimensionless numbers

In order to verify the main conditions of the asymptotic analysis, derived in Sec. III, we proceed to compute the following dimensionless numbers: the turbulent Mach number,  $M_t$ ; the turbulent Reynolds number,  $\text{Re}_\lambda$ , based on the Taylor microscale; as well as the turbulent Péclet number,  $\text{Pe}_t$ . All those numbers are extracted from the simulations at the initial position of the interface  $x = x_I$ , using the following definitions:

$$M_t \equiv \frac{\sqrt{\bar{k}}}{\bar{c}_s}, \quad \text{Re}_\lambda \equiv \frac{2\sqrt{15}}{3} \sqrt{\frac{\bar{\rho}\bar{k}^2}{\mu\bar{\varepsilon}}}, \quad \text{Pe}_t \equiv \frac{\bar{\rho}\bar{C}_p\nu_t}{\lambda}$$

with  $\nu_t = \frac{C_\mu\bar{k}^2}{\bar{\varepsilon}}$ ,  $\bar{k} = \frac{1}{2}\overline{u'_i u'_i}$ ,  $\bar{\varepsilon} = 2\nu\overline{(\partial_j u'_i)(\partial_j u'_i)}$ . (32)

These definitions involve the turbulent kinetic energy  $\bar{k}$ , its dissipation  $\bar{\varepsilon}$ , and the turbulent viscosity  $\nu_t$ . The constant  $C_\mu$  is set to 0.1 as in standard  $\bar{k} - \bar{\varepsilon}$  models [33].

First, the desired condition  $M_t \ll 1$  is met for the three configurations since the turbulent Mach number is always observed to remain lower than 0.14. Regarding the turbulent

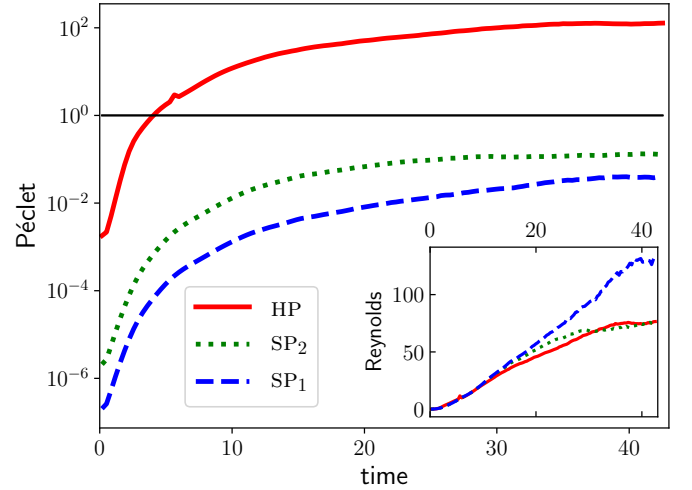


FIG. 1. Time evolution of the turbulent Péclet  $\text{Pe}_t$  number at the center of the mixing zone. Insert: Same evolution for the Reynolds  $\text{Re}_\lambda$  number.

Péclet number, its evolution is shown in Fig. 1. At large-enough times for the flow to be turbulent ( $t \gtrsim 15$ ), the Péclet reaches values on the order of  $10^{-2}$ ,  $10^{-1}$ , and  $10^2$ , respectively, for the low, intermediate, and high-Prandtl simulations. As for the Reynolds number,  $\text{Re}_\lambda$ , its value is shown in Fig. 1. It keeps increasing in time and finally reaches the value  $\text{Re}_\lambda \sim 115$  for the small-Prandtl simulation and  $\text{Re}_\lambda \sim 70$  for the other two configurations.

To sum up, the following conditions are reached for each simulations, from approximately  $t \gtrsim 15$ :

$$\begin{aligned} \text{SP}_1 : \text{Re}_t \gg 1 \text{ and } \text{Pe}_t \ll M_t \ll 1, \\ \text{SP}_2 : \text{Re}_t \gg 1 \text{ and } \text{Pe}_t \sim M_t \ll 1, \\ \text{HP} : \text{Re}_t \gg 1, M_t \ll 1 \text{ and } \text{Pe}_t \gg 1. \end{aligned}$$

Thus, the main conditions of relations (17) leading to the asymptotic expansion detailed in Sec. III B are verified for the simulations SP<sub>1</sub> and SP<sub>2</sub>. By contrast, the simulation HP evolves in the opposite Péclet limit.

Note that the secondary conditions introduced in Sec. III A are also verified in all three simulations. The Froude numbers are on the order or much larger than one, the relative concentration and density variances within the mixing zones are small and the mean pressure and temperature scales are much larger than the turbulent scale.

### C. General evolution of the flow

The development of the instability between the two fluids is illustrated in Fig. 2. The latter displays a volume rendering of the concentration at three different times and for the simulations SP<sub>1</sub> and HP. More precisely, the left and middle parts of the figure show the mixing zone shortly after the initial time ( $t = 4$ ) and at a transitional time ( $t = 17$ ). These times are only presented for the high-Péclet simulation HP. Indeed, until  $t \approx 17$ , the binary mixtures of the small- and high-Péclet simulations are visually indistinguishable. However, at later times, in the fully turbulent regime, a clear discrepancy between the two simulations is seen, as displayed in the right third of Fig. 2. In the high-Prandtl-simulation HP, the mixing

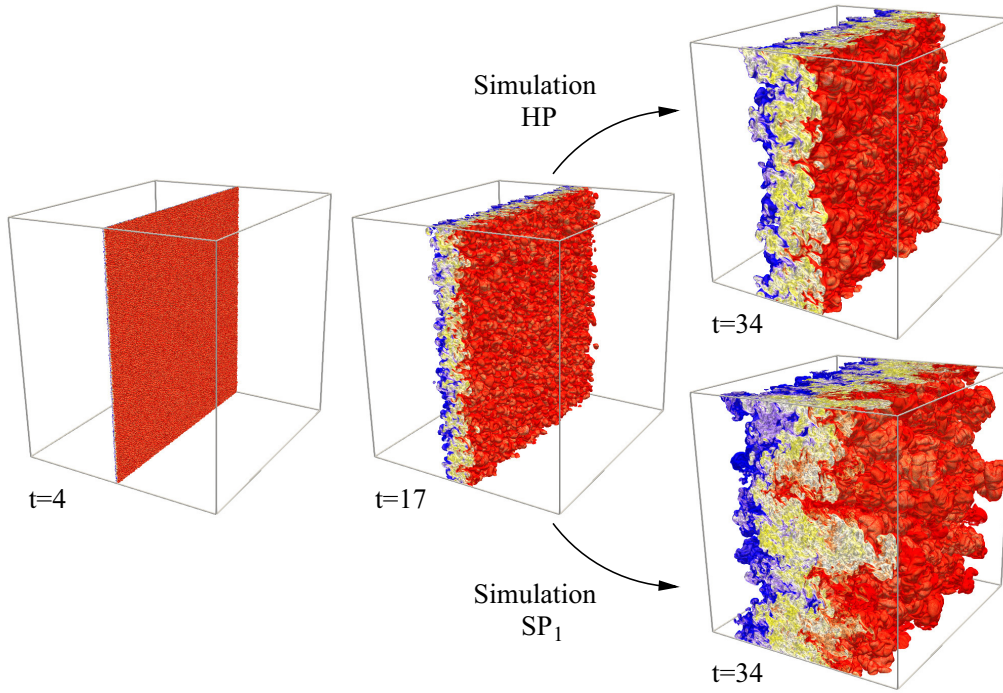


FIG. 2. Shaded volume rendering of the light fluid concentration made visible from  $c = 0.1$  (blue) to  $c = 0.9$  (red). The heavy fluid is on the right and the light one on the left. The gravity vector is oriented to the left along the  $x$  axis, i.e., from the heavy to the light side. The rendering is shown at three different times:  $t = 4$ ,  $t = 17$ , and  $t = 34$ . Visually identical figures are obtained for all three simulations at  $t = 4$  and  $t = 17$ . By contrast, large differences are observed between the high-Prandtl HP and the small-Prandtl  $SP_1$  simulations at the final time  $t = 34$ .

zone saturates, whereas in the small-Prandtl-simulation  $SP_1$ , the dominant and most energetic scales of turbulence keep increasing.

This discrepancy can be explained by the difference in the stability criteria obtained in the high- and small-Péclet limit, as detailed in Sec. III D. For the high-Péclet limit, the stability criterion is linked to the density gradient corrected by an adiabatic pressure gradient. This quantity can be integrated over the inhomogeneous direction to yield a dimensionless pseudoentropy:

$$S = \int_{x_0}^x \left( \frac{\partial_\xi \bar{P}}{\bar{\gamma}_1 \bar{P}} - \frac{\partial_\xi \bar{\rho}}{\bar{\rho}} \right) d\xi, \quad (33)$$

with the arbitrary integration origin  $x_0$  here chosen at  $x_0 = -30$ .

Given the orientation of the gravity in the simulations (leading to  $\partial_x \bar{P} < 0$ ) and the stability criterion (31), the stratification in the high-Péclet case is stable if  $S$  increases with  $x$  ( $\partial_x S > 0$ ), unstable if  $S$  decreases ( $\partial_x S < 0$ ) and neutral if  $S$  is constant ( $\partial_x S = 0$ ).

In the present simulations, the spatial profiles of the pseudoentropy  $S$  are not monotonous. These profiles are shown for the high- and small-Prandtl simulations in Fig. 3 at times  $t = 0$ ,  $t = 17$ , and  $t = 34$ . The initial profile of  $S$  is the same for all simulations and is imposed by the isothermal hydrostatic condition. More precisely, at  $t = 0$ , one observes a rapid decrease of  $S$  at the interface between both gases while  $S$  increases on each side of this interface. In other words, according to the

high-Péclet-number criterion (31), the interface is initially unstable while the subdomains it separates are stable. As mixing unfolds, the initial rapid interfacial decrease of  $S$  extends and flattens out until an almost constant profile is reached within the extent of the mixing zone. For the high-Prandtl-number simulation HP, this flat profile of  $S$  means that the stratification has reached an almost neutral state and that the instability

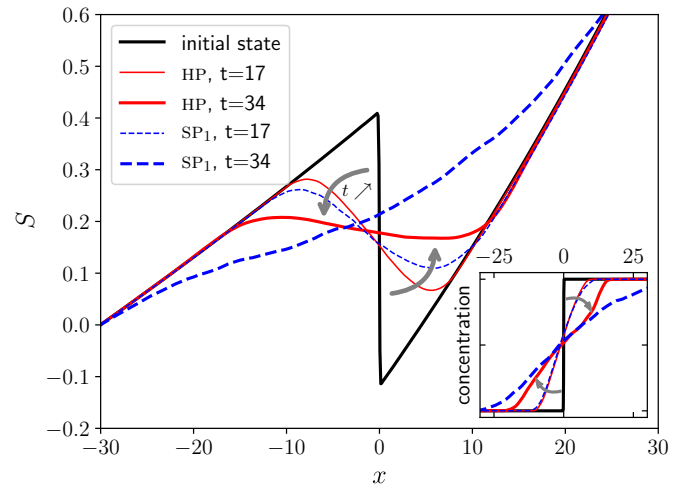


FIG. 3. Spatial profiles of the pseudoentropy  $S$ , given by (33) for the high- and small-Péclet simulations at times  $t = 0$ ,  $t = 17$ , and  $t = 34$ . Inset: Spatial profiles of the light fluid concentration at the same times.

is not fed any longer. Thus, turbulence starts decaying and eventually dissipates. The mixing zone stops growing.

This phenomenology is not observed for the small-Prandtl simulation  $SP_1$ . As can be seen in Fig. 3, for  $SP_1$ , the profile of  $S$  never stops diffusing. Even after crossing the high-Péclet neutral threshold, it keeps increasing over the whole spatial domain. To explain this major difference, one must recall that the stability criteria in the small- and high-Péclet limits are not the same. In the small-Péclet case, the stability of a stratification is determined by Eq. (30). It is completely independent of the entropy stratification and only depends on the gas constant gradient  $\partial_x \bar{c}$ . The latter exists if the two gases being mixed have different molar masses and if there is a mean concentration gradient. In the small-Prandtl simulations performed here, evolving in a small-Péclet regime, given the orientation of the gravity field and the initial repartition of the molar masses, the stability of the stratification is eventually given by the sign of  $\partial_x \bar{c}$ , the mean concentration gradient of the light fluid. More precisely, the stratification in the small-Péclet limit is stable if  $\bar{c}$  decreases with  $x$  ( $\partial_x \bar{c} < 0$ ), unstable if  $\bar{c}$  increases ( $\partial_x \bar{c} > 0$ ) and neutral if  $\bar{c}$  is constant ( $\partial_x \bar{c} = 0$ ). The mean concentration has a monotonously decreasing spatial profile at all times ( $\partial_x \bar{c} \leq 0$ ) as shown in the insert of Fig. 3. Therefore, the stratification of the small-Prandtl  $SP_1$  simulation is always unstable. As a result, the mixing zone grows in the small-Péclet regime until its fronts reach the limits of the domain.

As a conclusion, the different mixing width evolutions observed in simulations  $SP_1$  and HP are coherent with the stability criteria predicted in Sec. III D. These criteria reflect the influence of the Péclet number and are a direct consequence of the asymptotic approximation derived in Sec. III C. Thus, the qualitatively different behaviors between simulations  $SP_1$  and HP (identical except for the opacity value), is a first validation of the asymptotic results. A direct verification is proposed in the next subsection.

#### D. Validation of the asymptotic analysis

One of the main predictions of the asymptotic analysis is the order of magnitude of the pressure and temperature fluctuations, as given by Eq. (23). To assess this prediction, we plot in Fig. 4 the temporal evolutions of the ratios  $\eta_P$  and  $\eta_T$  at the center of the mixing zone, defined by:

$$\eta_P = \frac{\sqrt{P'P'}}{\overline{PM}_t^2} \quad \text{and} \quad \eta_T = \frac{\sqrt{T'T'}}{\overline{TPe}_t M_t}.$$

For Eq. (23) to be verified, these ratios must be on the order of 1. As can be seen in Fig. 4, the ratio  $\eta_P$  tends to 1 in the turbulent regime for each configuration, showing that the fluctuating pressure is on the order of  $M_t^2$ . This scaling is expected because it results from the small-turbulent-Mach-number asymptotics whatever the Péclet number. Since the turbulent Mach number hardly reaches 0.14, as previously mentioned, all three simulations evolve in a small-Mach regime and give rise to pressure fluctuations of the same order.

As for the ratio  $\eta_T$ , it is of order unity for the two small-Prandtl simulations  $SP_1$  and  $SP_2$  whose turbulent mixing occur in a small-Péclet regime. The prediction (23) is thus verified. On the opposite, the order of  $\eta_T$  in the high-Prandtl simulation

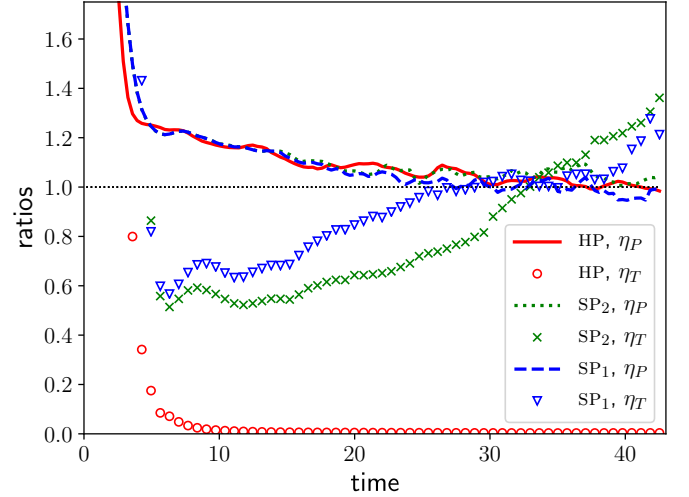


FIG. 4. Time evolution of ratios  $\eta_P$  and  $\eta_T$  at the center of the mixing zone.

HP significantly departs from the others:  $\eta_T$  actually tends toward zero. There is indeed no condition for the fluctuating temperature in the high-Péclet analysis [20].

The other major predictions derived from the asymptotic analysis of Sec. III C are the values of the fluctuating velocity divergence  $\text{div} \mathbf{u}'$  and of the fluctuating conduction term  $C'$ . These predictions are respectively expressed in Eqs. (24) and (25). To evaluate their quality, we compare “simulated” and “predicted” values of  $\text{div} \mathbf{u}'$  and  $C'$ . On the one hand, the “simulated” values are obtained by taking the fluctuating part of  $\text{div} \mathbf{u}$  and  $C$  computed from the actual fields using their definitions  $\text{div} \mathbf{u} = \partial_j u_j$  and  $C = \partial_j (\lambda \partial_j T)$ . On the other hand, the “predicted” values are directly computed as the right-hand side of Eqs. (24) and (25) using the same actual simulations.

Two-dimensional fields (slices in the plane  $y = 0$ ) are shown in Fig. 5 and 6 to compare the simulated and predicted values of  $C'$  and  $\text{div} \mathbf{u}'$ , respectively. They are extracted from the simulation  $SP_2$  at  $t = 34$ , a time at which the small-Péclet asymptotic results should apply according to Fig. 1. The same structures can indeed be identified in both parts of Fig. 5 and, since the color scale is the same, the overall agreement on the intensity of the fluctuating conduction  $C'$  fields can be guessed. The main difference comes from the occurrence of some localized extrema in the simulated field which seem to be filtered out by the use of formula (25). The same comments apply to the fluctuating velocity divergence shown in Fig. 6 including the filtering effect of the asymptotic expression Eq. (24). The striking likeness between Fig. 5 and 6 comes from the fact the stratification term is dominant in Eqs. (25) and (24) in that case and the mean flow is isothermal. Both fields then roughly look like  $u'_j (\frac{\partial_j \bar{p}}{\bar{p}} + \frac{\partial_j \bar{c}}{\bar{c}})$  and the large difference in the prefactors is hidden by the difference in color scale between both figures.

Figures 5 and 6 provide a qualitative assessment of the asymptotic results derived in Sec. III C. A quantitative validation can be performed by measuring the correlations of  $\text{div} \mathbf{u}'$  with other flow variables. For modeling purposes that will be made clear below in Sec. V, we focus on the correlations of  $\text{div} \mathbf{u}'$  with  $\rho'$  and  $u'_x$ , namely:  $\overline{\rho' \text{div} \mathbf{u}'}$  and  $\overline{u'_x \text{div} \mathbf{u}'}$ . Besides, the

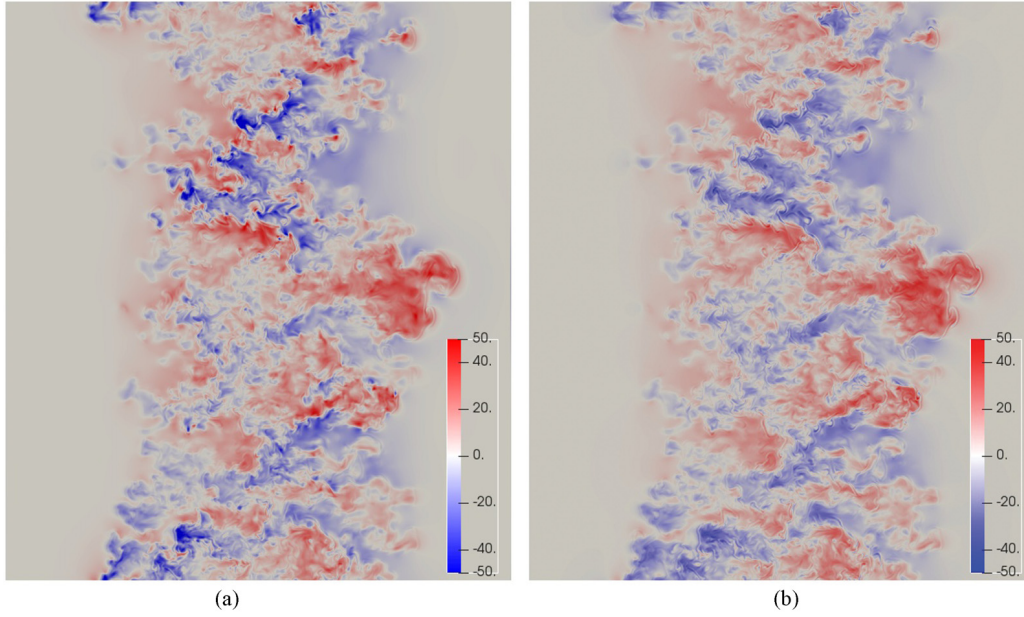


FIG. 5. Cuts in the plane  $y = 0$  at time  $t = 34$  for simulation  $SP_2$  displaying, respectively, (a) the fluctuating conduction term  $C'$  computed by using its definition  $C = \partial_j(\lambda \partial_j T)$  and (b) the asymptotic value of  $C'$  predicted by Eq. (25). The color scale is the same in each figure.

predicted value of  $\text{div} \mathbf{u}'$  is split into its two contributions: the one coming from the mean stratification and the one coming from molecular mixing effects. More precisely, from Eq. (24), the correlations  $\overline{\rho' \text{div} \mathbf{u}'}$  and  $\overline{u'_x \text{div} \mathbf{u}'}$  are expressed as:

$$\overline{q' \text{div} \mathbf{u}'} = \overline{q' \text{div} \mathbf{u}'}^{\text{strat.}} + \overline{q' \text{div} \mathbf{u}'}^{\text{mix.}}, \quad (34)$$

$$\text{with } \begin{cases} \overline{q' \text{div} \mathbf{u}'}^{\text{strat.}} = -\overline{q' u'_j} \left( \frac{\partial_j \bar{\rho}}{\bar{\rho}} + \frac{\partial_j \bar{r}}{\bar{r}} \right) \\ \overline{q' \text{div} \mathbf{u}'}^{\text{mix.}} = \frac{\Delta r}{\bar{r}} \overline{q' \left[ \frac{\partial_j (\rho \mathcal{D} \partial_j c')}{\rho} \right]'} \end{cases},$$

where the quantity  $q'$  stands for  $u'_x$  or  $\rho'$  and where  $\Delta r = \mathcal{R}/\mathcal{M}_l - \mathcal{R}/\mathcal{M}_h$ .

The simulated and predicted correlations  $\overline{\rho' \text{div} \mathbf{u}'}$  and  $\overline{u'_x \text{div} \mathbf{u}'}$  are shown in Fig. 7, along with the components of the predicted value, at times  $t = 17$  and  $t = 34$ . A good agreement between the simulation and the prediction is observed for both correlations at both times indicating that Eq. (24) provides quantitatively accurate estimations. The contributions of the stratification and of the molecular mixing have opposite signs because of the instability: the baroclinic production related to the stratification tends to intensify the turbulent mass

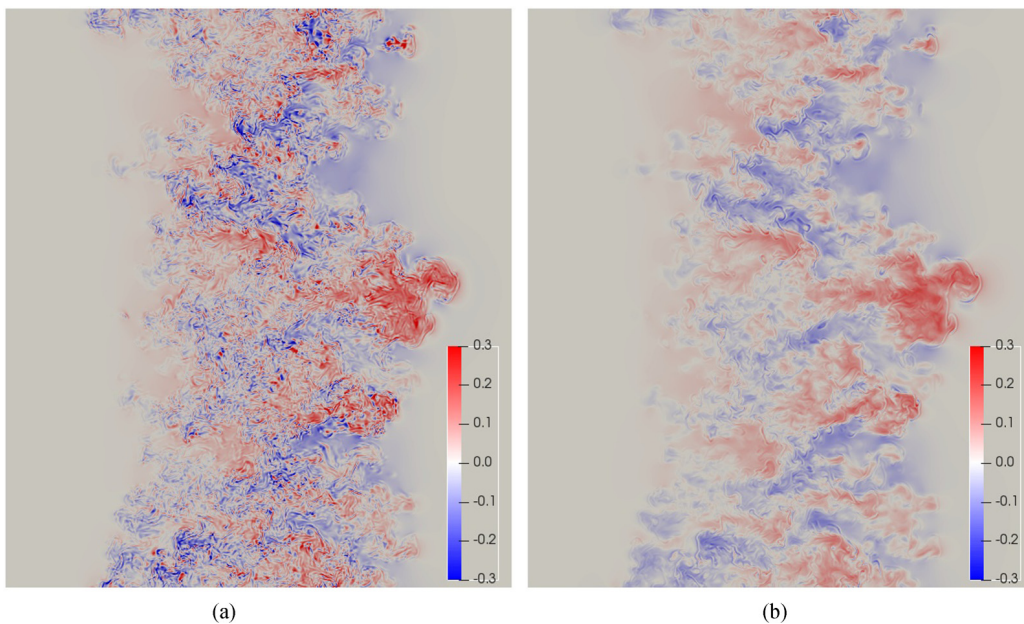


FIG. 6. Cuts in the plane  $y = 0$  at time  $t = 34$  for simulation  $SP_2$  displaying, respectively, (a) the fluctuating divergence  $\text{div} \mathbf{u}'$  computed by using its definition  $\text{div} \mathbf{u}' = \partial_j u'_j$  and (b) the value of  $\text{div} \mathbf{u}'$  predicted by Eq. (24). The color scale is the same in each figure.

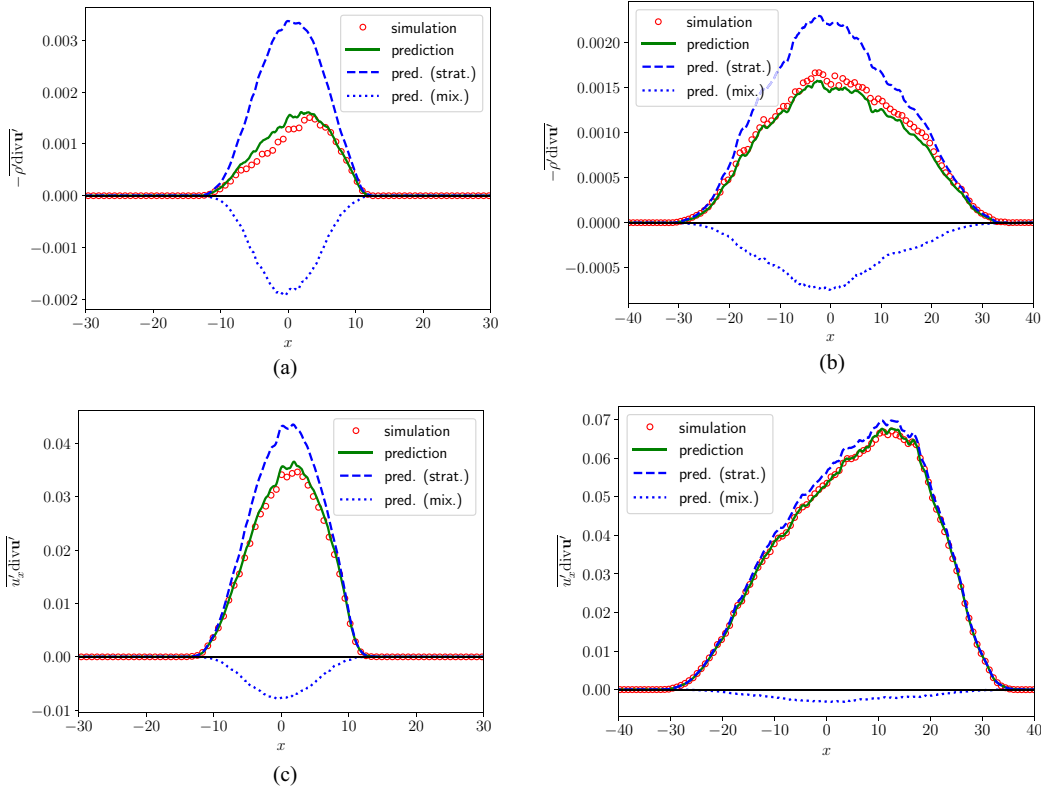


FIG. 7. Spatial profiles for simulation  $SP_2$  of (a)  $-\overline{\rho' \text{div} \mathbf{u}'}$  at  $t = 17$ , (b)  $-\overline{\rho' \text{div} \mathbf{u}'}$  at  $t = 34$ , (c)  $\overline{u'_x \text{div} \mathbf{u}'}$  at  $t = 17$ , and (d)  $\overline{u'_x \text{div} \mathbf{u}'}$  at  $t = 34$ . Comparison between the simulated and predicted values, computed using Eq. (24). The contributions from the stratification (“strat.”) and the molecular (“mix.”) terms to both predicted values are shown.

flux and density variance, whereas the molecular diffusion tends to act as a sink of the density correlations. As time elapses, the Reynolds number increases and the relative intensity of the molecular contribution is seen to decrease with respect to the stratification contribution.

By contrast, if the same comparisons as in Fig. 7 are performed using the high-Prandtl simulation HP instead of the small-Prandtl simulation  $SP_2$ , strong differences are observed as expected. Indeed, the small-Péclet prediction Eq. (24) can obviously not be applied to HP which evolves in a large-Péclet regime according to Fig. 1.

To summarize this section, the main results of the small Péclet–small Mach number approximation derived in Sec. III have been verified. The orders of magnitude of  $T'$  and  $P'$  and the values of  $\text{div} \mathbf{u}'$  and  $C'$  are all consistent with the asymptotic predictions.

## V. APPLICATION TO TURBULENCE MODELING

One of our main motivations for studying the small Péclet–small Mach number asymptotic limit is to understand how second-order one-point turbulence models can be designed or modified to account for this flow regime. In this section, we consider Reynolds average Navier-Stokes (RANS) modelization and focus on the Reynolds stress model (RSM) class because it requires less additional closures to take advantage of the results established in Sec. III C than two-equation models would do. A particular RSM called GSG model [26] is

used here to test modifications. This model is indeed particularly interesting for stellar applications since it is meant to treat variable density turbulent mixing zones submitted to a wide variety of convective instabilities. However, in its current formulation it is restricted to high Péclet numbers and need to be adapted to the small-Péclet limit.

### A. Adaptation of a Reynolds stress model

The GSG model [26,34] follows the evolutions of the correlations of the velocity and density fields, including the mass flux  $\overline{\rho' u'_i} / \bar{\rho}$  and the density variance  $\overline{\rho'^2} / \bar{\rho}^2$ . The evolution of the fluctuating density is given at first order by Eq. (29). Thus, the correlations  $\overline{u'_i \text{div} \mathbf{u}'}$  and  $\overline{\rho' \text{div} \mathbf{u}'}$  are among the main unknowns appearing in the evolution equations of  $\overline{\rho' u'_i} / \bar{\rho}$  and  $\overline{\rho'^2} / \bar{\rho}^2$ , respectively. In the small-Péclet limit, these terms can be closed by substituting the value of  $\text{div} \mathbf{u}'$  by its asymptotic expression Eq. (24). One obtains for  $Pe_r \ll 1$  with  $q'$  standing for  $u'_i$  or  $\rho'$ :

$$\overline{q' \text{div} \mathbf{u}'}|_{Pe_r \ll 1} = -\overline{q' u'_j} \left( \frac{\partial_j \bar{\rho}}{\bar{\rho}} + \frac{\partial_j \bar{r}}{\bar{r}} \right) + \overline{q' \text{div} \mathbf{u}'}^{\text{mix}},$$

where  $\overline{q' \text{div} \mathbf{u}'}^{\text{mix}}$  is the contribution to  $\text{div} \mathbf{u}'$  linked to molecular mixing. As a last step, we propose to model these molecular effects as a dissipation acting on density fluctuations:  $\overline{q' \text{div} \mathbf{u}'}^{\text{mix}} \propto \omega \frac{\rho' q'}{\bar{\rho}}$ . Thus, with this closure, the

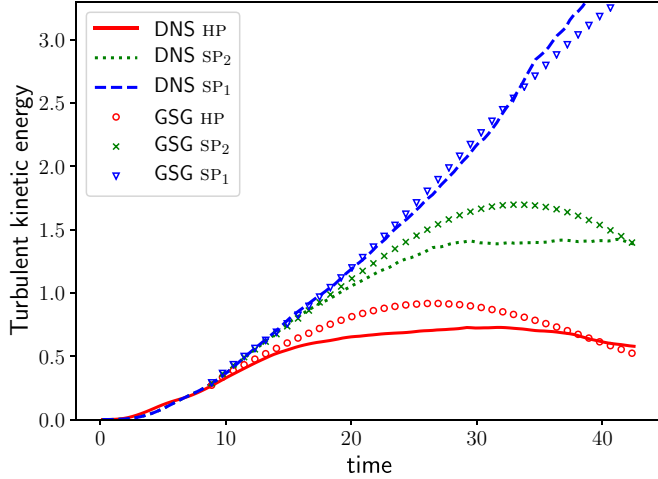


FIG. 8. Time evolution of the turbulent kinetic energy  $\tilde{k}$  at  $x = x_l$ . Comparison between the DNS and the 1D RANS simulations.

following model is obtained for  $\overline{u'_i \text{div} \mathbf{u}'}$  and  $\overline{\rho' \text{div} \mathbf{u}'}$  in the small-Péclet limit:

$$\overline{u'_i \text{div} \mathbf{u}'}|_{\text{Pe}_t \ll 1} = -\overline{u'_i u'_j} \left( \frac{\partial_j \bar{\rho}}{\bar{\rho}} + \frac{\partial_j \bar{r}}{\bar{r}} \right) + C_1 \omega \frac{\overline{\rho' u'_i}}{\bar{\rho}}, \quad (35)$$

$$\overline{\rho' \text{div} \mathbf{u}'}|_{\text{Pe}_t \ll 1} = -\overline{\rho' u'_i} \left( \frac{\partial_j \bar{\rho}}{\bar{\rho}} + \frac{\partial_j \bar{r}}{\bar{r}} \right) + C_2 \omega \frac{\overline{\rho'^2}}{\bar{\rho}}, \quad (36)$$

where  $C_1$  and  $C_2$  are constants and  $\omega = \bar{\varepsilon}/\bar{k}$  is the characteristic turbulent frequency.

The closures (35) and (36) are different from the ones retained in the initial large-Péclet formulation of the GSG model. Indeed, based on Eq. (28), the current formulation of the GSG model has been proposed for  $\text{Pe}_t \gg 1$  in Ref. [20]:

$$\overline{u'_i \text{div} \mathbf{u}'}|_{\text{Pe}_t \gg 1} = -\overline{u'_i u'_j} \frac{\partial_j \bar{P}}{\gamma_1 \bar{P}} + C_1 \omega \frac{\overline{\rho' u'_i}}{\bar{\rho}}, \quad (37)$$

$$\overline{\rho' \text{div} \mathbf{u}'}|_{\text{Pe}_t \gg 1} = -\overline{\rho' u'_i} \frac{\partial_j \bar{P}}{\gamma_1 \bar{P}} + C_2 \omega \frac{\overline{\rho'^2}}{\bar{\rho}}. \quad (38)$$

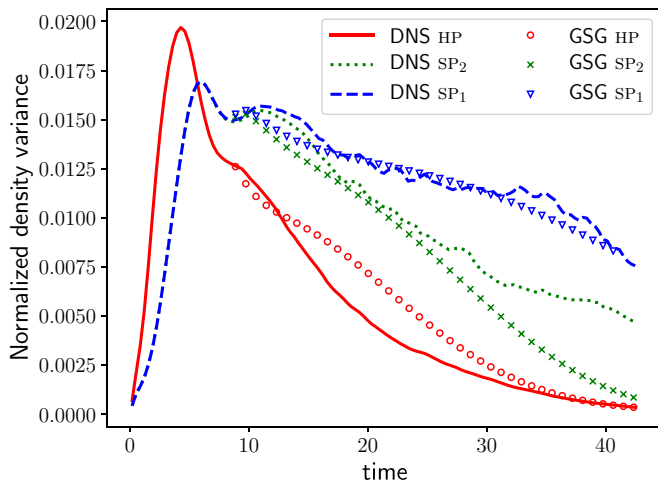


FIG. 9. Time evolution of the normalized density variance  $\overline{\rho'^2}/\bar{\rho}^2$  at  $x = x_l$ . Comparison between the DNS and the 1D RANS simulations.

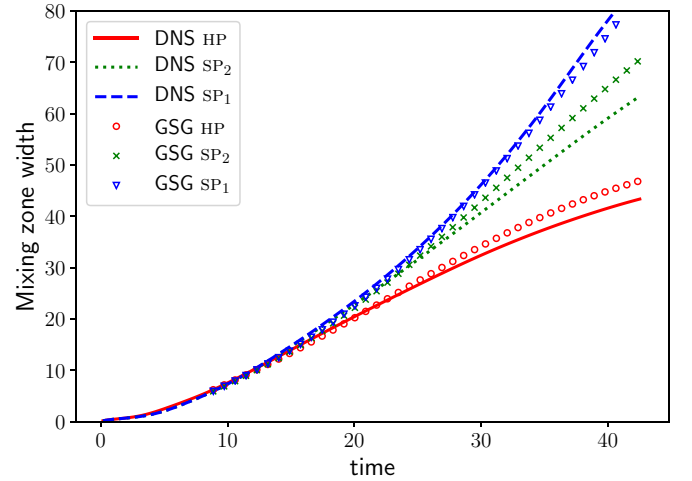


FIG. 10. Time evolution of the turbulent mixing zone width  $\mathcal{L}_{\text{TMZ}} = 6 \int_{L_x} \tilde{c}(1 - \tilde{c}) dx$ . Comparison between the DNS and the 1D RANS simulations.

Hence, the main adaptation of the GSG model to the small-Péclet limit requires the modification of the production terms arising in the density variance and turbulent mass flux equations. This difference does not only affect the levels of density-related correlations, it also modifies the buoyancy instability criterion to which the model is susceptible to react, as explained in Sec. III D. Finally, to bridge the range between small and large Péclet numbers, we propose to perform a weighted blending of the two limits in the form:

$$\overline{q' \text{div} \mathbf{u}'} = (1 - \omega_{\text{Pe}}) \overline{q' \text{div} \mathbf{u}'}|_{\text{Pe}_t \gg 1} + \omega_{\text{Pe}} \overline{q' \text{div} \mathbf{u}'}|_{\text{Pe}_t \ll 1}$$

$$\text{with } \omega_{\text{Pe}} = \frac{\text{Pe}_t^{\text{lim}}}{\text{Pe}_t^{\text{lim}} + \text{Pe}_t} \text{ and } \text{Pe}_t^{\text{lim}} = 2C_\mu = 0.2, \quad (39)$$

where the quantity  $q'$  stands for  $u'_i$  or  $\rho'$ . The value of  $\text{Pe}_t^{\text{lim}}$  is interpreted as a transition parameter between high- and small-Péclet regimes [refer to relation (32) for the precise definition of  $\text{Pe}_t$ ].

## B. Validation of the extended RSM

In order to validate the closure (39), the three DNS of the radiative Rayleigh-Taylor mixing described in Sec. IV A are compared to three 1D RANS simulations carried out with the modified GSG model. The latter are initialized at  $t = 9$  using 1D profiles for the averages and correlations computed from the DNS at the same time. Indeed, the model is derived in the high-Reynolds limit and does not take the molecular viscosity and diffusion coefficients into account. It is therefore unable to closely match the transition to turbulence of the DNS and should be turned on only when the flow is close to turbulence. The same set of model coefficients is used in the three cases.

Figures 8–10 compare turbulent quantities extracted from the three DNS SP<sub>1</sub>, SP<sub>2</sub>, and HP to the ones predicted by the GSG model adapted to all Péclet regimes using the blending (39). Figures 8 and 9 plot the temporal evolution of the turbulent kinetic energy  $k$  and the normalized density variance  $\overline{\rho'^2}/\bar{\rho}^2$  at the initial abscissa of the interface  $x = x_l$ , whereas

Fig. 10 plots the width of the turbulent mixing zone defined as  $\mathcal{L}_{\text{TMZ}} = 6 \int_{L_x} \tilde{c}(1 - \tilde{c}) dx$ .

It can be seen that the extended GSG model reproduces the main trends observed in the simulations and allows to capture the differences between high- and small-Péclet regimes. For instance, in the large-Péclet limit (HP), a decrease of the turbulent kinetic energy at  $x = x_l$  is observed during the last third of the computation together with a slowdown of the turbulent mixing zone (TMZ) expansion. This decline of the turbulent field has already been explained in Sec. IV C. It is due to the fact that the mean pseudoentropy profile  $S$  approaches its neutral value inside the TMZ so that the instability mechanism stops feeding the turbulent mixing zone, whereas viscosity still dissipates the turbulent kinetic energy.

By contrast, in the small-Péclet limit (SP<sub>1</sub>), the instability depends on the molar mass gradient which keeps always the same sign so that it endlessly transfers energy to the turbulent field. This explains the continuous growth in Fig. 8 and the accelerated expansion in Fig. 10.

The behavior of the density variance in Fig. 9 results from the competition between molecular diffusion tending to destroy the variance and turbulent transport of “fresh” pure fluid engulfed at the mixing zone edge and carried through the TMZ. Quicker expansion of the TMZ for SP<sub>1</sub> allows to maintain a slow decay of the variance, whereas molecular diffusion is almost not counterbalanced for HP.

Between these two limiting cases, the intermediate-Prandtl simulation SP<sub>2</sub> exhibits a more subtle balance between the different mechanisms. Beginning in a small-Péclet regime, it first follows the same evolution as SP<sub>1</sub>, but doing so, its turbulent diffusivity quickly increases and so does its Péclet number as shown in Fig. 1. When the latter becomes nonnegligible the instability production reduces and becomes of a similar order as the molecular dissipation leading to a marginal evolution of the turbulent kinetic energy. Transfer of pure fluid from the TMZ edges then slows down, letting the density variance decrease much quicker in SP<sub>2</sub> than in SP<sub>1</sub>. Capturing this limiting behavior is a challenge and the value  $\text{Pe}_t^{\text{lim}}$  in the blending of Eq. (39) is precisely chosen to get the transition in the right way.

Note that, plotted in Figs. 8 to 10, the original GSG model, with closures (37) and (38), would yield the same results as the large-Péclet limit (HP), whatever the value of  $\text{Pe}_t$ .

To conclude, implementation of Eq. (24) within the GSG RANS model proves successful in predicting the radiative RTI in the small-Péclet limit. Extending the closure to all Péclet regimes thanks to the blending Eq. (39) allows the RSM to correctly capture the effects of the relative intensity of the radiative transfer and the turbulent transport in the turbulent mixing case under consideration.

## VI. CONCLUSION

In this work, an asymptotic analysis of radiative mixing flows has been performed in the joint limit of small turbulent Mach number and small turbulent Péclet number. It predicts the scalings of pressure and temperature fluctuations together with approximations for the fluctuations of the thermal conduction and the velocity divergence fields.

The fluctuating velocity divergence turns out to be the cornerstone for the improvement of RANS turbulence modeling when the radiative conduction overwhelms the turbulent diffusivity. This work shows how to design turbulent models able to account for the effect of the relative magnitude of radiative conductivity and turbulent transport in the wide range of turbulent Péclet numbers encountered in stellar flows. Such an extension can easily be applied to augmented RSM tracking density correlations like BHR3 [35] or GSG [26,34] as shown here with the latter.

Radiative Rayleigh-Taylor turbulent mixing at an interface has been carefully considered with three goals in mind: First, validate the asymptotic predictions thanks to 3D DNS; second, validate their use in 1D RANS simulations; and, third, illustrate how large radiative conduction can lead to a qualitative change in the behavior of turbulent mixing zones by modifying the stability criteria.

## APPENDIX A: DESCRIPTIVE MATERIAL

The governing equations (1a)–(1d) need to be complemented with equations of state and closures for some terms like fluxes. These are precisely described in this Appendix.

Because the radiative field obeys the equilibrium diffusion approximation, the radiative pressure can be expressed as:

$$P^r = \frac{E^r}{3} \text{ with } E^r = a_R T^4,$$

where the radiation constant  $a_R = 4\sigma_{\text{SB}}/c_\ell$  is obtained from the Stefan-Boltzmann constant  $\sigma_{\text{SB}}$  and the light speed  $c_\ell$ . Concerning the material pressure  $P^m$ , we will assume, for the sake of simplicity, that the plasma is fully ionized and behaves as a perfect gas. As a result, the material pressure obeys the following equation of state:

$$P^m = \rho r T \text{ with } r = \sum_\alpha r_\alpha c_\alpha \text{ and } r_\alpha = \frac{\mathcal{R}(1 + \mathcal{Z}_\alpha)}{\mathcal{M}_\alpha}, \quad (\text{A1})$$

where  $\mathcal{R}$  is the ideal gas constant,  $\mathcal{M}_\alpha$  is the molar mass of ion  $\alpha$ , and  $\mathcal{Z}_\alpha$  is its ionization degree. As already mentioned, the Einstein convention for the summation of indices is not used for the Greek index  $\alpha$ . This simplified equation of state is only meant to avoid cumbersome expressions in the ensuing derivation and to allow for a better understanding of the physical meaning of the small-Péclet-number approximation to be derived. The general case of an equation of state for which  $P^m$  is an arbitrary function of  $\rho$ ,  $T$ , and  $c_\alpha$  is treated in Appendix C. For the same reasons, we will hereby assume that the specific heat at constant volume  $C_{v_\alpha}^m$  of each species  $\alpha$  is constant and that all species  $\alpha$  share the same polytropic coefficient  $\gamma_m$ . As a result, one has:

$$e^m = C_v^m T \text{ with } C_v^m = \sum_\alpha C_{v_\alpha}^m c_\alpha,$$

$$\text{and } \gamma_\alpha = 1 + \frac{r_\alpha}{C_{v_\alpha}^m} = \gamma_m \text{ for all } \alpha.$$

Similarly to the pressure  $P^m$ , the general case where  $e^m$  is an arbitrary function of  $\rho$ ,  $T$ , and  $c_\alpha$  is treated in Appendix C. Note also that  $C_v^m$  includes contributions from both ions and

electrons but not from photons. Given the equilibrium diffusion assumption, one may, however, define a global specific heat of the photon-ion-electron continuum by differentiating the total energy  $e$  with respect to the temperature  $T$  at constant density  $\rho$ . This yields the following total specific heat at constant volume  $C_v$ :

$$C_v = C_v^m + \frac{4a_R T^3}{\rho}.$$

This total specific heat depends on temperature and density as opposed to  $C_v^m$ .

In Eq. (1b), we also introduced the gravitational force  $\mathbf{g}$  and the viscosity tensor  $\Pi_{ij}$ . The latter is defined by:

$$\Pi_{ij} = -2\mu(S_{ij} - \frac{1}{3}\text{div}\mathbf{u}\delta_{ij}),$$

where  $S_{ij} = (\partial_j u_i + \partial_i u_j)/2$  and where  $\mu = \rho\nu$  is the dynamic viscosity of the plasma with  $\nu$  its kinematic viscosity. The associated dissipation is defined by:

$$\rho\varepsilon = -\Pi_{ij}S_{ji}.$$

In Eq. (1c), the diffusion flux of the species mass fraction  $c_\alpha$  is defined by a Fickian approximation of the form [36]:

$$\mathcal{F}_{\alpha j} = \begin{cases} -\rho\mathcal{D}^{(\alpha)}\partial_j c_\alpha & \text{for } \alpha = 1, \dots, N_s - 1, \\ -\sum_{\alpha=1}^{N_s-1} \mathcal{F}_{\alpha j} & \text{for } \alpha = N_s, \end{cases}$$

where  $\mathcal{D}^{(\alpha)}$  is the diffusion coefficient of the species  $\alpha$ . Note that the validation proposed in this work in Sec IV regards a binary mixture ( $N_s = 2$ ) which means that, for both gases, there is a single interspecific diffusion coefficient that will be noted  $\mathcal{D}$ .

Finally, the last unspecified term of Eqs. (1a)–(1d) is the energy flux  $\mathcal{F}_j$ . Given that  $e$  is the total energy,  $\mathcal{F}_j$  has two contributions, a material one  $\mathcal{F}_j^m$  and a radiative one  $\mathcal{F}_j^r$ :

$$\mathcal{F}_j = \mathcal{F}_j^m + \mathcal{F}_j^r.$$

The material term  $\mathcal{F}_j^m$  is itself split into a thermal conduction contribution and an enthalpy mixing one:

$$\mathcal{F}_j^m = -\lambda^m \partial_j T + h_{,\alpha}^m \mathcal{F}_{\alpha j},$$

where  $\lambda^m$  is the thermal conductivity of the plasma and  $h_{,\alpha}^m = \partial_{c_\alpha} h^m$  represents the enthalpy of species  $\alpha$ . As for the radiative flux, the equilibrium diffusion assumption allows to express it as:

$$\mathcal{F}_j^r = -\lambda^r \partial_j T \text{ with } \lambda^r = \frac{4c_\ell a_R T^3}{3\rho\kappa^r}.$$

In this expression,  $\kappa^r$  is the Rosseland opacity and is related to the Rosseland mean free path  $\Lambda^r$  by:

$$\kappa^r = \frac{1}{\rho\Lambda^r}.$$

To conclude this description, let us remark that a total conductivity  $\lambda$  can be defined by summing the radiative and material contributions:

$$\lambda = \lambda^m + \lambda^r.$$

From there, one can also define a total temperature diffusivity  $\chi$  using the total conductivity  $\lambda$  and the total specific heat  $C_v$ :

$$\chi = \frac{\lambda}{\rho C_v}.$$

This definition accounts for the contributions of matter and radiation.

From Eqs. (1a)–(1d) and using the definitions of this Appendix, equations for the total pressure and the common material and radiative temperature can be obtained with the form given in Eqs. (2) and (3). In these two equations,  $\mathcal{C}$  stands for the total conduction term and  $\mathcal{D}_P$  and  $\mathcal{D}_T$  account for the effects of molecular diffusion and dissipation on  $P$  and  $T$ :

$$\begin{aligned} \mathcal{C} &= \partial_j(\lambda\partial_j T), \\ \mathcal{D}_P &= \gamma_3 \sum_{\alpha} \frac{P_{,\alpha}}{\rho} \partial_j(\rho\mathcal{D}^{(\alpha)}\partial_j c_\alpha) \\ &\quad + (\gamma_3 - 1)\rho\left(\varepsilon + \sum_{\alpha} \mathcal{D}^{(\alpha)}\partial_j h_{,\alpha}^m \partial_j c_\alpha\right), \\ \mathcal{D}_T &= \sum_{\alpha} \frac{P_{,\alpha}}{\rho} \partial_j(\rho\mathcal{D}^{(\alpha)}\partial_j c_\alpha) + \rho\left(\varepsilon + \sum_{\alpha} \mathcal{D}^{(\alpha)}\partial_j h_{,\alpha}^m \partial_j c_\alpha\right). \end{aligned} \quad (\text{A2})$$

The coefficients  $\gamma_1$ ,  $\gamma_2$ , and  $\gamma_3$  are generalized adiabatic exponents defined for a continuum made of matter and radiation [27] by:

$$\begin{aligned} \gamma_1 &= \left. \frac{\rho}{P} \frac{\partial P}{\partial \rho} \right|_{s,c}, & \gamma_2 &= 1 + \left. \frac{\rho}{T} \frac{\partial T}{\partial \rho} \right|_{s,c} \\ \text{and } \gamma_3 &= 1 + \left. \frac{1}{\rho} \frac{\partial P}{\partial e} \right|_{\rho,c}, \end{aligned}$$

where  $s$  is the entropy. Note that with the notations found in Ref. [27], one has  $\gamma_1 = \Gamma_1$  but  $\gamma_2 = \Gamma_3$ . As for  $\gamma_3$ , it is not directly linked to an isentropic process and has been arbitrarily added to the list of adiabatic exponents for the sake of commodity. Note also that the generalized adiabatic exponents are usually different from one another and also from the ratio of specific heat  $\gamma$  defined by:

$$\gamma = \frac{C_p}{C_v},$$

where  $C_v$  is the total specific heat at constant volume, which has already been introduced, and  $C_p$  is the total specific heat at constant pressure. All these coefficients are also usually different from the adiabatic exponent  $\gamma_m$  characterizing the plasma without radiation. They nevertheless coincide for a perfect gas without radiation.

As a last note, Eqs. (2) and (3) are not affected by the simplifying assumptions made about the equation of state of the plasma in this Appendix. Equations (2) and (3) remain the same whether the plasma behaves as an ideal gas or not. The differences between two different equations of state would only appear in the actual values of the generalized adiabatic exponents, which definitions extend beyond the ideal gas framework.

**APPENDIX B: SECOND-ORDER CONTRIBUTIONS TO THE EVOLUTION  $\mathbf{u}'$ ,  $P'$ , AND  $T'$** 

The second- or higher-order terms appearing in Eqs. (8)–(10) are defined by:

$$\begin{aligned}\mathcal{R}_i^{\mathbf{u}} &= \frac{\partial_j(\overline{\rho u'_i u'_j})}{\overline{\rho}} \\ \mathcal{R}^P &= \overline{u'_j \partial_j P'} - (\gamma'_1 P' - \overline{\gamma'_1 P'}) \text{div} \overline{\mathbf{u}} - (\gamma'_1 \text{div} \mathbf{u}' - \overline{\gamma'_1 \text{div} \mathbf{u}'}) \overline{P} - \overline{\gamma}_1 (P' \text{div} \mathbf{u}' - \overline{P' \text{div} \mathbf{u}'}) + \gamma'_3 C' - \overline{\gamma'_3 C'} - (\gamma'_1 P' \text{div} \mathbf{u}' - \overline{\gamma'_1 P' \text{div} \mathbf{u}'}) \\ \mathcal{R}^T &= \overline{u'_j \partial_j T'} - (\gamma'_2 T' - \overline{\gamma'_2 T'}) \text{div} \overline{\mathbf{u}} - (\gamma'_2 \text{div} \mathbf{u}' - \overline{\gamma'_2 \text{div} \mathbf{u}'}) \overline{T} - (\overline{\gamma}_2 - 1) (T' \text{div} \mathbf{u}' - \overline{T' \text{div} \mathbf{u}'}) \\ &\quad + C' \left( \frac{1}{\rho C_v} \right)' - C' \left( \frac{1}{\rho C_v} \right)' - (\gamma'_2 T' \text{div} \mathbf{u}' - \overline{\gamma'_2 T' \text{div} \mathbf{u}'}).\end{aligned}$$

**APPENDIX C: NONIDEAL GASES AND SOURCE EFFECTS**

If the flow is not an ideal gas and source terms are considered, then the evolution equations of pressure (2) and temperature (3) written in Sec. II A would be modified in the following way:

$$\begin{aligned}D_t P &= -\gamma_1 P \text{div} \mathbf{u} + (\gamma_3 - 1) \mathcal{C} + \mathcal{S}_P + \mathcal{D}_P \\ D_t T &= -(\gamma_2 - 1) T \text{div} \mathbf{u} + \frac{\mathcal{C}}{\rho C_v} + \frac{\mathcal{S}_T}{\rho C_v} + \frac{\mathcal{D}_T}{\rho C_v},\end{aligned}$$

where the expression of already defined variables is unchanged. As for the additional terms  $\mathcal{S}_P$  and  $\mathcal{S}_T$ , they are expressed in terms of the source terms related to reactions  $\mathcal{S}_\alpha$ , matter  $\mathcal{S}^m$ , and radiation  $\mathcal{S}^r$ , such that:

$$\begin{aligned}\mathcal{S}_P &= (\gamma_3 - 1) \mathcal{S} - \sum_\alpha \left[ (\gamma_3 - 1) e_{,\alpha} - \frac{P_{,\alpha}}{\rho} \right] \mathcal{S}_\alpha, \\ \mathcal{S}_T &= \mathcal{S} - \sum_\alpha e_{,\alpha} \mathcal{S}_\alpha \text{ with } \mathcal{S} = \mathcal{S}^m + \mathcal{S}^r.\end{aligned}$$

The coefficients  $\gamma_1$ ,  $\gamma_2$ , and  $\gamma_3$  have been introduced in Ref. [37] as the generalized adiabatic coefficients regarding thermodynamics of hydroradiative flows. Joining the expressions from [27], they are defined in terms of differentials of temperature and density by:

$$\begin{aligned}\gamma_1 &= \frac{\rho P_{,\rho}}{P} + \frac{P_{,T}}{\rho e_{,T}} \left( 1 - \frac{\rho^2 e_{,\rho}}{P} \right) \\ \gamma_2 &= 1 + \frac{P - \rho^2 e_{,\rho}}{\rho e_{,T} T} \text{ and } \gamma_3 = 1 + \frac{P_{,T}}{\rho e_{,T}}.\end{aligned}$$

One can also defines the following ratio:

$$\gamma = \frac{C_p}{C_v} = 1 + \frac{P}{\rho P_{,\rho}} \frac{P_{,T}}{\rho e_{,T}} \left( 1 - \frac{\rho^2 e_{,\rho}}{P} \right),$$

where we recall that the shortcuts  $f_{,T}$  and  $f_{,\rho}$  stands for the differentiation with constant other variables in  $\{T, \rho, c_\alpha\}$ .

These coefficients characterize the equation of state. For a perfect gas without radiation, they are all equal to  $\gamma_m = \frac{C_p^m}{C_v^m}$  with  $C_p^m$  the material specific heat at constant pressure. Otherwise, they differ from this value.

While not taken into account in this study, the intensity of turbulent fluctuations, regarding the one of reactive source terms  $\mathcal{S}_{\text{react}}$ , may be characterized by  $\epsilon_{s0}$ .

In this way, the characteristic reaction time  $\tau^s$  would have been introduced so that the nondimensionalized source terms could be written:

$$\mathcal{S}_P^{s*} = \frac{\tau_0^{s'}}{P_0 \epsilon_{s0}} \mathcal{S}_P^s, \left( \frac{\mathcal{S}_T}{\rho C_v} \right)^{s*} = \frac{\tau_0^{s'}}{T_0 \epsilon_{s0}} \left( \frac{\mathcal{S}_T}{\rho C_v} \right)^s.$$

The Damkhöler number,  $\text{Da}$ , that characterizes the mean reaction rates would have been defined as:

$$\text{Da} = \frac{\tau_0}{\tau_0^s}.$$

Without the simplifications of Sec. II A, the source terms and the fluctuations  $\gamma$  are present in the next derivations. While the dimensionless equation of fluctuating velocity remains the same, the dimensionless equations of temperature and pressure become

$$\begin{aligned}D_t P' &= -\overline{\gamma}_1 \overline{P} \text{div} \mathbf{u}' + \left[ \frac{1}{\text{Pe}_t} \right] (\overline{\gamma}_3 - 1) C' - \left[ \frac{1}{\text{Fr}_s} \right] \overline{\gamma}_1 P' \partial_j \overline{u}_j \\ &\quad - [\text{Ka}_P] u'_j \partial_j \overline{P} - \left[ \frac{\epsilon_{\gamma 0}}{\text{Fr}_s} \right] \gamma'_1 \overline{P} \partial_j \overline{u}_j + \left[ \frac{\epsilon_{\gamma 0} \text{Ka}_T^2}{\text{Pe}_t} \right] \gamma'_3 \overline{C} \\ &\quad + \left[ \frac{\epsilon_{c0}}{\text{ScRe}_t} \right] \mathcal{D}'_P + [\text{Da} \epsilon_{s0}] \mathcal{S}'_P + O(2)\end{aligned}$$

$$\begin{aligned}D_t T' &= -(\overline{\gamma}_2 - 1) \overline{T} \text{div} \mathbf{u}' + \left[ \frac{1}{\text{Pe}_t} \right] \frac{C'}{\rho C_v} \\ &\quad - \left[ \frac{1}{\text{Fr}_s} \right] (\overline{\gamma}_2 - 1) T' \partial_j \overline{u}_j - [\text{Ka}_T] u'_j \partial_j \overline{T} \\ &\quad - \left[ \frac{\epsilon_{\gamma 0}}{\text{Fr}_s} \right] \gamma'_2 \overline{T} \partial_j \overline{u}_j + \left[ \frac{\epsilon_{\gamma 0} \text{Ka}_T^2}{\text{Pe}_t} \right] \left( \frac{1}{\rho C_v} \right)' \overline{C} \\ &\quad + \left[ \frac{\epsilon_{c0}}{\text{ScRe}_t} \right] \left( \frac{\mathcal{D}_T}{\rho C_v} \right)' + [\text{Da} \epsilon_{s0}] \left( \frac{\mathcal{S}_T}{\rho C_v} \right)' + O(2),\end{aligned}$$

with  $O(2)$  refers to terms involving products of fluctuations.

Again, if the simplifications and hypotheses of Sec. II A were not considered, while Eq. (23) would remain unchanged, the relations (24) and (25) of the asymptotic analysis would become, including also the source terms:

$$\begin{aligned} \operatorname{div} \mathbf{u}' &= -u'_j \frac{\bar{\gamma}}{\bar{\gamma}_1} \left( \frac{\partial_j \bar{P}}{\bar{P}} - x^P \frac{\partial_j \bar{T}}{\bar{T}} \right) - \frac{\bar{\gamma}}{\bar{\gamma}_1} (\gamma'_1 - x^P \gamma'_2) \partial_j \bar{u}_j + \frac{\bar{\gamma}}{\bar{\gamma}_1 \bar{P}} (\bar{S}_T + \bar{C}) \left[ \gamma'_3 - (\bar{\gamma}_3 - 1) \left( \frac{\bar{\rho} \bar{C}_v}{\rho C_v} \right)' \right] \\ &\quad + \frac{\bar{\gamma}}{\bar{\gamma}_1 \bar{P}} \sum_{\alpha} \left[ \bar{P}_{,\alpha} \mathcal{D}^{(\alpha)} \partial_{jj}^2 c'_{\alpha} + \left( \frac{P_{,\alpha} S_{\alpha}}{\rho} \right)' \right] \\ \frac{C'}{\bar{\gamma} \bar{\rho} \bar{C}_v} &= u'_j \left( \partial_j \bar{T} - \frac{\bar{\gamma}_2 - 1}{\bar{\gamma}_1} \bar{T} \frac{\partial_j \bar{P}}{\bar{P}} \right) + (\bar{\gamma}_2 - 1) \bar{T} \left( \frac{\gamma'_2}{\bar{\gamma}_2 - 1} - \frac{\gamma'_1}{\bar{\gamma}_1} \right) \partial_j \bar{u}_j + \left( \frac{\bar{C} + \bar{S}_T}{\bar{\rho} \bar{C}_v} \right) \left[ \frac{\bar{\gamma}_2 - 1}{\bar{\gamma}_3 - 1} x^P \frac{\gamma'_3}{\bar{\gamma}_1} - \left( \frac{\bar{\rho} \bar{C}_v}{\rho C_v} \right)' \right] \\ &\quad - \frac{S'_T}{\bar{\gamma} \bar{\rho} \bar{C}_v} + \frac{\bar{\gamma}_2 - 1}{\bar{\gamma}_3 - 1} \frac{x^P}{\bar{\gamma}_1 \bar{\rho} \bar{C}_v} \sum_{\alpha} \left( \frac{P_{,\alpha} S_{\alpha}}{\rho} \right)' + \left( \frac{\bar{\gamma}}{\bar{\gamma}_1} \frac{\bar{\gamma}_2 - 1}{\bar{\gamma}_3 - 1} x^P - 1 \right) \sum_{\alpha} \frac{\bar{P}_{,\alpha} \mathcal{D}^{(\alpha)} \partial_{jj}^2 c'_{\alpha}}{\bar{\gamma} \bar{\rho} \bar{C}_v} \\ \text{with } \bar{\gamma} &= \frac{\bar{\gamma}_1}{\bar{\gamma}_1 - (\bar{\gamma}_2 - 1)x^P}, x^P = \frac{(\bar{\gamma}_3 - 1)\bar{\rho} \bar{C}_v \bar{T}}{\bar{P}}. \end{aligned}$$

#### APPENDIX D: NUMERICAL METHOD

TRICLADE is a massively parallel code intended to solve turbulent mixing of perfect gases in a variable-density context [38,39]. The present computations are performed with an extension of the code to radiative equations implemented thanks to an operator splitting between the standard hydrodynamic viscodiffusive part and the radiative gray part including radiation-matter coupling and radiative diffusivity. In the radiative version of TRICLADE, the total energy equation (1d) is split into its material and radiative components. Hence, instead of Eq. (1d) the following two equations are solved:

$$\begin{aligned} \rho D_t e^m &= -P^m \operatorname{div} \mathbf{u} - \partial_j \mathcal{F}_j^m - \Omega^{m,r} + \rho \varepsilon, \\ \rho D_t (E^r / \rho) &= -P^r \operatorname{div} \mathbf{u} - \partial_j \mathcal{F}_j^r + \Omega^{m,r}, \end{aligned}$$

where  $\Omega^{m,r}$  is the radiation-matter exchange term:

$$\Omega^{m,r} = \rho \kappa^r c_{\ell} (a_R T_m^4 - E^r) \quad \text{with} \quad T_m = e^m / C_v^m.$$

It corresponds to a simplified version of the gray radiation hydrodynamics system derived in Ref. [40] within the flux-limited diffusion approximation. The asymptotic value 1/3 of

the optically thick limit is used here for the flux limiter and the Eddington factor, the corrections of order  $|\mathbf{u}|/c_{\ell}$  are neglected and the Planck mean interaction coefficient is taken equal to the opacity  $\kappa^r$  for the sake of simplicity.

For the hydrodynamic part of the code, the monotonic upstream centered scheme for conservation laws (MUSCL) finite-volume Godunov method referred to as M5 in Ref. [41] is used. With respect to the standard version of TRICLADE, only a slight modification of the HLLC numerical flux is required to account for the additional  $E^r$  variable.

As for the gray coupling diffusion subsystem for  $(e^m, E^r)$ , a simple implementation relies on the fact that TRICLADE only works on cartesian grids. It is solved by dimensional splitting into three successive 1D implicit systems. The nonlinear term  $T_m^4$  at final time step is linearized as in Commerçon [42]; in this way, when using three-point stencils to discretize the first-order derivative of  $E^r$ , each 1D implicit problem is solved by inverting one three-diagonal system for  $E^r$  followed by an update of  $e^m$ . To avoid anisotropic artifacts, alternate directions orders are used from one iteration to the next. This procedure is valid in the limit of vanishing decoupling like in the test cases of this article.

- [1] S. Chandrasekhar, *Principles of Stellar Dynamics*, Astrophysical monographs (Dover, London, 1960).
- [2] D. Prialnik, *An Introduction to the Theory of Stellar Structure and Evolution* (Cambridge University Press, Cambridge, UK, 2010).
- [3] E. A. Spiegel, Semiconvection, *Comments on Astrophysics and Space Physics* (1969), Vol. 1, p. 57.
- [4] C. Charbonnel and J.-P. Zahn, Thermohaline mixing: A physical mechanism governing the photospheric composition of low-mass giants, *Astron. Astrophys.* **467**, L15 (2007).
- [5] D. J. Stevenson, Formation of the giant planets, *Planet. Space Sci.* **30**, 755 (1982).
- [6] B. Paxton, M. Cantiello, P. Arras, L. Bildsten, E. F. Brown, A. Dotter, C. Mankovich, M. H. Montgomery, D. Stello, F. X.

- Timmes, and R. Townsend, Modules for experiments in stellar astrophysics (MESA): Planets, oscillations, rotation, and massive stars, *Astrophys. J. Suppl. Ser.* **208**, 4 (2013).
- [7] B. Paxton, R. Smolec, J. Schwab, A. Gaudy, L. Bildsten, M. Cantiello, A. Dotter, R. Farmer, J. A. Goldberg, A. S. Jermyn, S. M. Kanbur, P. Marchant, Anne. Thoul, R. H. D. Townsend, W. M. Wolf, M. Zhang, and F. X. Timmes, Modules for experiments in stellar astrophysics (MESA): Pulsating variable stars, rotation, convective boundaries, and energy conservation, *Astrophys. J. Suppl. Ser.* **243**, 10 (2019).
- [8] L. Prandtl, Bericht über untersuchungen zur ausgebildeten turbulenz, *Zs. angew. Math. Mech.* **5**, 136 (1925).
- [9] L. Biermann, Untersuchungen über den inneren Aufbau der Sterne. IV. Konvektionszonen im Innern der Sterne

- (Veröffentlichungen der Universitäts-Sternwarte Göttingen, Nr. 27.) mit 5 Abbildungen, *Zeitschrift für Astrophysik* **5**, 117 (1932).
- [10] J. P. Cox and R. T. Giuli, *Principles of Stellar Structure* (Gordon and Breach, New York, 1968).
- [11] E. Böhm-Vitense, Die Wasserstoffkonvektionszone der Sonne, *Z. Astrophys.* **32**, 135 (1953).
- [12] E. Böhm-Vitense, Über die Wasserstoffkonvektionszone in Sternen verschiedener Effektivtemperaturen und Leuchtkräfte, *Z. Astrophys.* **46**, 108 (1958).
- [13] V. M. Canuto, Stellar mixing—I. Formalism, *Astron. Astrophys.* **528**, A76, 2011.
- [14] V. M. Canuto, Stellar mixing—II. Double diffusion processes, *Astron. Astrophys.* **528**, A77 (2011).
- [15] E. A. Spiegel and G. Veronis, On the Boussinesq approximation for a compressible fluid, *Astrophys. J.* **131**, 442 (1960).
- [16] D. O. Gough, The anelastic approximation for thermal convection, *J. Atmos. Sci.* **26**, 448 (1969).
- [17] D. R. Durran, Improving the anelastic approximation, *J. Atmos. Sci.* **46**, 1453 (1989).
- [18] N. Botta, R. Klein, and A. Almgren, Dry atmosphere asymptotics, Technical Report PIK 55, Potsdam Institut für Klimafolgenforschung, 1999.
- [19] A. Shirgaonkar and S. Lele, On the extension of the Boussinesq approximation for inertia dominated flows, *Phys. Fluids* **18**, 066601 (2006).
- [20] O. Souillard, J. Griffond, and D. Souffland, Pseudocompressible approximation and statistical turbulence modeling: Application to shock tube flows, *Phys. Rev. E* **85**, 026307 (2012).
- [21] S. Chandrasekhar, *Radiative Transfer*, Dover Books on Intermediate and Advanced Mathematics (Dover, London, 1960).
- [22] E. A. Spiegel, Thermal turbulence at very small Prandtl number, *J. Geophys. Res.* **67**, 3063 (1962).
- [23] F. Lignières, The small-Péclet-number approximation in stellar radiative zones, *Astron. Astrophys.* **348**, 933 (1999).
- [24] A. Novotny, M. Ruzicka, and G. Thater, Rigorous derivation of the anelastic approximation to the Oberbeck–Boussinesq equations, *Asymp. Anal.* **75**, 93 (2011).
- [25] E. Feireisl and A. Novotný, Small Péclet number approximation as a singular limit of the full Navier-Stokes-Fourier system with radiation, *New Directions in Mathematical Fluid Mechanics* (Springer, Berlin, 2009), pp. 123–152.
- [26] O. Grégoire, D. Souffland, and S. Gauthier, A second-order turbulence model for gaseous mixtures induced by Richtmyer-Meshkov instability, *J. Turbul.* **6**, N29 (2005).
- [27] D. Mihalas and B. W. Mihalas, *Foundations of Radiation Hydrodynamics* (Courier Corporation, North Chelmsford, MA, 2013).
- [28] J. O. Hinze, *Turbulence*, 2nd ed. (McGraw–Hill, London, 1975).
- [29] V. Prat, Transport turbulent d’éléments chimiques dans les zones radiatives stellaires, Ph.D. thesis, Université de Toulouse, Université Toulouse III-Paul Sabatier, 2013.
- [30] R. W. Schmitt, Double diffusion in oceanography, *Annu. Rev. Fluid Mech.* **26**, 255 (1994).
- [31] P. Garaud, Double-diffusive convection at low Prandtl number, *Ann. Rev. Fluid Mech.* **50**, 275 (2018).
- [32] T. Radko, *Double-diffusive Convection* (Cambridge University Press, Cambridge, 2013).
- [33] R. Schiestel, *Modeling and Simulation of Turbulent Flows* (ISTE, London, 2010).
- [34] J. Griffond and O. Souillard, Evaluation of augmented RSM for interaction of homogeneous turbulent mixture with shock and refraction waves, *J. Turbul.* **15**, 569 (2014).
- [35] J. D. Schwarzkopf, D. Livescu, R. A. Gore, R. M. Rauenzahn, and J. R. Ristorcelli, Application of a second-moment closure model to mixing processes involving multicomponent miscible fluids, *J. Turbul.* **12**, N49 (2011).
- [36] V. Giovangigli, Multicomponent flow modeling, *Modeling and Simulation in Science, Engineering and Technology* (Birkhäuser Basel, Switzerland, 1999).
- [37] S. Chandrasekhar, *An Introduction to the Study of Stellar Structure* (Dover Publications, New York, 1957), Vol. 2.
- [38] S. Shanmuganathan, D. L. Youngs, J. Griffond, B. Thornber, and R. J. R. Williams, Accuracy of high-order density-based compressible methods in low Mach vortical flows, *Int. J. Numer. Methods Fluids* **74**, 335 (2014).
- [39] B. Thornber, J. Griffond, O. Poujade, N. Attal, H. Varshochi, P. Bigdelou, P. Ramaprabhu, B. Olson, J. Greenough, Y. Zhou, O. Schilling, K. A. Garside, R. J. R. Williams, C. A. Batha, P. A. Kuchugov, M. E. Ladonkina, V. F. Tishkin, N. V. Zmitrenko, V. B. Rozanov, and D. L. Youngs, Late-time growth rate, mixing, and anisotropy in the multimode narrowband Richtmyer-Meshkov instability: The  $\theta$ -group collaboration, *Phys. Fluids* **29**, 105107 (2017).
- [40] W. Zhang, L. Howell, A. Almgren, A. Burrows, and J. Bell, CASTRO: A new compressible astrophysical solver. II. Gray radiation hydrodynamics, *Astrophys. J. Suppl. Ser.* **196**, 20 (2011).
- [41] K. H. Kim and C. Kim, Accurate, efficient and monotonic numerical methods for multi-dimensional compressible flows: Part II: Multi-dimensional limiting process, *J. Comput. Phys.* **208**, 570 (2005).
- [42] B. Commerçon, R. Teyssier, E. Audit, P. Hennebelle, and G. Chabrier, Radiation hydrodynamics with adaptive mesh refinement and application to prestellar core collapse. I. Methods, *Astron. Astrophys.* **529**, A35 (2011).

**INTRODUCTION**

**Astrophysical context**

**Presence of turbulence in stellar interiors:**

occurs in a wide variety of regimes involving stable and unstable stratifications, mixing, shear, radiation losses...

generated and maintained by various mechanisms (rotation, instabilities, shearing...).

**Role of turbulence in stellar interiors:**

has major impacts on the life cycle of a star, can explain the abundance of some elements, may account for the dissipation of angular momentum observed in some stars, from [Lignières (1999)].

**Purpose**

To derive a statistical turbulent model describing stellar interiors which includes mixing and radiation effects (adapted for regimes of small and large Péclet numbers)

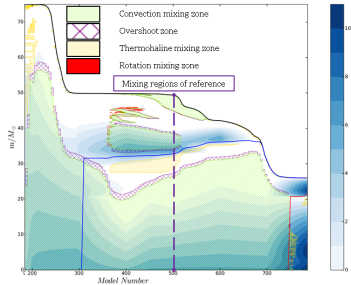


Figure 1: Kippenhahn diagram for the evolution of a 75 M<sub>⊙</sub> star (Model number 500 ⇔ 3.60 × 10<sup>6</sup> yrs) from MESA 1D code

**Double diffusion zone**

Comparison of modes of heat transport with a ratio of characteristic times:

**Péclet dimensionless number:**

$$Pe = \frac{\tau_{radiation}}{\tau_{turbulence}}$$

**Mixing zones**

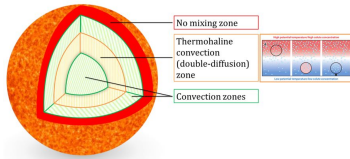


Figure 2: Schematic of mixing zones in a 75 M<sub>⊙</sub> star at 3.60 × 10<sup>6</sup> years of age (M<sub>⊙</sub> ⇔ solar mass).

**Mechanism of thermohaline mixing zone**

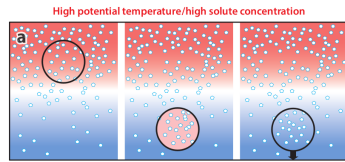


Figure 3: Schematic of double diffusion instability from [Garau (2017)]. Thermohaline convection is driven by two different density gradients which have different rates of diffusion.

**Turbulence models**

**Turbulence models for Pe ≫ 1:**

Reynolds Stress Models ⇒ GSG [Grégoire et al (2005)] conceived to work within the (Pe ≫ 1; M<sub>t</sub> ≪ 1) limits Those 2<sup>nd</sup> order models are used to describe a convective-type turbulence ⇒ deal with: u<sub>i</sub>u<sub>j</sub>, ρ<sub>i</sub>u<sub>j</sub>, ρ<sub>i</sub>ρ<sub>j</sub>.

**Turbulence models for Pe ≪ 1:**

Can the GSG model be adapted for the Pe ≪ 1 limit? Péclet effects appear in the evolution of ρ<sup>′</sup> ⇒ need to describe the following evolution equations:  
- the mass flux D<sub>t</sub>(ρ<sup>′</sup>u<sub>i</sub>) = u<sub>i</sub>divu<sup>′</sup> (unknown) + ... (source terms)  
- the density variance D<sub>t</sub>(ρ<sup>′2</sup>/2) = ρ<sup>′</sup>divu<sup>′</sup> (unknown) + ... (source terms)

**Method**

need to characterize divu<sup>′</sup>, asymptotic analysis with (Pe ≪ 1; M<sub>t</sub> ≪ 1) limits.  
- acoustical phenomena and temperature fluctuations equilibrate instantaneously.

**Stellar field: coupling flow and radiation fields**

**Flow field (mixed species α)**

**Characteristics:**

Variable density turbulent flow

Defined by ρ, u, e<sup>m</sup> and c<sub>α</sub>

**Simplifications:**

Ideal gas:

$$p^m = p^m(\rho, T, c) = \rho r T$$

$$e^m = e^m(\rho, T, c) = C_v^m T$$

With:

$$\gamma_\alpha = C_{p,\alpha}/C_{v,\alpha} = \gamma = C_p/C_v$$

$$r = r_\alpha c_\alpha \text{ and } C_v^m = C_{v,\alpha} c_\alpha$$

**Radiation field**

**Characteristics:**

Optically thick medium

Radiation in the diffusion limit

Defined by E<sup>r</sup>, P<sup>r</sup> and F<sup>r</sup>

**Simplifications:**

$$E^r = a_R T^4$$

$$P^r = a_R T^4/3 = E^r/3$$

$$F_j^r = -\lambda_j \partial_j T$$

**Stellar field**

**Characteristics:**

Matter and radiation have reached local equilibrium

Defined by ρ, u, c<sub>α</sub>, e<sup>m</sup> and E<sup>r</sup>

**Simplifications:**

$$T = T^m = T^r$$

**Dimensionless equations from governing equations with Reynolds average i.e.  $\bar{q} = q - q'$**

**Dimensionless equations:**

$$D_t u_i' = -\frac{1}{M_t^2} \frac{\partial_i p'}{\rho} - \frac{1}{Fr_s} u_j' \partial_j u_i' + \frac{1}{Fr_s} \frac{\partial_i \bar{p}}{\rho} - \frac{1}{Re_t} \left( \frac{\partial_j \Pi_{ij}}{\rho} \right)' + \text{Order 2} \quad (1a)$$

$$D_t p' = -\bar{\gamma} \bar{p} \text{div} u' + \frac{1}{Pe} (\bar{\gamma} - 1) C' - \frac{1}{Fr_s} \bar{\gamma}_1 P' \text{div} \bar{u} - Ka_p u_j' \partial_j \bar{p} + \frac{D_p'}{Sc Re_t} + \text{Order 2} \quad (1b)$$

$$D_t T' = -(\bar{\gamma} - 1) \bar{T} \text{div} u' + \frac{1}{Pe} \frac{C'}{\bar{C}_v} - \frac{\bar{\gamma} - 1}{Fr_s} T' \text{div} \bar{u} - Ka_T u_j' \partial_j \bar{T} + \frac{(\frac{\partial_j C_j'}{Sc Re_t})'}{Sc Re_t} + \text{Order 2} \quad (1c)$$

**Characterization of the flow:**

intensity of fluctuations:

$$M_t = \frac{v_0}{a_0}$$

mean field:

$$Fr_s = \frac{v_0}{S_0}, Fr_a = \frac{v_0}{S_0}, Ka_p = \frac{v_0}{L_0}, Ka_T = \frac{v_0}{L_0}$$

molecular transport and heat diffusion:

$$Re_t = \frac{v_0 L_0}{\nu_0}, Sc = \frac{\nu_0}{\chi_0}, Pr = \frac{\nu_0}{\chi_0}, Pe = \frac{v_0 L_0}{\chi_0} = Pr Re_t \text{ with } \chi_0 = \frac{\lambda_0}{\rho_0 c_{v0}}$$

**Asymptotic analysis**

**Asymptotic expansion of Eqs. (1)**

Main conditions: M<sub>t</sub> ≪ 1 and Pe ~ M<sub>t</sub> ≪ 1

Secondary conditions relevant to the flow:

Fr<sub>a</sub> ~ 1, Fr<sub>s</sub> ~ 1, Ka<sub>p</sub> ~ M<sub>t</sub>, Ka<sub>T</sub> ~ M<sub>t</sub>

**Consequences on the flow field**

the flow is in quasi-equilibrium,

the turbulent length scale is decoupled from the length scales of T and P.

**Expansions of fluctuating quantities**

The fluctuating quantities u<sup>′</sup>, p<sup>′</sup>, ρ<sup>′</sup>, c<sub>α</sub><sup>′</sup> are developed as functions of M<sub>t</sub>:

$$q' = q^{(0)} + M_t q^{(1)} + M_t^2 q^{(2)} + \mathcal{O}(M_t^3)$$

**First result**

$$\frac{p'}{\bar{p}} \sim M_t^2 \ll M_t \text{ and } \frac{T'}{\bar{T}} \sim Pe M_t \ll M_t \quad (2)$$

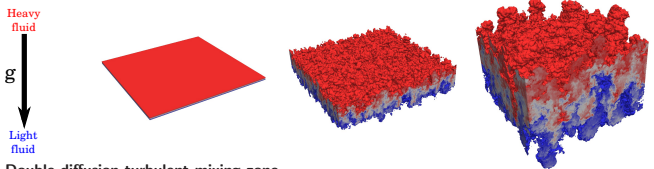
⇒ P<sup>′</sup> and T<sup>′</sup> are small compared to other thermodynamical variables fluctuations. They can be neglected with respect to these other variables, except when involved in gradients or diffusion terms.

**Second result**

$$C' = u_j' \left[ \bar{\rho} \bar{c}_\alpha \partial_j \bar{T} - (\bar{\rho} \bar{m} + 4 \bar{P}^r) \left( \frac{\partial_j \bar{p}^m}{\bar{p}^m} - \frac{\partial_j \bar{T}}{\bar{T}} \right) \right] - 4 \bar{P}^r \frac{c_\alpha}{\bar{T}} \mathcal{F}_j^r \quad (3)$$

$$\text{div} u' = -u_j' \left[ \frac{\partial_j \bar{p}^m}{\bar{p}^m} - \frac{\partial_j \bar{T}}{\bar{T}} \right] - \frac{r_\alpha}{\bar{T}} \partial_j \mathcal{F}_j^r \quad (4)$$

**Validation of the asymptotic analysis**



**Double diffusion turbulent mixing zone**

Currently: no hydro-radiative code ⇒ only a purely hydrodynamic one: TRICLADE.

However, we can still proceed to validate most of the asymptotic analysis, by imposing a very small Prandtl number (Pr = 2.5 · 10<sup>-3</sup>) ⇒ leads to a small Péclet number.

**Direct numerical simulation (DNS) of a mixing zone driven by RTI/DDI**

Two ideal gases with different molar masses and same γ initially separated by an interface.

Rayleigh-Taylor/Double diffusion instabilities (RTI/DDI): fundamental instabilities at work in the flow

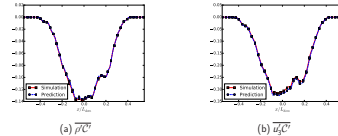


Figure 4: Comparison of the profiles of (a) p<sup>′</sup>C<sup>′</sup> and (b) u<sub>3</sub><sup>′</sup>C<sup>′</sup> with their predicted values as given by Eq. (3).

Figure 6: Cuts in the plane x<sub>1</sub> = 0 and at time t = 10 displaying respectively (a) the fluctuating conduction term C<sup>′</sup> and (b) its modelled value predicted by Eq. (3).

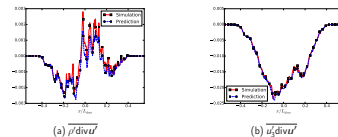


Figure 5: Comparison of the profiles of (a) p<sup>′</sup>div u<sup>′</sup> and (b) u<sub>3</sub><sup>′</sup>div u<sup>′</sup> with their predicted values as given by Eq. (4).

Figure 7: Cuts in the plane x<sub>1</sub> = 0 and at time t = 10 displaying respectively (a) the fluctuating velocity divergence div u<sup>′</sup> and (b) its modelled value predicted by Eq. (4).

⇒ Good agreement between predicted and simulated values of p<sup>′</sup>C<sup>′</sup> and u<sub>3</sub><sup>′</sup>C<sup>′</sup> with Eq. (3) and of p<sup>′</sup>div u<sup>′</sup> and u<sub>3</sub><sup>′</sup>div u<sup>′</sup> with Eq. (4)

⇒ Structures and levels of the divergence are well reproduced by Eq. (3) and Eq. (4)

**Comparison between small and high Péclet limits**

**Difference between the expressions of div u<sup>′</sup>**

It comes from the way the volume of fluid particles adjust to the mean gradients of pressure and temperature.

For Pe ≫ 1, from [Soulard et al (2012)]: div u<sup>′</sup> = -u<sub>j</sub><sup>′</sup> ∂<sub>j</sub> (P<sup>′</sup>/P̄) + ...

For Pe ≪ 1: div u<sup>′</sup> = -u<sub>j</sub><sup>′</sup> [∂<sub>j</sub> (P<sup>′m</sup>/P̄<sup>m</sup>) - ∂<sub>j</sub> (T<sup>′</sup>/T̄)] + ...

**Stability criterion of a mean stratification:**

For Pe ≫ 1:

$$\partial_{tt}^2 u_j' = -u_k' \left[ \frac{\partial_k \bar{p}}{\bar{p}} - \frac{\partial_k \bar{P}^r}{\bar{\gamma} \bar{P}^r} \right] \frac{\partial_j \bar{P}^r}{\bar{p}} + \dots$$

> 0 for stable stratification

For Pe ≪ 1 ⇒ asymptotic case of double diffusion instability (DDI)

$$\partial_{tt}^2 u_j' = u_k' \frac{\partial_k \bar{T} \partial_j \bar{P}^r}{\bar{T} \bar{p}} + \dots$$

< 0 for stable stratification

**Validation of the adaptation of the GSG model for small and large Péclet limits**

**Validation with GSG vs. ILES**

Two implicit large eddy simulations (ILES) of a RTI/DDI performed, different by heat diffusion coefficient:

λ = 0.2 and λ = 97.

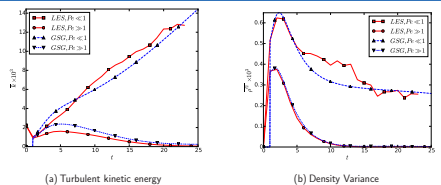


Figure 8: Time evolution of the turbulent kinetic energy and density variance at the center of the mixing zone (LES and GSG models).

**For Pe ≫ 1: stabilization of mean entropy stratification**

⇒ counters RTI ⇒ fast collapse of turbulent field

For Pe ≪ 1: DDI depends on molar mass gradient and grows

⇒ well captured by modified GSG model

**Conclusion**

**Results**

Small Péclet-small Mach number analysis was extended to radiative flows with mixing.

Closures for the evolution of density-linked correlations in a class of turbulent RSMs (GSG models) were derived.

Models can be used in stellar flows having small Péclet numbers.

**Future work**

To extend the validation to hydro-radiative flow mixing simulations for applications in stellar interiors.

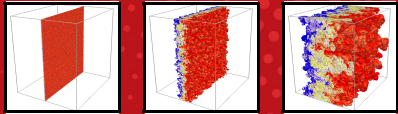
# Thesis defence (see hereinafter)

\* Thesis defence | Video conference (due to COVID-19)

Modelling turbulence subjected to strong radiation

March 29, 2021

## Thesis defence presentation

### Modelling of turbulence subjected to strong radiation

**Doctoral student:**  
J.-C. CHKAIR<sup>1</sup> (jean-cedric.chkair@cea.fr)

**Thesis supervisors:**  
X. BLANC<sup>2</sup> (blanc@ann.jussieu.fr)

**Thesis advisors:**  
O. SOULARD<sup>1</sup> (olivier.soulard@cea.fr)  
J. GRIFFOND<sup>1</sup> (jerome.griffond@cea.fr)

Thesis defence | March 29, 2021

**Introduction: turbulence and radiation in stars**

**Why studying turbulence coupled with radiation?**

- regime present in stellar interiors.

**Presence of turbulence in stellar interiors:**

- generated by various mechanisms (convection, rotation, instabilities, shear...)

**Impacts of turbulence:**

- transport of chemical elements in mixing zones,
- transport of heat due to strong radiation effects,
- ⇒ influence on stellar structure and composition.

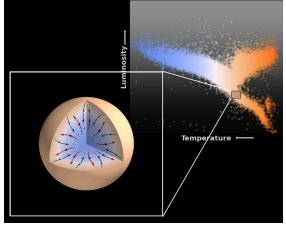


Figure: Convective zones in main-sequence stars.

Initial mass: 9/11 M<sub>⊙</sub> (massive), 2/3 M<sub>⊙</sub> (intermediate), low-mass (with M<sub>⊙</sub> the "Solar mass").

<sup>1</sup> CEA/DAM/DIF F-91297, Arpajon, France  
<sup>2</sup> Université de Paris, Laboratoire Jacques-Louis Lions, F-75013 Paris, France



### Radiative transport in stellar media

**Heat transfer:**

- comparison of radiation and turbulent convection processes with the turbulent Péclet number:

$$Pe_t = \frac{\tau_{\text{radiation}}}{\tau_{\text{turbulence}}}$$

- $(Pe_t \gg 1) \Rightarrow$  turbulence more efficient than radiation in heat transport,
- $(Pe_t \ll 1) \Rightarrow$  radiation more efficient than turbulence in heat transport,
- both regimes present in the transition phase from the main-sequence to the red-giant branch.

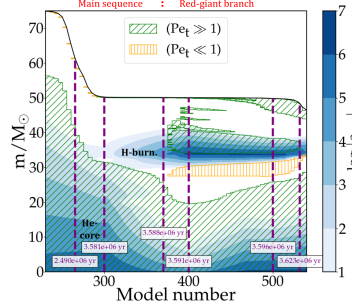


Figure: Temporal evolution diagram of a 75 M<sub>⊙</sub> star from t = 0.02 Myr to t = 3.7 Myr (from MESA), with:

- m the interior stellar mass,
- "model number" the non-linear timescale,
- ε<sub>nuc</sub> the nuclear reaction specific energy rate.



### Onset of (Pe<sub>t</sub> >> 1) and (Pe<sub>t</sub> << 1) convection

**Assumption:**

- negligible transport of species concentration.

**Negligible heat flux (Pe<sub>t</sub> >> 1):**

- negligible transport of heat,
- ⇒ adiabatic adjustment of pressure:

$$\rho_* = \rho_1 + \frac{\partial \rho}{\partial p} \Big|_{\text{ad}, \mu} (P_2 - P_1),$$

- unstable stratification (ρ<sub>\*</sub> < ρ<sub>2</sub>) if:

$$\frac{\partial P}{\partial p} \Big|_{\text{ad}, \mu} > \frac{\partial \rho / \partial r}{\partial \rho / \partial r}$$

**Large heat flux (Pe<sub>t</sub> << 1):**

- thermal equilibrium ⇒ T<sub>\*</sub> = T<sub>2</sub>,
- assuming μ<sub>\*</sub> = μ<sub>1</sub>:

$$\rho_* = \mu_1 \frac{1}{R T_2} \left( P_2 - \frac{1}{3} n_R T_2^4 \right),$$

- unstable stratification (ρ<sub>\*</sub> < ρ<sub>2</sub>) if:

$$\frac{\partial \mu}{\partial r} > 0$$



### "Ledoux" criterion for stellar convection

**Onset of stellar convection:**

- determined by the "Ledoux" criterion.

**Convective mixing zones (Pe<sub>t</sub> >> 1):**

- amplification of small perturbations around the mean stratification,
- unstable stratification if:

$$\nabla_s \cdot \frac{\nabla P}{\rho} > 0,$$

with  $\nabla_s \equiv \frac{\nabla P}{\gamma_1 P} - \frac{\nabla \rho}{\rho}$  and  $\gamma_1 = \frac{\rho}{P} \left( \frac{\partial P}{\partial p} \right)_{s, \mu}$ ,

where ∇ is the spatial gradient, s is the "pseudo-entropy" and γ<sub>1</sub> is a generalized adiabatic exponent.

**Thermohaline mixing zones (Pe<sub>t</sub> << 1):**

- double-diffusion instability caused by a destabilizing ∇μ and a stabilizing ∇T,
- unstable stratification if:

$$\frac{\nabla \mu}{\mu} \cdot \frac{\nabla P}{\rho} > 0,$$

**Characterization of turbulent regimes:**

**Convective mixing zones:**

- $Pe_t = Pr \cdot Re_t \gg 1$ ,
- heat transport by radiation  $\ll$  heat transport by turbulence,
- $M_t \ll 1$ ,
- $Re_t \gg 1$ ,
- $Pr \gtrsim P^m$ ,

**Thermohaline mixing zones:**

- $Pe_t = Pr \cdot Re_t \ll 1$ ,
- heat transport by radiation  $\gg$  heat transport by turbulence,
- $M_t \ll 1$ ,
- $Re_t \gg 1$ ,
- $Pr \gtrsim P^m$ ,

with  $P^r$  and  $P^m$  the radiative and matter pressure.

**Dimensionless numbers:**

$$M_t = \frac{u_0}{c_s}, Re_t = \frac{\nu_t}{\nu_v}, Pr = \frac{\nu_v}{\chi^r} \text{ and } Pe_t = \frac{\nu_t}{\chi^r}$$

$u_0$  the turbulent velocity,  $c_s$  the sound of speed,  $\nu_t$  the turbulent viscosity,  $\nu_v$  the kinematic viscosity and  $\chi^r$  the radiative diffusivity.

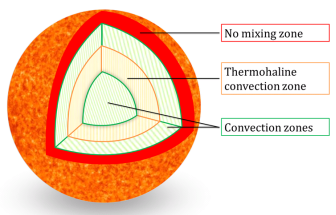


Figure: Turbulent mixing zones in a 75  $M_\odot$  red-giant star.

**Purpose:**

- derivation and validation of a turbulent statistical model that describes stellar interiors and including mixing and radiative effects (adapted to large and small Péclet numbers),
- for simplicity  $\Rightarrow$  turbulence modelling focused on convection and double-diffusion instabilities.

**Plan:**

- derivation and validation of the approach: asymptotic analysis within the ( $M_t \ll 1$ ;  $Pe_t \ll 1$ ) limits,
- adaptation of a ( $M_t \ll 1$ ;  $Pe_t \gg 1$ ) Reynolds stress model (RSM) to the ( $Pe_t \ll 1$ ) regime,
- validation of the modified model within the ( $Pe_t \gg 1$ ) and ( $Pe_t \ll 1$ ) limits,
- linear stability of a radiative Rayleigh-Taylor flow configuration with visco-diffusive effects  $\Rightarrow$  improvement of the model blending linking ( $Pe_t \gg 1$ ) and ( $Pe_t \ll 1$ ) limits.

- Asymptotic analysis
- Linear stability analysis
- Adaptation of a RSM model
- Conclusion and perspectives

**Asymptotic analysis in the ( $M_t \ll 1$ ) limit:**

- acoustical phenomena are filtered out,

**Asymptotic analysis in the ( $Pe_t \ll 1$ ) limit:**

- fast transport of temperature fluctuations  $\Rightarrow$  thermal equilibrium,

**Improvements compared to existing works:**

- mixing,
- radiative pressure  $P^r \gtrsim P^m$  matter pressure,
- (non-ideal equations of state),
- (nuclear reactions).

$\Rightarrow$  derive and validate a small Mach-small Péclet number approximation,

Hydro-radiative instantaneous compressible Navier-Stokes coupled with radiation in the diffusion limit:

$$\begin{cases} D_t \rho &= -\rho \operatorname{div} u & \text{continuity} \\ \rho D_t u_i &= -\partial_i P - \partial_j \Pi_{ij} + \rho g_i & \text{momentum} \\ \rho D_t c_\alpha &= -\partial_j \mathcal{F}_{\alpha j} & \text{concentration} \\ \rho D_t e^m &= \rho \varepsilon - Q_{c_\alpha} - P^m \operatorname{div} u - \partial_j \mathcal{F}_j^m & \text{material energy} \\ D_t E^r &= -(E^r + P^r) \operatorname{div} u - \partial_j \mathcal{F}_j^r & \text{radiative energy} \end{cases}$$

with:

- $D_t = \partial_t + u_j \partial_j$ : the Lagrangian time derivative,
- $\partial_j$ : the partial derivative with respect to the spatial cartesian coordinate  $x_j$ ,
- $\operatorname{div} u = \partial_j u_j$  the velocity divergence,
- "m" and "r" relates to matter and radiation.

**State variables:**

- $P = P^m + P^r$  the total pressure,
- $e = e^m + E^r / \rho$  the total specific energy,
- $T = T^m = T^r$  the temperature,
- $P^r = E^r / 3$  the radiative pressure,
- $E^r = a_R T^4$  the radiative energy.

$\Rightarrow$  mixture treated as an ideal gas with radiation.

Hydro-radiative instantaneous compressible Navier-Stokes coupled with radiation in the diffusion limit:

$$\begin{cases} D_t \rho &= -\rho \operatorname{div} u & \text{continuity} \\ \rho D_t u_i &= -\partial_i P - \partial_j \Pi_{ij} + \rho g_i & \text{momentum} \\ \rho D_t c_\alpha &= -\partial_j \mathcal{F}_{\alpha j} & \text{concentration} \\ \rho D_t e^m &= \rho \varepsilon - Q_{c_\alpha} - P^m \operatorname{div} u - \partial_j \mathcal{F}_j^m & \text{material energy} \\ D_t E^r &= -(E^r + P^r) \operatorname{div} u - \partial_j \mathcal{F}_j^r & \text{radiative energy} \end{cases}$$

**Molecular terms:**

- $\Pi_{ij}$  the viscosity tensor,
- $\mathcal{F}_{\alpha j} = -\rho D^{(\alpha)} \partial_j c_\alpha$  the diffusion flux of the species mass fraction  $c_\alpha$  where  $D^{(\alpha)}$  is its scalar diffusion coefficient,
- $\varepsilon$  the viscous dissipation rate,
- $Q_{c_\alpha} = \partial_j \left[ \sum_\alpha \partial c_\alpha h^{m|\rho, T, c_{\beta \neq \alpha}} \mathcal{F}_{\alpha j} \right]$  the enthalpy ( $h^m = e^m + P^m / \rho$ ) mixing.

**Material thermal flux:**

- $\mathcal{F}_j^m = -\lambda^m \partial_j T$  with  $\lambda^m$  the thermal conductivity.

**Radiative thermal flux:**

- $\mathcal{F}_j^r = -\lambda^r \partial_j T$  with  $\lambda^r = \frac{4 a_R c_\ell}{3} \frac{T^3}{\rho \kappa^r}$  the radiative conductivity,

where  $a_R$ ,  $c_\ell$  and  $\kappa^r$  are respectively the radiation constant, the speed of light and the Rosseland opacity.

**Governing equations:**

- ( $M_t \ll 1$ ) and ( $Pe_t \ll 1$ ) main effects: on ( $u, P, T$ ) fields,
- quantities  $q$  split into background component and a deviation:

Reynolds decomposition:  $q = \underbrace{\bar{q}}_{\text{statistical ensemble mean}} + \underbrace{q'}_{\text{fluctuation}}$

- ( $u', P', T'$ ) evolutions  $\Rightarrow$  rendered dimensionless with characteristic scales.

**Conditions:**

- $\exists n \geq 1$ ,

$$M_t \ll 1 \text{ and } Pe_t \sim M_t^n \ll 1,$$

- assuming:

$$Re_t \gtrsim 1,$$

- ( $u', \rho', P', \gamma', T'$ ) developed as:

$$q' = q^{(0)} + M_t q^{(1)} + M_t^2 q^{(2)} + \mathcal{O}(M_t^3).$$

**Results:**

- orders of magnitude:

$$\frac{P'}{P} \sim M_t^2 \text{ and } \frac{T'}{T} \sim Pe_t \cdot M_t,$$

- asymptotic expression:

$$\operatorname{div} u' = \underbrace{-u'_j \left[ \frac{\partial_j P^m}{P^m} - \frac{\partial_j T}{T} \right]}_{\text{stratification}} - \underbrace{\sum_\alpha \frac{r_\alpha}{\rho} \partial_j \mathcal{F}_{\alpha j}'}_{\text{molecular mixing}},$$

with:

- $r_\alpha$  the specific ideal gas constant of each species  $\alpha$  of concentration  $c_\alpha$ ,
- $r = \sum_\alpha r_\alpha c_\alpha$  the specific ideal gas constant of the mixture,
- $\mathcal{F}_{\alpha j} = -\rho D^{(\alpha)} \partial_j c_\alpha$  the scalar flux and  $D^{(\alpha)}$  the scalar diffusion coefficient.

cea Comparison of  $\text{divu}'$  in the  $(\text{Pe}_t \gg 1)$  and  $(\text{Pe}_t \ll 1)$  limits

Comparison of  $\text{divu}'$ :

■ For  $(\text{Pe}_t \gg 1)$  from Soular *et al.* [2012, Phys. Rev. E]:  $\text{divu}' = -u'_i \left[ \frac{\partial_i \bar{P}}{\gamma \bar{P}} \right] + \text{Molec. terms}$

■ For  $(\text{Pe}_t \ll 1)$ :  $\text{divu}' = -u'_i \left[ \frac{\partial_i \bar{P}^{\text{PM}}}{\bar{P}^{\text{PM}}} - \frac{\partial_i \bar{T}}{\bar{T}} \right] + \text{Molec. terms}$

Interpretation:

- stem from  $(\text{Ma}_t \ll 1)$  analyses applied to the evolution of  $P'$ ,
- different volume adjustment,
- contain mixing effects.

cea Inviscid stability criterion in the  $(\text{Pe}_t \gg 1)$  and  $(\text{Pe}_t \ll 1)$  limits

Configuration of the mean stratification:

- hydrostatic equilibrium:  $\partial_i \bar{P} = \bar{\rho} g_i$

Impact of  $\text{divu}'$  expressions:

- by inserting  $\text{divu}'$  expressions into  $\rho'$  linearized equation:

$$\partial_t \frac{\rho'}{\rho} = -\text{divu}' - u'_i \frac{\partial_i \bar{P}}{\bar{P}} \Rightarrow \begin{cases} \text{for } (\text{Pe}_t \gg 1), & \partial_t \frac{\rho'}{\rho} = u'_i \left( \frac{\partial_i \bar{P}}{\gamma \bar{P}} - \frac{\partial_i \bar{P}}{\bar{P}} \right), \\ \text{for } (\text{Pe}_t \ll 1), & \partial_t \frac{\rho'}{\rho} = u'_i \frac{\partial_i \bar{T}}{\bar{T}}, \end{cases}$$

- by inserting  $\partial_t \left( \frac{\rho'}{\rho} \right)$  into  $u'$  linearized equation:

$$\partial_t u'_i = \frac{\rho'}{\rho} \frac{\partial_i \bar{P}}{\bar{P}} \Rightarrow \partial_t (\partial_i u'_i) = \partial_t \left( \frac{\rho'}{\rho} \right) \frac{\partial_i \bar{P}}{\bar{P}} \Rightarrow \begin{cases} \text{for } (\text{Pe}_t \gg 1), & \partial_t^2 u'_i - \left( \frac{\partial_i \bar{P}}{\gamma \bar{P}} - \frac{\partial_i \bar{P}}{\bar{P}} \right) \frac{\partial_i \bar{P}}{\bar{P}} \partial_t u'_i = 0, \\ \text{for } (\text{Pe}_t \ll 1), & \partial_t^2 u'_i - \left( \frac{\partial_i \bar{T}}{\bar{T}} \right) \frac{\partial_i \bar{P}}{\bar{P}} \partial_t u'_i = 0. \end{cases}$$

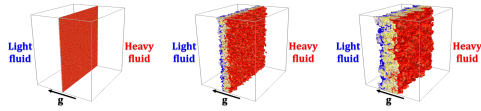
Inviscid stability criterion of the stratification:

- unstable provided:

$$\begin{cases} \text{for } (\text{Pe}_t \gg 1), & \left( \frac{\partial_i \bar{P}}{\gamma \bar{P}} - \frac{\partial_i \bar{P}}{\bar{P}} \right) \frac{\partial_i \bar{P}}{\bar{P}} > 0, \\ \text{for } (\text{Pe}_t \ll 1), & \frac{\partial_i \bar{T}}{\bar{T}} \frac{\partial_i \bar{P}}{\bar{P}} > 0. \end{cases}$$

- equivalent to the Ledoux stability criteria  $\Rightarrow$  highlights the role of  $\text{Pe}_t$ .

cea Validation of the approach: Rayleigh-Taylor instability (RTI)



NS (Numerical Simulations) of a turbulent mixing zone with the in-house code TRICLADE

- two ideal gases (of different molar masses  $M_h$  and  $M_l$ ) initially separated by an interface are mixed under the effect of gravity  $g$ ,
- usual mechanisms at work in stars,
- defined by the Atwood, Mihalas and Boltzmann dimensionless numbers:  
 $\mathcal{A}_t = \frac{M_h - M_l}{M_h + M_l} = 0.26$ ,  $R = \frac{\rho e^m}{E^2} = 1.24 > 1$  and  $\text{Bo} = \frac{\rho h^m c_{00}}{\text{arc} c T^4 / 4} = 3.75 \times 10^{-2} \ll 1$ ,
- homogeneous  $\kappa^t$  transport coefficient treated as a constant,

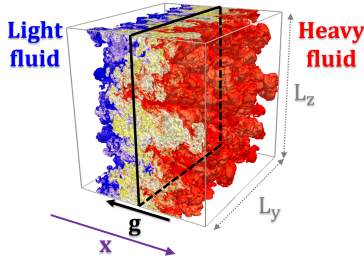
Opacity $\kappa^t$	Prandtl number Pr	Simulation acronym	Expected Péclet orders
8.64	$2.36 \times 10^{-4}$	SP <sub>1</sub>	$(\text{Pe}_t \ll 1)$
$8.64 \times 10^1$	$2.36 \times 10^{-3}$	SP <sub>2</sub>	$(\text{Pe}_t \lesssim 1)$
$8.64 \times 10^4$	2.36	HP	$(\text{Pe}_t \gg 1)$

Table: Interface parameters defining a hydrostatic equilibrium with an isothermal condition imposed.

cea Computation at the initial position of the interface

- statistically 1D  $\Rightarrow$  only depending on the inhomogeneous direction  $x$ ,
- statistical averages of any quantity  $q$  as:

$$\bar{q}(x) = \frac{1}{L_y L_z} \int \int q(x, y, z) dy dz$$



cea Verification of the conditions  $(\text{Ma}_t \ll 1)$  and  $(\text{Pe}_t \ll 1)$

$$\text{Ma}_t \equiv \frac{\sqrt{k}}{c_s}, \text{Re}_\lambda \equiv \frac{2\sqrt{15}}{3} \sqrt{\frac{\bar{P} k^2}{\mu_t \bar{\epsilon}}} \text{ and } \text{Pe}_t \equiv \frac{\bar{\rho} c_p \nu_t}{\lambda}$$

$\bar{k}$  the turbulent kinetic energy,  $\bar{\epsilon}$  its dissipation,  $c_s$  the speed of sound,  $\mu_t$  the dynamic viscosity,  $c_p$  the specific heat at constant pressure,  $\lambda$  the radiative conductivity and  $\nu_t$  the turbulent viscosity.

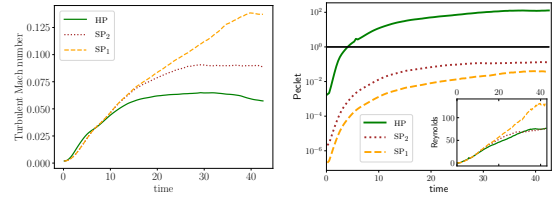


Figure: Time evolution of dimensionless parameters at the center of the turbulent mixing zone.

(HP, SP<sub>1</sub>, SP<sub>2</sub>)  $\Rightarrow$   $(\text{Ma}_t \ll 1)$ : limit verified &  $(\text{Re}_\lambda \gg 1)$ : turbulent regime reached.

(HP)  $\Rightarrow$   $(\text{Pe}_t \gg 1)$ : opposite evolution as (SP<sub>1</sub>),  
 (SP<sub>1</sub>)  $\Rightarrow$   $(\text{Pe}_t \ll 1)$ : condition verified,  
 (SP<sub>2</sub>)  $\Rightarrow$   $(\text{Pe}_t \lesssim 1)$ : intermediate regime reached.

cea Validation of the orders  $(P'/\bar{P} \sim \text{Ma}_t^2)$  and  $(T'/\bar{T} \sim \text{Pe}_t \cdot \text{Ma}_t)$

$$\eta_P = \frac{\sqrt{P' - \bar{P}'}}{\bar{P} \cdot \text{Ma}_t^2} \text{ and } \eta_T = \frac{\sqrt{T' - \bar{T}'}}{\bar{T} \cdot \text{Pe}_t \cdot \text{Ma}_t}$$

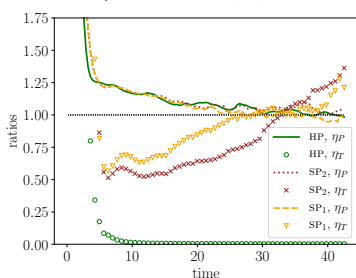


Figure: Time evolution of  $\eta_P$  and  $\eta_T$  ratios in the center of the turbulent mixing zone.

(SP<sub>1</sub>, SP<sub>2</sub>)  $\Rightarrow$   $(\eta_P \sim 1)$  &  $(\eta_T \sim 1)$ : consistency with the  $(\text{Ma}_t \ll 1; \text{Pe}_t \ll 1)$  approximation,  
 (HP)  $\Rightarrow$   $(\eta_P \sim 1)$  &  $(\eta_T \rightarrow 0)$ : no prediction on the order of  $T'$  in  $(\text{Ma}_t \ll 1)$  analyses.

cea SP<sub>2</sub> simulation and  $(\text{Pe}_t \ll 1)$  predicted  $\text{divu}'$

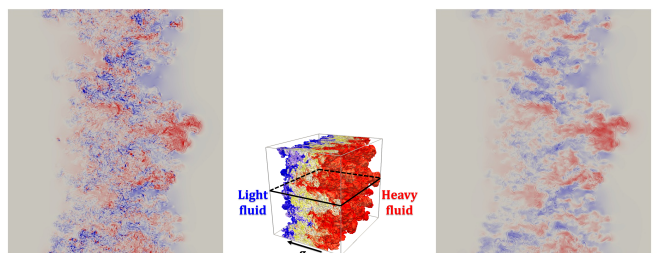


Figure: Cuts in the plane containing  $g$  at  $t = 34$  displaying (a)  $\partial_i u'_i$  of SP<sub>2</sub> and (b) its  $(\text{Pe}_t \ll 1)$  asymptotic value (same color scales).

(SP<sub>2</sub>): structures and levels of the divergence well reproduced by asymptotic values.

### Computation of $\text{div}u'$ -linked correlations along the x-axis

From the  $(Pe_t \ll 1)$  asymptotic expression:

$$\text{div}u' = \underbrace{-u'_x \left[ \frac{\partial \bar{p}^{pm}}{\partial x} - \frac{\partial \bar{T}}{\partial x} \right]}_{\text{stratification}} - \underbrace{\sum_{\alpha} \frac{r_{\alpha}}{\bar{T}} \partial_x \mathcal{F}_{\alpha}'}_{\text{molecular mixing}}$$

the correlations  $-\rho' \text{div}u'$  and  $u'_x \text{div}u'$  can be split into:

$$\begin{cases} -\rho' \text{div}u' = \underbrace{\rho' u'_x \left[ \frac{\partial \bar{p}^{pm}}{\partial x} - \frac{\partial \bar{T}}{\partial x} \right]}_{\text{strat.}} + \underbrace{\rho' \sum_{\alpha} \frac{r_{\alpha}}{\bar{T}} \partial_x \mathcal{F}_{\alpha}'}_{\text{mix.}} \\ u'_x \text{div}u' = \underbrace{-u'_x u'_x \left[ \frac{\partial \bar{p}^{pm}}{\partial x} - \frac{\partial \bar{T}}{\partial x} \right]}_{\text{strat.}} - \underbrace{u'_x \sum_{\alpha} \frac{r_{\alpha}}{\bar{T}} \partial_x \mathcal{F}_{\alpha}'}_{\text{mix.}} \end{cases}$$

and computed along the x-axis.

### SP<sub>2</sub> simulation and $(Pe_t \ll 1)$ predicted $\text{div}u'$ -linked correlations

Figure: Comparison at  $t = 34$  of the spatial profiles of (a)  $-\rho' \text{div}u'$  and (b)  $u'_x \text{div}u'$  of SP<sub>2</sub> with their  $(Pe_t \ll 1)$  prediction. ("strat.") and ("mix.") are contributions from the stratification and molecular terms.

(SP<sub>2</sub>): good agreement between simulated and predicted values.

("strat.")  $\Rightarrow$  positive sign due to baroclinic production : interpreted as production term.  
 ("mix.")  $\Rightarrow$  negative sign due to dissipation : interpreted as destruction term.

### Table of contents

- Asymptotic analysis
- Adaptation of a RSM model
- Linear stability analysis
- Conclusion and perspectives

### GSG ( $M_t \ll 1$ ) RSM turbulence model

Outcome of  $(M_t \ll 1)$  approximations:

- constraint on  $\text{div}u' \Rightarrow$  treatment of some compressibility effects,
- $\Rightarrow$  used to derive closed evolution equations for the **variance** and **flux** of the density field.

Reynolds Stress Models (RSM):

- second order model for convective turbulence:
  - $\bar{R}_{ij} = \overline{u'_i u'_j}$ : Reynolds stresses,
  - $\overline{\tau'' u''}$ : specific volume turbulent flux,
  - $\overline{\tau'' \tau''}$ : specific volume variance,
  - $\bar{\epsilon}$ : kinetic energy dissipation.
- GSG from Greigore *et al.* [2005, J. Turbul.] at CEA.
- $(M_t \ll 1)$ ,  $(Pe_t \ll 1)$  and  $(Re_t \gg 1)$  turbulence:
  - none in engineering applications,
  - but in stellar interiors  $\Rightarrow$  most Prandtl's mixing length models,
  - Canuto [2011, A&A]'s RSM exception  $\Rightarrow$  explicit dependency on  $Pe_t$ .

How to adapt the GSG ( $M_t \ll 1$ ) RSM turbulent model to the  $(Pe_t \ll 1)$  limit?

### Adaptation of the Langevin PDF model to the $(Pe_t \ll 1)$ limit

Purpose:

- derive expressions for unclosed terms in evolutions (with  $\bar{D}_i = \partial_i + \bar{u}_i \partial_i$ ):
  - specific volume flux:  $\bar{D}_i \overline{\tau'' u''} = \overline{u'_i \text{div}u'} + \dots$ ,
  - specific volume variance:  $\bar{D}_i \overline{\tau'' \tau''} = \overline{\tau'' \text{div}u'} + \dots$ ,
- $\Rightarrow$  derived from a stochastic Langevin model closing the evolutions of  $u''$  and  $\tau''$ ,
- in mass conservation, the only unknown appearing is  $\text{div}u'$ :

$$\bar{D}_i \frac{\tau''}{\bar{\tau}} = \left(1 + \frac{\tau''}{\bar{\tau}}\right) \left[ \text{div}u' - u'_i \frac{\partial \bar{\tau}}{\partial x_i} + \partial_i \left( \overline{\rho u'' \tau''} \right) \right] \quad (1)$$

Asymptotic expressions used in the GSG model:

- $(M_t \ll 1)$  approximation, compatible with the  $(Pe_t \gg 1)$  limit:
 
$$\text{div}u' = -u'_x \frac{\partial \bar{p}}{\partial x} + \text{Molec. terms}$$
- $(M_t \ll 1; Pe_t \ll 1)$  asymptotic analysis:
 
$$\text{div}u' = -u'_x \left[ \frac{\partial \bar{p}^{pm}}{\partial x} - \frac{\partial \bar{T}}{\partial x} \right] + \text{Molec. terms}$$

1<sup>st</sup> step to derive closures  $\Rightarrow$  inserting  $\text{div}u'$  in Eq. (1).

### Turbulence modelling in $(Pe_t \gg 1)$ and $(Pe_t \ll 1)$ limits

Evolution of  $\tau''$ :

$$\begin{cases} \text{for } (Pe_t \gg 1), \\ \bar{D}_i \frac{\tau''}{\bar{\tau}} = -u'_i \left( \frac{\partial \bar{\tau}}{\partial x_i} + \frac{\partial \bar{p}}{\partial x_i} \right) - C_{\rho 1} \bar{\omega} \frac{\tau''}{\bar{\tau}} + \sqrt{C_{\rho 0} \bar{\omega} \frac{\tau''}{\bar{\tau}}} W + \partial_i \left( \overline{\rho u'' \tau''} \right) - \overline{\rho u'' \tau''} \left( \frac{\partial \bar{p}}{\partial x_i} + \frac{\partial \bar{T}}{\partial x_i} \right), \\ \text{for } (Pe_t \ll 1), \\ \bar{D}_i \frac{\tau''}{\bar{\tau}} = -u'_i \frac{\partial \bar{\tau}}{\partial x_i} - C_{\rho 1} \bar{\omega} \frac{\tau''}{\bar{\tau}} + \sqrt{C_{\rho 0} \bar{\omega} \frac{\tau''}{\bar{\tau}}} W + \partial_i \left( \overline{\rho u'' \tau''} \right) - \overline{\rho u'' \tau''} \left( \frac{\partial \bar{p}}{\partial x_i} + \frac{\partial \bar{T}}{\partial x_i} \right). \end{cases}$$

Turbulence modelling:

- molecular diffusion closed with a Langevin model  $\Rightarrow$  interpreted as dissipation acting on  $\tau''$  with:
  - $C_{\rho 1}$  and  $C_{\rho 0}$  constants,
  - $\bar{\omega}$  the turbulent frequency,
  - $W$  the time derivative of a Brownian noise.

Reaction of  $\tau''$  to a mean stratification:

- $(Pe_t \gg 1)$ : readjusts to the pseudo-entropy gradient,
- $(Pe_t \ll 1)$ : readjusts to the molar-mass gradient,
- $\Rightarrow$  only difference, responsible for the change of the stability criterion.

2<sup>nd</sup> step to derive closures  $\Rightarrow$  modelling both  $(Pe_t \gg 1)$  and  $(Pe_t \ll 1)$  limits with a blending.

### Derivation of an "all-Péclet" turbulent RSM GSG model

Evolution of  $\tau''$  blending  $(Pe_t \gg 1)$  and  $(Pe_t \ll 1)$  limits:

$$\bar{D}_i \frac{\tau''}{\bar{\tau}} = -u'_i \left[ \omega_{Pe_t} \frac{\partial \bar{\tau}}{\partial x_i} + (1 - \omega_{Pe_t}) \left( \frac{\partial \bar{\tau}}{\partial x_i} + \frac{\partial \bar{p}}{\partial x_i} \right) \right] - C_{\rho 1} \bar{\omega} \frac{\tau''}{\bar{\tau}} + \sqrt{C_{\rho 0} \bar{\omega} \frac{\tau''}{\bar{\tau}}} W + \partial_i \left( \overline{\rho u'' \tau''} \right) - \overline{\rho u'' \tau''} \left( \frac{\partial \bar{p}}{\partial x_i} + \frac{\partial \bar{T}}{\partial x_i} \right)$$

Model blending:

- weighting function  $\omega_{Pe_t}$  of simple form with a fixed transition parameter  $Pe_t^{lim}$ :
 
$$\omega_{Pe_t} = \frac{Pe_t^{lim}}{Pe_t^{lim} + Pe_t} \quad \text{with} \quad \begin{cases} \text{for } Pe_t \rightarrow \infty, & \omega_{Pe_t} \rightarrow 0, \\ \text{for } Pe_t \rightarrow 0, & \omega_{Pe_t} \rightarrow 1. \end{cases}$$

3<sup>rd</sup> step to derive closures  $\Rightarrow$  multiply  $\left[ \bar{D}_i \frac{\tau''}{\bar{\tau}} = \dots \right]$  by  $\left( u''_i, \frac{\tau''}{\bar{\tau}} \right)$  and taking their averages.

Specific volume flux and variance evolutions are closed:

$$\begin{aligned} \bar{D}_i \overline{\tau'' u''} &= \left[ \omega_{Pe_t} \frac{\partial \bar{\tau}}{\partial x_i} + (1 - \omega_{Pe_t}) \left( \frac{\partial \bar{\tau}}{\partial x_i} + \frac{\partial \bar{p}}{\partial x_i} \right) \right] \bar{R}_{ij} + \dots \\ \bar{D}_i \overline{\tau'' \tau''} &= 2 \left[ \omega_{Pe_t} \frac{\partial \bar{\tau}}{\partial x_i} + (1 - \omega_{Pe_t}) \left( \frac{\partial \bar{\tau}}{\partial x_i} + \frac{\partial \bar{p}}{\partial x_i} \right) \right] \overline{\tau'' u''} + \dots \quad \text{with } \bar{D}_i = \partial_i + \bar{u}_i \partial_i \end{aligned}$$

### Validation of the extended GSG turbulence model

Validation of the modified GSG model closures:

- 1D-RANS simulations of RTI compared to NS simulations: SP<sub>1</sub> and HP,
- SP<sub>2</sub> used to calibrate the turbulent parameter  $Pe_t^{lim}$ .
- $\Rightarrow$  study of the impact of the  $(M_t \ll 1; Pe_t \ll 1)$  approximation on the RTI behaviour.

Stability of RTI:

HP turbulent state  $(Pe_t \gg 1)$ :

- stable if  $\left( \frac{\partial \bar{p}}{\partial x} - \frac{\partial \bar{p}}{\partial x} \right) \frac{\partial \bar{p}}{\partial x} < 0$ ,
- isentropic threshold reached,
- stabilization of the stratification.

SP<sub>1</sub> turbulent state  $(Pe_t \ll 1)$ :

- stable if  $\frac{\partial \bar{p}}{\partial x} \frac{\partial \bar{p}}{\partial x} < 0$ ,
- permanent evolution of the entropy,
- growth of the turbulent mixing zone.

Figure: Spatial pseudo-entropy profiles of HP and SP<sub>1</sub> DNS:

$$S = \int_{-30}^x \left( \frac{\partial \bar{p}}{\partial x} - \frac{\partial \bar{p}}{\partial x} \right) d\bar{x}$$

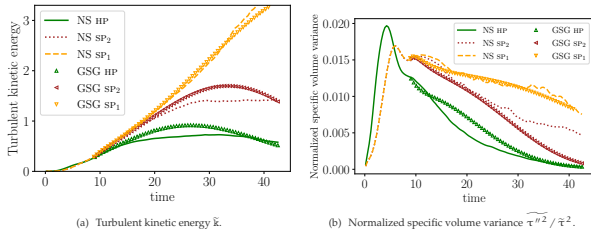


Figure: Time evolution of  $\bar{k}$  and  $\tilde{\tau}^2/\tau^2$  at the initial position of the interface. Comparison between the ID-RANS and the NS simulations.

- physics well captured by the model in different situations,
- (HP)  $\Rightarrow$  fast collapse of the turbulent field,
- (SP1)  $\Rightarrow$  kinetic energy keeps increasing,
- (SP2)  $\Rightarrow$  correct trends with fixed parameter  $Pe_t^{lim}$ .

- Asymptotic analysis
- Adaptation of a RSM model
- Linear stability analysis
- Conclusion and perspectives

Purpose:

- study the linear stability of the radiative binary mixture (ideal gas) considered in this work.

Motivations:

- current local inviscid stability criterion,

$$\text{unstable provided } \begin{cases} \text{for } (Pe_t \gg 1), & \left( \frac{\partial \bar{P}}{\partial T} - \frac{\partial \bar{P}}{\partial P} \right) \frac{\partial \bar{P}}{\partial P} > 0, \\ \text{for } (Pe_t \ll 1), & \frac{\partial \bar{P}}{\partial T} \frac{\partial \bar{P}}{\partial P} > 0, \end{cases}$$

- $\Rightarrow$  predicts the stability involving viscosity, scalar diffusion and radiative conductivity effects,
- current blending between  $(Pe_t \gg 1)$  and  $(Pe_t \ll 1)$  regimes with a calibrated  $Pe_t^{lim}$ ,

$$\omega_{Pe_t} = \frac{Pe_t^{lim}}{Pe_t^{lim} + Pe_t},$$

- $\Rightarrow$  propose another weighting function  $\omega_{Pe_t}$  for the blending based on physical considerations.
- $\Rightarrow$  matches the marginal stability criterion of the LSA with its analogue in the GSG RSM model.

Approach:

- based on compressible Navier-Stokes equations coupled with radiation,  $\Rightarrow$  satisfied by the basic flow  $\bar{q}$  of any quantity  $q$ .
- stratified RT (shear free) configuration under a gravity field  $\mathbf{g}$  along  $x_{||}$ -axis:
  - hydrostatic equilibrium  $\bar{u} = 0$ ,
  - isothermal  $\nabla T = 0$ .
- small disturbances  $q'$  of wavelength  $\left(\frac{2\pi}{k}\right)$  are superimposed to the base flow:  $q = \bar{q} + q'$ .
- quasi-homogeneous assumption over a limited domain:
  - $\frac{2\pi}{k} \ll \left| \frac{1}{\bar{q}} \right| \Rightarrow \nabla \bar{q} \approx \text{const.}$  and  $\bar{q} \approx \text{const.}$
- normal modes (i.e. eigenmodes of the Fourier transform):
  - $q' = \bar{q} e^{i(x \cdot k - \omega t)}$ ,  $\forall q' \in (\tau, u, P, T, c)$
- with:
  - $\mathbf{x} \equiv (x_{||}, x_{\perp}) \in \mathbb{R}^2$  the spatial coordinates,
  - $\mathbf{k} \equiv (k_{||}, k_{\perp}) \in \mathbb{R}^2$  the wavevector of norm  $k = \sqrt{k_{||}^2 + k_{\perp}^2}$ ,
  - $\omega \equiv \underbrace{\omega_r}_{\text{circular frequency}} + i \underbrace{\omega_i}_{\text{growth rate}} \in \mathbb{C}$ , where  $\omega_r = \Re(\omega)$  and  $\omega_i = \Im(\omega)$ .

Obtention of modes:

- derivation of  $(\forall M_t; \forall Pe_t)$  dispersion relation  $\Rightarrow$  degree 5 polynomial  $\Rightarrow$  5 roots  $\omega$

5 modes:

1 pair of acoustic modes:	1 pair of "oscillating" modes:	1 "non-oscillating" mode:
<ul style="list-style-type: none"> <li>stems from compressibility effects,</li> <li>filtered out in the <math>(M_t \ll 1)</math> limit.</li> </ul>	<ul style="list-style-type: none"> <li><math>\omega_r \neq 0</math>,</li> <li>if unstable, time-oscillations of the linear perturbation, amplified in an exponential envelope,</li> </ul>	<ul style="list-style-type: none"> <li><math>\omega_r = 0</math>,</li> <li>if unstable, pure exponential growth of the linear perturbation without oscillations.</li> </ul>

Marginal stability of the 5 modes:

- marginal stability of each mode  $m \in \{1, 5\}$  given by its neutrality hyper-surfaces  $\mathcal{N}_m$ :

$$\omega_i^m(p) = 0,$$

with:

- $p$  the set of parameters involved in the LSA,
- $\omega_i^m$  the growth rate of the root  $\omega^m$  corresponding to the mode  $m$ .

Stability of the flow for a given set of parameters  $p$ :

- stable if all modes are stable:  $\forall m, \omega_i^m(p) < 0$ ,
- unstable if at least one mode is unstable:  $\exists m, \omega_i^m(p) > 0$ ,
- marginally stable if:  $\max_{m \in \{1, 5\}} [\omega_i^m(p)] = 0$ .

Numerical resolution:

- with a non-dimensionalization, arbitrarily chosen,
- of the  $(\forall M_t; \forall Pe_t)$  dispersion relation.

Ledoux criterion:

- unstable in the  $(Pe_t \gg 1)$  limit if:

$$\nabla_s \cdot \frac{\nabla P}{\rho} > 0,$$

- unstable in the  $(Pe_t \ll 1)$  limit if:

$$\frac{\nabla r}{r} \cdot \frac{\nabla P}{\rho} > 0.$$

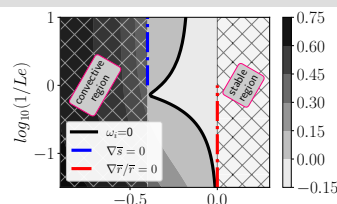


Figure: Map of stability in the  $[A_r, \log Le^{-1}]$  plane.

Dimensionless numbers:

$$A_r = \frac{M_b - M_a}{M} = \frac{\text{difference of molar masses}}{\text{sum of molar masses}},$$

$$Le^{-1} = \frac{D_c}{X_{\text{equi}}} = \frac{\text{scalar diffusion}}{\text{radiative conductivity}}.$$

$\Rightarrow$  intermediate zone can be investigated with the LSA.

Analytical expression for marginal stabilities, assuming  $(k = k_{\perp})$ :

$$\begin{aligned} & (\omega_i = 0, \omega_r \neq 0) \text{ in dispersion relation} \\ & \Rightarrow \mathcal{N}_{\text{Osc}} \text{ for the pair of "oscillating" modes,} \\ & (\omega_i = 0, \omega_r = 0) \text{ in dispersion relation} \\ & \Rightarrow \mathcal{N}_{\text{Non-osc}} \text{ for the "non-oscillating" mode:} \\ & \frac{\nabla \bar{P}}{\bar{P}} \cdot A_r \nabla \bar{c} (Le - \bar{\gamma}_3) + \frac{\nabla \bar{P}}{\bar{P}} \cdot \bar{\gamma} \nabla \bar{c} \\ & + (D_c k^2)^2 Sc \cdot Le \left[ 1 + \frac{\nabla \bar{P}}{\bar{P}} \cdot \frac{\bar{\gamma}}{k^2 \bar{c}^2} \frac{\nabla \bar{c}}{\bar{c}} \right] = 0. \end{aligned}$$

Parameters:

- $\bar{\gamma}_3$  a polytropic coefficient,
- $\bar{c}$  the speed of sound,
- $k$  the norm of the wavevector,
- $Sc$  the Schmidt number:  $Sc = \frac{\nu_v}{D_c} = \frac{\text{kinematic viscosity}}{\text{scalar diffusion}}$ .

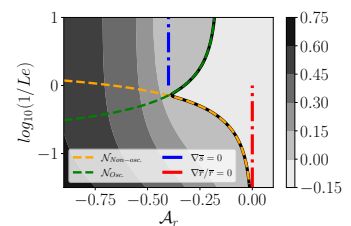


Figure: Map of stability in the  $[A_r, \log Le^{-1}]$  plane.

Dimensionless numbers:

$$A_r = \frac{M_b - M_a}{M} = \frac{\text{difference of molar masses}}{\text{sum of molar masses}},$$

$$Le^{-1} = \frac{D_c}{X_{\text{equi}}} = \frac{\text{scalar diffusion}}{\text{radiative conductivity}}.$$



## Analogy with the radiative turbulent RSM model

Implications for the turbulent RSM model:

- radiative conductivity effects studied,
- ⇒ use to improve the blending model of the GSG RSM model.
- ⇒ match the marginal stability of the LSA with the one given by the turbulence model.

Analogy between visco-diffusive coefficients:

- coefficients of systems: Navier-Stokes ↔ Turbulent GSG ,
- main analogy:

$$Le^{-1} \equiv \frac{D_r}{\chi^t} \leftrightarrow \frac{1}{\gamma} Pe_t \equiv \frac{\nu_t}{\chi^t} ,$$

with  $D_r$  the scalar diffusion,  $\chi^t$  the radiative diffusivity and  $\nu_t$  the turbulent diffusivity.

⇒ how to match marginal stabilities?



## Analogy between neutrality hyper-surfaces $\mathcal{N}_{Non-osc.}^0$ and $\mathcal{N}_{GSG}$

LSA ( $Le^{-1} \ll 1$ ) region ↔ ( $Pe_t \ll 1$ ) turbulent regime:

- flow stability dominated by the “non-oscillating” mode ( $\mathcal{N}_{Non-osc.}$  marginal limit),
- marginal stability in the ( $D_r k^2 \rightarrow 0$ ) limit:

$$\mathcal{N}_{Non-osc.}^0 : \frac{\nabla \bar{P}}{\bar{P}} \cdot (1 - \gamma_3 Le^{-1}) \frac{\nabla \bar{T}}{\bar{T}} + \frac{\nabla \bar{P}}{\bar{P}} \cdot (\gamma Le^{-1}) \nabla \bar{s} = 0 .$$

GSG marginal “fingering” stability of a RT flow:

- from the adapted turbulent model system, the stability criterion is:

$$\left[ \omega_{Pe_t} \frac{\nabla \bar{T}}{\bar{T}} + (1 - \omega_{Pe_t}) \left( \frac{\nabla \bar{T}}{\bar{T}} + \frac{\nabla \bar{P}}{\bar{P}} \right) \right] \cdot \frac{\nabla \bar{P}}{\bar{P}} > 0 \quad \text{with } \omega_{Pe_t} \in [0, 1] \text{ the weighting function,}$$

- marginal stability of the GSG model driven by an equivalent neutrality hyper-surface:

$$\mathcal{N}_{GSG} : \frac{\nabla \bar{P}}{\bar{P}} \cdot (\omega_{Pe_t}) \frac{\nabla \bar{T}}{\bar{T}} + \frac{\nabla \bar{P}}{\bar{P}} \cdot (1 - \omega_{Pe_t}) \nabla \bar{s} = 0 .$$



## Blending model “b” proposed from the LSA

Neutrality hyper-surfaces:

$$\begin{cases} \mathcal{N}_{Non-osc.}^0 : \frac{\nabla \bar{P}}{\bar{P}} \cdot (1 - \gamma_3 Le^{-1}) \frac{\nabla \bar{T}}{\bar{T}} + \frac{\nabla \bar{P}}{\bar{P}} \cdot (\gamma Le^{-1}) \nabla \bar{s} = 0 , \\ \mathcal{N}_{GSG} : \frac{\nabla \bar{P}}{\bar{P}} \cdot (\omega_{Pe_t}) \frac{\nabla \bar{T}}{\bar{T}} + \frac{\nabla \bar{P}}{\bar{P}} \cdot (1 - \omega_{Pe_t}) \nabla \bar{s} = 0 . \end{cases}$$

Blending “b”:

- keep the arbitrary form:  $\omega_{Pe_t} = \frac{Pe_t^{lim}}{Pe_t^{lim} + Pe_t}$ ,
- only impose  $Pe_t^{lim}$  so that it matches the stability curve in the ( $Pe_t \ll 1$ ) limit:  $Pe_t^{lim} \rightarrow 1$ ,
- ⇒  $\omega_{Pe_t}^b \equiv \frac{1}{1 + Pe_t}$ ,
- $\mathcal{N}_{GSG}^b$  joins smoothly the neutral curves ( $\nabla \bar{s} = 0$ ) and ( $\frac{\nabla \bar{T}}{\bar{T}} = 0$ ).

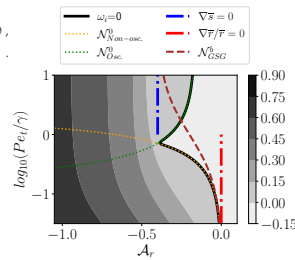


Figure: Map of stability in the  $[A_r, \log(\frac{Pe_t}{\tau})]$  plane.



## 1D-RANS simulations with the blending model “b”

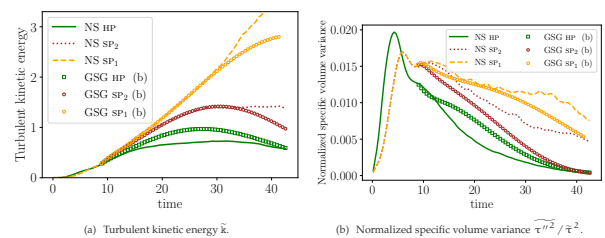


Figure: Time evolution of  $\tilde{k}$  and  $\tilde{\tau}^{\nu 2} / \tilde{\tau}^2$  at the initial position of the interface. Comparison between the 1D-RANS with the blending model “b” and the NS simulations.

- (HP, SP<sub>1</sub>, SP<sub>2</sub> “b”) ⇒ model blending “b” shows quite satisfactory agreement with NS,
- (HP, SP<sub>1</sub>, SP<sub>2</sub> “b”) ⇒ correct trends obtained from a physically sounded derivation.



## Table of contents

- Asymptotic analysis
- Adaptation of a RSM model
- Linear stability analysis
- Conclusion and perspectives



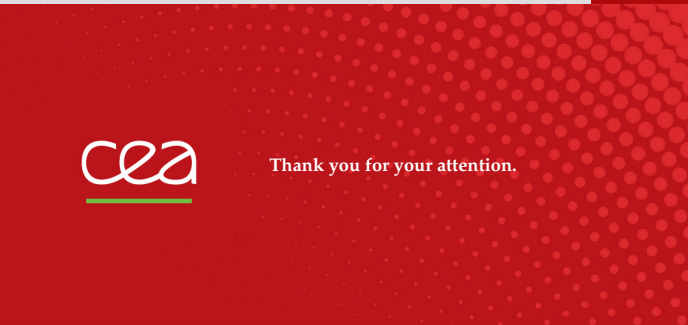
## Conclusion and perspectives

### Conclusion

- $Pe_t \equiv$  key parameter defining convective ( $Pe_t \gg 1$ ) and thermohaline ( $Pe_t \ll 1$ ) mixing.
- ( $Ma \ll 1, Pe_t \ll 1$ ) approximation with mixing and radiative effects was derived and validated:
  - prediction for P' and T' orders,
  - divu' asymptotic expression.
- a statistical RSM model (GSG) was adapted and validated in ( $Pe_t \gg 1$ ) and ( $Pe_t \ll 1$ ) regimes,
- linear stability of a radiative stratified binary mixture was studied:
  - role played by radiative diffusion was highlighted,
  - $Le \equiv$  key parameter defining the switch from “oscillating” to “non-oscillating” modes that drive the instability,
  - improvement of the blending model which deals with intermediate  $Pe_t$  regimes.

### Perspectives

- implementation of the new CSG model in an astrophysical code (or under a mixing length model),
- many multiphysical processes in stellar flows still not accounted for: nuclear reaction, shear, magnetism...



Thank you for your attention.



## Thesis defence speech

### Beginning of the presentation

My work regards **turbulence modelling of flow fields** that are **strongly coupled to radiation**.

#### Slide 1

Such regimes are found in **stellar interiors**, where **turbulence** is generated and maintained by a large amount of mechanisms. Among them, we may quote convection, double-diffusion instabilities or shear for instance. The development of these turbulent zones have a major impact on the internal **structure** and the **composition** of stars. Indeed, they entail, among others, the **transport** and the **mixing** of stellar isotopes, as well as a **strong radiative transfer**.

#### Slide 2

Regarding **radiation transfer**, its efficiency in the **transport of heat** competes with **turbulent convection**. These processes can be compared with the **turbulent Péclet number**. This non-dimensional number compares the characteristic timescale of heat transport **by radiation** to the one **by turbulence**. Thus, a small Péclet number indicates that **radiation is much more efficient** than **turbulence** at transporting heat, while a **large Péclet number** implies the contrary. On the right, I have represented these regimes during the **early phases** of evolution of a **massive star**. **High Péclet regimes** are displayed in green and **low Péclet ones** in orange. They are shown along the **Lagrangian mass** of the star with respect to the “model numbers”. These “model numbers” represent a **non-linear time scale** that adapts to the **pace** of stellar evolution. This example shows that turbulence is present in stars **within small and high Péclet regimes**. In order to highlight the **physical properties** of these two particular turbulent regimes, I propose to provide a **short example** based on a simple **stellar flow configuration**.

#### Slide 3

Let us consider a **small parcel a fluid** displacing radially from its **equilibrium position** and **in opposition** to the direction of the gravitational field. Before being displaced, the particle is considered to **have the same characteristics** as its environment. The initial state is considered in **hydrostatic equilibrium** so that the pressure **of the top fluid** is smaller than the pressure **of the bottom one**. Then, this displacement is assumed slow with respect to the speed of sound, which corresponds to an **acoustic equilibrium**. Hence, the pressure of the particle will **adjust instantaneously** to its environment. **However**, the particle density is **not necessarily equal** to the density of its **new environment**. Two specific situations may occur: in the first case, if the particle is **less dense** than its **surrounding**, it will **keep on rising** due to **buoyancy forces**. Then, the displacement of the particle is **amplified** and the stratification is said “**unstable**”. In the opposite case, the particle **may fall back** towards its **initial position**. Its displacement is **damped** and, hence, the stratification will be said “**stable**”. In order to determine the stability of the stratification **in the astrophysical context**, we will consider the **two asymptotic Péclet regimes**.

#### Slide 4

For simplicity, the transport of **species mass fraction** is neglected. If the **heat flux** is **negligible**, it corresponds to a **high Péclet situation**. The mass particle will then **undergo an adiabatic adjustment** of its pressure. By comparing the **density** of the particle to the one of its **new environment**, a **stability condition** for the **stratification** is obtained. It relies on the **pressure partial derivative** with respect to the **density**, **compared** to its **adiabatic analog**. In the **small Péclet case**, the **heat flux** is **so high** that it implies **thermal equilibrium**. It means that the temperature of the particle **adjusts instantaneously** to its environment. And if **no changes** of composition

are considered within this mass particle, the stability of the stratification will depend on **the gradient of mean molecular weight**, equivalent to an **effective molar mass gradient**.

### Slide 5

Both of these conditions can be rewritten in terms of a **pseudo-entropy gradient** times a **pressure gradient** for stellar **standard** convective regions and in terms of a **molar mass gradient** times a **pressure gradient** for small Péclet turbulent zones. These relations are known in the astrophysical formalism as the **Ledoux criterion**. Moreover, in the stellar context, small Péclet regimes characterize a **double-diffusion process** called **thermohaline mixing**. As just explained, it stems from a **destabilizing mean molecular weight** supplemented by a **stabilizing temperature gradient**.

### Slide 6

To summarize this introduction, we have seen that **standard convective** and **thermohaline turbulent regions** are characterized by **opposite asymptotic orders** of Péclet numbers. In the first case, turbulence prevails over radiation in the transport of heat. And in the second case, this is the contrary. However, both zones share a **small Mach number** and a **large Reynolds number**. One last property may be quoted. For **massive stars**, the contribution of **radiative pressure** with respect to its material counterpart is **not negligible**.

### Slide 7

The main purpose of my work consists in **deriving** and **validating** a **turbulent statistical model** that describes stellar interiors and that **accounts** for **mixing** and **radiation** effects, so that **high and small Péclet compressible stellar flows** can be **captured accurately**. For the **sake of simplicity**, we will focus on **modelling turbulence** generated by **convective** and **double-diffusive instabilities**. Other effects, such as shear for example, should be included to describe a realistic stellar interior. This presentation articulates as follow: - first, a **small Mach-small Péclet** asymptotic analysis is derived and validated so that a simplified approximation of the real flow can be formulated. - second, we will focus on a particular turbulent model, available at the CEA. This is a **small-Mach** Reynolds Stress Model, compatible with the **high Péclet regime**. It will be adapted to the limit of **infinitely small Péclet numbers**. - it follows the **validation** of this model for **"all-Péclet" asymptotic regimes**. - at last, we will study the **linear stability** of a **stratified equilibrium** of a **binary mixture** submitted to a **gravitational field**. Some of the results of this **stability analysis** will be used in order to improve the **model blending** proposed in our **"all Péclet"** turbulent RSM model.

### Slide 8

Let us start with the **core of this thesis**, that-is-to say the description of the **asymptotic analysis** in the limit of **infinitely small turbulent Mach** and **turbulent Péclet** numbers.

### Slide 9

On the one hand, **small Mach approximations** allow to consider **all acoustical phenomena** to equilibrate instantaneously with their environment. On the other hand, **small Péclet approximations** allow the assumption of **temperature fluctuations** equilibrating instantaneously with their environment. It results in a **thermal equilibrium** of the field due to **radiative diffusion**. Besides, **small Péclet analyses** are usually derived jointly with their small Mach counterpart, that they **complete** and **modify**. However, **none** of the current studies present in literature accounts for the **presence of mixing** or **nuclear reactions effects**. In this way, the capture of **double-diffusion instabilities** such as the **thermohaline convection** seems compromised.

Besides, these studies consider generally the **radiative pressure** to be **negligible** with respect to **its material counterpart**. Their applications may then not apply to **massive stars**. In the end, **non-ideal equations of state** may be used in stellar interiors. Hence, the purpose is to **derive** and **validate** a small Mach-small Péclet approximation involving the previous effects and adapted for the interiors of massive stars. Although the approximation derived in the manuscript treats these four points, we will only restrain ourselves to the two first ones in this presentation.

#### Slide 10

The starting point of this analysis is the **governing hydro-radiative system**, which is defined by the **Navier-Stokes usual set of conservation laws**, coupled with **radiation**, treated in the **diffusion limit**. Note that they are here expressed in the cartesian frame. Along with the **mass**, **momentum** and **material energy** conservations, an advection-diffusion equation for the concentration and a radiative energy equation are added to the system. From there, the superscripts “m” and “r” will refer respectively to the **material** and the **radiative quantities**. The **extensive variables** such as the **pressure** and the **total specific energy** are defined as the sum of their matter and radiative parts. The **radiative energy** and **pressure** are expressed in terms of the temperature **raised to the power of four** and proportional to the radiation constant. For the sake of simplicity, we will consider the case of a **radiative mixture of ideal gases**, considered itself as an **ideal gas**, and submitted to an **homogeneous gravity**.

#### Slide 11

Along with the **viscous terms** appearing in the **momentum** and the **material energy equation**, the molecular terms involve also **scalar diffusive terms**. More precisely, the **scalar flux of species concentration** is defined as a **Fickian approximation**. The latter arises also in the **enthalpy mixing term** of the **material energy equation**. Besides, as for the **material thermal flux**, the **radiative flux** takes also the form of a **Fourier law**. Its corresponding **radiative conductivity** depends on the **temperature**, the **opacity**, and in a lesser extent, on the **density**.

#### Slide 12

Since the small-Mach and the small-Péclet effects deal with the **physical properties** of the **turbulent velocity**, **pressure** and **temperature**, this approximation will focus on their evolutions. Each quantity of these equations are then **split** into a **background component** and a **deviation** from this background. The **turbulence modelling context** of this work entails to consider the background quantities as **statistical ensemble means**, and their deviations as their **corresponding fluctuations**. Then, the **fluctuating velocity, pressure and temperature evolution equations** are rendered **dimensionless** with the use of characteristic scales, which are chosen **relevant for stellar flows**. From there, the **main conditions** defining the behaviour of the field are: - the turbulent Mach number, **being small**, - and the turbulent Péclet number, **being of the same order or even smaller**. We will also assume that the **Reynolds number is not small**, so that **viscous effects** have to be taken into account. All fluctuating quantities are then developed as **functions** of the Mach number and re-inserted into the evolution equations of **these fluctuations**.

#### Slide 13

Once the asymptotic analysis is derived, **two main results** are obtained in a **dimensional form**. **First**, the **predictions** for the orders of magnitude of the **fluctuating pressure and temperature** are derived. As in usual small Mach approximations, the pressure fluctuations are of the order of the **Mach squared**. Furthermore, we observe that the order of temperature fluctuations has an **explicit dependancy** on the Péclet number. **Second**, the **asymptotic expression** of the **fluc-**

tuating velocity divergence is derived. It stems from both **pressure and thermal equilibria**. Moreover, it can be split into **two contributions**. The first term is related to the **mean stratification**. It expresses the **volume adjustment** of a flow particle moving along a **pressure and temperature gradient**. The second term is related to **mixing** and shows that the volume of this mass element **may** also be modified by **the molecular diffusion of species**. This asymptotic expression can be compared to **another one**, derived in the high Péclet limit.

### Slide 14

As we can see, the adjustment **related to the mean stratification** is not the same in both cases because, here, **in the high Péclet situation**, the volume of the flow particle adjusts to a **total pressure gradient**. Besides, this difference between large and small Péclet asymptotic expressions have important **repercussions** on the **stability criterion** of the mean stratification.

### Slide 15

In order to illustrate this statement, we can study the **linear inviscid stability** of a stratified radiative flow that satisfies **hydrostatic equilibrium**. For this purpose, we insert the asymptotic expressions of the **divergence term in blue** in the **linearized equation** for the **fluctuating density**. Then, by using the **fluctuating velocity equation** and reinserting the previous results, we obtain that the **stability of the stratification** depends on **the sign of the pseudo-entropy gradient in the high Péclet limit**, and it depends on **the molar mass gradient in the small Péclet situation**. These criteria are equivalent to the **Ledoux criterion** shown in the beginning of the presentation. As a result, it **puts forward the role played by the Péclet number** in the **characterization of stellar turbulent mixing zones**.

### Slide 16

All of these results **need now to be verified**. To this aim, we study the **development of a turbulent mixing zone** induced by a **radiative Rayleigh-Taylor instability**. Hence, we consider two ideal gases, initially separated by an interface. We can see that the **heavier fluid of greater molar mass** falls over the **lighter one** under the **effect of gravity**. The mean state is chosen at **hydrostatic equilibrium** and with an **imposed isothermal condition**. Although this configuration **does not occur** in stellar interiors, it **combines the elementary mechanisms at work** in such media. Furthermore, the field is characterized by **three dimensionless numbers**. The **contrast of molar masses** is defined by the Atwood number, which is **not small**. As for the **contributions of the radiative field**, they are assessed with respect to the **Mihalas number  $R$**  and the **Boltzmann number  $Bo$** . The first one defines the **rate of material to radiative energy**, and shows that the **matter pressure and energy** prevail over the **radiative ones**. The second one defines **the ratio of the material enthalpy to the radiative flux**: thus, the latter **overwhelms the enthalpy one**. We can note that such conditions can be met in the **interiors of massive stars**, where the radiative pressure is **not negligible** with respect to its material equivalent. Three **Numerical Simulations** are then performed with the **compressible Navier-Stokes code TRICLADE**, in which radiation has been **implemented**. The three simulations differ only from the value of the **opacity**, treated as a constant in the code, and hence, **from the value of the radiative conductivity**. This leads to **two small Prandtl simulations SP1 and SP2**, as well as a **high Prandtl one** named HP. These numerical parameters are chosen in order to reach **certain orders of Péclet number at the center of the mixing zone**. While **the first and the last simulations** are meant to show the **discrepancies** of the behaviour of the flow field between **both asymptotic regimes**, the **intermediate small Péclet simulation** aims to **test the limits** of the approximation.

**Slide 17**

In this video (see Fig. C.6), the **small and the large Péclet simulations** are displayed respectively at the top and at the bottom. More precisely, they represent a slice containing the gravity vector directed from right to left, and displaying the **shadowgraphy**, the **pseudo-entropy** and the **temperature fields**. Each of these quantities **share the same color scales**, except for the temperature one in the small Péclet situation, **which has been reduced**. The ombroscopy computes roughly the **transverse Laplacian of density**, which is representative of the **density fluctuations**. The latter seems to **stabilize** after a certain amount of time **in the high Péclet situation** and the **density variance** seems to **keep evolving** in the **opposite limit**. The evolution of the **pseudo-entropy gradient** appears to become **statistically bounded in the high Péclet limit** whereas its gradient looks **statistically growing** in the other case, and without reaching any form of equilibrium. Finally, the contrast of temperature is **more pronounced** in the high-Péclet simulation. As for the small-Péclet situation, as expected, the large heat flux **smoothes out** the fluctuations of temperature. To summarize, the behaviour of the turbulent mixing zone has shown to meet **strong discrepancies** when the Péclet number reaches **infinitely small values**. This work aims then to **shed light** on the **physical properties** of such **turbulent field**.

**Slide 18**

By noticing that the problem is **statistically mono-dimensional**, we proceed to compute **statistical averages** along the x-axis by **integration** over the **transverse homogeneous directions**.

**Slide 19**

The turbulent Mach, Péclet and Reynolds numbers are displayed **at the center of the mixing zone** for the three “Prandtl” simulations with respect to a **dimensionless time**. On the left, the Mach number remains always under the value of 0.14 **for each numerical simulation** which is one of the desired condition. On the right, the flow **becomes turbulent at approximately the time 15** where **large Reynolds numbers** are observed. The Péclet number reaches the value of **10 to the power 2** for the **High Prandtl simulation**. It tends to **10 to the minus 2** and to **10 to the minus 1** for respectively SP1 and SP2. Hence, each of these configurations have reached **the expected Péclet order desired**. Indeed, while the condition of the asymptotic analysis is verified **for SP1**, HP evolves **in the opposite regime**. As for SP2, its Péclet number tends **well** towards **intermediate small values**.

**Slide 20**

Regarding the predictions of the fluctuating state variables, **two ratios** involving the orders of pressure and temperature fluctuations are displayed again **at the initial position of the interface**. **First**, the fluctuations of pressure tends towards the **squared Mach number** in each simulation, which is consistent with the **usual results** of small Mach approximations, and this, **whatever the value of the Péclet number is**. **Second**, the temperature ratio tends towards 1 **for both small Prandtl numerical simulations** which verifies the prediction of **the asymptotic analysis**, even in **intermediate regimes**. However, this ratio **drops fastly to naught** in the High Prandtl case. There is indeed **no condition** related to the **high Péclet analysis** in usual small-Mach approximations.

**Slide 21**

We now pass to the validation of the predictive asymptotic expression of the **divergence term**, derived in the small-Péclet approximation. To do so, we proceed to **extract 2 dimensional fields**, defined as the **slices** in the **plane orthogonal to the interface** and containing the gravity vector,

as shown here. On the left, we have computed the exact value of the divergence term which is obtained by **differentiation of the fluctuating velocity**. On the right, we have **calculated the asymptotic prediction** derived in the analysis. Since the color scales are the same in both figures, we can argue that the **turbulent structures and levels seem to be well captured** by the asymptotic values. The **only discrepancies** observed stem from **some localized extrema** which seem to be **filtered out** by the small-Mach small-Péclet formula.

### Slide 22

After this qualitative validation, a **quantitative verification** is proposed with the use of computed correlations, which are **related to the divergence term**. Just as the divergence term, these correlations **can be split into two contributions**, related to the mean stratification and to molecular diffusion. As illustrated here, they are extracted along the **whole inhomogeneous axis** of the flow field.

### Slide 23

A good agreement between the **intermediate small Prandtl simulation** (in brown) and the **small Péclet prediction** (in orange) of **both correlations** is observed. As for the **contributions related to the stratification** (in blue) and **to molecular diffusion** (in magenta), they have **opposite signs** in each case. Hence, referring to the current configuration we have chosen, this can be associated to the **mechanisms of the instability**. Indeed, if we look at the left side for instance, the **baroclinic production related to the mean stratification** tends to **increase the density variance**, whereas **molecular mixing tends to dissipate it**. As a result, both contributions can be respectively interpreted as a **production** and a **destruction term** in the context of **turbulence modelling**.

### Slide 24

Now that the approach has been validated, we can proceed to the **adaptation** of the **RSM turbulent model**.

### Slide 25

One of the outcomes of **small-Mach approximations** regard a **peculiar constraint** imposed to the fluctuating velocity divergence. The derived expression may allow to characterize **some compressibility effects** and may be used in order to derive **some closures** for the evolution equations **of the density variance** and **of the mass flux**. If these equations are supplemented by equations **for the Reynolds Stresses** and **for the kinetic energy dissipation**, they define the basis of a **class of RSM turbulent models**. Then, referring to our current framework, flows combining **small Mach, small Péclet and high Reynolds numbers** are rarely, if not ever, **seen in engineering applications**. However, they are often observed in **stellar interiors** where most efforts regarding turbulence modelling regard **calibrated Prandtl's models** based on the mixing length theory. We can nonetheless quote a notable exception of **RSM iso-volume model**, which has been derived by **Canuto** and that involves **an explicit dependancy** on the Péclet number. From now on, we will focus on an **existing RSM**, available at the CEA and known as **the GSG model**. The objective will be then to adapt this GSG model, **originally conceived for the treatment of compressible gaseous mixtures**, to the **small Péclet limit**.

### Slide 26

The purpose of this part is to derive **closures** for production terms in the evolutions of **the specific volume flux and variance**, where the **correlations implying the divergence term** appear, as shown here in blue. This GSG model has been derived **from a stochastic Langevin model**

that **closes the evolutions** of the fluctuating **velocity** and **specific volume**. By writing the **mass conservation equation**, we notice that the **only unknown** is the **divergence term** (appearing here in blue). The first step to derive these closures is then to **insert** the asymptotic expressions of the divergence term, respectively stemming from the **small Mach approximation** and from the **current small Mach-small Péclet asymptotic analysis**, into this continuity equation.

**Slide 27**

The evolution of the **fluctuating specific volume** is then obtained in **both Péclet asymptotic limits**, provided that **third order correlations linked to tau second** are neglected. Here, **molecular diffusion terms** are closed using a **Langevin model**. Hence, they are interpreted as a **dissipation term** acting on the **variance of tau second**. Besides, we will assume that **their modelization** in both Péclet regimes is identical. Then, the main difference between both cases comes from **the way the relative specific volume reacts to the mean stratification**: - in the high Péclet limit, it varies when the **pseudo-entropy gradient** is different from naught, - and in the small Péclet limit, it varies when **it is the molar mass gradient** that is different from zero. This difference has been **previously proven** to be **responsible** for the **modification of the stability criterion** of a mean stratification. From there, the second step consists in **blending the range between both asymptotic Péclet regimes**.

**Slide 28**

To this aim, we choose to introduce a **weighted function of a simple form**, with a calibrated parameter (**noted Péclet limit**) such that the **specific volume evolution equation** takes a more general form. The main modification stems from the **terms related to the stratification**. They are interpreted as a **convex combination** between the **molar mass gradient** and the **pseudo-entropy gradient**. As a result, when the Péclet number tends towards **an asymptotic value**, the evolution of **tau second** follows the **rightful Péclet equation**. And when the Péclet number has an **intermediate value**, the calibrated parameter **control** the **transition** between asymptotic regimes. The third step to derive the **desired closures** is then to **multiply this equation** by  $u$  second and  $\tau$  second, and then to take their averages. These RSM closures can then be derived in the **specific volume flux** and **variance equations**, as shown here. What remains now is the **validation of the turbulent model for any Péclet regime**.

**Slide 29**

To do so, the three previous **numerical simulations** are compared to the **mono-dimensional RANS simulations**, run with the **modified GSG** model. While the Small and High Prandtl simulations are meant to **compare the behaviour between the flow fields**, the intermediate Prandtl simulation is used to **calibrate the parameter Péclet limit** of the blending function. In this context, the **spatial profiles of the pseudo-entropy** and of the **concentration** of HP and SP1, are represented with respect to the x-axis. As a recall, **both fields are initially stably stratified** at both sides of an **unstable interface**. In the high Péclet situation, the **stability criterion** depends on the **sign of pseudo-entropy gradient**. At late times, the flow tends **towards a marginal stability** where we can observe an **isentropic threshold around the interface**. This corresponds to a **stabilization of the stratification**. In the small Péclet limit, the stability criterion depends on the **sign of molar mass gradient**. Hence, because of the form of the concentration profile, the field **cannot reach an equilibrium**, and thus, the **pseudo-entropy gradient keeps growing**. This case corresponds to a **permanent increase of the turbulent mixing zone**.

### Slide 30

In this frame, the **turbulent kinetic energy** and the **normalized specific volume variance** of **Navier-Stokes** and **RANS** simulations are **extracted** at the center of the mixing zone **with respect to a dimensionless time**. Globally, the **extended turbulent GSG model** follows the **main trends** observed in Navier-Stokes simulations. This proves that this RANS model seems to be able to **capture the differences of flow behaviours** in both Péclet regimes. In the large Péclet limit, the **kinetic energy** decreases during the **last third of the simulation**. This is due to the fact that the **pseudo-entropy profile** approaches its **neutral value** inside the **turbulent mixing zone**. Indeed, the instability mechanism **stops feeding** the turbulent mixing zone whereas **viscosity** still **dissipates the kinetic energy**. In opposition, the latter **keeps growing** in the small Péclet limit and **endlessly transfers energy to the turbulent field**. Besides, the **higher levels of density variance** observed in the previous video for this small Péclet case seems to be accurately **reproduced by the model**. As a result, despite the fact that the adaptation of the GSG model affects **only a limited part** of the turbulent system, we can argue that **significant discrepancies** are still **accurately captured** in both asymptotic limits. Furthermore, the **intermediate Péclet RANS simulation** follows **quite satisfying trends** with the **calibrated blending**.

### Slide 31

We now pass to the last part of this presentation and focus on the **linear stability** of the radiative flow field.

### Slide 32

This study regards a **binary mixture of ideal gases** based on the **radiative Rayleigh-Taylor configuration already described previously**. The motivations concern two points. **First**, the current local criterion that have been derived for the stability of the stratification is **inviscid** and hence, it does not account for **visco-diffusive transport coefficients**. We wish then to predict the stability of the field with respect to **viscous** and **diffusive effects**, and in particular, with respect to **radiative conductivity**. **Second**, since the current blending has been calibrated with respect to **phenomenological considerations**, we wish to propose another blending that stems, this time, from **physical groundings**. The method that we propose here is to **match the stability conditions**, derived in the LSA, with its equivalent ones, **derived from the turbulent system**.

### Slide 33

The linear analysis lies on the **same set of governing equations** introduced earlier and which is followed by the base flow. We assume the **binary flow** to **initially respect an hydrostatic equilibrium** and **having an imposed isothermal condition**. Then, the **wavelengths of the linear perturbations**, which are superimposed to the basic flow, are considered to be **much smaller** than any other **gradient length scale**. It leads to an **homogeneous approach** where **basic quantities** and **their gradients** can be considered constant with respect to **any other perturbation** inserted into the system. We seek **normal modes** in the form of **plane waves** where the **complex frequency  $\omega$**  can be split into a real part corresponding to the **circular frequency** and into an imaginary part, defining the **growth rate of the perturbation**.

### Slide 34

From there, the derivation of the general dispersion relation is obtained by taking the **determinant of the Fourier-transformed linear system**. This “all-Mach” and “all-Péclet” dispersion relation gives a **polynomial of degree 5** and hence, its 5 roots lead to the derivation of **5 modes**. We have a **pair of acoustic modes**, which stem from compressibility effects, and which can be

filtered out in the small-Mach regime. We have a pair of **oscillating modes**, which, **when unstable**, correspond to the **exponential amplification of the linear perturbation**, that oscillates with respect to time. And finally, we have **1 non-oscillating mode**, which, **when unstable**, correspond also to the **exponential amplification of the perturbation**, but **without** oscillating.

**Slide 35**

The **marginal stability of each of the 5 modes** is given by the fact that their **growth rate is equal to zero**. As shown here, this **neutrality hyper-surface** is obtained for the whole set of parameters involved in the analysis. It defines the limit between **the stable and the unstable region**. Accordingly, the **whole stability** of the flow field depends on the stability of the 5 modes. In the first case, if **all of them** are stable, **then** the flow is stable. In the second case, if at least **one of them** is unstable, **then** the flow becomes unstable. Hence, the **marginal stability** of the field is obtained when the **maximum of all growth rates** is equal to zero.

**Slide 36**

From there, we can compute numerically a **stability map** by choosing arbitrarily a **set of non-dimensionalization parameters**. This Atwood number defines the contrast of specific ideal constants, or an equivalent opposite Atwood number related to the **contrast of molar masses**. It represents one of the axis of the stability map along with the **inverse Lewis number** that characterizes the rate of **scalar diffusion to radiative diffusivity**. Hence, if we look at the color bar of the stability map, the **marginal stability curve** is seen to **separate the unstable zone** (*here*, on the left) and the **stable one** (*here*, on the right). If we consider an **horizontal displacement**, **when the Atwood number increases**, the **contrast of molar masses** decreases and then, after reaching a contrast of zero, the field **becomes stable**, whatever the other conditions are. In the opposite direction, as showed by the iso-values, the flow **becomes more and more unstable**. Hence, in our current configuration, the **stratification is unstable**, on the left, and **stable**, on the right. If we consider now a **vertical displacement**, the rate of **scalar diffusion to radiative diffusivity** decreases with the increase of the **inverse Lewis number**. Moreover, we can represent the **inviscid stability conditions** derived in the small Mach-small Péclet asymptotic analysis. We notice that the **convectively stable and unstable regions** from the Ledoux criterion match those of the LSA. Besides, the limits of these regions correspond exactly to the **zero gradients of pseudo-entropy** and of **molar mass** as defined by the boundaries of these inequalities. What remains is the investigation of the stability of the field **in the intermediate zone**.

**Slide 37**

From the general dispersion relation, we can derive **neutrality hyper surfaces** corresponding to **marginal stabilities in the limits of purely oscillating or purely non-oscillating transverse modes**. We assume that **the first unstable mode is always the transverse one**. An example is shown **for the non-oscillating mode** here. Each of these curves follows **continuous evolutions** and matches accurately the **marginal stability branches** defined with respect to the whole flow in the intermediate zone. While the pair of oscillating modes **dominates** the field **in the high inverse Lewis numbers regime**, the non-oscillating mode **dominates** in the **weak ones**. Hence, the marginal stability of the flow follows **different trends** in the limit **where radiative conduction is high** and **where it is low**, with respect to scalar diffusion.

**Slide 38**

Since the **efficiency of radiative conductivity** has been highlighted in the previous stability criteria, we can use this results to **improve the fitted blending model used in the turbulent model**.

The idea is then to **match the marginal stability condition of the LSA with the one derived from the RANS system**. To do so, we proceed to perform an **analogy** between **visco-diffusive coefficients** of each set of equations. The main consequence is that **the inverse Lewis number** can be directly **associated** to the **turbulent Péclet number**. Under our conditions, these **two dimensionless numbers** are then considered to follow **analog behaviours** with respect to their own governing system.

### Slide 39

As a result, in the context of **turbulence modelling**, the LSA has shown that the **flow stability** is **dominated** by the “non-oscillating” mode **in the small Péclet limit**. By taking a **convenient limit** of the neutrality hypersurface, so that it can be used in a **turbulence context**, we obtain a condition **for marginal stability**. From the GSG model, the **stability criterion** depends on the **blending function omega** and is recalled here **for each asymptotic Péclet regime**. Hence the **marginal limit** of this condition **takes a simple form** that can be compared to the other one.

### Slide 40

These expressions are recalled here. A blending model “b” is proposed such that **this neutrality hypersurface** is interpreted as a **convex combination** between **molar mass** and **pseudo-entropy gradients**. Hence, this drives **the stability of the field** with respect to the **asymptotic Péclet regime considered**. We impose this blending to match the stability curve in **ONLY** the small Péclet limit. Hence, as shown on the stability map, **the corresponding neutrality hyper-surface** joins smoothly both asymptotic Péclet limits.

### Slide 41

The temporal evolutions of **the turbulent kinetic energy and density variance** are shown once again **for the three previous Navier-Stokes simulations**, and then compared **to the new GSG simulations run with this blending “b”**. Although the asymptotic RANS simulations do not seem affected by the blending, we can see that, **while some improvements can still be carried out**, a quite satisfactory agreement is obtained for SP2.

### Slide 42

To summarize this presentation,

### Slide 43

We have seen that the Péclet number **is a key parameter** allowing to characterize **turbulent standard convective zones** and **thermohaline regions, in stellar interiors**. An approximation of stellar flows has been **derived** and **validated** in the limit of **infinitely small Péclet numbers**. The main outcomes **have regarded** an estimation for the orders of **pressure and temperature fluctuations**, as well as an asymptotic expression for the fluctuating velocity divergence, which involves **mixing** and **radiative effects**. We have then used this term **to adapt a turbulent RANS model to the small Péclet regime**, and we have **validated it** for **all asymptotic Péclet limits**. Finally, we have performed a stability analysis of a **radiative mixture** which **highlighted the role of the Lewis number** in the **identification of unstable flows** with respect to the intensity of radiative diffusivity. The marginal stability condition derived from the LSA has allowed to improve the blending of the GSG model, which is **now based on a sound reasoning**. Hence, this modified RANS model can be directly used **in an astrophysical code** and even put **under the form of a Prandtl’s model**. In the future, this work may be extended to a **more accurate study of the stellar plasma**. The latter may involve many other **physical effects** such as ionization processes or nuclear reactions for instance.

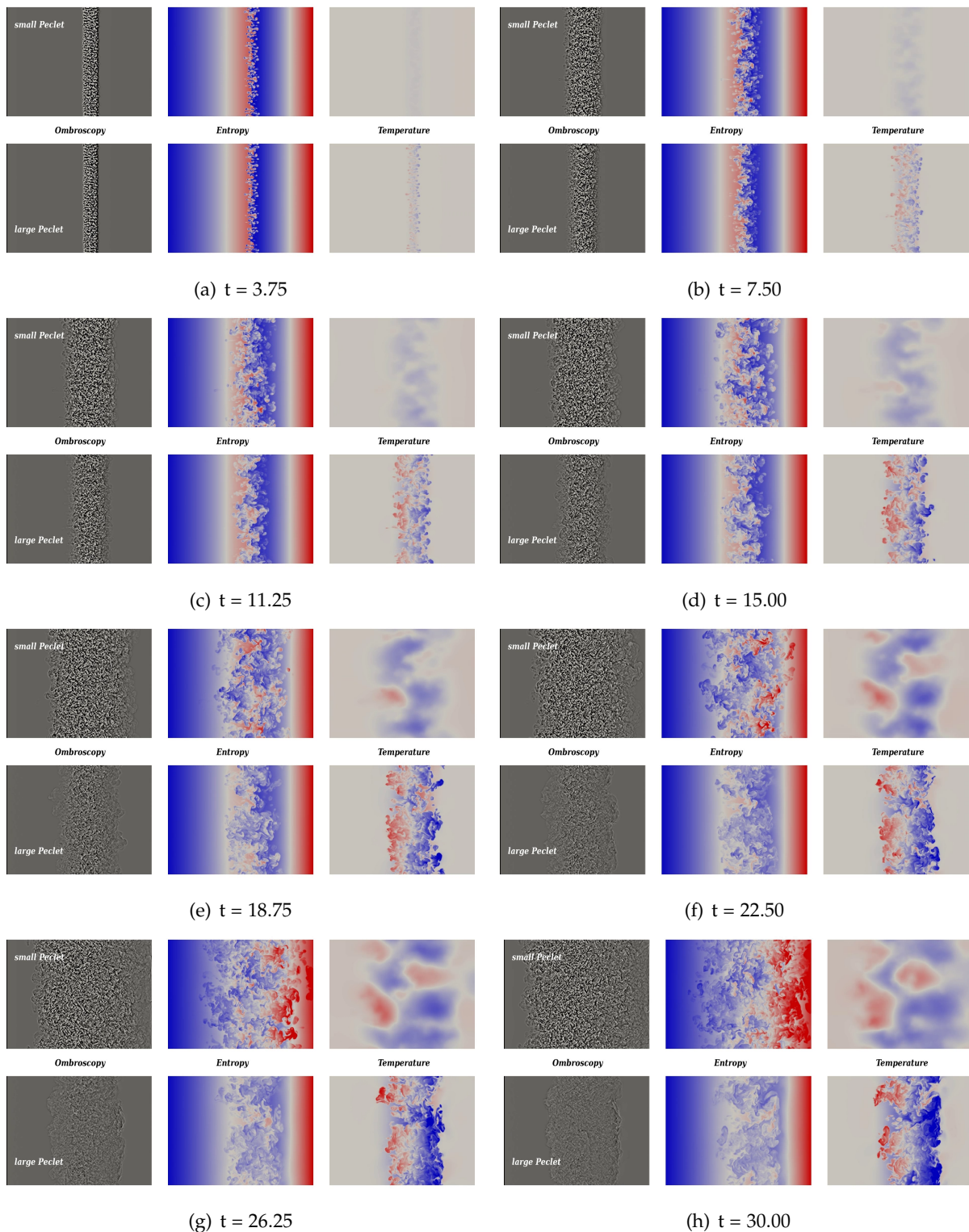


Figure C.6 – Screenshots of the video ([slide 17](#)) displaying the ( $Pe_t \ll 1$ ) (top) and the ( $Pe_t \gg 1$ ) (bottom) simulations at dimensionless times. Slices containing the gravity vector directed from right to left, and displaying the ombroscopy, the pseudo-entropy and the temperature fields. Each quantity shares the same color scale, except for the temperature one in the ( $Pe_t \ll 1$ ) situation that has been reduced.

End of the presentation



# Bibliography

- Almgren, A., Bell, J., Nonaka, A. & Zingale, M., *Low Mach number modeling of type Ia supernovae. III. reactions*, The Astrophysical Journal, vol. 684, 1: 449 (2008) [38](#)
- Almgren, A. S., Bell, J. B., Rendleman, C. A. & Zingale, M., *Low Mach number modeling of type Ia supernovae. I. Hydrodynamics*, The Astrophysical Journal, vol. 637, 2: 922 (2006a) [38](#)
- Almgren, A. S., Bell, J. B., Rendleman, C. A. & Zingale, M., *Low Mach number modeling of type Ia supernovae. II. energy evolution*, The Astrophysical Journal, vol. 649, 2: 927 (2006b) [38](#)
- Arnault, P., *Modeling viscosity and diffusion of plasma for pure elements and multicomponent mixtures from weakly to strongly coupled regimes*, High Energy Density Physics, vol. 9, 4: 711 (2013) [33](#), [154](#)
- Asplund, M., Grevesse, N., Sauval, A. J. & Scott, P., *The chemical composition of the Sun*, Annual Review of Astronomy and Astrophysics, vol. 47 [5](#), [14](#), [29](#), [153](#)
- Bailly, P., Champion, M. & Garréton, D., *Counter-gradient diffusion in a confined turbulent premixed flame*, Physics of Fluids, vol. 9, 3: 766 (1997) [83](#)
- Baines, P. & Gill, A., *On thermohaline convection with linear gradients*, Journal of Fluid Mechanics, vol. 37, 2: 289 (1969) [28](#)
- Besnard, D., Haas, J. & Rauenzahn, R., *Statistical modeling of shock-interface interaction*, Physica D: Nonlinear Phenomena, vol. 37, 1-3: 227 (1989) [28](#), [80](#), [152](#)
- Biermann, L., *Untersuchungen über den inneren Aufbau der Sterne. IV. Konvektionszonen im Innern der Sterne.*(Veröffentlichungen der Universitäts-Sternwarte Göttingen, Nr. 27.) Mit 5 Abbildungen., Zeitschrift für Astrophysik, vol. 5: 117 (1932) [xiv](#), [24](#)
- Böhm-Vitense, E., *Die Wasserstoffkonvektionszone der Sonne (The hydrogen convection zone of the Sun)*, Z. Ap, vol. 32: 135 (1953) [xiv](#), [24](#)
- Böhm-Vitense, E., *Über die wasserstoffkonvektionszone in sternern verschiedener effektivetemperaturen und leuchtkrafte*, Z. Astrophys, vol. 46: 108 (1958) [xiv](#), [24](#)

## Bibliography

---

- Botta, N., Klein, R. & Almgren, A., *Asymptotic analysis of a dry atmosphere*, ENUMATH, Jyväskylä, Finland [xiv](#), [38](#)
- Brown, J. M., Garaud, P. & Stellmach, S., *Chemical transport and spontaneous layer formation in fingering convection in astrophysics*, *The Astrophysical Journal*, vol. 768, 1: 34 (2013) [27](#), [28](#), [33](#), [154](#)
- Browning, M. K., Brun, A. S. & Toomre, J., *Simulations of core convection in rotating A-type stars: differential rotation and overshooting*, *The Astrophysical Journal*, vol. 601, 1: 512 (2004) [80](#)
- C. Caso, e. a., *Review of particle physics* (1998) [5](#), [12](#)
- Canuto, V., *Turbulent convection: old and new models*, *The Astrophysical Journal*, vol. 467: 385 (1996) [26](#), [80](#)
- Canuto, V., *Stellar mixing-I. Formalism*, *Astronomy & Astrophysics*, vol. 528: A76 (2011a) [xiv](#), [28](#), [80](#), [146](#), [147](#), [150](#), [152](#), [174](#), [175](#)
- Canuto, V., *Stellar mixing-III. The case of a passive tracer*, *Astronomy & Astrophysics*, vol. 528: A78 (2011b) [28](#), [152](#)
- Canuto, V., *Stellar Mixing-IV. The angular momentum problem*, *Astronomy & Astrophysics*, vol. 528: A79 (2011c) [28](#), [152](#)
- Canuto, V., *Stellar mixing-V. Overshooting*, *Astronomy & Astrophysics*, vol. 528: A80 (2011d) [28](#), [152](#)
- Canuto, V. & Mazzitelli, I., *Stellar turbulent convection: a new model and applications*, *The Astrophysical Journal*, vol. 370: 295 (1991) [26](#), [80](#)
- Canuto, V. & Mazzitelli, I., *Further improvements of a new model for turbulent convection in stars*, *The Astrophysical Journal*, vol. 389: 724 (1992) [26](#), [80](#)
- Canuto, V. M., *Stellar mixing - II. Double diffusion processes*, *A&A*, vol. 528: A77 (2011e) [xiv](#), [28](#), [146](#), [150](#), [152](#), [174](#)
- Chandrasekhar, S., *An introduction to the study of stellar structure*, vol. 2, Courier Corporation (1957) [16](#), [42](#), [178](#), [191](#)
- Chandrasekhar, S., *Principles of stellar dynamics*, psd [xiii](#), [16](#), [19](#), [149](#)
- Charbonnel, C. & Zahn, J.-P., *Thermohaline mixing: a physical mechanism governing the photospheric composition of low-mass giants*, *Astronomy & Astrophysics*, vol. 467, 1: L15 (2007) [xiii](#), [26](#), [149](#)
- Chassaing, P., *The modeling of variable density turbulent flows. A review of first-order closure schemes*, *Flow, turbulence and combustion*, vol. 66, 4: 293 (2001) [83](#)
- Choi, J., Dotter, A., Conroy, C., Cantiello, M., Paxton, B. & Johnson, B. D., *Mesa isochrones and stellar tracks (MIST). I. Solar-scaled models*, *The Astrophysical Journal*, vol. 823, 2: 102 (2016) [29](#), [153](#)

- Cohen, E. & Taylor, B., *The 1986 CODATA recommended values of the fundamental physical constants*, Journal of Research, vol. 92: 85 (1987a) [5](#), [13](#)
- Cohen, E. & Taylor, B., *Physics Today* (1995) [5](#), [13](#)
- Cohen, E. R. & Taylor, B. N., *The 1986 adjustment of the fundamental physical constants*, Rev. Mod. Phys., vol. 59: 1121 (1987b) [5](#), [13](#)
- Commercon, B., Teyssier, R., Audit, E., Hennebelle, P. & Chabrier, G., *Radiation hydrodynamics with adaptive mesh refinement and application to prestellar core collapse-I. Methods*, Astronomy & Astrophysics, vol. 529: A35 (2011) [62](#)
- Cox, J. P. & Giuli, R. T., *Principles of Stellar Structure*, New York (1968) [xiv](#), [24](#), [29](#), [152](#), [178](#)
- Daly, B. J. & Harlow, F. H., *Transport equations in turbulence*, The Physics of Fluids, vol. 13, 11: 2634 (1970) [82](#)
- de Charentenay, J., Thévenin, D. & Zamuner, B., *DNS of Turbulent H<sub>2</sub>/O<sub>2</sub> Premixed Flames Using Compressible and Low-Mach Number Formulations*, Direct and Large-Eddy Simulation IV, p. 129–136, Springer (2001) [38](#)
- Denissenkov, P. A., *Numerical simulations of thermohaline convection: implications for extra-mixing in low-mass RGB stars*, The Astrophysical Journal, vol. 723, 1: 563 (2010) [27](#)
- Dotter, A., *MESA Isochrones and Stellar Tracks (MIST) 0: Methods for the construction of stellar isochrones*, The Astrophysical Journal Supplement Series, vol. 222, 1: 8 (2016) [29](#), [153](#)
- Durrán, D. R., *Improving the anelastic approximation*, Journal of the atmospheric sciences, vol. 46, 11: 1453 (1989) [xiv](#), [38](#)
- Eddington, A., *On the radiative equilibrium of the stars*, Monthly Notices of the Royal Astronomical Society, vol. 77: 16 (1916) [16](#)
- Eggleton, P. P., Dearborn, D. S. & Lattanzio, J. C., *Deep mixing of 3He: reconciling Big Bang and stellar nucleosynthesis*, Science, vol. 314, 5805: 1580 (2006) [31](#), [153](#)
- Einfeldt, B., *On Godunov-type methods for gas dynamics*, SIAM Journal on Numerical Analysis, vol. 25, 2: 294 (1988) [196](#)
- Feireisl, E. & Novotný, A., *Small Péclet number approximation as a singular limit of the full Navier-Stokes-Fourier system with radiation*, New Directions in Mathematical Fluid Mechanics, p. 123–152, Springer (2009) [xv](#), [38](#), [55](#)
- Garaud, P., *Double-diffusive convection at low Prandtl number*, Annual Review of Fluid Mechanics, vol. 50: 275 (2018) [27](#), [28](#), [38](#), [58](#), [98](#), [107](#), [109](#), [132](#), [133](#), [134](#), [136](#), [138](#), [143](#), [160](#), [169](#), [172](#)
- Gauthier, S. & Bonnet, M., *A k- $\epsilon$  model for turbulent mixing in shock-tube flows induced by Rayleigh-Taylor instability*, Physics of Fluids A: Fluid Dynamics, vol. 2, 9: 1685 (1990) [83](#)
- Giovangigli, V., *Multicomponent flow modeling*, Science China Mathematics, vol. 55, 2: 285 (2012) [39](#), [41](#), [156](#), [190](#)

## Bibliography

---

- Gough, D., *The anelastic approximation for thermal convection*, Journal of the atmospheric sciences, vol. 26, 3: 448 (1969) [xiv](#), [38](#), [55](#), [56](#)
- Griffond, J. & Souldard, O., *Evaluation of augmented RSM for interaction of homogeneous turbulent mixture with shock and rarefaction waves*, Journal of Turbulence, vol. 15, 9: 569 (2014) [39](#), [165](#)
- Griffond, J., Souldard, O. & Souffland, D., *A turbulent mixing Reynolds stress model fitted to match linear interaction analysis predictions*, Physica Scripta, vol. 2010, T142: 014059 (2010) [81](#), [82](#)
- Grégoire, O., Souffland, D. & Gauthier, S., *A second-order turbulence model for gaseous mixtures induced by Richtmyer—Meshkov instability*, Journal of Turbulence, vol. 6, 6: N29 (2005) [28](#), [80](#), [81](#), [82](#), [151](#), [152](#), [165](#)
- Harten, A., Lax, P. D. & Leer, B. v., *On upstream differencing and Godunov-type schemes for hyperbolic conservation laws*, SIAM review, vol. 25, 1: 35 (1983) [193](#)
- Heiter, U., Kupka, F., Barban, C., Weiss, W., Goupil, M.-J., Schmidt, W., Katz, D. & Garrido, R., *New grids of ATLAS9 atmospheres I: Influence of convection treatments on model structure and on observable quantities*, Astronomy & Astrophysics, vol. 392, 2: 619 (2002) [26](#), [80](#)
- Henyey, L., Vardya, M. & Bodenheimer, P., *Studies in Stellar Evolution. III. The Calculation of Model Envelopes.*, The Astrophysical Journal, vol. 142: 841 (1965) [29](#), [152](#)
- Joyce, M. & Chaboyer, B., *Not all stars are the sun: empirical calibration of the mixing length for metal-poor stars using one-dimensional stellar evolution models*, The Astrophysical Journal, vol. 856, 1: 10 (2018) [25](#)
- Kato, S., *Overstable convection in a medium stratified in mean molecular weight*, Publications of the Astronomical Society of Japan, vol. 18: 374 (1966) [21](#), [23](#), [153](#)
- Kim, K. H. & Kim, C., *Accurate, efficient and monotonic numerical methods for multi-dimensional compressible flows: Part II: Multi-dimensional limiting process*, Journal of computational physics, vol. 208, 2: 570 (2005) [62](#)
- Kippenhahn, R., *A, Weigert*, Stellar Structure and Evolution [26](#), [80](#)
- Kippenhahn, R., Ruschenplatt, G. & Thomas, H.-C., *The time scale of thermohaline mixing in stars*, Astronomy and Astrophysics, vol. 91: 175 (1980) [27](#)
- Kuznetsov, V. & Sabelnikov, V., *Turbulence and combustion*, Hemisphere, New York [80](#)
- Landau, L. & Lifshitz, E., *Statistical Physics* (1958) [21](#)
- Lane, J. H., *Charles Grafton Page*, American Journal of Science, vol. 48: 1 (1869) [16](#)
- Launder, B. E., Reece, G. J. & Rodi, W., *Progress in the development of a Reynolds-stress turbulence closure*, Journal of fluid mechanics, vol. 68, 3: 537 (1975) [80](#), [83](#)
- Ledoux, P., *Stellar stability*, Astrophysics II: Stellar Structure / Astrophysik II: Sternaufbau, p. 605–688, Springer (1958) [21](#)

- Lignieres, F., *The small-Peclet-number approximation in stellar radiative zones*, *Astronomy & Astrophysics*, vol. 348: 933 (1999) [xv](#), [26](#), [38](#), [52](#), [55](#), [56](#), [151](#)
- Livescu, D., *Turbulence with large thermal and compositional density variations*, *Annual Review of Fluid Mechanics*, vol. 52: 309 (2020) [80](#)
- Maeder, A., *Physics, Formation and Evolution of Rotating Stars* (Springer, Berlin Heidelberg) (2009) [16](#), [17](#)
- Maity, P. & Kumar, K., *Zero-Prandtl-number convection with slow rotation*, *Physics of Fluids*, vol. 26, 10: 104103 (2014) [38](#)
- Meakin, C. A. & Arnett, D., *Turbulent convection in stellar interiors. I. Hydrodynamic simulation*, *The Astrophysical Journal*, vol. 667, 1: 448 (2007) [80](#)
- Mihalas, D. & Mihalas, B. W., *Foundations of radiation hydrodynamics*, Courier Corporation (2013) [19](#), [39](#), [43](#), [63](#), [155](#), [156](#), [161](#), [178](#), [182](#)
- Nishikawa, H. & Kitamura, K., *Very simple, carbuncle-free, boundary-layer-resolving, rotated-hybrid Riemann solvers*, *Journal of Computational Physics*, vol. 227, 4: 2560 (2008) [196](#)
- Novotny, A., Ruzicka, M. & Thater, G., *Rigorous derivation of the anelastic approximation to the Oberbeck–Boussinesq equations*, *Asymptotic Analysis*, vol. 75, 1-2: 93 (2011) [xv](#), [38](#), [55](#), [56](#), [151](#)
- Paxton, B., Bildsten, L., Dotter, A., Herwig, F., Lesaffre, P. & Timmes, F., *Modules for experiments in stellar astrophysics (MESA)*, *The Astrophysical Journal Supplement Series*, vol. 192, 1: 3 (2010) [29](#), [152](#)
- Paxton, B., Cantiello, M., Arras, P., Bildsten, L., Brown, E. F., Dotter, A., Mankovich, C., Montgomery, M., Stello, D., Timmes, F. *et al.*, *Modules for experiments in stellar astrophysics (MESA): planets, oscillations, rotation, and massive stars*, *The Astrophysical Journal Supplement Series*, vol. 208, 1: 4 (2013) [xiv](#), [29](#), [150](#)
- Paxton, B., Marchant, P., Schwab, J., Bauer, E. B., Bildsten, L., Cantiello, M., Dessart, L., Farmer, R., Hu, H., Langer, N. *et al.*, *Modules for experiments in stellar astrophysics (MESA): binaries, pulsations, and explosions*, *The Astrophysical Journal Supplement Series*, vol. 220, 1: 15 (2015) [29](#)
- Paxton, B., Schwab, J., Bauer, E. B., Bildsten, L., Blinnikov, S., Duffell, P., Farmer, R., Goldberg, J. A., Marchant, P., Sorokina, E. *et al.*, *Modules for Experiments in Stellar Astrophysics (MESA): Convective Boundaries, Element Diffusion, and Massive Star Explosions*, *The Astrophysical Journal Supplement Series*, vol. 234, 2: 34 (2018) [29](#), [196](#)
- Paxton, B., Smolec, R., Schwab, J., Gautschy, A., Bildsten, L., Cantiello, M., Dotter, A., Farmer, R., Goldberg, J. A., Jermyn, A. S. *et al.*, *Modules for experiments in stellar astrophysics (MESA): Pulsating variable stars, rotation, convective boundaries, and energy conservation*, *The Astrophysical Journal Supplement Series*, vol. 243, 1: 10 (2019) [xiv](#), [29](#), [150](#)
- Pomraning, G. C., *The equations of radiation hydrodynamics*, Courier Corporation (2005) [197](#), [198](#)

## Bibliography

---

- Pope, S., *On the relationship between stochastic Lagrangian models of turbulence and second-moment closures*, *Physics of Fluids*, vol. 6, 2: 973 (1994) [83](#)
- Pope, S., *Modeling Mixing and Reaction in Turbulence Combustion*, Rap. tech., CORNELL UNIV ITHACA NY DEPT OF MECHANICAL AND AEROSPACE ENGINEERING (2000) [86](#), [199](#)
- Pope, S. B., *PDF methods for turbulent reactive flows*, *Progress in energy and combustion science*, vol. 11, 2: 119 (1985) [80](#), [86](#)
- Prandtl, L., *Bericht uber Untersuchungen zur ausgebildeten Turbulenz*, *Zs. angew. Math. Mech.*, vol. 5: 136 (1925) [xiv](#), [xv](#), [24](#), [145](#), [146](#), [147](#), [150](#), [152](#), [174](#), [175](#)
- Prat, V., *Transport turbulent d'éléments chimiques dans les zones radiatives stellaires*, Thèse de doctorat, Université de Toulouse, Université Toulouse III-Paul Sabatier (2013) [26](#), [38](#), [80](#)
- Prialnik, D., *An introduction to the theory of stellar structure and evolution*, Cambridge University Press (2000) [xiii](#), [16](#), [17](#), [18](#), [19](#), [30](#), [149](#)
- Rotta, J., *Statistische theorie nichthomogener turbulenz*, *Zeitschrift für Physik*, vol. 129, 6: 547 (1951) [83](#)
- Sagaut, P. & Cambon, C., *Incompressible Homogeneous Anisotropic Turbulence: Buoyancy Force and Mean Stratification*, *Homogeneous Turbulence Dynamics*, p. 485–533, Springer (2018) [80](#)
- Salaris, M. & Cassisi, S., *Chemical element transport in stellar evolution models*, *Royal Society open science*, vol. 4, 8: 170192 (2017) [23](#), [24](#), [28](#), [152](#)
- Sanz, J., Masse, L. & Clavin, P., *The linear Darrieus-Landau and Rayleigh-Taylor instabilities in inertial confinement fusion revisited*, *Physics of plasmas*, vol. 13, 10: 102702 (2006) [38](#)
- Schiestel, R., *Modeling and simulation of turbulent flows*, vol. 4, John Wiley and Sons (2010) [28](#), [45](#), [64](#), [80](#), [152](#), [162](#), [183](#)
- Schmitt, R. W., *Double diffusion in oceanography*, *Annual Review of Fluid Mechanics*, vol. 26, 1: 255 (1994) [38](#), [58](#)
- Schwarzschild, K., *On the equilibrium of the Sun's atmosphere*, *WisGo*, vol. 195: 41 (1906) [16](#)
- Shanmuganathan, S., Youngs, D., Griffond, J., Thornber, B. & Williams, R., *Accuracy of high-order density-based compressible methods in low Mach vortical flows*, *International Journal for Numerical Methods in Fluids*, vol. 74, 5: 335 (2014) [61](#)
- Shimomura, Y., *Turbulent transport modeling in low Mach number flows*, *Physics of Fluids*, vol. 11, 10: 3136 (1999) [80](#)
- Shirgaonkar, A. A. & Lele, S. K., *On the extension of the Boussinesq approximation for inertia dominated flows*, *Physics of Fluids*, vol. 18, 6: 066601 (2006) [xiv](#), [38](#)
- So, R., Zhao, C. & Gatski, T., *Predicting buoyant shear flows using anisotropic dissipation rate models*, *Flow, turbulence and combustion*, vol. 63, 1-4: 193 (2000) [80](#)

- Soulard, O., Griffond, J. & Souffland, D., *Pseudocompressible approximation and statistical turbulence modeling: Application to shock tube flows*, Physical Review E, vol. 85, 2: 026307 (2012) [xiv](#), [xvi](#), [2](#), [51](#), [55](#), [56](#), [69](#), [73](#), [76](#), [80](#), [83](#), [112](#), [150](#), [159](#), [163](#), [165](#), [169](#)
- Spiegel, E., *Semiconvection*, Comments on Astrophysics and Space Physics, vol. 1: 57 (1969) [xiii](#), [149](#)
- Spiegel, E. A., *Thermal turbulence at very small Prandtl number*, Journal of Geophysical Research, vol. 67, 8: 3063 (1962) [xv](#), [38](#), [52](#), [151](#)
- Spiegel, E. A. & Veronis, G., *On the Boussinesq approximation for a compressible fluid.*, The Astrophysical Journal, vol. 131: 442 (1960) [xiv](#), [xv](#), [98](#)
- Stevenson, D. J., *Formation of the giant planets*, Planetary and Space Science, vol. 30, 8: 755 (1982) [xiii](#), [149](#)
- Tassoul, M., Fontaine, G. & Winget, D., *Evolutionary models for pulsation studies of white dwarfs*, The Astrophysical Journal Supplement Series, vol. 72: 335 (1990) [26](#)
- Thornber, B., Griffond, J., Poujade, O., Attal, N., Varshochi, H., Bigdelou, P., Ramaprabhu, P., Olson, B., Greenough, J., Zhou, Y. *et al.*, *Late-time growth rate, mixing, and anisotropy in the multimode narrowband Richtmyer–Meshkov instability: The  $\theta$ -group collaboration*, Physics of Fluids, vol. 29, 10: 105107 (2017) [61](#)
- Toro, E. F., *Riemann solvers and numerical methods for fluid dynamics : a practical introduction*, Springer Science & Business Media (2013) [192](#), [193](#), [196](#)
- Traxler, A., Garaud, P. & Stellmach, S., *Numerically determined transport laws for fingering (“thermohaline”) convection in astrophysics*, The Astrophysical Journal Letters, vol. 728, 2: L29 (2011) [26](#)
- Ulrich, R. K., *Thermohaline Convection in Stellar Interiors.*, The Astrophysical Journal, vol. 172: 165 (1972) [26](#), [27](#), [29](#), [31](#), [152](#), [153](#)
- Viallet, M., Meakin, C., Prat, V. & Arnett, D., *Toward a consistent use of overshooting parametrizations in 1D stellar evolution codes*, Astronomy & Astrophysics, vol. 580: A61 (2015) [80](#)
- Wachlin, F. C., Vauclair, S. & Althaus, L. G., *Fingering convection in red giants revisited*, Astronomy & Astrophysics, vol. 570: A58 (2014) [26](#)
- Weiss, A. & Charbonnel, C., *Mixing along the Red Giant Branch*, Memorie della Societa Astronomica Italiana, vol. 75: 347 (2004) [26](#), [80](#)
- Zahn, J.-P., *Convective penetration in stellar interiors*, Astronomy and Astrophysics, vol. 252: 179 (1991) [80](#)
- Zhang, W., Howell, L., Almgren, A., Burrows, A. & Bell, J., *CASTRO: A new compressible astrophysical solver. II. Gray radiation hydrodynamics*, The Astrophysical Journal Supplement Series, vol. 196, 2: 20 (2011) [61](#)
- Zhou, Y., *Rayleigh–Taylor and Richtmyer–Meshkov instability induced flow, turbulence, and mixing. II*, Physics Reports, vol. 723: 1 (2017) [81](#)